17th
INTERNATIONAL CONGRESS
of the Geological Society of Greece

BULLETIN OF THE GEOLOGICAL
SOCIETY OF GREECE, SP. PUBL.

EXTENDED ABSTRACT 151

Utilizing engineering geological database for urban geohazard assessment: a case study from Thessaloniki, Greece

Kokkala A.[1], Marinos V.[2], Papathanassiou G.[1]
(1) School of Geology, Aristotle University of Thessaloniki, Thessaloniki, Greece, kokkalaaliki@gmail.com
(2) School of Civil Engineering, National Technical University of Athens, Athens, Greece

Introduction

This research presents an advanced engineering geological database, designed to comprehensively manage extensive geological and geotechnical data (Kokkala, 2023). Based on the Tunnel Information and Analysis System (TIAS) framework (AGS, 1999; Marinos et al., 2013), the database integrates information from numerous boreholes and geotechnical investigations conducted in Thessaloniki's urban area, northern Greece, focusing on Quaternary and Neogene sediments, as well as fill deposits. Its primary aim is to reduce geological uncertainties and address geotechnical challenges critical for urban safety and planning, by means of numerous database applications (Kokkala and Marinos, 2022). Emphasizing the utility of big data management, the study explores how geological heterogeneity, subsurface variations, and engineering geological conditions can be better understood to mitigate geohazards (e.g. liquefaction as the application example used here) and support early-stage infrastructure design.

Methods

In this study, Standard Penetration Test (SPT) and Cone Penetration Test (CPT) results were analyzed to investigate liquefaction susceptibility and potential in an area located at the vicinity of Thessaloniki airport (Figure 1), as a database application for urban geohazard assessment. Based on the outcome arisen by the geotechnical investigation, it was concluded that the subsoil profile predominantly consists of sandy clays and silts, interspersed with medium-density sand layers. Two distinct sub-areas (A and B), differentiated based on their proximity to the stream located to the south, were analyzed to evaluate in situ conditions and liquefaction susceptibility.

A series of cross-sections, such as the example shown in Figure 2, was developed to illustrate the distribution of the Soil Behavior Type Index-SBTn (Ic) based on the liquefaction susceptibility criterion proposed by Robertson and Wride (1998). Further analysis involved the assessment of the liquefaction potential index (LPI) alongside estimations of vertical and lateral displacements for each sub-area, utilizing the available CPT data. For this purpose, two distinct seismic scenarios were considered: the first one involves the activation of the Anthemoundas fault, resulting in a seismic event with a magnitude of M 6.9 and peak ground acceleration of 0.4 g, while the second scenario refers to the activation of the Gerakarou fault, generating a seismic event with a magnitude of M 7.0 and peak ground acceleration of 0.5 g (Lin and Smerzini, 2022).

Results

The analysis revealed stratigraphic differences between the sub-areas. Sub-area A exhibited a higher concentration of coarse-grained materials in places, whereas sub-area B was dominated by fine-grained deposits, reflecting variations in the depositional environment. In most soil columns, LPI values exceeding 5% were observed throughout the study area under the first seismic scenario, indicating a high to very high liquefaction potential. Additionally, vertical displacements ranged from 16 to 19 cm and lateral displacements reached up to 220 cm were estimated under both seismic scenarios for the two sub-areas.

Conclusions

This study highlights the essential role of integrating primary geological and geotechnical data into a well-structured database for detailed geohazard analysis. The proposed methodology showcases the utility of an engineering geological database in evaluating and mitigating liquefaction, providing critical insights for enhancing urban safety and optimizing infrastructure design.

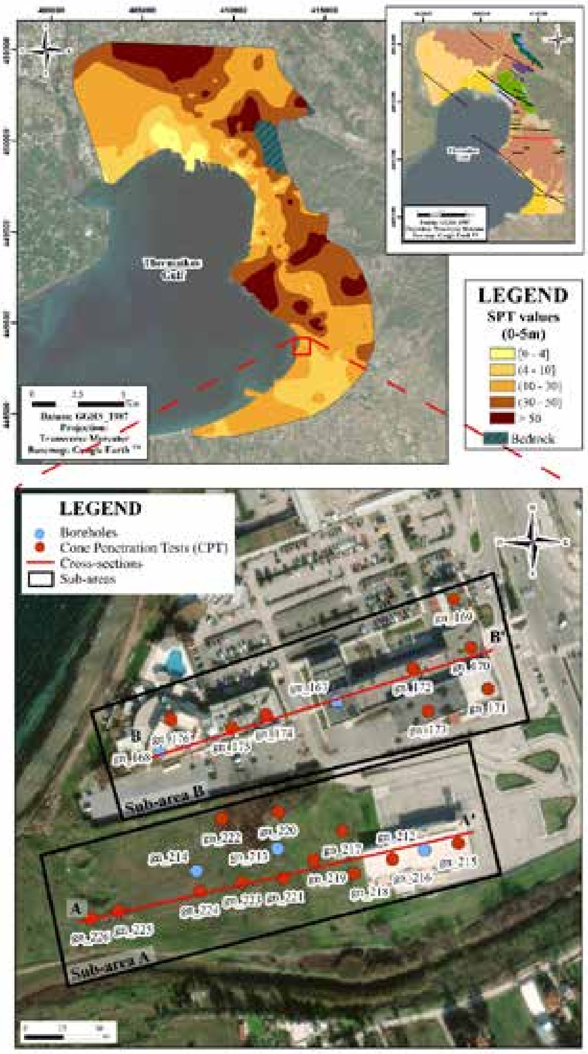

Figure 1. Spatial distribution map of SPT for depth 0-5 m accompained by the updated engineering geological map of Thessaloniki city (for detailed engineering geological map refer to Kokkala and Marinos, 2022, from Rozos *et al.*, 1998), illustrating the studied area used as an engineering geological database application (Kokkala, 2023).

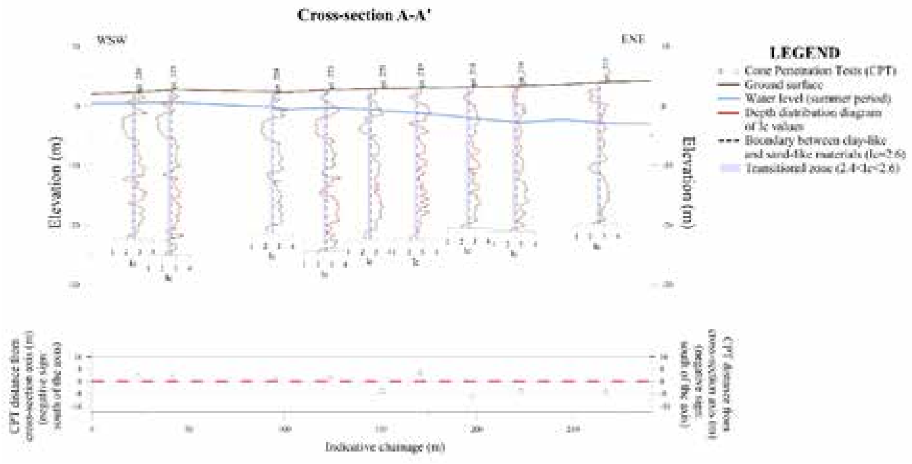

Figure 2. Cross-section A-A’ (see Figure 1), presenting the graphical distribution of Ic values (Kokkala, 2023).

Acknowledgements

The research was funded by the Hellenic Foundation for Research and Innovation (HFRI) through the HFRI PhD Fellowship grant (Fellowship Number: 99319). The authors extend their gratitude to the Central Laboratory of Public Works, Geognosi S.A., Attiko Metro S.A., Egnatia Odos S.A., and the National Cadastre and Mapping Agency S.A. for generously providing the data used in this study.

References

Association of Geotechnical and Geoenvironmental Specialists (AGS), 1999. Electronic Transfer of Geotechnical and Geoenvironmental Data, 3rd ed.

Kokkala, A., 2023. Engineering geological assessment and classification of Thessaloniki’s urban area formations using a geotechnical database. Research on the technical behavior and applications in the design of engineering projects. Ph.D. Thesis, Aristotle University of Thessaloniki, Thessaloniki, 570 p.

Kokkala, A., Marinos, V., 2022. An engineering geological database for managing, planning and protecting intelligent cities: The case of Thessaloniki city in Northern Greece. Engineering Geology 301, 106617, https://doi.org/10.1016/j.enggeo.2022.106617

Lin, J., Smerzini. C., 2022. Variability of physics-based simulated ground motions in Thessaloniki urban area and its implications for seismic risk assessment. Frontiers in Earth Science, 10: 951781. https://doi.org/10.3389/feart.2022.951781

Marinos, V., Prountzopoulos, G., Fortsakis, P., Koumoutsakos, D., Korkaris, K., Papouli, D., 2013. Tunnel information and analysis system: a geotechnical database for tunnels. Geotechnical and Geological Engineering 31, 891–910, https://doi.org/10.1007/s10706-012-9570-x

Robertson, P.K., Wride, C.E., 1998. Evaluating cyclic liquefaction potential using the cone penetration test. Canadian Geotechnical Journal, 35 (3): 442–459

Rozos, D., Apostolidis, E., Hadzinakos, I., 1998. Engineering-Geological Map of the Wider Thessaloniki Area, 1:25,000 Scale. I.G.M.E, Athens

17th INTERNATIONAL CONGRESS
of the Geological Society of Greece

BULLETIN OF THE GEOLOGICAL SOCIETY OF GREECE, SP. PUBL.

EXTENDED ABSTRACT 152

Diapiric structures in evaporites of Western Greece as potential geoenergy storage areas

Kokkalas S.[1], Psarros V.[1], Koutsovitis P.[1]
(1) Department of Geology, University of Patras, Greece, skokalas@upatras.gr

Introduction-Research background

The capture and storage of CO_2 is an important process as it helps to prevent the negative impacts of CO_2 emissions in the atmosphere, such as the greenhouse effect and ocean acidification among others. On the other hand, the storage of H_2 is an environment-friendly process, as it allows for large-scale controlled and flexible energy conversion. Storage of both hydrogen and carbon dioxide in salt caverns has emerged recently as a favorable option due to its numerous benefits, such as the high withdrawal capacity, favorable mechanical properties, and enhanced safety (Tackie-Otoo & Haq, 2024). Despite the increasing demand in geo-energy storage, there is limited relevant literature, mainly on underground geoenergy storage in geological structures in Greece (Arvanitis et al., 2020; Makri et al., 2022). Triassic evaporites diapirism, which involves the buoyant uprise of large evaporite masses through piercing and displacing, are either reaching the surface or halting at a depth, as is evidenced in several seismic profiles. They mainly occur in Western Greece along the Ionian zone, such as in the areas of Aitolo-Akarnania, Hepirus, the Ionian islands, as well as in the Western Peloponnese (Underhill, 1988; Kamberis et al., 2022; Soto et al., 2024). Salt caverns provide significantly higher storage volumes compared to traditional fuel tanks, making them ideal for large-scale energy storage (Fig. 1). The geological suitability for geo-energy storage in salt caverns is determined by certain fundamental geological criteria such as: i) the depth of the storage cavities, ii) the minimum thickness of the salt formation, (iii) the mineralogical composition of the salt formations and (iv) the petrophysical properties of the host rock (i.e., low porosity and permeability, pore structure etc.), in order to ensure that the supercritical gas remains in the cavity and to prevent the potential risk of leakage.

The above criteria for geological suitability for subsurface storage were examined and evaluated in some representative areas in Western Greece, where evaporitic rock samples were collected and analyzed, by applying several laboratory techniques, upon samples from the areas of Katouna (Aitolo-Akarnania), Pagos (Corfu), and various sites in the proximity to Preveza (Kanalaki-Aidonia-Chimadio). Based on the interpretation of these preliminary results, and the percentage of coverage of the required geological criteria for underground energy storage, the prospects of underground storage in artificial cavities in evaporite rock formations are discussed and the adverse factors that require further study in the future research stages are presented.

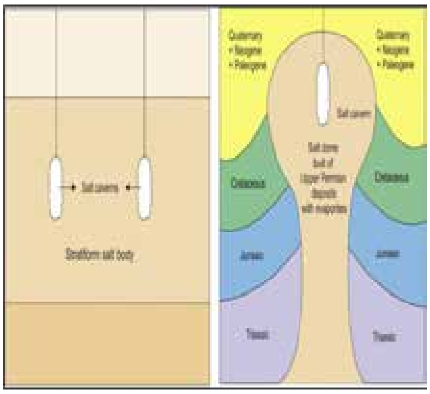

Figure 1. Salt cavern in a salt diapiric structure (Tarkowski and Czapowski 2018).

CO_2 and H_2, as representative gases for underground gas storage, exhibit significant differences in physical properties, particularly in density and viscosity. Storage of CO_2 in salt caverns is a promising solution, since it not only provides permanent storage but can also operate as a renewable and sustainable method for utilizing CO_2 as a valuable industrial resource.

For the underground storage of geoenergy, salt caverns are currently considered to offer the most promising option owing to their low investment cost, high sealing capacity, the inert nature of salt structures, and the low cushion gas requirement (Fig. 1; Caglayan et al., 2020). Rock salt properties such as permeability, porosity, and pore pressure, are crucial parameters to consider for hydrogen storage and to evaluate potential migration (AbuAisha and Billiotte, 2021).

Several sites for hydrogen storage in salt caverns in UK (Teeside), USA (Clemens Dome, Moss Bluff) operate for nearly 50 years, at depths below 1 km, demonstrating that underground storage is a technically-feasible option (Landinger and Crotogino, 2007; Tarkowski, 2019). For the Greek region a total cavern storage potential mainly onshore (within 50 km from the shore) is estimated around 10^2 TWh (Caglayan et al., 2020).

Geological setting

Although the Ionian Zone has been extensively studied, having attracted the interest for hydrocarbon exploration in Greece (Zelilidis et al., 2015), there is still much ambiguity in the deeper structures of the crust of the External Hellenides. Western Greece is considered as a region with mainly thin, or possibly coexistence of thin and thick-skinned deformation of the Mesozoic-Cenozoic succession above the Triassic evaporites and Permian sequences (Kokkalas et al., 2013). The Ionian Zone consists of sedimentary rocks ranging from Triassic evaporites at the base, to Jurassic–upper Eocene carbonates with minor cherts and shales (Karakitsios, 1995; Rigakis et al., 2007; Karakitsios et al., 2015; Bourli et al., 2019; Kamberis et al., 2022). Thick Upper Eocene to Miocene flysch deposits overlie the carbonate sequence (Avramidis et al., 2002; Vakalas et al., 2024). The Ionian Zone boundary towards the west is marked by intrusive evaporites that represent the lowest detachment level of individual overthrust sheets in the External Hellenides.

The Ionian Zone consists of three distinct stratigraphic sequences (Karakitsios, 2013): a) a pre-rift sequence (Triassic – Early Jurassic) represented by a thick evaporitic succession (with an estimated thickness that exceeds 2 km) overlain by shallow marine carbonates. Regarding the depositional environment, the alternating sulphate and carbonate constituents correspond probably to an arid and shallow depositional setting (Karakitsios, 1995). Evaporites are often related to extensive exposures of dissolution breccia of Triassic age (Triassic breccia); b) a syn-rift sequence (Early to Late Jurassic) where the basin was compartmentalized, and a half-graben geometry was favored, as reflected in variations in sediment type (pelagic carbonates and deep water clastics) and thickness (Karakitsios, 2013). During this stage, the evaporites were mobilized forming several types of diapiric structures; c) A post-rift sequence (Early Cretaceous to Eocene) marking by the deposition of pelagic limestones.

However, new insights into the evolutionary structural model of the Ionian fold-and-thrust belt in central-south Albania and Western Greece have been revealed, based on significant information provided from detailed fieldwork and new seismic data, suggesting an alternative model that places the rifting stage earlier in the Triassic and demonstrating the clear influence of salt tectonics since the Early Jurassic (Hernandez et al., 2019; Vakalas et al., 2023; Soto et al., 2024).

Methods

Fieldwork and preliminary sampling were conducted in five areas along western Greece, specifically on Corfu Island (Pagoi), in several sites of Preveza region (Aidonia, Chimadio and Tsouknida) and along a continuous road outcrop near Katouna area (Table 1). The rock samples were carefully selected to avoid areas of high dissolution and internal fracturing, in order to comply with the requirements for each of the following analytical techniques. For the determination of the mineralogical and quantitative composition of the samples, X-Ray Powder Diffraction analyses (XRD) and Fourier-Transform Infrared Spectrometry (FTIR) were conducted. For the characterization of their petrophysical properties, such as porosity, pore size distribution (PSD), permeability and specific surface area, Brunauer-Emmett-Teller (BET) analysis with nitrogen and Mercury Injection Capillary Pressure (MICP) analysis (Table 2), were carried out in parallel, in the facilities of the Department of Material Sciences and FORTH/ICE-HT (Upatras), respectively. Investigation of the sealing capacity and pore-throat-aperture size distribution in samples was conducted via mercury porosimetry using the latest Micromeritics Autopore III porosimeter, which is capable of injecting non-wetting phase (mercury) in user-defined, step-like pressure increments (0.5 to 2 psi) up to 60,000 psi (~413 MPa) into an evacuated, cleaned, and dried rock sample.

Results

The analyzed evaporite samples can generally be distinguished into those being rich in gypsum and those being rich in anhydrite (Table 1). The samples have a dominance of gypsum in the samples Pg2, KAT, KAT1, KAT2, Aid2, whereas anhydrite is the predominant phase in samples Pg1, Pg3, and Chm1b.

Mercury porosimetry showed porosity values that range from 0.17% to 5.06% (Table 2), with a wide distribution of pore diameters D (Fig. 2). The mean pore-throat diameter values in the samples indicate macroporous materials, with samples Pg2, Chm_1b and Aid2 showing the lowest mean values (0.55-0.57 μm), whereas the highest value is shown in sample KAT1 (1.10 μm). Since these samples were collected from surface outcrops, a reference evaporite sample (Mo1#7) from a borehole in southwest Montenegro at a depth of ~ 3 km, (kindly provided by Energean Montenegro Ltd.) was used for comparison; it showed a mean PSD value of 0.19 μm (Table 2). The permeability exhibits relatively low values, ranging from 0.01549 to 0.46367 mD. For comparison the reference sample Mo1#7 showed a permeability of 0.00587 mD.

Table 1. Results of XRD-analysis in the studied samples.

Samples ID	Location	Mineral content (in %)						
		Gypsum	Anhydrite	Halite	Dolomite	Calcite	Celestite	Quartz
KAT	Katouna	30	4	9	10	17	7	20
KAT 1	Katouna	35	4	13	13	21	6	5
KAT 2	Katouna	36	3	11	9	20	8	9
Aid2	Aidonia (Preveza)	98	-	-	<2	-	-	-
Chm	Chimadio (Preveza)	15	-	-	-	85	-	-
Chm_1b	Chimadio (Preveza)	4	30	<3	<3	34	<3	27
Tsk	Tsouknida (Preveza)	10	-	-	-	90	-	-
Pg 1	Pagoi (Corfu)	4	43	<3	<3	44	<3	7
Pg 2	Pagoi (Corfu)	37	<3	8	10	18	7	18
Pg 3	Pagoi (Corfu)	4	30	<3	<3	30	<3	29

In order to additionally investigate the presence and size of the micro-mesopores BET-analysis was performed, which has a different resolution capability than MICP. The BET-analysis confirmed the wide distribution of pore width ranging from micropores (width 1.6-3 nm), mainly mesopores (width 7-10 nm), and also macropores (width 50-100 nm). A mean pore diameter of approximately 3.8 nm is observed, indicating the presence of micro-mesoporosity in the samples, which would be unfeasible to determine by applying only the mercury porosimetry measurement technique. Furthermore, the specific surface area shows values ranging from 19.9 to 22.7 m^2/g.

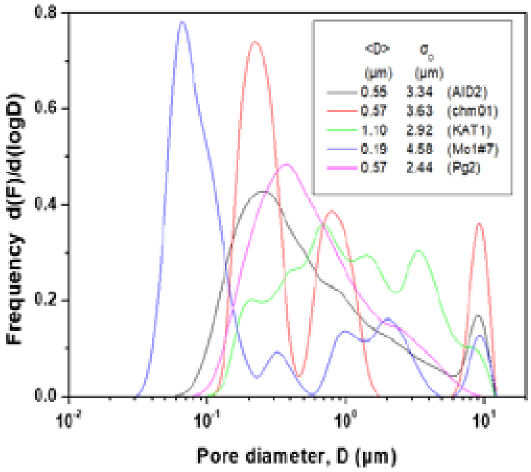

Figure 2. Pore size distribution diagram of the samples from the MICP analysis.

In the BET analyses, it is observed that all samples belong to the type III isotherm adsorption. Type III isothermal adsorption is convex on the P/Po axis throughout the entire adsorption process, and for this reason, there are no inflection points (Fig. 3). From the types of adsorption-desorption isotherm (type III), which are not common, it appears that there is little interaction between the gas and the adsorbing surface. Regarding the type of hysteresis loop, all samples exhibit an H3-type hysteresis loop, which appears only in the mesoporous structure due to capillary condensation, and this is confirmed by the pore size distribution (PSD) assessed through analytical techniques. This indicates that the pores exhibit slit-like shapes and it is considered that materials with such characteristics tend to behave as microporous materials, regardless of the PSD.

Table 2. Results from MICP-analysis in selected samples.

Sample	Pore volume, V_p (cm³/g)	Specific surface area, S_p (m²/g)	Porosity (%)	Mean value of PSD (μm)	Standard deviation of PSD (μm)	Tortuosity τ	$k = \varphi < D_p >^2 / (16\tau)$ (mD)
Aid2	0.0220	0.258	4.74	0.55	3.34	2.217	0.40422
Chm1b	0.0007	0.007	0.17	0.57	3.63	2.229	0.01549
KAT1	0.0028	0.018	0.63	1.10	2.92	2.228	0.21384
Pg2	0.0235	0.222	5.06	0.57	2.44	2.216	0.46367
Mo1#7	0.0020	0.079	0.58	0.19	4.58	2.229	0.00587

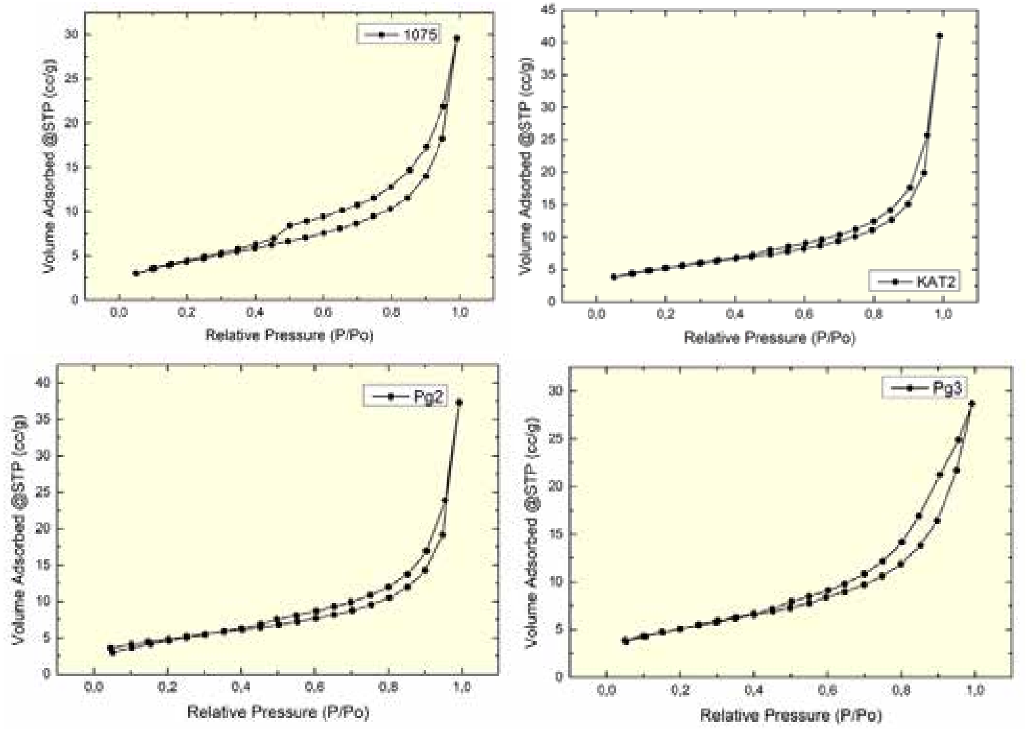

Figure 3. Isotherm absorption curves and hysteresis loops for the examined samples in BET analysis.

Discussion-Conclusions

The porosity of the studied evaporite samples appear to exhibit a complex structure involving micro-, meso-, and macropores, and potentially interconnected pores (microcavities due to dissolution). The range of their pore size (diameter) distribution values was estimated by combining results from both BET and MICP techniques, as there is a different resolution capability between these techniques. In general, the porosity of the samples shows low values ranging from 0.17 to 5% and relatively low permeabilities (0.01-0.46 mD). Since these are preliminary data and the research is still ongoing on this subject, more data will be required from other evaporitic rock sites in western Greece to have a better overview of their petrophysical properties.

The halite (NaCl) at a percentage higher than 95%, the depth of the cavity formation (which ideally should range between a min of 800 m and max of 1300 m for the higher capacity of hydrogen storage), and the ideal thickness of the evaporite formation, in the range of 150-200 m, are some of the most important required factors for the underground geological storage of carbon dioxide and hydrogen in salt cavities to be considered.

Existing data from boreholes and seismic interpretations of salt structures (pillows, plugs and diapirs) in western Greece (Fig. 4, Kamberis et al., 2022; Soto et al., 2024), suggest that in the area of Filiates the presence of thick halite appears at a non-ideal depth of 1700 m and deeper, as anhydrite predominates at shallower depths (from 300-1600 m in Filiates-1 well). In Delvinaki, halite predominates at the desired depth (700-1000 m) with sufficient thickness (approx. 400 m) and minimal presence of dolomite. In Tryfos, (Aitolo-Akarnania) and Parakalamos, although the formation depth is ideal, the lack of halite and the presence mainly of anhydrite-gypsum and dolostone sequence requires further investigation and analyses, mainly due to the slower dissolution of the formation compared to halite and issues of stability and sealing of the walls of the artificially formed cavity. Despite that, the visco-plastic properties of evaporitic rocks may improve their sealing function, since they have the ability for “self-sealing” the potential microfractures under cyclic stress (Lyu et al., 2023). Thus, detailed studies on the mechanical properties of the evaporitic rocks are crucial when selecting a site for underground storage.

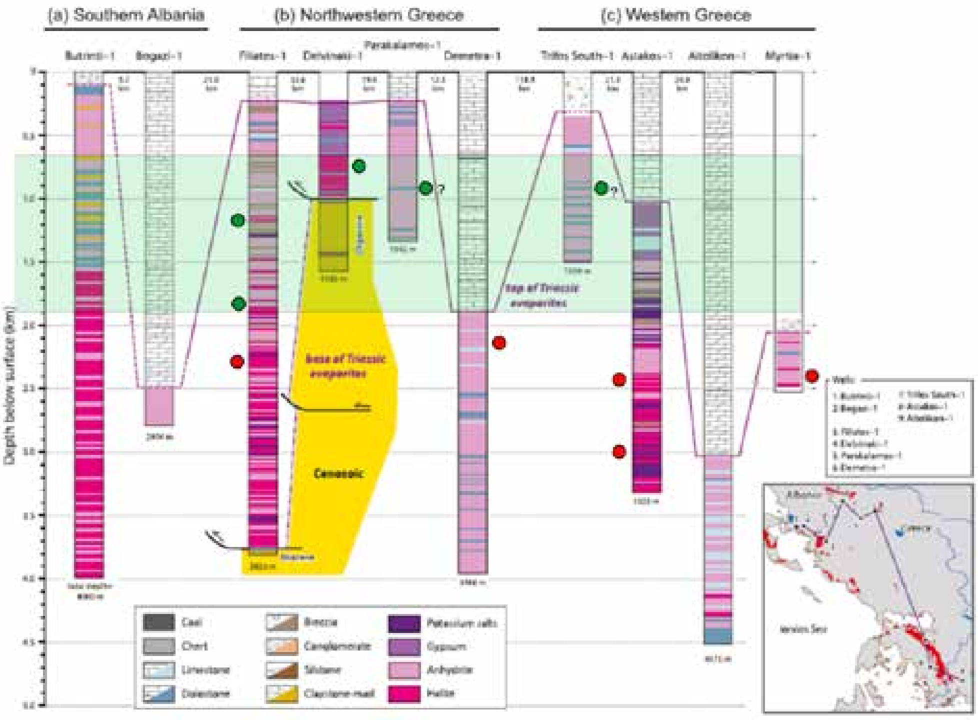

Figure 4. Triassic evaporite sequences with well correlation in north-western and western Greece and inset showing the position of wells and main outcrops of Triassic evaporites in the Ionian zone (from Soto et al., 2024). Original figure is modified showing the ideal depths for subsurface geoenergy storage with green shading, while green/red circles indicate the potential sites with favorable/unfavorable conditions for storage, respectively, based on combined depth/lithology selection criteria.

Although until recently, the construction of artificial cavities in evaporitic formations has been carried out exclusively in areas with a high percentage of halite (>95%), recent studies have shown that salt-rich gypsum rocks can also be characterized as high-quality seals for hydrocarbon reservoirs, due to their strong plasticity, and their excellent petrophysical and mechanical properties (Lyu et al., 2023). However, the effect of cyclic loading on their sealing capacity in a cavity needs further investigation, which limits progress in such storage plans (Lyu et al., 2023). Furthermore, a recent experimental study suggests that the geochemical reactivity of hydrogen with salt cavern minerals (halite-anhydrite-gypsum) is very weak at relatively low temperatures, within short period of time with hydrogen treatment, demonstrating high stability and integrity of salt caverns during short hydrogen storage cycles, with no major alterations in pore structure analysis (Fatah et al., 2024).

Based on these new published data (Fig. 4), and in conjunction with the analytical results of the present study, areas such as Pagoi (Corfu Island) and Katouna (Aitolo-Akarnania region), exhibit promising petrophysical characteristics, which, together with the aforementioned areas of Delvinaki and Filiates (mostly based on the available well data and the seismic profile interpretations; Soto et al., 2024), provide favorable prospects for further research as potential underground storage sites for H_2 and/or CO_2. The areas of Corfu and Trifos (north of Katouna) in Aitolo-Akarnania have been proposed also by Arvanitis et al. (2020), as potential H_2 storage sites, based mainly on their storage capacity (367 km^3), taking as a scenario a capsule-shaped cavern, with dimensions of 300 m height and 60 m in diameter, at a depth of 650 m.

It is also worth to mention that a significant issue in the development of such areas for subsurface storage of hydrogen is the lack of a specific legislation that regulates, based on technical-geological and economic-technical criteria, the entire process related to underground hydrogen storage, from the selection of the site to the injection process, including the monitoring and an action plan after the exploitation of the storage facility.

Acknowledgements

We would like to thank our colleague Ass. Prof. P. Lampropoulou (University of Patras) for her assistance with XRD analysis, Prof. G. Avgouropoulos and Dr. St. Tombros (Department of Material Science, University of Patras) for their help with BET-analysis and Dr. Ch. Tsakiroglou for conducting the MICP-analysis in FORTH/ICE-HT at the University of Patras.

References

AbuAisha, M., Billiotte, J., 2021. A discussion on hydrogen migration in rock salt for tight underground storage with an insight into a laboratory setup. Journal of Energy Storage 38, art. #102589.

Arvanitis, A., Koutsovitis, P., Koukouzas, N., Tyroglou, P., Karapanos, D., Karkalis, C., Pomonis, P., 2020. Potential sites for underground energy and CO_2 storage in Greece: A geological and petrological approach. Energies 13, art. #2707.

Avramidis, P., Zelilidis, A., Vakalas, I., Kontopoulos, N., 2002. Interactions between tectonic activity and eustatic sea-level changes in the Pindos and Mesohellenic Basins, NW Greece: Basin evolution and hydrocarbon potential. Journal of Petroleum Geology 25(1), 53–82.

Bourli, N., Pantopoulos, G., Maravelis, A. G., Zoumpoulis, E., Iliopoulos, G., Pomoni-Papaioannou, F., et al., 2019. Late Cretaceous to early Eocene geological history of the eastern Ionian Basin, southwestern Greece: A sedimentological approach. Cretaceous Research 98, 47–71.

Caglayan, D.G., Weber N., Heinrichs, H., Linßen, J., Robinious, M., Kukla, P.A., Stolten D., 2020. Technical Potential of Salt Caverns for Hydrogen Storage in Europe. International Journal of Hydrogen Energy 45, 6793-6805.

Fatah, A., Al-Yaseri, A., Theravalappil, R., Radwan, O., Amao, A., Al-Qasim, A., 2024. Geochemical reactions and pore structure analysis of anhydrite/gypsum/halite bearing reservoirs relevant to subsurface hydrogen storage in salt caverns. Fuel 371, Part A. art. #131857,

Hernández, P., Pérez Martín, R., Pita, J.P., Ponte, A., Rubio, B., Malmcrona, Y., Chambers, A., Martin, A., Cascone, L., Konstantopoulos, T., et al., 2019. New structural and petroleum system models of the Ionian Zone, North-Western Greece. In 15th International Congress of the Geological Society of Greece, Athens, Greece, p. 527–528.

Kamberis, E., Kokinou, E., Koci, F., Lioni, K., Alves, T.M., Velaj, T., 2022. Triassic evaporites and the structural architecture of the External Hellenides and Albanides (SE Europe): Controls on the petroleum and geoenergy systems of Greece and Albania. International Journal of Earth Sciences 111(3), 789–821.

Karakitsios, V., 1995. The influence of preexisting structure and halokinesis on organic matter preservation and thrust system evolution in the Ionian Basin, Northwest Greece. AAPG Bulletin 79(7), 960–980.

Karakitsios, V., 2013. Western Greece and Ionian Sea petroleum systems. AAPG Bulletin 97(9), 1567–1595.

Kokkalas, S., Kamberis, E., Xypolias, P., Sotiropoulos, S., Koukouvelas, I., 2013. Coexistence of thin- and thick-skinned tectonics in Zakynthos area (western Greece): Insights from seismic sections and regional seismicity. Tectonophysics 597–598, 73–84.

Landinger, H., Crotogino, F., 2007. The role of large-scale hydrogen storage for future renewable energy utilisation. In Second international renewable energy storage conference (IRES II), 19-21.

Lyu, X., Yun, L., Xu, J., Liu, H., Yu, X., Peng, P., Ouyang, M., Luo, Y., 2023. Sealing capacity evolution of gypsum salt caprocks under multi-cycle alternating stress during operations of underground gas storage. Journal of Petroleum Science and Engineering 220, art. #111244.

Makri, V.I., Bellas, S., Gaganis, V., 2021. Assessing Natural Gas Versus CO_2 Potential Underground Storage Sites in Greece: A Pragmatic Approach. Materials Proceedings 5(1), 98.

Rigakis, N., Nikolaou, K., Marnelis, F., Pakos, T., 2007. The utility of oil shows in the hydrocarbon exploration of western Greece. Bulletin of the Geological Society of Greece 40(2), 959–971.

Soto, J. I., Tranos, M. D., Bega, Z., Dooley, T. P., Hernández, P., Hudec, M. R., et al. 2024. Contrasting styles of salt-tectonic processes in the Ionian Zone (Greece and Albania): Integrating surface geology, subsurface data, and experimental models. Tectonics, 43, e2023TC008104, https://doi.org/10.1029/2023TC008104.

Tackie-Otoo, B.N., Haq, M.B., 2024. A comprehensive review on geo-storage of H_2 in salt caverns: Prospect and research advances. Fuel 356, p. 129609.

Tarkowski R. 2019. Underground hydrogen storage: characteristics and prospects. Renew Sustain Energy Rev. 105, 86-94.

Tarkowski, R., Czapowski, G., 2018. Salt domes in Poland-Potential sites for hydrogen storage in caverns. International Journal of Hydrogen Energy, 43, 21414-21427.

Vakalas, I., Kokkalas, S., Konstantopoulos, P., Tzimeas, C., Kampolis, I., Tsiglifi, H., et al., 2023. Implications of salt diapirism in syn-depositional architecture of a carbonate margin-to-edge transition: An example from Plataria syncline, Ionian Zone, NW Greece. Applied Sciences 13(2), 7043.

Zelilidis, A., Maravelis, A.G., Tserolas, P., Konstantopoulos, P.A., 2015. An overview of the petroleum systems in the Ionian Zone, onshore NW Greece and Albania. Journal of Petroleum Geology 38(3), 331–348.

17th INTERNATIONAL CONGRESS
of the Geological Society of Greece

BULLETIN OF THE GEOLOGICAL SOCIETY OF GREECE, SP. PUBL.

EXTENDED ABSTRACT 153

The Argo-Beachrock Project: web mapping and geovisualisation of beachrocks using UAS along the coast of the Argolic Gulf, Greece

Kolaiti E.[1], Soulakellis N.[2], Tataris G.[2], Mourtzas N.[3]

(1) Society for the Study of Ancient Coastlines - AKTES NPO; National Hellenic Research Foundation, Institute of Historical Research; University of Nottingham, Department of Classics and Archaeology; Chalandri, Athens, Greece, kolaitieleni@gmail.com (2) University of the Aegean, Department of Geography, Cartography and Geoinformatics Laboratory, Mytilene, Lesvos, Greece (3) Society for the Study of Ancient Coastlines - AKTES NPO; University of Nottingham, Department of Classics and Archaeology; Chalandri, Athens, Greece

Research Highlights

Web mapping and geovisualisation of beachrocks using UAS along the littoral zone of the Argolic Gulf: a methodological approach to surveying the nearshore zone, with advantages and constraints for bathymetric reconstruction.

Introduction - Background

Beachrocks are rocky coastal deposits that form during relatively short periods along the shoreline within the intertidal zone, under complex physicochemical (e.g., Ginsburg, 1953; Taylor and Illing, 1969; Moore, 1973; Hanor, 1978; Meyers, 1987) and biological (e.g., Webb *et al.*, 1999; Neumeier, 1999) cementation processes. They consist of coastal sediments, such as sand, gravels, pebbles, cobbles and other coarse materials of both clastic and biogenic origin, and even of anthropogenic origin (e.g., ancient remains), usually cemented with calcium carbonate, high/low magnesian calcite and aragonite. It is generally accepted that beachrock lithification takes place in the intertidal zone (e.g., Scholle and Ulmer-Scholle, 2003; Vousdoukas *et al.*, 2007; Mauz *et al.*, 2015). In microtidal environments such as this, in the central Aegean where the maximum and mean tidal ranges do not exceed 0.30 m and 0.15 m, respectively (HNHS, 2015), the cementation of coastal sediments exceeds the tidal range and expands into the swash, saturated, zone (Gifford, 1995; Kolaiti *et al.*, 2017; Kolaiti, 2019). Diagenesis is similar in both the intertidal and the swash and backwash zones, and the cementation results are indistinguishable (Bernier and Dalongeville, 1996). Therefore, beachrocks demarcate an ancient coast during their formation, with the base of the seaward end of a beachrock slab, in its well-preserved parts that have not undergone erosion or fragmentation, representing the mean low tide of a former sea level (e.g., Kolaiti and Mourtzas, 2023). Different sea level stands form distinct beachrock slabs at various elevations that correspond to different generations of a fossilized palaeoshoreline (e.g., Vousdoukas *et al.*, 2007; Desruelles *et al.*, 2009; Mauz *et al.*, 2015 and references therein; Mourtzas and Kolaiti, 2020). The loose, unconsolidated, sandy/sandy-gravel sediments laid on the sea bottom between two different beachrock generations represent a period of relative sea level (rsl) change (e.g., Desruelles *et al.*, 2009). Fossils, organic material or archaeological remains embedded in a beachrock are a *terminus post quem* for the beachrock formation, postdating the embedded material (Kolaiti, 2019).

The study of beachrocks provides valuable knowledge about the ancient environmental, geological, sedimentological, and geomorphological conditions that prevailed in the littoral zone during their formation process (Mauz *et al.*, 2015 and references therein). Their development along a sandy coastline contributes to mitigating the effects of marine erosion, i.e., the irreversible retreat of the coastline caused by natural (e.g., storms, waves, ocean currents, sea level rise) and anthropogenic (e.g., residential and touristic development, coastal infrastructure) processes in the coastal zone. This results in a systematic alteration of the coastscape, with the sea covering large sections of the vulnerable sandy beach. The submerged beachrock slabs in the nearshore zone due to relative sea level rise can act as natural barriers against coastal erosion, despite the loss of sediment during their initial cementation, thus changing the seascape and affecting the coastal morphodynamics (Psomiadis *et al.*, 2010). On the other hand, the rsl rise results in exposure of beachrocks along the contemporary coast (typical example from the study area: the Ververonta beachrock), which were previously buried under beach sediments, thus turning a sandy beach into rocky. This may have several social-economic impacts on the touristic exploitation of a beach and requires appropriate coastal management (Vousdoukas et al., 2009), in order to avoid inconsiderate destruction by locals (typical example from the study area: the Plaka-Drepano beachrock). As an alternative protection measure against coastal erosion, of lower cost and more environmentally friendly than heavy engineering structures, several studies have focused on coastal ground improvement based on bio-stimulation, that is cementation of coastal sediments on the erosion-prone beach following the formation process of beachrocks and using local bacteria and seawater (e.g., Danjo and Kawasaki, 2016; Saitis *et al.*, 2022).

Due to their lateral spread and, often, their significant thickness, beachrocks contribute to the preservation of biodiversity in the nearshore marine ecosystems, effectively acting as a natural reef on the sandy seabed and a safe habitat of several species of marine life (seaweed, algae, organisms, fish, etc.).

Finally, recently initiated experimental researches attempt to link beachrocks with natural CO_2 storage exploring their role in reducing the environmental footprint of a region, as it has been demonstrated for CO_2 sequestration in sandstone reservoirs (e.g., Koukouzas *et al.*, 2018; Gholami and Raza, 2022).

Project area - Objective

The pilot area for the implementation of the Argo-Beachrock Project is the nearshore of the south Argolic Peninsula, from the southern part of the Saronic Gulf, at the eastern edge of the Hydra Strait, to the mouth of the Argolic Gulf, on the western coast of the Myrtoan Sea. The study area stretches across 255 km of coastline and includes 20 locations with beachrock formations, which collectively cover a total length of 20 km (Fig. 1).

This area was chosen partly because numerous submerged beachrock generations have already been recorded at various locations and depths, indicating distinct ancient lithified beaches formed during different periods. Notably, it includes the deepest recorded occurrence of Holocene beachrock observed in Greece to date (i.e., -8.85 m below mean sea level, Tigani coast, Tyros Bay) (Kolaiti, 2019). Additionally, it is a region undergoing systematic tourism development.

Figure 1. Map of the project area. The survey areas are indicated by red bullets.

The objectives of the Argo-Beachrock Project could be outlined as follows:

- UAV mapping and documenting of beachrock formations, including UAV and underwater survey, and depth measuring and validation.
- Analysis and processing of spatial data, production of high-resolution orthophoto maps, digital surface models (DSM), and 3D models.
- Visualisation of 2D information on an open-access web-map platform, creation of thematic maps, photographic material.
- Understanding coastal dynamics, environmental conditions, and natural processes through the comprehension and synthesis of all available data on the formation and evolution of beachrocks.
- Creating a comprehensive database (incl. location, depth per generation, mineralogical composition, if available, and absolute and indirect dating for each survey site), thus enhancing scientific knowledge and providing data available for future research.

- Disseminating the project results in order to raise public awareness of the importance of coastal protection through the study and preservation of beachrock formations, highlighting their role in mitigating erosion and preserving ecosystems. Collaboration with local communities, researchers, and stakeholders.

Methods

The submerged beachrock formations throughout the survey area have been previously mapped, their features (length, width and thickness) recorded, and the depth of the seaward and landward end of the top and base of each beachrock generation in each location were measured during previous snorkel geological surveys using customary methods. The depth measurements were subsequently corrected for tide at the time of the surveys with respect to mean sea level and for the effect of atmospheric pressure on the sea level (Kolaiti, 2019, 2024).

In this study, aerial digital photogrammetry was applied to produce high-resolution digital surface models (DSM) of the seashore and nearshore zone in all the survey areas. The low altitude imagery captured during aerial surveys conducted in two different periods (October 2024 and April 2025), under extremely calm wind conditions (<1 bf), in order to achieve the best shoreline reconstruction and avoid any distortion in the coastline position caused by sea waves and water refraction. High-resolution images have been acquired using an RTK DJI Mavic 3E with global shutter camera (FOV 84^o, 24mm lens equivalent, 20MPixel, ¾ sensor size) in aerial surveys. Side overlap was set at 60%, frontal overlap at 80%, and flight speed at 4-7 m/sec. During the two survey periods 30 flights were conducted, of a maximum duration 20 min each, depending on the extent of the survey area. The relative height of the flights was 80 m with terrain follow adjustments, whereas in two sites (Tyros and Plaka-Drepano) a flight height of 60 m and 40 m was applied, in order to compare the images in shallow waters. At the 80 m-flight level, the resulting ground sample distance (GSD) was 2.2 cm/pixel, which produced a high detailed orthomosaic. A total of 4,534 images were collected, while the sum of the 20 survey areas amounts to 454 ha (4.54 km^2).

The image-based 3D modelling process was carried out using Agisoft Metashape Pro software. The GGRS 1987 coordinate system was used, with Geoid Model D applied for vertical adjustments. After the modelling process was completed, the following outputs were produced for each surveyed site: (i) 3D dense point cloud (in LAS/LAZ format) (ii) mesh (in FBX format) (iii) GeoTIFF Digital Surface Model (DSM) with a spatial resolution of 8.5 cm, and (iv) orthomosaic with a spatial resolution of 2.1 cm.

The 3D modelling workflow involved several key steps: (a) *Sparse Point Cloud Generation*: an initial sparse point cloud was created as a preliminary representation of the geometry derived from UAV-acquired imagery using the Structure from Motion (SfM) algorithm, (b) *Dense Point Cloud Generation*: high-resolution dense point clouds were generated from the aligned images using multi-view stereo algorithms, after feature detection with the Scale-Invariant Feature Transform (SIFT) algorithm. The dense point cloud enhanced model precision by capturing detailed surface features necessary for accurate representation, (c) *3D Mesh Creation*: The dense point cloud data was interpolated to construct 3D meshes, providing a continuous surface representation, and (d) *3D mesh Texturing*: the 3D meshes were textured to produce a photorealistic visual output.

This systematic approach ensured the generation of high-precision 3D models suitable for detailed analysis and visualisation (Papadopoulou *et al*., 2021, 2022).

Results - Discussion

The orthomosaics generated from the Argo-Beachrock Project's geospatial survey were used to delineate the boundaries of each beachrock generation, now submerged in the nearshore zone of each surveyed area, to assess its current situation (e.g., erosion, fragmentation), and to identify remains of ancient structures integrated into the beachrock formations.

For each surveyed area, a comprehensive suite of geospatial products has been generated, including detailed 3D models, high-resolution visualisations, orthophoto maps, and associated datasets. These outputs are integral to the project's objectives and will be made publicly available on open-access platforms by the project's conclusion. The data dissemination strategy includes the following components:

- *Web-Map Platform*: an interactive web map will enable users to visually explore all orthomosaics. This platform will allow seamless navigation, zooming, and layer toggling for enhanced spatial analysis and visualisation. The web map will cater to diverse user needs, from researchers and planners to educators and the general public.

- *YouTube Channel for 3D models*: a dedicated YouTube channel will host a collection of 3D animated maps, providing dynamic visualisations of the generated 3D models. These animations will facilitate an in-depth visual inspection of the models, showcasing intricate surface details and the spatial relationships within each survey area. The channel will serve as an accessible resource for presentations, educational purposes, and broader dissemination to non-specialist audiences.

By leveraging open-access platforms, the project ensures that these datasets are preserved and accessible for future research, education, and practical applications. This approach promotes collaboration, supports transparency, and maximizes the impact of the generated geospatial resources.

Next, we provide an example of the photogrammetric mapping and visualisation data generated for one out of the twenty survey sites (Figs. 2 and 3).

Figure 2. Part of the orthomosaic of the Plaka beach (Drepano, N Argolic Gulf), providing a clear and detailed image of the beachrock formation extending to a depth of -1.20±0.05 m below mean sea level.

Figure 3. Part of the 3D model of the Plaka beach (Drepano, N Argolic Gulf), corresponding to the same coastal zone as Figure 2.

The depths in the nearshore zone, as derived from the Digital Surface Models (DSMs) produced in the context of the Argo-Beachrock Project, were compared with those obtained through mechanical methods during previous snorkel geological surveys. The comparison shows a good match in shallow waters (up to a maximum depth of 2 m), with deviations well below the mean tidal range. However, this comparison is not meaningful for greater depths.

Shallow-water bathymetry is a dynamic and evolving field of research, with modern drone imagery-based methods enabling unprecedented levels of detail and accuracy (Makris *et al.*, 2024 and references therein). Among the methodologies commonly employed in the literature, spectral and geometry-based approaches are predominant. These techniques are often utilized individually or in combination to enhance bathymetric accuracy and resolution.

In the context of the present study, the produced Digital Surface Models (DSMs) were utilized exclusively for geovisualisation purposes rather than as a true bathymetric dataset. This distinction aligns with prior research, where DSMs derived from drone-based imagery are often leveraged for visual representation but they lack the precision required for accurate depth measurements in bathymetric studies, as it is widely accepted that the accuracy of DSMs decreases with increasing water depth (Sefercik *et al.*, 2024 and references therein).

Conclusions

By combining UAV image-based 3D modelling, field observations, and systematic documentation of coastal natural features and manmade structures, alongside the use of geovisualisation tools, we can better understand the extent of past marine transgression and coastline retreat driven by ongoing relative sea level rise along the entire coast of the Argolic Gulf during the Late Holocene.

Modern methodological approaches to studying the dynamic coastal system have proven invaluable tools for monitoring and managing one of the wealthiest littoral zones of the Peloponnese, which is experiencing steady tourist growth. However, this region, rich in natural geomorphs and cultural heritage, has already been significantly affected by rising sea levels over both prehistoric and historic timescales. It will face even greater challenges as sea levels continues to rise at an accelerating rate, in line with global temperature increases, a dire consequence of climate change.

Beyond the methodological aspects, the results of this fully open-access research project will assist scientists, local communities, and stakeholders to design early response systems for coastal retreat, extreme weather events, and civil protection and adaptation measures, ultimately contributing to a sustainable regional development. More analytically, integration of UAV-based remote sensing and advanced geovisualisation techniques has significantly enhanced the accuracy and efficiency of coastal monitoring and analysis. Geovisualisation platforms further enable interactive exploration and interpretation of 2D and 3D data, fostering a deeper understanding of spatial-temporal trends and facilitating data-driven decision-making for coastal management and climate resilience strategies. Finally, UAV-based mapping can serve as a foundation for the long-term monitoring of the changes in the coastal zone over time.

Acknowledgements

The Argo-Beachrock Project was implemented with the support of the Athanasios C. Laskaridis Charitable Foundation within the framework of "*Points of Support*", a co-funded programme by 10 public benefit foundations. The project was assigned to the Society for the Study of Ancient Coastlines NPO – AKTES on October 1, 2024, and was carried out in close and effective collaboration with the Cartography and Geoinformatics Laboratory, Department of Geography, University of the Aegean. It was completed on May 31, 2025. The final deliverables are displayed on the *ArcGis Enterprise Portal* of the University of the Aegean (https://sdi-portal.aegean.gr/portal/apps/experiencebuilder/experience/?id=602a22c307b34e7cb0211f0f6b58220e), uploaded on the fully open access *sketchfab platform* (https://sketchfab.com/aegean_cartolab/collections/the-argo-beachrock-project), and published on the *AKTES YouTube channel* (https://www.youtube.com/@aktes7509/playlists).

References

Bernier, P., Dalongeville, R., 1996. Mediterranean coastal changes recorded in beachrock cementation. Zeit. Geomorphol. NF, Suppl.-Bd, 102, 185–198.

Danjo, T., Kawasaki, S., 2016. Microbially Induced Sand Cementation Method Using Pararhodobacter sp. Strain SO1, Inspired by Beachrock Formation Mechanism. Materials Transactions, 57(3), 428-437.

Desruelles, S., Fouache, É., Çiner, A., Dalongeville, R., Pavlopoulos, K., Kosun, E., Coquinot, Y., Potdevin, J.-L., 2009. Beachrocks and sea level changes since Middle Holocene: Comparison between the Insular Group of Mykonos-Delos-Rhenia (Cyclades, Greece) and the southern coast of Turkey. Global and Planetary Change, 66(1), 19-33.

Gholami, R., Raza, A., 2022. CO_2 sequestration in sandstone reservoirs: How does reactive flow alter trapping mechanisms? Fuel, 324, part C, 124781.

Gifford, J.A., 1995. The physical geology of the western Messara and Kommos. In: Shaw, J.W., Shaw, M.C. (Eds.), Kommos I: the Kommos Region and Houses of the Minoan Town, 30-90, Princeton University Press, NJ.

Ginsburg, N.R., 1953. Beach rock in south Florida. Journal of Sedimentary Petrology, 23, 85-92.

Hanor, S.J., 1978. Precipitation of beachrock cements: mixing of marine and meteoric waters vs CO2-degassing. Journal of Sedimentary Petrology, 48, 489-501.

HNHS - Hellenic Navy Hydrographic Service, 2015. Statistical data on sea level from Greek ports, 2nd revised edition.

Kolaiti, E., 2019. Changes in the anthropogenic environment along the eastern coast of the Peloponnese on the basis of archaeological and morphological indicators of the Late Holocene relative sea level changes. Proposing a geoarchaeological method of approach. Ph.D. Thesis, University of the Peloponnese, Kalamata, 674 p. (available at www.didaktorika.gr/eadd.)

Kolaiti, E., 2024. The 'vanished port' of ancient Asine: a geoarchaeological approach, in: Xanthopoulou, M. et al. (Eds), Archaeological Work in the Peloponnese 3 (Proceedings of the 3rd International Scientific Meeting AWOP3 - 2021, University of the Peloponnese Kalamata, Greece), 821-835.

Kolaiti, E., Mourtzas, N., 2023. Late Holocene relative sea-level changes and coastal landscape readings in the island group of Mykonos, Delos, and Rheneia (Cyclades, Greece). Mediterranean Geoscience Reviews, 5(3), 99-128.

Kolaiti, E., Papadopoulos, G., Morhange, C., Vacchi, M., Triantafyllou, I., Mourtzas, N., 2017. Palaeoenvironmental evolution of the ancient harbour of Lechaion (Corinth Gulf, Greece): were changes driven by human impacts and gradual coastal processes or catastrophic tsunamis? Marine Geology, 392, 105-121.

Koukouzas, N., Kypritidou, Z., Purser, G., Rochelle, C.A., Vasilatos, C., Tsoukalas, N., 2018. Assessment of the impact of CO_2 storage in sandstone formations by experimental studies and geochemical modeling: The case of the Mesohellenic Trough, NW Greece. International Journal of Greenhouse Gas Control, 71, 116-132.

Makris, A., Nicodemou, V.C., Alevizos, E., Oikonomidis, I., Alexakis, D.D., Roussos, A., 2024. Refraction-Aware Structure from Motion for Airborne Bathymetry. Remote Sensing, 16(22), 4253.

Mauz, B., Vacchi, M., Green, A., Hoffmann, G., Cooper, A., 2015. Beachrock: a tool for reconstructing relative sea level in the far-field. Marine Geology, 362, 1-16.

Meyers, J.H., 1987. Marine vadose beachrock cementation by cryptocrystalline magnesian calcite, Maui, Hawaii. Journal of Sedimentary Petrology, 57, 558-570.

Moore, C.H., 1973. Intertidal carbonate cementation in Grand Cayman, West Indies. Journal of Sedimentary Petrology, 43, 591-602.

Mourtzas, N., Kolaiti, E., 2020. Palaeogeographic reconstruction of the Messara Gulf and Matala Bay (Crete, Greece): coastal response to sea level changes during prehistoric and historic times. Alpine and Mediterranean Quaternary 33(1), 61-87.

Neumeier, U., 1999. Experimental modeling of beachrock cementation under microbial influence. Sedimentary Geology, 126, 35-46.

Papadopoulou, E.E., Papakonstantinou, A., Zouros, N., Soulakellis, N., 2021. Scale-variant flight planning for the creation of 3d geovisualization and augmented reality maps of geosites: The case of Voulgaris Gorge, Lesvos, Greece. Applied Sciences, 11(22), 11(22), 10733.

Papadopoulou, E.E., Papakonstantinou, A., Vasilakos, C., Zouros, N., Tataris, G., Proestakis, S., Soulakellis, N., 2022. Scale issues for geoheritage 3D mapping: The case of Lesvos Geopark, Greece. International Journal of Geoheritage and Parks, 10(3), 435-446.

Psomiadis, D., Albanakis, K., Tsourlos, P., 2010. Evaluation of sea-level rise impact on cemented and uncemented beach. Case study from Thassos Island, Greece. Scientific Annals, School of Geology, Aristotle University of Thessaloniki (Proceedings of the XIX CBGA Congress, Thessaloniki, Greece), Special Volume 99, 483-48.

Saitis, G., Karkani, A., Koutsopoulou, E., Tsanakas, K., Kawasaki, S., Evelpidou, N., 2022. Beachrock Formation Mechanism Using Multiproxy Experimental Data from Natural and Artificial Beachrocks: Insights for a Potential Soft Engineering Method. Journal Marine Science and Engineering, 10, 87.

Scholle, P.A., Ulmer-Scholle, D.S., 2003. A color guide to the petrography of carbonate rocks: grains, textures, porosity, diagenesis. American Association of Petroleum Geologists, Tulsa, Oklahoma.

Sefercik, U.G., Nazar, M., Aydin, I., Büyüksalih, G., Gazioglu, C., Bayirhan, I., 2024. Comparative analyses for determining shallow water bathymetry potential of multispectral UAVs: case study in Tavsan Island, Sea of Marmara. Frontiers in Marine Science, 11, 1388704.

Taylor, M.C.J., Illing, V.L., 1969. Holocene intertidal calcium carbonate cementation, Qatar, Persian Gulf. Sedimentology, 12, 69-107.

Vousdoukas, M., Velegrakis, A., Plomaritis, T.A., 2007. Beachrock occurrence, characteristics, formation mechanisms and impacts. Earth-Science Reviews, 85, 23-46.

Vousdoukas, M.I., Velegrakis, F., Kontogianni, A., Makrykosta, E.-N., 2009. Implications of the cementation of beach sediments for the recreational use of the beach. Tourism Management, 30(4), 544-552.

Webb, G.E., Jell, J.S., Baker, J.C., 1999. Cryptic intertidal microbialites in beachrock, Heron Island, Great Barrier Reef: implications for the origin of microcrystalline beachrock cement. Sedimentary Geology, 126 (1–4), 317-334.

17th INTERNATIONAL CONGRESS
of the Geological Society of Greece

BULLETIN OF THE GEOLOGICAL
SOCIETY OF GREECE, SP. PUBL.

EXTENDED ABSTRACT 154

The Corinth Canal (Greece): monumentality and protection

Kolaiti E.[1], Zouros N.[2], Mourtzas N.[3]

(1) Society for the Study of Ancient Coastlines - AKTES NPO; National Hellenic Research Foundation, Institute of Historical Research; University of Nottingham, Department of Classics and Archaeology; Chalandri, Athens, Greece, kolaitieleni@gmail.com (2) University of the Aegean, Department of Geography, Mytilene, Lesvos, Greece; Natural History Museum of the Lesvos Petrified Forest (3) Society for the Study of Ancient Coastlines - AKTES NPO; University of Nottingham, Department of Classics and Archaeology; Chalandri, Athens, Greece

Introduction

The Corinth Canal is an artificial waterway in Greece that connects the Corinth and Saronic Gulfs. It crosses the narrow Isthmus of Corinth, a 79 m high ridge which once linked the Peloponnese peninsula to the Greek mainland, creating a natural barrier between the Ionian and Aegean Seas. The Canal extends in a straight line for 6,343 m. It is 24.60 m wide at the sea surface narrowing to 21.30 m at its bottom, while the water height in it ranges from 7.50 to 8 m (CorinthCanal). In this paper, we present an overview of the technical aspects of this admirable engineering work tracking the historical route of its opening from antiquity until the late 19th century and briefly describe the accompanying infrastructure works and the ongoing interventions, mainly driven by the geotectonic setting of the area. We argue for the monumentality of the Corinth Canal that mandate its future preservation and we propose a framework of actions to protect this prominent heritage.

The diolkos and the history of the canal

The idea of avoiding the dangerous and long circumnavigation of the Peloponnese taking advantage of the strategic position of the Isthmus of Corinth dates back to the late 7th – early 6th century BC, when ancient Corinth flourished, ruled by the tyrant Periander, having two harbours (Lechaion in Corinth Gulf and Kenchreai in Saronic Gulf) and a fleet to control maritime traffic on both seas. It was then that a paved trackway along the isthmus was constructed, the famous *diolkos*, across which goods and small boats, mainly warships, were hauled and transported on a platform (*olkos*). It followed the path of the present-day canal for a length of about 8 km. It was 3.40-6.0 m wide and carried two grooves in the middle, spaced 1.50 m apart. It ended on a paved quay on its western side, where it has been excavated for 255 m and 204 m on the Peloponnese (Kolaiti *et al.*, 2017) and Sterea Hellas sides, respectively, whereas its eastern end facing the Saronic Gulf, located in the area of ancient Schinous (today's Kalamaki) has not been found yet. Several phases of reconstruction followed during the 5th and 4th centuries BC. It remained in use until the AD 9th century (Ministry of Culture and Sports, 2012).

Strabo (1.3.11) reports that Dimitrios Poliorkitis (307 BC) planned to cut a passage through the Isthmus of Corinth, but he was prevented by his engineers, and also Julius Caesar (AD 44) and Caligula (AD 37) had probably the same intention. The most important works were carried out by Nero in AD 67, who, using slaves (at least 6,000 Jewish prisoners), began excavations on both sides of the Isthmus with notable progress, remains of which are either still visible (e.g. Nero's relief) or recorded (e.g. trenches, pits) during the construction of the modern canal (Gerster, 1884). The project was eventually interrupted due to either logistic difficulties or political instability (CorinthCanal). This was certainly the commencement of an ambitious project. The Venetians attempted to resume it in 1687 but were unsuccessful.

In 1830, Ioannis Kapodistrias, the first Governor of the new Greek State, assigned the project to the French engineer Virle d'Uct, who estimated that an enormous amount of 40 million gold francs would be needed for its completion. In 1869, the inauguration of the Suez Canal revived interest in constructing the Corinth Canal, and the government of Thrasyvoulos Zaimis passed a law "on the Isthmus canalization", under the provisions of which in 1870 a contract was signed with French entrepreneurs, but it was not implemented due to lack of funds (Papafotiou, 2010). In 1882, the French company 'Société Internationale du Canal Maritime de Corinthe' was formed with the purpose of completing and operating the Corinth Canal. The 99-year canal's concession, granted by a royal decree in 1881 to Hungarian General, canal architect, and engineer Istvan Türr, was transferred to the French company (Société Internationale). The project commenced on April 23, 1882, based on Nero's plans and the final design by the Hungarian engineer Bella Gerster. In 1890, the company was dissolved and put into liquidation, and the project halted. However, efforts to secure additional funding succeeded, and constructions was resumed by the Greek construction company 'Geniki Etaireia Ergolipsion', founded in 1889 (Pepelasis, 2010). With a generous contribution from Greek benefactor Andreas Syggros, the canal opened with great ceremony on July 25, 1893 (CorinthCanal).

Isthmus Infrastructure: The bridges

The 19th-century railway bridge was blown by the German occupying troops during their withdrawal from Greece in 1944, to be later rebuilt in the late 1940's. Two submersible road bridges operate at both ends of the canal (Posidonia and Istmia), which continuously facilitate the communication between central Greece and the Peloponnese.

In the late 1990s, as part of the construction projects of the new P.A.TH.E. motorway and the high-speed railway line Athens-

Thessaloniki funded by the European Union, the design of the new canal bridges was decided. The initial design was based on the geometric characteristics of the new alignments, while ensuring the stability of the bridges with the least possible excavations in the canal's slopes so that its shape would not be altered. The span of the bridges was determined after the idea of widening the canal was rejected. However, the geotectonic setting of the Isthmus area finally played a decisive role in the final position and foundation of the new bridges. The secondary tectonic activation of the faults crossing the Corinth Isthmus, as it was evidenced by their quantitative and qualitative tectonic analysis, and the thorough study of the stratigraphic, lithological and neotectonic features of the canal's slopes, demonstrated that the abutments and the piers of the new bridges had been positioned in different tectonic blocks on both sides of the canal (Peloponnese and Attica). This led to the redesign of the new bridges and the implementation of specific construction techniques using seismic isolation bearings. The new motorway and railway bridges were opened to traffic in 1997 and 2003, respectively.

The geological and geotectonic context of the Corinth Isthmus

The Corinth Isthmus is crossed by at least 46 large-scale normal faults, traverse to its direction, which have caused successive displacements on the Plio-Pleistocene and Quaternary strata, and on the recent artificial deposits from the Isthmus excavation, affecting the morphology on both sides of the canal. The faults have a NE-SW direction, with the fault mirrors dipping toward S, SE, and WNW at 60°-85°, and strike-slip lineation plunging S and SW. They have been repeatedly activated within a NNE-SNE extensional regime and are still considered to be active (Fig. 1A, 1B). With a total visible displacement of 7.50-21 m during the Quaternary, they have caused the gradual rotation of the tectonic blocks they delimit by about 10° toward the SE. The Corinth Isthmus is affected by two vectors of tectonic displacement: uplift and extensional fault-induced subsidence, which may be accompanied by block rotations. Neogene and Quaternary sediments are cut by numerous, nearly E-W striking, sub-vertical normal faults, which can be observed all along the canal. As these faults belong to two different groups dipping toward N and S, respectively, the isthmus has been interpreted as a horst (Fig. 1C). The oldest sediments are at the base of the central horst block, dominated on the NW by white and grey calcareous silts (Fig. 1B). There is an upwards transition within the central horst block from freshwater or brackish facies to sediments of a marine environment (Papanikolaou *et al.*, 2015; Mourtzas and Kolaiti, 2017 and references therein).

The crossing area of the new bridges consists of three distinct tectonic blocks, each of an average width of 60 m, bounded by four main normal faults striking NW-SE to NNE-NNW and dipping toward SE to SSW at angles 70°-90°, with a visible displacement of 4-5 m (Fig. 1D, 1E). The faults have been activated during various neotectonic deformation phases, causing a gradual displacement toward the SE and a counter-clockwise rotation of about 10°. The main faults and the accompanied parallel small-scale structures were surveyed, not only on both slopes, but also in deep trenches that were excavated parallel to the canal axis, while their geometric and kinematic features were measured (Fig. 1E). The stratigraphy of the Neogene and Quaternary units on both the canal's slopes was mapped and the relative position of the layers within the distinct tectonic blocks was recorded, thus ascertaining their spatial continuity (Fig. 1D, 1E). Moreover, the lithology, physical characteristics, and mechanical properties of the layers were determined by means of drilling of fifteen boreholes and wells (Fig. 1D). The identification of recent fault activations that have resulted in displacements of several centimetres, which are visible even in the debris of the canal's excavations, imposed the positioning of the abutments and piers of the bridges within the same tectonic block with their axes parallel to the direction of the fault lines, in order to avoid failures in case of differential movements (Mourtzas and Kolaiti, 2017 and references therein).

Landslides and Recent interventions

The high (>60 m), steep, marly slopes of the Corinth Canal, prone to landslides, have caused ongoing instability, rock falls, and slide of large volumes of materials since almost the inception of the canal, leading to interruptions in vessel passage and even extended closures. In addition to geological factors (e.g., rock type and structure, steep gradients, active tectonism, seismic activity, lack of vegetation, soil erosion), human-related factors (e.g., excavation, construction, undermining, sabotage) have further increased slope vulnerability to failure. Between 1923 and 1997, it is estimated that approximately 900,000 m^3 of material fell into the canal, resulting in a total closure period of eight years (CorinthCanal). The destructive 1981 Alkyonides earthquake sequence (24.2.1981 M=6.7, 25.2.1981 M=6.4, 4.3.1981 M=6.3) at the eastern end of Corinth Gulf, resulted in two major ruptures in the Isthmus horst, fault activation and displacement, and rock failure and serious landslides in the canal's slopes. The ENE-WSW trending Kalamaki-Isthmia normal fault downthrown to SSE, located at the eastern tip of the canal, was passively ruptured by up to 6 cm during the 1981 earthquake sequence (Papanikolaou *et al.*, 2015; Mourtzas and Kolaiti, 2017 and references therein). Between November 2020 and February 2021, frequent landslides occurred, culminating in a major collapse of 15,000-20,000 m^3 on February 3, 2021 (CorinthCanal), mainly near the wastewater treatment plant on the Peloponnese side. This serious instability resulted in the closure of the canal and disruption of navigation through it. Although the landslides affected the upper part of the slope over a 100 m-stretch near the wastewater bridge, they did not impact the bridge's stability.

In November 2021, the final design of the slope restoration project was approved by the Ministry of Infrastructure and Transportation

–now responsible for the design and construction of the slope restoration works at the request of the

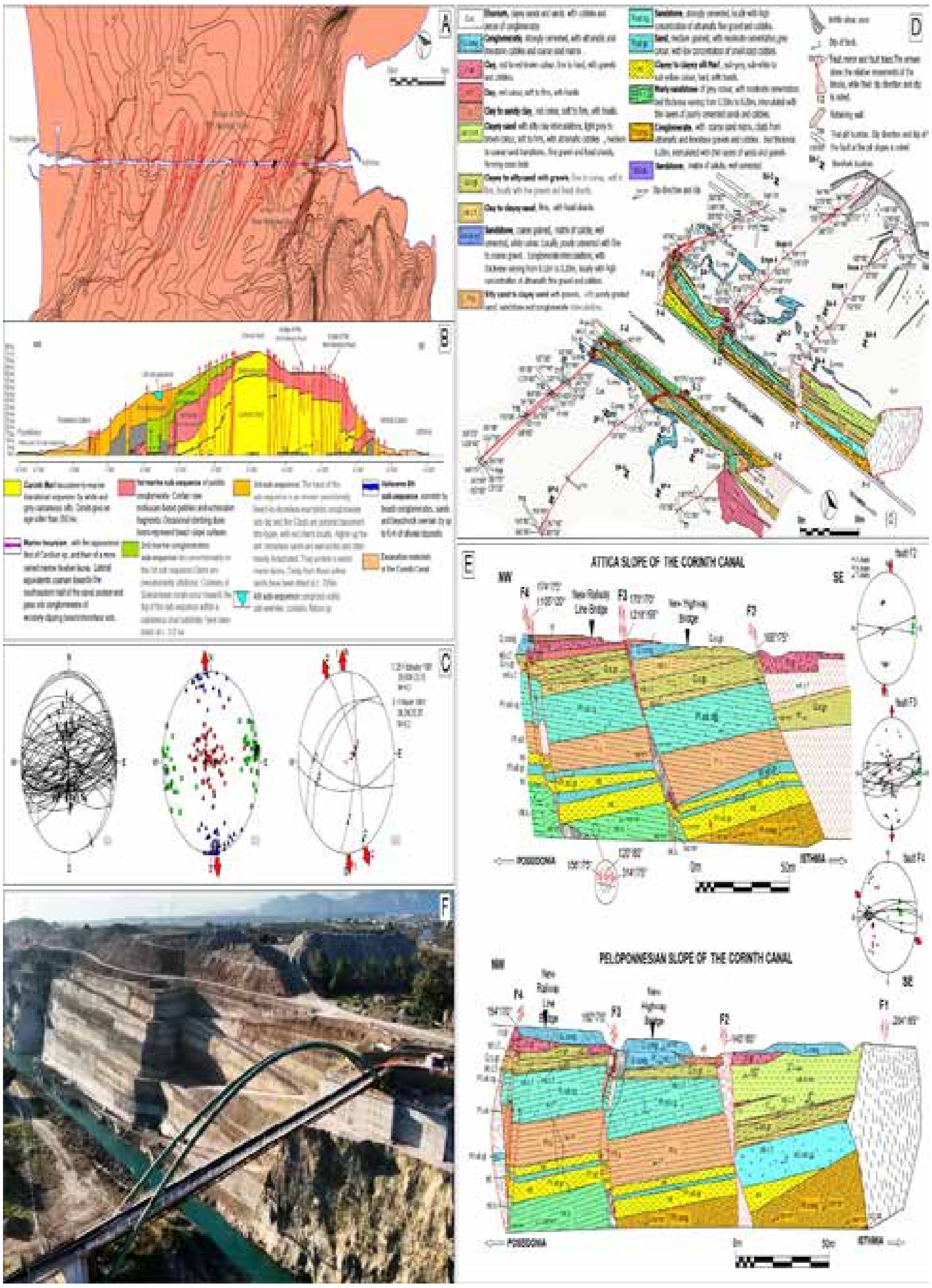

Figure 1. A: Plan view, and B: Longitudinal section of the Isthmus horst, indicating the geological structure and main faults. C: (i) Stereogram, and (ii) calculated stress axes of the Isthmus main faults, and (iii) focal mechanism solutions of the 1981 Alkyonides earthquake sequence. D: Geological plan view, and E: Front views of the two slopes of the Corinth Canal in the area of the new bridges, indicating the main faults that demarcate the tectonic blocks and their palaeostress analysis. F: Aerial view of the slope stabilisation works in 2022 at the area of the wastewater treatment plant on the Peloponnese side, showing the slope excavations and, in the foreground, the wastewater bridge [A, B, C, D, E: after Mourtzas and Kolaiti (2017) and references therein, F: modified from Papamanolakis].

Corinth Canal S.A.– especially characterized as a ‘*complex and special national-level project*’ (Dec. 29307/Σ6651/3.2.2021). Due to its urgent nature for civil protection ensuring public safety and restoring normal navigation, the project is exempting from environmental approval (Dec. 103435/6635/9.2.2021), with the only obligation for the operating company to submit an Environmental Impact Study for the operation and maintenance of the canal within two years from the exemption. In December 2021, the project was assigned to the contacting company AKTOR S.A., with a budget of 30.57 million euros and a completion period of 24 months. The restoration engineering works are divided into two distinct phases: Phase A includes slope excavations for a total length of 600 m on both sides of the wastewater bridge, creation of three terraces (10 m-wide with intermediate slopes 6 m/11 m/9 m/8 m high), construction of permanent roads-ramps for heavy vehicles, strengthening with piles of the southern pier of the wastewater bridge, slope stabilisation with anchors and grouting, hydraulic works for surface water drainage management, construction and waterproofing of the western and eastern embankments. Phase B involves the construction of a toe pile wall to prevent coastal erosion and slope undermining.

The first phase of the project has been completed, leaving a significant environmental footprint (Fig. 1F). The second phase has not yet started. Furthermore, the recent approval by the Ministry of Infrastructure and Transportation to replace the seismic isolation bearings of the new motorway bridge, at the request of Olympia Odos S.A. (concessionaire of the Elefsis-Corinth-Patras-Pyrgos Motorway), and the looming plans of widening the canal (Papafotiou, 2022), will further alter this outstanding landmark, without substantial financial benefits for the Corinth Canal S.A. (A.E.DI.K), the company which exercises and exploits the rights associated with the Corinth Canal. Although outside the scope of this paper, the long-term viability of the company remains crucial. Official data (Growthfund) shows that the Corinth Canal handles over 11,000 vessels annually, mainly tourist ships. Published financial statements for the period 2019-2023 (GEMI-Publicity) reveal net profits of 1 million euros in 2019 when the canal's passage was unhindered, but losses of over 3.3 million euros in 2021 and 1.7 million euros in 2022, due to the canal's closure for restoration after the 2020-landslides.

Monumentality of the Corinth Canal or Infrastructure and Monumentality

The term '*monumentality*', introduced by several scientists with different connotations, is hard to define in a few words, although several methodological approaches and tools explore its concept, mainly for ancient civilisations (Buccellati, 2019). Despite the unfruitful attempts to find a unifying definition for the complex notion of monumentality (Levenson, 2019), it has been adopted by architectural and archaeological theory, while it has a broader approval to other disciplines and different types of structures, which reflect the cultural and socio-political context they belong to. Osborne (2014) argues that '*monumentality is something more than the shape, or size, or visibility, or permanence of the monument – though these variables absolutely carry their own significance. Monumentality lies in the meaning created by the relationship that is negotiated between object and person, and between object and the surrounding constellation of values and symbols in a culture*'. Others support that monumentality exceeds physical scale and it is '*a combination of great technical ingenuity, extraordinarily high levels of skill, the devotion of vast amounts of time to build the monument, the type and range of the resources invested and the sheer size of the task*' (Brunke *et al.*, 2016). Monumental structures can be related to four primary attributes: permanence of the structure, the place or the memory (lasting endurance: connection to the past and projection into the future), integration within a specific landscape or urban environment, statement of vision, compelling effect, strength, and social and political relations, and, projection of public values, symbols, and political authority (Brunke *et al.*, 2016; Hageneuer and van der Heyden, 2016; Horn and Proudfoot, 2016). Although there has been much discussion of monumentality, it is mainly focused on monumental architectures, in diverse archaeological and historical contexts. Infrastructures (e.g. dams, bridges, canals, roads, power stations, etc.) are often overlooked in discussions, due to the weakness of perception of their symbolic power or the profound effects they have on society. Nevertheless, large-scale technical works are undeniably significant in terms of constructional energetics and social impact. According to Levenson (2019), they possess a distinct form of monumentality rooted in their capacity to innovate, improve daily life, and create social dependencies, arguably making them even more integral to the survival of societies than palaces, temples, or other public buildings. Infrastructure and monumentality intersect in how large-scale constructions embody both functional utility and symbolic significance. Beyond serving as tools for transportation and labour, they synthesise surrounding landscape, public space, and architecture (MIT Center for Advanced Urbanism, 2016). Large-scale technical projects, while fulfilling essential societal functions, can also be monumental in design and impact, symbolizing power, progress, and cultural significance.

Under these considerations, the Corinth Canal is an infrastructure necessary for navigation, primarily designed for function, efficiency, and sustainability. The canal connected the Saronic with the Corinth Gulfs, thus making navigation faster (time), easier (risk), and more environmentally-friendly (energy). Its geographic and geopolitical position renders it to '*a communication hub between the Aegean and Ionian Seas*' (Dec. 29307/Σ6651/3.2.2021). The opening of the canal, in fact, created a man-made, geographic boundary between the Greek mainland (Sterea Hellas) and the Peloponnese, the latter now shaping the largest island of Greece. From this perspective, the canal is an outstanding landmark. The geology and faulting of the Isthmus horst adds an invaluable value to the Corinth

Canal. Crossed by at least 46 normal and oblique normal faults, all recognised and surveyed (Mourtzas and Kolaiti, 2017), the canal's slopes compose an open geo-archive, providing a great opportunity to visualise them. This unique structure shapes an '*impressive mega-trench*' (Papanikolaou *et al.*, 2015), a precious geoheritage (Velitzelos *et al.*, 2003).

Its monumentality, on the other hand, lies in its symbolic and cultural importance, emphasising permanence, vision, political power, and historical significance. First conceived 2,300 years ago, the initial design plans date back to the 1st century AD. Remains from Nero's works testify to the ambitious idea and efforts to implement the grand project. The canal's construction was organized and completed only after the emergence of the Modern Greek state. The various actors of this grand project, either known or unknown, may have had different motivations, but its completion is the result of the development policy of the Prime Minister Charilaos Trikoupis, who, through major infrastructure projects, aimed to create a modern, economically developed state and provide models for future growth. The project was also deemed necessary by the international trade and shipping conditions of the time. Though the Corinth Canal was a 2,300-year-old dream, it was the technological progress of the 19th-century Industrial Revolution that ultimately drove its realisation. Therefore, large-scale public projects, such as the Corinth Canal, serve to enhance community infrastructure and identity, reflecting the vision of their inspirers, and the cultural values and technological advancements of the society, in most cases tied to political power. It is authoritatively perceived as '*a unique landmark*' and '*a project-symbol, completely identified with the modernization of Greece*' (Hellenic Republic, 2022).

The Corinth Canal is tightly connected to the collective historical memory of the WWII period. Images of the blow up of the railway bridge by the Germans and knocking of locomotives and wagons down into the canal to block it, remain still strong to remind this period of the Greek history. Landscape transformations (e.g. earth movements) and bunkers still preserved there, reveal the strategic importance the isthmus had for the German occupiers, contributing to the historical memory.

The approaching method of '*constructional energetics*' would help to understand the canal monumentality in numbers. Records of the cost of the individual constructional processes (e.g. excavation, debris transportation, labour, etc.), aids in understanding the resources required and calculating the energy expended (Buccelatti, 2019). Beyond the quantitative approach, the study of the workforce (skills, composition, social setting) would be interesting. Therefore, the consequential correlation between cost and final result, given the limitations of data availability, adequacy, and accuracy, provides a better understanding of what the canal meant to those who produced it. Urban changes imposed by the needs of construction in the project's area can also signal its social impact, such as the creation of two settlements, Posidonia (divided in two sections, area: 139,000 m^2 and 72,000 m^2) and Isthmia (area: 144,000 m^2) (Papafotiou, 2010) to house the people occupied in the project and their families.

In addition, the huge quantities (millions of cubic metres) of excavated material from the opening of the canal and recent construction activities, have actually reshaped the landscape of the Isthmus territories (e.g., the artificial slopes on the road leading from Isthmia to Loutraki), offering insights into the design process. Recent approaches to moving grounds from the 'AlpTransit Infrastructure' project (new rail link crossing the Alps and connecting Germany to Italy through Switzerland) highlight how depots, landfills, and wastelands are shaping a collective imagination about the idea of landscape, giving rise to major political, economic, and ecological implications (Pradel, 2020).

From an engineering point of view, the Corinth Canal has no parallel in Greece and Europe. It is numbered among the three existing canals in the world, and is an excellent technological achievement of the time. Its engineering uniqueness has been authoritatively recognised: '*together with the Panama and Suez Canals, (it) constitutes the three technical canals that exist in the world today*' (Dec. 29307/Σ6651/3.2.2021). Furthermore, the implementation of the canal project opened new routes to mobilisation of scarce capital and technical know-how for the construction of public infrastructure through the collective entrepreneurial initiatives of S.A. banks (Pepelasis, 2010). Together with the construction of the 1,548 km-long national railway network, were decisive for the establishment of an integrated national economy and administrative centralization, both required for the building of the newly Greek state (Papayiannakis, 1982; Pepelasis, 2010). In particular, the mobilisation of national technical know-how was seminal to the Greek technical community. A notable example is Greek engineer-entrepreneur Antonios Z. Matsas, co-founder of 'Geniki Etaireia Ergolipsion', who replaced the foreign engineer Istvan Türr after the liquidation of the French company, ultimately leading to the canal's completion.

The long-lasting project of the canal's opening evokes the perception of a connection to a distant past, while its continuous operation for over 130 years reinforces a sense of permanence. Integrated into the unique geotectonic landscape of the Isthmus, the canal stands as a striking and timeless landmark with a dominant form, whose monumentality is constantly experienced. In terms of reception, it commemorates people, events, eras, practices, and techniques—not only from its creation, but also its lasting impact—embedded both in the structure and in collective memory (Belavilas, 2015). Numerous textual and artistic sources depict the canal, in an iconic way, further enhancing this shared memory.

Thoughts on the future of the Corinth Canal

Nowadays navigation through the canal appears to be limited to mainly tourist vessels, as large ships prefer other easier sea routes in the open sea than a restricted canal to get from the Ionian to the Aegean Sea, thus downgrading its economic importance. The Corinth Canal is mainly a tourist attraction, thus its widening to accommodate ships larger than its current capacity seems to have no effect in conjunction with the exorbitant construction costs and the loss of its monumentality. After all, this proposal was rejected during the design of the new bridges in the 1990s. Although it seems that the Greek state is moving in this direction [‘*the Canal should not only be a project that facilitates navigation, but also in itself be a visitable destination in order to highlight the overall tourism product of the region*’ (Hellenic Republic, 2022)], at the same time the Ministry of Infrastructure and Transportation approves large-scale interventions for slope stabilisation on the Peloponnese side, without any environmental restrictions under the guise of urgent user safety, sadly causing significant alterations in the physiognomy of this unique monument. Immediate restoration of the canal’s slope to its original form by a reinforced earth wall is required, while any future interventions of this scale will invalidate its monumentality.

Unfortunately, political decisions appear to be driven by development policies, yet they lack a clear strategy for ensuring the long-term viability of the canal. However, it seems that only an alternative management of the Corinth Canal, while maintaining its existing function, creates a development perspective. The production and promotion of a new tourism product is suggested, which will offer an immersive experience and tour of the canal through its historic path. Though it be focused on the Corinth Canal highlighting its monumental qualities and geological features, will also include accompanying monuments (e.g. ancient diolkos, bunkers, new bridges, submersible bridges, etc.). This tourism product would be flexible, catering to different types of tourism (both conventional and alternative), visitor demand, and available time, while ensuring accessibility and safety to visitors of all ages.

The Corinth Canal, a prominent engineering project of the time with an outstanding universal value, is a monumental infrastructure, highlighting how certain structures, while fulfilling necessary functions, transcend their utility and become symbols of cultural identity, history, and human achievement. It should have long since been classified as a recent monument of Greek cultural heritage, fully protected and subject to sustainable interventions under the provisions of Law No. 3028/2002, as in force. In addition, coordinated efforts ought to make the competent bodies so that the area of the Corinth Canal could be designated UNESCO World Heritage Site, recognizing its global significance both historically and culturally, as well as for its geological features. Thinking that *‘monuments have shaped and are still shaping contemporary views on the past*’ (Bußmann, 2019), we marvel at how this monumental, man-made ‘*mega-trench*’ shapes perceptions of the geotectonic processes reflected on its slopes. It is our duty to preserve engineering achievements and historical memory for present and future generations, thereby substantially enhancing our social and cultural identity.

References

Belavilas, N., 2015. On monuments and memory: the material aspects of history, in: Papadimitriou, N., Anagnostopoulos, A. (Eds), The past in the present: Memory, history, and antiquity in modern Greece, 64-82.

Brunke, H., Bukowiecki, E., Cancik-Kirschbaum, E. *et al.*, 2016. Thinking Big. Research in Monumental Constructions in Antiquity. eTopoi - Journal of Ancient Studies, Spec.Vol. 6, 250–305.

Buccellati, F., 2019. Monumentality: Research Approaches and Methodology, in: Buccellati., F, Hageneuer, S., van der Heyden, S., Levenson, F. (Eds), Size Matters – Understanding Monumentality Across Ancient Civilizations, 41-63.

Bußmann, R. 2019. Monumentality in context – a reply from Egyptology, in: Buccellati., F., Hageneuer, S., van der Heyden, S., Levenson, F. (Eds), Size Matters – Understanding Monumentality Across Ancient Civilizations, 99-104.

CorinthCanal, Corinth Canal S.A. (A.E.DI.K.). The Canal - Specifications - The history of the canal - Press release of January 15, 2021, retrieved from: https://corinthcanal.com/the-canal/?lang=en.

Papamanolakis, M., Korinthognosia (YouTube channel). Latest news about the small wagon found in the Corinth Canal, retrieved from: https://www.youtube.com/Papamanolakis.

Dec. 29307/Σ6651/3.2.2021. Ministerial Decision No 29307/Σ6651 3 February 2021, Ministry of Infrastructure and Transportation.

Dec. 103435/6635/9.2.2021. Decision of the G. D. of Env. Policy No 103435/6635 9/12/2021, Ministry of Environment and Energy.

GEMI-Publicity. Financial Reports: A.E.DI.K. S.A., retrieved from: https://publicity.businessportal.gr/.

Gerster, B., 1884. L’Isthme de Corinthe, tentatives de percement dans l’antiquité. BCH, 8, 225-232.

GrowthFund. Corinth Canal S.A. (AEDIK), retrieved from: https://growthfund.gr/corinth-canal-sa/.

Hageneuer, S., van der Heyden, S., 2016. Perceiving monumentality, in: Buccellati., F, Hageneuer, S., van der Heyden, S., Levenson, F. (Eds), Size Matters – Understanding Monumentality Across Ancient Civilizations, 65-89.

Hellenic Republic, 2022. Hellenic Republic, Information note on the visit of Prime Minister Kyriakos Mitsotakis to the Corinth Canal, retrieved from: https://www.primeminister.gr/2022/07/01/29702.

Horn, E.T., Proudfoot, P.R., 2016. Ideas of monumentality in architecture. Quadrant, 60(9), no. 529, 75-80.

Kolaiti, E., Papadopoulos, G.A., Morhange, C., Vacchi, M., Triantafyllou, I., Mourtzas, N.D., 2017. Palaeoenvironmental evolution of the ancient harbor of Lechaion (Corinth Gulf, Greece): Were changes driven by human impacts and gradual coastal processes or catastrophic tsunamis? Marine Geology, 392, 105-121.

Levenson, F., 2019. Monuments and Monumentality – different perspectives, in: Buccellati., F, Hageneuer, S., van der Heyden, S., Levenson, F. (Eds), Size Matters – Understanding Monumentality Across Ancient Civilizations, 17-39.

Ministry of Culture and Sports. Diolkos of Corinthian Isthmus, retrieved from: http://odysseus.culture.gr/.

MIT Center for Advanced Urbanism, 2016. Infrastructural Monument. Princeton Architectural Press.

Mourtzas N., Kolaiti E., 2017. Relative sea level changes on the NE coast of the Peloponnese after the late roman period: the ancient Corinth harbours of Lechaion and Kenchreai, in: D. Katsonopoloulou, D. (ed.), Ancient Helike and Aigialeia: Poseidon God of Earthquakes and Waters Cult and Sanctuaries, 275-308.

Osborne, J.F., 2014. Monuments and Monumentality, in: Osborne, J.F. (ed.), Approaching Monumentality in Archaeology, IEMA Proceedings, 1-19.

Papafotiou, A.E., 2010. The Corinth Canal: a technological miracle of the 19th century, retrieved from: https://www.teepelop.gr/.

Papafotiou, A.E., 2022. The Corinth Canal – a pharaonic intervention with negligible results, retrieved from: https://gnomipoliton.com/2022/.

Papanikolaou, D., Triantaphyllou, M., Pallikarakis, A., Migiros, G., 2015. Active faulting at the Corinth Canal based on surface observations, borehole data and paleoenvironmental interpretations. Passive rupture during the 1981 earthquake sequence? Geomorphology, 237, 65-78.

Papayiannakis, L., 1982. Greek Railways (1882-1910) Geopolitical, economic, and social aspects, MIET.

Pepelasis, I.S., 2010. Entrepreneurial Typologies in a Young Nation State: Evidence from the founding charters of Greek Société Anonymes, 1830-1909. Discussion Paper No 200, Athens Univ. Econ. Business, 1-24, available at: https://www.dept.aueb.gr/sites/.

Pradel, C., 2020. Moving Ground. The Construction of AlpTransit Infrastructure and its Monumental Landscapes, Ardeth, 7, 67-83.

Société Internationale. Numistoria, retrieved from: https://numistoria.com/.

Velitzelos, E., Mountrakis, D., Zouros, N., Soulakellis, N., 2003. Atlas of the Geological Monuments of the Aegean. Ministry of the Aegean, Adam editions.

BULLETIN OF THE GEOLOGICAL SOCIETY OF GREECE, SP. PUBL.

EXTENDED ABSTRACT 155

Synergies for geo- education: materials and initiatives from Psiloritis UNESCO Global Geopark and the Center for Environmental Education and Sustainability of Anogia, (Crete) Greece.

Kolendrianou M .[1], Kefalogianni Z.[2], Kalomoiri A. [2], Fassoulas C. [1,3]

(1) Psiloritis UNESCO Global Geopark, Anogia, Greece, info@psiloritisgeopark.gr (2) Center for Environmental Education and Sustainability of Anogia, Anogia, Greece, (3) Natural History Museum of Crete- University of Crete, Heraklion, Greece

Research Highlights

The present work includes a summary of the main materials used and initiatives undertaken by Psiloritis UNESCO Global Geopark and the Center for Environmental Education and Sustainability of Anogia for the education of children and adults on Geology and Geology- related topics in the area of Psiloritis UNESCO Global Geopark, (Crete) Greece.

Introduction / Background

UNESCO Global Geoparks (UGGps) are single, unified geographical areas with exceptional geological features of international significance. They are managed with a holistic approach towards the protection, education and sustainable development of their territories, adopting a bottom-up approach through the active involvement of their local communities in their efforts (UNESCO, 2024). For any UGGp, education at all levels is one of the main focus areas of its operation (UNESCO, 2015). It is essential for a UGGp to develop and perform educational activities to disseminate knowledge and raise awareness on geodiversity and its connections to biodiversity and other traits of the tangible and intangible cultural heritage, with the purpose to educate and inspire on the significance of the territory and to increase local involvement and engage the audiences into more effective conservation.

Many UGGps form synergies with specialized educational institutions, at the national or local level, to achieve better pedagogical and more widespread results in their initiatives for education. One such example is the cooperation between Psiloritis UGGp and the Center for Environmental Education and Sustainability (CEES) of Anogia. CEESs are an institution of multiple different centers throughout Greece, established by the Greek Ministry of Education, Religious Affairs and Sports as a bridge between the school and society. In the CEESs' philosophy of operation, emphasis is put on the need to raise interest in all forms of life towards the development of an environmental ethic and by linking the education for the environment and sustainability with the need to also instill a system of values.

Objectives

Presently, there are 213 UGGps in 48 countries and, even though they produce numerous and innovative educational materials, the amount of published works on UGGp- education still remains limited in comparison to research on other topics concerning UGGps and with an availability of resources not much broader than that of local implementation and dissemination through conference participation (Martínez-Martín *et al*., 2023). The present work aims to present the materials, programs and digital tools developed and used for education by Psiloritis UGGp and its education partner, the CEES of Anogia, as they are currently being implemented in the area.

Area

Psiloritis Geopark was established in 2001 and since 2015 it has been recognized as a UGGp. It is located in the central part of the island of Crete (Greece) with the mountain of Psiloritis, or ancient Idi (2456m), being the main point of reference for the territory, thus, also providing the name for the Geopark. It has a total area of 1272 km^2, including villages and settlements from 8 different Municipalities and a population of approximately 38.000 residents. The complex topography of the area and the variety of rocks combined with the isolation of the entire island of Crete, make the mountainous mass of the geopark a hotspot for biodiversity and endemism, leading to the inclusion of ~56% of the territory in the European NATURA 2000 Network. The connection of the area with the people has been strong and persistent since the times of antiquity, as can be demonstrated by the numerous findings and monuments spanning from the Minoan era to the Roman times and the many religious and cultural monuments of our days. The intangible cultural heritage of Psiloritis is also worldwide famous with the traditional handicrafts, cuisine, and music being only some of the examples.

Concerning the geodiversity of Psiloritis UGGp, it spans over a period of about 360 million years, with a variety of rocks attributed in 7 different tectonic nappes and ranging from the most common limestones and dolomites to the more rare stromatolites and ophiolites. The fossils of Psiloritis UGGp also bear witness to its history and evolution of life, including findings such as the rare Fodele fossils (corals, brachiopods and bivalves of about 360-300 million years ago) or the most recent fossils from terrestrial vertebrates (dwarf elephants and deer, giant mice from the Pleistocene) as evidence of a special adaptation mechanism to island life.

The geodiversity of the Geopark bears witness to the geological history of the area that has been (and is still being) dominated by tectonism, uplift of the mountains and karstic erosion. Large- and small-scale folds and faults and all kinds of karstic features (surface and subterranean) appear throughout the area of Psiloritis, providing the opportunity for the visitor to find all the evidence that explain the formation of the high mountains and their continuous transformation through the creation of impressive gorges, mystical caves and fertile plateaus, as well as fascinating landscapes.

Results and Discussion

Psiloritis UGGp and Anogia CEES are both institutions with a long history of operation in the area (Psiloritis Geopark was established in 2001 and Anogia CEES in 2006), offering formal and non- formal educational activities in the wider area of Psiloritis. Both organizations have so far informed and trained thousands of students, teachers and also local professionals, residents and visitors. It is characteristically mentioned that for the year 2024, Psiloritis UGGp and Anogia CEES received a total of approximately 1035 children aged 5-18 (students, scouts), with whom educational activities were implemented either indoors or in the field. Most of the developed materials and tools used within this context, could be broadly categorized in the following general thematic categories: Geodiversity, Biodiversity, Human History/ Traditions and Arts, Sustainable way of life. These are briefly presented in the table below (Table) according to the typology of each material that is currently being implemented, its title and a brief description, the thematic category it falls into, whether it's being implemented by the staff of Psiloritis UGGp, Anogia CEES or by the two in cooperation and finally, the age of the audiences each material is addressed to.

Table. Summary of main materials for education implemented by Psiloritis UGGp and Anogia CEES, at the area of Psiloritis UGGp.

#	Typology of material	Title	Brief description	Thematic Category	Partner that implements the activity	Age of targeted audience
1	Multiple	Visit to the Psiloritis UGGp Information Center.	Includes informative and educational materials and small experimental displays, dioramas (cave, mountain ecosystem and traditional house), an exhibition of local products, while there is also a small collection of rocks and fossils from the geopark area as well as digital educational tools and references to the SDGs.	Geodiversity, Biodiversity, Human History and Traditions, Sustainable way of life	Psiloritis UGGp	NS
2	Educational program, field visit, simple experiments, hands- on activities	Meet Psiloritis UNESCO Global Geopark!	Includes a presentation on what is a UGGp and what are its purposes, Geopark networks, examples of geosites from Psiloritis UGGp, interpretation of the main geological processes (complementarily with simple experiments or displays) characteristic of the geodiversity and geological history of Psiloritis UGGp (and Crete), holistic approach of UGGps and links between geodiversity, biodiversity and human history and traditions. The presentation is usually followed by a field visit and/ or worksheets, hands- on activities.	Geodiversity	Psiloritis UGGp & Anogia CEES	NS

3a	Educational program	Where is the water?	Aims to explore the processes of karst erosion that have formed the relief of Psiloritis and the relationship between underground water and water availability/ management issues in the area. It may be followed by a field visit (#3c) in one of the caves of Psiloritis UGGp that are open for visitors.	Geodiversity	Anogia CEES	Kindergarten - mid-Elementary School students
3b	Educational program	When water hugged the stone…				Mid-Elementary-High School students and adult students
3c	Field visit	Discovering the secret world of caves!	This field visit incudes a visit in one of the three open for visitors caves of Psiloritis UGGp, where the students experience the geology of caves and their unique biodiversity and local legends.	Geodiversity, Biodiversity, Human History and Traditions		Elementary-High School students and adult students
4a	Hands-on activity	What makes the most common rock of Psiloritis UGGp special?	This aims to highlight the diversity of karst formations, including posters of caves, gorges, plateaus and karst springs and complementary smaller cards depicting characteristic plants, animals or human activities linked to them, that the students need to “match”. This activity is used independently (during public outreach events) or follows the implementation of #2 or #5a (when there isn’t an option for a field visit).	Geodiversity, Biodiversity	Psiloritis UGGp	Elementary-High School students and adults (during public outreach events)
4b		Threats for mountain ecosystems!	Includes 12 cards with different threats for mountain ecosystems (soil erosion, pollution, habitat fragmentation etc.) with pictures from the territory and different Greek mountains. This activity is used independently (during public outreach events) or follows the implementation of #2 or #5a. It can also be implemented in the field, where the students try to identify in- situ a bad practice from the cards (if present) and discuss if other threats could apply in the territory.	Geodiversity, Biodiversity, Sustainable way of life		
5a	Educational program, field visit, worksheets, hands- on activities	Biodiversity and Psiloritis UGGp.	Includes a presentation on what is a UGGp and what are its purposes, interpretation of geodiversity and biodiversity and how they are linked, introduction to endemic plants and animals of Psiloritis UGGp- mainly focusing on the species’ history and threats. The presentation is usually followed by a field visit and/ or worksheets, hands- on activities in the Information Center or in the field.	Geodiversity, Biodiversity	Psiloritis UGGp	mid-Elementary -High School students
5b		In the land of Amalthea: earth, scent, life!	Includes a presentation on the typical ecosystems of Psiloritis, examples of local biodiversity and endemism, the concepts of diversity in nature and society and familiarization with the scientific approach of studying the natural world. The presentation is usually followed by a field visit and/ or worksheets, hands- on activities in the Information Center or in the field.	Geodiversity, Biodiversity	Anogia CEES	Elementary-High School students and adult students
6	Educational program, hands- on activities	A tale from Psiloritis UGGp!	Includes a presentation on what is geology and what is a UGGp, what could be a geosite and what could not (with visual examples from the territory), who are the people of the Geopark (who studies rocks? what are the main professions of the people in our geopark?), interactive narration of a local myth and activities exploring the characters/ natural setting of the story.	Geodiversity, Human History/ Traditions and Arts	Psiloritis UGGp	Kindergarten - mid-Elementary School students

7	Educational program, worksheets, activity book	How does the natural environment give birth to civilization?	This is a program that aims to highlight the connections between the natural environment of Psiloritis and the cultural heritage of its people, focusing on the local economy and the traditional arts (especially loom weaving).	Geodiversity, Human History/ Traditions and Arts	Anogia CEES	Kindergarten -High School students and adult students
8	Educational program, field visit	Visiting the shepherd's shelter!	This program aims to present the shepherd's way of life in Psiloritis, highlighting the role of the natural environment, through a field visit in a mountain plateau to experientially explore concepts of ecosystem services and visit a mitato (traditional shepherd's refuge built with the dry- stone walling practice).	Geodiversity, Biodiversity, Human History/ Traditions and Arts	Anogia CEES	Kindergarten -High School students and adult students
9	Educational kit	The underground journey of water.	Explores the relationship between limestone and water, the underground journey of water through the rocks, the formation of karst structures and the ecosystems and biodiversity found in them. The kit includes theoretical background for the teacher, instructions and materials for different activities e.g. crosswords, board games.	Geodiversity, Biodiversity	Psiloritis UGGp	Elementary -High School students
10	Educational kit	Climate Change and Island Geoparks.	Explores themes such as climate change, the "footprint" of the modern lifestyle and the natural phenomena associated with the effects of these factors. The kit includes theoretical background for the teacher, instructions and materials for different activities e.g., card- games, board game.	Sustainable way of life	Psiloritis UGGp	Mid Elementary -High School students
11	Digital tool	e-Geodiscover app (available for two different geo-trails)	This is an app for mobile devices (smartphones, tablets) that aims to provide knowledge about the geology, culture and environment of the geopark, as well as map reading, orientation and navigation skills, in the form of a pop-up "hidden treasure" quiz, which the child follows along an easy and smooth short route in the area of the Stefana plateau (Mygia's geo- trail) and/or in Gonies geo- trail.	Geodiversity, Biodiversity, Human History/ Traditions and Arts	Psiloritis UGGp	NS
12	Network for collaboration on education	National Thematic Network entitled "Feeling the memory of the Earth through geodiversity, Geoparks and anthropogenic activities"	Anogia CEES has established this Thematic Network with the aim to connect teachers and educators all over Greece, interested in topics related to geodiversity and UGGps and keep them engaged through a series of actions and initiatives (trainings, production of textbooks and education material etc.).	Geodiversity, Biodiversity, Human History/ Traditions and Arts	Anogia CEES	Teachers of all levels, Educators
13	Training seminars, field visits	Multiple themes	Both partners design, organize and implement training seminars (many times jointly) addressed to adult professionals of the area (e.g., teacher trainings, seminars for local producers). These seminars usually include a series of theoretical presentations from experts, followed by field visits to experience the examples and good practices, regarding each topic.	Geodiversity, Biodiversity, Human History and Traditions, Sustainable way of life	Psiloritis UGGp & Anogia CEES	Adults

14	Public events	Multiple themes	Both partners design, organize and implement public events (many times jointly), addressed to issues that concern the local communities with the purpose to responsibly inform and sensitize them. These events may concern public talks on Natural heritage & Conservation, Natural Hazards, debates on Clean Energy etc. and on many occasions they are organized within the context of International Days.	Geodiversity, Biodiversity, Human History and Traditions, Sustainable way of life	Psiloritis UGGp & Anogia CEES	NS
15	Partnerships-synergies	Multiple partnerships	Both partners have a close cooperation between each other, but they have also developed numerous synergies with other Educational/ Research Institutions over the years to further support their initiatives concerning education.	Geodiversity, Biodiversity, Human History and Traditions, Sustainable way of life	Psiloritis UGGp & Anogia CEES	NS

NS: Not- Specified (for "Age of targeted audience"), when there is no limit to the age of the targeted audiences to whom the material/ activity is addressed to, but is modified for different ages and situation of implementation (educational activity, public outreach event etc.).

Figure 1. Picture from a school visit in the geosite Petradolakia after an educational program at CEES of Anogia (left) and at the geosite Vossakos Folds during a three-day teacher- training seminar in 2019, within the context of the National Thematic Network of CEES of Anogia "Feeling the memory of the Earth through geodiversity, Geoparks and anthropogenic activities" with the cooperation of Psiloritis UGGp (right).

Based on the quantity and multidisciplinarity of the materials provided for geo- education and geology- related topics in Psiloritis UGGp (Table), it becomes once again evident that these territories are important loci for the interpretation and education on themes and phenomena related to the formation and conservation of the natural world. In Psiloritis UGGp, educational activities are implemented by the staff of the organization as well as by the Anogia CEES, one of the geopark' s partners for education within the territory. Interestingly, even though the educators in the CEES of Anogia are not trained geologists, they have exhibited a consistent passion for geo- education since the early years of their operation, recognizing the importance of the local geodiversity and promoting it through the numerous education programs and initiatives they implement (Table). The excellent cooperation between Anogia CEES and Psiloritis UGGp has provided high- quality (scientifically and pedagogically) education materials and initiatives, educating an overall of approximately 10.000 students and 5.000 teachers on relevant topics (Fig. 1) in the territory so far (data from Anogia CEES).

Both organizations have developed and are implementing activities in the form of complete and structured educational programs or individual materials (activity books, short experiments etc.) for students of different levels, but also adults that may be university students, teachers or professionals of the area, receiving training on Geopark- related subjects in the form of workshops. Other forms of education initiatives may include field trips, textbooks and other activities performed during special occasions (i.e., celebration of International Days, special visits etc.) (Catana & Brilha, 2020; Rossi et al., 2022) also potentially aiming at locals or visitors, within the context of communication/ public outreach- that share some goals and principles with education- on what concerns the interpretation of the natural world of a territory (Crofts et al., 2020).

A wide range of pedagogical techniques is embedded in these educational activities: step-based education, familiarization and empowerment games, field studies, observation and orientation games, experiments that visualize natural processes, inquiry-based learning and many more, while at the same time they enhance critical thinking, cooperation between students/ student groups, and empirical knowledge. The multidisciplinary approach and the promotion of links between themes is obvious in most materials while the successful communication between the organizations itself can be seen in the complementarity of some of the materials/ initiatives e.g., the CEES of Anogia has a greater experience in organizing training seminars for teachers and educators and Psiloritis UGGp has a larger set of options of digital tools (Tab. #11; Fig.2; Fassoulas *et al.*, 2022). All the above observations (quantitatively, qualitatively) generally agree with findings and conclusions from Catana & Brilha (2020) and Rossi *et al.*, (2022) on the mode of how educational tools and activities are designed and executed in most geopark territories.

Furthermore, with reference to the seventeen United Nations Sustainable Development Goals (SDGs), the potential of the tools presented here can easily be grasped within the context of SDG 4 “Quality Education” and SDG 17 “Partnership for the Goals”. Additional SDGs can also be observed in, for example, materials #4b- 5b (Table) that are clearly linked to SDG 15 “Life on Land” and material #10 (Table) that is linked to SDG 13 “Climate Action”. Furthermore, other stand- alone activities and individual actions from initiatives #13, 14, 15 (Table)- that are not mentioned here in detail for reasons of space availability and overall relevance- are directly related to SDGs focusing on the triplet People- Prosperity- Planet. This further underlines the role of UGGps as areas for the promotion of the natural sciences but, also, sustainability (Catana & Brilha, 2020; da Silva, 2020).

Figure 2. Picture from a school visit where the e-Geodiscover app was used by students following Mygia’s geo-trail.

Conclusions

Geology is all around us through the rocks and minerals that we use, the processes that shape our surroundings and the very substrate we walk on! However, as a scientific field, it unfortunately still remains rather unpopular and non-understandable by most of the public. UGGps as organizations and as territories are, indeed, playing a significant role addressing this issue, since they have the background and experience to “translate” this often-inaccessible knowledge for the local communities (students and adults) in a way that is scientifically and pedagogically appropriate. Thus, educational tools developed and implemented in UGGp territories, especially in cooperation with local educational partners, are numerous, innovative and extremely useful if one considers the overall limited and very much needed interpretive and teaching resources on geology for the more effective protection of this aspect of the natural heritage of our territories. Extending the conversation to other relevant issues of sustainability such as the climate crisis, natural hazards, water availability and many more, we could find ourselves in the position to also inform, sensitize, engage, and prepare members of local communities on matters that are extremely pressing nowadays. The impact of this effort increases significantly if we, as organizations, share all these tools and practices within our networks and more broadly into the scientific community and other conservation organizations and protected areas, with whom we share the same goals.

References

Catana, M. M., Brilha, J. B., 2020. The role of UNESCO global geoparks in promoting geosciences education for sustainability. Geoheritage 12 (1), 1.

Crofts, R., Gordon, J.E., Brilha, J., Gray, M., Gunn, J., Larwood, J., Santucci, V.L., Tormey, D., Worboys, G.L., 2020. Guidelines for geoconservation in protected and conserved areas. Best Practice Protected Area Guidelines Series No. 31. Gland, Switzerland: IUCN.

da Silva, E. M. R., 2020. The contribution of the European UNESCO Global Geoparks for the 2030 Agenda for Sustainable Development–a study based on several data sources. Ph.D. Thesis, Universidade NOVA de Lisboa, Portugal, 344p.

Fassoulas, C., Nikolakakis, E., Staridas, S., 2022. Digital tools to serve geotourism and sustainable development at Psiloritis UNESCO Global Geopark in COVID times and beyond. Geosciences 12 (2), 78.

Martínez-Martín, J. E., Mariñoso, P. E., Rosado-González, E. M., Sá, A. A., 2023. UNESCO Global Geoparks vs. Education: A 10-Year Bibliometric Analysis. Geoheritage 15(1), 34.

Rossi, G.S., Motta Garcia, M.G., Marie Bourotte, C.L., 2022. Educational Materials on Geosciences: Analysis from UNESCO Global Geoparks and Potential for Application to Protected Areas. Geoconservation Research 5(2): 165-194.

UNESCO, 2015. Operational Guidelines for UNESCO Global Geoparks. https://unesdoc.unesco.org/ark:/48223/pf0000391354. Accessed 21 January 2025.

UNESCO, 2024. UNESCO Global Geoparks (UGGp). https://en.unesco.org/global-geoparks. Accessed 21 January 2025.

17th INTERNATIONAL CONGRESS
of the Geological Society of Greece

BULLETIN OF THE GEOLOGICAL SOCIETY OF GREECE, SP. PUBL.

EXTENDED ABSTRACT 156

The Role of Fairy Tales in Fostering Geoscience Understanding in Early Childhood

Kolyva P. [1], Koumoutsakou O.[1], Antonarakou A.[1]
(1) Department of Geology and Geoenvironment, Kapodistrian University, Athens, Greece, pavlinak03@yahoo.com

Introduction

Storytelling through oral traditions has long been a powerful way to pass down cultural values and beliefs while nurturing imagination and creativity in children. Similarly, children's literature plays a pivotal role in education by effectively blending learning with entertainment (Pulimeno et al., 2020). This research is a small case study in which the use of fairy tales and storytelling, in general, is examined to understand geoscience and its subsections, such as earthquakes. Regarding the utilization of fairy tales as instructional resources, an extensive examination of a wide range of fairy tales was undertaken, focusing on their various attributes and potential educational significance. A fairy tale about earthquakes was created and evaluated with primary school children.

The Evolution and Impact of Fairy Tales: From Cultural Narratives to Educational and Scientific Insights

Fairy tales stimulate creativity and emotional development by embodying deep themes, offering comfort and security even when exploring conflict or danger. They nurture emotional intelligence, impart moral lessons, and inspire critical thinking. These stories are vital tools for fostering creativity, moral maturity, and thoughtful engagement with the world. (Bakaraki et al., 2018).

Fairy tales have transitioned from oral traditions to a significant presence in mass media, with geomythology—a field studying myths tied to geological phenomena—revealing how narratives about earthquakes, tsunamis, and volcanic eruptions reflect cultural efforts to explain natural events (Rahman, 2017; Dewi, 2024; Piccardi & Masse, 2007; Vitaliano, 2007). These myths, often holding sacred and cultural significance, provide valuable insights into geological science and resilience-building, especially for children living in areas prone to natural disasters (Dewi, 2024). Local myths have also contributed to addressing geological challenges, with geological terminology itself drawing inspiration from mythological figures (Vitaliano, 2007). Prominent authors like Jules Verne, Arthur Conan Doyle, and H.P. Lovecraft have integrated geological concepts into their adventure and fantasy literature, illustrating how literature can blend science and storytelling (Gargallo, 2023).

Research Methodology:

The research was conducted as a small-scale case study involving a class of 20 second-grade students from a primary school in Vasiliko Evoias, Greece. The prototype fairy tale was introduced during the school's annual earthquake drill. Data collection methods included direct observation, semi-structured interviews with the teachers, and a post-activity reflection task using visual prompts tailored for children. The research aimed to evaluate student engagement, their conceptual understanding of earthquakes, and their emotional response to the narrative.

Developing a Prototype Fairy Tale to Educate Children About Earthquakes

The initial phase of this research involved an exploration of effective strategies for the implementation of fairy tale-based instruction within the context of elementary science classrooms (Kwon & Lee, 2010). To investigate the pedagogical effectiveness of fairy tales in geoscience education, a prototype fairy tale was developed specifically for preschool and elementary school-aged children. This narrative addresses the phenomenon of earthquakes, emphasizing the importance of preparedness and mitigation strategies to minimize potential damage, destruction, and human loss. The protagonist of this tale is a small rock named Rhea, who embarks on a journey to the Earth's surface to convey an urgent message about an impending earthquake.

The prototype fairy tale was introduced to elementary school students during their annual earthquake drill. Teachers observed that the students were highly engaged throughout the process. The classroom was soon filled with exciting questions and discussions about earthquakes, sparked by the captivating story. The fairy tale not only ignited children's imaginations but also stimulated their critical thinking skills, helping them understand the appropriate actions to take during an earthquake. Importantly, these results demonstrate that incorporating fairy tales into children's education can effectively cultivate valuable character traits.

Mitigating the Risk of Misconceptions

To prevent the development of misconceptions, the fairy tale content was co-reviewed by a geoscience expert and an early childhood education specialist. Scientific elements, such as the causes of earthquakes and safety measures, were presented clearly and accurately within the fictional framework. Educators facilitated follow-up discussions to reinforce key concepts and clarify any confusion that might arise between fiction and scientific fact.

Discussion of Results

Teachers reported increased attentiveness and participation from students, indicating the effectiveness of the narrative-driven approach. Many students could accurately recall appropriate earthquake safety measures, such as "Drop, Cover, and Hold On," and showed greater confidence in discussing natural disasters. Some students even shared how they planned to inform family members about what they had learned. These findings suggest that the integration of storytelling not only supported cognitive learning but also fostered emotional readiness and resilience. The use of relatable characters like Rhea helped students better internalize abstract scientific ideas, which is consistent with previous research emphasizing the benefits of narrative pedagogy (Dewi, 2024; Fleer, 2013).

Enhancing Scientific Learning and Motivation Through Fairy Tale-Based Pedagogy

This research revealed that students effectively connected fairy tales to their personal experiences and actively engaged in classroom activities incorporating them. Many expressed increased interest in science classes, attributing this to the engaging nature of the fairy tale-based approach. This method not only motivated students to study diligently but also facilitated a deeper understanding of scientific concepts in context.

The study concluded that instruction using fairy tales is an effective pedagogical approach that enhances learning motivation, fosters scientific inquiry, provides opportunities to apply scientific concepts, and cultivates a positive attitude toward science.

Conclusion

Recognizing the crucial role of imagination in early childhood science education is vital (Fleer, 2013). Children's literature and storytelling could help promote "*students' global development and well-being when included in school curricular activities*" (Pulimeno, et al., 2020). This study offers promising evidence that integrating scientifically accurate storytelling into early education can not only reduce fear and confusion about natural disasters but also lay the groundwork for informed and resilient future citizens. Further research with larger samples and longitudinal follow-ups is recommended to explore the long-term impact of this approach.

Acknowledgments

I would like to express my sincere gratitude to the teachers and elementary school children who have given their time to be respondents in this research, to my professor for her invaluable guidance, and to my sister for her significant contributions throughout the project.

References

Bakaraki, M.P., Dourbois, T., Kosiva, A. (2024). Therapeutic and developmental benefits of fairy tales in early childhood: A mini-review. Brazilian Journal of Science, 3(8), 19-23. https://doi.org/10.14295/bjs.v3i8.600

Dewi, D.J.K. 2024 Storytelling to develop resilience in early childhood in facing earthquake disasters. Proceedings of the International Conference on Current Issues in Education (ICCIE 2023), Atlantis Press, pp. 410-420. Doi: 10.2991/978-2-38476-245-3_43

Fleer, M. (2013). Affective Imagination in Science Education: Determining the Emotional Nature of Scientific and Technological Learning of Young Children. Research in Science Education, 43, 2085-2106. https://doi.org/10.1007/S11165-012-9344-8

Gargallo, J. (2023). Geology and literary fiction. BOLETÍN GEOLÓGICO Y MINERO. https://doi.org/10.21701/bolgeomin/134.1/004

Kwon, N., & Lee, K. (2010). The Development and Application of Strategies using Fairy Tales in Elementary School Science Instruction. Journal of the Korean Association for Research in Science Education, 30, 1-12. https://doi.org/10.14697/JKASE.2010.30.1.001

Piccardi, L., & Masse, W. (2007). Myth and geology. Geological Society, London, Special Publications, 273, 366-368. https://doi.org/10.1144/GSL.SP.2007.273

Pulimeno, M., Piscitelli, P., Colazzo, S. (2019). Children's literature to promote students' global development and well-being. Health Promotion Perspectives, 2020, 10(1), 13-23. https://hpp.tbzmed.ac.ir/Article/hpp-31914

Rahman, F. (2017). The Revival of Local Fairy Tales for Children Education. Theory and Practice in Language Studies, Vol. 7, No. 5, pp. 336-344. http://dx.doi.org/10.17507/tpls.0705.02

Sherbaeva, Z. (2021). Fairy Tales World Specifics in the Perception of a Child. Bulletin of Science and Practice. https://doi.org/10.33619/2414-2948/69/36

Vitaliano, D. (2007). Geomythology: geological origins of myths and legends. Geological Society, London, Special Publications, 273, 1 - 7. https://doi.org/10.1144/GSL.SP.2007.273.01.01

BULLETIN OF THE GEOLOGICAL SOCIETY OF GREECE, SP. PUBL.

EXTENDED ABSTRACT 157

Application of the educational proposal for geoscience: geology in secondary education through educational geopaths in the urban environment

Kontokostas G.E.[1,], Antonarakou A.[1]

(1) National and Kapodistrian University of Athens, Faculty of Geology and Geoenvironment, Panepistimiopolis, Zografos, Greece, geokon@geol.uoa.gr

Introduction / Background

The research project, entitled: An educational walk in the historical centre of Athens, is an innovative educational proposal that approaches different scientific fields in an interdisciplinary way. Conducted as part of the research work (project) by 14 school girls and 13 school boys of secondary education of the high school, during the second semester of the 2019-2020 school year. In addition to the historical, social and literary approach to the selected sites, this educational process uses the area around the square in Monastiraki in the light of urban geology and can increase children's knowledge and improve their attitude towards geosciences.

1. Background and Objectives

A route guide was prepared by the students, in which each site, along with its historical and cultural characteristics, describes the geological and hydrological potential of the area.

In the course of the educational process, using techniques entailed in the scientific/educational methodology by inquiry, suggesting educational walking paths through the historical center of Athens, (Dermott, L.,1996), Selected places of the walk trail served our educational aims: Ag, Asomaton-Monastiraki-Eridanos-Stoa of Attalos-Roman Agora –Hadrian's Library-Kapnikarea.

The locations chosen for the route served our educational purposes. I am referring, for example, to the optimal understanding of the formation of rocks, the recognition of the type of rocks, information on the geological and hydrographic potential, in pupils of the Secondary Education of Attica.

2. Research Methodology

The research sample consist of 14 school girls and 13 school boys of secondary education of the high school. In this research the educational aims for the students were: a) to recognize rocks b) to be informed about geological and hydrological potential, and finally, c) to understand the geological notions in time and in space, that means to recognize the geological time and to comprehend the rock cycle (Kaliet al.,2003). The educational goals of our proposal were: a) to inform students about the urban environment of Attica, b) to show that geology is an attractive and important science, c) to study geological phenomena with an interdependence procedure with geosciences and d) to view physical phenomena with a holistic approach, improving students' ecological consciousness.

In this work, we attempted to follow research steps, (Kalkanis, 2010) set forth by inquiry-based learning (Dermott, 1996) : a) trigger for interest, b) reminder of basic knowledge/formulation of hypotheses, c) experimentation/trials, d)formulation of conclusions, e) applications/generalization according to learning.

Trigger of interest (step 1) : Initially, the students visited the exterior and interior of the Temple of Kapnikarea, where they noted with interest the diversification of the rocks and the geological relief of the area.

Reminder of basic knowledge/formulation of hypotheses: Then the necessary knowledge was presented in the way presented by the relevant school lesson of the analytical program (orogenesis, types of rocks) and by the most widely used international reference books (Kali, 2003, Tillery, 1996), - ways of rock formation and the cycle of rocks, so that the pupils could formulate hypotheses. Then, the male and female students completed an appropriately coded questionnaire (pre-test), (Bakopoulou, 2016). The pre-test examined if the students are informed of the geological and hydrological potential of the area , if they could recognize rocks (marbles, granites, limestone and fossils) and if they know the rock cycle.

Experimentation/trials: After studying the relevant literature (Bouras, 2017), the students researched the area and the sites through the internet, collecting historical, cultural and geological information, and visited the places around the area of the square in Monastiraki. They revisited the sites, observed and studied the stones with the aid of a magnifying glass in different buildings. Then they selected sites of hydrological interest (rivers, wells) and of geological interest, combining building materials (limestone, marble and granite).

Formulation of conclusions: Then, we asked the students to summarize their conclusions and to write down observations and comments. Finally, they designed a suitable route with the selected locations and entered it in a mobile application with all the relevant information.

Applications/generalization according to learning: The successful completion of the students' survey prompted them to suggest additional routes in the surrounding area. Finally, we asked them (increasing the difficulty further) to generalize their conclusions by interpreting the creation of other sedimentary, siliceous and metamorphic rocks. They also completed a post-test questionnaire.

3. Results

The control group was also the experimental group. After the questionnaires were deleted (pre-tests are different from post-tests), the answers and observations were compared, and the following was recorded as regards the main research questions and objectives: In general, the pre-tests showed difficulties in identifying the different rocks, in understanding the geological processes and the cyclicity of the rocks. On the contrary, their responses to the post-test after the completion of the project and following the methodological steps, showed that all the students had understood the geological processes and the cycle of rocks in geological time, had the ability to recognize rocks and learned about the geological and hydrological potential of the area (Figure 1).

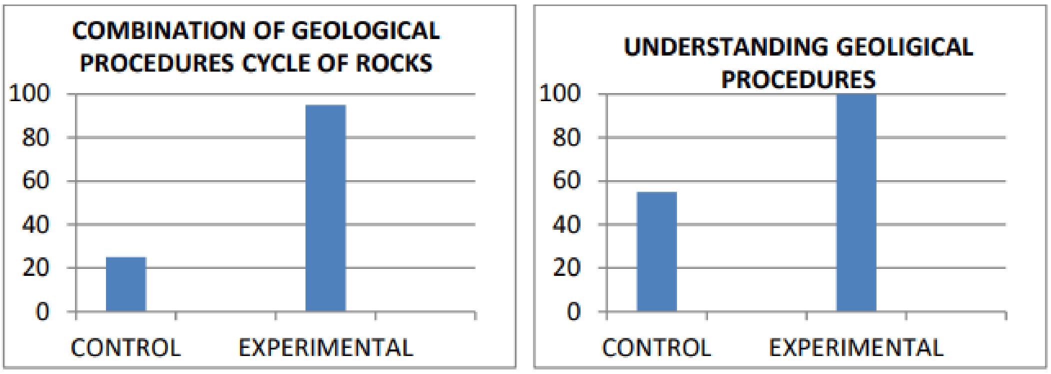

Figure 1 a. We observed an improvement in a) the understanding of geological processes by the pupils (%) and (b) the combination of geological processes in the rock cyclicity by the pupils (%), before and after the teaching intervention, respectively.

4. Conclusions

The results of the post-test show that all the pupils in the class understood the geological processes (Figure 1a) and the rock cycle (Figure 1b). The children's own design of the georoutes proved to be functional and highly useful in terms of understanding and interpreting the phenomena involved. After the educational intervention the pupils improved their geological knowledge, developed their critical thinking, their creativity and found the science of geology interesting.

Figure 2 A mobile app that acts as a compass for our route.

References

Καλκάνης, Γ.Θ., 2010. ΕκΠαιδευτικό ΕΡΓΑΣΤΗΡΙΟ και ΕκΠαιδευτικές ΤΕΧΝΟΛΟΓΙΕΣ, Ι. το Εργαστήριο, ΙΙ. οι Τεχνολογίες, Αθήνα (in Greek).

Bakopoulou, A., Antonarakou, A., Loizos, S., Zambetakis –Lekkas, 2016. Development and precodification of a lithosphere questionnaire as a tool in educational research (Geosciences). Bulletin of the Geological Society of Greece, 50(1), 201-208 https://doi.org/10.12681/bgsg.11720

Bloom, B.S. (Ed.), 1984. Taxonomy of educational objectives. 1: Cognitive domain. White Plains, Longman, NY.

Bouras, Ch., 2017, Byzantine Athens. 10th-12th centuries, Routledge – Benaki Museum, Athens.

Dermott, L.,1996. Physics by Inquiry: Physics Education Group University of Washington, Washington.

Kali, Y., Orion, N. & Eylon, B-S, 2003. The effect of knowledge integration activities on students' perceptions of the Earth's crust as a cyclic system. Journal of Research in Science Teaching, 40(6), 545–565.

Manion, L, Cohen, L., and Morrison, K., 2000. Methodologia ekpaideftikis erevnas, publ. Metaixmio, 737 pp. (in Greek), Athens.

Zervopoulou, A., Pavlides, S., 2016. Geological mapping in urban areas. a case study from the inner city of Thessaloniki, Greece. Bulletin of the Geological Society of Greece, 50 (2), 1027-1023 https://doi.org/10.12681/bgsg.11807.

17th INTERNATIONAL CONGRESS
of the Geological Society of Greece

BULLETIN OF THE GEOLOGICAL
SOCIETY OF GREECE, SP. PUBL.

EXTENDED ABSTRACT 158

Interpretation of CPTu data for mining slope stability assessment in reclamation projects: The case of pit Lake Most, Czech Republic

Kontopidis O.N.[1], Theocharis A.I.[2], Koukouzas N.C.[3], Burda J.[4,5], Zevgolis I.E.[1]

(1) School of Mining and Metallurgical Engineering, National Technical University of Athens, Greece izevgolis@metal.ntua.gr *(2) Department of Civil Engineering, University of Patras, Greece (3) Chemical Process & Energy Resources Institute, Centre for Research & Technology Hellas, Athens, Greece (4) Brown Coal Research Institute (VUHU), Most, Czech Republic (5) Faculty of Mining and Geology, VSB Technical University Ostrava, 17 Listopadu 2172-15,70800 Ostrava, Czech Republic*

Spoil heterogeneity poses geotechnical challenges during mine reclamation. CPTu data-driven slope stability analyses are crucial for safe and effective restoration.

Introduction

During the last decades, coal (also in the form of lignite) has been the main raw material for electricity production. The leading European producing countries include Germany, Czech Republic, Poland and Greece (BGR, 2014, Euracoal, 2017, EY, 2014). Due to the climate crisis, lignite mines have now entered a final phase in Europe and worldwide, heading towards decarbonization. As the transition to the post-lignite era is underway, the choice of land use after mine closure is a crucial decision, and must obviously be in line with the expectations of local communities and with the principles of sustainable development (Pavloudakis *et al*., 2009).

One of the most common practices of restoring a mine is the formation of a lake within its excavation. The creation of lakes can be done either artificially or naturally through hydrological processes, such as rainfall or groundwater infiltration. Lakes offer local communities social, recreational, ecological and economic benefits by landscaping and revegetation, creating aquatic life and maintaining water quality. However, the creation of lakes in lignite mines may cause instabilities and landslide phenomena, with social and economic consequences (Zevgolis *et al*., 2019). The elevation of the aquifer during flooding affects the stability of the slopes by increasing the water pressures of the submerged soil pores. However, increasing the water body within open excavation also acts as a supporting force, and lake creation has been reported to improve slope stability as lake height increases (Kontopidis *et al*., 2022).

The surface exploitation of lignite requires the extraction, transport and deposition of the overlying intermediate soil layers called spoil materials (spoils). According to estimates, spoil heaps reach 1.45 Gt annually worldwide (Bian *et al*., 2012). The disposal spoil takes place mainly in areas where the mining phase has been completed, so that there is the possibility of restoring the paid areas with the aim of minimal environmental impact during the transition to the post-lignite era. The variability of their characteristics and the absence of good deposition practices result in geotechnical problems, including slope stability issues, which need to be investigated both during the deposition phase and during the restoration phase of the area.

This work deals with the assessment of stability issues in the area of the artificial lake Most in the Czech Republic, which was formed in a former surface lignite mine with an average excavation depth of 100 m. At the current boundaries of the lake, spoil materials were deposited during the operation of the mine, forming artificial slopes. Due to the uncertainty about the properties of spoil, 24 cone penetration tests were performed around the lake by measuring pore pressure (CPTu) at depths up to 50 m, mainly within spoils. Raw test data were used to evaluate them and estimate undrained shear strength (c_u) based on empirical correlations. The stability analysis was performed using the commercial software Slide2 applying the limit equilibrium method.

CPTu raw data interpretation

In 2020, 5 years after the final elevation of the lake Most, 24 CPTu were performed with measurement of pore pressures, at depths up to 50 m. The purpose of the tests was to investigate and identify adverse soil conditions in terms of lake's banks stability. Figure 1 shows a sketch of Lake Most (floor plan) with the relative locations of the CPTu tests. A star symbol indicates test P20 whose primary results are shown in Figure 2. CPTu raw data consist of cone tip resistance (q_c), sleeve friction (f_s), friction ratio (R_F) and pore water pressure (u_2). Cone tip resistance (q_c) is observed to increase with depth smoothly from 2 MPa at the surface to 5 MPa at the depth of 40 m and then increase relatively sharply up to 15 MPa. Local peaks, such as those occurring at depths of 22 m, 33 m and 45 m, may be due to the presence of isolated conglomerates which momentarily hinder the advance of the cone. Sleeve friction (f_s) shows a similar increase from 0.1 MPa on the surface to 0.2 MPa at a depth of 40 m and in the last 10 m increases sharply to 0.6 with 0.8 MPa. The friction ratio (R_F) varies from 2% to 6%, while two peaks of 10% are observed at 15 m and 25 m. In the first 20 m the average R_F value is about 3.5%, while from 20 m to 45 m the average value increases to 5%. Pore water pressure (u_2) shows a small rate of increase up to 120 kPa at a depth of 40 m with no local peaks.

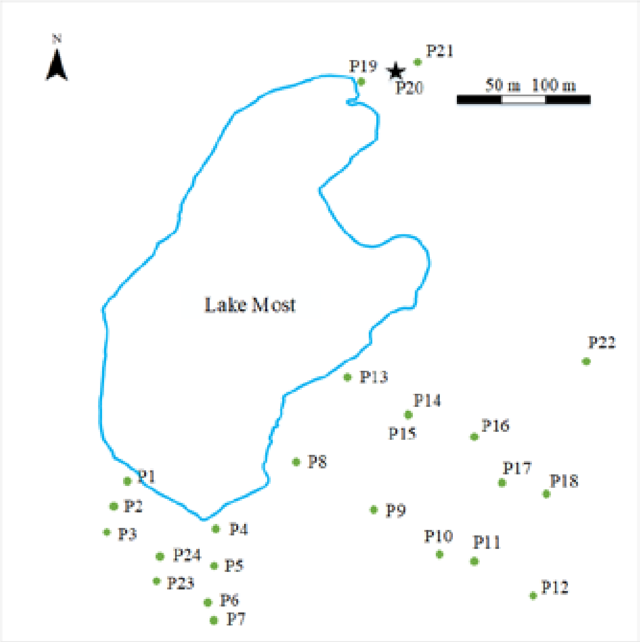

Figure 1. Overview of the lake Most with the locations of the CPTu tests.

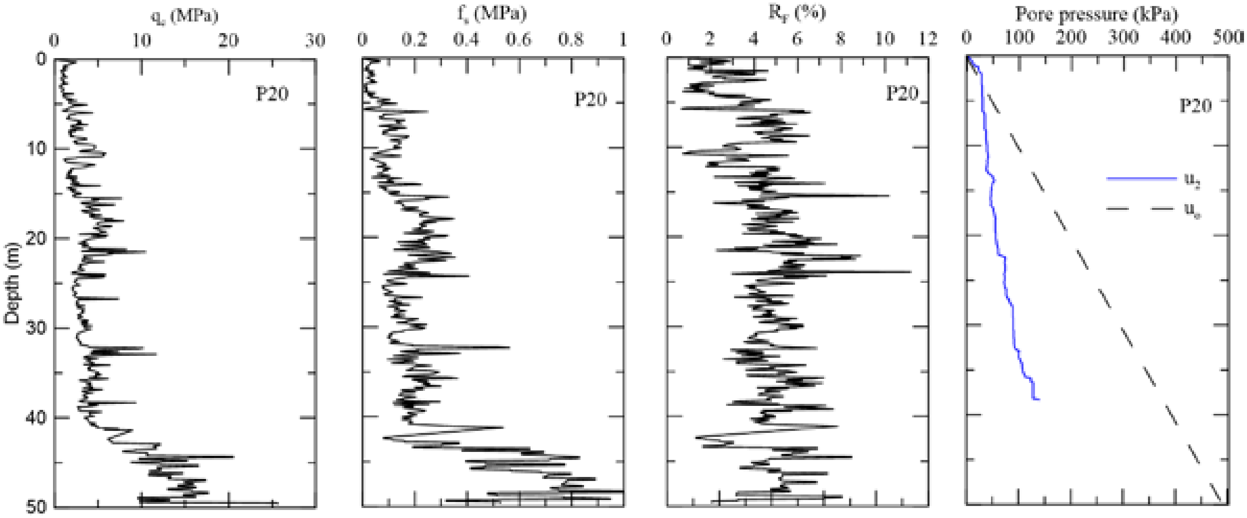

Figure 2. Measurements of q_c, f_s, R_F, and u_2 with depth for test P20.

The measurement of pore pressure allows for improved interpretation of soil conditions. In particular, several diagrams have been proposed for the determination of soil types by CPTu using the combined overburden stress (σ_v)-corrected total tip resistance (Q_t), overburden stress-corrected sleeve friction (F_r), and pore pressure, u_2. In this paper the following I_c index is used (Robertson, 2009, Mayne, 2014):

$$I_c = ((3.47 - \log Q_t)^2 + (\log F_r + 1.22)^2)^{0.5} I_c = ((3.47 - \log Q_t)^2 + (\log F_r + 1.22)^2)^{0.5} \quad (1)$$

Figure 3 presents the soil classification as a function of depth for the P20 test according to the I_c index. The values on the horizontal axis correspond to specific values of I_c associated with specific soil types. Up to 5 m sandy silty and silty sand are the main soil type and then up to 10 m sandy silt/silty sand. At a depth of 10 m to 42 m, clay prevails with sporadic silty layers. In the last 8 m, until the end of the test, silty clay is returned. Generally based on the 24 CPTu, the soil type mainly in fine-grained soils, i.e. silt, silty clays and clays.

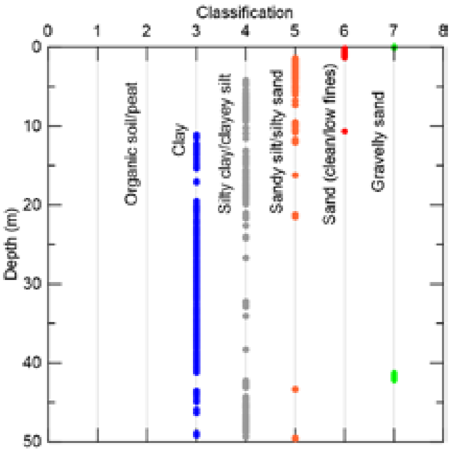

Figure 3. Soil classification using I_c index for test P20.

The undrained shear strength (c_u) is calculated based on the values of pore-pressure-corrected cone resistance (q_t):

$$c_u = \frac{q_t-\sigma_{vo}}{N_{kt}}c_u = \frac{q_t-\sigma_{vo}}{N_{kt}} \quad (2)$$

where N_{kt} is a factor taking values 10 to 18. In the context of this analysis, the mean value N_{kt}=14 was used (Robertson, 2009). Initially, a regression analysis of the q_t population was performed where a trendline equation was derived:

$$q_t = 0.12D + 1.27\ (\mathrm{MPa})q_t = 0.12D + 1.27\ (\mathrm{MPa}) \quad (3)$$

where D is the depth.
The equation (2) was used for the function of undrained shear strength (c_u). For the calculation of total stress σ_{vo} a constant value of unit weight γ=18.2 kN/m³ was considered as the population mean. Figure 4 illustrates the change of c_u with depth. Therefore, the mean function (c_u) is obtained:

$$c_u = 7.27D + 90.7c_u = 7.27D + 90.7 \ (c_u \text{ in kPa, D in m}) \quad (4)$$

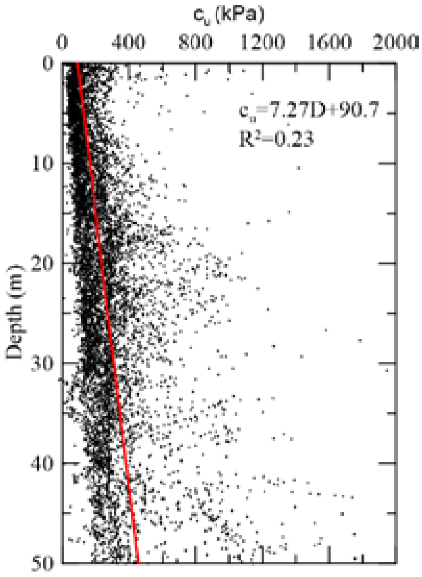

Figure 4. Variation of c_u as a function of depth.

Slope stability analysis

Slope stability analyses were performed with Slide2 software (Rocscience, 2019). The strength of spoils is determined by the function c_u=7.27D+90.7 (Eq. 4). Figure 5 illustrates a typical slope model considered for stability analysis. Specifically, the analyses are performed on two-layer slopes of (H) 100 m and inclination (β) 11°, where a clayey layer with φ´=9.5° and c´=57 kPa underling spoils. An unfavorable condition in lignite mines, usually, is the presence of weak zones at the marl-lignite or between the layers of lignite. In this work, an inclined (β_z=3°) weak zone is located at the base of spoils with low strength (φ´= 6°, c´= 6 kPa) is considered (Mikroutsikos *et al*., 2021). This weak zone was simulated with a weak layer interface condition (proposed in limit equilibrium analysis to simulate narrow layers or interfaces with low strength) through software tools (Rocscience, 2023). Table 1 shows the strength values for the layers considered in the slope model.

Table 1. Input strength values.

Layer	**Strength**
Spoils	c_u=7.27D+90.7
Weak zone	φ´= 6°, c´= 6 kPa
Clay	φ´= 9.5°, c´= 57 kPa

The analyses used the advanced method “cuckoo” search for non-circular surfaces, which does not require the surface to be determined from the outset, but determines it through linear sections and optimization of solutions. To calculate the safety factor, the Spencer method was used, which satisfies the equations of equilibrium of both forces and moments. The Mohr-Coulomb failure criterion was used to determine the shear strength of the clayey layer and the weak zone. The lake was considered to have been filled by about 1/3 (so the ratio of the level of the lake (H_w) to the height of the slope is H_w/H = 0.3) as the most critical condition for the stability where the safety factor (FS) becomes minimal (Zevgolis *et al*., 2021). Finally, steady-state flow conditions were considered with the water table defined by H'_w = 0.1H at the left limit of the slope and the height of the lake on the right.

Figure 6 illustrates the non-circular/bi-linear failure surface which travels along the weak zone and daylights at the toe of slope. The safety factor (FS) is equal to 1.19, which is deemed tolerable for temporary mining slopes. However, this value is insufficient for civil engineering slopes, especially when considered in the context of reclamation projects, where a minimum FS of 1.4 is required. This higher standard is crucial to ensure the stability and safety of the slopes in the long term, as reclamation projects often involve the restoration of disturbed land and the safeguarding of the surrounding environment.

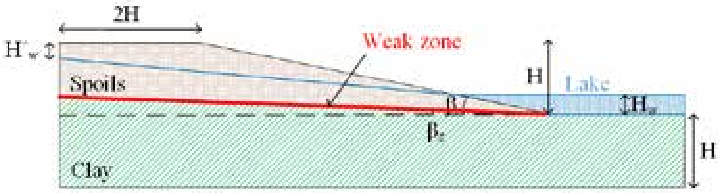

Figure 5. Two-layered slope model with inclined weak zone.

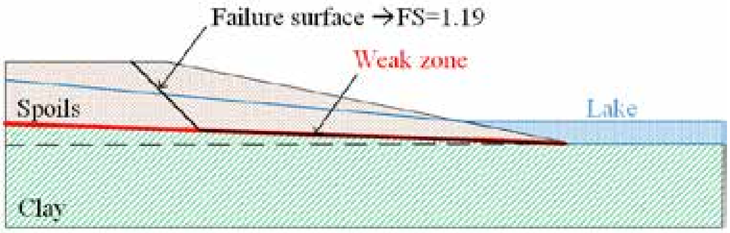

Figure 6. Bi-linear failure surface with FS=1.19.

Conclusions

This paper deals with slope stability in the area of the artificial lake Most in the Czech Republic, which was formed in a former surface lignite mine with an average excavation depth of 100 m. A key element of the slopes and their stability is the existence of spoi materials from the excavations of lignite mines. To investigate the characteristics of spoil materials around the lake, 24 cone penetration tests were performed by measuring pore pressure (CPTu) at

depths up to 50 m. Each test produced different deep primary results, confirming uncertainty and spatial variability as the main characteristics of the nature of spoil materials. Through the empirical soil index I_c spoils are mainly characterized as fine-grained materials, silts, silty clays and clays. Due to the presence of several types of soils in random spatial arrangement, it was not possible to locate a distinct stratigraphy. Consequently, a single soil material with significant heterogeneity was assumed. Evaluation of CPTu results showed that undrained shear strength c_u increases as a function of depth. The strength c_u was calculated through empirical correlations from the total cone peak resistance (q_t). A regression analysis of q_t resulted in the change function with the depth D q_t=0.12D+1.27 (in MPa). The change function of q_t derived the function of change of c_u=7.27D+90.7 (in kPa).
The use of CPTu data, although displaying some data dispersion, proved valuable for characterizing the soil properties and informing the stability analysis. The stability analysis revealed a safety factor (FS) of 1.19, deemed acceptable for temporary mining slopes but inadequate for long-term stability in civil engineering applications, especially reclamation projects. A minimum FS of 1.4 is recommended for such projects to ensure stability and safety. The analysis employed a two-layer slope model incorporating an inclined weak zone, a common feature in lignite mines, further emphasizing the need for a higher FS. The lower FS obtained highlights the potential for slope instability and underlines the risks associated with insufficient consideration of long-term stability requirements during reclamation.

Acknowledgements

This research has received funding from the European Union's Research Fund for Coal and Steel (RFCS) under the project "MidSafe" grant agreement No. 101157379 and the Hellenic Foundation for Research under the 5th Call for HFRI PhD Fellowships (Fellowship Number: 61518400).

References

BGR 2014. Energy study 2014: reserves, resources and availability of energy resources,Hanover. Federal Institute for Geosciences and Natural Resources (BGR).

Bian, Z., Miao, X., Lei, S., Chen, S.-E., Wang, W. & Struthers, S. 2012. The challenges of reusing mining and mineral-processing wastes. Science, 337, 702-703.

Euracoal 2017. Annual Report. European Association for Coal and Lignite,Brussels, Belgium.

EY 2014. European lignite mines benchmarking—sanitized report.

Kontopidis, O.N, Theocharis, A.I., Koukouzas, N.C. & Zevgolis, I.E. 2022. Stability of open pit lignite excavations during flooding. Comparison of a simplified analytical tool with limit equilibrium computational analysis. Górnictwo Odkrywkowe, 63.

Kontopidis, O., Theocharis. A.I., Zevgolis, I.E., Koukouzas. N.C. (2022). Stability of open pit lignite excavations during flooding: comparison of a simplified analytical tool with limit equilibrium computational analysis, Górnictwo Odkrywkowe – Surface Mining (ISSN 0043-2075), Poltegor-Instytut, Vol. LXIII, Nr. 3, p. 4-9

Mayne, P. Interpretation of geotechnical parameters from seismic piezocone tests. Proceedings, 3rd international symposium on cone penetration testing, 2014. 47-73.

Mikroutsikos, A., Theocharis, A.I., Koukouzas, N.C. & Zevgolis, I.E. 2021. Slope stability of deep surface coal mines in the presence of a weak zone. Geomechanics and Geophysics for Geo-energy and Geo-resources, 7, 1-17.

Pavloudakis, F., Galetakis, M. & Roumpos, C. 2009. A spatial decision support system for the optimal environmental reclamation of open-pit coal mines in Greece. International Journal of Mining, Reclamation and Environment, 291-303.

Robertson, P. K. 2009. Interpretation of cone penetration tests—a unified approach. Canadian geotechnical journal, 46, 1337-1355.

Rocscience 2019. Slide2 Version 7.0 - 2D Limit Equilibrium Slope Stability Analysis. https://www.rocscience.com/, Toronto, Ontario, Canada.

Rocscience 2023. Slide2 User Guide. Documentation/Slide model/Boundaries/Weak Layer Overview. https://www.rocscience.com/help/slide2/documentation/slide-model/boundaries/weak-layer/weak-layer-overview. Accessed on 10-1-2025. Toronto, Ontario, Canada.

Zevgolis, I.E, Mikroutsikos, A., Theocharis A.I. & Koukouzas, N.C. 2021. The effect of water filling on slope stability of open pits: A numerical investigation. The Evolution of Geotech-25 Years of Innovation. CRC Press.

Zevgolis, I.E., Deliveris, A.V. & Koukouzas, N. C. 2019. Slope failure incidents and other stability concerns in surface lignite mines in Greece. Journal of Sustainable Mining, 18, 182-19

17th INTERNATIONAL CONGRESS of the Geological Society of Greece

BULLETIN OF THE GEOLOGICAL SOCIETY OF GREECE, SP. PUBL.

EXTENDED ABSTRACT 159

A semi-quantitative multi-hazard approach for Tailings Storage Facilities

Kontopidis O.N.[1], Theocharis A.I.[2], Zevgolis I.E.[1]
(1) School of Mining and Metallurgical Engineering, National Technical University of Athens, Greece izevgolis@metal.ntua.gr (2) Department of Civil Engineering, University of Patras, Greece

A semi-quantitative approach presents a new way to assess multiple natural hazards' interactions affecting the stability of tailings storage facilities, leading to a semi-quantitative hazard index.

Introduction

The extraction and exploitation of raw materials are necessary activities for the sustainable development of society and the evolution of technology. The mining sector consists of successive stages initiating from the extraction of raw material to the storage and management of waste. Mine wastes include overlying soils that are removed to reveal the mineral, spoil materials with a content of raw material below the cut of grade and tailings. Tailings are defined as the waste of ore processing during the removal of economically important components (Vick, 1990). These can be in solid or liquid form (slurry) depending on the drying and deposition techniques chosen by the enrichment plants. The tailings, in the form of slurry, are transported by pipelines from the enrichment plant to the Tailings Storage Facilities (TSFs). TSFs are high-risk infrastructures as tailings contain a high pollutant load mainly due to the chemicals used to extract minerals. Also, the volume of tailings stored is in the order of millions of cubic meters. In general, tailings storage is often recognized as the most important source of environmental impact for many mining activities (Vick, 1990). A large number of TSFs are located in countries with a severe mining sector such as the USA, Canada, Brazil, Chile, South Africa and Australia (Piciullo *et al.*, 2022).

TSFs, like any infrastructure, interact with and are affected by the environmental conditions of the surrounding area. These conditions are related to the particular geological, hydrogeological, geotechnical, climatic and topographical characteristics of the area, which potentially constitute sources of natural hazards. Infrastructures with components that perform various functions (storage, transportation, drainage), such as TSFs, tend to show vulnerability to multiple natural hazards. Indicative components are pipelines, dams, geomembranes, spillways and impoundments. In the recent past, attempts are made to review significant failures over the last 100 years by statistically recording the natural hazards and more generally the conditions under which TSFs have failed (Azam & Li, 2010; Piciullo *et al.*, 2022; Rico *et al.*, 2008). In this direction, on line bases are also moving, indicatively mentioning the CSP2-Tailings Dam Failures. The difference between single and multi-hazard is important, as. In a multi-hazard framework, the consequences of interrelated hazards in the components are often more significant than those deriving from individual hazard summation. These failure mechanisms, most frequently mentioned as "failure modes", are defines as the ways, or modes, in which something (in this case the various components of the TSF) might fail.

This paper presents a new way to assess the interaction of natural hazards among them, and natural hazards with failure modes of TSFs. A semi-quantitative multi-hazard method developed by Liu *et al.*, 2021, hereinafter Liu's method, is adapted for TSFs. This method evaluates each hazard individually, builds triggering interactions between hazards and failure modes using adjusted factors, and aims to quantify the multi-hazard intensity of different scenarios, which trigger specific failure modes. This method has been applied once in the wider mining sector and specifically in post-mining lignite regions (Nalmpant-Sarikaki *et al.*, 2023).

Methodology

Three categories of methodologies are typically encountered to explore the interaction of hazards and calculate the multi-hazard intensity: qualitative and semi-quantitative quantitative. Focusing on semi-quantitative methods, they either use correlation coefficients or calibrate hazard occurrence characteristics to capture the interaction of hazards. The current work is based on a semi-quantitative method, which is described in four main steps. The initial step involves the identification of the main hazards in the study area as typically conducted in risk assessment. In the case of TSFs, the hazard categories are related to the specific conditions of the surrounding area as described above (geological, hydrogeological, geotechnical, climatic and topographical characteristics of the area). Anthropogenic (technological hazards) also affect TSFs and are often combined with natural ones to trigger a failure mode. However, in this work, only natural hazards are employed and the scenarios that will be developed consider only natural hazards. It focuses on the methodological framework and does not extend to a large number of natural hazards that could potentially threaten the area. Thus, four natural hazards are considered for this analysis, specifically earthquake, rainfall, flooding and landslide. Individual hazards are characterized based on their predisposing factors and associated triggering factors. For example, a landslide is influenced by its predisposing factors, such as the topography of the ground and the soil conditions, and can be triggered by climate conditions, e.g., heavy rainfall (Zevgolis, Deliveris *et al*., 2019). Moreover, in a multi-hazard scenario, a landslide can be triggered by other hazards, such as flooding and earthquakes.

The second step deals with typical failure modes identification. The most critical components of TSFs are the tailings dam as they are earthen confining structures whose failure results in the release of tailings. As geotechnical works similar to earthen water dams and levees, they mainly present geotechnical failure modes. The failure modes that will be considered in this work are the overtopping, the slope instability, the liquefaction, the foundation failure, the internal erosion and the external erosion (Clarkson & Williams, 2021).

- Overtopping can occur from excessive inflows (flooding), malfunctioning spillway or outlet structures, insufficient spillway capacity, dam settlement, external landslide into reservoir, or by waves driven by wind running up and overtopping the dam (Clarkson & Williams, 2021).
- Slope instability refers to the failure of the upstream and downstream slopes of the dam either due to static or dynamic loading.
- Liquefaction is the instant loss of saturated soil's strength in response to strong ground shaking. A particular type, which the upstream constructed dams face, is the static liquefaction, namely the brittle loss of strength in loose, saturated, nonplastic or low plasticity soil under monotonic loading (i.e., static rather than dynamic).
- Foundation failure has three components, the overcoming of the bearing capacity, the development of excessive settlements and its permeability, which will result in the seepage of water and tailings under the dam body.
- Internal erosion (called "piping" by dam engineers) of a tailings dam takes place when water that seeps through the dam carries soil particles away from the embankment, filters, drains, foundation or abutments of the dam. If the seepage that discharges at the downstream side of the dam carries particles of soil, an elongated cavity or "pipe" may be eroded backward (working upstream) toward the reservoir through the embankment, foundation or abutment. When a backward-eroding pipe reaches the reservoir, a catastrophic breaching of the dam can occur (ASDSO).
- Surface erosion is a physical process that occurs when tailings flow removes soil particles from the surface of the dam so that its cross section to thin.
- An additional failure mode is the structural failure, which refers to any non-earth-related parts, such as corrosion of pumps and fractures in reinforced concrete. However, this failure mode is ignored in this study.

The third step deals with interactions between natural hazards and failure modes determining multi-hazard scenarios. Although the type of interactions between hazards and failure modes can be of diverse types such as trigger and coincidence (when they occur simultaneously and independently), hazards that act as triggering factors for other hazards are associated to failure modes to define multi-hazard scenarios. Scenarios in the form of "chains" will therefore be built, with cause-and-effect relationships.

The final (fourth) step focuses on identifying the level of interactions among hazards and failure modes. This assessment is based on the intensity of individual hazards and the level interaction of a hazard that causes a failure mode. The multi-hazard analysis demonstrates that interacting hazards can be more destructive as the principles of Liu's method demonstrate. Thus, it is challenging to consider multiple hazards and not only assess single ones because the overall risk is underestimated in the latter case.

Application

The application of Liu's method requires the selection of a study area to assign intensity values to natural hazards according to characteristics such as seismicity, precipitation and topography as well as the history of hazard occurrence in the area surrounding the TSF. It does not require knowledge of the technical specifications of a specific TSF. The identification of failure modes and their interaction with hazards is generally applicable, regardless of the specific study area. The indicative area employed in this work refers to the area of Halkidiki in the central Macedonia in northern Greece. In Halkidiki, due to intense mining operations, various TSFs with dry tailings have been constructed. Table 1 presents the identified natural hazards that potentially affect the study area and their initial intensities considering its location, topography and the historical data. There are six intensity classes ranging from 0 to 5; the higher the number, the greater the hazard intensity, and zero means that the hazard has no impact.

The earthquake's initial intensity is related to the classification of Greek seismic hazard. According to the latest Greek seismic code, the country was divided into three seismic hazard zones. Regarding the horizontal peak ground acceleration, the study area falls into zone II. In addition, according to National Observatory of Athens two strong earthquakes have occurred in the past in the wider area, 1932 Ierissos earthquake and 1978 Thessaloniki earthquake with M=7 and 6 respectively. Therefore, the initial intensity was selected as three. Precipitation data reserved from the Hellenic National

Meteorological Service. The annual precipitation of the Halkidiki area has a moderate value, 400-450 mm, with a low to moderate duration regarding the recordings; thus, the initial intensity was selected as two. Flooding is expected, locally, on both sides of the riverbeds and streams and considering the value given to rainfall the initial intensity selected equally as 2. Finally, initial intensity for landslides is selected as 4 due to mine wastes heaps prone to instabilities. Regarding bedrock formations, there are amphibolites – amphibolitic gneisses and biotic gneisses. These rock types exhibit high strength, whenever their rock mass characteristics indicate gravitational-movement type landslides governed by their discontinuities.

Table 1. Initial intensities of hazards (scale 0-5).

Natural hazards	Initial intensity
Earthquake (EQ)	3
Rainfall (RF)	2
Flooding (FL)	2
Landslide (LA)	4

The triggering relationships among hazards and between hazards and failure modes are summarized by hazard matrices, as shown in Figure 1 and Figure 2, respectively. The interactions among them are categorized into two levels: dark blue indicates high probability of interaction; light blue indicates low probability of interaction. In Figure 1 the diagonal cells are filled with dashes and represent the interaction of each hazard with itself, which is meaningful because the current study is focused on interactions between different hazards. Indicatively, earthquake has a high probability of triggering landslide, the flood has a low probability to trigger landslide, and the earthquake is unlikely to trigger rain and vice versa. Regarding the interaction between hazards and failure modes, flooding has a high probability to trigger overtopping, the landslide has a low probability to trigger external erosion and finally the earthquake is not associated with internal and external erosion as these phenomena are inextricably related to the action of water.

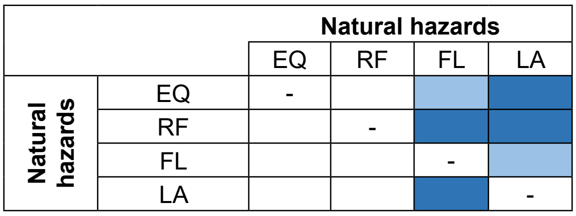

		Natural hazards			
		EQ	RF	FL	LA
Natural hazards	EQ	-		▨	🟦
	RF		-	🟦	🟦
	FL			-	▨
	LA			🟦	-

Figure 1. Interaction matrix of natural hazards; dark blue cells: high probability of interaction, light blue cells: low probability of interaction, white cells: no interaction.

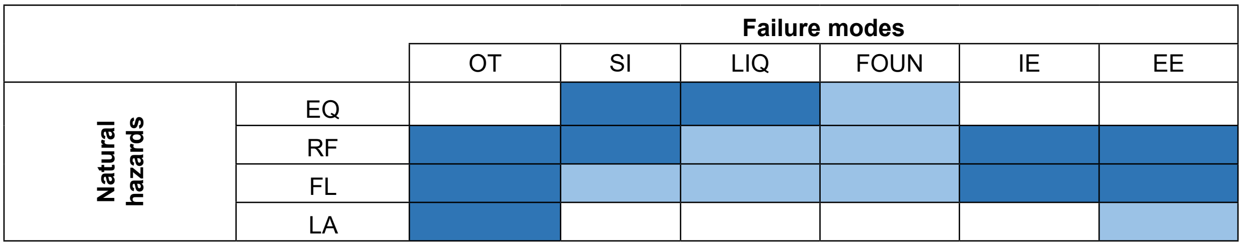

		Failure modes					
		OT	SI	LIQ	FOUN	IE	EE
Natural hazards	EQ		🟦	🟦	▨		
	RF	🟦	🟦	▨	▨	🟦	🟦
	FL	🟦	▨	▨	▨	🟦	🟦
	LA	🟦					▨

Figure 2. Interaction matrix between natural hazards and failure modes. OT= overtopping, SI=slope instabilities, LIQ= liquefaction, FOUN= foundation failure, IE= internal erosion, EE= external erosion.

The above qualitative characterization of the interactions is converted into semi-quantitative by introducing some sub-coefficients of approximation of the initial intensities of hazards. In the context of multi-hazard analysis, the intensities of hazards are greater when they occur in combination compared to the simple hazards analysis approach. Liu’s method proposes multiplying the initial intensities by coefficients from 1.1 to 1.5 depending on the initial intensity value and the type of correlation (low or high) among hazards. Coefficient 1.1 is applied when the initial intensity value equals to 1-2 and there is a low interaction while on the other side 1.5 with initial intensity value 5 and high interaction. Liu’s method presents a detailed table for coefficients. The same principle applies to this work and in addition the coefficients are similarly applied to the correlation between hazards and failure modes.

The combination of Figure 1 and Figure 2 results in scenarios development. The scenarios consist of 2 hazards and a failure mode. In particular, a primary hazard causes a second hazard which in turn causes a failure mode. The scenarios are therefore in the form of a chain, for example, rainfall trigger flooding and the latter trigger overtopping. Thus, the building of scenarios involves pairing elements (hazards or failure modes) according to the degree of interaction observed between them. Earthquake and rainfall cannot be triggered by the other hazards (as shown in Figure 1) so, they cannot be placed as second hazards in the multi-hazards scenarios. The final multi-hazard intensity (MH) is calculated by summing up the trigger and the triggered hazard's adjusted intensity.

Table 2 presents all scenarios sorted by failure modes. Each scenario receives an MH, so for each failure mode a total MH summing up the individual MH corresponding to each failure mode is obtained. In addition, It is determined a higher (each hazard has an initial intensity of 5 and high probability to trigger other hazards or failure mode) and a lower (each hazard has an initial intensity of 1 and low probability to trigger other hazards or failure mode) limit. The range is normalized (0-1), and the MH is scaled accordingly through Norm. MH to improve visualization of scenario intensities. Table 2 presents scenarios shorted by failure mode to assess their criticality according to MH. Similarly, we could short them by hazards to find their criticality. Overtopping appears to be the most critical failure mode as 0.438 is the highest norm. MH. This is because FL and LA has high interaction with it as well as LA, which is involved in 4 out of 6 scenarios has an initial intensity of 4. SI, LIQ and FOUN have equal MH as 3 scenarios lead to them and FL acts as triggering hazards for each failure mode. They present low MH as FL and RF receive the lowest initial intensity of 2. IE shows slightly higher MH than SI, LIQ and FOUN because although equally similarly in 3 scenarios, FL has low interaction with IE. In final, EE appears to be the second most critical after OT, as LA has low interaction with EE while LA has high interaction with OT. Therefore, the criticality of FM depends on the number of scenarios involved, on the initial intensities of hazards and on the type of interaction between hazards and between hazards and between hazards and failure modes.

Table 2. Multi-hazards scenarios shorted by failure modes (FM). OT= overtopping, SI=slope instabilities, LIQ= liquefaction, FOUN= foundation failure, IE= internal erosion, EE= external erosion

FM	Scenario	Total MH	Min total MH	Max total MH	Norm. MH
OT	EQ → FL → OT	46.8	13.2	90	0.438
	RF → FL → OT				
	LA → FL → OT				
	EQ → LA → OT				
	RF → LA → OT				
	FL → LA → OT				
SI	EQ → FL → SI	18.4	6.6	45	0.307
	RF → FL → SI				
	LA → FL → SI				
LIQ	EQ → FL → LIQ	18.4	6.6	45	0.307
	RF → FL → LIQ				
	LA → FL → LIQ				
FOUN	EQ → FL → FOUN	18.4	6.6	45	0.307
	RF → FL → FOUN				
	LA → FL → FOUN				
IE	EQ → FL → IE	19.6	6.6	45	0.339
	RF → FL → IE				
	LA → FL → IE				
EE	EQ → FL → EE	44.4	13.2	90	0.406
	RF → FL → EE				
	LA → FL → EE				
	EQ → LA → EE				
	RF → LA → EE				
	FL → LA → EE				

Conclusions

The present work adjusted an existing multi-hazard methodology, originally designed to analyze the interaction of natural and technological hazards, adapting it to fit a framework of interactions between hazards and failure modes in the context of TSFs. Multi-hazard analysis constitutes a critical component of modern risk assessment; this assessment must also include a detailed analysis of the consequences of TSF failures in the downstream region. The initial steps involved identifying the most significant natural hazards and possible failure modes of TSFs. The region of Halkidiki, operating intense mining, was selected as an indicative area. Then, the hazards' initial intensities and levels of interaction determined using appropriate interaction matrixes. The initial intensities were modified and increased, and the resulting values were appropriately summed up to create various multi-hazard scenario intensities (MH). The ultimate objective was to identify the most critical failure by comparing various scenarios via the total multi-hazard (MH) intensities. The study showed that the criticality of failure mode for this methodology is a function of the number of scenarios involved, the initial intensities of hazards and the type of interaction among hazards and between hazards and failure modes. Based on the analysis overtopping is the most critical, with external erosion following. Finally, some limitations of the modified method and the general assumptions considered in this work should be mentioned. The scenarios were built under the premise of developing a cause-and-effect relationship among their components. However, in nature this assumption does not always apply. For example, earthquakes and rainfall, although independent, can occur simultaneously without having a causal relationship. Rainfall and earthquakes are not triggered by other hazards. Subsequently, they were not placed as second components in scenarios, consequently, they were not included as direct triggering factors of failure modes. In future work, these interactions will be better studied, and anthropogenic-technological hazards will be included in the analysis.

Acknowledgements

The research work was supported by the Hellenic Foundation for Research and Innovation (HFRI) under the 5th Call for HFRI PhD Fellowships (Fellowship Number: 61518400).

References

Azam, S., & Li, Q. (2010). Tailings dam failures: a review of the last one hundred years. Geotechnical news, 28(4), 50-54.

Clarkson, L., & Williams, D. (2021). An overview of conventional tailings dam geotechnical failure mechanisms. Mining, Metallurgy & Exploration, 38(3), 1305-1328.

CSP2- Tailings Dam Failures. (2024). Retrieved 11/12/2024 http://www.csp2.org/tsf-failures-from-1915

Liu, B., Han, X., Qin, L., Xu, W., & Fan, J. (2021). Multi-hazard risk mapping for coupling of natural and technological hazards. Geomatics, Natural Hazards and Risk, 12(1), 2544-2560. doi:10.1080/19475705.2021.1969451

Nalmpant-Sarikaki, D. M., Theocharis, A. I., Koukouzas, N. C., Benardos, A. G., & Zevgolis, I. E. (2023). Multi-Risk Assessment in Post-Mining Lignite Areas. Materials Proceedings, 15(1), 65.

Piciullo, L., Storrøsten, E. B., Liu, Z., Nadim, F., & Lacasse, S. (2022). A new look at the statistics of tailings dam failures. Engineering Geology, 303, 106657.

Rico, M., Benito, G., Salgueiro, A., Díez-Herrero, A., & Pereira, H. (2008). Reported tailings dam failures: a review of the European incidents in the worldwide context. Journal of hazardous materials, 152(2), 846-852.

Vick, S. G. (1990). Planning, Design, and Analysis of Tailings Dams. Vick, S. G. (1990). BiTech Publishers Ltd.

Zevgolis, I. E., Deliveris, A. V., & Koukouzas, N. C. (2019). Slope failure incidents and other stability concerns in surface lignite mines in Greece. Journal of Sustainable Mining, 18(4), 182-197.

BULLETIN OF THE GEOLOGICAL SOCIETY OF GREECE, SP. PUBL.

EXTENDED ABSTRACT 160

The role of the museums in the geoscience education

Efterpi Koskeridou[1], Christos Psarras[1], Evangelia Rentoumi[1], Ioannis Giaourtsakis[1], Marija Bosniak[2]

(1) Faculty of Geology and Geoenvironment, National and Kapodistrian University of Athens, Greece, ekosker@ geol.uoa.gr (2), Croatian Natural History Museum, Zagreb, Croatia

Introduction

Museum curators and museum staff working in the field of education face the challenges of enrolling museums in the geoscience education. The knowledge gained from the scientific work on museums' collections is transferred and communicated to public using various tools. That way public is acquainted with the current and ongoing research in the museums, has the opportunity to be part of it, and it is educated on various topics.

In this paper we show ways of communicating with the audience based on the examples from the Museum of Paleontology and Geology of the National and Kapodistrian University of Athens, Greece and the Croatian Natural History Museum, Zagreb, Croatia.

Objectives

The goal of this work is to highlight the role of museums in Geosciences and education, acting as a mediator between scientific research and public understanding. By combining traditional and digital tools, museums potentially offer learning opportunities to diverse audiences, from the general public to university students and educators. This work demonstrates how museums can communicate the complex concepts of Natural History, containing geological and paleontological terms, by fostering curiosity and providing accessible educational experiences that enamor people to science. By showcasing innovative methodologies and case studies, we underscore the importance of museums as dynamic hubs of learning and science communication.

Methods

Museum education encompass various tools that can be used in the science communication, e.g., exhibitions, catalogues related to the exhibitions and collections, workshops, lectures, conferences, flyers, etc. Examples here presented are based on the incorporation of virtual tools in the museum work, which are in recent time becoming more and more popular and applied.

First example is a new virtual online tour at the Museum of Paleontology and Geology of Athens, titled: Advanced Tour and Education Services in the virtual Paleontology and Geology Museum/v-PalM.

Second example is a virtual exhibition "Oysters of the ancient seas" available on the website of the Croatian Natural History Museum.

Results

Museum of Geology and Paleontology

- The Museum of Geology and Paleontology at the National and Kapodistrian University of Athens has long been a beacon for scientific research and public education in the fields of Paleontology and Earth Sciences in Greece. Founded in the 19th century, the institute's roots go back to the founding of the Hellenic Society of Naturalists in 1835, which began collecting specimens of animals, plants, fossils, rocks and minerals. These early collections laid the foundations for one of the most important paleontological and geological museums in Greece. Throughout its history, the Museum has grown through continuous acquisitions, research and collaborations, so that today it can preserve a rich selection of more than one million specimens documenting more than 550 million years of the Earths' geological history.

A significant enhancement to the Museum's educational output has recently been the "v-PalM" project (fig. 1), which has developed a dynamic virtual experience to increase the museum's reach and educational effectiveness. Through the collaboration with the National Technical University of Athens and the technology company OMEGA, the project has successfully integrated 3D models, multimedia content, games and interactive educational programs, offering a digital extension of the museum's physical exhibits (Konstantakis *et al*., 2023; Thanou *et al*., 2023). In this virtual museum, visitors can explore thematic educational material such as the organisms and evolution of life during the Paleozoic, Mesozoic and Cenozoic Eras, the famous Pikermian Fauna, examples of island dwarfism in Greece and the evolution of marine organisms through time. Each program is carefully coordinated with the exhibits that are on display in the actual Museum exhibition. For the first time, these educational programs have been specifically designed to engage the public with the Museum's unique collection and enhance the learning experience through the use of detailed illustrations of specimens, 3D models and in-depth information.

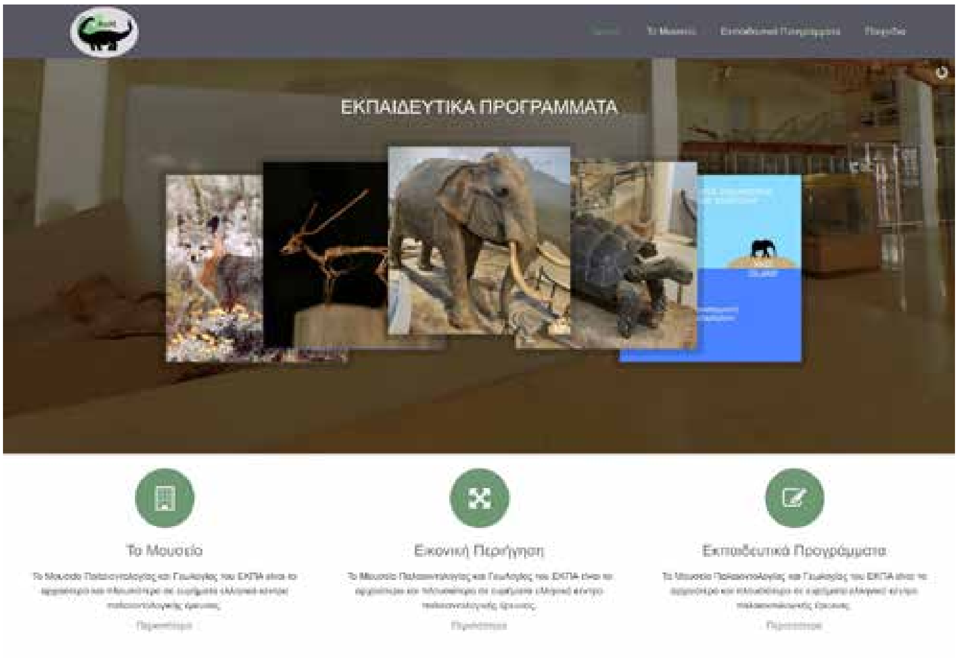

Figure 1. V-Palm Web application.

Furthermore, the Museum's impact on the educational landscape goes beyond its exhibits and digital initiatives. It has long been a center for educating students in fields such as Geology, Paleontology and Museology, providing hands-on learning opportunities through its extensive collections and research programs. The Museum hosts a variety of educational initiatives, including fieldwork, workshops and guided tours, providing opportunities for both school groups, university students and the general public to engage with the sciences of Geology and Paleontology. The Museum, through the expansion of educational offers, particularly through digital platforms such as the "v-PalM" project, makes science learning more accessible, especially for those who cannot visit the Museum in person, and promotes a deeper understanding of the natural world.

The completion of the "v-PalM" project is a milestone in the museum's mission to make science education more accessible and interesting for several target groups. By integrating advanced technology with curated educational content, the Museum has not only enriched its physical exhibitions through illustrations and paleoenvironmental reconstructions but has also made a lasting impact on the way Earth Science education is delivered in Greece. Visitors –whether in person or virtually– can now experience an interactive and enriching learning environment that emphasizes on the importance of scientific knowledge and understanding our planet's past, present and future.

Croatian Natural History Museum

- Due to the earthquake, renovation of the museum building and work on the new permanent exhibition, Croatian Natural History Museum was closed for public from 2020 until 2024. In order to continue presenting the museum collections, virtual exhibition "Oysters of the ancient seas" was prepared. That was the first virtual exhibition of the CNHM completely prepared from the scratch in the virtual environment. For the purposes of the exhibition, virtual exhibits of the Middle Miocene oysters were presented not only as photographs, but also as 3D scanned objects, that could be moved in various directions, as the visitors decided. The exhibition involved a guide in each section, who would briefly describe what can be seen in this part of the exhibition. Storytelling was a great part of the preparation of this exhibition, since the texts for the exhibition' guide were prepared based on the work with a communicator.

Currently, the exhibition is presented in its classical form in the renovated CNHM museum building. Together with original specimens of the fossil and recent oysters, 3D prints of fossil oysters are available for touching. That way, visitors having disabilities can feel the morphology of the fossil oysters and imagine how they looked like. Additionally, one original specimen of partial fossil oyster-reef can be studied by the magnifier and visitors can look for various inhabitants preserved as fossils, e.g., oysters, coralline algae, corals, bryozoans, etc. We noticed the positive feedback of visitors on these types of exhibits, enabling them to discover for themselves something that is not so familiar to them on everyday basis, and encouraging them to find out more.

Methods used in geoscience education include also workshops and seminars. As museum curators, we can be involved in the education of the pupils and students, as well as the schoolteachers.

One of the examples of geoscience education is the action called “Meet the Earth - Peek under the microscope” organized by the Croatian Geological Society since 2013 (e.g., Galović & Bošnjak, 2014). Geologists from various institutions are involved in this promotion of geoscience, as well as students. In the agreement with schools, geoscientists show various exhibits of macro samples of minerals, rocks, fossils, and petroleum, and thin sections of different fossils and crystals using the microscopes. Geological maps, posters from conferences, and geological models can also be shown. This type of exhibition can be followed by a presentation. Exhibiting specimens from different geological field, the students and teachers can learn more about geoscience, and specifics of each discipline.

Other example of educating teachers is the Spring seminar, organized by the Education and Teacher Training Agency, Croatia and the Croatian Geological Summer School. Each year, under one topic researchers hold lectures to the teachers of geography, taking in account the curriculum of the geographic class for the current year. Topics include various geoscience themes, e.g., vulcanism, climatic changes, catastrophic events, etc.

Conclusions

Museums are crucial in promoting and educating people about geosciences by serving as accessible platforms that combine science, culture, and education. The two examples presented here in the two museums illustrate how museums are modernized to meet the needs of modern educational practices. By adopting tools like 3D modeling, virtual exhibitions, and interactive workshops, museums are extending their reach to visitors but also enhancing their experience. These initiatives display the importance of museums not just as repositories of knowledge but as active participants in its acquisition and promotion. Finally, continued collaboration between museums, researchers, and educators is necessary for the further enhancement and impact of geoscience education worldwide.

References

Galović, L., Bošnjak, M., 2014: Meet the Earth – Peek under the microscope!’’ – promotion of geology and geoheritage protection. XVI Serbian Geological Congress “ Optimal research and sustainable usage of the geological resources”, Belgrade, Serbia, p. 846-849.

Konstantakis, M., Trichopoulos, G., Aliprantis, J., Michalakis, K., Caridakis, G., Thanou, A., Zafeiropoulos, A., Sklavounou, S., Psarras, C., Papavassiliou, S., Koskeridou, E., 2023. An Enhanced Methodology for Creating Digital Twins within a Paleontological Museum Using Photogrammetry and Laser Scanning Techniques. Heritage 6(9), 5967-5980.

Thanou, A., Stavropoulou, G., Tsitseklis, K., Zafeiropoulos, A., Orfanidou, V., Kotsopoulos, K., Papastamatiou, N., Koskeridou, E., Giaourtsakis, I., Filis, P., Papavassiliou S., 2023. A Dynamic Interactive Virtual Museum for Enhancing Students Engagement. 13th Pan-Hellenic and International Conference “ICT in Education”, Kavala, Greece, p. 235-242.

17th INTERNATIONAL CONGRESS of the Geological Society of Greece

BULLETIN OF THE GEOLOGICAL SOCIETY OF GREECE, SP. PUBL.

EXTENDED ABSTRACT 161

Ultrasonic analysis of the structural stones of the Parthenon at the Acropolis of Athens - Investigation of the physical / mechanical properties and integrity control of the grouted Joints

Kosmas P.[1], Loupasakis C.[1], Eleftheriou V.[2], Christodoulopoulou R.[2], Vrouva A.[2]

(1) Laboratory of Engineering Geology and Hydrogeology, School of Mining and Metallurgical Engineering, National Technical University of Athens, Athens, Greece, kosmas.panagiotis9@gmail.com

(2) Acropolis Restoration Service, Ministry of Culture and Sports, Athens, Greece

In this research, a non-destructive ultrasonic method was used to evaluate both the physicomechanical properties of the Parthenon's stones and the integrity of the grouted joints in the restoration works. Over 600 measurements of ultrasound velocity were conducted: 320 measurements for estimating the physicomechanical characteristics and 280 for assessing the integrity of the joints (Fig 1).

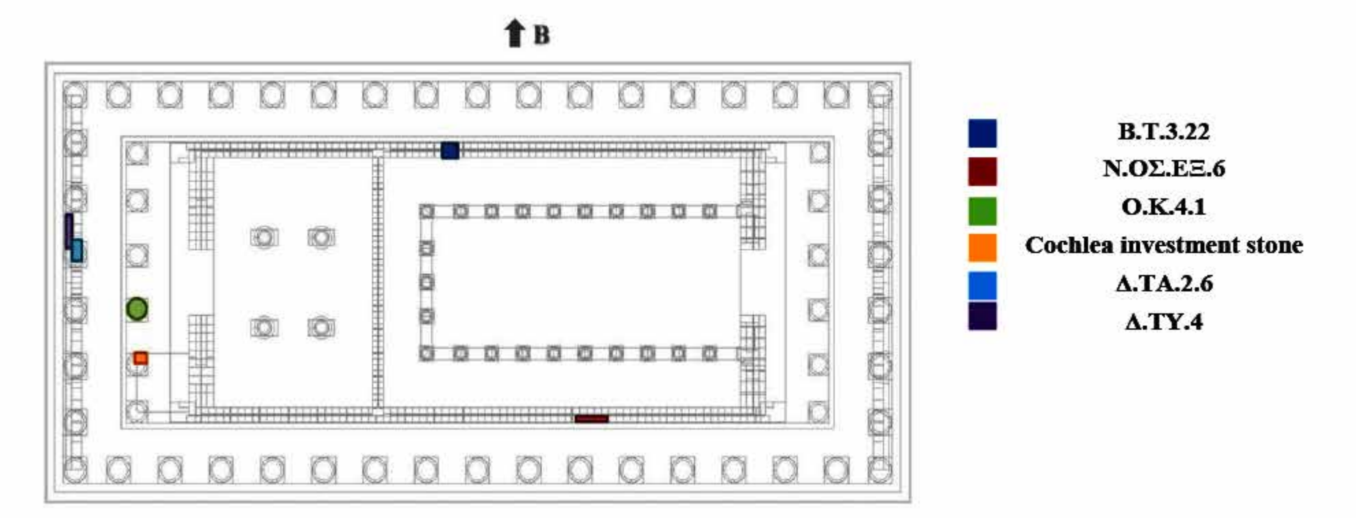

Figure1.Parthenon's layout. The physical location of the measured structural stones.

The measurements were made with the PUNDIT ultrasonic pulse propagation measurement device using P-wave piezoelectric transducers at 54 kHz, 150 kHz, and 250 kHz. After several measurements, it was concluded that, due to the roughness of the surfaces, plasticine was best suited as a contact material. Additionally, the transducers that provided the most consistent readings were those at 54 kHz, especially when used for the evaluation of the integrity of the joints.

The physicomechanical properties of the marbles were determined by taking measurements perpendicular and parallel to the unconformities (bedding or schistosity). The distance between the transducers was 10 cm, and distance between two successive rows 3 cm. A canvas was designed over the surfaces to ensure an accurate distance was maintained between the transducers (Fig 2). Physical pressure was applied to the transducers to ensure proper contact.

The properties of the Dionysos marble, after applying the above-described procedure, are presented in Table 1, and those of the Pentelikon marble are presented in Table 2. It should be noted that, according to Skoulikidis (2000) and Korres & Mpouras (1983) the density of Dionysos and Pentelic marble is 2720 kg/m^3 and 2720 to 2710 kg/m^3, respectively.

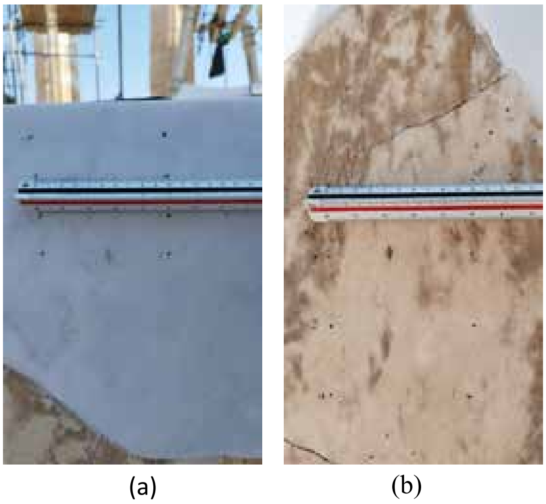

Figure 2. a) "New" Dionysos and b) "Ancient" Pentelic marble with the canvas designed for measuring the physicomechanical properties.

Table1.The physicomechanical properties estimated for the Dionysos marble (Pd: Density, Eo: modulus of elasticity, v: Poisson's ratio, Go: shear modulus).

Transducers parallel to the unconformities				
Code No.	**Marble**	**Pd (kN /m3)**	**Eo (Gpa)**	**Go (Gpa)**
BT322	Dionysos	27.2	12.68~13.14	5.13~5.31
ΝΟΣΕΞ6	Dionysos	27.2	20.52~23.23	8.30~9.40
Transducers perpendicular to the unconformities				
Code No.	**Marble**	**Pd (kN /m3)**	**Eo (Gpa)**	**Go (Gpa)**
BT322	Dionysos	27.2	11.99~12.84	4.85~5.20
ΝΟΣΕΞ6	Dionysos	27.2	12.74~15.43	5.16~6.24
ΝΟΣΕΞ6	Dionysos	27.2	20.00~21.50	8.09~8.70

Table2. The physicomechanical properties estimated for the Pentelikon marble (Pd: Density, Eo: modulus of elasticity, v: Poisson's ratio, Go: shear modulus).

Transducers perpendicular to the unconformities				
Code No.	**Marble**	**Pd (kN /m^3)**	**Eo (Gpa)**	**Go (Gpa)**
BT322	Pentelikon	27.1-27.2	10.20~15.45	4.13~6.25
ΝΟΣΕΞ6	Pentelikon	27.1-27.2	8.26~ 14.80	3.34~5.99
ΝΟΣΕΞ6	Pentelikon	27.1-27.2	9.78~ 12.67	3.96~ 5.13
O.K.4.1	Pentelikon	27.1-27.2	5.55~15.28	2.25~ 6.18
ΔΤΥ4	Pentelikon	27.1-27.2	7.78~8.32	3.15~3.37
ΔΤΑ2.6 1o	Pentelikon	27.1-27.2	9.34~11.76	3.77~ 4.76
ΔΤΑ2.6 2o	Pentelikon	27.1-27.2	7.47~13.47	3.02 – 5.45
Transducers parallel to the unconformities				
BT322	Pentelikon	27.1-27.2	15.76~19.44	6.38~7.85
ΝΟΣΕΞ6	Pentelikon	27.1-27.2	14.17~26.49	5.74~10.72
ΝΟΣΕΞ6	Pentelikon	27.1-27.2	27.61~29.76	11.17~12.04
ΔΤΑ2.6 1o	Pentelikon	27.1-27.2	11.43~22.47	4.63~9.10

The measurements conducted for assessing the integrity of the joints are based on a two-step procedure. An initial measurement is taken with the transducers placed 2 cm from both sides of the joint, followed by a second measurement at a distance of 4 cm. After the completion of the measurements, the PUNDIT provides a clear reading of the depth of the open joint. The process is repeated until a sufficient number of readings, indicating a clear value of the depth of the open joint, is provided. Note that an open joint is considered to be the part of the joint not filled with grout, or the part where grout has detached due to shrinkage from the walls of the joint.

(a) (b)

Figure 3. (a) Joint between ancient and ancient marble pieces and (b) joint between ancient and new marble. The canvas designed for measuring the integrity of the joints is clearly illustrated.

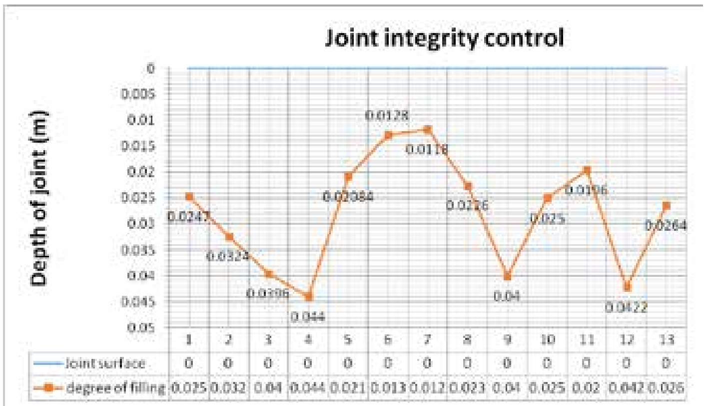

	1	2	3	4	5	6	7	8	9	10	11	12	13
Joint surface	0	0	0	0	0	0	0	0	0	0	0	0	0
degree of filling	0.025	0.032	0.04	0.044	0.021	0.013	0.012	0.023	0.04	0.025	0.02	0.042	0.026

Figure 4. Graph presenting the depth of the open joint; the part of the joint that failed to get properly filed with grout. The graph presents the readings obtained at the joint depicted in Figure3.a.

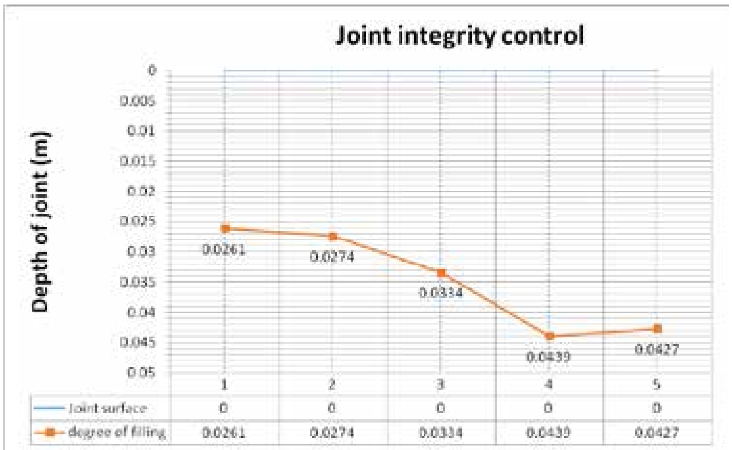

	1	2	3	4	5
Joint surface	0	0	0	0	0
degree of filling	0.0261	0.0274	0.0334	0.0439	0.0427

Figure 5. Graph presenting the depth of the open joint; the part of the joint that failed to get properly filed with grout. The graph presents the readings obtained at the joint depicted in Figure3.b.

Measurements of ultrasound velocity was used to examine Dionysos “new” and Pentelic “old” marble, which have been used to construct and reconstruct the Parthenon from antiquity to the present.

According to the ultrasonic measurements, both marbles’ properties appear to be compatible to each other.

Furthermore, higher values of the dynamic characteristics (shear modulus and dynamic modulus of elasticity) are noted in the measurements made parallel to the marbles’ unconformities (bedding or schistosity) than those perpendicular.

Additionally, the superficial deterioration—such as cellular corrosion or gypsum formation—ultimately affects only the marbles’ surface and not their interior structure and characteristics. This indicates that even though there is significant surface damage, which obviously and irrevocably alters the stone’s external relief, it does not damage their mechanical properties.

When evaluating the integrity of the joints, it can be safely stated that the joints are shielded, as the mean depth of the open cracks is less than 2 cm, with only a few identified as reaching the maximum depth of 5 cm. As the ultrasound machine does not allow for the determination of the cracks’ width, capillary cracks can only be observed along the joints.

References

Asef M.R., Farrokhrouz M. (2017): A semi-empirical relation between static and dynamic elastic modulus; Journal of Petroleum Science and Engineering 157, pp.359-363.

Christaras, B., (1994): Anisotropy effects on the elastic parameters of rocks; determination using ultrasonic techniques. 7o Intern. Congr. Geol. Soc. Gr.4, pp. 381-387.

Christaras B. (1996): Particularities In Studying The Fpysical And Mechanical Properties Of Stones In Monuments. Examples From The Mediterranean Basin. 8th International Congress on the Deterioration and Conservation of Stone, Berlin, pp. 819-829.

Christaras B. (1997): Estimation Of Damage At The Surface Of Stones Using Non Destructive Techniques. STREMAH V (5th Int. Congr. Structural Studies, Repairs and Maintaince of Historical Buildings). San Sebastian. Advances in Architectural Series of Computetional Mechanics Publications, Southampton, pp. 121-128.

Korres M. and Mpouros Ch. (1983): Study for the restoration of the Parthenon, Athens. Ministry of Culture and Sports - Acropolis Restoration Service (YSMA).

Salvatici T., Centauro I., Segabinazzi E., Intrieri E., Garzonio G.A., (2023): Non destructive methods applied for in situ mechanical diagnosis: Florentine historical buildings in Pietra Serena, Salvatici et al. Heritage Science, pp.1-11.

Skoulikidis Th. (2000): Erosion and conservation of structural monuments, Heraklion, University of Crete Press.

17th INTERNATIONAL CONGRESS
of the Geological Society of Greece

BULLETIN OF THE GEOLOGICAL
SOCIETY OF GREECE, SP. PUBL.

EXTENDED ABSTRACT 162

The Koziakas Mélange Unit: New perspectives on Its Mesozoic paleogeographic and geotectonic evolution (Central Greece)

Kostaki G.[1], Gawlick H.-J.[2], Kilias A.[1], Missoni S., Ghon G.[2], Katrivanos E.[1]

(1) Aristotle University Thessaloniki, Thessaloniki, Greece, gkostaki@geo.auth.gr (2) Montanuniversität Leoben, Leoben, Austria

The Koziakas ophiolites in central Greece, along with their underlying mélanges, represent a part of the obducted Neo-Tethys ophiolites. During the Middle to early Late Jurassic, west-directed ophiolite obduction led to the formation of various mélanges, incorporating blocks from the Triassic Neo-Tethys Ocean floor (radiolarites) and the outer open-marine shelf (Hallstatt Facies). The Middle to Late Triassic Hallstatt Limestones, in particular, are crucial in defining the migration path of the obducting ophiolites. During Oxfordian, obduction stopped, and a shallow-water carbonate platform devolved on top of the ophiolites, shedding material into the remaining underfilled foreland basin in front of the obducted ophiolites. In the latest Jurassic to early Early Cretaceous, mountain uplift and erosion began, and the erosional products of this evolving continent were transported into this foreland basin. During the Tertiary (Eocene-Oligocene), the Koziakas ophiolite and mélange system thrust westward as a whole, together with Pindos unit, over the Gavrovo carbonate platform.

Background/Objectives

The Koziakas mélange unit, traditionally referred to as the Koziakas massif, is located in central Greece and is geologically characterized by an ophiolite nappe and associated underlying Jurassic mélanges. The unit was thrust southwestward as a whole during the Early Cretaceous over the Early Cretaceous Boeotian ‘flysch’, and during subsequent Paleocene-Eocene tectonics, it was displaced together with the Boeotian ‘flysch’ over the Late Cretaceous Thymiama succession or directly onto the Paleocene-Eocene Pindos orogenic sediments (Bortolotti *et al*., 2004, Chiari *et al.,* 2012; Fig. 1a). To the east of the Koziakas mélange unit, a Neogene basin developed, primarily receiving erosional products from the ophiolites to the west. The Koziakas ophiolites crop out between the well-known Pindos and Vourinos ophiolites to the north and the Othrys and Argolis ophiolites to the south, forming part of an ophiolite belt whose derivation remains a subject of ongoing debate. Several geodynamic models have been proposed to interpret the origin of these ophiolites, with the most prevalent divided on whether they originated: a) from a parautochthonous Triassic-Jurassic oceanic basin (Pindos Ocean) or b) represent remnants of a far-traveled ophiolite nappe stack derived from the Triassic-Jurassic Neo-Tethys Ocean floor located east of the Pelagonian units (see Robertson, 2012, for an extended review). To unravel the origin of these ophiolites is essential to understanding the Mesozoic paleogeography and mountain-building processes. A key aspect of this understanding is the study of the sedimentary and facies evolution of the passive continental margin(s) that existed prior to plate convergence and ophiolite obduction. Comprehending their evolution would assist in determining the number of the oceanic realms involved, as a multi-ocean reconstruction requires the presence of multiple passive continental margins. An important contribution to this is the study of mélanges formed in front of the advancing ophiolites, as they contain material that provide critical insights into the route taken by the ophiolites during their emplacement. A typical Triassic-Jurassic passive continental margin adjacent to an oceanic realm, from which the ophiolites originate, is characterized by shallow-water carbonates on the central shelf and open-marine carbonates dominating the outer shelf. During the obduction processes, the arrangement of the passive continental margin is disrupted, leading to the formation of a nappe stack and associated trench-like deep water basins in the lower plate position (Frisch & Gawlick, 2003). These trench-like deep-water basins receive synorogenic sediments derived from formations of the passive margin and the ophiolites, while experiencing thrusting into the foreland following the ophiolite emplacement (Gawlick & Missoni, 2019). As a result, the synorogenic sediments within these basins can undergo deformation, with most of their primary sedimentological characteristics being destructed by subsequent tectonics. However, in some cases, distinctive primary sedimentary features can still be observed in such sedimentary mélanges (in sense of Festa *et al*., 2016). During the overthrust of the higher nappe (i.e., obducting ophiolites), material from the lower plate (former passive continental margin sedimentary rocks) can also be scraped off and incorporated into such mélanges (Schmid *et al*., 2008). These mélanges are characterized by a fine-grain matrix incorporating diverse exotic blocks and mass-transport deposits (Gawlick & Missoni, 2019). In this paper, we present new stratigraphic and paleontological data from the Koziakas mélange unit, integrated with structural observations to provide new insights toward a comprehensive understanding. Our analysis focuses on the carbonate exotic blocks incorporated within the mélange associated with the obduction of Koziakas ophiolites. These exotic blocks serve as a valuable tool for reconstructing the original configuration of the overridden passive continental margin. Moreover, we conducted microfacies analyses on a sedimentary sequence composed of carbonate resediments intercalated in radiolarites. This sedimentary sequence, which overlies the Koziakas mélange with the incorporated exotic carbonate and radiolarite blocks, offers new insights into the subsequent events after the ophiolite emplacement. By combining our diverse data, we aim to contribute to the ongoing discussion surrounding the provenance of the ophiolites and the geotectonic evolution of the Hellenides during the Middle Jurassic to Early Cretaceous. Specifically, we address whether a Triassic-Jurassic Pindos Ocean or Pindos Basin existed and investigate the timing and direction of ophiolite obduction on the Pelagonian margin(s), providing new geodynamic implications and perspectives on the Mesozoic paleogeography of the region.

Methods

In the laboratory, approximately 100 thin sections, each measuring 5 cm x 5 cm, were prepared for detailed examination. Microfacies analyses were conducted to identify microfossils and paleontological characteristics, aiming to determine the paleogeographical environment and the age of the original deposition of the various components and blocks within the studied successions. For conodont age dating, carbonate samples were subjected to 10% diluted acetic acid digestion to dissolve the rock matrix, with the resulting residues examined under a binocular microscope.

Results

Microfacies analysis and conodont age dating were conducted on samples from various outcrops of the Koziakas mélange unit, situated on the eastern slopes of the Koziakas massif, west of the Koziakas ophiolites. This mélange comprises a lower section dominated by an argillaceous-radiolaritic matrix of Middle to early Late Jurassic age, containing, beside Triassic radiolarite pebbles, exotic open-marine Late Triassic carbonate blocks and slides of varying sizes and colors, resembling typical Hallstatt Limestones. Overlying this mélange follow basin-fill sediments consisting of thick, multicolored Late Jurassic radiolarites intercalated by carbonate turbidites and oolitic limestones, transitioning at higher stratigraphic levels into Late Jurassic to earliest Cretaceous shallow-water carbonate-clastic resediments (Fig. 1b, c).

- *Conodont age dating and microfacies analysis on open-marine carbonate blocks*: Samples from exotic blocks and mass-transport deposits within the Jurassic matrix of the Koziakas mélange were collected along the local road connecting Gorgogyri to Kori, as well in the vicinity of the Monastery of Vytoumas (Fig. 1d, e). Sample GR (62), obtained from a polymictic breccia, yielded conodont taxa such as *Gladigondolella*-ME, *Gladigondolella* cf. *malayensis*, *Paragondolella foliata*, and *Paragondolella* cf. *inclinata*, indicating a latest Longobardian to earliest Carnian age. Sample GR (69), collected from a filament limestone block beneath radiolarites with turbidites containing shallow-water debris, revealed taxa *Gladigondolella*-ME, *Paragondolella foliata*, *Paragondolella* cf. *inclinata*, and *Paragondolella polygnathiformis*, suggesting a lowermost Carnian (Cordevolian) age. Sample GR (70), collected from a grey micritic limestone block with red chert nodules, included taxa *Epigondolella rigoi* and *Norigondolella hallstattensis*, indicating an Early Norian age. Sample GR (71), derived from a polymictic breccia, contained the conodont *Paragondolella polygnathiformis*, corresponding to a Carnian age. Sample GR (235), obtained from mass-transport deposits with grey and red limestones, included *Metapolygnathus* cf. *commusti*, suggesting the Carnian/Norian boundary; *Epigondolella slovakensis*, indicative of Alaunian 2-3; and *Epigondolella bidentata*, corresponding to the Sevatian. Sample GR (236), collected from a reddish limestone block, yielded conodont taxa *Paragondolella polygnathiformis* and *Paragondolella nodosa*, indicating Tuvalian 3/1, as well as *Metapolygnathus* sp., suggesting the Carnian/Norian boundary. Sample GR (237), derived from a reddish limestone block, included several species of the latest Carnian (Orchard). Sample GR (238), also collected from a reddish limestone block, yielded *Paragondolella polygnathiformis* and *Paragondolella carpathica*, which are indicative of Tuvalian 2. Sample GR (240), obtained from a grey limestone block, included *Epigondolella rigoi*, indicating Lacian 2 age. Finally, sample GR (43) was collected from a medium-bedded grey siliceous limestone block and thin section analysis revealed a dark reddish-grey pelagic non-laminated wackestone with radiolarians, filaments, and a biofabric characterized by loose packing, medium sorting, and size variation of bioclasts. These facies suggest open-marine deposition on an outer shelf, with most radiolarians recrystallized into quartz.
- *Microfacies analysis of shallow-water carbonate-clastic resediments*: Shallow-water carbonate-clastic resediments are observed near Kori village, occurring at the higher stratigraphic levels of the Late Jurassic radiolarite sequence (Fig. 1f, g). Based on the examination of thin sections, the microfacies of the collected samples are identified as bioclastic packstones and grainstones, with shallow-water bioclasts being the most frequent components. In these thin sections, the bioclasts consist of bryozoans, foraminifera, crinoids, and debris from reef-building organisms. The presence of encrusting organisms is characteristic, such as the microencruster *Crescentiella morronensis* (Crescenti). Additionally, other bioclasts, such as calcareous algae *Thaumatoporella*, foraminifera *Litualinida*, and *Aptychus*, have been identified. These taxa indicate reefal facies from the Tithonian age. In specific thin sections, reworked shallow-water bioclasts are observed to be mixed with older Late Triassic clasts containing the benthic foraminifera *Aulotortus sinuosus*. The identification of radiolarian wackestone containing poorly preserved calpionellids, such as *Crassicollaria brevis* or *Calpionella elliptica*, mixed in the resediments suggests that the oldest age of redeposition can be estimated as Berriasian (Ghon *et al.*, 2018).

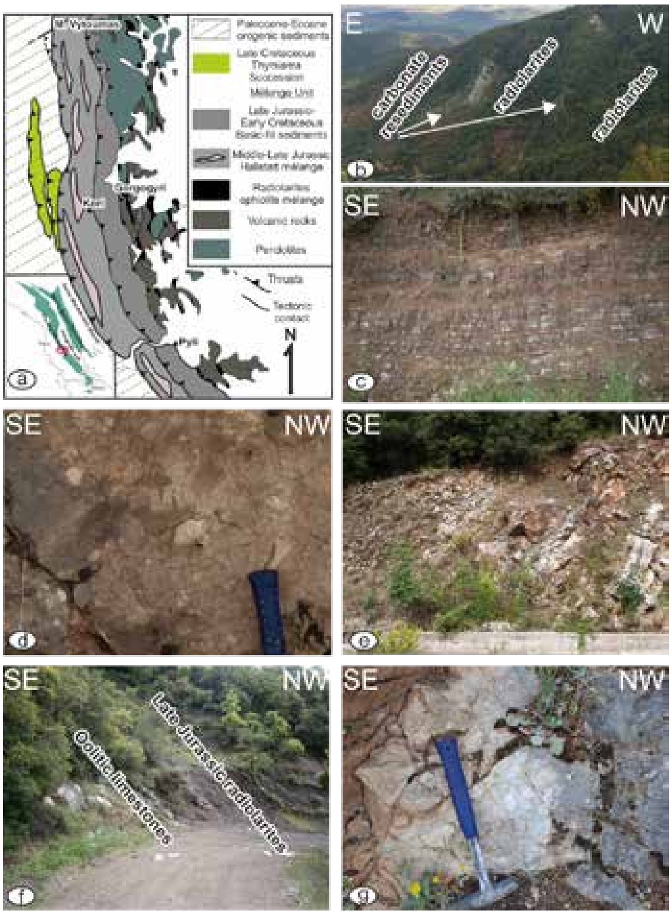

Figure 1. a) Simplified geological map of Koziakas massif (modified after Chiari et al., 2012). b) Panoramic view of the Late Jurassic-Early Cretaceous carbonate resediments intercalated in radiolarites. c) Radiolarite sequence. d) Polymictic breccia with Hallstatt components. e) Hallstatt Limestone block within Middle to early Late Jurassic argillaceous-radiolaritic matrix. f) Late Jurassic radiolarites intercalated by oolitic limestones. g) Late Jurassic to earliest Cretaceous shallow-water carbonate-clastic resediments.

Discussion/Conclusions

Carbonate rocks originating from formations of the outer passive continental margin (Hallstatt Facies) are often found as exotic blocks incorporated within mélanges, a phenomenon widely observed in collisional belts (Gawlick & Missoni, 2019). These exotic blocks serve as valuable tools for reconstructing the original configuration of passive continental margins, as demonstrated in studies of the Dinarides, Albanides, and more recently, the Hellenides (Kostaki *et al.*, 2024, and references therein). Similarly, the exotic open-marine carbonate blocks within the Koziakas mélange provide critical insights into the disrupted architecture of the former passive margin preceding ophiolite obduction. Our analysis reveals that these blocks, spanning ages from the latest Ladinian–earliest Carnian, Late Carnian, and the entire Norian, correspond to a dismembered Triassic Hallstatt Limestone succession characterized by distinctive lithology, microfacies, and stratigraphy. The Hallstatt Facies were originally deposited on the outer shelf during the Middle Anisian to Rhaetian, along with the continental slope Meliata Facies, shaping the eastern Adriatic passive continental margin that faced Neo-Tethys Ocean to the east (e.g., Sudar *et al.*, 2013; Fig. 2a). However, in most instances, the Hallstatt Facies have been disrupted during Middle-Late Jurassic ophiolite obduction and preserved as components or complete successions within massive blocks and slides found in Middle to Late Jurassic far-traveled mélanges along the Alpine-Carpathian-Dinaridic collisional belt (e.g., Gawlick & Frisch, 2003). The Hallstatt Facies can be subdivided into (Gawlick *et al.*, 2018): the reef-proximal facies, characterized by light grey hemipelagic limestones intercalated with shallow-water turbidites, and the distal outer shelf facies, which consists of variously colored limestones. Within the distal outer shelf facies, two types are recognized (Krystyn, 2008): a) the famous fossil-rich facies featuring red bioclastic condensed limestone layers with local enrichment in cephalopods, and b) the facies poor in megafauna, characterized by red to whitish to grey bedded limestones with local enrichment in filaments, radiolarians and echinoderms. The biostratigraphy of the latter facies primarily relies on conodonts. In the Hellenides, the reef-proximal facies are well-represented by Middle Triassic to Early Jurassic cherty limestones intercalated with turbidites with shallow-water material, notably observed in the Argolis Peninsula, Orthis, and Hydra (Baumgartner, 1985, Ferrière *et al.*, 2016). These limestones are interpreted as west-directed, far-traveled nappes associated with a Jurassic obduction of ophiolites originating from an oceanic realm east of the Pelagonian units (for an alternative view, see Clift & Robertson, 1990). Representing the central shelf dominated by shallow-water carbonates, the Pelagonian units served as a source for sedimentary input into the adjacent reef-proximal outer shelf environment during the Middle Triassic to Early Jurassic. A west-directed ophiolite obduction over the Pelagonian units during the late Middle to early Late Jurassic aligns with our structural observations and other published works (e.g., Kilias *et al.*, 2010, Bortollotti *et al*. 2012, and references therein). In the Avdella mélange, an equivavent mélange to the Koziakas mélange, NW-SE trending asymmetric tight to sub-isoclinal folds with a predominant top-to-the-SW sense of movement are well-preserved and associated with the emplacement of the Pindos ophiolites (Kostaki *et al.*, 2024). Additionally, ductile to semi-ductile shear zones, characterized by well-developed cinematic indicators (e.g. σ-clasts, shear bands, S-C-C` structures), clearly show a west to southwestward sense of shear, although, in some places, they are affected by the younger Tertiary brittle deformation, which typically characterizes the post-obduction phase. Furthermore, similar to the Koziakas mélange, the Avdella mélange contains open-marine Triassic blocks, from which a dismembered Hallstatt succession has been reconstructed (Kostaki *et al.*, 2024). Both mélanges, exhibiting identical characteristics, developed during the Middle to early Late Jurassic as a result of westward ophiolite obduction. Ahead of the advancing ophiolites, trench-like deep-water basins formed, receiving material from the progressing nappe stack, including Hallstatt Facies and ophiolites (Fig. 2b). These basins were subsequently sheared and incorporated into the nappe stack, resulting in the characteristic features of mélanges. Notably, the reconstructed Hallstatt succession from exotic blocks within the Avdella and Koziakas mélanges closely resemble the complete open-marine Middle Triassic to Early Jurassic succession preserved in the Western Pindos, indicating that the Western Pindos succession is the paleogeographic source of the open-marine exotic blocks (complete correlation in Kostaki *et al.*, 2024, Kostaki, 2024). This succession, attributed to the Hallstatt Facies due to its identical lithological and stratigraphic characteristics, represents the distal outer shelf facies. The original deposition of the Western Pindos succession is identified as taking place on the outer shelf from the Middle Triassic until the Early Jurassic east of the Pelagonian units, constituting the easternmost segment of the Adriatic plate (Kostaki *et al.*, 2024). During the late Middle to early Late Jurassic, the west-directed obduction of the Neo-Tethys ophiolites led to the formation of a nappe stack (Fig. 2b**)**. As a result, the Western Pindos succession also became part of this nappe stack and was subsequently bulldozed westward, providing material to trench-like deep-water basins that later evolved into mélanges. This Jurassic westward movement, reflected in both the mélanges and the ophiolites (Kilias, 2024), ultimately transported the Western Pindos succession onto the foreland, reaching the inner parts of the Pelagonian units. Consequently, in its new position during the early Late Jurassic, the Western Pindos succession underwent new sedimentation, resulting in its coverage by a subsequent Late Jurassic to Paleogene sequence. This sequence contributed to a misconception regarding its original deposition, which was perceived as parautochthonous and referred to as Pindos basin. Our biostratigraphic analysis of the exotic blocks found in the Koziakas mélange indicates that the lowermost Carnian blocks are characterized by the influence of shallow-water material, suggesting their original deposition in proximity to the central shelf. This interpretation aligns with the development of the Wetterstein Carbonate Platform, which evolved during the Late Ladinian and lasted until the Early Carnian, shedding debris into the outer shelf region.

Furthermore, our study of the Koziakas mélange unit provides additional insights into nappe stacking processes, the timing of events, and the Middle Jurassic to Early Cretaceous paleogeography. Based on our structural observations, the Koziakas mélange unit can be divided into three tectono-sedimentary sub-units: a) an ophiolitic mélange at the base, consisting exclusively of components derived from the ophiolites and their radiolarite cover, predominantly Triassic radiolarite components (see also Chiari *et al.*, 2012); b) a mélange upsection, dominated by Triassic Hallstatt limestone blocks within an argillaceous-radiolaritic matrix; c) an overlying sequence of radiolarites intercalated by carbonate turbidites and oolitic limestones, transitioning at higher stratigraphic levels into shallow-water carbonate-clastic resediments. The formation of ophiolitic mélanges occurred at the base of the advancing ophiolites, following the onset of intra-oceanic subduction and the development of metamorphic soles. Radiometric dating and geochemical analysis indicate a Middle Jurassic age (174 ± 3 Ma and 161 ± 1 Ma) for the formation of Koziakas ophiolites' metamorphic sole within a MORB-type lithosphere influenced by IAT characteristics (Pomonis *et al.*, 2002). This setting initiated a west-directed ophiolite obduction onto the passive continental margin during the Bajocian-Bathonian, imbricating the lower plate and leading to the formation of trench-like deep-water basins (Fig. 2b). These basins received material from the advancing nappe stack, which later evolved into the mélange with the Hallstatt blocks (Fig. 2c). The timing of ophiolite obduction and the formation of trench-like deep-water basins as Middle to early Late Jurassic is supported by biostratigraphic data obtained from equivalent mélanges across the Albanides and Dinarides (Gawlick *et al.*, 2017), aligning with radiolarian age dating from the Koziakas mélange, which indicate a latest Bajocian to Early Callovian age (Chiari *et al.*, 2012). This is further supported by the evolution of Kimmeridgian–Tithonian shallow-water platforms atop the obducted ophiolites, suggesting that ophiolite emplacement over the Pelagonian units predates the formation of these platforms (Kostaki *et al.*, 2013, 2024). By that time, the nappe stack had advanced into the foreland, and the progressing basin system developed into a trench-like foreland basin in front of the obducted Koziakas ophiolites, where the radiolarite sequence of the Koziakas was deposited above the mélange with the Hallstatt blocks (Fig. 2c, d). Extending for several meters, this radiolarite sequence reflects a period of relative tectonic silence during the Oxfordian to the Kimmeridgian, as indicated by radiolarian age dating (Kostaki, 2024). The influence of a shallow-water environment from the Kimmeridgian-Tithonian platform atop of the ophiolites during the late Oxfordian to Tithonian became evident through the deposition of radiolarites intercalated with carbonate turbidites and oolitic limestones. Subsequently, from the latest Tithonian onwards, erosional products of this platform were redeposited in this remaining underfilled foreland basin, forming carbonate-clastic resediments. Microfacies analysis of these resediments reveals Kimmeridgian Saccocoma-bearing limestones and Tithonian shallow-water clasts mixed with Late Triassic carbonate clasts. This phase of erosion is attributed to the tectonic uplift of the accreted former Pelagonian margin from the Tithonian onwards, initially affecting the Late Jurassic shallow-water platform, then the ophiolites and their radiolarite cover, and later extending to the Triassic to Early Jurassic shallow-water Pelagonian carbonates. The ongoing uplift and unroofing led to further westward transport of the ophiolites and the overlying shallow-water platform, bringing them closer to the under-filled foreland basin (Fig 2d). In this setting, erosional products, including reworked Late Jurassic shallow-water platform clasts and Triassic carbonate clasts, were redeposited, forming carbonate-clastic resediments. The basin remained under-filled, allowing sedimentation to continue until the earliest Cretaceous (Ghon *et al.*, 2018). In contrast to the Koziakas setting, which partially escaped complete overthrusting by the ophiolites and allowed for prolonged sedimentation with minimal deformation of the basin fill sediments, the Avdella mélange was totally overthrust by the ophiolites, exhibiting the typical characteristics of a mélange.

Our perspective aligns with paleogeographic reconstructions of other regions within the Alpine-Carpathian-Dinaridic belt, characterized by a well-organized passive continental margin consisting of a central shelf (the Pelagonian unit) and an outer shelf dominated by Hallstatt Facies. In the Hellenides, these facies are represented by the Triassic–Early Jurassic Western Pindos succession, which we interpret as a west-directed, far-traveled nappe during Middle to early Late Jurassic. Our findings support the existence of a single Neo-Tethys Ocean located east of the broader Adria, with the Pelagonian unit forming its easternmost continuation without any interruption of an autonomous Pindos Ocean or a Triassic-Jurassic deep-water Pindos Basin.

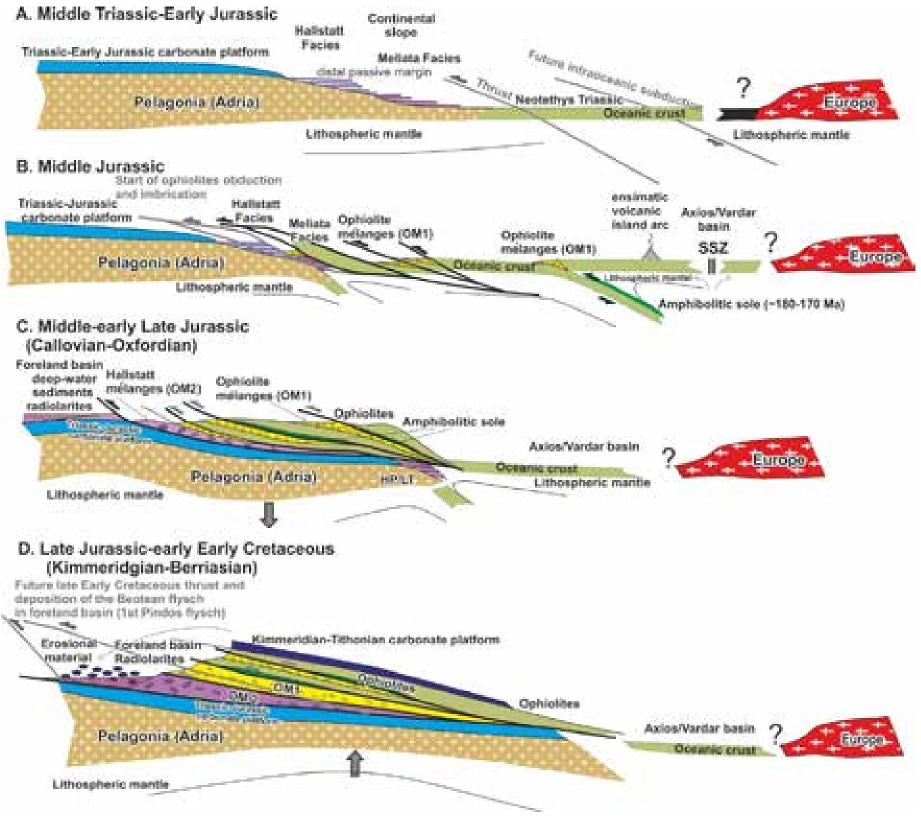

Figure 2. Reconstruction of the Middle Triassic to Early Cretaceous paleogeographic and geotectonic evolution.

Acknowledgements

We acknowledge the late Sigrid Missoni, whose contributions to this research were invaluable. The assistance of Dr. Agni

Vamvaka and Dr. Aristides Sfeikos during fieldwork is greatly appreciated. We also thank the editors for their support throughout the publication process.

References

Baumgartner, P.O., 1985. Jurassic sedimentary evolution and nappe emplacement in the Argolis Peninsula (Peloponnesus; Greece). Mémoires de la Société Helvétique des Sciences Naturelles 99, 111 p.

Bortolotti, V., Chiari, M., Marcucci, M., Marroni, M., Pandolfi, L., Principi, G., Saccani, E., 2004. Comparison among the Albanian and Greek ophiolites: In search of constraints for the evolution of the Mesozoic Tethys Ocean. Ofioliti 29(1), 19-35.

Bortolotti, V., Chiari, M., Marroni, M., Pandolfi, L., Principi, G., Saccani, E., 2012. Geodynamic evolution of ophiolites from Albania and Greece (Dinaric-Hellenic –belt): one, two or more oceanic basins? International Journal of Earth Sciences 102, 783-811.

Chiari, M., Bortolotti, V., Marcucci, M.C. and Saccani, E., 2012. Radiolarian Biostratigraphy and Geochemistry of the Koziakas Massif Ophiolites (Greece). Bulletin de la Societe Geologique de France 183, 287-306.

Clift, P.D. and Robertson, A.H.F., 1990. Deep-water basins within the Mesozoic carbonate platform of Argolis, Greece. Journal of the Geological Society London 147, 825-836.

Ferrière, J., Baumgarthner, P.O., Chanier, F., 2016. The Maliac Ocean: the origin of the Tethyan Hellenic ophiolites. International Journal Earth Sciences 105, 1941-1963.

Festa, A., Ogata, K., Pini, G.A., Dilek, Y., Alonso, J.L., 2016. Origin and significance of the olistostromes in the evolution of the orogenic belts: a global syntheisis. Gondwana Research 39, 180-203.

Frisch, W., Gawlick, H.J., 2003. The nappe structure of the central Nothern Calcareous Alps and its disintegration during Miocene tectonic extrusion-A contribution to understanding the orogenic evolution of the Eastern Alps. International Journal of Earth Science 92, 712-727.

Gawlick, H.-J., Frisch, W., 2003. The Middle to Late Jurassic carbonate clastic radiolaritic flysch sediments in the Northern Calcareous Alps: sedimentology, basin evolution and tectonics - an overview. Neues Jahrbuch für Geologie und Paläontologie, Abh. 230, 163–213

Gawlick, H.-J., Sudar, M.N., Missoni, S., Suzuki, H., Lein, R., Jovanovic, D., 2017. Triassic- Jurassic geodynamic evolution of the Dinaridic Ophiolite Belt (Inner Dinarides, SW Serbia). Journal of Alpine Geology 55, 1–167.

Gawlick, H.-J., Missoni, S., Sudar, M.N., Suzuki, H., Meres, S., Lein, R., Jovanovic, D., 2018. The Jurassic Hallstatt Mélange of the Inner Dinarides (SW Serbia): implications for Triassic-Jurassic geodynamic and palaeogeographic reconstructions of the Western Tethyan realm. Neues Jahrbuch Geologie Paläontologie, Abh. 288, 1–47.

Gawlick, H.-J., Missoni, S., 2019. Middle-Late Jurassic sedimentary melange formation related to ophiolite obduction in the Alpine-Carpathian-Dinaridic Mountain Range. Godwana Research 74, 144-172.

Ghon, G., Gawlick, H.-J., Missoni, S., Djeric, N., Kilias, A., Gorican, S., 2018. Age and microfacies of a carbonate-clastic radiolaritic basin fill above the Koziakas Mélange (Hellenides, Greece). XXI International Congress of CBGA, Salzburg, Austria.

Kilias, A., Frisch, W., Avgerinas, A., Dunkl, I., Falalakis, G., Gawlick, H.-J., 2010. Alpine architecture and kinematics of deformation of the northern Pelagonian nappe pile in the Hellenides. Austrian Journal of Earth Sciences 103/1, 4-28.

Kilias, A., (2024). The Alpine Geological History of the Hellenides from the Triassic to the Present—Compression vs. Extension, a Dynamic Pair for Orogen Structural Configuration: A Synthesis. Geosciences 14, 10.

Kostaki, G., Kilias, A., Gawlick, H-J., Schlagintweit, F., 2013. Kimmeridgian- Tithonian shallow-water platform clasts from mass flows on top of the Vardar/Axios ophiolites. Bulletin of the Geological Society of Greece 47, 184–193.

Kostaki, G., Gawlick, H.-J., Missoni, S., Kilias, A., Katrivanos, E., 2024. New stratigraphic and paleontological data from carbonates related to the Vourinos-Pindos ophiolite emplacement: Implications for the provenance of the ophiolites (Hellenides). Journal of Geological Society of London 181.

Kostaki, G., 2024. Late Jurassic-Early Cretaceous shallow water sediments on the top of the Tethyan ophiolites of the Hellenides (Northern Greece). Ph.D. Thesis, Aristotle University of Thessaloniki, Thessaloniki, 200 p.

Krystyn, L., 2008. The Hallstatt pelagics- Norian and Rhaetian Fossillagerstaetten of Hallstatt. Berichte der Geologischen Bundesanstalt Wien 76, 81-98.

Pomonis, P., Tsikouras, B., Hatzipanagiotou, K., 2002. Origin, evolution and radiometric dating of the sub-ophiolitic metamorphic rocks from the Koziakas ophiolite (W. Thessaly, Greece). Neues Jahrbuch für Mineral, Abh. 177, 255-276.

Robertson, A.H.F., 2012. Late Paleozoic-Cenozoic tectonic development of Greece and Albania in context of alternative reconstructions of Tethys in the Eastern Mediterranean region. International Geology Review 54, 373-454.

Schmid, S.M., Bernoulli, D., Fugenschuh, B., Matenco, L., Scheffer, S., Schuster, R., Tischler, M., Ustaszewski, K., 2008. The Alpine-Carpathian-Dinaric orogenic system: correlation and evolution of tectonic units. Swiss Journal of Geosciences 101, 139-183.

Sudar, M.N., Gawlick, H.-J., Lein, R., Missoni, S., Kovacs, S., Jovanovic, D., 2013. Depositional environment, age and facies of the Middle Triassic Bulog and Rid formation in the Inner Dinarides (Zlatidor Mountain, SW Serbia): evidence for the Anisian break-up of the Neotethys Ocean. Neues Jahrbuch fur Geologie und Palaontologie, Abh. 269, 291-320.

17th INTERNATIONAL CONGRESS
of the Geological Society of Greece

BULLETIN OF THE GEOLOGICAL SOCIETY OF GREECE, SP. PUBL.

EXTENDED ABSTRACT 163

Assessing Climate Extremes as Drivers of Geohazards in Greece

Kostopoulou E.[1], Giannakopoulos C.[2], Nefros C.[3], Loupasakis C.[3]

(1) Department of Geography, University of the Aegean, Greece, ekostopoulou@aegean.gr (2) Institute for Environmental Research and Sustainable Development, National Observatory of Athens, Greece, (3) School of Mining and Metallurgical Engineering, National Technical University of Athens, Athens 15780, Greece

Climate extremes have become more frequent and intense in recent years due to global climate change, leading to an increased risk of geohazard occurrences. Extreme events, such as heavy precipitation, can contribute directly to the occurrence of geohazards, including floods and landslides. Additionally, prolonged heatwaves can directly lead to increased soil erosion and indirectly to more frequent and intense wildfires, which, in turn, can increase landslide hazard, by reducing vegetation cover and destabilizing the soil. This study examines historical climate data and future projections, to identify potential climatic changes, which may induce geohazards in Greece.

Introduction

The Mediterranean, a climate change hotspot, is warming 20% faster than the global average (Lionello and Scarascia, 2018; MedECC, 2020; IPCC, 2021), with Greece, as part of the region, following a similar trend. The impact of climate change becomes evident with the increasing variability in temperature, precipitation, and wind patterns leading to more frequent and severe climatic extremes (Giannakopoulos et al., 2011; Lelieveld et al., 2012; Zittis et al., 2016; 2014, Politi et al., 2022, Kostopoulou and Giannakopoulos, 2023 Kostopoulou et al., 2024). Rising temperatures and shifting rainfall patterns exacerbate soil erosion, increase the frequency of floods, and destabilize slopes. This study focuses on the assessment of climate extreme indices in Greece and their direct and indirect impacts on potential future geohazards. Using climate data from the Copernicus Climate Change Service/Climate Data Store (https://cds.climate.copernicus.eu/) we analyze climate variables, indices, based on historical data and projections of future climate scenarios. The ERA5-Land is a global land-surface climate reanalysis produced by the European Centre for Medium-Range Weather Forecasts (ECMWF), providing data at various temporal resolutions from 1950 onward (Muñoz-Sabater et al., 2021). The high-resolution regional climate model data were extracted from the EURO-CORDEX database (Jacob et al., 2014). The climate projections cover the period 1971–2100 and have been used to examine future changes. The projections were estimated for two future emissions scenarios, the moderate RCP4.5 and the more extreme RCP8.5 (Moss et al., 2010). Furthermore, we study maps from the European Climate Risk Typology (https://european-crt.org/) projecting changes in representative climate indices, under the high-emissions 'RCP8.5' global warming scenario, which are related to specific hazards in Greece at regional scale. In the following sections, historical and model-projected time series of temperature and precipitation are analyzed. Subsequently, changes in climate indices and hazard indicators across Greece are presented.

Time Series Analysis of Climate Data and Projections

Reanalysis data from the ERA5-Land dataset are used to describe present climate conditions in Greece. Over the historical period 1950–2022, the mean annual temperature (TM) averaged 13.9°C. In the first half of the period, the annual TM was 13.6°C, while in the second half, it increased to 14.2°C. Anomalies from the 1991–2020 mean range from -1.5°C to 0.8°C, with nine of the ten warmest years occurring after 2010.

Increasing trends are particularly observed in daily mean, minimum, and maximum temperatures (hereafter TM, TN, and TX) on both annual and seasonal scales. Figure 1 illustrates the variations in TN and TX during winter (December to February – DJF) and summer (June to August – JJA) over the historical period. Both seasons show increasing trends, with summer temperatures exhibiting a steeper rise. Focusing on the positive anomalies, we observed deviations of 2.1°C and 1.5°C for TN, and 2.4°C and 2.3°C for TX in winter and summer, respectively, compared to the 30-year average for the period 1991–2020. However, when comparing to the average of the earlier 30-year period (1951–1980), the positive deviations reach up to 2.3°C for TN in both winter and summer, 2.9°C for winter TX, and 3.1°C for summer TX. Hence, both seasonal TN and TX are increasing in Greece, with TX exhibiting a faster rate of warming. The increasing temperatures can contribute to more frequent and severe wildfires, which, in turn, increase the risk of soil erosion (Depountis et al., 2020) and landslides (Nefros and Loupasakis, 2023), especially in mountainous areas. The rise in temperatures may also lead to increased droughts, further stressing water resources and enhancing the risk of desertification in certain regions.

Warming is projected to continue in the future, with both seasonal TN and TX expected to rise further in Greece. Figure 2 shows future projections for the near term (2021–2040), medium term (2041–2060), and long term (2081–

2100). As revealed under both RCP4.5 and RCP8.5 scenarios, not only TX and TN are projected to increase, but the number of heatwave days (TX exceeding 35° C) is expected to rise, while the number of frost days (TN below 0° C) is anticipated to decline. Moreover, according to the CORDEX-EUR-11 climate model, TX and TN are anticipated to increase, with changes ranging from 2°C to over 4°C by the end of the 21st century under the RCP4.5 and RCP8.5 scenarios, respectively.

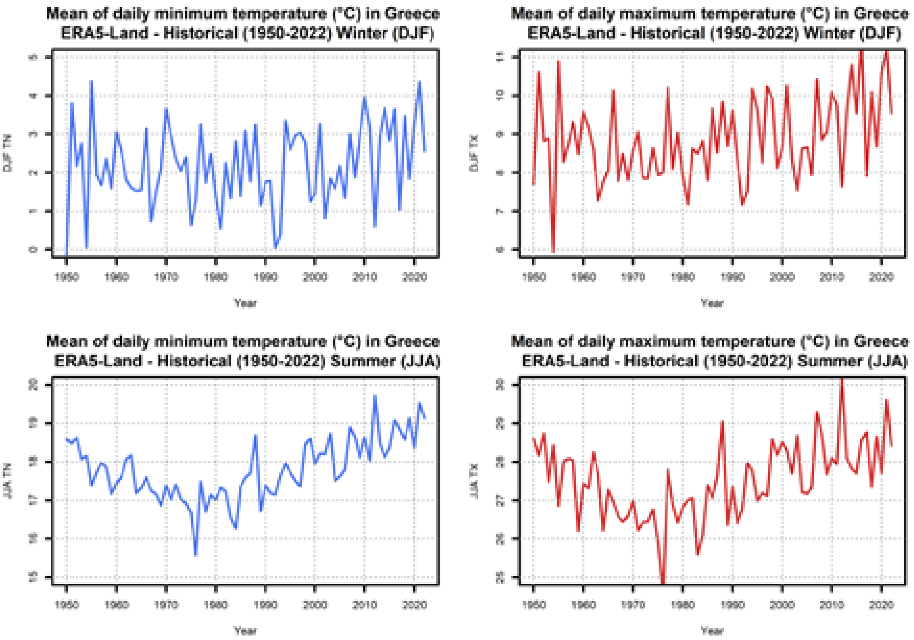

Figure 1. Variations in TN -mean daily minimum (blue) and TX -maximum (red) temperatures over the historical period 1950–2022 during winter (top) and summer (bottom) in Greece.

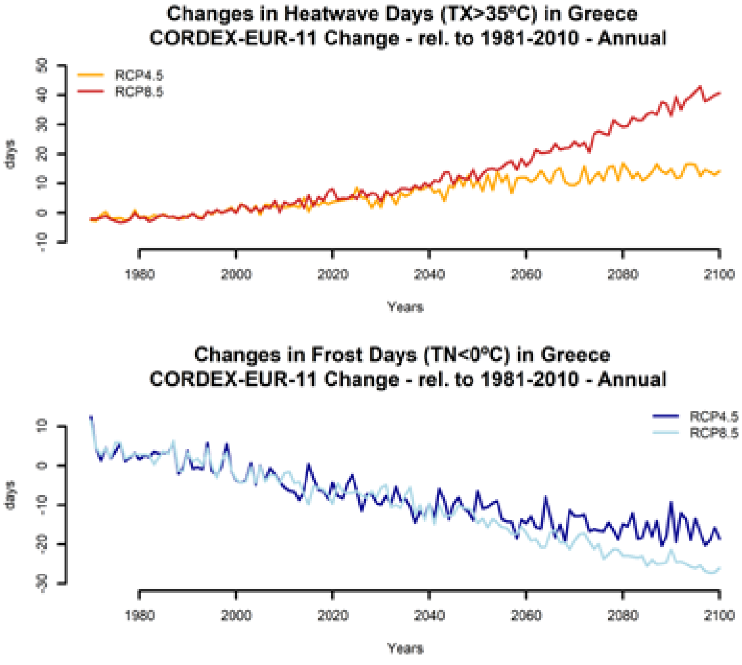

Figure 2. Simulated changes in the number of days with TX above 35°C (top) and TN below 0°C (bottom) in Greece, relative to the 30-year historical period 1981–2010.

Concerning precipitation, the mean daily accumulated precipitation fluctuates around its average over the historical period 1950-2022 (Figure 3, left column panels), with both wetter and drier years evident. An increasing trend has been observed in the annual maximum 1-day precipitation over the past decade, although this is not a long-term pattern and the trend remains uncertain. However, a more distinct trend is evident in the annual mean daily evaporation, likely driven by the rising temperatures. Regarding future changes (Figure 3, right column panels), the mean daily accumulated precipitation is projected to slightly decrease in the medium term (2041–2060) under both RCP4.5 and RCP8.5 scenarios, with a more pronounced decline under RCP8.5 in the long term (2081–2100). The annual maximum 1-day precipitation is expected to increase under both scenarios, particularly under RCP8.5, with an approximate increase of 5 mm per day. The combined effect of these changes suggests that while daily precipitation may decrease, precipitation on wet days could become more intense. The scenarios do not show a clear trend in the annual mean daily evaporation. The Standardized Precipitation Index (SPI; McKee et al., 1993) is of particular relevance, as it shows changes in precipitation relative to the average of a reference period and defines precipitation anomalies over time (i.e., dry and wet spells). The two maps shown in Figure 3, located at the far right of the figure, present the annual index values calculated over a 6-month period (SPI-6) for the medium and long term under RCP8.5. This index is typically used to identify short-term trends in precipitation. In both cases, negative values of the index are observed over Greece, indicating that the region is expected to experience drier-than-normal conditions. More specifically, the SPI-6 suggests moderate drought conditions in the medium term, which could become more severe towards the long-term period.

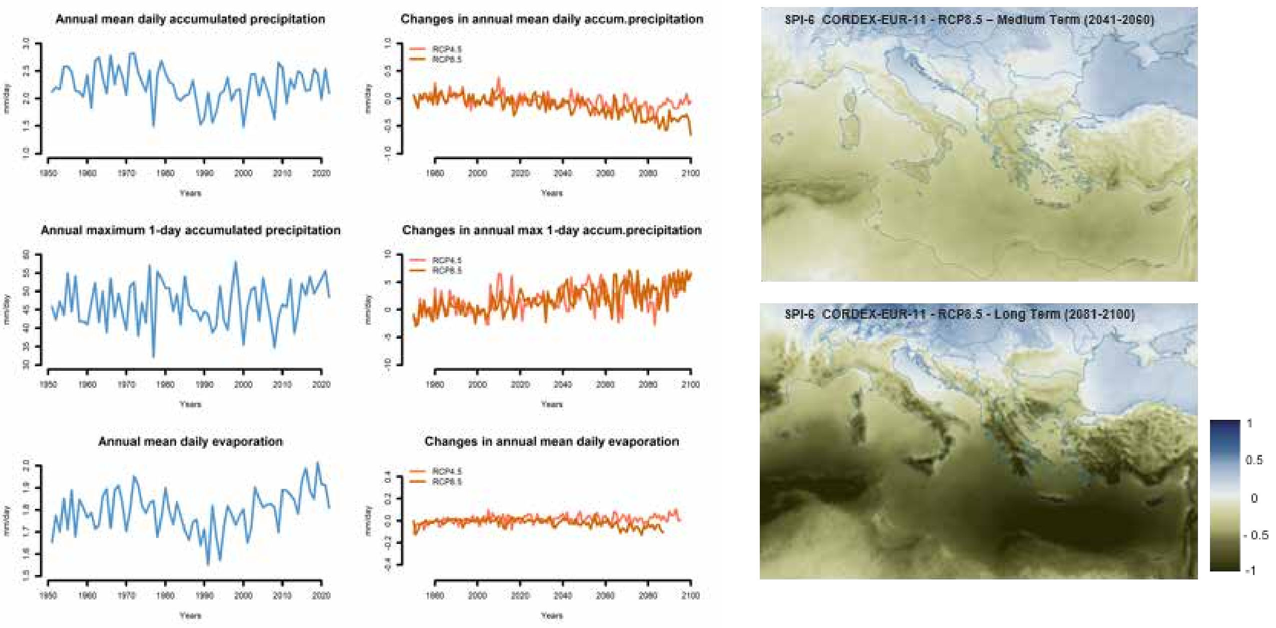

Figure 3. The diagrams show the observed values (left) and simulated changes (right) in mean daily precipitation (top), maximum 1-day precipitation (middle), and daily evaporation (bottom) in Greece. The maps, located at the far right of the figure, depict the annual SPI-6 under RCP8.5 for the medium term (2041–2060, top) and the long term (2081–2100, bottom).

Spatial Representation of Changes in Climate Indices and Hazard Indicators

Subsequently, data from the European Climate Risk Typology (European CRT, Carter et al., 2018) are utilized to examine the spatial distribution of projected climate index changes in Greece at regional unit scale (NUTS3 scale). The European CRT provides a systematic framework for assessing and classifying climate risks across Europe, facilitating a comprehensive understanding of their spatial distribution and intensity. This approach supports researchers and policymakers in developing targeted, region-specific climate adaptation strategies.

Extreme climate indices potentially related to the occurrence of specific hazards are shown and discussed. For example, the combined effect of increased temperatures and consecutive dry days creates favorable conditions for the development of drought hazards. Similarly, projections of changes in the number of consecutive wet days and extreme precipitation events provide insights into the potential for flood hazards. These maps present changes for the medium term (in this case the period 2036-2065, with respect to the reference period 1981-2010) under the RCP8.5 scenario.

The projected changes in heatwave days (TX > 35°C) are shown in Figure 4a. The Greek region is expected to experience positive changes across the entire area. Most regions are projected to see an additional 6–15 heatwave days by the mid-21st century. Notably, increases are observed in the islands of the eastern Aegean Sea. The most impacted areas, highlighted in red, are located in the central continental parts of the country. Increases are also observed in consecutive dry days (Figure 4b), with the eastern and southern parts of the country projected to experience the greatest impact. The number of consecutive dry days (precipitation < 1mm) may increase by 8 days in eastern Peloponnese and by 11 days in eastern Crete. In line with this finding, the next index refers to changes in wet spells, using the number of consecutive wet days (precipitation > 1mm). Here, we observe minimal changes, indicating a future trend toward increasing dryness in the region. The fourth index, presented in Figure 4d, shows the projected changes in heavy precipitation days. All Greek sub-regions show negative trends in heavy precipitation events. However, it is important to note that smaller-scale extreme events, such as localized heavy rainfall, may not be accurately captured by the model's long-term projections, particularly in areas with complex topography (e.g., mountains or coastal regions). As a result, extreme precipitation events may still occur despite the overall negative trend.

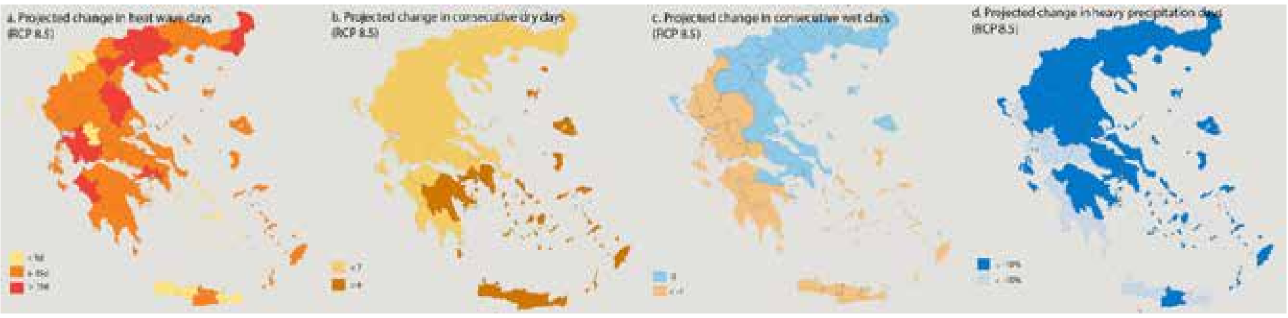

Figure 4. Projected changes under RCP8.5 in (a) heatwave days, (b) consecutive dry days, (c) consecutive wet days, and (d) heavy precipitation days (data source: european-crt.org).

Finally, maps showing several hazards over Greece were reproduced from the European CRT datasets. Figure 5 presents four types of hazards related to climate conditions. The indicator that defines 'Drought hazard' utilizes the Standardized Precipitation-Evapotranspiration Index (SPEI; Vicente-Serrano et al., 2010) at nine month timescales to provide a measure of meteorological drought. Negative values of SPEI reflect regions where precipitation over a nine-month period is reduced. Although most of the Greek region shows values below the European average, the light colors in northeastern Greece, the small islands of the Aegean, and eastern Crete indicates regions more susceptible to drought. This is of particular importance, especially for eastern Crete and the Cyclades islands in the Aegean, which are among the driest areas of the country and at high risk of desertification. The "Fluvial flooding" indicator highlights areas susceptible to flooding in the event of a 1-in-100-year fluvial flood. Parts of northeastern Greece, as well as the regions of Larissa, Voiotia, Ileia, Thesprotia, and especially Evros, are identified as areas prone to fluvial flooding. The "Landslide hazard" indicator highlights areas with moderate or higher susceptibility to landslides, considering both predisposing and triggering factors. While steep slopes are a key factor influencing landslide susceptibility, landslide hazard is determined by combining susceptibility with triggering factors, such as intense precipitation (Nadim et al., 2006). Landslides in Greece are usually triggered by heavy rainfall, seismic activity, and human activity such as deforestation, and constructions on geologically unstable or steep terrain. Changes in soil erosion can also impact landslide susceptibility (Huang et al., 2020), significantly also heighten the landslides hazard in various regions. Moreover, high temperatures and prolonged dry spells may exacerbate soil erosion, which can further increase landslides susceptibility. This indicator identifies several Greek sub-regions with values above the European average, indicating a higher susceptibility to landslides. The "Wildfire hazard" indicator uses data on past wildfire occurrences, vegetation types, climate variables, and the Canadian Forest Fire Weather Index (FWI; Van Wagner, 1987) to identify regions at risk. Most of Greece shows values above the European average, which can be attributed to the combination of rising temperatures and extended dry periods, particularly in subregions located in the eastern and southern parts of the country. Similarly, the increased wildfire hazard is expected to indirectly affect the occurrence of geohazards, such as soil erosion and landslides.

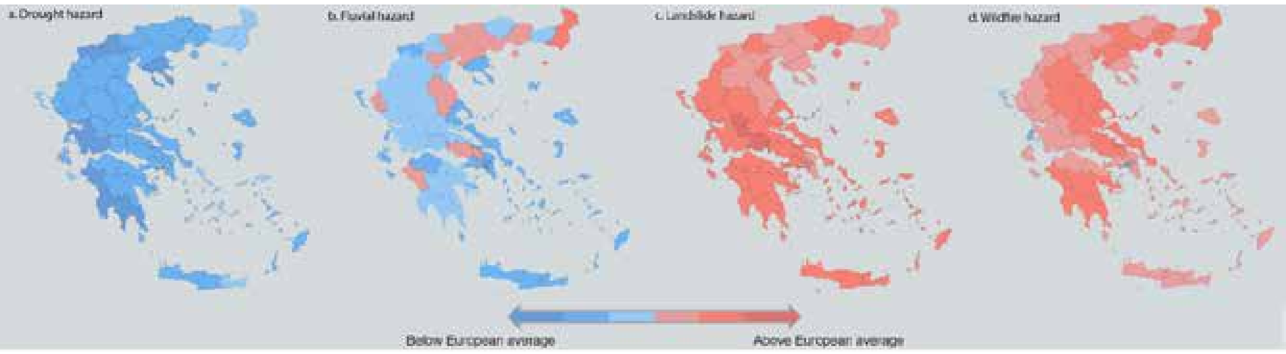

Figure 5. Estimated hazards under RCP8.5 for (a) drought, (b) fluvial flooding, (c) landslides, and (d) wildfires (data source: european-crt.org).

Conclusions

Analysis of climate data reveals a clear warming trend across Greece, with annual and seasonal temperatures rising, especially during summer. Projections suggest further warming of 2°C to beyond 4°C, by the century's end, depending on emission scenarios. Combined with prolonged dry spells, this will lead to more frequent and intense heatwaves, droughts, and wildfire risks, and in turn, to an increased occurrence of geohazards. While precipitation trends remain variable, heavy rainfall events do not show a clear increase, though models have difficulty capturing localized extremes. Future projections indicate a decline in mean daily accumulated precipitation, but an increase in the individual daily rainfall amounts, raising the risk of both droughts and floods, which can, in turn, impact accordingly soil erosion and landslides. The SPI-6 indicates drier conditions, especially under high-emission scenarios. Eastern and southern Greece is most vulnerable to drought, while coastal and mountainous areas face increased flooding, landslides, and soil erosion. Wildfire risks will also rise, especially in the east and south. These findings highlight the need for targeted adaptation strategies to mitigate extreme climate impacts on geohazards, particularly in high-risk regions.

Acknowledgements

We acknowledge the use of data from the Copernicus Climate Change Service (C3S) and the Climate Data Store (CDS), specifically the ERA5-Land dataset and the CORDEX-EUR-11 climate model data. We also thank the European Climate Risk Typology for contributing essential data on climate risk indicators.

References

Carter, J.G, Hincks, S, Vlastaras, V, Connelly, A., Handley, J., 2018. European Climate Risk Typology. [ONLINE] Available at: http://european-crt.org/index.html

Depountis, N., Michalopoulou, M., Kavoura, K., Nikolakopoulos, K., Sabatakakis, N., 2020. Estimating Soil Erosion Rate Changes in Areas Affected by Wildfires. ISPRS International Journal of Geo-Information 9, 562.

Giannakopoulos, C., Kostopoulou, E., Varotsos, K.V., Tziotziou, K., Plitharas, A., 2011. An integrated assessment of climate change impacts for Greece in the near future. Reg Environ Change 11, 829–843.

Huang, F., Jiawu C., Zhen D., Chi Y., Jinsong H., Qinghui J., Zhilu C., Shu L., 2020. Landslide Susceptibility Prediction Considering Regional Soil Erosion Based on Machine-Learning Models. ISPRS International Journal of Geo-Information 9, no. 6, 377.

IPCC, 2021. Climate Change 2021: The Physical Science Basis. Contribution of Working Group I to the Sixth Assessment Report of the Intergovernmental Panel on Climate Change[Masson-Delmotte, V., P. Zhai, A. Pirani, S.L. Connors, C. Péan, S. Berger, N. Caud, Y. Chen, L. Goldfarb, M.I. Gomis, M. Huang, K. Leitzell, E. Lonnoy, J.B.R. Matthews, T.K. Maycock, T. Waterfield, O. Yelekçi, R. Yu, and B. Zhou (eds.)]. Cambridge University Press, Cambridge, United Kingdom and New York, NY, USA.

Jacob, D., Petersen, J., Eggert, B., Alias, A., Christensen, O.B., Bouwer, L.M., Braun, A., Colette, A., Déqué, M.; Georgievski, G., et al., 2014. EURO-CORDEX: New high-resolution climate change projections for European impact research. Reg Environ. Change 14, 563–578.

Kostopoulou, E., Giannakopoulos, C., 2023. Projected Changes in Extreme Wet and Dry Conditions in Greece. Climate 11(3), 49.

Kostopoulou, E., Giannakopoulos, C., Mirasgedis, S., 2024. Aspects of Climate Change in Greece. In: Darques, R., Sidiropoulos, G., Kalabokidis, K. (eds) The Geography of Greece. World Regional Geography Book Series. Springer.

Lelieveld, J., Hadjinicolaou, P., Kostopoulou, E., Chenoweth, J., El Maayar, M., Giannakopoulos, C., Hannides, C., Lange, M.A., Tanarhte, M., Tyrlis, E., Xoplaki, E., 2012. Climate change and impacts in the Eastern Mediterranean and the Middle East. Climatic Change 114, 667–687.

Lelieveld J, Hadjinicolaou P, Kostopoulou E, Giannakopoulos C, Pozzer A, Tanarhte M, Tyrlis E., 2014. Model projected heat extremes and air pollution in the eastern Mediterranean and Middle East in the twenty-first century. Regional Environmental Change 14, 1937-1949.

McKee, T.B., Doesken, N.J., Kleist, J., 1993. The relationship of drought frequency and duration to time scale. In: Proceedings of the Eighth Conference on Applied Climatology, Anaheim, California, 17–22 January 1993. Boston, AMS, 179–184.

MedECC, 2020. Climate and Environmental Change in the Mediterranean Basin – Current Situation and Risks for the Future. First Mediterranean Assessment Report [Cramer, W., Guiot, J., Marini, K. (eds.)] Union for the Mediterranean, Plan Bleu, UNEP/MAP, Marseille, France, 632pp.

Moss, R.H., Edmonds, J.A., Hibbard, K.A., Manning, M.R., Rose, S.K., Van Vuuren, D.P., Carter, T.R., Emori, S., Kainuma, M., Kram, T., 2010. The next generation of scenarios for climate change research and assessment. Nature 463, 747–756.

Muñoz-Sabater, J., Dutra, E., Agustí-Panareda, A., Albergel, C., Arduini, G., Balsamo, G., Boussetta, S., Choulga, M., Harrigan, S., Hersbach, H., Martens, B., Miralles, D. G., Piles, M., Rodríguez-Fernández, N. J., Zsoter, E., Buontempo, C., and Thépaut, J.-N., 2021. ERA5-Land: A state-of-the-art global reanalysis dataset for land applications, Earth Syst. Sci. Data 13, 4349–4383.

Nadim, F., Jaedicke, C., Smebye, H., Kalsnes, B., 2006. Assessment of global landslide hazard hotspots. International Centre for Geohazards (ICG) / Norwegian Geotechnical Institute (NGI), Oslo, Norway. IPL Project C102

Nefros, C., Loupasakis, C., 2023. Landslide Risk Management in Areas Affected by Wildfires or Floods: A Comprehensive Framework Integrating GIS, Remote Sensing Techniques, and Regional Climate Models. Bull. Geol. Soc. Greece 60 (1), 27–68.

Politi, N., Vlachogiannis, D., Sfetsos, A., Nastos, P.T., 2023. High resolution projections for extreme temperatures and precipitation over Greece. Clim Dyn 61, 633–667.

Vicente-Serrano, S.M., Beguería, S., López-Moreno, J.I., 2010. A multi-scalar drought index sensitive to global warming: the standardized precipitation evapotranspiration index - SPEI. Journal of Climate 23 (7), 1696-1718.

Van Wagner, C.E. 1987. Development and structure of the Canadian forest fire weather index system. Forestry Technical Report 35. Canadian Forestry Service.

Zittis, G., Hadjinicolaou, P., Fnais, M., Lelieveld, J., 2016. Projected changes in heat wave characteristics in the eastern Mediterranean and the Middle East. Reg Environ Change 16, 1863–1876.

Submarine geomorphological structures in the Ionian Sea, Greece

Kothri S.[1], Nomikou P.[1], Loreto M.F.[2], Ranero R.C.[3,4], Lampridou D.[1], Nikoli E.[1], Merino I.[5], Ferrante V.[2], Poulos S.[1], Ganas A.[6]

(1) National and Kapodistrian University of Athens, Athens, Greece, skothri@geol.uoa.gr, (2) CNR – ISMAR, Istituto di Scienze Marine, Bologna, Italy, (3) Institució Catalana de Recerca i Estudis Avançats, ICREA, Barcelona, Spain, (4) Barcelona Center for Subsurface Imaging, ICM, CSIC, Barcelona, Spain, (5) Faculty of Geosciences, University of Bremen, Bremen, Germany, (6) Institute of Geodynamics – National Observatory of Athens, Greece

Introduction

The underwater geomorphology of tectonically active regions is essential for understanding seismic hazards, particularly in areas with a history of destructive earthquakes. The Ionian Sea, situated at the convergence of major tectonic domains in the Mediterranean, represents a region of significant scientific interest (Fig.1). It likely features an upper crustal fault system overlying the megathrust fault system of the Hellenic Subduction Zone, trending NW-SE to NNW-SSE, which contributes to its high seismic hazard potential (Ranero et al., 2023).

Figure 1. The location of the study area in relation to continental Greece (the bathymetry is from EMODnet, while in red are shown simplified fault lines of on- and offshore Greece)

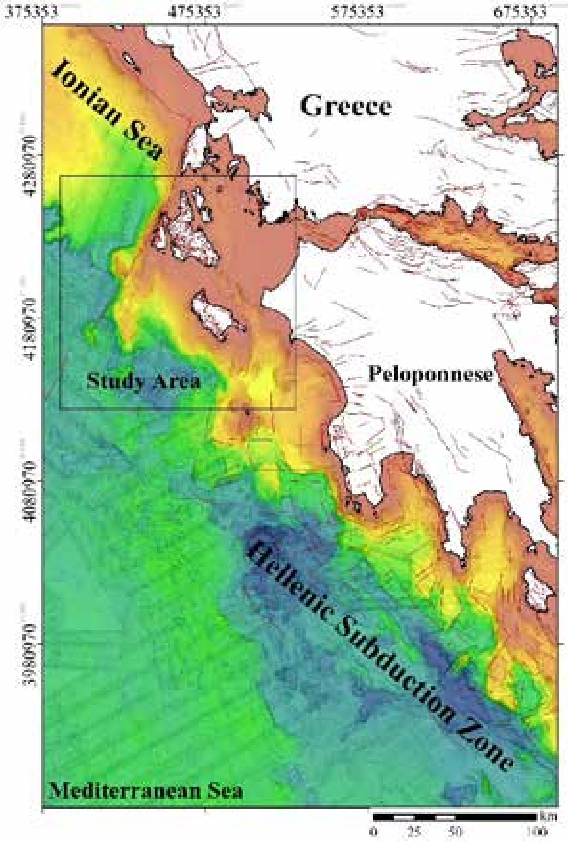

The POSEIDON Eurofleet+ cruise (10–22 June 2023) aboard Research Vessel (R/V) *Laura Bassi* focused on mapping the tectonic structure of the Ionian Sea, particularly near the western Peloponnese and Ionian Islands, including Lefkada, Cephalonia, and Zakynthos (Fig.1). This region is characterized by a complex fault network and exhibits the highest instrumentally recorded seismic activity in the Mediterranean, often associated with tsunamigenic potential, as exemplified by the 1953 Cephalonia Mw ~6.8 earthquake (Stiros et al., 1994).

Methods

During the cruise, approximately 1,940 km of high-resolution swath bathymetry data were collected using the keel-mounted EM304 (Kongsberg Maritime) system. To enhance data accuracy, adjustments were made to optimize swath width, and sound velocity profiles (SVP) were acquired in shallow and deep waters to correct refraction errors. Data acquisition was performed using SIS and Quincy software, while processing—including sound speed corrections, line cleaning, and CUBE surface creation—was completed using Qimera software. The processed data was gridded at a 50 m resolution.

The high-resolution bathymetric data were then integrated with medium-resolution data from the EMODnet database, along with single- and multibeam datasets provided by the Hellenic Navy Hydrographic Service (HNHS) (Fig.2). These combined datasets were visualized and analyzed using the ESRI GIS software suite, producing a comprehensive morpho-bathymetric map of the region.

The bathymetric data reveal a rugged seafloor with significant variability, especially in the northern sections. Offshore Lefkada Island, a well-defined continental slope extends from 150 m to 680 m water depth, marked by amphitheater-shaped canyon heads at the continental shelf's edge. This area can be divided into two distinct zones: a relatively flat section up to 600 m depth, hosting sediment waves in the northern part, and deeper regions characterized by NE-SW trending canyons. These canyons exhibit flanks indicating multiple, coalescent and nested landslides, with their mouths reaching depths of nearly 2800 m (Fig.2).

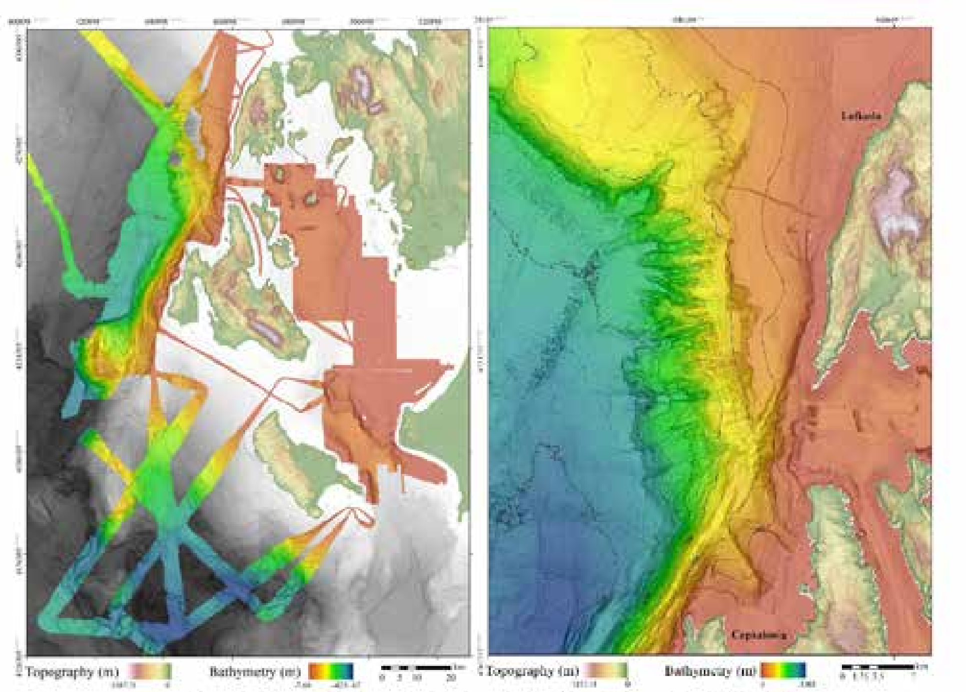

Figure 2. Integrated bathymetric data from the Poseidon Cruise and the HNHS (left) and offshore Lefkada region (right)

Results

The bathymetry of Cephalonia and Zakynthos shows stark contrasts. Northwest of Cephalonia, a steep (>40°) slope connects the abyssal plain to a narrow continental shelf or directly to the coastline. Southward, the slope becomes gentler (~21°) with NE-SW trending steps along the Cephalonia Transform Fault (CTF) system, forming a corrugated seabed (Fig. 4). The CTF trends in a NE-SW direction and extends morphologically to the northern edge of Cephalonia. To the west, the CTF system connects to the Lixouri Seamount, which transitions from a N-S to an E-W orientation. Another Unnamed Seamount further south features steep (36°), triangular, E-dipping faces (Fig.3).

The SW-facing slopes of Cephalonia and Zakynthos are even steeper, with angles up to 40° (Fig. 4), lacking features like canyons or gullies, but are marked by crescent-shaped landslide scars and large-scale landslides, such as a 51 km-long and 2 km-wide feature south of the Paliki Peninsula (Cephalonia) and Zakynthos. These areas display morphological steps indicative of landslides, with E to ENE-dipping detachment planes. The Argostoli Ridge runs NNE-SSW and is bounded by the CTF system and several crescent-shaped landslide scars. Further south, this ridge fragments and collapses. The southernmost area features two elongated abyssal basins reaching depths of 4230 m and 4220 m (Fig.3).

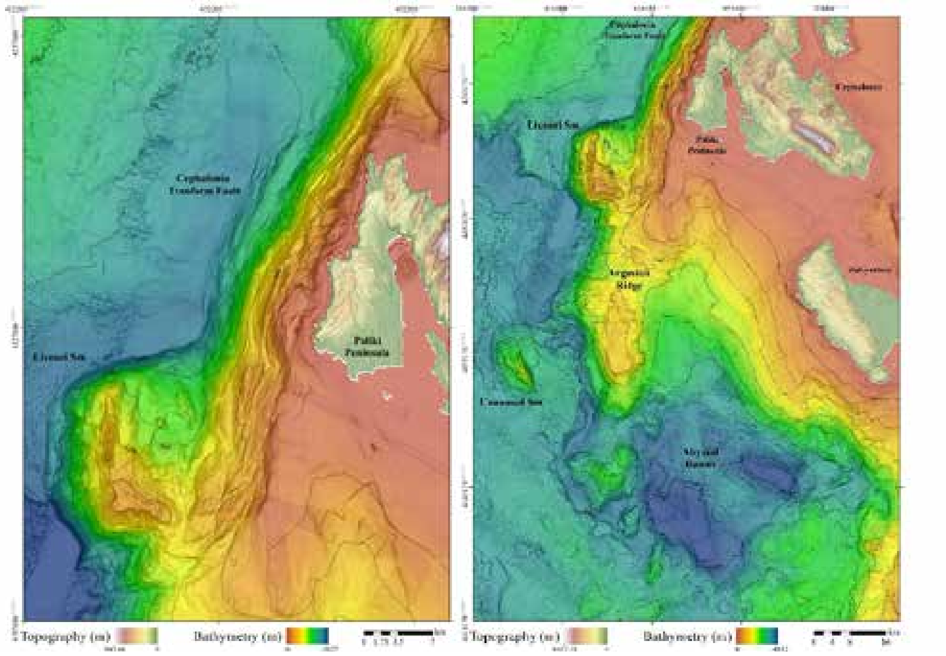

Figure 3. The Cephalonia Transform Fault and the Lixouri Seamount (left) and the SW Cephalonia and Zakynthos area (right)

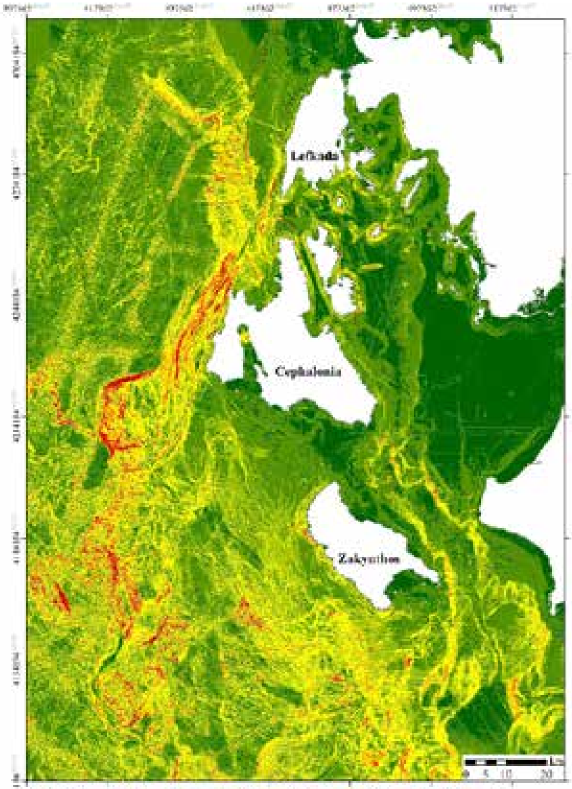

Figure 4. Morphological slope map of the Ionian Sea

Acknowledgements

We acknowledge the professional and dedicated work of the master, officers and crew of the R/V Laura Bassi as well as the technical parties that made this acquisition possible.

References

Ranero C. R., Nomikou P., Loreto M.F., Merino I., Ferrante V., Lampridou D., Nikoli E., Poulos S., 2023. POSEIDON: New data on offshore structures in the west Peloponnese - Ionian Islands Domain and implications for seismic hazards. Bulletin of the Geological Society of Greece, Sp. Publ. 11, 28-31.

Stiros, S.C., et al.,1994. The 1953 earthquake in Cephalonia (western Hellenic arc): coastal uplift and halotectonic faulting. Geophys. J. Int.

17th INTERNATIONAL CONGRESS of the Geological Society of Greece

BULLETIN OF THE GEOLOGICAL SOCIETY OF GREECE, SP. PUBL.

EXTENDED ABSTRACT 165

Heavy metal concentrations in indoor house dusts from the city of Thessaloniki, N. Greece: a small-scale study

Kotsakostoudi Ch.[1], Bourliva A.[2], Mytiglaki Ch.[1], Papadopoulou L.[1], Kantiranis N.[1]

(1) Department of Mineralogy-Petrology-Economic Geology, School of Geology, Aristotle University of Thessaloniki, 54124 Thessaloniki, Greece, kchristina91@gmail.com

(2) Soil Science Laboratory, School of Agriculture, Faculty of Agriculture, Forestry and Natural Environment, Aristotle University of Thessaloniki, 541 24Thessaloniki, Greece

Introduction

Heavy metals in indoor environments have raised growing concern due to their potential adverse health effects, especially in residential settings where individuals, including vulnerable populations such as children and the elderly, spend a significant amount of time (Cheng et al., 2018). Among various indoor substrates, house dust serves as a significant reservoir for heavy metal contamination, often reflecting the combined influence of outdoor pollution, household activities, and the use of materials containing toxic metals. These metals, including lead (Pb), cadmium (Cd), arsenic (As), and chromium (Cr), can be introduced into indoor spaces through numerous pathways, such as outdoor air deposition, contaminated building materials, household products, and the wear and tear of everyday items (Isley et al., 2021).

The presence of these toxic elements in house dust poses serious health risks, with evidence linking exposure to neurological, respiratory, and developmental disorders, particularly in children. Furthermore, long-term exposure to even low concentrations of heavy metals can contribute to chronic health conditions, including cancer, kidney damage, and cardiovascular diseases (Thomas et al., 2009). The variability in the distribution and concentration of heavy metals across different homes highlights the complex interplay between environmental factors, socio-economic status, and lifestyle choices, making the study of house dust as a vector for heavy metal exposure a crucial area of research.

This study aims to explore the concentration of heavy metals in house dust from diverse residential settings in the city of Thessaloniki, with an emphasis on understanding the indoor environmental quality and promoting healthier living spaces.

Materials and Methods

A total of 10 house dust samples were collected from residences within the city of Thessaloniki (Fig1). An effort was made to ensure that the selected residences are uniformly distributed within the city. Sampling was performed during June 2024. House dust was collected by vacuuming repeatedly hard floor surfaces of all living spaces in the house. Vacuum bags were sealed, labeled and stored. Dust samples were sieved to 150 μm using a stainless-steel sieve and analyzed for seven (7) trace metals: arsenic (As), chromium (Cr), copper (Cu), manganese (Mn), nickel (Ni), lead (Pb) and zinc (Zn) as they are known to occur in potentially toxic concentrations in residential environments and to allow comparison with other international dust studies (Isley et al., 2021). Trace metal concentrations were determined via pXRF. A Bruker S1 Titan 600 with a 4 W Rh X-ray tube, 5 mm spot size, a silicon drift detector (resolution < 145 eV), and the inbuilt Geoexploration mode, a factory calibration method for soils, was applied for pXRF analysis. The analysis was conducted in three energy ranges (15, 30 and 50 kV) for 30 s each (a total of 90 s). The elemental contents calculated with the Geoexploration mode were calibrated using certified reference materials (CRMs); calibration curves with R^2 values higher than 0.9 were obtained.

Results and Discussion

The summary statistics of heavy metals in house dusts are given in Table 1 and graphically shown in Figure 2. Heavy metals in house dusts exhibited ranges as: 4 to 11 mg kg^{-1} for As, 106 to 279 mg kg^{-1} for Cr, 62 to 614 mg kg^{-1} for Cu, 263 to 544 mg kg^{-1} for Mn, 23 to 160 mg kg^{-1} for Ni, 22 to 77 mg kg^{-1} for Pb and 339 to 885 mg kg^{-1} for Zn. The median concentration values are following a descending order as: Zn > Mn > Cr > Cu > Ni > Pb > As in line with previous studies (Kelepertzis et al., 2020). In particular, sampled house dusts exhibited higher contents in Zn (650 mg kg^{-1}) followed by Mn (384 mg kg^{-1}), Cr (179 mg kg^{-1}) and Cu (166 mg kg^{-1}), while As presented the lowest concentrations (9 mg kg^{-1}).

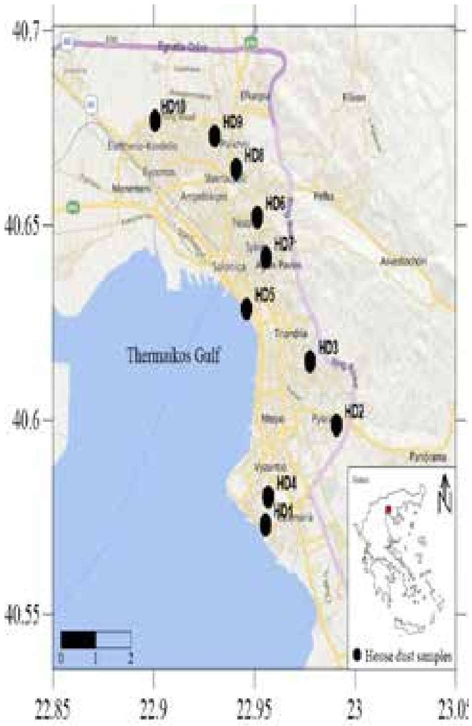

Figure 1. Map of house dust sampling sites in the city of Thessaloniki, N. Greece.

Compared to global crustal values (Isley et al., 2021), most of the elements (except Mn and Ni) are presented moderately to significantly enriched in house dust samples (Fig. 2). Specifically, enrichment ranges of 1-2.6 for As, 1.5-4.0 for Cr, 1.6-15.7 for Cu, 0.7-1.5 for Mn, 0.4-2.9 fon Ni, 1.3-4.5 for Pb and 5.1-13.2 for Zn, were estimated. On the contrary, heavy metal levels (except Cr and Mn) are relatively lower (Fig. 2) than those reported for a dataset of 2265 vacuum dust samples from 35 countries (Isley et al., 2021).

Table 1. Summary statistics of heavy metal contents (mg kg^{-1}) in house dust samples. Background crustal values and international vacuum dust values are also given.

Element	Indoor house dusts (n=10)					Upper Continental Crust [2]	Global Crustal Values[3]	International Vacuum Dust Values[4]
	Mean	SD[1]	Median	Minimum	Maximum			
As	8	3	9	4	11	4.8	4.2	25
Cr	185	49	179	106	279	92	69	128
Cu	204	158	166	62	614	28	39	264
Mn	392	92	384	263	544	1000	363	333
Ni	66	43	50	23	160	47	55	78
Pb	51	21	52	22	77	17	17	224
Zn	623	197	650	339	885	67	67	1470

1: standard deviation, 2: Rudnick & Gao, 2004, 3: Isley et al., 2021, 4: average values from 35 countries (Isley et al., 2021)

Although a direct comparison of heavy metal contents is difficult due to the different sampling protocols, analytical procedures and examined dust fractions, the obtained elemental contents were compared with reported values worldwide (Table 2). As shown, heavy metal contents were relatively higher than those reported for residences from Turkey, Croatia or Ghana; however the sampled house dusts are relatively enriched in Cr and Mn compared to other Greek cities such as Athens (Kelepertzis et al., 2019). Moreover, sampled residential environments display elevated Cr, Mn and Ni contents compared to data from an international vacuum dust analysis program including values from 35 countries worldwide (Isley et al., 2021). Specifically, median Cr levels of 179 mg kg^{-1} were recorded, in contrast to 86 mg kg^{-1} exported from a dataset of 2265 samples from 35 countries. Though Cr sources mainly reflect natural inputs from ultramafic rocks and soils, anthropogenic or industrial inputs cannot be excluded.

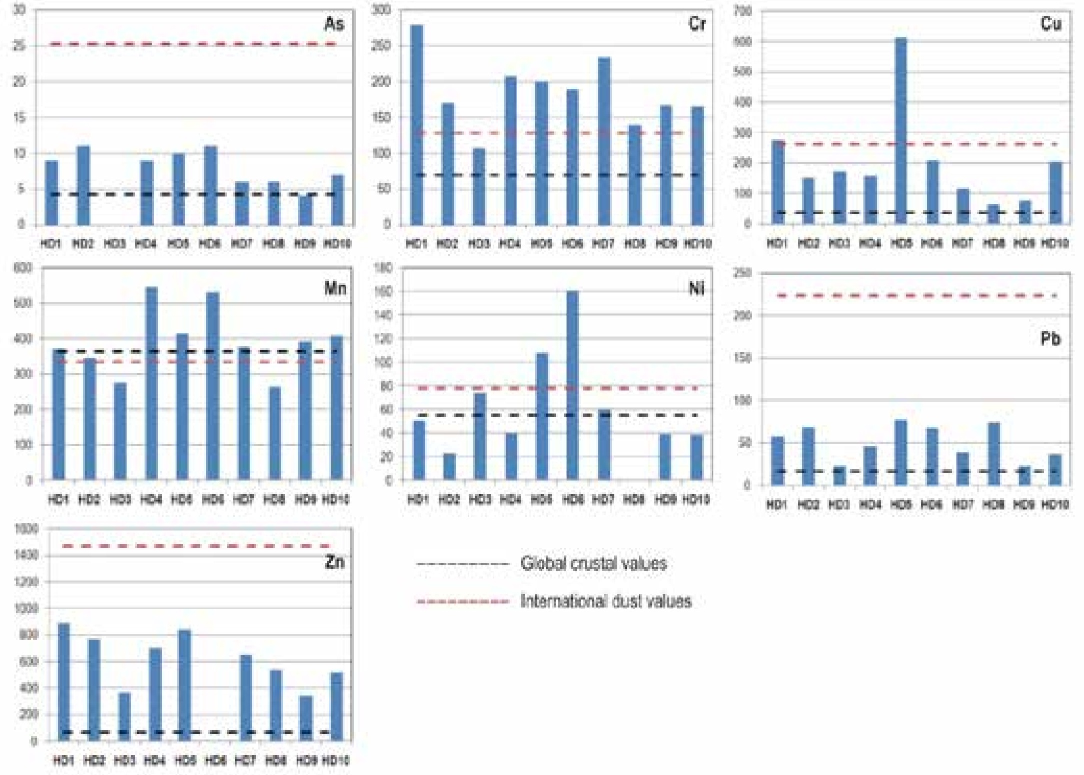

Figure 2. Heavy metal contents (mg kg^{-1}) in house dust samples. Global crustal elemental concentrations (black dashed line, data in Table 1) and international dust values (red dashed line, data in Table 1).

Table 2. Bibliographic data of median heavy metal contents in indoor dust from previous studies.

Study areas	n	Concentrations (mg kg^{-1})							References
		As	Cr	Cu	Mn	Ni	Pb	Zn	
Thessaloniki, Greece	10	9.0	179	166	384	50	52	650	This study
Volos, Greece	24	31.7	163.0	167	274	81	63.2	785	Kelepertzis et al., 2020
Athens, Greece	43		82.9	217	132	89.5	92.2	786	Kelepertzis et al., 2019
Greece	35	6.9	97.9	158	230	52.3	57.0	664	Isley et al., 2021
Australia	1310	19	86	186	246	36	126	1260	Doyi et al., 2019
UK	32			301	524	53.1	150	622	Turner & Simmonds, 2006
Turkey	85	4.41	23.8	65.7	65.9	32.3	27.5	263	Gul et al., 2023
Croatia	34	4.5	88.5	133	225	32.5	59	669	Isley et al., 2021
Ghana	54	1.75	51	55.5	161.5	17	60.5	114	Isley et al., 2021
International vacuum dust values (mean of 35 countries)	2265	13.3	86	176	257	39	94	1110	Isley et al., 2021

To decipher the influence of anthropogenic activities on indoor dust concentrations, Enrichment Factors (EFs) were calculated for As, Cr, Cu, Ni, Pb, and Zn by normalizing vacuum dust trace metal ratios to ratios from global crustal values selected from relevant crustal assessments in the literature and the results are illustrated in Figure 3. The EF was calculated using the following equation:

$$EF = \left(\frac{C_n}{C_{ref}}\right)_{sample} / \left(\frac{B_n}{B_{ref}}\right)_{background}$$

where $(C_n/C_{ref})_{sample}$ and $(B_n/B_{ref})_{background}$ refer to the concentration ratios of a target metal and the reference metal in the house dust samples and the background material, respectively (Yuen et al. 2012). In this study, aluminum (Al) was taken as a normalization factor and concentrations of elements in the upper crust (Rudnick and Gao, 2004) were taken as background values.

An enrichment factor (EF) less than 2 indicates natural conditions, while EFs larger than 2 suggest anthropogenic influence (Isley et al., 2021). Overall, enrichment of Zn was the greatest, followed by Cu > Pb > Cr > As. Zinc and copper returned values EF > 2 in all sampled house dusts, while EFs for As, Cr and Pb were above 2 in more than 80% of the sampled residences. Specifically, the median EF values of Zn (13.7), Cu (8.8), Pb (4.3), Cr (3.1) and As (2.4) were higher than 2, implying that these heavy metals in house dusts are related to anthropogenic activities (Kelepertzis et al., 2020). For instance, pigments of the wall paints are an important source of heavy metals in household dust (Chattopadhyay et al., 2003). On the contrary, the median EFs for Ni (1.5) and Mn (0.6) indicate a minimal enrichment, which therefore, is linked to the lithogenic component of the house dust mainly inherited from the outdoor soil. However, Ni moderate enrichment in 40% of the sampled residences (maximum values of 4) cannot exclude an anthropogenic input. Moreover, EF values did not exhibit great variability among sampled house dusts suggesting the absence of local anthropogenic activities adjacent to the sampled residential environments. However, residences close to city center presented significantly higher EF values reflecting possible outdoor input from adjacent roadside environments as enhanced heavy metal contents in road dusts have already been reported (Bourliva et al., 2018).

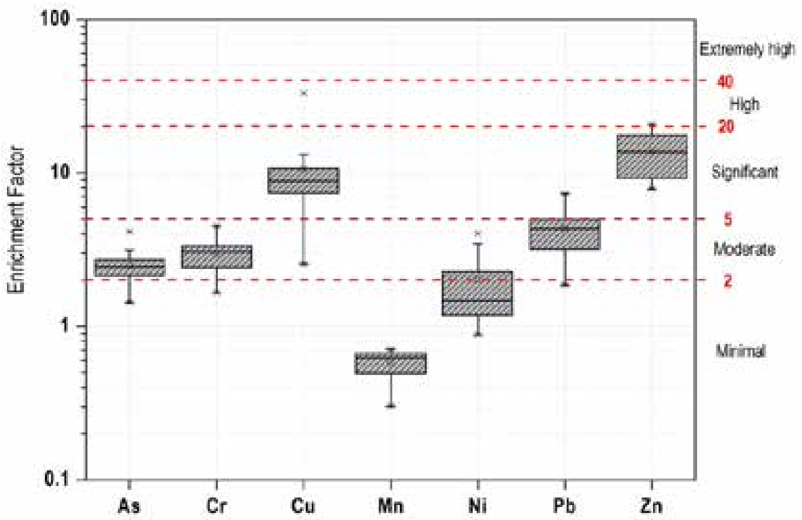

Figure 3. Box plots of enrichment factor (EF) calculations for the assessed trace metals in house dusts, normalized against the reference element Al. Red dashed lines indicate the level of enrichment.

Conclusions

People spend increasing amount of time at home, yet household environments remain understudied. The present study investigated the heavy metal contents in house dust samples from 10 residences within the city of Thessaloniki. Concentration values exhibited a descending order as: Zn > Mn > Cr > Cu > Ni > Pb > As, while concentration levels of these elements were high when compared with those from countries such as Turkey and Croatia. Moreover, the concentrations of As, Cu, Pb and Zn are lower than that of a global vacuum dust dataset. However, Cr levels were relatively higher than those reported from other countries or areas. Values of EFs larger than 2 suggested anthropogenic inputs (except of Ni and Mn), while higher EF values in residences close to city center suggest vehicular traffic as a factor contributing to the rise of heavy metal levels in household environments. Thus, distance to city center could be suggested as an important consideration for the choice of housing.

References

Bourliva, A., Kantiranis, N., Papadopoulou, L., Aidona, E., Christophoridis, C., Kollias, P., Evgenakis, M., Fytianos, K., 2018. Seasonal and spatial variations of magnetic susceptibility and potentially toxic elements (PTEs) in road dusts of Thessaloniki city, Greece: A one-year monitoring period. Science of the Total Environment 639, 417-427.

Chattopadhyay, G., Lin, C.P., Feitz, A.J., 2003. Household dust metal levels in the Sydney metropolitan area. Environmental Research 93, 301-307.

Cheng, Z., Chen, L.-J., Li, H.-H., Lin, J.-Q., Yang, Z.-B., Yang, Y.-X., Xu, X.-X., Xian, J.-R., Shao, J.-R., Zhu, X.-M., 2018. Characteristics and health risk assessment of heavy metals exposure via household dust from urban area in Chengdu, China. Science of the Total Environment 619-620, 621-629.

Doyi, I.N.Y., Isley, C.F., Soltani, N.S., Taylor, M.P., 2019. Human exposure and risk associated with trace element concentrations in indoor dust from Australian homes. Environment International 133, 105-125

Gul, H.K., Gullu, G., Babaei, P., Nikravan, A., Kurt-Karakus, P.B., Salihoglu, G., 2023. Assessment of house dust trace elements and human exposure in Ankara, Turkey. Environmental Science and Pollution Research 30, 7718–7735.

Isley, C.F., Fry, K.L., Liu, X., Filippelli, G.M., Entwistle, J.A., Martin, A.P., Kah, M., Meza-Figueroa, D., et al., 2021. International Analysis of Sources and Human Health Risk Associated with Trace Metal Contaminants in Residential Indoor Dust. Environmental Science and Technology 56, 1053-1068.

Kelepertzis, E., Argyraki, A., Botsou, F., Aidona, E., Szabó, Á., Szabó, C., 2019. Tracking the occurrence of anthropogenic magnetic particles and potentially toxic elements (PTEs) in house dust using magnetic and geochemical analyses. Environmental Pollution 245, 909-920.

Kelepertzis, E., Argyraki, A., Chrastný, V., Botsou, F., Skordas, K., Komárek, M., Fouskas, A., 2020. Metal(loid) and isotopic tracing of Pb in soils, road and house dusts from the industrial area of Volos (central Greece). Science of the Total Environment 725, 138300.

Rudnick, R.L., Gao, S., 2004. Composition of the continental crust, in: Rudnick, R.L. (Ed.), The Crust, 1–64.

Thomas, L.D., Hodgson, S., Nieuwenhuijsen, M., Jarup, L., 2009. Early kidney damage in population exposed to cadmium and other heavy metals. Environmental Health Perspectives 117, 181-184.

Turner, A., Simmonds, L., 2006. Elemental concentrations and metal bioaccessibility in UK household dust. Science of the Total Environment 371, 74-81.

Yuen, J.Q., Olin, P.H., Lim, H.S., Benner, S.G., Sutherland, R.A., Ziegler, A.D., 2012. Accumulation of potentially toxic elements in road deposited sediments in residential and light industrial neighborhoods of Singapore. Journal of Environmental Management 101, 151–163.

17th INTERNATIONAL CONGRESS
of the Geological Society of Greece

BULLETIN OF THE GEOLOGICAL SOCIETY OF GREECE, SP. PUBL.

EXTENDED ABSTRACT 166

New *Clypeaster* fossils from South Crete (Rodakino, Rethymno)

Kotsomitopoulou A.[1], Tsaparas N.[1], Galazoudi E.[1]

(1) National and Kapodistrian University of Athens, Athens, Greece, artemiskots@gmail.com

Introduction

The study area is located near the village of Rodakino in the southwestern part of the Rethymno prefecture (Crete). In this region, the marine Neogene deposits overly the Phyllite-Quartzite unit, which structure the wider area.

The Neogene deposits of Crete are extensive covering a large part of the island. Many researchers have described them throughout the years, classifying them into four lithostratigraphic units ranging from Upper Tortonian to Lower Pleistocene. From oldest to youngest these units are: Tefeli Group (conglomerates and coarse-grained sands to claystone and siltstone with turbidites), Vrysses Group (white marls, calcarenites and bio-calcarenites of Tortonian-Messinian age), Foinikia Group (marls and marly silts of lower Pleistocene age) and Agia Galini Group (conglomerates and coarse-grained sands of lower-middle Pleistocene age) (van Hinsbergen & Meulenkamp, 2006; Tortorici et al., 2010).

The fossiliferous section is 20 meters thick and consists of fine marly sandstones alternating with blue marls. In detail, from the bottom of the section and for 5 meters, thick layers of marly sandstones (~ 70cm) alternate with very thin layers (~5cm), while towards the top, the marly layers are thicker (~ 20 cm). The studied sea urchins were found in the marly sandstones from the first 5m of the outcrop.

Objectives

The purpose of this paper is to present findings from a new fossiliferous site in Crete with echinoids of the genus *Clypeaster*, a taxon now extinct from the Mediterranean. Additionally, data about the age of the studied site were based on calcareous nannoplankton.

Materials and methods

Samples and data collected during the area's mapping were used to create the stratigraphical section. The *Clypeaster* species were identified according to Marcopoulou-Diakantoni (1985), by measuring length (l), width (L), height (h), ratio width-length (L/l) and ratio height-width (h/L).

The material was transported to the Laboratory of Historical Geology and Biogeosciences (Department of Geology and Geoenvironment, National and Kapodistrian University of Athens), where it was cleaned and, when necessary, reconstructed to restore its original shape in cases of fracturing.

A preliminary investigation was conducted on the age of the section based on calcareous nannofossils, but it needs further and more detailed analysis. The sample preparation for the study of calcareous nannoplankton followed standard smear slide techniques. The slides were analyzed using a polarising light microscope LEICA DMLP at 1,250×..

Results

Five different *Clypeaster* species were determined: *Clypeaster altus, C. calabrus, C. campalanatus f. portentosus, C. tauriqus, and C. altostratus*. Several of the specimens could not identified in species level as they were not well preserved. The descriptions of the species presented herein were created according to Markopoulou-Diakantoni (1985), Kroh (2005) and Tsaparas (2005).

Classification

Phylum: Echinodermata KLEIN 1734
Subphylum: Echinozoa HECKEL in ZITTEL, 1895
Class: Echinoidea LESKE, 1778
Subclass: Euechinoidea BRONN, 1860
Superorder: Gnathostomata ZITTEL, 1879
Order: Clypeasteroida A. AGASSIZ, 1873
Suborder: Clypeasterina A. AGASSIZ, 1872
Family: Clypeasteridae L. AGASSIZ, 1835
Genus: Clypeaster LAMARCK, 1801

***Clypeaster campanulatus f. portentosus* MICHELIN, 1861**

(Figure 1.a, b)

Large size species with long pentagonal shape. It has slightly curved edges and very distinct surface ridging and it's characterized by a very elevated petal area, which gives the animal the shape of a bell. The sides are very inclined and not well developed, while the petals are curved and slightly open. Its underside is particularly flat.

Clypeaster altus **KLEIN, 1734**

(Figure 1.c)

Pentagonal symmetry, elongated, angular on the front and almost straight on the back. Its upper side is erect, the upper surface is relatively high, erect, hypoconical and thick on the sides. Sides very poorly developed and oblique like petals, with their edges rounded and thick. The lower surface is smooth and has prominent peripatetic grooves. The upper side sports a madreporite with ten pores. Ambulacral zones are protruding and petal shaped, with their sides open.

Clypeaster calabrus **SEGUENZA, 1880**

(Figure 1.d)

Medium to large sized, elongated with pentagonal shape. Its front side is blunt and pointed and its back side is transversely truncated, with well-defined recess and a margin that gets thinner from the front to the back side. The margin of the test is rounded off.

Clypeaster tauricus **DESOR, 1859**

(Figure 1.e)

Medium height, with its test size pentagonal, elongated and angular, with the 5 points rounded off. The ambulacral zones are petal like in shape, long, protruding, wide open and form a bulge when they come to the side. The lower surface is smooth, the peristome is not well developed while the peripectorium is small and circular.

Clypeaster alticostatus **MICHELIN 1861**

(Figure 1.f)

Large sized species, with its upper surface very elevated and conical and the madreporite plate submerged. Its sides are underdeveloped, thick and curved, and less extended. The periphery is slightly elongated and the ambulacral zones are petal and almost lance like. The test margin is thin and slightly angular.

Table 1. Measurements of the *Clypeaster* species

Species	Length (l)	Width (L)	Height (h)	L/l	h/l
C. campanulatus f. portentonsus	228	181	96	0.79	0.42
C. altus	152	135	64	0.88	0.42
C. calabrus	158	134	72	0.86	0.45
C. tauricus	189	151	70	0.80	0.37
C. alticostatus	165	142	68	0.86	0.41

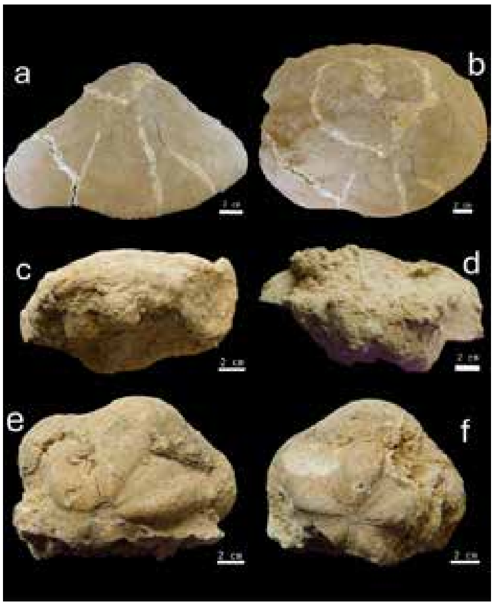

Figure 1. ***a, b. Clypeaster campanulatus*** **f.** ***portentosus. C: Clypeaster altus d. Clypeaster calabrus. E. Clypeaster tauricus. F. Clypeaster alticostatus***

Several specimens of the large benthic foraminifera *Heterostegina* were found on the echinoids (Figure 2) and in the sediment that was collected after cleaning the specimens. This large benthic calcareous foraminifer is a circum-tropical nummulitid foraminifer with photosymbionts, which prefers forereef environments (Boudagher-Fadel, 2008; Benedetti *et al*., 2017).
The micropaleontological analysis for calcareous nannoplankton (Young *et al*., 2022) of the sediment from the interior of a sea urchin determined two species of the genus *Discoaster* : *Discoaster variabilis* MARTINI AND BRAMLETTE, 1963 and *Discoaster exilis* MARTINI AND BRAMLETTE, 1963 (Figure 3).

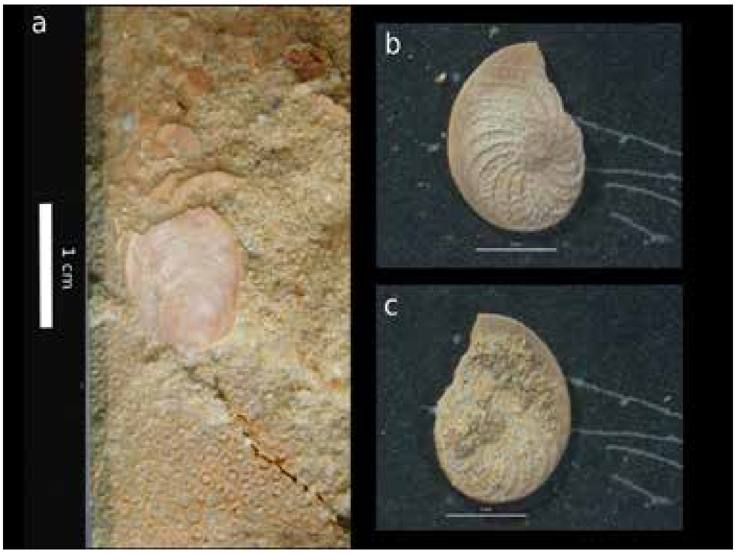

Figure 2. *Heterostegina* members found on the echinoids

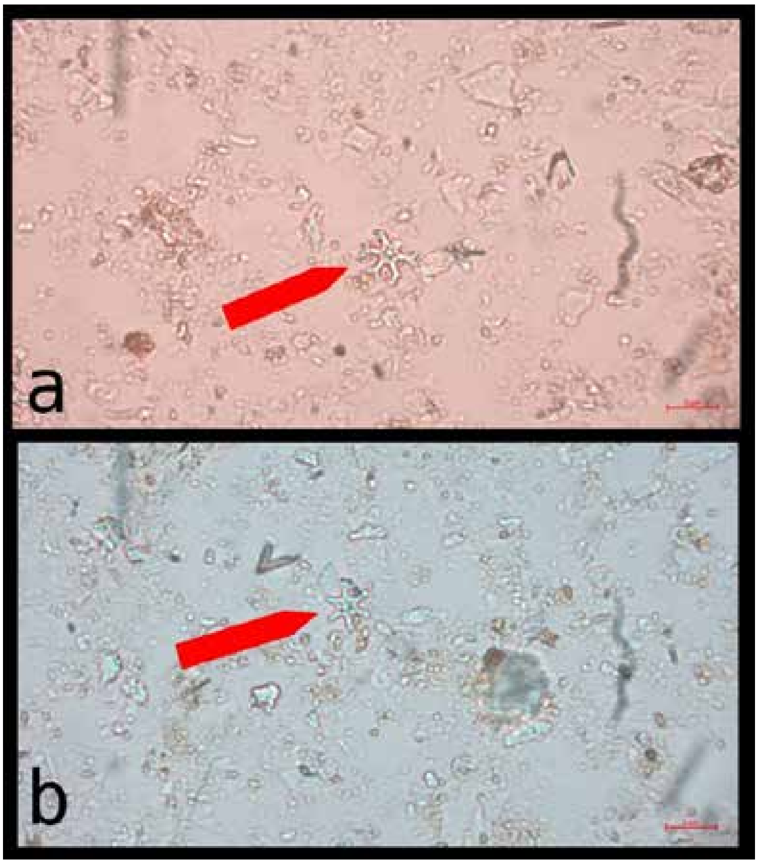

Figure 3. a. *Discoaster variabilis.* b. *Discoaster exilis*

Conclusions

After measurements were made, the following *Clypeaster* species were determined*: C. altus, C. calabrus, C. campalanatus f. portentonsus, C. tauriqus, C. alticostatus*. Based on the presence of *Discoaster variabilis* and *Discoaster exilis* individuals that were found in the sediment, their age was identified as Middle Tortonian (NN9-NN10). Further study on calcareous nannoplankton will determine the age. The environmental conditions inferred from the presence of *Heterostegina*, which coexisted with the sea urchins, suggest a shallow, warm marine environment, similar to that of Gavdos, where comparable findings had been reported.

Acknowledgements

We would like to thank Mr. Nils Sappok for his kind gesture to provide us with the large, complete specimen of *Clypeaster* for our study and for indicating the location where he found it. This enabled us to conduct extensive sampling, the results of which are presented in this paper.

References

Aubry, M.P, 1984. Handbook of Cenozoic Nannoplankton Book 1: Ortholithae (Discoasters), Micropaleontology Press, The American Museum of Natural History.

Benedetti, A., Less G., Parente M., Pignatti J., Cahuzac B., Torres-Silva A.I. & Dieter Buhl D., 2017. Heterostegina matteuccii sp. nov. (Foraminiferida: Nummulitidae) from the lower Oligocene of Sicily and Aquitaine: a possible transatlantic immigrant. Journal of Systematic Palaeontology, 16(2), 87–110.

BouDagher-Fadel, M. K. (2008). Evolution and Geological Significance of Larger Benthic Foraminifera (Vol. 21). Elsevier. https://doi.org/10.1016/S0920-5446(08)00012-5

Kroh, A., 2005. Catalogus Fossilium Austriae. Band 2. Echinoidea neogenica. Österreichische Akademie der Wissenschaften.

Markopoulou-Diakantoni, A., 1985. Morphology and Evolution of the Genus Clypeaster (Clypeasteroida). Aristotle University of Thessaloniki. (in Greek)

Tortorici L., Caputo R., Monaco C., 2010. Late Neogene to Quaternary contractional structures in Crete (Greece), Tectonophysics, 483 (3–4), 203-213.

Tsaparas, N., 2005. Contribution to the history of sedimentation of the upper Cenozoic marine formations in Gavdos island. Faculty of Geology and Geoenvironment. Ph.D. Thesis, National and Kapodistrian University of Athens, 325 p. (in Greek).

van Hinsbergen, D.J.J., Meulenkamp, J.E., 2006. Neogene supradetachment basin development on Crete (Greece) during exhumation of the South Aegean core complex. Basin Research, 18(1), 103–124.

Young, J.R., Bown P.R., Lees J.A., 2022. Nannotax3 website. International Nannoplankton Association.

17th INTERNATIONAL CONGRESS
of the Geological Society of Greece

BULLETIN OF THE GEOLOGICAL SOCIETY OF GREECE, SP. PUBL.

EXTENDED ABSTRACT 167

Measurements of soil gas emissions (radon and thoron) in the municipality of occidental Lesbos, Stypsis – Petras, and correlation with tectonic structures (rift zone) of the subsidence coast of Petra

Koukoulis A.[1], Xenakis M.[1]
(1) H.S.G.M.E., Athens, Greece, akoukoulis@eagme.gr

Panoramic view of the measurement area.

Summary

In this work, a radiological, geological and tectonic approach is carried out, for the evaluation of radon-thorium soil, in two predetermined areas of Petra, which have been designed by PPC RENEWABLES S.M.S.A. for the needs of geothermal research conducted in the region. The objective of the HSGME service project was to identify the optimal pathways for radon increase in the soil and their possible connection to the mapped tectonic structures and the corresponding optimal geothermal fluid pathways in the research area.

The most important results of the work are that radon and thoron concentrations in the soil, which reach high levels of up to 57.448 and 10.357 Bq/cm3 respectively, are independent of the activity of local geological formations and are fed by deeper bottom horizons via fault zones. The spatial distribution of radon shows high concentrations with growths of about 200 to 400m on the ground, correlated with the corresponding tectonic structures.

From the shape and the particular characteristics of the distribution of soil gases (radon and thoron), the data so far change, and from the lines of the mapped tectonic structures, we have the identification of rift zones, with optimal circulation of soil gases and possibly also of geothermal fluids.

Methodology-Measures

In situ measurements (N=435) were performed at predetermined positions of a 400m orthocanonical cell grid, with some thickening in the center of the squares and at the 200m edge vertices, which cover the entire area of the research field with a total of 87 situations (Fig. 1).

For each location, underground air is pumped to a depth of about 50cm, and radon and thoron are measured on site using an automatic semi conductor detector (RTM-1688-2, Sarad), for an average time of about 45 minutes. At the same time, with the help of special detectors (Camberra smart probes), the variation of activity on the ground surface, three radiological parameters is recorded (Fig. 2) :

(a) total contamination of α-β-γ radiation, by the Radiagem 2000 instrument and the SABG 15 probe

b) the equivalent dose rate when detecting a gamma photon flux by the Radiagem 2000 instrument and the external 2΄X2΄ SG-2R gamma probe

c) total γ radiation, by scintillation meter SPP2 (Saphymo-Stel).

The measurements of these quantities (Table 1) give a satisfactory consistency of the arguments in favour of the activity of the radiation emitted by the ground in the field of research, and above all make it possible to assess the origin of the high concentrations of radon in the soil, since it is known that among the factors that influence it are geology, geotectonic, radiology, geothermal field, etc., with which an investigation is attempted.

Discussion of the results

In the study area, radon-thoron increases are independent of the type of volcano and the primary or secondary stages of volcanism (Fig. 3, 4), which have a high radiological background, several times higher than that of other regions of the country (Table 1, Fig. 5, 6). However, there is no direct relationship between radon-thoron and volcanism, which is essentially identical (Fig. 2, Fig. 9. 10, 11) to the upper unit of lavas of Hehct 1974, or to that of the subalkaline potassic series (shoshonites) as identified by G. Piper 1992, and which is more uranium-rich and potassic, with accessory minerals responsible for uranium concentrations, selective aggregation of thorite-titanite-allanite-zirconium-apatite (Koukoulis A. et al., IGME, 2001).

A few kilometers from the Stypsi geothermal field, there are high concentrations of radon and thoron in the ground, with small isolated developments (about 200-400m on the ground), which are located both in the research field and its extension, which requires further research (Fig. 7, 8).

On the descending side of the Avlaki and Petra faults, maximum radon values were recorded in the upper unit of lavas (53.522Bq/cm3) and in the alluvial deposits (48.015Bq/cm3), which structure individual soil extentions (about 200-400m), at the boundaries of the research field, suggesting a possible expansion beyond these.

On these margins and approximately above the Petra ring road, private and municipal water supply and irrigation wells have been recorded, with high temperatures (25-45°C), at depths of a few tens of meters, which is considered particularly encouraging for further research.

In the field of research, the individual high concentrations of radon, with a growth of more than about 600m, have a NE-SW direction, which is affected by deep long-range faults, which form the important sunkens of the island.

This development of high radon concentrations seems to have been dismembered towards the SW, under the influence of the more frequent and later NW-SE faults. In the fragment descending echelon to SW of the NW-SE faults, the highest radon concentrations in the research field were recorded (45.175 and 55.578 Bq/cm3), with NW direction and a development greater than 400m in the upper unit of lavas.

Further research is also needed in the north-western extension of the search area, in which the high concentrations of thoron appear (maximum value 10.357 Bq/m3), with a NW-SE direction of about 200m on the ground.

References

Hecht, J. (1974): Geological mapping of at a scale of 1:50.000, I.G.M.E.

Koukoulis, A., 1982. The granitoids of the Vrondou massif, Serres, Greece, Magmatic typology and evolution, Mineralogy and geochemistry of uranium and thorium, 3rd cycle thesis (Mineral and Energy Raw Materials), I.N.P.L. (E.N.S.G.), Nancy, France, 179 pp.

Koukoulis, A., Karageorgiou, E.D., Pergamalis, F., (2001). Uranium detection research on the island of Lesvos, IGME Report, Athens p.173.

Koukoulis A., 2016a. Primary radiological investigation (radon-thoron, etc.) of the urban and suburban area of Volos (under geological control), IGME Report, Athens, p. 61.

Koukoulis A., 2016b. Primary radiological investigation (radon-thhoron, etc.) of the urban and suburban area of Igoumenitsa (under geological control), IGME Report, Athens, p. 67.

Koukoulis A, 2024. Primary radiological investigation (radon-thoron, etc.) of the urban and suburban area of Lamia (under geological control), EAGME Report, Athens, p. 57.

Pe-Piper, G. and Piper, D.J.W. (1992): Geochemical variation with time in high-K Cenozoic volcanic rocks of shoshonite petrogenesis. Journal of Volcanology and Geothermal Research, 53 pp. 371-387.

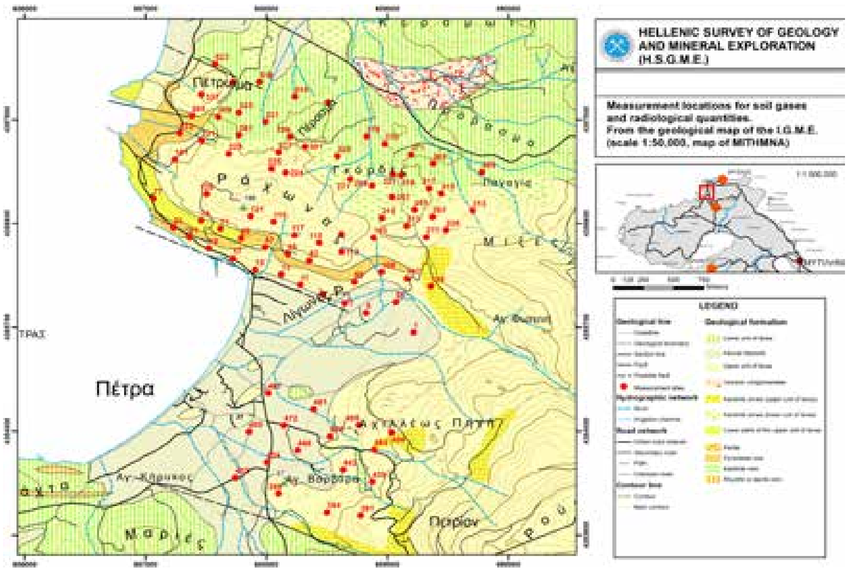

Figure 1: Soil measurement locations in the predefined research area, on a geological map of the I.G.M.E. (excerpt from sheet MITHMNA, scale 1:50,000).

Radon-thoron analyzer RTM-1688-2 (Sarad) Radiagem 2000 (Camberra)

Alpha beta gamma probe SABG 15 Gamma external 2´X2´ probe SG-2R

Scintillation meter SPP2 (Saphymo–Stel)

Figure 2 : Radio Measuring Instruments

Table 1: Statistical descriptive data of the soil measurements in the area between Stypsi and Petra (Lesvos). In parentheses, corresponding data from the urban and suburban areas of Lamia, Volos and Igoumenitsa (Koukoulis A., 2016 a-b and Koukoulis A.2024).

Measurements	On the ground surface			At a depth of 50cm (approximately)	
Radiation measurement	α-β-γ	γ		γ	
Radiological Size	Total Radiation contamination α-β-γ	Dose rate	Total Radiation γ	Thoron	Radon
Measuring instrument	SABG 15 & RADIAGEM 2000	SG-2R & RADIAGEM 2000	SPP2	RTM 1688-2	
Unit of measurement	Bq/cm2	nSv/h	c/s (SPP2)	Bq/m3	Bq/m3
Number of measurements	87 (238_211_160)	87 (238_213_160)	87 (238_163_160)	87 (238_133_160)	87 (238_214_160)
Minimum measurement value	0,61 (0,01_0,22_0,21)	3170 (248_242_371)	50 (5_5_10)	25 (40_84_42)	290 (46_78_72)
Maximum measurement value	1,99 (0,76_1,51_0,88)	10900 (4080_3000_2960)	180 (75_40_75)	10357 (4206_16324_28223)	57448 (33290_36522_153781)
Average measurements	1,21 (0,45_0,44_0,42)	6258 (1196_1083_1240)	99 (22_21_22)	1297 (707_1144_2069)	16622 (4016_5920_12582)
Standard deviation of measurements (σ)	0,32 (0,12_0,12_0,10)	1972 (514_462_430)	32 (8,49_5,98_7,90)	1698 (771_1559_2959)	13040 (5422_6191_14323)
Coefficient of dispersion of measurements (σ/ȳ)	0,26 (0,28_0,27_0,23)	0,32 (0,43_0,43_0,35)	0,32 (0,39_0,29_0,35)	1,31 (1,09_1,36_1,43)	0,78 (1,35_1,05_1,14)

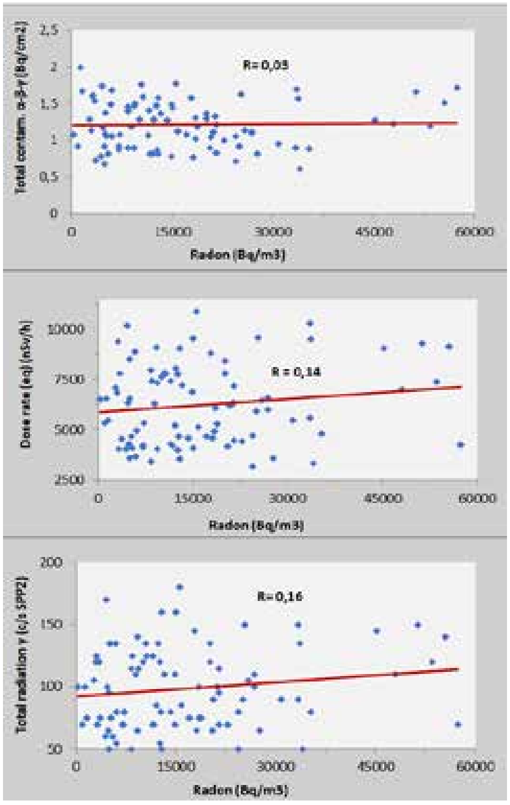

Figure 3: Independent increase in radon from surface soil activity, expressed as:: (i) the total contamination α-β-γ radiations, (ii) the equivalent dose rate, and (iii) the total γ radiation (correlation coefficients almost zero, R=0.03-0.16).

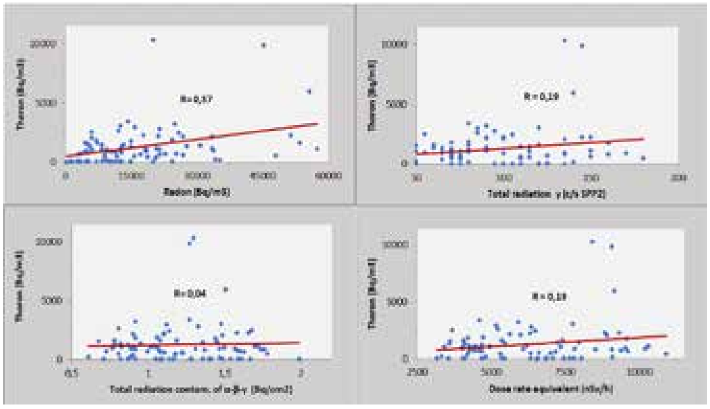

Figure 4 : Relatively independent increase between thoron and radon (r=0.37) and greater independence of thoron from soil activity (r=0.04-0.19) expressed as: i) surfacic contamination of α-β-γ radiation, ii) equivalent dose rate and iii) total γ radiation.

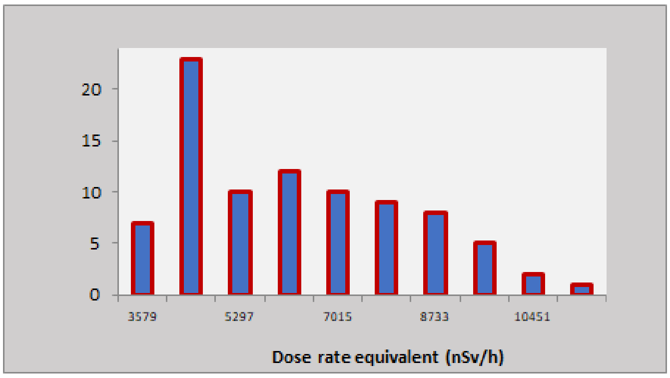

Figure 5 : High values of soil activity in the research area with the equivalent dose rate being above normal levels (1μSv/h) and slightly increased (3.17μSv/h-10.9 μSv/h).

Geological formation		Symbols	0-2,5 KBq/m3	2,5-5 KBq/m3	5-10 KBq/m3	10-15 KBq/m3	15-20 KBq/m3	20-25 KBq/m3	25-30 KBq/m3	30-40 KBq/m3	40-50 KBq/m3	50-60 KBq/m3	Total
Upper unit of lavas		Ng-ul	1	5	4	7	6	4	5	2	0	2	36
	Lower parts	Ng-ul1	1	1	1								3
	Kaolinite zone	kl Ng-ul			1								1
	Limits	Ng-ul/Ng-pc		1		1				1	1	1	5
Pyroclastic row		Ng-pc	1		1								2
Lover unit of lavas		Ng-ll		2	5	2	1	3	1	3			17
	Kaolinite zone	kl Ng-ll	1	1	3	3	0	2				1	11
Alluvial deposits		Q.al			3	4	2	2			1		12
		Total	4	10	18	17	9	11	6	6	2	4	87

Table 2: Relationship of soil radon with geological formations of the field of investigation (number of measurements in some classes from 0-60KBq/m3)

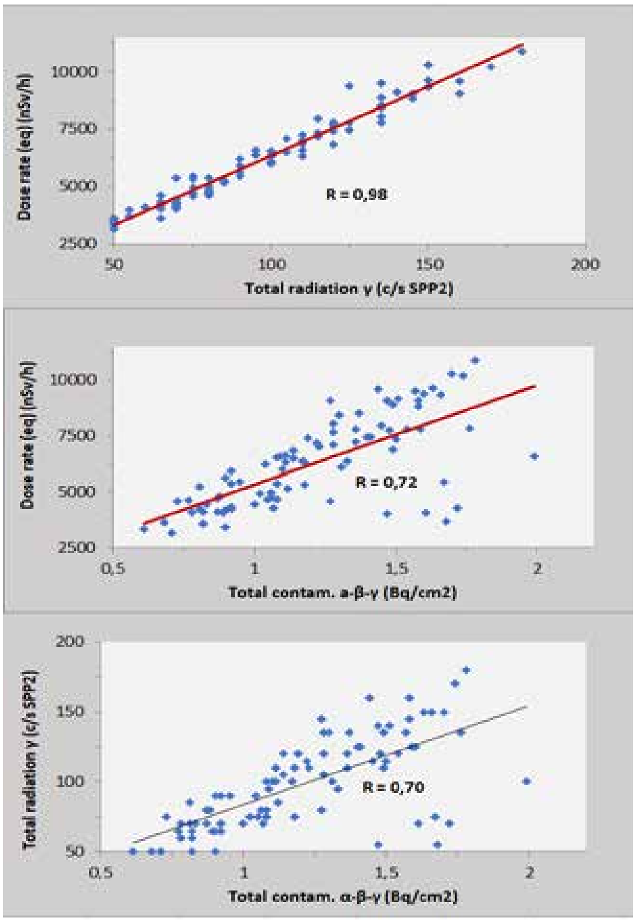

Figure 6 : Strong correlations between radiological values measured at the soil surface, with very strong correlation coefficients (R≥0.70 and up to 0.98).

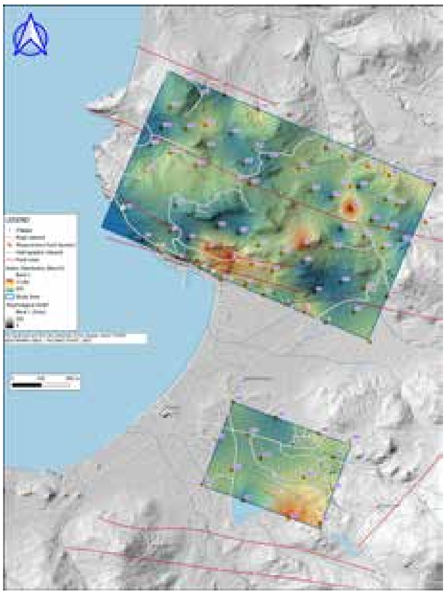

Figure 7: Spatial distribution of radon

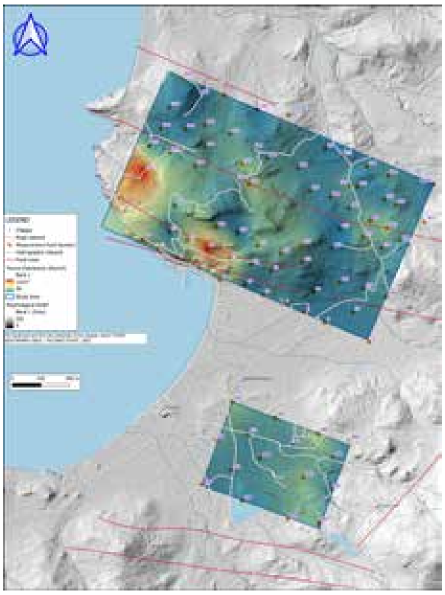

Figure 8 : Spatial distribution of thoron

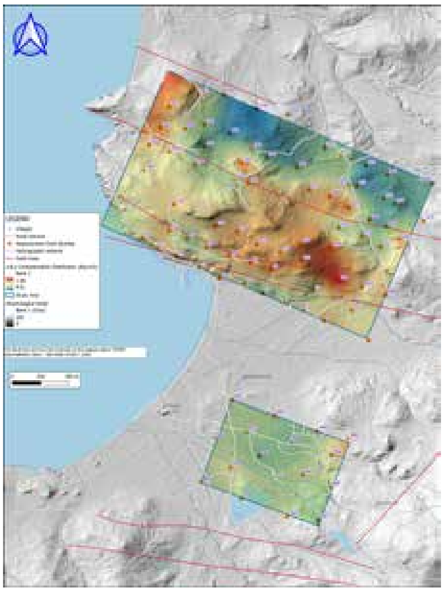

Figure 9 : Spatial distribution of total contamination of radiations α-β-γ

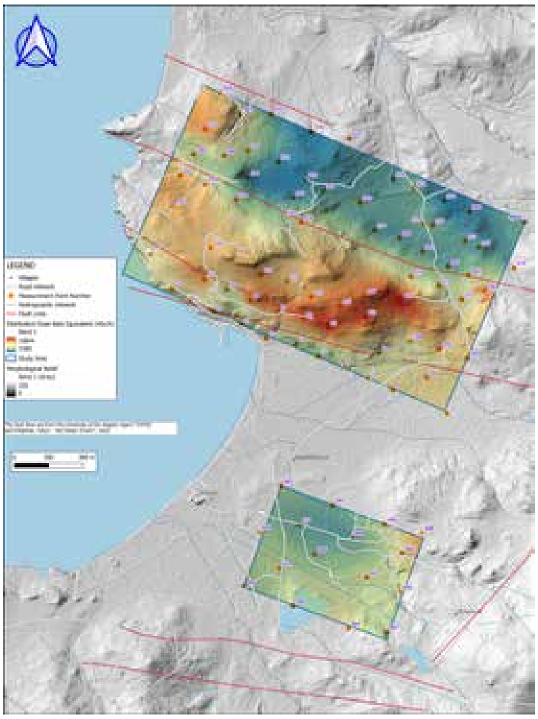

Figure 10 : Spatial distribution of dose rate equivalent

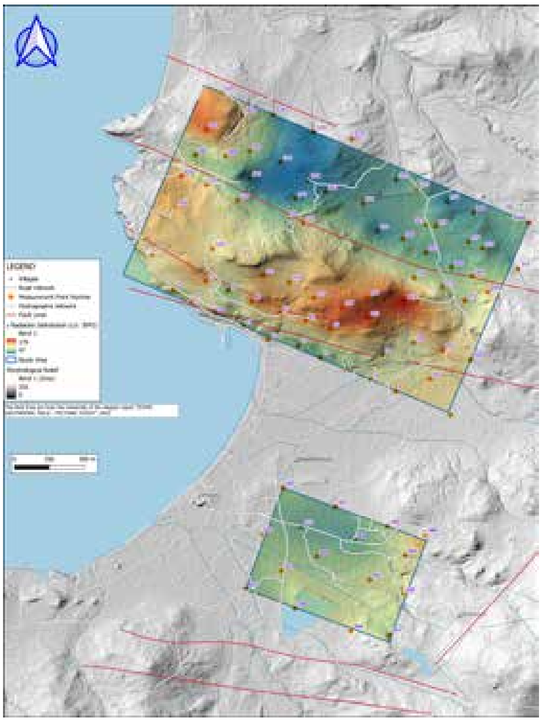

Figure 11 : Spatial distribution of total radiation γ

17th INTERNATIONAL CONGRESS of the Geological Society of Greece

BULLETIN OF THE GEOLOGICAL SOCIETY OF GREECE, SP. PUBL.

EXTENDED ABSTRACT 168

Foraminiferal response to a giant shallow-marine pyroclastic-flow-eruption from ancestral Santorini discovered by IODP Expedition 398 - Objectives, challenges and results of deep drilling into Christiana-Santorini-Kolumbo volcanic field

Koukousioura O.[1,2], Nomikou P.[3], Woodhouse A.[4], Chiyonobu S.[5], Polymenakou P.[6], Druitt T.[7], Kutterolf S.[8], Ronge T.[9], Beethe S.[10], Bernard A.[11], Berthod C.[12], Chen H.[13], Clark A.[14], DeBari S.[15], Della Sala S.[16], Fernandez-Perez T.I.[17], Gertisser R.[18], Hübscher C.[19], Johnston R.M.[20], Jones C.[21], Joshi K.B.[22], Katsigera A.[3], Kilias S.[3], Kletetschka G.[23], Li X.[24], Manga M.[25], McCanta M.[26], McIntosh I.[27], Metcalfe A.[7], Morris A.[28], Pank K.[8], Papadimitriou V.[3,6], Peccia A.[29], Preine J.[19], Tominaga M.[30], Yamamoto Y.[31], Yoshimoto T.[31], Papanikolaou D.[3]

(1) Aristotle University of Thessaloniki, Thessaloniki, Greece, okoukous@geo.auth.gr (2) University of Cologne, Cologne, Germany (3) National and Kapodistrian University of Athens, Athens, Greece (4) Cardiff University, Cardiff, UK (5) Akita University, Akita, Japan (6) Hellenic Centre for Marine Research, Heraklion, Greece (7) University Clermont-Auvergne, CNRS, IRD, OPGC, Clermont-Ferrand, France (8) GEOMAR Helmholtz Centre for Ocean Research Kiel, Kiel, Germany (9) International Ocean Discovery Program, Texas A&M University, Texas, US (10) Oregon State University, Corvallis, US (11) Université de Pau et des Pays de l'Adour, Pau, France (12) Centre National de la Recherche Scientifique (CNRS), Paris, France (13) China University of Geosciences, Beijing, China (14) University of Tasmania, Hobart, Australia (15) Western Washington University, Bellingham, US (16) University of Oxford, Oxford, UK (17) Kent State University, Kent, USA (18) Keele University, Keele, UK (19) University of Hamburg, Hamburg, Germany (20) University of South Florida, Tampa, US (21) University of California, Riverside, US (22) National Centre for Earth Science Studies, Thiruvananthapuram, India (23) University of Alaska Fairbanks, Fairbanks, US (24) Ocean University of China, Qingdao, China (25) University of California, Berkeley, US (26) University of Tennessee, Knoxville, US (27) Japan Agency for Marine-Earth Science and Technology, Yokosuka, Japan (28) Plymouth University, Plymouth, UK (29) Columbia University, New York, US (30) Woods Hole Oceanographic Institution, Woods Hole, US (31) Kobe University, Kobe, Japan

International Ocean Discovery Program Expedition 398 'Hellenic-Arc-Volcanic-Field' took place in the Christiana-Santorini-Kolumbo Volcanic-Field (CSKVF) in the central Hellenic Volcanic Arc. The CSKVF is one of the most hazardous volcano-tectonic regions in the world, as the volcano has produced many and highly explosive eruptions in the past and could be of a threat for at least eastern Mediterranean (Druitt *et al.*, 1999; Nomikou *et al.*, 2013, 2019). This volcanic field produced the notorious Late Bronze age Minoan eruption that is considered to have contributed to the fall of an entire civilization (Bruins et al., 2008). The overall objectives of the expedition were to investigate the links and feedbacks between volcanism/magmatism, crustal tectonics and sea level, to groundtruth the seismic stratigraphy of the Santorini caldera, to reconstruct the subsidence history of the southern Aegean Sea and to search for deep life inside and outside of Santorini caldera (Druitt *et al.*, 2022).

IODP Expedition 398 was conducted with the R/V JOIDES Resolution, from 11 December 2022 to 10 February 2023. During the expedition despite the very challenging drilling conditions, twelve sites were drilled, for a total of 7345 meter in 28 holes, retrieving 780 cores with a total recovery of 3356 meters (Druitt *et al.*, 2024b; Figure 1). Outside of Santorini caldera, drilling penetrated the thick basin fills of the crustal rift system hosting the CSKVF, and identified more than 1000 tephra layers, some known from onland and others formerly unknown. The seismic stratigraphy was groundtruthed (Preine *et al.*, 2024), detailed age-depth constraints were provided mainly by biostratigraphy. Drilling penetrated the Alpine basement and ancient life DNA was recovered, proving that most of the volcano-tectonic history of the CSK field, as the volcano-sedimentary sequences, lies under the sea.

One of the first results, constrained by a multidisciplinary approach and highlighting the hazards of submarine explosive eruptions, includes the discovery of a giant rhyolitic pumice, the Archaeos Tuff, as the result of a shallow marine eruption of ancestral Santorini Volcano (Druitt *et al.*, 2024a). The Archaeos Tuff was emplaced during the Middle Pleistocene at water depths of 200 to 1000 m, as suggested by foraminiferal and calcareous nannoplankton biostratigraphic markers and benthic foraminiferal paleodepth indicators. It formed a 90 km^3 volcaniclastic megaturbidite up to 150m thick in the marine basins (Druitt *et al.*, 2024a), six times bigger than the pyroclastic current deposit from the Minoan eruption (~15 km^3; Karstens *et al.*, 2023).

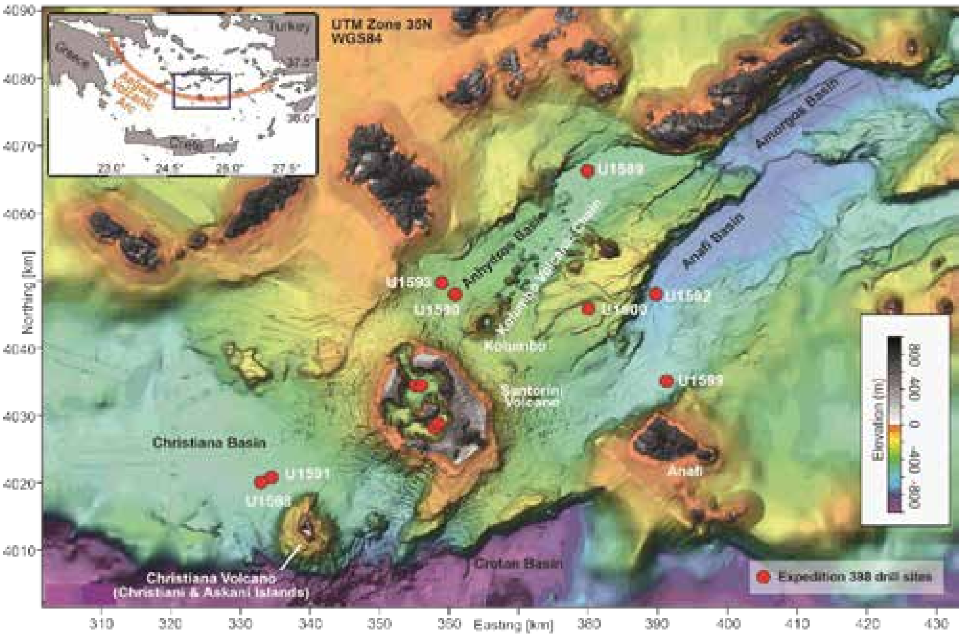

Figure 1. The IODP Expedition 398 drill sites (modified by Druitt *et al.*, 2024a).

These kind of large explosive volcanic eruptions from island arcs pour pyroclastic currents into marine basins, causing high plumes of ash, earthquakes and associated tsunamis and severely affecting coastal communities and infrastructures. Marine ecosystems are particularly vulnerable to eruptions and their consequences (ocean acidification, fertilization, debris flows, increased temperatures, ash falls) leading to diversity changes and even biodiversity loss (e.g., Finger and Lipps, 1981; Hart *et al.*, 2022). The effects in foraminiferal microfauna of such extreme events, as volcanic eruptions, were investigated in the sediments deposited prior and after the emplacement of Archaeos Tuff.

The exact intervals before, during and after this pyroclastic flow (for interval details on the Archaeos Tuff see Druitt *et al.*, 2024a) were studied in six cores along the different basins, and here we present our preliminary results on its impacts on foraminiferal community structure. During deposition of the submarine pumice, benthic foraminifera species were severely affected both in terms of density and diversity, with survivor infaunal species, shelf species and damaged specimens likely representing downslope reworking. Some samples were barren even from accompanying ostracods, molluscs and pteropods, while planktonic foraminifera were also rarely present. Following deposition of the pumice, the foraminiferal repopulation took place, with high numbers and diversity values, suggesting the recovery of the stressed environment and the restoration of the oligotrophic and well-oxygenated conditions.

Our findings highlight the foraminiferal fauna ability to tolerate major catastrophic events in their environment and to recover and recolonize, which is both admirable and extremely useful as a tool to interpret biostratigraphic correlations and paleoenvironmental conditions.

Acknowledgements

We are thankful to the International Ocean Discovery Program (IODP), the technical staff of the JOIDES Resolution, and all of the shipboard personnel for a great expedition. We also thank the member organizations of IODP for financial aid, and the Municipality of Thera for help in preparing for the expedition.

References

Bruins, H.J., MacGillivray, J.A., Synolakis, C.E., Benjamini, C., Keller, J., Kisch, H.J., Klügel, A., van der Plicht, J., 2008. Geoarchaeological tsunami deposits at Palaikastro (Crete) and the late Minoan IA eruption of Santorini. Journal of Archaeological Science 35(1), 191-212.

Druitt, T.H., Edwards, L., Mellors, R.M., Pyle, D.M., Sparks, R.S.J., Lanphere, M., Davies, M., Barreirio, B., 1999. Santorini Volcano. Memoir - Geological Society of London 19, 165pp.

Druitt, T., Kutterolf, S., Höfig, T.W., 2022. Expedition 398 Scientific Prospectus: Hellenic Arc Volcanic Field. International Ocean Discovery Program. https://doi.org/10.14379/iodp.sp.398.2022

Druitt, T., Kutterolf, S., Ronge, T.A., Hübscher, C., Nomikou, P., Preine, J., Gertisser, R., Karstens, J., Keller, J., Koukousioura, O., Manga, M., Metcalfe, A., McCanta, M., McIntosh, I., Pank, K., Woodhouse, A., Beethe, S., Berthod, C., Chiyonobu, S., Chen, H., Clark, A., DeBari, S., Johnston, R., Peccia, A., Yamamoto, Y., Bernard, A., Fernandez Perez, T., Jones, C., Joshi, K.B., Kletetschka, G., Li, X., Morris, A., Polymenakou, P., Tominaga, M., Papanikolaou, D., Wang, K.-L., Lee, H.-Y., 2024a. Giant offshore pumice deposit records a shallow submarine explosive eruption of ancestral Santorini. Communications Earth and Environment 5, 24.

Druitt, T.H., Kutterolf, S., Ronge, T.A., Beethe, S., Bernard, A., Berthod, C., Chen, H., Chiyonobu, S., Clark, A., DeBari, S., Fernandez Perez, T.I., Gertisser, R., Hübscher, C., Johnston, R.M., Jones, C., Joshi, K.B., Kletetschka, G., Koukousioura, O., Li, X., Manga, M., McCanta, M., McIntosh, I., Morris, A., Nomikou, P., Pank, K., Peccia, A., Polymenakou, P.N., Preine, J., Tominaga, M., Woodhouse, A., and Yamamoto, Y., 2024b. Expedition 398 summary, in: Druitt, T.H., Kutterolf, S., Ronge, T.A., and the Expedition 398 Scientists, Hellenic Arc Volcanic Field. Proceedings of the International Ocean Discovery Program, 398: College Station, TX (International Ocean Discovery Program). https://doi.org/10.14379/iodp.proc.398.101.2024

Finger, K.L., Lipps, J.H., 1981. Foraminiferal decimation and repopulation in an active volcanic caldera, Deception Island, Antarctica. Micropaleontology 27, 111-139.

Hart, M.B., Fisher, J.K., Smart, C.W., Speers, R., Wall-Palmer, D., 2022. Re-colonization of hostile environments by benthic foraminifera: an example from Montserrat, Lesser Antilles Volcanic Arc. Micropaleontology 68(1), 1-27.

Karstens, J., Preine, J., Crutchley, G.J., Kutterolf, S., van der Bilt, W.G.M., Hooft, E.E.E., Druitt, T.H., Schmid, F., Cederstrøm, J.M., Hübscher, C., Nomikou, P., Carey, S., Kühn, M., Elger, J., Berndt, C., 2023. Revised Minoan eruption volume as benchmark for large volcanic eruptions. Nature Communications 14, 2497.

Nomikou, P., Papanikolaou, D., Alexandri, M., Sakellariou, D., Rousakis, G., 2013. Submarine volcanoes along the Aegean volcanic arc. Tectonophysics 597-598, 123-146.

Nomikou, P., Hübscher, C., Carey, S., 2019. The Christiana-Santorini-Kolumbo Volcanic Field. Elements 15(3), 171-176.

Preine, J., Karstens, J., Hübscher, C., Druitt, T., Kutterolf, S., Nomikou, P., Manga, M., Gertisser, R., Pank, K., Beethe, S., Berthod, C., Crutchley, G., McIntosh, I., Ronge, T., Tominaga, M., Clark, A., DeBari, S., Johnston, R., Mateo, Z., Peccia, A., Jones, C., Kletetschka, G., Metcalfe, A., Bernard, A., Chen, H., Chiyonobu, S., Fernandez-Perez, T., Joshi, K.B., Koukousioura, O., McCanta, M., Morris, A., Polymenakou, P., Woodhouse, A., Yamamoto, Y., Wang, K.-L., Lee, H.-Y., Li, X., Papanikolaou, D., 2024. Hazardous explosive eruptions of a recharging multi-cyclic island arc caldera. Nature Geoscience 17, 323-331.

17th INTERNATIONAL CONGRESS
of the Geological Society of Greece

BULLETIN OF THE GEOLOGICAL SOCIETY OF GREECE, SP. PUBL.

EXTENDED ABSTRACT 169

Late Quaternary dynamics of paleoenvironments and ecosystems in the Gulf of Corinth (eastern Mediterranean): IODP Expedition 381

Koukousioura O.[1,2], Panagiotopoulos K.,[1,3], Fatourou E.[4], Kafetzidou A.[4], Diz P.[5], Kouli K.[4], Grunert P.[1]

(1) University of Cologne, Cologne, Germany (2) Aristotle University of Thessaloniki, Thessaloniki, Greece, okoukous@geo.auth.gr (3) Forschungszentrum Jülich, Jülich, Germany (4) National and Kapodistrian University of Athens, Athens, Greece (5) Universidade de Vigo, Vigo, Spain

Abundance and assemblage composition of benthic foraminifera, dinoflagellate cysts and pollen grains were analysed together with sedimentological (grain size) and geochemical (organic and inorganic carbon content, XRF, benthic foraminifera oxygen and carbon isotopes) proxies to investigate paleoenvironmental changes recorded in the Gulf of Corinth during MIS 1-5, from IODP Expedition 381 core M0080. The Gulf of Corinth is a relatively young (<5 Ma) and active continental rift zone in the eastern Mediterranean Sea, with a length of about 120 km (McNeil *et al.*, 2019a and references therein; Gawthrope et al., 2022). The Gulf is currently connected to the Ionian Sea through a shallow sill (Rion sill; 60 m-deep) and to the Aegean Sea via the Corinth Canal (Isthmus; 6 km-wide). The eastern part is divided by the Perachora Peninsula into the Lecheon Gulf in the south, and the Alkyonides Gulf in the north, a shallow semi-enclosed sub-basin within the northeastern part of the Gulf of Corinth, where core M0080 is located (Fig. 1; McNeil et al., 2019b). The closed drainage system and the high sedimentation rates (approx. 0.5-3 mm/yr; McNeil et al., 2019a) make the study area a natural laboratory for the investigation of the complex interaction between sedimentary input, tectonics and climate through the basin's evolution.

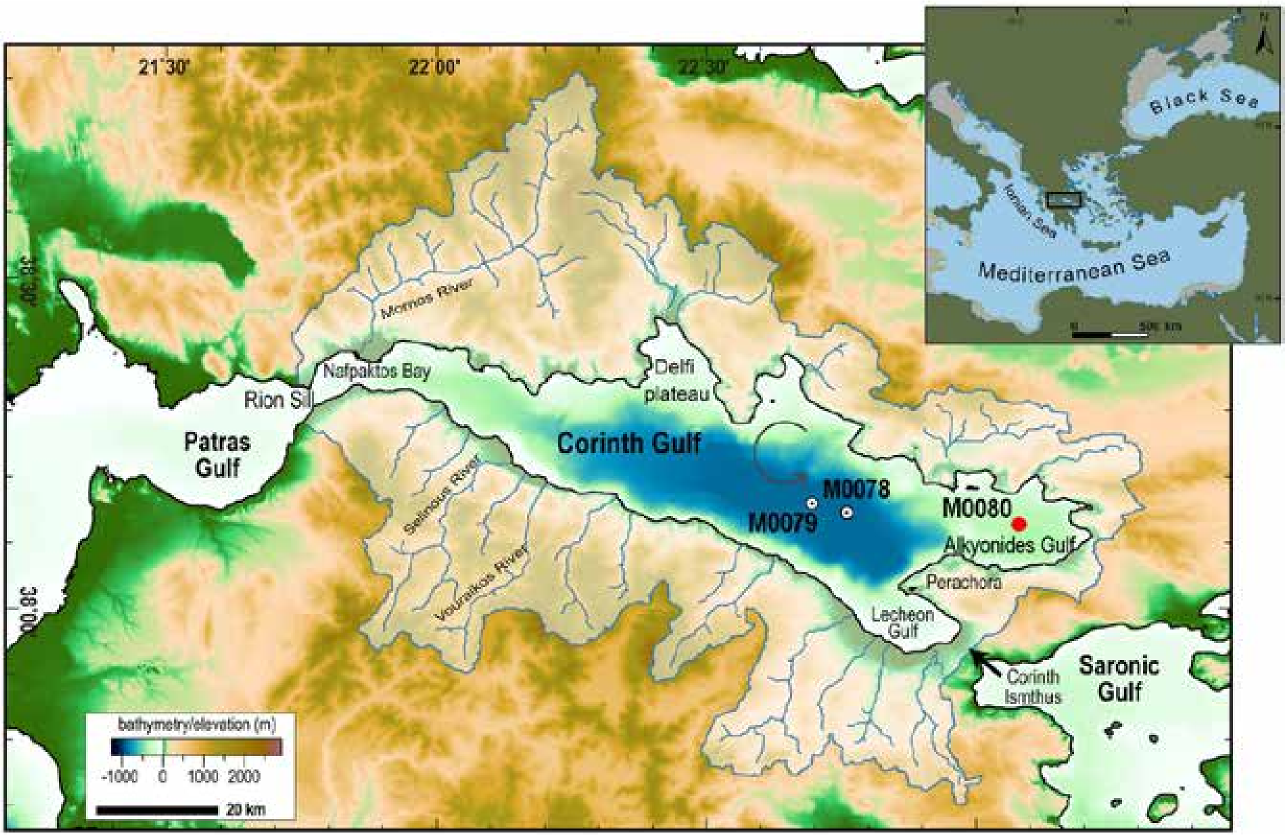

Figure 1. The IODP Expedition 381 drill sites with the location of M0080 indicated by the red dot (modified from Fatourou *et al.*, 2023 and Kafetzidou *et al.*, 2023).

The benthic foraminiferal, dinocyst and pollen records are highly variable during both the Last Interglacial complex and the Holocene. Infaunal foraminiferal species characterize these assemblages with high abundances of *Bolivina* spp.,

Melonis affinis, *Bulimina* spp. and *Cassidulina carinata*, indicating mesotrophic to eutrophic marine conditions, with marine dinocysts (*Nemaosphaeropsis labyrinthus*, *Spinifireties ramosus*) and montane trees likely to have occurred during high sea-levels. During glacial and interstadial intervals, benthic foraminifers are very low in numbers or even absent, whereas abundant brackish dinocysts (*Pyxidinopsis psilata*) suggest a sea-level drop below sill level and the subsequent (semi-)isolation of the basin. Inorganic carbon content and elemental counts varied following the inferred sea-level fluctuations, while the benthic foraminifera oxygen isotope record is discontinuous and conditioned to the presence of well-preserved benthic foraminifera. The beginning of the Holocene is marked by the re-establishment of marine conditions as the sea-level rose above the sill and the basin re-connected to the Mediterranean Sea.
Ongoing high-resolution studies and a refinement of the age model will improve our understanding of paleoenvironmental changes in the Gulf of Corinth during glacial and interglacial stages and allow us to define the factors driving changes in this unique active rift of the eastern Mediterranean.

Acknowledgements

This study is funded through projects GR 5285/3-1 "*Late Quaternary dynamics of marine paleoenvironments and ecosystems in the Gulf of Corinth (eastern Mediterranean)*" and PA 2664/8-1 "*Linking marine and terrestrial ecosystem responses to climate variability since the Last interglacial in the Eastern Mediterranean*" of the Deutsche Forschungsgemeinschaft (DFG).

References

Fatourou, E., Kafetzidou, A., Marret, F., Panagiotopoulos, K., Kouli, K., 2023. Late Quaternary Ponto-Caspian dinoflagellate cyst assemblages from the Gulf of Corinth, Central Greece (eastern Mediterranean Sea). Marine Micropaleontology 179, 102211.

Gawthrope, R.L., Fabregas, N., Pechlivanidou, S., Ford, M., Collier, R.E.L., Carter, G.D.O., McNeil, L.C., Shillington, D.J., 2022. Late Quaternary mud-dominated, basin-floor sedimentation of the Gulf of Corinth, Greece: Implications for deep-water depositional processes and controls on syn-rift sedimentation. Basin Research 34, 1567-1600.

Kafetzidou, A., Fatourou, E., Panagiotopoulos, K., Marret, F., Kouli, K., 2023. Vegetation Composition in a Typical Mediterranean Setting (Gulf of Corinth, Greece) during Successive Quaternary Climatic Cycles. Quaternary 6(2), 30.

McNeil, L.C., Shillington, D.J., Carter, G.D.O., Everest, J.D., Gawthorpe, R.L., Miller, C., Phillips, M.P., Collier, R.E.Ll., Cvetkoska, A., De Gelder, G., Diz, P., Doan, M.-L., Ford, M., Geraga, M., Gillespie, J., Hemelsdaël, R., Herrero-Bervera, E., Ismaiel, M., Janikian, L., Kouli, K., Le Ber, E., Li, S., Maffione, M., Mahoney, C., Machlus, M.L., Michas, G., Nixon, C.W., Oflaz, S.A., Omale, A.P., Panagiotopoulos, K., Pechlivanidou, S., Sauer, S., Seguin, J., Sergiou, S., Zakharova, N.V., Green, S., 2019a. High-resolution record reveals climate-driven environmental and sedimentary changes in an active rift. Scientific Reports 9, 3116.

McNeill, L.C., Shillington, D.J., Carter, G.D.O., Everest J.D., Le Ber E., Collier R.E., Cvetkoska A., De Gelder G., Diz P., Doan M.L., Ford M., Gawthorpe R.L., Geraga M., Gillespie J., Hemelsdaël R., Herrero-Bervera E., Ismaiel M., Janikian L., Kouli K., Li S., Machlus M.L., Maffione M., Mahoney C., Michas G., Miller C., Nixon C.W., Oflaz S.A., Omale A.P., Panagiotopoulos K., Pechlivanidou S., Phillips M.P., Sauer S., Seguin J., Sergiou S., Zakharova N.V., 2019b. Site M0078, in Program, I.O.D.P. (Ed.), McNeill, L.C., Shillington, D.J., Carter, G.D.O., and the Expedition 381 Participants, Corinth Active Rift Development. Proceedings of the International Ocean Discovery Program. International Ocean Discovery Program, College Station, Texas.

BULLETIN OF THE GEOLOGICAL SOCIETY OF GREECE, SP. PUBL.

EXTENDED ABSTRACT 170

Characterization of Sandstone Formations in the Mesohellenic Trough for CO_2 Storage: Insights from the Integration of Optical Mineralogy, Geochemistry, and Automated Imaging Techniques

Koukouzas N.[1], Tyrologou P.[1], Stergiou C.L.[2,3], Carneiro J.[4], Fernández-Canteli P.[5], Karatrantou C.[1], Asimakopoulou S.[1],

(1) Chemical Process & Energy Resources Institute (CPERI), Centre for Research and Technology Hellas (CERTH), 15125 Athens, Greece, koukouzas@certh.gr (2) Chemical Process & Energy Resources Institute (CPERI), Centre for Research and Technology Hellas (CERTH), 50200 Ptolemaida, Greece (3) School of Geology, Aristotle University of Thessaloniki (AUTH), 54124 Thessaloniki, Greece (4) ICT/IIFA, Geosciences Department, Universidade de Évora, 7000-671 Évora, Portugal (5) Instituto Geológico y Minero de España (IGME-CSIC), 28003 Madrid, Spain

Introduction

Carbon Capture, Utilization, and Storage (CCUS) is critical for reducing CO_2 emissions from industry and energy generation, aligning with net-zero goals under the Paris Agreement (Koukouzas *et al.,* 2021). CCUS captures CO_2 for reuse or secure storage in geological formations, including saline aquifers and depleted fields, offering flexibility through enhanced recovery and mineralization (Koukouzas *et al.,* 2018, 2021, Tyrologou *et al.,* 2023). While cost remains a challenge, technological advancements and successful projects (e.g. Sleipner, Norway) highlight its potential for supporting the low-carbon transition (Tyrologou *et al.,* 2023).

The Horizon 2020-funded PilotSTRATEGY project advances CO_2 storage research in Southern and Eastern Europe, focusing on deep saline aquifers in five basins, including the Mesohellenic Trough (M.T.) in northern Greece (e.g. Ayala *et al.,* 2023, Berrezueta *et al.,* 2023, Tyrologou *et al.,* 2023, Ordóñez *et al.,* 2024). Geological modeling in the M.T. identified the Pentalofos and Eptachori Formations (Fms) as prime storage sites, with capacities of 1 Gt and 0.85 Gt, respectively (Koukouzas *et al.,* 2021). Petrophysical studies confirm low porosity and water permeability in specific sedimentary strata, designating sedimentary layers in the Eptachori, Pentalofos, and Tsotyli Fms as effective cap rocks for secure CO_2 storage (Tyrologou *et al.,* 2023). This publication presents preliminary findings on the geological characterization of sandstone formations in the M.T. using a multidisciplinary approach. Methods include thin section analysis under optical and SEM microscopy for grain and texture evaluation, XRD and XRF for mineralogical and chemical characterization, and automated image analysis for macro-porosity assessment.

Geological Setting

The Mesohellenic Trough (M.T.) is a Tertiary sedimentary basin along the suture zone between the Apulian platform and the Pelagonian nappe, marking the Hellenide orogenic belt boundary (Vamvaka *et al.,* 2006, Fig. 1a). Extending over 200 km in length and 40 km in width, it features five siliciclastic formations – Krania, Eptachori, Pentalofos, Tsotyli, and Ondria – deposited from the Late Eocene to the Middle Miocene in environments varying from fan-deltas to turbiditic sandstones, and deltaic sediments, reflecting a transition from marine to terrestrial settings (Vamvaka *et al.,* 2006). The asymmetrical syncline, with up to 4.5 km thick sediments near Grevena, reflects orogenic and extensional tectonics. Its evolution involves Eocene-Oligocene and Miocene faults and N-S extension linked to recent seismicity, shaping fault zones and river alignments (Tyrologou *et al.,* 2023).

Methods

Three sedimentary rock samples were selected for study, originating from the Tsotyli (sample Tsot-1; marly sandstone; Burdigalian; Lower Miocene), Eptachori (sample Ept-2; fine sandstone; Rupelian; Upper Oligocene), and Pentalofos (sample Pent-3; sandstone; Chattian-Aquitanian; Upper Oligocene-Lower Miocene) Fms of the M.T. (Figs 1b-g). Three thin-polished sections were prepared at the School of Geology, AUTH, and analyzed using a ZEISS Axioskop 40 polarizing microscope to examine mineral composition. SEM-EDS analysis was conducted with a JEOL JSM-IT500 equipped with an OXFORD INCA X-ACT system at Analytical Services Unit, CPERI, CERTH, under 20 kV accelerating voltage, 0.4 mA probe current, 20 s analysis time, and ~1 μm beam diameter in BSE mode. Elemental mapping revealed mineralogical variations, and pore characteristics were evaluated with representative photomicrographs. Automated image analysis (×200 magnification, BSE mode) was performed using ImageJ software (Schneider *et al.*, 2012).

X-ray diffractometry (XRD) was performed using a Bruker D8 Advance diffractometer with a CuKα anode (λ = 0.1542 nm) operating at 40 kV and 30 mA at the School of Geology, AUTH. The counting statistics of the XRD study were, step size: 0.019° 2θ, start angle: 3.000°, end angle: 93.009° and scan speed: 0.19° 2θ/s. Rietveld refinement

were implemented by using the Profex5 (v.5.2.7, Doebelin and Kleeberg, 2015) software acquiring semi-quantitative estimates on the abundance of the mineral phases and on the chemical composition of the analyzed samples.
X-ray fluorescence (XRF) analysis was conducted using a Bruker S4-PIONEER WDXRF system at the School of Geology, AUTH, to determine the geochemical composition of the samples. Equipped with a Rh lamp, five crystals, and dual detectors, the system operated at 50–60 kV, analyzing Ka and La lines for elements. Corrections for spectral overlaps and matrix effects ensured accuracy.

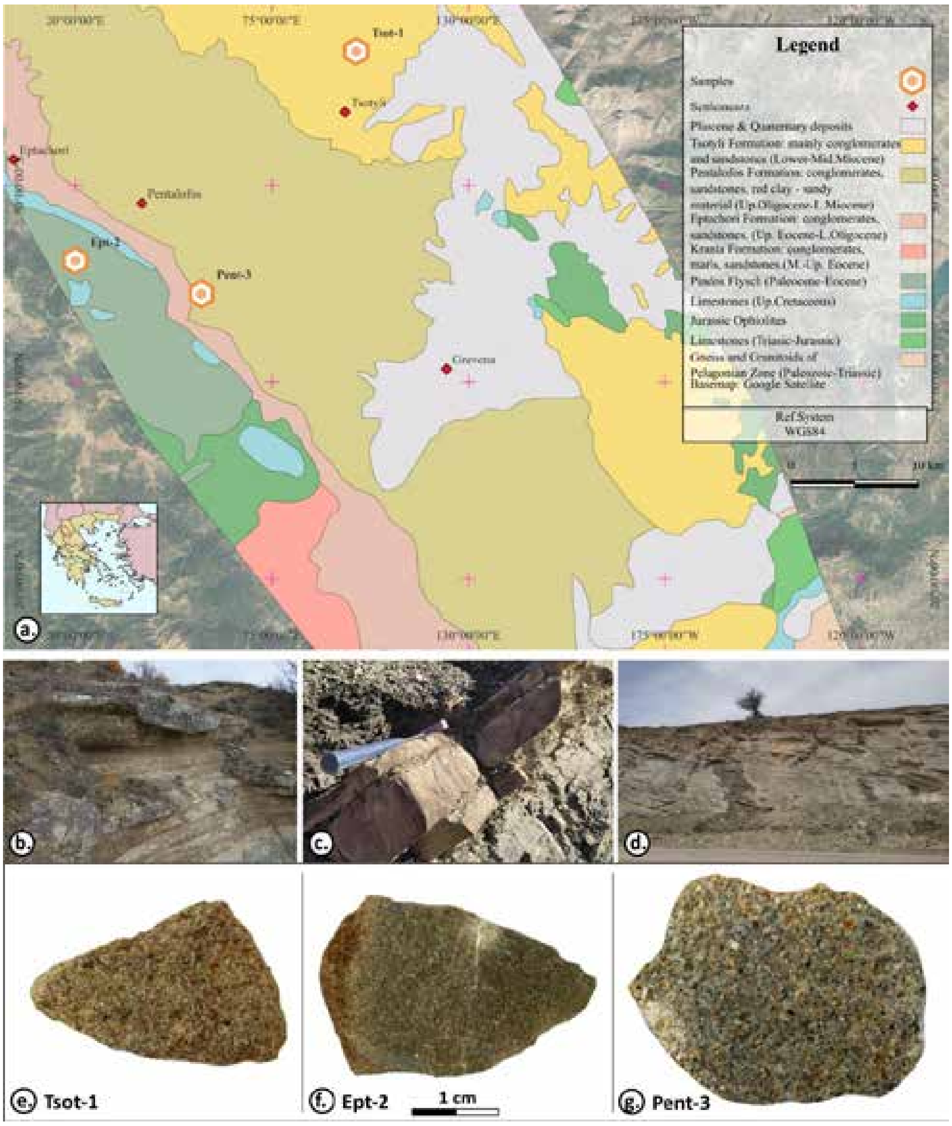

Figure 1. a. Geological map of the Mesohellenic Trough at Grevena region, showing the sampling locations of Tsot-1, Ept-2 and Pent-3 samples (modified after Savoyat & Monopolis, 1972, Bornovas & Rondogianni-Tsiambaou, 1983). b-d. Field photographs of the sampled outcrops (b: Tsot-1, c: Ept-2, Pent-3: d). d-f. Macro-photographs of the analyzed samples.

Results & Discussion

Field survey and macroscopic observations revealed that Tsot-1, Ept-2, and Pent-3 outcrops share similarities, including their light-colored sandstones, medium bedding (200 to 600 mm in thickness), and slightly weathered (Grade 1) tabular rock masses, and very strong material strength (100-250 MPa, Fig. 1b-d). However, they differ in texture, features, and bedding orientation: Tsot-1 lacks fossils, has a homogeneous marly texture, and bedding striking 322°/12°, Ept-2 exhibits burrows, plant fragments, Liesegang discoloration, and bedding striking 122°/33°, while Pent-3 shows alternating clast-rich and mudstone units with diverse compositions and bedding striking 128°/33°.

Optical microscopy and SEM-EDS analysis and petrographic examination of bulk samples and thin-polished sections from Tsot-1, Ept-2, and Pent-3 highlighted distinct mineralogical and compositional characteristics. In Tsot-1, the identified minerals include calcite (30 wt.%), quartz (29 wt.%), and albite (21 wt.%), minor muscovite, chlorite, dolomite and aragonite, as well as microcline, zircon and jacobsite in traces (Table 1, Figs 2a, 3a). The sample consists of well-cemented grains dominated in average by Si (52 wt.%) and Ca (24 wt.%), with additional Al (11 wt.%), K (11 wt.%), Fe (7.0 wt.%), Mg (4.0 wt.%), and Na (3.0 wt.%, Table 3). Macro-pores are rounded to irregular, averaging 45 μm in width, and the siliceous cement is locally crystalline, containing up to 9.9 wt.% Fe (Tables 2, 3). Sample Ept-2 includes quartz (37 wt.%), calcite (29 wt.%), albite (13 wt.%) and muscovite (13 wt.%), minor dolomite and chamosite, while as traces are found biotite, titanite, pyrite, crichtonite, actinolite and zircon (Table 1, Figs 2b, 3b). It is well-cemented, with a bulk composition dominated by Ca (<53 wt.%) and Si (≤26 wt.%), alongside Mg (<8.8 wt.%), Fe (<8.3 wt.%), and Al (3.7 wt.%, Table 3). The calcareous microcrystalline cement contains up to 41 wt.% Si and 18 wt.% Fe, with macro-pores averaging 66 μm and smaller pores at 11 μm (Tables 2, 3). In Pent-3, calcite (41 wt.%), dolomite (18 wt.%), quartz (15 wt.%), and albite (12 wt.%) are found, while minor minerals include microcline, muscovite and aragonite, with trace amounts of chlorite, titanite, chromite, pyrite, Fe-chromite, actinolite, apatite, andradite and enstatite (Table 1, Figs 2c, 3c). The sample displays the largest grains among the analyzed material, with grains occasionally exceeding 500 μm, with a dominantly calcareous composition (61 wt.%) and cement enriched in Mg and Si (Fig. 3c). Rare elongated macro-pores average 65 μm, while smaller pores within the cement average 6.0 μm.

Table 1. Sample identification numbers, localities (coordinates), main, minor and trace mineralogy. Abundances (%) of the main and minor mineral phases are given after the Rietveld refinement.

Sample	Coordinates WGS84 (Latitude/Longitude)	Main minerals	Minor minerals	Trace mineralogy	Qtz/ Fsp ratio
Tsot-1	N 40.3075°/ E 21.3354°	Cal: 30%, Qz: 29%, Ab: 21%	Ms: 7.2%, Chl: 7.1%, Dol: 4.5%, Arg: 1.4%,	Mc, Zrn, Jcb	1.4
Ept-2	N 40.1535°/ E 21.0824°	Qz: 37%, Cal: 29%, Ab: 13%, Ms: 13%,	Dol: 4.6%, Chm: 3.1%	Bt, Ttn, Py, Cic, Act, Zrn	2.9
Pent-3	N 40.1332°/ E 21.1997°	Cal: 41% , Dol: 18%, Qz: 15%, Ab: 12%	Mc: 8.0%, Ms: 4.3%, Arg: 2.6%	Chl, Ttn, Chr, Py, Fe-Chr, Act, Ap, Adr, En	0.8

Abbreviations: Ab = Albite, Act = actinolite, Adr = andradite, Ap = apatite, Arg = aragonite, Bt = biotite, Cal = calcite, Chl = chlorite, Chm = chamosite, Cic = crichtonite, Chr = chromite, Dol = dolomite, Fe-Chr = Iron-chromite, Fsp = feldspar, Mc = microcline, Ms = muscovite, Py = pyrite, Ttn = titanite, Qz = quartz, Zrn = zircon.

Relative abundances of quartz and feldspars (albite, microcline) were obtained by XRD analysis and plotted in the QFR (Quartz-Feldspar-Rock fragments) triangular classification diagram (McBride, 1963). The analyzed samples fall within the "Feldspathic litharenite" field, with Tsot-1 and Ept-2 clustering closely, while Pent-3 exhibits relative enrichment in lithic fragments (Fig. 2d). In addition, the mineralogical analysis conducted via XRD and Rietveld refinement, revealed that for sample Tsot-1 the quartz/feldspar (albite) ratio is 1.38 (Table 1), while Ca/Si ratio of 0.6 complements SEM-EDS results (Ca/Si = 0.5), indicating a consistent siliceous matrix (Table 3). Sample Ept-2 has a quartz/feldspar (albite) ratio of 2.9 (Table 1). Although SEM-EDS geochemistry highlights a Ca-enriched matrix (Ca ≤53 wt.%), the Rietveld refinement analysis revealed a siliceous chemical composition (25 wt.% Si) with a Ca/Si ratio of 0.5, underscoring the complex interplay between primary mineral inputs and diagenetic processes (Table 3). The quartz/feldspar (albite, microcline) ratio of 0.8 for sample Pent-3, reflects feldspathic contributions, while the Rietveld-derived Ca/Si ratio of 1.5 aligns with SEM-EDS findings (Ca/Si = 1.5), indicating a calcite-dominated cement matrix (Tables 1 & 3).

Bulk geochemical analysis applying XRF spectrometry reveals the compositional variability among samples Tsot-1, Ept-2, and Pent-3, with calcium and silica identified as the most enriched elements (Table 3). Sample Tsot-1 (25 wt.% SiO_2) is slightly siliceous, Ept-2 (36 wt.% SiO_2) is dominantly siliceous, and Pent-3 (42 wt.% CaO) is dominantly calcareous (Table 3). These findings align closely with the semi-quantitative mineralogical data derived from XRD and SEM-EDS analyses. In sample Tsot-1, the XRF results support the mineralogical profile established by XRD, where calcite (30 wt.%) and siliceous components, quartz (29 wt.%) and albite (19 wt.%), collectively constitute 50 wt.%, confirming its slightly siliceous composition. For Ept-2, XRF results indicating a dominantly siliceous composition (36 wt.% SiO_2) are consistent with the XRD data, which identified quartz (37 wt.%) as the primary phase, followed by calcite (29 wt.%). Similarly, the calcareous dominance of Pent-3 (42 wt.% CaO by XRF) corroborates XRD findings, which showed calcite as the most abundant phase (41 wt.%). The XRF data also reveal insights into trace element distributions, particularly for Ept-2, which exhibits the highest enrichment in minor elements, including Cr (1680 ppm) and V (990 ppm), alongside Co, Cu, Ni, and Zn (Table 3). These variations in trace element content are associated to minor mineral phases, such as chromite and pyrite, which were detected through the SEM-EDS analysis of the thin-polished sections (Table 1, Fig. 3c), and suggest a significant contribution of detrital material, likely derived from the erosion of ophiolitic basement rocks surrounding the Mesohellenic Trough.

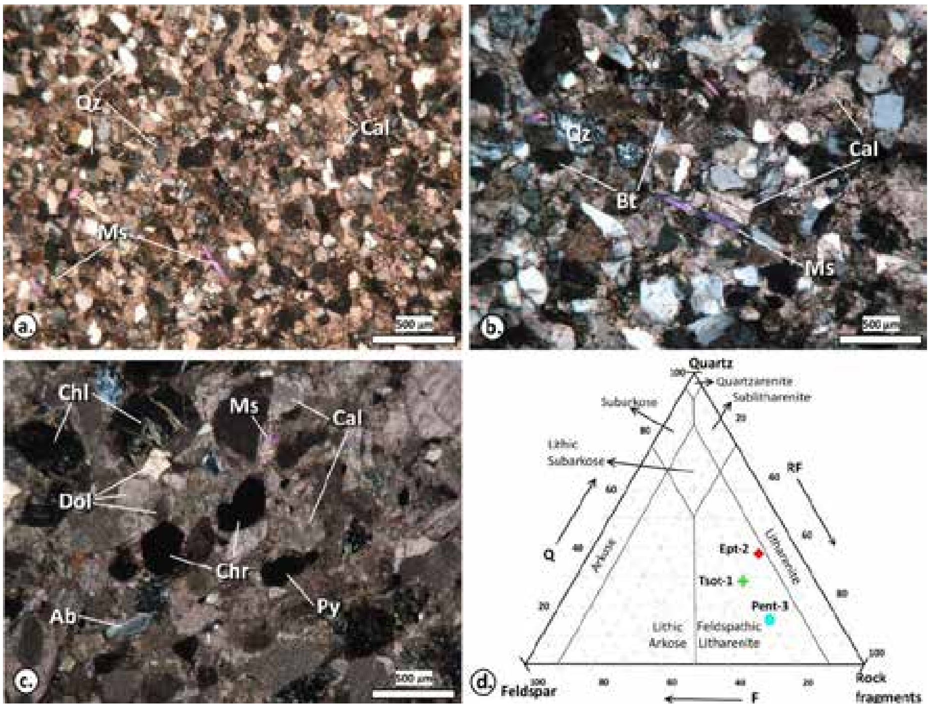

Figure 2. Photomicrographs of the studied samples: a. Well-cemented quartz (Qz), calcite (Cal) and muscovite (Ms) in sample Tsot-1. b Quartz (Qz), biotite (Bt), calcite (Cal) and muscovite (Ms) in sample Ept-2. c. Calcite (Cal) and dolomite (Dol) with chlorite (Chl) and minor albite (Ab), chromite (Chr) and pyrite (Py) in sample Pent-3. Dolomite was identified by SEM-EDS analysis. d. QFR (Quartz-Feldspar-Rock fragments) triangular plot diagram for classification of the studied samples after McBride (1963).

Table 2. Average morphometric characteristics by SEM-EDS analysis of the pores width between grains and in cement for samples Tsot-1, Ept-2, and Pent-3, along with macro-porosity data obtained through automated image analysis.

	Average morphometric characteristics				**Macro-porosity data**				
Sample	**Pores between grains**	**Pore shape**	**Pores in cement**	**Pore shape**	**Sample**	**MIN**	**MAX**	**STDEV**	**AVG**
Tsot-1	45 μm (n = 12)	Irregular, rounded, elongated	-	-	**Tsot-1** (n = 5)	1.4	1.9	0.2	1.7
Ept-2	66 μm (n = 8)		11 μm (n = 5)	Rounded	**Ept-2** (n = 9)	1.7	1.9	0.1	1.8
Pent-3	65 μm (n = 4)	Irregular, elongated	6.0 μm (n = 3)	Rounded	**Pent-3** (n = 12)	1.0	4.0	1.4	2.0

Abbreviation: average = AVG, maximum = MAX, minimum = MIN, standard deviation = STDEV.

The maximum porosity (4%) measured after automated image analysis is related to sample Pent-3 (Table 2). The results are in accordance with these previously published where porosity was measured at 6.0%, 7.4% and, 4.9 to 10.8% for the samples Tsot-1, Ept-2 and Pent-3, respectively (Tyrologou *et al.,* 2023). The lower porosity values from ImageJ analysis compared to petrophysical testing reflect differences in methodology, as ImageJ focuses on 2D observable pores, potentially overlooking micro-porosity (Figs 3d-f). Petrophysical testing, measuring bulk porosity provides a more comprehensive view of the porosity of the samples. Despite this, ImageJ remains a valuable and cost-effective tool for identifying porosity trends and comparing samples, particularly for macro- and meso-pores.

Table 3. Bulk geochemical composition, determined through elemental mapping via SEM-EDS, XRD and Rietveld refinement, and XRF analysis of major elements in samples Tsot-1, Ept-2, and Pent-3. Values are in weight percent (wt.%), except for the trace elements where they are reported in parts per million (ppm).

Element by SEM-EDS	**Si**	**Al**	**Fe**	**Ca**	**Mg**	**Na**	**K**	**Mn**	**Ti**	**P**	**Ca/Si**	
Tsot-1 in average (n = 6)	52	11	7.0	24	4.0	3.0	11	n.a.	n.a.	n.a.	0.5	
Ept-2 in average (n = 6)	26	3.7	8.3	53	8.8	n.a.	n.a.	n.a.	n.a.	n.a.	2.0	
Pent-3 in average (n = 6)	21	3.3	3.6	48	7.9	1.8	1.4	n.a.	n.a.	n.a.	2.3	
Element by XRD	**Si**	**Al**	**Fe**	**Ca**	**Mg**	**Na**	**K**	**Mn**	**Ti**	**P**	**Ca:Si**	
Tsot-1	23	4.3	0.8	14	1.8	1.8	0.7	n.a.	n.a.	n.a.	0.6	
Ept-2	25	4.0	1.1	13	0.8	1.1	0.8	n.a.	n.a.	n.a.	0.5	
Pent-3	14	2.8	0.1	21	2.3	1.0	1.4	n.a.	n.a.	n.a.	1.5	
Element by XRF	**SiO_2**	**Al_2O_3**	**Fe_2O_3**	**CaO**	**MgO**	**Na_2O**	**K_2O**	**MnO**	**TiO_2**	**P_2O_5**	**LOI**	**Total**
Tsot-1	35	7.0	2.7	31	4.2	1.0	2.2	0.1	0.3	0.08	17	100
Ept-2	36	6.6	3.3	26	7.2	0.7	1.4	0.1	0.4	0.1	18	100
Pent-3	16	2.9	1.2	42	6.0	0.4	0.9	0.03	0.1	0.06	30	100
Trace element by XRF	**Ba**	**Co**	**Cr**	**Cu**	**Ni**	**Rb**	**Sc**	**Sr**	**V**	**Zn**	**Zr**	**Total**
Tsot-1	189	7.0	749	14	112	192	bdl	298	650	31	100	
Ept-2	149	13	1680	23	221	95	bdl	342	990	38	113	
Pent-3	66	4.0	512	7.0	78	82	bdl	242	306	15	54	

Abbreviations: LOI = Loss of ignition, n.a. = not available.

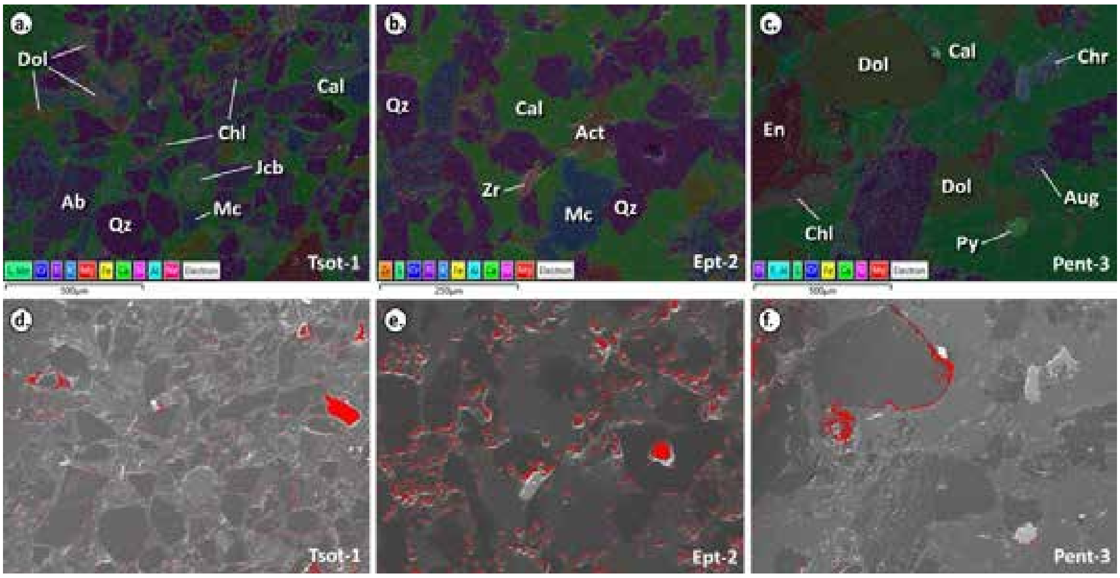

Figure 3. Representative photomicrographs illustrate elemental mapping (a–b) and porosity assessment (d–f) via automated image analysis for samples Tsot-1, Ept-2, and Pent-3. The calculated porosity values are 1.8% for Tsot-1 (d), 1.9% for Ept-2 (e), and 1.1% for Pent-3 (f).

Conclusions and Ongoing Research

The combined mineralogical, geochemical, and textural analysis of samples Tsot-1, Ept-2, and Pent-3 reveals significant variability in depositional environments and diagenetic processes. In addition, SEM-EDS analysis and automated image analysis enables fast, cost-effective macro-porosity characterization. Sample Tsot-1, with its siliceous dominance, moderate macro-porosity, and traces of microcline and zircon, suggests deposition in a high-energy environment with significant siliciclastic input, consistent with its well-bedded sandstone structure. Sample Ept-2, characterized by its carbonate-rich composition and microcrystalline cement, indicates deposition in a marine-influenced or lacustrine setting, supported by bedding features and burrow evidence. In contrast, the complex mineralogy of sample Pent-3, including high calcite content and inclusions like titanite and chromite, reflects a mixed depositional environment influenced by the erosion of the ophiolitic rocks surrounding the Mesohellenic Trough.

These findings highlight the interplay between provenance, depositional energy, and diagenetic processes in shaping the regional sedimentary formations, offering insights into the tectonic and sedimentological evolution of the basin.

Acknowledgements

This research was funded by the EU Horizon 2020 program under grant No. 101022664 (PilotSTRATEGY). The funders had no role in study design, data collection, analysis, publication decisions, or manuscript preparation. Special thanks to Agnes Vamvaka, Dina Ghikas, and Anna Mpatsi for their assistance in field sample collection. XRF analyses were conducted under a service agreement between CERTH and the Laboratory of Mineralogy and Petrology, Faculty of Geology, AUTH.

References

Ayala, C., Benjumea, B., Mediato, J.F., García-Crespo, J., Clariana, P., Soto, R., Rubio, F., Rey-Moral, C., Pueyo, E.L., Martín-León, J., García, A.G., Fernández-Canteli, P. Martinez Orio, R., 2023. Developing a new innovative methodology to integrate geophysical techniques into characterization of potential CO_2 storage sites: Lopín structure (Southern Ebro basin, Spain), in: Miocic, J.M., Heinemann, N., Edlmann, K., Alcalde, J., Schultz, R.A. (Eds.), Enabling Secure Subsurface Storage in Future Energy Systems, The Geological Society of London, Lyell Collections, 528, 227–243.

Berrezueta, E., Kovacs, T., Herrera-Franco, G., Mora-Frank, C., Caicedo-Potosí, J., Carrion-Mero, P., Carneiro, J., 2023. Laboratory studies on CO_2-brine-rock interaction: an analysis of research trends and current knowledge. International Journal of Greenhouse Gas Control 123, 103842.

Bornovas, J., Rondogianni-Tsiambaou, Th., 1983. Geological Map of Greece, 1:500.000. 2nd edition, Institute of Geology and Mineral Exlporation, Athens.

Doebelin, N., Kleeberg, R., 2015. Profex: a graphical user interface for the Rietveld refinement program BGMN. Journal of Applied Crystallography 48(5), 1573-1580.

Koukouzas N., Kypritidou Z., Purser G., Rochelle, C.A., Vasilatos, Ch., Tsoukalas, N., 2018. Assessment of the impact of CO_2 storage in sandstone formations by experimental studies and geochemical modeling: The case of the Mesohellenic Trough, NW Greece. International Journal of Greenhouse Gas Control 71, 116–132.

Koukouzas, N., Tyrologou, P., Karapanos, D., Carneiro, J., Pereira, P., de Mesquita Lobo Veloso, F., Koutsovitis, P., Karkalis, C., Manoukian, E., Karametou, R., 2021. Carbon Capture, Utilisation and Storage as a Defense Tool against Climate Change: Current Developments in West Macedonia (Greece). Energies 14, 3321.

McBride, E.F., 1963. A classification of common sandstones. Journal of Sedimentary Petrology 33, 664–669.

Ordóñez, B., Mediato, J., Kovacs, T., Martínez-Martínez, J., Fernández-Canteli, P., González-Menéndez, L., del Moral, B., Berrezueta, E., 2024. Experimental geochemical assessment of a seal-reservoir system exposed to supercritical CO_2: A case study from the Ebro Basin, Spain. International Journal of Greenhouse Gas Control 137, 104233.

Savoyat, E., Monopolis, D., 1972. Geological map sheet Grevena, 1:50.000. Institute of Geology and Mineral Exlporation, Athens.

Schneider, C.A., Rasband, W.S., Eliceiri, K.W., 2012. NIH Image to ImageJ: 25 years of image analysis. Nature Methods 9(7), 671–675.

Tyrologou, P., Vamvaka, A., Koukouzas, N., Pedro, J., Fleury, M., Carneiro, J., Ribeiro, C., Ghikas, D., Mpatsi, A., Barradas, J.P., Faria, P., de Mesquita Lobo Veloso, F., 2023. Progress for carbon dioxide geological storage in West Macedonia: A field and laboratory-based survey. Open Research Europe 3, 85.

Vamvaka, A., Kilias, A., Mountrakis, D., Papaoikonomou, J., 2006. Geometry and structural evolution of the Mesohellenic Trough (Greece): a new approach, in: Robertson, A.H.F., Mountrakis, D. (Eds.), Tectonic Development of the Eastern Mediterranean Region, Geological Society, London, Special Publications 260(1), 521-538.

17th INTERNATIONAL CONGRESS
of the Geological Society of Greece

BULLETIN OF THE GEOLOGICAL
SOCIETY OF GREECE, SP. PUBL.

EXTENDED ABSTRACT 171

Unveiling the Potential of AI in Geoscience Education: A Student-Centered Perspective

Koumoutsakou O.[1], Antonarakou A.[1]
(1) Department of Geology and Geoenvironment, University of Athens, Ilisia, Greece, okoumout@geol.uoa.gr

Introduction / Background

According to a recent survey by the Digital Education Council, 86% of students globally incorporate artificial intelligence into their studies, with 24% using it every day and 54% using it at least once a week (Digital Education Council, 2024). This highlights the growing integration of AI into students' academic routines. Integrating Artificial Intelligence (AI) into geoscience education is rapidly transforming the learning landscape, presenting unprecedented opportunities and significant ethical challenges (Patra et al., 2024). This research explores the multifaceted impact of AI on geoscience students, focusing on their perspectives regarding the future of their field in this era of technological advancement. It draws upon a range of studies that examine the practical applications, ethical dilemmas, and prospects of AI in Earth sciences.

AI's Role in Geoscience Education

AI is becoming increasingly prevalent in geoscience, from data collection and processing to complex modeling and interpretation (Sun et al., 2024; Zhao et al., 2024). Artificial intelligence techniques, such as machine learning (ML) and deep learning (DL), allow for the analysis of large datasets, improving our insights into Earth's systems (Sun et al., 2024). "AI can help students analyze satellite imagery to detect land-use changes, monitor environmental degradation, and study natural disasters. In mineral exploration, AI algorithms can identify mineral deposits based on geophysical data patterns" (Sun et al., 2024). AI can also improve the analysis of seismic data, enhance our understanding of the Earth's interior, and aid in the prediction of earthquakes. Furthermore, AI techniques can optimize climate modeling, making the process more accurate and efficient despite its complexity and time demands (Sun et al., 2024).

Furthermore, AI tools such as ChatGPT, Gemini, etc., can help with tasks such as scientific writing, data interpretation, and hypothesis generation (Baucon et al., 2024). GeologyOracle, a specialized artificial intelligence system created by Baucon and his colleagues, can handle complex geoscientific tasks, interpret geological sites, and provide support in educational environments (Baucon et al., 2024). Such tools can accelerate scientific discovery, automate research tasks, and support educators, students, and geotourists (Baucon et al., 2024). However, this technological integration also presents considerable challenges.

Ethical Considerations and Student Perspectives

Ethical concerns are central to discussions of AI in education. Plagiarism and academic integrity present significant challenges, as students might rely on AI to produce written content, potentially hindering the development of their skills (Assapari et al., 2025; Patra et al., 2024; Weijemars et al., 2023). There is a concern that some students may use AI to complete assignments, bypassing plagiarism detectors, and there are concerns regarding the authenticity of written work. Additionally, the potential for AI to generate biased or inaccurate information raises questions about the reliability of these tools in an academic setting (Ghotbi & Ho, 2021).

Student perceptions of AI in education are varied

While many recognize the potential benefits of AI, particularly for improving learning and research activities, there are also concerns about over-reliance on technology, its impact on critical thinking, and the need for human oversight (Patra et al., 2024; Sarwari & Adnan, 2024; Kumar & Ramanm, 2022; Crawford et al., 2024). Many students find AI tools like ChatGPT valuable for everyday learning activities, as they provide access to information anytime and anywhere without limitations. "However, they also prefer traditional teaching methods and consider human teachers indispensable" (Patra et al., 2024; Sarwari & Andnan, 2024).

Research conducted among 94 geoscience students in Mumbai (Patra et al., 2024) revealed that most students disapprove of AI-generated texts bypassing plagiarism detection, emphasizing their concern for academic integrity. There is also concern that using AI may diminish critical thinking and problem-solving skills. Furthermore, some students believe AI should be excluded from specific academic processes, like admissions, exams, and placements, due to concerns about accuracy and fairness (Kumar & Raman, 2022).

The Future of Geoscience in the AI Era

Although challenges exist, AI is anticipated to become increasingly important in shaping the future of geoscience (Zhao et al., 2024, Sun et al., 2024). Many scientists envision a hybrid environment where AI and numerical models coexist, working collaboratively to solve complex environmental issues (Sun et al., 2024). Advancing explainable and physics-based AI models is crucial for improving accuracy and building trust (Sun et al., 2024). It is also important to address the ethical implications of AI in geoscience, including algorithmic bias and data privacy (Ghotbi & Ho, 2021; Sun et al., 2024; Zhao et al., 2024).

AI is also anticipated to aid in creating personalized learning experiences that are customized to meet the specific needs of each student and support educators in providing effective interventions (Burner et al., 2025; Miller, 2025). AI-powered tools can provide tailored feedback, assist with language barriers, and offer adaptive testing, which is particularly beneficial for international students (Wang et al., 2023). However, some scholars highlight gaps in understanding the long-term psychosocial effects of AI usage in education (Crawford et al., 2024).

According to Sun et al. (2024), the success of AI in geoscience will rely on collaboration between computer scientists, mathematicians, and geoscientists to develop tailored tools and training. It is critical to foster a culture of innovation and ethical AI use, educating students on the importance of critical thinking and responsible application of AI technologies (Sun et al., 2024; Baucon et al., 2024; Patra et al., 2024; Ghotbi & Ho, 2021).

Preliminary research results

The preliminary results of our survey of students and graduates of Earth Science in Greece reveal important findings about students' understanding, use, and opinions about Artificial Intelligence (AI). Although AI is embedded in their daily lives, a small percentage of students remain unaware of its presence. The majority use AI tools mainly for information access, data analysis, and task automation, with a particular focus on geoscientific data. Familiarity with these tools ranges from moderate to high, with voice assistants and recommendation systems emerging as more popular applications. However, the use of more specialized tools, such as for music production, video, navigation or translation tools, and bibliographic analysis, remains in high demand, much more frequently than the use of chatbots. Students appear divided on the reliability of AI responses, with several expressing concerns about privacy and human autonomy, while very few feel adequately informed about the ethical issues arising from its use.

Conclusion

The integration of AI in geoscience education is a complex, evolving process that requires a balanced approach. AI is expected to assist in developing tailored learning experiences that address the unique needs of each student (AI-powered personalized learning systems, adoption of artificial intelligence). (Sun et al., 2024; Zhao et al., 2024; Sarwari & Andnan, 2024; Wang et al., 2023). Students have expressed concern regarding potential over-reliance on AI, and their role as future geoscientists in a rapidly changing world (Patra et al., 2024; Kumar & Raman, 2022; Crawford et al., 2024; Ghotbi & Ho, 2021). Therefore, the future of geoscience in the AI era will depend on our capacity to integrate these technologies responsibly and ethically while prioritizing human expertise, critical thinking, and environmental responsibility.

Acknowledgments

Thank you to all the students who participated in my research questionnaire. Your valuable insights were greatly appreciated and contributed significantly to this study.

References

Assapari, M.M., Hidayati, R., Mukti, S.R.W. (2025). Unlocking the Future: EFL Students' Insights on Artificial Intelligences for Academic Writing. Indonesian Journal of Artificial Intelligence and Data Mining (IJAIDM) Vol. 8, No. 1, March 2025, pp. 120 – 129. doi: http://dx.doi.org/10.24014/ijaidm.v8i1.30307

Baucon, A., de Carvalho, C.N. (2024). Can AI Get a Degree in Geoscience? Performance Analysis of a GPT-Based Artificial Intelligence System Trained for Earth Science (GeologyOracle). Geoheritage 16, 121 (2024). https://doi.org/10.1007/s12371-024-01011-2

Burner, T.; Lindvig, Y.; Wærness, J.I. "We Should Not Be Like a Dinosaur"—Using AI Technologies to Provide Formative Feedback to Students. Educ. Sci. 2025, 15, 58. https://doi.org/10.3390/educsci15010058

Crawford, J., Allen, K. A., Pani, B., & Cowling, M. (2024). When artificial intelligence substitutes humans in higher education: the cost of loneliness, student success, and retention. Studies in Higher Education, 49(5), 883–897. https://doi.org/10.1080/03075079.2024.2326956

Digital Education Council (2024). Digital Education Council Global AI Student Survey 2024. https://www.digitaleducationcouncil.

com/post/digital-education-council-global-ai-student-survey-2024 (retrieved 9/1/2025)

Ghotbi N., Ho M.T. (2021). Moral Awareness of College Students Regarding Artificial Intelligence. Asian Bioeth Rev. 2021 Sep 3;13(4):421-433. doi: 10.1007/s41649-021-00182-2. PMID: 34616496; PMCID: PMC8486910

Kumar, V.V. R and Raman, R. (2022). Student Perceptions on Artificial Intelligence (AI) in higher education, 2022 IEEE Integrated STEM Education Conference (ISEC), Princeton, NJ, USA, 2022, pp. 450-454, doi: 10.1109/ISEC54952.2022.10025165.

Miller, M.D. (2025). Generative AI as a challenge to faculty development: ugly advice at the dawn of generative AI. (ch. 13, pp. 179-191). In: Generative AI in Higher Education, (Eds.: Kätlin Pulk & Riina Koris), https://doi.org/10.4337/9781035326020

Patra, S., Singha, T. S., Kanvinde, M., Mazumder, A., and Kanjilal, S. (2024). Harnessing AI for Geosciences Education: A Deep Dive into ChatGPT's Impact,/ChatGPT in Geoscience Education: Revolutionizing Learning or Ethical Minefield? ((b), EGU General Assembly 2024, Vienna, Austria, 14–19 Apr 2024, EGU24-16918, https://doi.org/10.5194/gc-2023-7, 2024., https://doi.org/10.5194/egusphere-egu24-16918, (b) 2024.

Sarwari, A. Q., & Mohd Adnan, H. (2024). The effectiveness of artificial intelligence (AI) on daily educational activities of undergraduates in a modern and diversified university environment. Advances in Mobile Learning Educational Research, 4(1), 927-930. https://doi.org/10.25082/AMLER.2024.01.004

Sun, Z., ten Brink, T., Carande, W., Koren, G., Cristea, N., Jorgenson, C., Janga, B., Asamani, G. P., Achan, S., Mahoney, M., Huang, Q., Mehrabian, A. Munasinghe, T., Liu, Z., Margolis, A., Webley, P., Gong, B., Rao, Y., Burgess, A., Huang, A., Sandoval, L., Pagán, B. R. and Duzgun, S. (2024) Towards practical artificial intelligence in Earth sciences. Comput Geosci 28, 1305–1329 (2024). https://doi.org/10.1007/s10596-024-10317-7

Zhao, T., Wang, S., Ouyang, C., Chen, M., Liu, Ch., Zhang, J., Yu, L., Wang, F., Xie, Y., Li, J., Wang, F., Grunwald, S., Wong, B., Zhang, F., Qian, Z., Xu, Y. J., Yu, C., Han, W., Sun, T., Wang, L. (2024). Artificial intelligence for geoscience: Progress, challenges, and perspectives. The Innovation. Vol. 5 100691. 10.1016/j.xinn.2024.100691.

Wang, T., Lund, B. D., Marengo, A. Pagano, A., Mannuru, N. R., Teel, Z. A., & Pange, J. (2023). Exploring the Potential Impact of Artificial Intelligence (AI) on International Students in Higher Education: Generative AI, Chatbots, Analytics, and International Student Success. Applied Sciences 13(11):6716, doi: 10.3390/app13116716

Weijermars, R., Waheed, U. B., Suleymanli, K. (2023). Will ChatGPT and Related AI Tools Alter the Future of Geosciences and Petroleum Engineering? First Break 41(6):53-61 doi: 10.3997/1365-2397.fb2023043

17th INTERNATIONAL CONGRESS
of the Geological Society of Greece

BULLETIN OF THE GEOLOGICAL
SOCIETY OF GREECE, SP. PUBL.

EXTENDED ABSTRACT 172

An insight to grain size composition of the beach sediment along the north coast of the Messiniakos Gulf (Greek Mainland).

Koumpou[1] V., Poulos[1] S.E., Karditsa[2] A., Petrakis[3] S., Kapsimalis[3] V.
(1) Laboratory of Physical Geography, Section of Geography and Climatology, Department of Geology and Geoenvironment, Panepistimioupolis-Zografou 15794, Attiki, Greece.
(2) Department of Post Managerment and Shipping, National and Kapodistrian University of Athens, Psahcna, Evia, Greece
(3) Instiute of Oceanography, National Centre for Marine Research, 46,7 km Athens Sounio ave., P.C. 19013, Anavyssos, Attiki, Greece

Introduction

Among the processes that govern the formation and evolution of beach zones is the grain-size of beach material; the latter together with slope have recognized as key geomorphological elements for characterizing the beaches as they appear interrelated with each other and with the oceanographic conditions (Carter, 1988; Wright and Short, 1984).

The scope of the present study is to provide an insight to the grain size distribution of the sediments consisting of both subaerial and submarine sectors of beach zone that extends along the north coastline of the Messiniakos Gulf from Messini to Kalamata with a West – East trending shoreline, a length of 21 km and an average width of 20 m. It is exposed to southerly wind-generated waves, with average significant wave height of 1.2 m and period of 7.6 s (Koumpou et al., 2018). The subaerial beach zone gentles smoothly, having rhythmic morphological features (e.g. beach cusps, berms) at its central and western part and crescentic / longshore bars at its subaqueous part. In addition, low dunes, river mouths (central and western sector) and artificial coastal structures (eastern sector) are also present.

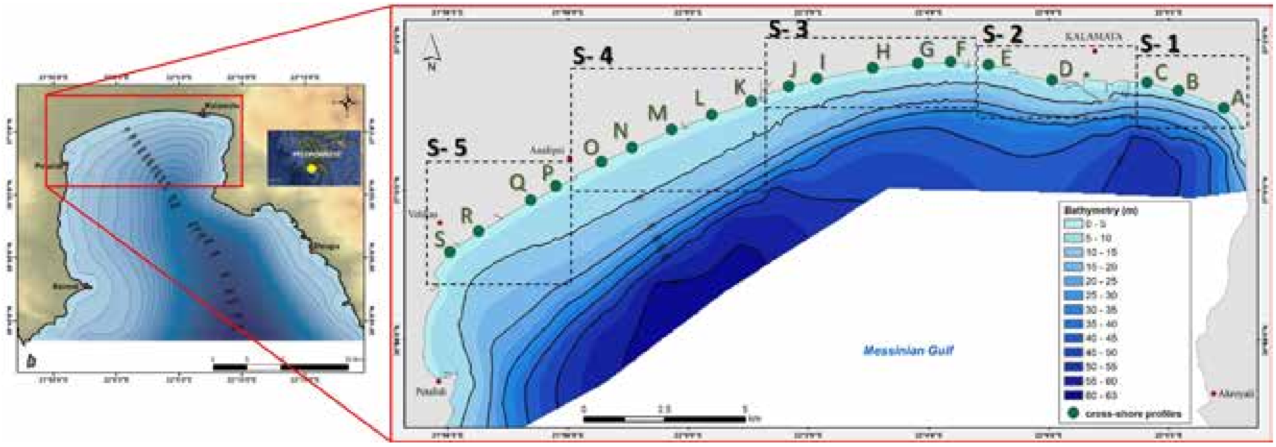

Figure 1. The study area with the positions of the shore-normal profiles (A-S) and the five beach sectors (1-5).

Methods

Nineteen (19) shore-normal profiles (A to S, from east to west) (Fig.1) were measured with the use of a Leica Distance Meter (subaerial part) and a Portable Handy Depth Sounder Hondex PS-7 (subaqueous part). For the geographical position of the profiles a Topcon GPS was used. 118 ssurficial (upper 2 cm) sediment samples were selected along these profiles, i.e., 60 subaerial, 19 from the beach face (shoreline) and 39 subaqueous samples (see Table A).

Subsequently sediment samples >625μm were subjected to dry sieving according to the Folk (1974) procedure, whilst sediment samples (<625 μm) were analyzed with a Sedigraph-Micrometrics using X-rays (type III PLUS). The statistical elaboration of the grain size identification included the determination of the graphical mean grain size (Mz; equation 1), the graphical standard deviation (σI; equation 2) and the mean diameter (D50), while the samples were classified according to their content in gravels, sand and mud following the Folk' (1974).

Results

The subaerial, beach-face and subaqueous slopes of the 19 normal to shoreline profiles (A-S) are presented in Table 1, while the types of sediment samples, according to their grain size composition, is presented in Table 2.

Table 1. Average slopes of subaerial, subaqueous and beacface of the 5 beach sectors (T1-T5)

Sectors	**1A**	**T1B**	**T-2a**	**T2b**	**T3a**	**T3b**	**T4**	**T5a**	**T5b**
Profiles	**A**	**B, C**	**D**	**E**	**F, G**	**H, I, J**	**K, L, M, N, O**	**P, Q, R**	**S**
Backshore (%)	0.07	0.115 (±0.045)	0.21	0.11	0.065 (±0.005)	0.145 (±0.055)	0.03 (±0.01)	0.105 (±0.015)	0.13
Beach face (%)	0.15	0.13 (±0.01)	0.16	0.19	0.16 (±0.02)	0.175 ±(0.025)	0.105 (±0.015)	0.10	0.11
Foreshore (%)	0.04	0.03 (±0.01)	0.01	0.01	0.035 (±0.025)	0.03 ±0.02	0.015 (±0.005)	0.01	0.01

Table 2. Types of sediment according to their size at the 5 beach sectors (T1-T5)

Sectors	**T1A**	**T1B**	**T2a**	**T2b**	**T3a**	**T3b**	**T4**	**T5a**	**T5b**
Profiles	**A**	**B, C**	**D**	**E**	**F, G**	**H, I, J**	**K, L, M, N, O**	**P, Q, R**	**S**
2,0-2,5							g(S)-gS		
1,5-2,0	G					sG-gS-(g)S	g(S)-gS	(g)S	
1,0-1,5	G	(g)S			sG	gS	(g)S - gS -sG	(g)S -S	
0,5-1	G	G-sG		(g)S	G	(g)S	gS -sG	G	(g)S
0-0,5	G	G	G	G	G	G-sG	(g)S - gS -sG	sG -G	G
0	G	gS -sG	sG	gS	gS	sG-gS	S -sG	sG-gS	gS
1,5-2,5	S	sG	G	(g)S	S-gS	(g)S-sG	(g)S -sG	sG	S
4-5	S	(g)S-S	mS	S	S	S-mS	S-mS	mS -S	sM
5-7,5	S	S		S	S	S-mS	mS	mS	sM
7,5-10	mS	mS		S	S	S-mS	mS	sM	sM
10-15	mS	mS		S	S	S-mS	mS	M	M
15-20	mS	mS			sM	sM	mS - sM		

Key. G: Gravel; S: Sand; M: Mud; sG: sandy Gravel; (g)S: slightly sandy Gravel; gS: gravelly Sand; sG: sandy Gravel; mS: muddy Sand; sM: sandy Mud

Discussion and Conclusions

The beach zone along the northern coast of the Messiniakos Gulf consists predominantly of mixed sediments, with sand-sized material being the primary component. As expected, the subaerial sediments are coarser, with gravel-sized particles being as significant as the sand-sized ones. In contrast, the subaqueous sediments are dominated by sand, particularly in water depths greater than 2 meters. Beyond 5 meters of depth, the proportion of mud increases, becoming the dominant sediment type at depths exceeding 15 meters. Along the beach face (±0.5 m), the sediment consists of a mixture of sand and gravel in varying ratios. Additionally, the results of the grain size analysis align with the classification of the 19 profiles into five main sectors, based on shoreline orientation and beach slope (Table 1).

There is a notable similarity between the eastern Sector 1 and the central Sector 3, particularly in the slopes of their beach face and shoreface. Both end sectors are characterized by relatively coarser material and exhibit similar slopes. This similarity is likely influenced by the original terrestrial material and the presence of coastal structures, such as port breakwaters, in the eastern Sector. The observed differences between the sectors may be attributed to variations in sediment input from rivers discharging along the shore, combined with the effects of longshore sediment transport in the nearshore zone and wave runup on the subaerial beach.

References

Carter, R.W.G., 1988. *Coastal Environments: An Introduction to the Physical, Ecological, and Cultural Systems of Coastlines*; Academic Press: London, UK.

Folk, R. L. (1980). *Petrology of sedimentary rocks*. Hemphill publishing company.

Koumpou V., Petrakis S., Karditsa A., Kapsimalis V. and Poulos S., 2018. Morphological changes induced by storm event, along the Messini- Kalamata beach zone. 12th Panhellenic Symposium of Oceanography & Fisheries, Corfu, 30 May – 3 June 2018, p.93.

Wright, L.;and Short, A., 1984. Morphodynamic variability of surf zones and beaches: A synthesis. *Mar. Geol*, *56*, 93–118.

17th INTERNATIONAL CONGRESS of the Geological Society of Greece

BULLETIN OF THE GEOLOGICAL SOCIETY OF GREECE, SP. PUBL.

EXTENDED ABSTRACT 173

A systematic review of grey literature in Greek universities repositories to uncover Greek UNESCO Global Geoparks

Alexandros Aristotelis Koupatsiaris[1], Hara Drinia[1]

(1) Department of Geology and Geoenvironment, National and Kapodistrian University of Athens, 15784 Athens, Greece, alkoup@geol.uoa.gr

Research Highlights

A systematic review of grey literature from Greek university repositories reveals a growing interest in UNESCO Global Geoparks, primarily focusing on geotourism, geology, management, and education, but also identifies gaps in social sciences and community engagement. Future research should adopt a holistic approach, integrating socio-economic, cultural, and environmental aspects, while enhancing geoenvironmental education and stakeholder involvement to support the United Nations' seventeen Sustainable Development Goals.

Introduction / Background

Our world is experiencing rapid urbanization, interconnectivity, and environmental changes. The global population is projected to reach 9.7 billion by 2030 and 10.4 billion by 2050. Currently, 55% of the population lives in urban areas, a figure expected to rise to 68% by 2050. This trend impacts land use, biodiversity, and ecosystems, with significant urban land development anticipated by 2030 (Fragkias, 2013). Environmental challenges, such as pollution, erosion, desertification, deforestation, fires, intensified agriculture, overgrazing, invasive species, overfishing (Scoullos, 2008), climate change, greenhouse effects, droughts, floods, habitat loss, chemical pollution (Krasny, 2020), environmental emergencies, and anthropogenic impacts on economic systems, global warming, natural disasters, declining biodiversity, land degradation, water pollution, mineral resource exploitation, coastal vulnerability, and geodiversity alterations (Peppoloni et al., 2022) threaten our planet's natural capital (Gray, 2018). These issues necessitate proactive measures and community involvement to protect our environment for future generations.

UNESCO Global Geoparks (UGGps) play a crucial role in sustainable development by managing areas with significant geological heritage. Established in 2000 and supported by UNESCO since 2001, these UGGps promote awareness of societal issues through geoconservation, geotourism, and geoeducation, enhancing community well-being and sustainability (Zouros, 2016). There are currently 213 UGGps in 48 countries. In Greece, nine areas are designated as UGGps (Lesvos Island UGGp, Psiloritis UGGp, Chelmos-Vouraikos UGGp, Vikos-Aoos UGGp, Sitia UGGp, Grevena-Kozani UGGp, Kefalonia-Ithaca UGGp, Lavreotiki UGGp, Meteora-Pyli UGGp), with one more in the nomination process (Nisyros aspiring UGGp).

Greece's geotectonic position offers a rich geological landscape, making its UGGps invaluable. These sites serve as "natural geological laboratories," chronicling Earth's history from the Proterozoic Eon to today and providing insights into tectonics, sedimentation, volcanic activity, and landscape evolution. The geoconservation and sustainable development of these UGGps are crucial. Scientific research helps formulate effective conservation strategies. Greek UGGps also serve as effective platforms for teaching about the environment, enhancing public awareness of the connections between geology, ecology, culture, and sustainability (Koupatsiaris et al., 2023). They promote social, economic, and cultural growth through educational programs, geotourism, and geoethics (Zafeiropoulos et al., 2021). The study of UGGps supports interdisciplinary research in geosciences and geoconservation, informing global efforts in sustainability and environmental stewardship.

Objectives

The systematic review aims to evaluate the repositories of Greek universities to identify and catalog research topics related to Greek UGGps. It seeks to provide a comprehensive overview of the research landscape, highlight underexplored areas, and suggest directions for future research, offering insights to the academic community, policymakers, and stakeholders.

The research questions addressed are:

- What research topics and themes are covered in Greek university grey literature about Greek UGGps?
- What research gaps exist in this literature?
- What are the potential future research directions for Greek UGGps?
-

Methods

This study gathers research evidence on Greek UGGps to guide future research studies. Using a systematic review approach, specific steps were followed to ensure replicability and reliability. The criteria included publications from Greek university repositories published between 2000 and 2022, using the keyword “Geopark.” The search focused on publications primarily discussing Geoparks as holistic entities, rather than specific geological or other features within Geopark boundaries. A total of 138 items were accessed, with 28 theses deemed relevant after applying selection criteria. The process followed PRISMA guidelines for a thorough review (Figure 1).

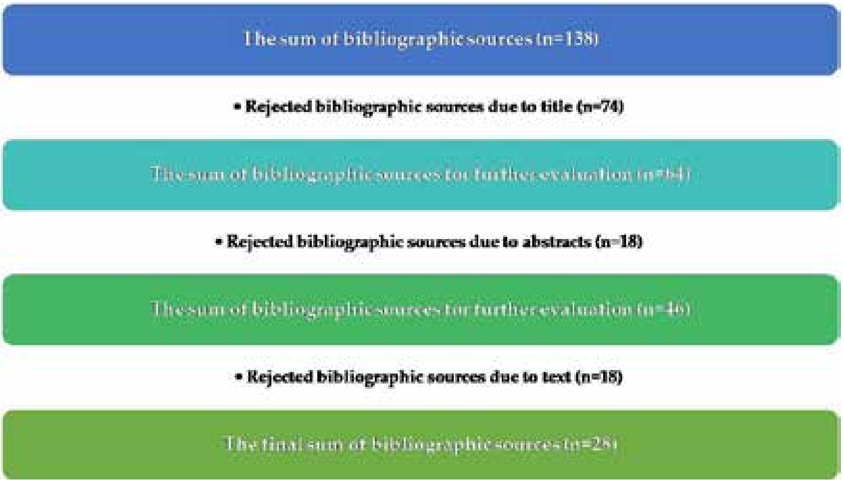

Figure 1. Flow chart for the grey literature review in Greek university repositories.

Limitations included reliance on a single keyword and variations in search capabilities across institutions, which may have resulted in omissions. External literature from global databases related to Greek UGGps was not examined.

Results

The review identified 28 theses on UGGPs: 23 master’s, 3 graduate, and 2 doctoral theses. This indicates a growing academic interest, although there was a notable dip in publications during 2021 due to the SARS-CoV-2 pandemic (Figure 2).

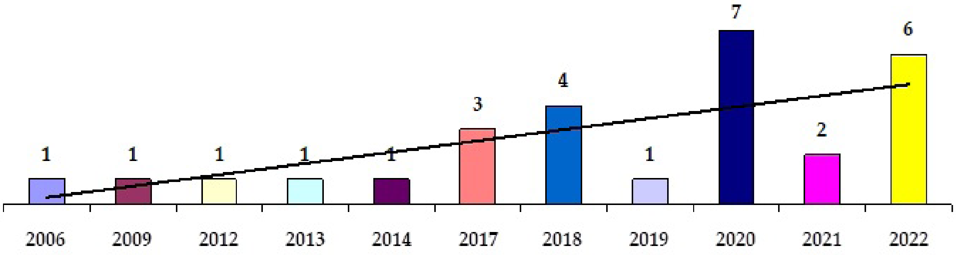

Figure 2. Distribution of the theses by the year of publication in Greek university repositories.

Most theses were found at the University of the Aegean (n=9), likely due to its collaboration with the Lesvos Island UGGp, followed by the Hellenic Open University (n=6) and the National Kapodistrian University of Athens (n=4) (Figure 3).

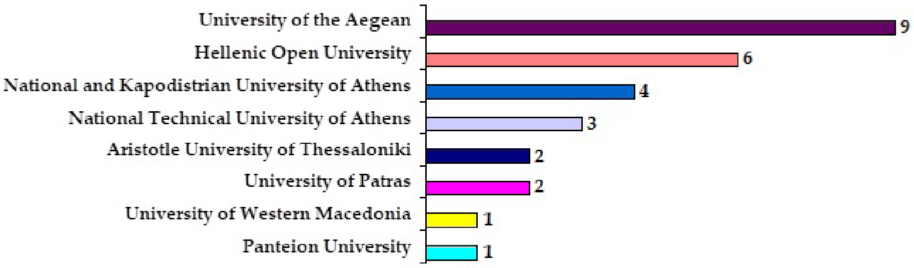

Figure 3. Distribution of the theses by Greek university repositories.

The Department of Geography had the most theses (n=7), followed by the Department of Geology and Geoenvironment at the National and Kapodistrian University of Athens (n=4) and the Tourism Business Administration at the Hellenic Open University (n=4) (Figure 4).

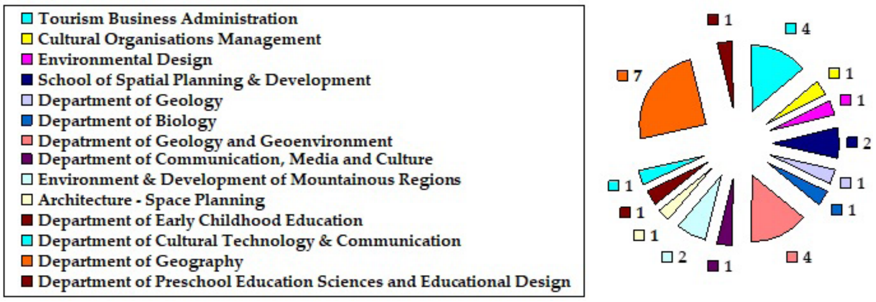

Figure 4. Distribution of the theses by Greek university department.

The 28 university theses focused on Lesvos Island (n=11) and Sitia UGGps (n=6), with newer UGGps like Grevena-Kozani, Kefalonia-Ithaca, and Lavreotiki having fewer studies due to their recent establishment (Figure 5).

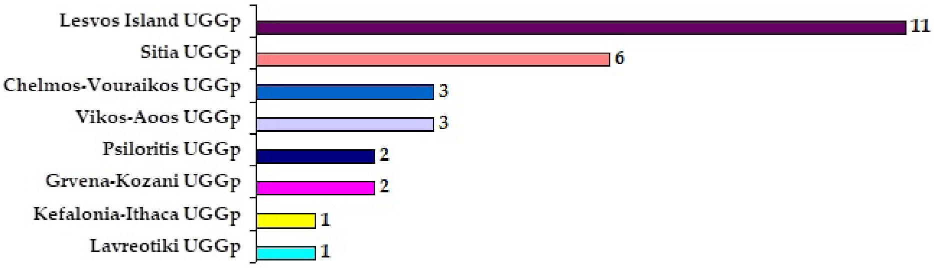

Figure 5. Distribution of the theses according to their Greek UNESCO Global Geopark focus.

Research topics included geotourism (n=7), geodiversity and geology (n=6), sustainable management (n=4), and geoeducation (n=4). Other areas were geoinformatics, biodiversity, cartography, cultural development, spatial planning, and georoute promotion, highlighting the multidisciplinary nature of UGGps studies (Figure 6).

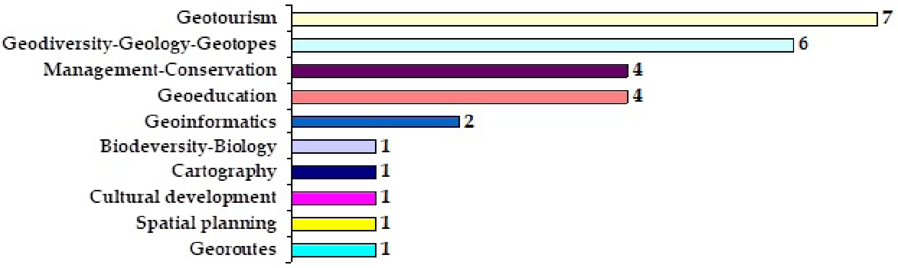

Figure 6. Content classification of the grey literature in Greek university repositories.

Conclusions

This review underscores the importance of Greek UGGps as globally recognized assets supporting scientific research and societal contributions. It addresses key global issues such as urbanization, environmental challenges, and the alienation from nature, emphasizing the need for new sustainability and resilience policies. Greece, renowned for its geological richness, hosts nine UGGps, offering opportunities for geoconservation, geodiversity and biodiversity, and cultural appreciation. The review focused on grey literature from Greek universities to identify research gaps and align domestic efforts with international trends. There is strong academic interest in Greek UGGps, particularly in geology, biology, tourism, and culture.

Recent proposals, such as Martini et al. (2022), suggest a roadmap for UGGps focusing on climate change, water resources, sustainable tourism, and community engagement. International research emphasizes interdisciplinary studies and community involvement. Stoffelen's (2020) review focused on geomorphological aspects, while Herrera-Franco et al. (2021) noted this area's dominance in research, particularly in Asia and Europe. Ferreira et al. (2023) highlighted the need to explore UGGps' role in sustainable development and their benefits to local populations. Evaluations of the International Geoscience and Geoparks Programme showed UGGps' contributions to the United Nation's Sustainable Development Goals, including quality education (UNESCO, 2019). However, educational topics remain underrepresented in research.

Greek research aligns with international trends but often focuses on geotourism, geology, and management, with limited attention to social and humanitarian aspects. To fully harness the potential of UGGps, Greek studies should expand to include social development and stakeholder engagement, drawing from successful international models aligning with the United Nations' Sustainable Development Goals and fostering a sense of belonging and responsibility among future generations in Greece and beyond (Koupatsiaris et al., 2023). Addressing these research gaps can enhance the role of UGGps in environmental awareness, sustainability, and education, providing a roadmap for future academic research.

Future research within UGGps, highlighted in the grey literature of Greek university repositories, should focus on:

- Socio-economic and cultural aspects: Explore the socio-cultural dimensions of UGGps, integrating historical and cultural narratives with geological significance. This holistic approach can transform UGGps into cultural and economic hubs, enhancing their role in local identity and advancement.
- Collaborative management and governance: Investigate stakeholder participation in UGGps management, involving local communities, students, and special interest groups. Innovative governance structures can improve UGGps' visibility and recognition, reflecting their significance in local culture.
- Climate change and environmental challenges: UGGps can educate the public on climate change and resilience. They serve as living laboratories for studying environmental impacts and engaging communities in climate action through science initiatives, contributing to public health and well-being.
- Geoenvironmental education: Emphasize education with a focus on integrating UGGps into educational curricula to raise awareness about geoconservation, sustainability, and environmental challenges. This can enhance public understanding and foster a sense of responsibility towards preserving geological heritage.

By addressing these areas, future research can strengthen the role of Greek UGGps in promoting sustainability.

Acknowledgements

The authors extend their heartfelt thanks to the organizing committee of the 17th International Congress of the Geological Society of Greece and the anonymous reviewers for their thorough consideration of this extended abstract.

References

Ferreira, D.R., Valdati, J., 2023. Geoparks and Sustainable Development: Systematic Review. Geoheritage 15, 6. https://doi.org/10.1007/s12371-022-00775-9

Fragkias, M., Güneralp, B., Seto, K.C., Goodness, J., 2013. A synthesis of global urbanization projections, in: Elmqvist, T., Fragkias, M., Goodness, J., Günerlap, B., Marcotullio, P.J., McDonald, R.I., Parnell, S., Schewenius, M., Sendstad, M., Seto, K.C., et al. (Eds.), Urbanization, Biodiversity and Ecosystem Services: Challenges and Opportunities, 409-435.

Gray, M., 2018. The Confused Position of the Geosciences within the "Natural Capital" and "Ecosystem Services" Approaches. Ecosystem Services 34, 106-112. https://doi.org/10.1016/j.ecoser.2018.10.000

Herrera-Franco, G., Montalván-Burbano, N., Carrión-Mero, P., Jaya-Montalvo, M., Gurumendi-Noriega, M. 2021. Worldwide Research on Geoparks through Bibliometric Analysis. Sustainability 13, 1175. https://doi.org/10.3390/su13031175

Koupatsiaris, A.A., Drinia, H., 2023. Exploring Greek UNESCO Global Geoparks: A Systematic Review of Grey Literature on Greek Universities and Future Research Avenues for Sustainable Development. *Geosciences 13*(10), 296. https://doi.org/10.3390/geosciences13100296

Krasny, M.E., 2020. Advancing environmental education practice, Cornell University Press.

Martini, G., Zouros, N., Zhang, J., Jin, X., Komoo, I., Border, M., Watanabe, M., Frey, M.L., Rangnes, K., et al., 2022. UNESCO Global Geoparks in the "World After": A Multiple Goals Roadmap Proposal for Future Discussion. Episodes 45, 29-35. https://doi.org/10.18814/epiiugs/2021/021002

Peppoloni, S., Di Capua, G., 2022. Geoethics: Manifesto for an Ethics of Responsibility towards the Earth, Springer International Publishing.

Scoullos, M., Alambei, B., Kouroutos, B., Malotidi, M., Mantzara, M., Psallidas, B. (Eds.) Environmental Education and Education for Sustainable Development in Protected Areas: Educational Material, MIO-ECSDE. (In Greek).

Stoffelen, A., 2020. Where is the Community in Geoparks? A Systematic Literature Review and Call for Attention to the Societal Embedding of Geoparks. Area 52, 97-104. https://doi.org/10.1111/area.12549

UNESCO, 2019. International Geoscience and Geoparks Programme, in: Evaluation of the International Geosciences and

Geoparks Programme, Zhechkov, R., Hinohosa, C., Knee, P., Pinzon, L., Buchs, D., Chernet, T. (Eds.), IOS/EVS/PI/182.

Zafeiropoulos, G., Drinia, H., Antonarakou, A., Zouros, N., 2021. From Geoheritage to Geoeducation, Geoethics and Geotourism: A Critical Evaluation of the Greek Region. *Geosciences 11*(9), 381. https://doi.org/10.3390/geosciences11090381

Zouros, N., 2016. Global Geoparks Network and the new UNESCO Global Geoparks Programme. Bulletin of the Geological Society of Greece 50, 284-292. https://doi.org/10.12681/bgsg.11729

17th INTERNATIONAL CONGRESS
of the Geological Society of Greece

BULLETIN OF THE GEOLOGICAL SOCIETY OF GREECE, SP. PUBL.

EXTENDED ABSTRACT 174

Assessing Educators’ Sense of Place and Geoethical Awareness at the 4th Summer School of Sitia UNESCO Global Geopark

Alexandros Aristotelis Koupatsiaris[1], Hara Drinia[1]
(1) Department of Geology and Geoenvironment, National and Kapodistrian University of Athens, 15784 Athens, Greece, alkoup@geol.uoa.gr

Introduction / Background

The environment is shaped by a complex interplay of natural and human influences affecting ecological balance, quality of life, public health, cultural traditions, and aesthetic values. Current environmental challenges, intensified by urbanization, threaten natural resources and cultural and geological heritage. The United Nations’ Sustainable Development Goals provide a strategic framework to address these issues. In the Anthropocene Era, it is crucial to adopt modern geoenvironmental strategies grounded in geoethics (Koupatsiaris et al., 2024). Pro-environmental behavior, aimed at enhancing environmental quality and sustainability, is essential for confronting these challenges.

UNESCO Global Geoparks (UGGps) play a vital role in conserving and promoting areas with notable geodiversity, biodiversity, and geotourism, while also advancing education, public understanding, sustainability, and resilience. These UGGps inspire a sense of belonging and responsibility, encouraging local communities to re-evaluate their heritage through tourism and eco-friendly activities (Fassoulas et al., 2010). At present, there are 213 UGGps across 48 countries, with Greece hosting nine, including the Sitia UGGp, established in 2015. It is located on the eastern edge of Crete, encompassing an area of 713.5 km^2 with internationally significant geology.

For over six decades, environmental education has aimed to develop environmentally conscious citizens capable of addressing complex environmental problems (Krasny, 2020). Geoeducation integrates natural and cultural features with geology to raise awareness and foster participation in geoconservation efforts (Gordon, 2019). Place-based education (Sobel, 2004) emphasizes the importance of local geoenvironments in a globalized world, countering the alienation from nature. The sense of place (Kudryavtsev et al., 2012), a key concept in environmental education, involves the connections people have with locations, influenced by physical, psychological, and emotional factors (Semken et al., 2009). It intersects with geoethics (Peppoloni et al., 2022), which explores the ethical dimensions of human interactions with the natural environment, promoting sustainability, environmental responsibility, and social justice.

Objectives

In response to the increasing global interest in geoenvironmental education, geoheritage, geoconservation, and geoethics, this study presents a novel approach to exploring the interrelations between sense of place and geoethical awareness within the context of UGGps. The research addresses the following questions:

- What changes occur in participants’ sense of place (including place attachment and place meaning) and geoethical awareness before and after attending the summer school?
- Is there a relationship between place attachment, place meaning, and geoethical awareness among the summer school participants?
-

Methods

The study was conducted during the 4th Summer School of Environmental Education on Geotopes and Sustainability at the Sitia UNESCO Global Geopark from June 29 to July 4, 2024, involving 50 educators from Greece. A quasi-experimental design with a single experimental group and a pre-post technique was employed. Convenience sampling resulted in 41 questionnaires at the start and 36 at the end, with 33 matched pre-post questionnaires analyzed. The comprehensive survey included four sections: Section A (place attachment)—12 items, Section B (place meaning)—28 items, Section C (geoethical awareness)—32 items, and Section D (demographics)—15 items. The place attachment scale was adapted from Williams and Vaske (2003), and the place meaning scale was a modified version of Young’s (1999) scale. A new geoethical awareness scale was developed based on geoethics literature. All items used a Likert scale from 1 to 5. Ethical standards were strictly followed. Data analysis was conducted using IBM SPSS Statistics version 29. Normality tests (Kolmogorov–Smirnov and Shapiro–Wilk) indicated a non-normal distribution ($p > 0.05$), so non-parametric tests (Spearman’s rho, and Wilcoxon signed-rank) were used for correlation analyses and multiple linear regression.

Results

The questionnaire’s internal consistency was assessed using Cronbach’s Alpha. Section A had $\alpha = 0.942$ (pre) and $\alpha = 0.929$ (post) with 12 items. Section B had $\alpha = 0.917$ (pre) and $\alpha = 0.914$ (post) with 28 items. Section C had $\alpha = 0.945$ (pre) and $\alpha =$

0.955 (post) with 32 items. For all 72 items, both pre- and post-summer school consistency was α = 0.967.

Among participants, 36.4% were male and 63.6% female. Age distribution: 9.1% were 25–34, 27.3% were 35–44, 33.3% were 45–54, and 30.3% were 55 and above. Educational qualifications included 66.7% with a postgraduate degree, 24.2% with an undergraduate degree, and 9.1% with a Ph.D. Employment varied: 6.1% in kindergarten, 30.3% in primary school, 33.3% in middle school, 21.2% in high school, and 6.1% in other institutions.

In analyzing the ‘’Place Attachment’’ section of the questionnaire, notable changes in participants’ responses were observed before and after attending the summer school (Table 2).

Table 2. Distribution of mean value, standard deviation, and total score for place attachment.

Items		**PRE M.V.**	**PRE S.D.**	**POST M.V.**	**POST S.D.**	**SUM PRE**	**SUM POST**
A1	I feel Sitia Geopark is part of me.	3.58	0.204	4.06	0.168	118	134
A3	Sitia Geopark is very special for me.	3.79	0.178	4.33	0.142	125	143
A5	I identify strongly with Sitia Geopark.	3.39	0.162	3.88	0.161	112	128
A7	I am very attached to Sitia Geopark.	3.36	0.203	4.12	0.167	111	136
A9	Visiting Sitia Geopark says a lot about who I am.	3.52	0.145	4.12	0.149	116	136
A11	Sitia Geopark means a lot to me.	3.48	0.185	4.18	0.154	115	138
Total (place identity)		3.52	0.157	4.12	0.137	697	815
A2	Sitia Geopark is the best place for what I like to do.	3.39	0.157	3.79	0.167	112	125
A4	No other place can compare to Sitia Geopark.	2.58	0.123	3.24	0.163	85	107
A6	I get more satisfaction out of visiting Sitia Geopark than any other.	3.12	0.167	3.61	0.157	103	119
A8	Doing what I do at Sitia Geopark is more important to me than doing it in any other place.	3.24	0.174	3.61	0.130	107	119
A10	I wouldn’t substitute any other area for doing the types of things I do at Sitia Geopark.	2.82	0.154	3.24	0.180	93	107
A12	The things I do at Sitia Geopark I would enjoy doing just as much at a similar site.	3.30	0.119	3.39	0.137	89	86
Total (place dependence)		3.08	0.115	3.48	0.113	589	663
Total (place attachment)		3.30	0.130	3.80	0.118	1286	1478

Note: Odd-numbered items measure place identity, and even-numbered items measure place dependence. The final item is reverse-scored. Responses are based on a Likert scale where 1 corresponds to ‘’Strongly disagree,’’ 2 to ‘’Disagree,’’ 3 to ‘’Neither disagree nor agree,’’ 4 to ‘’Agree,’’ a nd 5 to ‘’Strongly agree.’’

Overall, the measure of place attachment, which includes both place identity and place dependence, showed a notable increase. The average score for place attachment rose from 3.30 (S.D. = 0.130) before the summer school to 3.80 (S.D. = 0.118) after the event. The total score for place attachment also increased from 1286 to 1478 units. Participation in the summer school positively influenced participants’ place attachment, enhancing their emotional connections and deepening their bonds with Sitia UGGp in the context of geoenvironmental education.

The analysis of the ‘’Place Meaning’’ section revealed significant shifts in participants’ perceptions of Sitia UGGp both before and after their attendance at the summer school (Table 3).

Table 3. Distribution of mean value, standard deviation, and total score for place meaning.

Sitia Geopark is for me:		**PRE M.V.**	**PRE S.D.**	**POST M.V.**	**POST S.D.**	**SUM PRE**	**SUM POST**
B1	Ancient place	3.52	0.200	4.03	0.177	116	133
B2	Pristine place	3.61	0.213	4.21	0.167	119	139
B3	Scenic place	3.70	0.215	4.36	0.156	122	144
B4	Beautiful place	4.30	0.141	4.58	0.115	142	151
B5	Remote place	4.03	0.197	4.18	0.182	133	138
B6	Unique place	4.15	0.152	4.64	0.105	137	153
B7	Important place to preserve	4.55	0.116	4.73	0.090	150	156
B8	Authentic place	4.55	0.107	4.70	0.111	150	155
B9	Privilege to visit	3.73	0.191	4.42	0.131	123	146
B10	Relaxing place	4.21	0.136	4.70	0.081	139	155
B11	Important place for local culture	4.12	0.143	4.64	0.105	136	153
B12	Overdeveloped place	1.64	0.143	1.73	0.152	144	141
B13	Unusual place	3.94	0.174	4.42	0.138	130	146

B14	Scientific valuable place	4.09	0.165	4.33	0.155	135	143
B15	Ecologically important place	4.42	0.151	4.58	0.123	146	151
B16	Place for fun	2.85	0.209	3.15	0.243	94	104
B17	Threatened place	3.76	0.151	4.09	0.171	74	63
B18	Crowded place	1.70	0.141	1.82	0.177	142	138
B19	Dangerous place	1.58	0.151	1.94	0.184	140	134
B20	Interesting place	4.3	0.111	4.48	0.131	142	148
B21	Educational place	4.18	0.127	4.48	0.098	138	148
B22	Tranquil place	4.52	0.088	4.64	0.085	149	153
B23	Spiritually valuable place	2.79	0.188	3.15	0.247	92	104
B24	Fragile place	4.00	0.144	4.39	0.123	132	145
B25	Wilderness place	3.85	0.169	4.15	0.200	127	137
B26	Historical place	4.06	0.130	4.24	0.180	134	140
B27	Place for adventure	4.15	0.116	4.61	0.144	137	152
B28	Tourism place	3.52	0.200	3.94	0.204	116	130
Total (place meaning)		3.71	0.089	4.05	0.085	3639	3900

Note: Items 12, 17, 18, and 19 are reverse-scored. This instrument uses a Likert scale where 1 corresponds to ‘‘Does not fit at all,’’, 2 to ‘‘Fits to some extent,’’ 3 to ‘‘Neither fits nor does not fit,’’ 4 to ‘‘Fits sufficiently well,’’ and 5 to ‘‘Fits perfectly.’’

Overall, the comprehensive measure of place meaning increased from a mean of 3.71 (S.D. = 0.089) to 4.05 (S.D. = 0.085). This reflects a stronger alignment with the idea that Sitia UGGp ‘‘fits perfectly’’ with the positive attributes assessed. The total score for place meaning rose from 3639 to 3900 units. Participation in the summer school significantly enhanced participants’ perceptions of the symbolic meanings of Sitia UGGp, reinforcing its cultural, ecological, and aesthetic value.

The analysis of the ‘‘Geoethical Awareness’’ section revealed significant shifts in participants’ perceptions regarding geoethical issues before and after attending the summer school (Table 4).

Table 4. Distribution of mean value, standard deviation, and total score for geoethical awareness.

Items		**PRE M.V.**	**PRE S.D.**	**POST M.V.**	**POST S.D.**	**SUM PRE**	**SUM POST**
C1	The preservation of geoheritage is essential for maintaining cultural and scientific values in Sitia Geopark.	4.33	0.112	4.70	0.081	143	155
C2	Public awareness programs about geoheritage in Sitia Geopark significantly enhance community appreciation and protection efforts.	4.42	0.098	4.70	0.081	146	155
C3	Effective geoconservation strategies in Sitia Geopark are crucial for protecting geological features from degradation.	4.39	0.106	4.64	0.085	145	153
C4	Geoconservation in Sitia Geopark should be integrated into local development plans to ensure the sustainable use of geological resources.	4.42	0.107	4.58	0.098	146	151
C5	Geotourism activities within Sitia Geopark should prioritize sustainability.	4.45	0.098	4.58	0.107	147	151
C6	The promotion of geotourism in Sitia Geopark can help boost local economies without compromising geological integrity.	4.30	0.141	4.52	0.098	142	149
C7	It is important to recognize and protect the geodiversity of Sitia Geopark as it contributes to ecological balance.	4.48	0.098	4.58	0.098	148	151
C8	Educational programs about geodiversity in Sitia Geopark can foster a deeper understanding of geological processes among visitors.	4.33	0.120	4.55	0.098	143	150
C9	The protection of biodiversity within Sitia Geopark is as important as preserving geological features.	4.18	0.187	4.73	0.079	138	156
C10	Biodiversity and geodiversity conservation in Sitia Geopark should be managed in a complementary manner.	3.88	0.167	4.15	0.175	128	137
C11	Responsible use of georesources within Sitia Geopark can support local communities without harming the environment.	4.09	0.159	4.42	0.098	135	146
C12	Regulations on the extraction of geosources in Sitia Geopark are necessary to prevent environmental degradation.	4.12	0.183	4.58	0.107	136	151
C13	Sustainable water management practices are essential to maintain the ecological balance within Sitia Geopark.	4.30	0.119	4.58	0.087	142	151
C14	Community involvement in water management decisions within Sitia Geopark can lead to more effective conservation outcomes.	4.18	0.119	4.55	0.098	138	150
C15	Sitia Geopark should implement strategies to mitigate the impacts of the climate crisis on its geological and biological resources.	4.33	0.128	4.48	0.116	143	148

C16	Raising awareness about the climate crisis in Sitia Geopark can motivate visitors and locals to adopt more sustainable practices.	4.27	0.117	4.45	0.116	141	147
C17	Risk prevention measures are necessary to protect both geological and human resources within Sitia Geopark.	4.39	0.115	4.42	0.098	145	146
C18	Adequate infrastructure and planning can significantly reduce the risks of natural disasters within Sitia Geopark.	4.18	0.134	4.45	0.107	138	147
C19	Sitia Geopark must develop adaptive strategies to cope with environmental changes and their impacts.	4.06	0.130	4.36	0.114	134	144
C20	Continuous research and monitoring are vital for effective adaptation to changing conditions within Sitia Geopark.	4.33	0.104	4.58	0.098	143	151
C21	All activities within Sitia Geopark should be guided by principles of sustainability to ensure long-term conservation.	4.55	0.107	4.70	0.081	150	155
C22	Sustainable development within Sitia Geopark can serve as a model for other protected areas.	4.36	0.114	4.48	0.088	144	148
C23	Enhancing the resilience of Sitia Geopark's ecosystems is crucial for coping with environmental pressures.	4.00	0.179	4.39	0.123	132	145
C24	Community resilience in Sitia Geopark can be bolstered through education and involvement in conservation efforts.	4.15	0.158	4.55	0.098	137	150
C25	Active community engagement is crucial for the success of conservation initiatives in Sitia Geopark.	4.33	0.104	4.48	0.116	143	148
C26	Local communities should have a significant role in decision-making processes related to Sitia Geopark.	4.18	0.134	4.45	0.116	138	147
C27	Strong environmental advocacy initiatives are essential for raising awareness about conservation issues within Sitia Geopark.	4.42	0.098	4.67	0.083	146	154
C28	Collaborating with environmental advocacy groups can amplify the impact of conservation efforts within Sitia Geopark.	4.42	0.087	4.45	0.163	146	147
C29	Programs that connect visitors emotionally to Sitia Geopark can lead to stronger conservation efforts.	4.30	0.111	4.52	0.098	142	149
C30	Ecological experiences within Sitia Geopark should be designed to foster a sense of responsibility towards nature.	4.45	0.116	4.70	0.092	147	155
C31	Geoenvironmental education programs are essential for raising awareness about the importance of geological conservation in Sitia Geopark.	4.27	0.109	4.39	0.162	141	145
C32	Schools and educational institutions should be actively involved in geoenvironmental education initiatives within Sitia Geopark.	4.52	0.098	4.61	0.097	149	152
Total (geoethical awareness)		4.30	0.770	4.53	0.069	4536	4784

Note: Items 1–2 evaluate the geoheritage value; items 3–4 focus on the geoconservation; items 5–6 examine geotourism; items 7–8 address the geodiversity; items 9–10 pertain to the biodiversity; items 11–12 consider georesources; items 13–14 discuss water management; items 15–16 relate to climate crisis issues; items 17–18 involve risk prevention; items 19–20 explore adaptation to changes; items 21–22 assess sustainability; items 23–24 reflect on resilience; items 25–26 cover community engagement; items 27–28 focus on environmental advocacy; items 29–30 evaluate the value of concrete ecological feelings; and items 31–32 consider the geoenvironmental education potential. The instrument uses a Likert scale as follows: 1 corresponds to ''Strongly disagree,'' 2 to ''Disagree,'' 3 to ''Neither disagree nor agree,'' 4 to ''Agree,'' and 5 to ''Strongly agree.''

Overall, the average rating for geoethical awareness increased from 4.30 (S.D. = 0.770) to 4.53 (S.D. = 0.069), with total scores rising from 4536 to 4784, highlighting the program's positive impact on participants' understanding and attitudes towards geoethical issues. These findings demonstrate a marked enhancement in geoethical awareness, with increased agreement on management, sustainability, preservation, community involvement, and advocacy. The summer school enhanced participants' commitment to geoethical principles, supporting geoconservation efforts in Sitia UGGp.

To explore the relationships between key scales of the questionnaire —place attachment (Scale A), place meaning (Scale B), and geoethical awareness (Scale C)—Spearman's rho correlation coefficients were calculated. The strongest correlation was observed between place attachment and place meaning ($\rho = 0.734$, $p < 0.001$, N = 33), indicating a strong link between emotional connection and perceived significance. Place meaning and geoethical awareness also showed a significant correlation ($\rho = 0.699$, $p < 0.001$), as did place attachment and geoethical awareness ($\rho = 0.664$, $p < 0.001$). All correlations were positive and significant, indicating interconnectedness of the scales and suggesting that the summer school enhanced participants' understanding of geoethical issues at Sitia UGGp.

A Wilcoxon signed-rank test was used to evaluate the impact of the summer school program on participants' connection to Sitia UGGp by comparing median place attachment levels before (APRE) and after (APOST) the program. This test is suitable for related samples. Notably, 30 of 33 participants reported a stronger connection post-program, while only 2 reported a decrease, and 1 remained unchanged. The test showed a statistically significant difference ($Z = -4.785$, $p < 0.001$), confirming the changes were not due to chance. The median place attachment score increased from 41.00 to 45.00, indicating a stronger connection to Sitia UGGp. The total scores for place attachment for each participant illustrate a clear trend toward stronger connections with

Sitia UGGp (Figure 1).

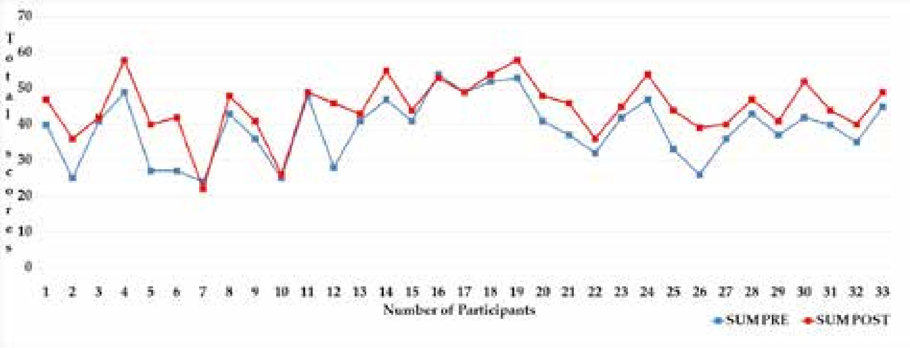

Figure 1. Distribution of total place attachment scores among summer school participants.

The results from the Wilcoxon signed-rank test and descriptive statistics demonstrate that the summer school significantly enhanced participants' attachment to Sitia UGGp. The increased median scores and the large number of participants reporting stronger connections highlight the program's success in deepening emotional and cognitive bonds with Sitia UGGp. This underscores the effectiveness of the summer school in fostering greater appreciation and attachment among participants.

To assess the summer school's impact on participants' perceptions of the Sitia UGGp's significance, a Wilcoxon signed-rank test compared median place meaning scores before (BPRE) and after (BPOST) the program. Of the 33 participants, 28 reported an enhanced perception of the site's importance, while only 2 noted a decrease, and 3 remained unchanged. The test showed a statistically significant difference ($Z = -4.282$, $p < 0.001$), indicating the changes were not due to chance. The median score for place meaning increased from 110.00 to 121.00 after the program. The upward shift in total scores for place meaning reflects a notable enhancement in participants' valuation of the Sitia UGGp, attributable to the summer school experience (Figure 2).

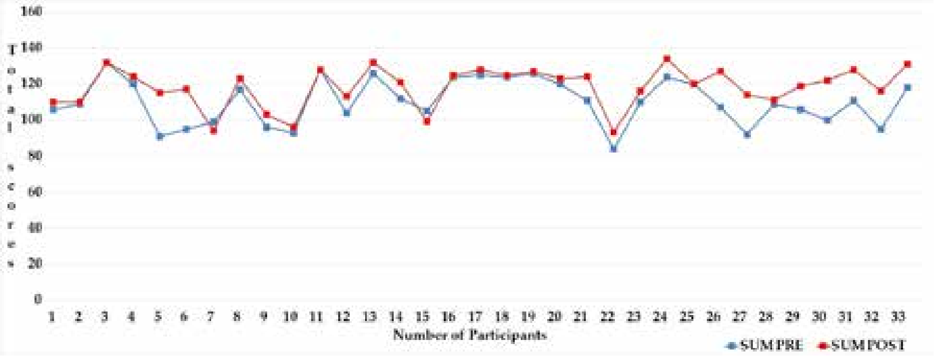

Figure 2. Distribution of total place meaning scores among summer school participants.

The results show that the summer school positively influenced participants' perceptions of the importance of the Sitia UGGp. The significant increase in median place meaning scores underscores the program's effectiveness in enhancing appreciation and recognition of the site's cultural and natural value. This highlights the role of educational initiatives in elevating the significance of heritage sites.

A Wilcoxon signed-rank test was also used to evaluate the impact of the summer school on participants' geoethical awareness, comparing median scores before (CPRE) and after (CPOST) the program. Among 33 participants, 26 reported increased geoethical awareness, 4 experienced a decrease, and 3 showed no change. The test revealed a statistically significant difference ($Z = -4.085$, $p < 0.001$), indicating the changes were not due to chance. The median geoethical awareness score rose from 139.00 to 152.00, demonstrating a significant improvement following the summer school. The notable increase in total scores for geoethical awareness indicates a positive shift in participants' geoethical perceptions of the Sitia UGGp, reflecting the summer school's effectiveness in enhancing their awareness (Figure 3).

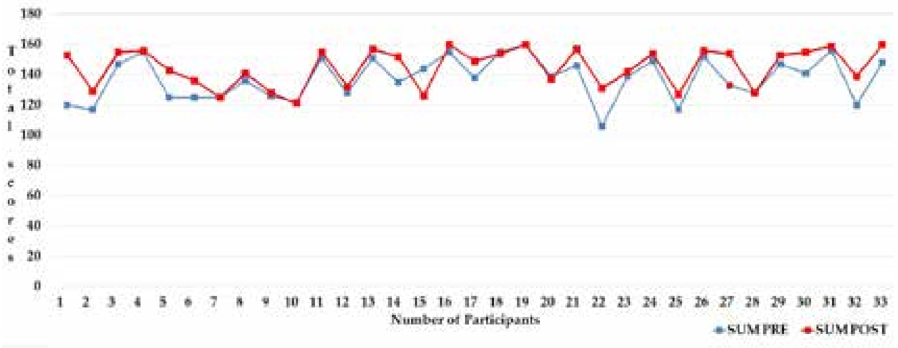

Figure 3. Distribution of total geoethical awareness scores among summer school participants.

The results show that the summer school significantly enhanced participants’ geoethical awareness regarding the Sitia UGGp. The increase in median scores underscores the program’s success in deepening understanding of ethical considerations. These findings affirm the summer school’s effectiveness in enhancing geoethical perspectives and achieving its educational goals.

To explore the potential for predicting geoethical awareness (CPRE), a multiple linear regression analysis was conducted. The goal was to identify variables that reliably predict geoethical awareness before the summer school. Independent variables included place attachment (APRE), place meaning (BPRE), gender, years of teaching experience, and other factors related to environmental involvement. The stepwise procedure revealed that place attachment (APRE) and place meaning (BPRE) significantly contributed to the model, with an adjusted R^2 of 0.583, explaining 58.3% of the variance in geoethical awareness. ANOVA confirmed statistically significant differences for place attachment [$F(1,29) = 34.330$, $p < 0.001$] and place meaning [$F(2,28) = 21.990$, $p < 0.001$]. The regression equation is: Geoethical Awareness = 2.128 + 0.281 × Place Attachment + 0.332 × Place Meaning. A one-unit increase in place attachment predicts a 0.281 unit increase in geoethical awareness, while a one-unit increase in place meaning predicts a 0.332 unit increase. Place attachment showed a stronger effect, with a standardized coefficient $B = 0.458$. Multicollinearity checks showed no significant issues (max $VIF < 5$, $Tolerance > 0.2$), and the Durbin–Watson value (1.928) indicated independent residuals. Residuals met normal distribution assumptions, with Spearman’s rho showing no significant correlation ($\rho = -0.128$, $p = 0.477$).

In summary, place attachment and place meaning are significant predictors of geoethical awareness, with place attachment being a stronger predictor. The model’s reliability is confirmed by meeting statistical assumptions, highlighting the importance of emotional and cognitive connections in fostering geoethical awareness.

Conclusions

In the realm of geosciences, safeguarding biotic, abiotic, and cultural elements is crucial for sustainability and resilience. Geoconservation emphasizes geodiversity and biodiversity, highlighting biological, geological, and cultural heritage. Developing a strong sense of place can foster a responsible and cooperative world, enhancing emotional connections and promoting protective behaviors. Geoethics provides a framework for viewing Earth as a system of complex relationships, advocating sustainable practices.

This study on sense of place and geoethics at the Sitia UGGp found high reliability in scales measuring place attachment, place meaning, and geoethical awareness, both before and after summer school. Significant increases in these scales indicated enhanced emotional connections and understanding. Positive correlations among the scales highlighted their interrelation, with regression analysis confirming place attachment and place meaning as predictors of geoethical awareness.

Future research could explore changes in geoethical awareness over time, use interdisciplinary approaches for holistic understanding, and conduct comparative studies across UGGps. Investigating how awareness translates into behaviors and evaluating geoenvironmental education programs could enhance effectiveness. Validating the geoethical awareness scale in diverse contexts is also important.

This research has limitations, including a small sample size, lack of a control group, and potential biases. The focus on Sitia UGGp may limit applicability to other regions.

Acknowledgements

The authors want to express gratitude to the 4th Summer School of Environmental Education on Geotopes and Sustainability organizing committee at Sitia UNESCO Global Geopark and all the participants involved in our study. They also extend their heartfelt thanks to the organizing committee of the 17th International Congress of the Geological Society of Greece and the anonymous reviewers for their thorough consideration of this extended abstract.

References

Fassoulas, C., Staridas, S., Perakis, V., Mavrokosta, C., 2013. Revealing the Geoheritage of Eastern Crete through the Development of Sitia Geopark, Crete, Greece. Bulletin of the Geological Society of Greece 47, 1004-1016. https://doi.org/10.12681/bgsg.11143

Gordon, J.E., 2019. Geoconservation Principles and Protected Area Management. International Journal of Geoheritage and Parks 7, 199-210. https://doi.org/10.1016/j.ijgeop.2019.12.005

Koupatsiaris, A.A., Drinia, H., 2024. Expanding Geoethics: Interrelations with Geoenvironmental Education and Sense of Place. Sustainability 16, 1819. https://doi.org/10.3390/su16051819

Krasny, M.E., 2020. Advancing environmental education practice, Cornell University Press.

Kudryavtsev, A., Stedman, R., Krasny, M., 2012. Sense of Place in Environmental Education. Environmental Education Research 18, 229-250. https://doi.org/10.1080/13504622.2011.609615

Peppoloni, S., Di Capua, G., 2022. Geoethics: Manifesto for an Ethics of Responsibility towards the Earth, Springer International Publishing.

Semken, S., Freeman, C.B., Watts, N.B., Neakrase, J.J., Dial, R.E., Baker, D.R., 2009. Factors that Influence Sense of Place as a Learning Outcome and Assessment Measure of Place-Based Geoscience Teaching. The Electronic Journal for Research in Science and Mathematics Education 13, 136–159.

Sobel, D., 2004. Place-based education: Connecting classrooms and communities, 2nd ed. The Orion Society.

Williams, D., Vaske, J., 2003. The Measurement of Place Attachment: Validity and Generalizability of a Psychometric Approach. Forest Science 49, 830-840. https://doi.org/10.1093/forestscience/49.6.830

Young, M., 1999. The Social Construction of Tourist Places. Australian Geographer 30, 373-389. https://doi.org/10.1080/00049189993648

17th INTERNATIONAL CONGRESS
of the Geological Society of Greece

BULLETIN OF THE GEOLOGICAL
SOCIETY OF GREECE, SP. PUBL.

EXTENDED ABSTRACT 175

Fault–based recurrence models and occurrence probabilities of large earthquakes (M≥6.0) in the Corinth Rift, Greece

Kourouklas C. [1], Bonatis P.[1], Papadimitriou E.[1], Karakostas V.[1]
(1) Geophysics Department, School of Geology, Aristotle University of Thessaloniki, Thessaloniki, Greece, ckourouk@geo.auth.gr.

Research Highlights

- The M^{3}6.0 earthquakes recurrence times, T_r, exhibit high variability from 40 to 1500 years, with the southern Corinth Rift fault segments reaching values up to 350 years and their antithetic ones ranging from 400 to 1500 years.
- The fault segments in the Corinth Rift can be devided into three groups, according to their recurrence behaviour, with some of them exhibiting significantly lower renewal model probabilities than the Poisson model, others showing nearly equal probabilities, and one segment where the renewal model probabilities are much higher than the Poisson one.
-

Introduction

The main objectives of the current study include the determination of the mean recurrence time, T_r, of large (M^{3}6.0) earthquakes associated with the major fault segments of the Corinth Rift, Greece, and the estimation of the conditional occurrence probabilities of an impending M^{3}6.0 earthquake on each major fault segment.

The recurrence behavior of large earthquakes (e.g. M^{3}6.0) on specific fault segments is one of the primary input parameters for developing long–term Earthquake Rupture Forecast (ERF) models. These models integrate a series of parameters (maximum observed magnitude, fault dimensions, long–term slip rates, available recurrence times) to estimate the occurrence likelihood of nearly characteristic magnitude earthquakes in a specific time span. The primary output of such models is the mean recurrence time, which can later be used for the application of statistical models, which, in turn, return the likelihood of the occurrence of near characteristic magnitude earthquakes over specific time intervals and can be based on either a time–independent or an elastic rebound motivated renewal assumption.

A precise and robust estimation of T_r requires the inclusion of as many large earthquakes associated with individual fault segments as possible, including both historical and instrumental data along with the selection of the appropriate statistical model. However, large earthquakes associated with specific fault segments are often limited, with only a few cases having about 3 to 10 observations due to the long duration required for stress accumulation and the short time span of available large earthquake records.

To address these challenges and limitations, an alternative approach is the estimation of T_r through the application of the seismic moment rate conservation method (Field *et al.*, 1999). This method defines the mean recurrence time as the ratio of the maximum expected seismic moment corresponding to a large earthquake with the maximum observed magnitude (M_{max}) occurring on a given fault segment, to the seismic moment that might be released by the respective fault segment due to the tectonic loading, assuming a nearly characteristic earthquake model. This approach can provide more precise T_r estimates because the overall rate and size distribution of earthquakes should reflect the tectonic loading in the brittle part of the crust, and this function is typically constrained by the principle of seismic moment rate conservation.

Seismotectonic Setting of Corinth Rift

The Corinth Rift, a prominent E–W oriented elongated graben stretching over 100 km in length, separates the Peloponnese from mainland Greece. It exhibits a remarkable extension rate that varies spatially, with the western section extending at approximately 10 mm/yr and the eastern section at around 5.5 mm/yr (Briole *et al.*, 2021). As a result, the Corinth Rift is one of the most seismically active regions, frequently experiencing large (M^{3}6.0) earthquakes during both the instrumental and historical seismicity periods (Papazachos & Papazachou, 2003), with the most recent one being the 1995 M_w=6.5 Aigion earthquake (Bernard *et al.*, 1997). The intense seismic activity along the Corinth Rift has made it one of the most well studied areas, resulting in the detailed determination of its main fault segments. Information on the M≥6.0 earthquakes are derived from the catalogue provided by Papazachos & Papazachou (2003) and regional parametric earthquake catalog of the Geophysics Department of the Aristotle University of Thessaloniki, consisting of 35 large earthquakes since 373 BC. Studies by Console *et al.* (2013, 2015), after concluding that the large earthquakes catalog could be considered as complete after 1700 AD (since 1714 AD) as well as Kourouklas (2022), suggest that they are not regularly distributed but they are clustered in time. This latter dataset includes 22 M≥6.0 earthquakes (Figure 1).

The southern margin of the Corinth Rift is bounded by eight (8) normal faults, listed from west to east as Psathopyrgos (FS 01), Aigion (FS 02), Eliki (FS 03), Akrata (FS 04), Xylokastro (FS 05), Perachora (FS 06), Skinos (FS 07) and Alepochori

(FS 08) fault segments (Figure 1). Their strike values are almost the same 260° – 280° and their dip angles vary between 30° and 45°. The northeastern boundary of study area is demarcated by the Kapareli fault segment (FS 09), also a normal fault with a strike of 50° and a dip angle of 50°. The fault segment lengths range from 8 km (Akrata Fault Segment) to 22 km (Eliki Fault Segment). All their geometrical and kinematic were summarized by Console *et al.* (2013, and references therein). To the north the Delfoi (FS 10), Makrygialos (FS 11), Sykia (FS 12) and Marathias (FS 13) fault segments are defined from east to west (Figure 1; Ganas 2024, and references therein). Their lengths range from 10 km (Makrygialos and Sykia fault segments) to 18 km (Delfoi fault segment).

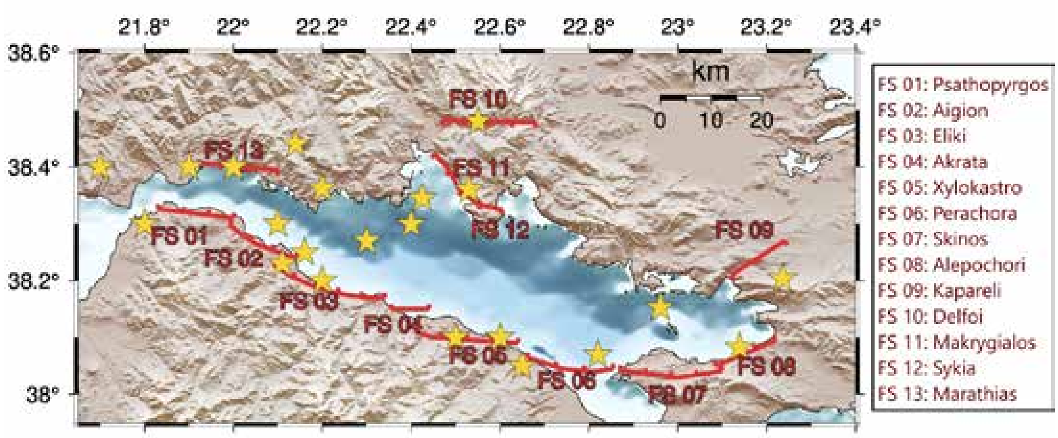

Figure 1. Geomorphological map of Corinth Rift, where the major normal fault segments are represented by red solid lines. Yellow stars depict the *M*^{3}6.0 earthquakes occurred in the study area since 1714.

Although the number of large earthquakes (both historical and instrumental) is adequate for regional statistical studies, the number of recurrence intervals become limited when subdivided into subsets associated with specific fault segments. For this reason, Kourouklas (2022, and references therein) attempted to associate the 22 M≥6.0 earthquakes since 1714 with their respective causative fault segments. The analysis suggested that 2 out of 8 fault segments of the western Corinth Rift were associated with two (2) M≥6.0 earthquakes each (Psathopyrgos and Eliki). The Aigion fault segment was linked to four (4) events, whereas the Xylokastro and Perachora segments were each associated with three (3). The Alepochori and Skinos fault segments were associated with one (1) M≥6.0 earthquake each. It is noteworthy that the Akrata fault segment, the shortest in length, has not been associated with any M≥6.0 earthquake since 1714. Similarly, the Kapareli fault segment was also associated with only one (1) M≥6.0 earthquake. In the northern part, the Delfoi, Makrygialos and Sykia segments were associated with one (1) M≥6.0 historical earthquake each, whereas the Marathias fault was linked to two (2) such events. Thus, although the study area is among the most seismically active areas where several large earthquakes rather frequently take place, the insufficient number of M≥6.0 earthquake events per segment restricts the ability to determine T_r by using their observational recurrence intervals as input.

Method

We estimated the mean recurrence time, T_r, by applying the seismic moment rate conservation technique (Field *et al.*, 1999) in the absence of a sufficient number of recurrence intervals for each of the 13 normal faults in the Corinth Rift. This technique assumes that a large earthquake of nearly characteristic magnitude can release the total accumulated seismic moment on a fault. It takes into account the maximum observed magnitude (M_{max_obs}) and its corresponding uncertainty (ΔM) and the maximum seismic moment corresponding to the accumulated strain on the specific fault segment due to tectonic loading. The mean recurrence time is then calculated as the ratio of the seismic moment rate that can be released by the maximum magnitude earthquake to the seismic moment due to strain accumulation on the fault:

$$T_r = \frac{M_{o\,max}}{\mu L w V} \quad (1)$$

where $M_{o,\,max}$ is the maximum possible seismic moment released by a large earthquake with a magnitude within the range $M_{max\_obs} \pm \Delta M$. μ is the shear modulus, whose typical value for faults in the Earth's crust is equal to 3.3 × 10^5 bar ($\mu = 3.3\times10^5$ bar), L and w *are* the length and width of the fault segment (in km), respectively, and V the long–term slip rate.

The maximum expected seismic moment is computed via the definition of seismic moment. The variability of T_r is also computed via the method of formal error propagation technique proposed by Peruzza *et al.* (2010), considering the uncertainties related to the maximum magnitude and slip rate values. Knowing the variability of mean recurrence time, the standard deviation, *σ*, can then be easily calculated. The advantage of this approach is that, once T_r and *σ* are estimated, the corresponding aperiodicity values, *α*, can be calculated as the coefficient of variation, C_v, of T_r, which is the second appropriate parameter of renewal model applications (Pace *et al.*, 2016).

Using the estimated T_r and *σ* as the primary inputs, we model the *M*≥6.0 earthquakes recurrence times by applying both the time–independent Poisson model and the Brownian Passage Time (BPT; Matthews *et al.*, 2002) renewal model, aiming at the estimation of the occurrence probabilities of the next *M*≥6.0 earthquake to be occurred on each fault segment for the next 10, 20 and 30 years, starting from 1 January 2025.

The Poisson process can be expressed by the exponential distribution with probability density function (pdf) given by:

$$f(t|T_r) = \frac{1}{T_r}\exp\{-\frac{t}{T_r}\} \quad (2)$$

where T_r is the mean recurrence time of large earthquakes associated with a specific fault segment. To model the occurrence of large earthquakes as a renewal process, the BPT distribution is applied. The PDF of the BPT model is given by:

$$f(t|T_r,\alpha) = \left(\frac{T_r}{2\pi\alpha^2 t^3}\right)^{1/2}\exp\{-\frac{(t-T_r)^2}{2T_r\alpha t}\} \quad (3)$$

where T_r is also the mean recurrence time and *α* is the aperiodicity, which can be considered as analogous to the coefficient of variation, C_v, of the normal distribution.

The occurrence probabilities of a next large earthquake on certain fault in a specific time span can be computed by applying the simple Poisson probability model given by:

$$P(t \le T \le t + \delta t) = 1 - e^{-\delta t/T_r} \quad (4)$$

where $\delta t\delta t$ is the forecast duration and the conditional probability corresponding to the BPT renewal given by:

$$P(t \le T \le t + \delta t) = \frac{\int_t^{t+\delta t} f(t)dt}{\int_t^{\infty} f(t)dt} \quad (5)$$

where *t* is relative to the date of last earthquake, conditioned by the fact that it has been $t + \delta tt + \delta t$ years since the last one.

Alternatively, the occurrence probabilities of the next large earthquake can be evaluated by the estimation of the hazard function, *H(t)*, of both Exponential and BPT models. This analysis is particularly useful for predicting future rupture scenarios as the values of the hazard function or, in other words, the hazard rate is equivalent to the conditional probability estimate within a specific time span. The hazard function of a given distribution can be easily defined using its corresponding probability density, *f(t)*, and cumulative density, *F(t)*, functions as follows:

$$H(t) = \frac{f(t)}{S(t)} = \frac{f(t)}{1-F(t)} \quad (6)$$

where *S(t)* is the survival function of the distribution.

Application & Results

The mean recurrence times, T_r, of M≥6.0 earthquakes are estimated through Equation (1) after defining all the appropriate parameters for the application of the seismic moment rate conservation method. These parameters include the fault dimensions (*L*, *w*), the maximum observed magnitude, M_{max_obs}, their long-term slip rates (*V*) and the corresponding uncertainties (*ΔM* and *σV*, respectively) which are summarized in Kourouklas (2022). It should be noted that for the definition of the long-term slip rates assigned to each fault segment, 60% of the geodetic slip rates proposed by Briole *et al.* (2021) are used. As previously mentioned, the Akrata fault segment was not associated with any *M*≥6.0 earthquake and the estimation of the mean recurrence time and the maximum expected magnitude, were calculated using scaling relations, The absence of any *M*≥6.0 earthquake associated with this fault segment prevents the estimation of any elapsed time, which is necessary for renewal recurrence modeling. For this reason, the Akrata fault segment is excluded from the next steps of the statistical analysis.

The estimated T_r values (Figure 2a) range from a few years (Akrata fault segment; T_r=35 years) to about 1500 years (Makrygialos fault segment; T_r=1511.5 years). These variations are clearly related to the dimensions and slip rates of each segment, which results in different stressing rate values and maximum observed magnitudes. Starting from the southern Corinth Rift fault zone (excluding the Akrata fault segment), mean recurrence times vary from almost 120 years (Psathopyrgos fault segment; T_r=119.4 years) to 359 years (Skinos fault segment; T_r=359.3 years) (Figure 2a). The T_r of *M*≥6.0 earthquakes increase from the western part to the eastern one (Figure 2a), due to the gradual decrease of deformation rates from the western to eastern part of our study area. Regarding the respective *Cv* values, it is reported that they exhibit minimal variations, ranging from 0.6 to 0.7 in 6 out of 7 cases (Psathopyrgos, Aigion, Xylokastro, Perachora, Skinos, Alepochori). This suggests that the recurrence behavior of *M*≥6.0 earthquakes associated with these fault segments can be characterized as slightly aperiodic. On the other hand, results of our analysis for *M*≥6.0 earthquakes associated with the Eliki fault segment indicates that its recurrence behavior can be characterized as highly aperiodic (almost random), given that its *Cv* value is equal to 0.9 (*Cv*=0.9).

Moving to the mean recurrence time results for the northern part, higher values are reported, ranging from 426 years to 1511 years. Specifically, the T_r of *M*≥6.0 earthquakes associated with the Kapareli fault segment is found equal to 426 years, with a *Cv* value of 0.6. The mean recurrence time for the Delfoi fault segment is equal to T_r=933.1 years, whereas the T_r of *M*≥6.0 earthquakes associated with Makrygialos and Sykia fault segments are even larger, with T_r=1511.5 years and T_r=1070.1 years, respectively. The mean recurrence time of *M*≥6.0 earthquakes associated with the Marathias fault segment is T_r=546.1 years. The coefficient of variation for all four these cases (Delfoi, Makrygialos, Sykia, Marathias) is estimated equal to *Cv*=0.7.

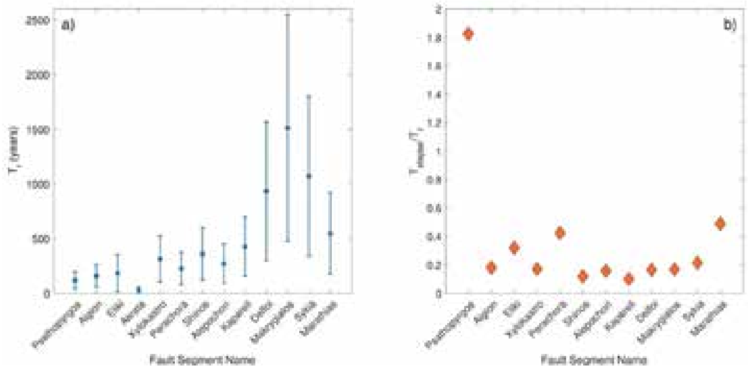

Figure 2. (a) Mean recurrence time, T_r, estimates of *M*≥6.0 earthquakes (blue circles), along with their ±1σ (vertical blue solid line) for the 13 normal fault segments of the Corinth Rift. (b) The ratio of elapsed time, T_e, of the last *M*≥6.0 earthquake that occurred in each fault segment (except from Akrata fault segment) and the mean recurrence time, T_r, estimates.

One more important factor for the statistical modeling of T_r, especially for time–dependent approaches, is the elapsed time, T_e, since the last earthquake. Specifically, the ratio of T_e over T_r can serve as an initial indicator of the stage of the earthquake cycle for a given fault. Values of this ratio approaching zero indicate the early stage of a new earthquake cycle, while more increased values indicate that the fault is closer to the next rupture. Figure 2b shows the ratio of the elapsed time to the mean recurrence time for the seven fault segments. The smallest value is reported for the Aigion fault segment, which is the most recently ruptured (T_e = 28.57 years). For 10 out of the other 11 fault segments, the ratio ranges between 0.17 and 0.55, also showing that the elapsed time is considerably shorter than the mean recurrence time. This suggests that these faults are likely in the early stages of their seismic cycle. The only case in which the ratio is larger than 1.0 is the Psathopyrgos fault segment (Figure 2b), meaning that the elapsed time since the last *M*≥6.0 is much larger than the estimated T_r.

Next, we applied the exponential and BPT distributions, representing the Poisson and renewal models, using the mean recurrence time, T_r, and *Cv* values obtained from the seismic moment rate conservation approach. The ultimate goal is to model the recurrence behavior of the *M*≥6.0 earthquakes associated with the normal faults of the study area. We focused primarily on the hazard functions of both statistical models, as their (hazard) rates can be considered equivalent to the conditional probability estimates over a specific time span. Figure 3 shows the hazard functions of the exponential and BPT distributions for the seven (7) fault segments of the southern part (Psathopyrgos, Aigion, Eliki, Xylokastro, Perachora, Skinos and Alepochori), in which their significant differences in modeling T_r are highlighted.

Starting from the Psathopyrgos fault segment (Figure 3a) the constant hazard rate of the Poisson model (blue solid line) is considerably lower than the hazard rate of the BPT model (red solid line), which exhibits a decreasing trend, at the time corresponding to T_e (until 31-12-2024). On the other hand, in the case of the Aigion fault segment (Figure 3b), the most recently ruptured segment in the study area, the hazard function values of the Poisson model (blue solid line) are considerably larger than the values obtained from the application of the BPT, at the time corresponding to T_e. The BPT model application on the Eliki fault segment (Figure 3c) reports hazard rates slightly higher than those of the Poisson model around the time corresponding to the elapsed time (black dashed line in Figure 3c). More specifically, the BPT hazard function values exhibit an increasing trend for the next 10, 20 and 30 years after 31-12-2024. Similarly, for the Aigion fault segment, the hazard function values of the Poisson model (blue solid line) are considerably larger than the values of the BPT model for the recurrence behavior of the *M*≥6.0 earthquakes associated with the Xylokastro fault segment (Figure 3d), indicating that the fault segment is at an early stage of a new earthquake cycle at time *t* corresponding to the elapsed time. For the Perachora fault segment both models report almost equal hazard rates (Figure 3e) and lastly, for the Skinos and Alepochori fault segments (Figures 3f and 3g, respectively) the hazard function values of the BPT model are significantly lower than the ones of the Poisson model at time *t* corresponding to the elapsed time, highlighting that both segments are at an early stage of a new earthquake cycle according to the renewal model.

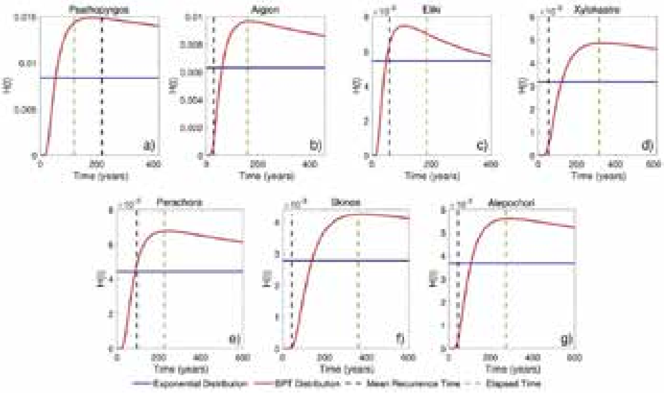

Figure 3. Hazard functions, *H(t)*, for the Psathopyrgos (a), Aigion (b), Eliki (c), Xylokastro (d), Perachora (e), Skinos (f) and Alepochori (g) fault segments according to the Exponential (blue solid lines) and the BPT (solid red lines) distributions. Vertical dashed lines denote the elapsed time since the last *M*≥6.0 earthquake (*t* = 0) occurred on each fault segment, whereas the vertical dashed black lines denote the mean recurrence time of *M*≥6.0 earthquake for each fault segment.

Focusing on the recurrence modeling results for the five (5) fault segments of the northern Corinth Rift fault zone, in 4 out of 5 cases the hazard rate values of the renewal model are significantly lower than those of the Poisson model. Specifically, the statistical modeling of *M*≥6.0 earthquakes associated with the Kapareli (Figure 4a), Delfoi (Figure 4b), Makrygialos (Figure 4c) and Sykia (Figure 4d) fault segments show that the hazard rate estimates of the time–independent Poisson model are considerably higher (blue solid lines in Figures 4a, 4b, 4c and 4d) than the ones of the BPT model (solid red lines). More specifically, for the Kapareli fault segment, the BPT model hazard function values are almost zero at the time corresponding to the elapsed time, whereas the constant hazard rate of the Poisson mode is equal to 2.4×10^{-3}. Statistical modeling for Delfoi, Makrygialos and Sykia fault segments indicates slightly different results for the renewal model, with its hazard function values exhibiting an increasing trend for the next 10, 20 and 30 years after elapsed time (vertical dashed black lines in Figures 4b, 4c and 4d) in all cases. On the contrary, the recurrence modeling of *M*≥6.0 earthquakes associated with the Marathias fault segment (Figure 4e) reports hazard rates slightly higher than the ones of the Poisson model around the time corresponding to the elapsed time.

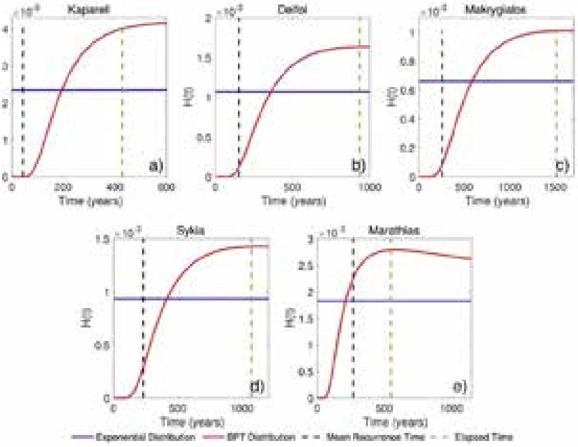

Figure 4. Hazard functions, *H(t)*, for the Kapareli (a), Delfoi (b), Makrygialos (c), Sykia (d) and Marathias (e) fault segments according to the Exponential (blue solid lines) and the BPT (solid red lines) distributions. The vertical dashed lines denote the elapsed time since the last *M*≥6.0 earthquake (*t* = 0) occurred on each fault segment, whereas the vertical dashed black lines denote the mean recurrence time of *M*≥6.0 earthquake for each fault segment.

Conclusions

In this study, we present both time–dependent and time–independent recurrence models to investigate the mean recurrence time of $M \geq 6.0$ earthquakes associated with the main normal faults of the Corinth Rift. We used the most detailed available input data (fault network model, long–term slip rates) for the estimation of the mean recurrence time, T_r, by applying the physics–based seismic moment rate conservation method. The results show that T_r ranges from about 40 years to almost 1500 years, depending on the combination of the input parameters. The statistical analysis of T_r via the Exponential and BPT distributions (representing the Poisson and a renewal model, respectively) reveals that the recurrence behavior of the Corinth Rift fault segments can be divided into three distinct groups. The first group includes fault segments where the elapsed time since the last earthquake is considerable smaller than the T_r. This group includes the Aigion, Xylokastro, Skinos, Alepochori, Kapareli, Delfoi, Makrygialos and Sykia fault segments. For all these cases the renewal model's hazard function values and the corresponding conditional occurrence probabilities for the next 10, 20 and 30 years show significant differences among the two applied models, with the BPT model yielding much lower values than the Poisson model. These findings indicate that the aforementioned fault segments are at an early stage of a new earthquake cycle according to the renewal model. The second group includes the Eliki, Perachora and Marathias fault segments for which the hazard rates of both models are almost equal, resulting in similar occurrence probabilities for the next 10, 20 and 30 years. The last group includes only the Psathopyrgos fault segment for which the BPT model reports significantly larger hazard rate values than the Poisson model. The Psathopyrgos fault segment is the only case where the elapsed time since the last $M \geq 6.0$ earthquake exceeds the mean recurrence time, indicating that from a statistical point of view, it is at a later stage of a new earthquake cycle. Consequently, the occurrence probabilities for the next $M \geq 6.0$ earthquake to occur in the next 10, 20 and 30 years are the highest within the study area. The results of our analysis could serve as the basis for fault–based large earthquake occurrence models. By considering time–dependent occurrence models in probabilistic seismic hazard analysis (PSHA) one can account for epistemic uncertainties, quantify the range of seismic hazard for a given exceedance probability and illustrate which model assumptions lead to the most significant variations in the estimated seismic hazard (Akinci *et al.*, 2017). By utilizing these models, stakeholders can better determine when and where protective measures are most urgently needed, particularly in regions with higher short-term earthquake probabilities, leading to more effective seismic risk management.

Acknowledgements

Funded by the European Union

This research is financially supported by the artEmis Project funded by the European Union, under Grant Agreement nr 101061712. Views and opinions expressed are however those of the author(s) only and do not necessarily reflect those of the European Union or European Commission – Euratom. Neither the European Union nor the granting authority can be held responsible for them.

References

Akinci, A., Vannoli, P., Falcone, G., Taroni, M., Tiberti, M.M., Murru, M., Burrato, P., Mariucci, M.T., 2017. When time and faults matters: Towards a time-dependent probabilistic SHA in Calabria, Italy. Bulletin of Earthquake Engineering 15, 2497-2524.

Bernard, P., Briole, P., Meyer, B., Lyon-Caen, H., Gomez, J.-M., Tiberi, C., Berge, C., Cattin, R., Hatzfeld, D., Lachet, C., Lebrun, B., Deschamps, A., Courboulex, F., Larroque, C., Rigo, A., Massonet, D., Papadimitriou, P., Kassaras, I., Diagourtas, D., Makropoulos, K., Veis, G., Papazisi, E., Mitsakaki, C., Karakostas, V., Papadimitriou, E., Papanastassiou, D., Chouliaras, G., Stavrakakis, G., 1997. The Ms = 6.2, June 15, 1995 Aigion earthquake (Greece): Evidence for low angle normal faulting in the Corinth rift. Journal of Seismology 1, 131–150. Doi:https://doi.org/10.1023/A:1009795618839.

Briole, P., Ganas, A., Elias, P., Dimitrov, D., 2021. The GPS velocity field of Aegean. New observations, contribution of the earthquakes, crustal blocks model, Geophysical Journal International 226, 468-492.

Console, R., Falcone, G., Karakostas, V., Murru, M., Papadimitriou, E., Rhoades, D., 2013. Renewal models and coseismic stress transfer in the Corinth Gulf, Greece, fault system/ Journal of Geophysical Research, Solid Earth 118, 3655–3673. Doi:https://doi.org/10.1002/jgrb.50277.

Console, R., Carluccio, R., Papadimitriou, E., Karakostas, V., 2015. Synthetic earthquake catalogs simulating seismic activity in the Corinth Gulf, Greece, fault system. Journal of Geophysical Research 120, 326–343. Doi:https://doi.org.10.1002/2014JB011765.

Field, E.H., Jackson, D.D., Dolan, J.F., 1999. A mutually consistent seismic hazard source model for Southern California. Bulletin of Seismological Society of America 89, 559–578.

Ganas, A., 2024. NOAFAULTS KMZ layer Version 6.0 (version 6.0) [Data set]. Zenodo. Doi: https://doi.org/10.5281/zenodo.13168947

Kourouklas, C., 2022. Determination and simulation of strong earthquakes' recurrence times in Greece via the application of stochastic models: contribution on seismic hazard assessment. Ph.D. Thesis, Aristotle University of Thessaloniki,

Thessaloniki, 329 p. Doi: http://dx.doi.org/10.12681/eadd/53270

Matthews, M.V., Ellsworth, W.L., Reasenberg, P.A., 2002. A Brownian model for recurrent earthquakes, Bulletin of Seismological Society of America 92, 2233–2250.

Pace, B., Visini, F., Peruzza, L., (2016). FiSH: MATLAB Tools to Turn Fault Data into Seismic-Hazard Models, Seismological Research Letters, 87, 375-386.

Papazachos, B.C., Papazachou, C.C., 2003. The earthquakes of Greece, Ziti Publications.

Peruzza, L., Pace, B., Cavallini, F., 2010. Error propagation in time- dependent probability of occurrence for characteristic earthquakes in Italy, Journal of Seismology, 14, 119–141.

17th INTERNATIONAL CONGRESS
of the Geological Society of Greece

BULLETIN OF THE GEOLOGICAL SOCIETY OF GREECE, SP. PUBL.

EXTENDED ABSTRACT 176

A preliminary petrographic approach to the pyroclastic rocks (tuffs) of Tilos island

Petros Koutsovitis[1], Gerasimina Pahaki[1], Vasileios Giamas[1], and Lemonia Kalantzi[1]
(1) University of Patras, Greece, pkoutsovitis@upatras.gr

Introduction

Volcanism in the Aegean results after the subduction of the African plate beneath the European. The present-day active volcanic arc consists of five major volcanic centers (Sousaki, Methana-Aegina, Milos-Antimilos, Santorini-Kolumbo, and Nisyros-Kos). In the eastern Aegean, several large-scale volcanic eruptions took place during Late Pleistocene, which produced large quantities and relatively thick layers of pumice and vitric ash. These were distributed throughout various regions, but they are more evident in proximity to the volcanic centers. Their origin is mainly associated with the phreatomagmatic volcanic eruption of Nisyros volcano at eastern flank, which corresponds to the Kyra sequence at 161 ka (Sterba, 2007; Sterba *et al.,* 2011). Pyroclastic deposits in the form of pumice from this eruption have been recorded not only to the southeast at Tilos island but also to the north at Kalymnos Island, and to the east at Datça peninsula in Turkey, expanding over an area of approximately 3000 km^2. KPT pyroclastic deposits have been investigated by Smith *et al.* (1996) and Steinhauser *et al*. (2007) in order to refine the chemical fingerprint of the KPT eruption

Explosive rhyolitic eruptions form one of the most hazardous catastrophic events that can occur on earth (Allen 1999). The eruption of the Kos Plateau Tuff (KPT) produced massive rhyolitic fallout, high-density pyroclastic flows, and massive ignimbrites (Allen, 2001). The inflow of seawater to the magmatic chamber at the early stages of the eruption can be considered as the mechanism that led to a phreatomagmatic type of eruption. The fact that the lithic breccia is followed by the deposition of ignimbrites forms an important volcanological feature which implies the collapse of the caldera and links with its initial stages. This feature has also been noticed in the Minoan eruption of Santorini (Heiken and McCoy,1984). During caldera collapse, the pressure and the mass flux increase simultaneously (Wilson *et al.,* 1980; Carey and Sparks, 1986; Carey and Sigurdsson, 1989). Pyroclastic deposits withhold information about the eruption and/or mass flux nevertheless the precise classification of internal stratigraphy and lithofacies combined with petrographical and geochemical results can pose fundamental objectives regarding the dynamics of the eruption.

Geological Setting

The non-volcanic island of Tilos lies to the southeast of the volcanic islands of Kos and Nisyros. Stratigraphically, Tilos consists of biosparudites limestones and dolomites, locally representing the 'Hallstatt' phase. These rocks date from Triassic to the Lower Jurassic. Furthermore, it consists of Upper Jurassic thin-bedded pelagic plate micritic limestones, Upper Cretaceous pelagic biomicritic limestones as well as pyroclastic deposits from the KPT eruption (Stadlbauer, 1988; Johannes and Sterba, 2007). The pyroclastic rocks are mostly represented by tuffs and pumices, which in most cases correspond to acid compositions (e.g., rhyolite), and date to the Quaternary. According to Allen and Cas (1998), Tilos pyroclastic rocks are subdivided into i) ash-rich facies (~1 meter), ii) pumice-rich facies (~50 centimeters) and iii) pumiceous ignimbrites. The pumiceous ignimbrites, which are correlated with the E stromatographic unit of Nisyros (Allen and Cas, 1998), contain basaltic lithic fragments (Figure 1a) and are rather restricted in only a few outcrops in the field. Based on field observations, pumice-rich facies underlain the ash-rich facies. The ash-rich facies are coarse-grained and exhibit internal wavy and irregular bedforms (Figure 1b), whilst pumice-rich facies display fine lithic lapilli. The lithic clasts of this layer are rather small in size (< 40 centimeters) and the matrix material is fine-grained compared to the overlying pumiceous ignimbrite.

Figure 1. (a) Field photograph from the lower pyroclastic unit, comprising of lithic fragments, many of which are basaltic, (b) Field photograph from pumice succession of pyroclastic tuffs.

Materials and Methods

Twenty rock samples were collected from Tilos Island. These were macroscopically classified into two major groups i) pumices and ii) basaltic lithic fragments taking into account field observations as well. All samples were subsequently crushed and pulverized for conducting bulk mineralogy investigation through X-ray Diffractometry (XRD) as well as polished thin sections were prepared for conducting petrographic examination through transmitted light optical microscopy. Bulk mineralogy of the studied samples was determined using a Bruker D8 Advance Diffractometer with Ni-filtered CuKα radiation at the Research Laboratory of Rocks and Minerals of the University of Patras. The scanning angle (2θ) interval was 2–70° with an angular step size of 0.015° and a time step of 0.1 s. Subsequently, mineral phases were determined using the DIFFRACplus EVA 12® software (Bruker-AXS GmbH, Karlsruhe, Germany) and the ICDD Powder Diffraction File of PDF-2 2006. Petrographic examination was performed using a polarizing petrographic microscope (Leitz Ortholux II POL-BK Ltd., Midland, ON, Canada) at the Research Laboratory of Rocks and Minerals of the University of Patras.

Results-Discussion

In the present study, three main types of pyroclastic rocks were observed based on field observations. Most of the thin layers are ash-rich layers and pumice-rich layers that collapsed and flattened as they were re-heated, whereas in some cases the pumice clasts have relatively high vescularity, revealing high intensity phases. The matrix material is quite friable and finely crystalline, with yellow ash dominating the most outcrops. Lithic fragments show a diversity (e.g., basaltic, pumice) and in restricted outcrops has also established obsidian. Basaltic lithic fragments are mainly found within the lower pyroclastic unit (Figure 1a) are well preserved and have been subjected to only minor alterations. Pumice samples show an excellent color contrast between the various clasts (red, orange, brown, etc.) and the compressed ash (white). The pinkish to brownish hue characteristic for some samples is mainly due to oxidation but could also related to the presence of xenoliths (i.e., basaltic blocks; Figure 2b).

Pyroclastic rocks present vitrophyritic texture and contain plagioclase (mainly albite-oligoclase), clinopyroxenes (augite) and alkali feldspars. They also contain tubular fragments of pumice as well as bonded clay margins on glassy and crystalline surfaces, which record the initial stage of diagenesis in this semi-molten pumice breccia. These clay margins in many cases enclose crystalline and glassy fragments. In some cases, microfossils were also established within the matrix. The pyroclastic texture of most tuffs is not so evidently identified. Basaltic lithic fragments contain plagioclase, clinopyroxene, and alkali feldspars (Figure 3). Despite the glassy and fine-grained nature of the studied rocks, they display trachytic texture and, in some cases, glomeroporphyritic textures (Figure 3).

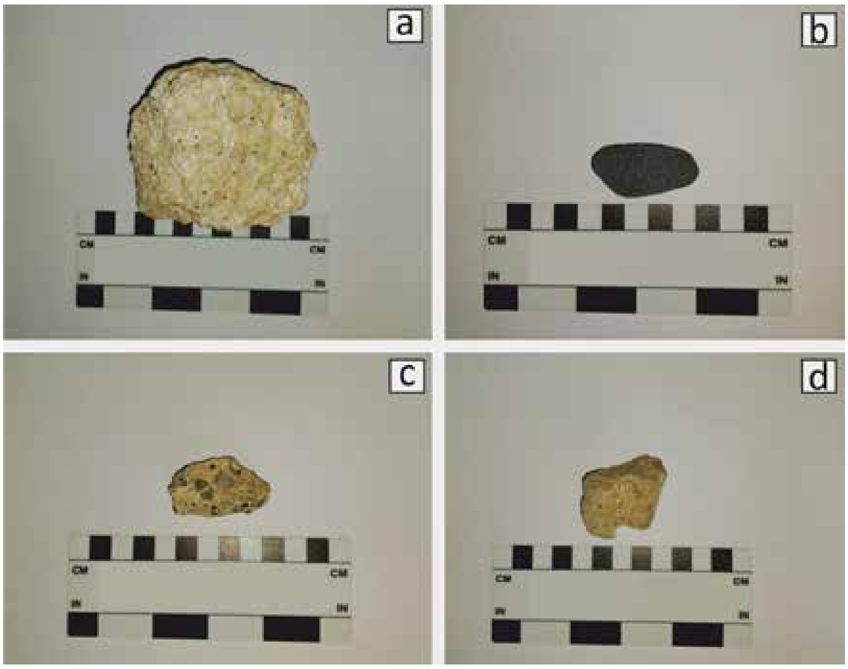

Figure 2: Representative samples from Tilos Island, a) Vesicular pumice, b) Basaltic lithic fragment, c) Pumice with individual clasts, and d) Pumice with low porosity.

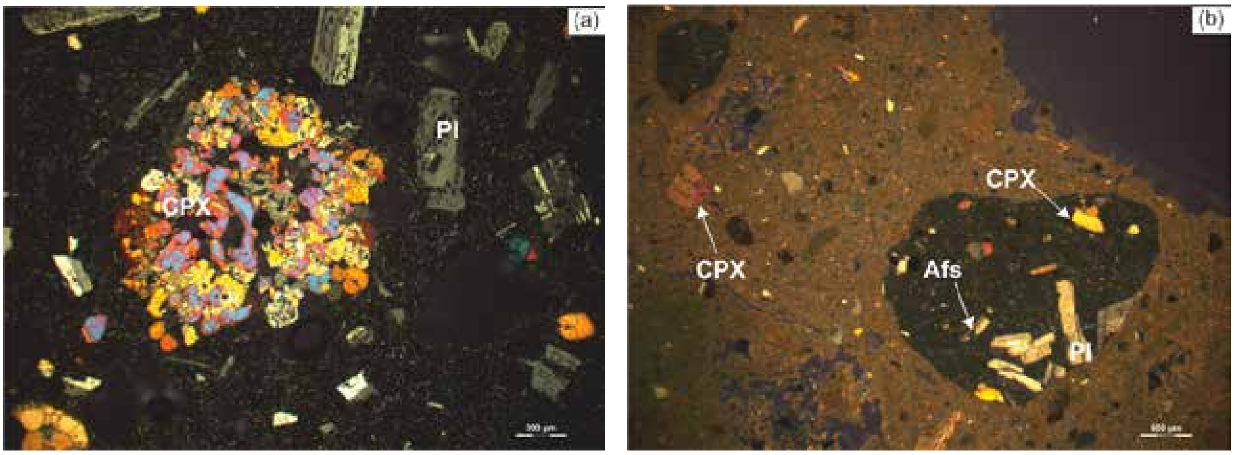

Figure 3. Photomicrographs of: (a) hornblende basaltic lithic fragment with quenched glomerophyric clinopyroxenes (CPX) and plagioclase (Pl) and b) pyroclastic lapilli tuff with devitrified glass with clinopyroxene (CPX) phenocryst and basaltic lithic fragment with clinopyroxene phenocrysts (CPX), plagioclase (Pl) and alkali feldspar (AFS).

Conclusion

The internal stratigraphy and the deposition of the lithofacies reflect a dynamic high-intensity eruption. In particular, the deposition of these basaltic lithic fragments seems to be vent-derived, resulting from the deposition of voluminous ignimbrites. For the case of Tilos, the conduit type of lithic fragments can be an eruptive indicator. Also, the textural changes in the vesicularity of the pumice show possibly two stages of depressurization and the influence of the volatiles during the phreatomagmatic eruption. These patterns have a strong impact, and their understanding would be critical for potential hazard assessment. Through a more comprehensive volcanological view, further investigation combining field observations and detailed mineral chemistry analyses of the fluid inclusion on the lithic fragments and the pumice will highlight the importance of volatiles in post-caldera forming reactions.

References

Allen, S. R. (2001). Reconstruction of a major caldera-forming eruption from pyroclastic deposit characteristics: Kos Plateau Tuff, eastern Aegean Sea. Journal of Volcanology and Geothermal Research, 105, 141–162.

Carey, S., & Sigurdsson, H. (1989). The intensity of plinian eruptions. Bulleting of Volcanology, 51, 28–40.

Carey, S., & Sparks,. (1986). Quantitative models of the fallout and dispersal of tephra from volcanic eruption columns. *Bulleting of Volcanology*, 48, 109–125.

Caliro, S., Chiodini, G., Galluzzo, D., Granieri, D., La Rocca, M., Saccorotti, G., Ventura, G., 2005. Recent activity of Nisyros volcano (Greece) inferred from structural, geochemical and seismological data. Bulletin of Volcanology 67, 358–369.

Johannes, D.I., Sterba., J.H, 2007, Anwendung der Neutronen Aktivierungsanalyse zum Aufbau der Chemostratigraphie einer vulkanischen Eruptionssequenz auf Tilos und Nisyros, Griechenland., pages 7-120.

Heiken, G., & Jr, M. (1984). Caldera development during the Minoan eruption, Thira, Cyclades, Greece. *J. Geophys. Res.*, *89*(B10), 8441–8462.

Nomikou, P., Krassakis, P., Kazana, S., Papanikolaou, D., Koukouzas, N. 2021. The Volcanic Relief within the Kos-Nisyros-Tilos Tectonic Graben at the Eastern Edge of the Aegean Volcanic Arc, Greece and Geohazard Implications, Geosciences 11, 231.

R, A. S., & Cas,. (2001). Transport of pyroclastic flows across the sea during the explosive, rhyolitic eruption of the Kos Plateau Tuff, Greece. *Bulletin of Volcanology*, *62*(6), 441–456.

R, A. S., Stadlbauer, E., & Keller, J. (1999). Stratigraphy of the Kos Plateau Tuff: product of a major Quaternary explosive rhyolitic eruption in the eastern Aegean, Greece. *International Journal of Earth Sciences*, *88*(1), 132–156.

Smith, P.E., York, D., Chen, Y., Evensen, N.M., 1996. Single crystal 40Ar–39Ar dating of a Late Quaternary paroxysm on Kos, Greece: concordance of terrestrial and marine ages. Geophys. Res. Lett. 23, 3047–3050.

Stadlbauer, E., 1988. Vulkanologisch-geochemische Analyse eines jungen Ignimbrites: Der Kos-Plateau-Tuff (Südost-Ägäis). PhD thesis, Freiburg.

Steinhauser, G., Sterba, J.H., Bichler, M., 2007. Chemical fingerprints of pumice from Cappadocia (Turkey) and Kos (Greece) for archaeological applications. Appl. Radiat. Isot. 65, 488–503

Sterba, J.H., 2007. Anwendung der Neutronen-Aktivierungsanalyse zum Aufbau der Chemostratigraphie einer vulkanischen Eruptionssequenz auf Tilos und Nisyros, Griechenland. Ph.D. Thesis, Vienna University of Technology

Sterba, J.H., Steinhauser, G., Bichler, M., 2011. On the geochemistry of the Kyra eruption sequence of Nisyros volcano on

Nisyros and Tilos, Greece. Applied Radiation and Isotopes 69, 1605–1612.

Vougioukalakis, G., 1993. Volcanic stratigraphy and evolution of Nisyros island (Abstracts). Bull. Geol. Soc. Greece 1993, 28, 239–258

.Wilson, L., Stephen, & George, W. (1980). Explosive volcanic eruptions — IV. The control of magma properties and conduit geometry on eruption column behaviour. Geophysical Journal of the Royal Astronomical Society, 63, 117-148

17th INTERNATIONAL CONGRESS
of the Geological Society of Greece

BULLETIN OF THE GEOLOGICAL
SOCIETY OF GREECE, SP. PUBL.

EXTENDED ABSTRACT 177

A preliminary petrographic approach of the altered Triassic volcanic lavas in Argolis, Greece

Petros Koutsovitis[1], Aikaterini Papaioannou[1]
(1) University of Patras, Department of Geology, GR-26504 Patras, Greece
E-mail address: pkoutsovitis@upatras.

Introduction

In the northeastern Peloponnese lies the region of Argolis, an area of significant geological interest, as its geotectonic position belongs to the Sub-Pelagonian zone, characterized by intense and extensive tectonism, involving the presence of five distinct tectonic units. These comprise of: i) Trapezona Unit (M. Triassic - L. Jurassic: limestones, radiolarites, lavas), ii) Demaina Ophiolite Unit (L. – L. Cretaceous: ophiolites, basalts, pillow lavas, limestones, radiolarites, dolerites), iii) Adheres Melange Unit (Palaeocene – Eocene: silt, sandstone, marl and Triassic: limestones, radiolarites and Jurassic: metagranodiorites, andesites, basalts, mineralized sediments, dolomites), iv) Iliokastron Melange Unit (ophiolite melange), v) Faniskos Unit (L. Cretaceous: above the "Trapezona" and "Demaina Ophiolite Unit" units). The region primarily consists of Triassic and Jurassic-aged rocks (Bortolotti et al., 2003; Celet & Ferriere, 1978; Jacobshagen et al., 1978; Gioni, 2021). The study was mostly focused on the Middle Unit, occurring in Central and Northern Argolis (Bortolotti et al., 2001, 2002; Baumgartner, 1985). This investigation integrates field observations with detailed microscopic analyses of the most representative rock samples. Emphasis was given to interpret alteration effects that are a key characteristic of these rocks. The Triassic basaltic rocks of the Middle Unit are classified as trachybasalts (Saccani et al., 2015), mostly in the form of pillow lavas, with OIB and E-MORB geochemical signatures (Baumgartner, 1985; Dostal et al., 1991). The vast majority of these exposed rocks in the field exhibit evidence of low-grade metamorphism and metasomatic processes. The research focuses on characterizing the secondary processes that influenced the Triassic volcanic lavas of the area, with an emphasis on their petrographic and mineralogical classification.

Results - Discussion

The most representative samples were selected for the preparation of thin sections. Through pulverization, the samples were prepared for analyses via X-ray diffractometry (XRD). In addition, the Petrographic study was carried out using an optical microscope for observation of the rocks' mineralogical characteristics.

Residual phases of primary minerals were recorded, due to the significant degree of alteration. These mainly include clinopyroxene (Cpx) and plagioclase (Pl), with the presence of plagioclases being more Ca-rich in their center (An) and more Na-rich at the periphery (Ab), exhibiting the albitization phenomenon. The microcrystals of clinopyroxene appear altered and with intense colors throughout the fundamental mass of the samples. It is observed that the entire glass has been transformed into secondary chlorite, actinolite, and montmorillonite. Additionally, we have the presence of accessory mineral of ilmenite (Ilm), as well as secondary alteration of primary mineralogical components with concurrent formation of chlorite (Chl), epidote (Ep), prehnite (Prh), calcite (Cc) with characteristic zoning and the form of spherical mineral amygdales, while in small-length veinlets analcime (Anl), as well as other zeolites (Zeo), are present.

Additionally, in certain samples, actinolite (Act) and tremolite (Tr) were observed replacing clinopyroxene (Cpx), while there are also microlites of alkaline feldspars (K-feld) and paragonite (Pg). The phenocrysts of quartz (Qz) represent a secondary phase, complementary to chlorite, and they are intensely deformed. The modal composition of secondary zeolites found in some of the samples is estimated to be ~10 vol.%. The type of zeolite observed in most of the samples from the area is Mordenite, as well as Analcime. Specifically, the zeolites appearing in the form of small-sized crystals were observed filling voids and microfractures, indicating hydrothermal processes and a low degree of metamorphism.

The petrographic study of the Triassic lavas of Argolis reveals the significant secondary processes that occurred after the intense volcanic activity during the Triassic period. These processes are generally common for the various Triassic lavas of the Hellenic region (Castorina et al. 2020 - Koutsovitis et al. 2012 - Magganas et al. 1997 - Magganas and Kyriakopoulos 2005 - Pe-Piper and Piper 2002). However, in the study area, the significant involvement of zeolites in the secondary phases stands out, as they locally constitute the dominant metasomatic phase, fully replacing the primary phases. A more precise characterization of the zeolitic phases requires further investigation through mineral chemical analyses methods, while it is also deemed necessary to conduct geochemical analyses to detect trace element variations during the secondary processes.

References

Bortolotti, B., D'Souza, J., Fantini, M., & Megginson, W. L. (2002). Privatization and the sources of performance improvement in the global telecommunications industry. Telecommunications Policy, 26(5-6), 243-268.

Bortolotti, V., Carras, N., Chiari, M., Fazzuoli, M., Marcucci, M., Photiades, A., & Principi, G. (2003). The Argolis Peninsula in the palaeogeographic and geodynamic frame of the Hellenides. Ofioliti, 28(2), 79-94.

Castorina, F., Magganas, A., Masi, U., & Kyriakopoulos, K. (2020). Geochemical and Sr-Nd isotopic evidence for petrogenesis and geodynamic setting of Lower-Middle Triassic volcanogenic rocks from central Greece: Implications for the Neotethyan Pindos ocean. Mineralogy and Petrology, 114, 39-56.

Koutsovitis, P., Magganas, A., Ntaflos, T., Koukouzas, N., Rassios, A.E., Soukis, K., 2020. Petrogenetic constraints on the origin and formation of the Hellenic Triassic rift-related lavas. Lithos 368-369, 105604.

Saccani, E. (2015). A new method of discriminating different types of post-Archean ophiolitic basalts and their tectonic significance using Th-Nb and Ce-Dy-Yb systematics. Geoscience Frontiers, 6(4), 481-501.

17th INTERNATIONAL CONGRESS
of the Geological Society of Greece

BULLETIN OF THE GEOLOGICAL SOCIETY OF GREECE, SP. PUBL.

EXTENDED ABSTRACT 178

Petrographic evidence for the metamorphic conditions in ultramafic rocks at Makrymalli - Evia Island

Petros Koutsovitis[1], Konstantinos Tetisis[1], Georgia Kolovadi[1]
(1) University of Patras, Department of Geology, GR-26504 Patras, Greece
E-mail address: pkoutsovitis@upatras.gr

Introduction

The aim of this announcement is to highlight the greenschist facies as the main metamorphic facies that affected the ultramafic rocks of the Makrymalli area, based on petrographic data. Makrymalli is a region in central Evia (Central Greece). In geotectonic terms, the region belongs to the Pelagonian zone and is mainly comprised of mafic and ultramafic volcanic and sedimentary rocks (Danelian and Robertson, 2001). The extensive ophiolitic complex that represents the ultramafic rocks of the area consists mainly of harzburgites (Danelian and Robertson, 2001), variably serpentinized, including both serpentinites and serpentinized harzburgites, although serpentinized lherzolites were also identified. Their metamorphic grade is classified as greenschist facies, though some evidence suggests that, on local scale, metamorphic conditions may have been more intense (Simantov et al., 1990). These ophiolites are related to the subduction of the oceanic crust of the Tethys Ocean and the subsequent closure of the Pindos and Vardar Oceanic basins; the Pelagonian platform host ophiolitic thrust sheets from both basins.

Results- Discussion

The samples analyzed in this study comprise of serpentinized harzburgites, lherzolites and also serpentinites. They are clearly serpentinized, with lizardite and antigorite occurring in rather balanced amounts. Serpentinization occurs at rates of 75% to 85% on average in microscopic sections. Uralitization is also observed in certain lherzolites, at the expense of relict clinopyroxene. Mesh textures are frequently observed especially in the highly serpentinized varieties. The presence of lizardite and antigorite in the ultramafic rocks of Makrymalli in rather balanced amounts, suggests that metamorphism did not exceed greenschist facies (~320°C - 340°C, $P \approx 6\text{-}7$ kbar; Guillot et al., 2015). This is further supported by the fact that spinel rims were not altered to Cr-magnetites but also because orthopyroxene bastites were pseudomorphically retained their former crystal appearance. These metamorphic conditions are evidently lower than those that were established for the adjacent East Thessaly serpentinites, where the predominance of antigorite corresponds to blueschist facies metamorphism (~ 360–400 °C, $P \approx 11\text{–}12$ kbar) (Koutsovitis, 2017). Furthermore, thin crosscutting chrysotile veinlets, as well as the presence of talc and minor chlorite, point to retrograde low-metamorphic conditions during exhumation. Serpentinization subsequently led to the formation of Fe-oxides such as magnetite in the serpentinite matrix. In some of the serpentinized lherzolites, distinct deformation and undulose extinction was observed in clinopyroxene crystals, suggesting local deformation phenomena. Serpentinites in few cases were locally subjected to local mylotinization and even brecciation, being characterized by their mylonitic fabric and by the higher modal amount of antigorite.

References

Danelian, T., Robertson, A.H.F., 2001. Neotethyan evolution of eastern Greece (Pagondas Mélange, Evia island) inferred from radiolarian biostratigraphy and the geochemistry of associated extrusive rocks. Geological Magazine (3) 138, 345–363.

Guillot, S., Schwartz, S., Reynard, B., Agard, P., Prigent, C., 2015. Tectonic significance of serpentinites. Tectonophysics 646, 1–19.

Koutsovitis, P., 2017. High-pressure subduction-related serpentinites and metarodingites from East Thessaly (Greece): Implications for their metamorphic, geochemical and geodynamic evolution in the Hellenic–Dinaric ophiolite context, Lithos 276, 122-145.

Simantov, J., Economou, C., Bertrand, J., 1990. Metamorphic rocks associated with the central Euboea ophiolite (southern Greece). Some new occurrences. In Ophiolites and Oceanic Crust (eds J. Malpas, E. M. Moores and C. Xenophontos), pp. 285–94. Ophiolites and Oceanic Crustal Analogues. Proceedings of the International Symposium “Troodos 1987”. Geological Survey Department Cyprus, Nicosia.

17th INTERNATIONAL CONGRESS of the Geological Society of Greece

BULLETIN OF THE GEOLOGICAL SOCIETY OF GREECE, SP. PUBL.

EXTENDED ABSTRACT 179

An outline on some of the recently reported granitoids from St. Martin Island

Petros Koutsovitis[1,*], Michiel J. van der Meulen[2], Tirza van Daalen[2], Pavlos Tyrologou[3], Nikolaos Koukouzas[3], Alkiviadis Sideridis[1], Christos Karkalis[3], Michel Grégoire[2], Petros Petrounias[1], Theodoros Ntaflos[5], Konstantinos Lentas[6]

(1) University of Patras, Department of Geology, GR-26504 Patras, Greece
(2) TNO, Geological Survey of the Netherlands, P.O. Box 80015, 2508 TA, Utrecht, the Netherlands
(3) Centre for Research and Technology, Hellas (CERTH), Egialias 52, Marousi 15125, Attica, Greece
(4) Géosciences Environnement Toulouse (GET), CNRS, UPS, IRD, CNES, Université de Toulouse, Observatoire Midi Pyrénées (OMP), 14 Av. E. Belin, 31400 Toulouse, France
(5) University of Vienna, Department of Lithospheric Research, Althanstr. 14, Vienna, Austria
(6) National Observatory of Athens, Institute of Geodynamics, Lofos Nymfon, Athens 11810, Greece
** Corresponding author: Tel.: +30 2610997737; E-mail address: pkoutsovitis@upatras.gr.*

Introduction

St. Martin is located at the northern parts of the Lesser Antilles (Caribbean). Oligocene magmatic rocks include plutonic intrusions and volcanics (Davidson et al., 1993). Their age has been determined between 26 to 31 Ma relying upon K-Ar data (Davidson et al., 1993). The plutonic granitoids mostly comprise of tonalites, quartz-monzodiorites and granodiorites (Davidson et al., 1993, Noury et al. 2021, Koutsovitis et al. 2025). Granitoid plutonism is assigned to subduction and subsequent convergence of the Farallon, South American and North American plates (Lidiak and Jolly, 1996).

For the purposes of the present announcement, we briefly outline some of the findings, recently outlined in detail by Koutsovitis et al. (2025), concerning some of the St. martin granitoids that encompass relatively high modal amounts of mafic minerals.

Results

The recently reported St. Martin melatonalites (Koutsovitis et al. 2025), clearly correspond to granitoids, with their total modal composition of quartz, plagioclase and alkali feldspars exceeding 50 vol.%. Most participating mineral phases are medium grained, suggesting plutonic crystallization condition. Their modal composition was determined through point counting and CIPW calculations. Accessory minerals were determined through microprobe facility. Classification relied upon normative Q, A, P percentages. Their M' colour index, based on the mafic minerals, suggests that these are in fact melatonalites with elevated M' values. They are also characterized by the following features: i) relatively restricted modal amount of quartz, ii) higher normative anorthite than albite, iii) participation of cordierite, orthopyroxene and phlogopite. iv) low LOI contents, in accordance with the presence of phlogopite and complete absence of any alteration effects. Accessory minerals comprise of ilmenite, Ti-magnetite and apatite.

Plagioclase of the St. Martin melatonalites are characterized by their relatively high An components, displaying normal compositional zoning (Koutsovitis et al. 2025); K-feldspars are absent. Orthopyroxenes are enstatites with moderate Mg#, low Al, Cr and Ni contents (Koutsovitis et al. 2025). Clinopyroxenes and amphiboles are absent, in contrast to the other granodiorites present in St. Martin. Phlogopites display rather enhanced Ti and Ba contents, whereas cordierites exhibit rather high Mg values. Geochemical results show that the melatonalites are characterized by their enhanced Ti, Fe and Mg contents (Koutsovitis et al. 2025). Based upon various geochemical classification plots, these rocks correspond to low-K, calcic and magnesian granitoids, with a transitional character between calc-alkaline to tholeiitic (Koutsovitis et al. 2025).

Discussion-Conclusions

Apparently, the presence of cordierite within the melatonalites signifies that these may correspond to S-type granitoids. This is further supported by their peraluminous character (Koutsovitis et al. 2025). However, this is not consistent with their very low-K, as well as their behavior in Harker binary plots, pointing to an I-type character. Furthermore, additional major and trace element ratios comply with restricted involvement of sediments in the source and were more affected by hydrous and slab-derived fluids (Koutsovitis et al. 2025). Geothermometry applications reveal relatively high temperatures for the melatonalites compared to the other granitoids. Pressure calculations show that these were crystallized at the relatively deep parts of the arc (Koutsovitis et al. 2025). It seems that these rocks formed at the early stages of subduction and may likely represent one of the few traces of CLIP influence, associated with early hybridization of the mantle wedge (Koutsovitis et al. 2025).

References

Davidson, J., Boghossian, N.D., Wilson, M., 1993. The Geochemistry of the Igneous Rock Suite of St Martin, Northern Lesser Antilles. Journal of Petrology, 34 (5), pp. 839-866. https://doi.org/10.1093/petrology/34.5.839

Lidiak, E.G., Jolly, W.T., 1996. Circum-Caribbean granitoids: Characteristics and Origin. Int. Geol. Rev. 38, 1098 – 1133. https://doi.org/10.1080/00206819709465385.

Noury, M., Philippon, M., Cornee, J.-J., Bernet, M., Bruguier, O., Montheil, L., Legendre, L., Dugamin, E., Bonno, M., Münch, P., 2021. Evolution of a shallow volcanic arc pluton during arc migration: a tectono-thermal integrated study of the St. Martin granodiorites (Northern Lesser Antilles). Geochem. Geophys. Geosyst. 22, e2020GC009627. https://doi.org/10.1029/2020GC009627.

Koutsovitis, P., van der Meulen, M.J., van Daalen, T., Tyrologou, P., Koukouzas, N., Sideridis, A., Karkalis, C., Grégoire, M., Petrounias, P., Ntaflos, T., Lentas, K., 2025. Granitoids from St. Martin/Maarten Island, Caribbean: Insights on the role of mantle processes in the Lesser Antilles arc. Lithos 494–495, 107926. https://doi.org/10.1016/j.lithos.2024.107926

17th INTERNATIONAL CONGRESS
of the Geological Society of Greece

BULLETIN OF THE GEOLOGICAL SOCIETY OF GREECE, SP. PUBL.

EXTENDED ABSTRACT 180

Mineral mapping using satellite multispectral and hyperspectral data for a pyrite mine in the frame of the m4mining project

Evlampia Kouzeli[1], Olga Sykioti,[2] Konstantinos Nikolakopoulos[1], Saeid Asadzadeh[3], Friederike Koerting[4], Daniel Schläpfer[5]

[1] *GIS and Remote Sensing Lab, Department of Geology, University of Patras, Patras 26504, Greece; e.kouzeli@upatras.gr (E.K.); knikolakop@upatras.gr (K.N.)*
[2] *National Observatory of Athens, Institute for Astronomy, Astrophysics, Space Applications and Remote Sensing, Athens Greece; sykioti@noa.gr (O.S.)*
[3] *Helmholtz Centre Potsdam, GFZ German Research Centre for Geosciences,14473, Potsdam, Germany; saeid@gfz-potsdam.de (S.A.);*
[4] *Norsk Elektro Optikk AS—HySpex Division, Østensjøvei 34, 0667 Oslo, Norway; friederike@neo.no (F.K.);*
[5] *ReSe Applications LLC Langeggweg 3 9500 Wil Switzerland daniel@rese-apps.com (D.S.)*

Introduction and objectives

Mafic sulfide deposits in Cyprus were studied by Hannington et al. (1998) and Adamides et al. (2010). They are composed mostly of pyrite (Parvaz, 2014). The acid mine drainage (AMD) is the result of sulfide minerals and waste oxidation due to exposure to water and oxygen conditions affecting large areas. The case study is the Memi inactive pyrite mine in Nicosia, Cyprus. Herein, we applied Remote Sensing (RS) techniques for the monitoring of the mine area. To this purpose, the Visible Near Infrared and Shortwave Infrared (VNIR-SWIR) spectral bands of multispectral (MSI) and hyperspectral satellite imagery (HSI) were used. More specifically, a combination of Sentinel-2, WorldView-3 (WV3), both VNIR and SWIR, and Environmental Mapping and Analysis Program (EnMap) data were employed. Two different spectral libraries, namely the United States Geological Survey (USGS) and Jet Propulsion Laboratory (JPL) spectral libraries, and three spectral processing methods were selected to analyze the data in the frame of the m4mining project.

The m4mining project aims to provide an integrated remote sensing approach for mapping and monitoring active and inactive mining sites. MSI and HSI imaging are combined with in situ measurements and are utilized for material identification from the detailed mine face to the site scale using unmanned aerial vehicles (UAVs) and satellite sensors. Central to the proposed work is a synergistic combination of UAV and satellite-based processing algorithms, workflows, and decision-making tools at timescales required to impact active operations and environmental and risk management of tailings and waste sites.

This study aims to investigate the suitability of EnMap, Sentinel-2, and WV3 data for the detection and mapping of minerals related to pyrite -AMD.

Data and methodology

The Memi mine is located in Nicosia district, Cyprus (35° 2’30.11”N, 33° 2’19.61”E). Six minerals (Table 1, Figure 1) namely hematite, goethite, ferrihydrite, jarosite, schwertmannite, and copiapite (hereafter endmembers) were selected for AMD identification within the inactive pyrite mine study area. USGS and JPL spectral libraries were used to retrieve the spectral signatures of hematite, goethite, and jarosite which were convolved to EnMap, Sentinel-2, and WV3 spectral bands while spectral signatures of ferrihydrite, schwertmannite, and copiapite were not available in the JPL library.

The endmember selection criteria were the grain size and the spectral purity of the sample. A spectral signature with fine to medium grain size approximated the grain size of the minerals in the study area while the spectral purity defined the presence and/or the absence of contaminants. We selected spectral signatures with the least possible contaminants and a fine to medium grain size.

Table 1. Description of endmembers used in this study. For each mineral in the second column, the first row corresponds to the spectral signature name in the USGS spectral library, and the second row corresponds to the spectral signature name in the JPL spectral library. The spectrum title and information were retrieved from the corresponding ancillary file of each mineral from each spectral library.

Mineral	Spectrum title	Reference
Hematite	Hematite_FE2602_BECKb Hematite alpha Fe 2O 3 [oxide-none-fine-o01a]	Meerdink et al, 2019 Kokaly et al., 2017 Baldridge et al., 2009
Goethite	Goethite_HS36.3_BECKb Goethite alpha Fe^3+O(OH) [hydroxide-none-fine-oh02a]	
Ferrihydrite	Ferrihydrite_GDS75_Syn_F6_BECKb	
Jarosite	Jarosite_JR2501_(K)_BECKb Jarosite KFe 3^3+(SO 4) 2(OH) 6 [sulfate-none-fine-so07a]	
Schwertmannite	Schwertmannite_BZ93-1_BECKb	
Copiapite	Copiapite_GDS21_BECKb	

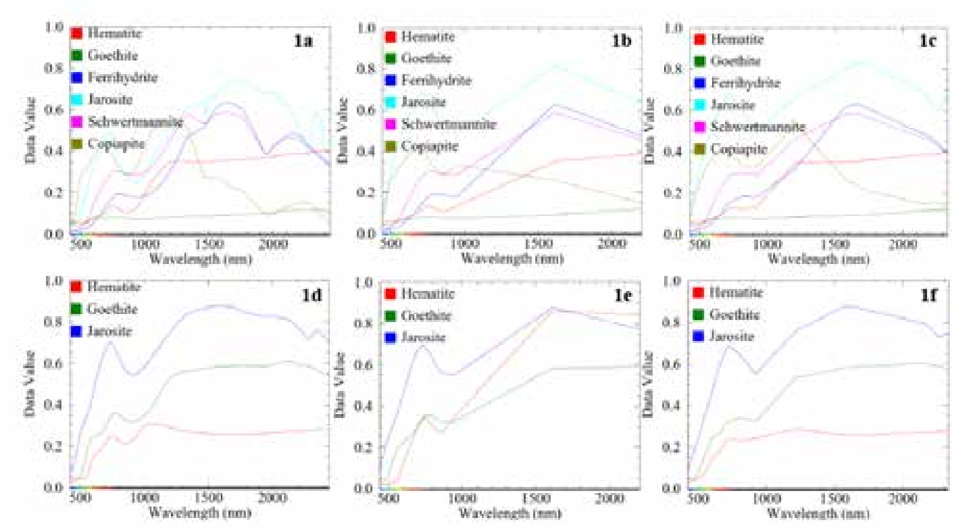

Figure 1. Mineral spectral signatures used in this study, (a) retrieved from the USGS spectral library convolved to the EnMap spectral bands; (b) retrieved from the USGS spectral library convolved to the Sentinel-2 spectral bands; (c) retrieved from the USGS spectral library convolved to the WV3 VNIR and SWIR spectral bands; (d) retrieved from the JPL spectral library convolved to the EnMap spectral bands; (e) retrieved from the JPL spectral library convolved to the Sentinel-2 spectral bands; (f) retrieved from the JPL spectral library convolved to WV3 VNIR and SWIR spectral bands.

For the purpose of this study, a Sentinel-2 Level 2A VNIR-SWIR image (12 spectral bands) was used, acquired on 2024/07/26. The archived WV3-VNIR and SWIR datasets (16 spectral bands) were also used (acquired on 2018/04/03-VNIR and 2020/09/12-SWIR). The WV3 data were atmospherically corrected by ReSe Applications. Although the WV3 data were acquired on two different dates, namely 2020 and 2018, after atmospheric corrections they were handled as one dataset (a total of 16 spectral bands). The atmospherically corrected EnMap data (acquired 2024/07/14) VNIR-SWIR (224 spectral bands) were conceded by the Helmholtz Centre Potsdam - GFZ German Research Centre for Geosciences (GFZ). The EnMap spectral bands 131-135 (1342.82-1390.48nm) were set as bad bands and excluded from the analysis. The spatial resolutions of EnMap, Sentinel-2, and WV3 data used in this study are 30m, 10m, and 3.7m respectively. The EnMap, Sentinel-2, and WV3 datasets were analyzed as layer-stacked (VNIR-SWIR) data: one layer stack for each sensor (EnMap, Sentinel-2, and WV3). To discriminate the spectral bands between the different types of sensors, we hereafter named the EnMap spectral bands Ebx (e.g. Eb1), the Sentinel-2 ones Sbx (e.g. Sb1), and WV3 ones Wbx (e.g. Wb1). The reflectance values were between 0 and 1 and each scene was cropped to the mine area extent. The mineral reflectance values issued from the spectral libraries vary between 0 and 1 as well. An NDVI threshold of 0.25 was applied to mask vegetation.

Three different processing methods were employed: spectral indices (SI), band depth (BD) analysis using continuum removal, and spectral angle mapping (SAM). The selected spectral indices used in this study are given in Table 2 and some of the results are presented in Figure 2. For BD and SAM calculations, six USGS endmembers and three JPL endmembers were used to detect the wavelength/band of the minerals' diagnostic absorption features (Sykioti et al, 2023) and compare the spectral angle between the spectral vectors of image pixels and reference spectra, respectively. Moreover, in BD, pixels with absorption <0.01 were masked while the threshold angle for SAM was set to 0.35 for EnMap (USGS endmember), 0.30 for EnMap (JPL endmember), 0.40 for Sentinel-2 (USGS & JPL endmembers), and 0.25 for WV3 (USGS and JPL endmembers).

Table 2. Overview of used spectral indices applied to this study. The SIs for EnMap and Sentinel-2 were retrieved from van der Meer et al. (2014), Ge et al. (2020), and the Index DataBase (https://www.indexdatabase.de/, accessed 02/11/2025). The SIs for WV3 were retrieved from Hildebrand (2022).

Spectral Index	EnMap	Sentinel-2	WV3
Ferrous Iron	(Eb216/Eb60) + (Eb22/Eb37)	(Sb12/Sb8a) + (Sb3/Sb4)	(Wb13/Wb7) + (Wb3/Wb5)
Ferric Iron	(Eb37/Eb22)	(Sb4/Sb2)	Wb5/Wb3
Ferric Oxides	(Eb164/Eb60)	(Sb11/Sb8a)	Wb11/Wb7

Results and Conclusions

SI maps: Using the SIs, we mapped ferric iron, ferrous iron, and ferric oxides in different spectral and spatial resolutions (Figure 2). As seen in Figure 2, generally, the SI ferrous iron values obtained were higher than the SI ferric iron ones. Furthermore, the EnMap and Sentinel-2 ferric iron maps were presented a similar spatial pattern and generally the same SI values. On the other hand, the SI ferrous iron showed higher values in EnMap data than in Sentinel-2 data. As for WV3, we observed locally high values (mostly on the roads) but generally, the SI values were lower than the corresponding ones in the EnMap and Sentinel-2 data.

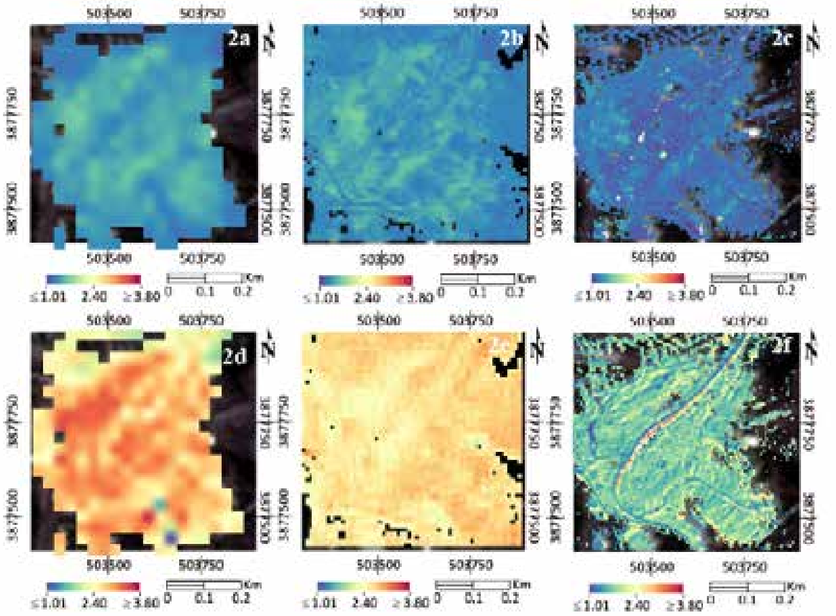

Figure 2. SI maps of ferric iron index applied on (a) EnMap (2024/07/14); (b) Sentinel-2 (2024/07/26); and (c) WV3 (2020/2018) and ferrous iron index applied on (d) EnMap (2024/07/14); (e) Sentinel-2 (2024/07/26); and (f) WV3 (2020/2018). For comparison purposes, all images have a common color scale (1.01-3.80). The background image is the TCI of Sentinel-2 (2024/07/26). SI values <1.01, indicating the absence of the material, are masked.

Absorption maps: the absorption feature maps (BD method) were also created from each one of the EnMap, Sentinel-2, and WV3 datasets. Based on the maximum absorption features observed within each endmember spectrum (issued from both the USGS and JPL spectral libraries and for each endmember), we located the unique diagnostic feature which was not observed in the other mineral spectral signatures and thus, it spectrally differentiates the specific mineral from the others. The spectral bands/wavelengths corresponding to these absorption features were presented in Table 3 and Figure 3. In Figure 3, we presented indicative the hematite, goethite, and jarosite absorption maps. In particular for the EnMap dataset, we identified more than one characteristic absorption features for each endmember. However in Table 3, for EnMap, we presented the spectral band with the highest absorption of all other bands.

Table 3. Wavelength position (and corresponding band) and corresponding band depths (in the continuum removed (CR) spectra) of the characteristic diagnostic absorption feature of each one of the six minerals, namely hematite, goethite, ferrihydrite, schwertmannite, copiapite, and jarosite in (a) EnMap, (b) Sentinel-2 and (c) WV3 spectral bands retrieved from both USGS and JPL spectral libraries. Not available: mineral's spectral signature was not available in the specific spectral library, and -: no spectral feature was detected that differentiates this mineral from the others.

	EnMap		**Sentinel-2**	**WV3**	
Endmember	USGS	JPL	JPL	USGS	JPL
Hematite	871.7nm (Eb76) CR value 0.45	540.4nm (Eb26) CR value 0.40	864.7nm (Sb9) CR value 0.63	660.3nm (Wb5) CR value 0.64	546.6nm (Wb3) CR value 0.53
Goethite	501.2nm (Eb18) CR value 0.77	482.4nm (Eb14) CR value 0.38	664.6nm (Sb4) CR value 0.94	-	660.3nm (Wb5) CR value 0.95
Ferrihydrite	515.6nm (Eb21) CR value 0.34	Not available	Not available	-	Not available
Jarosite	2265.7nm (Eb196) CR value 0.61	439.7nm (Eb5) CR value 0.75	-	-	2259.8nm (Wb15) CR value 0.95
Schwertmannite	482.4 (Eb196) CR value 0.34	Not available	Not available	-	Not available
Copiapite	879.6nm (Eb77) CR value 0.59	Not available	Not available	-	Not available

Concerning the USGS endmembers, for hematite the characteristic absorption features were possible to define with EnMap and WV3 data. For goethite, ferrihydrite, jarosite, schwertmannite, and copiapite, this was possible only with the EnMap dataset. For Sentinel-2 data, no characteristic absorption feature was identified for these minerals. As for the JPL endmembers, hematite and goethite were differentiated with EnMap, Sentinel-2, and WV3 data while jarosite only with EnMap and WV3. The corresponding absorption maps (1-CR values) are presented in Figure 3.

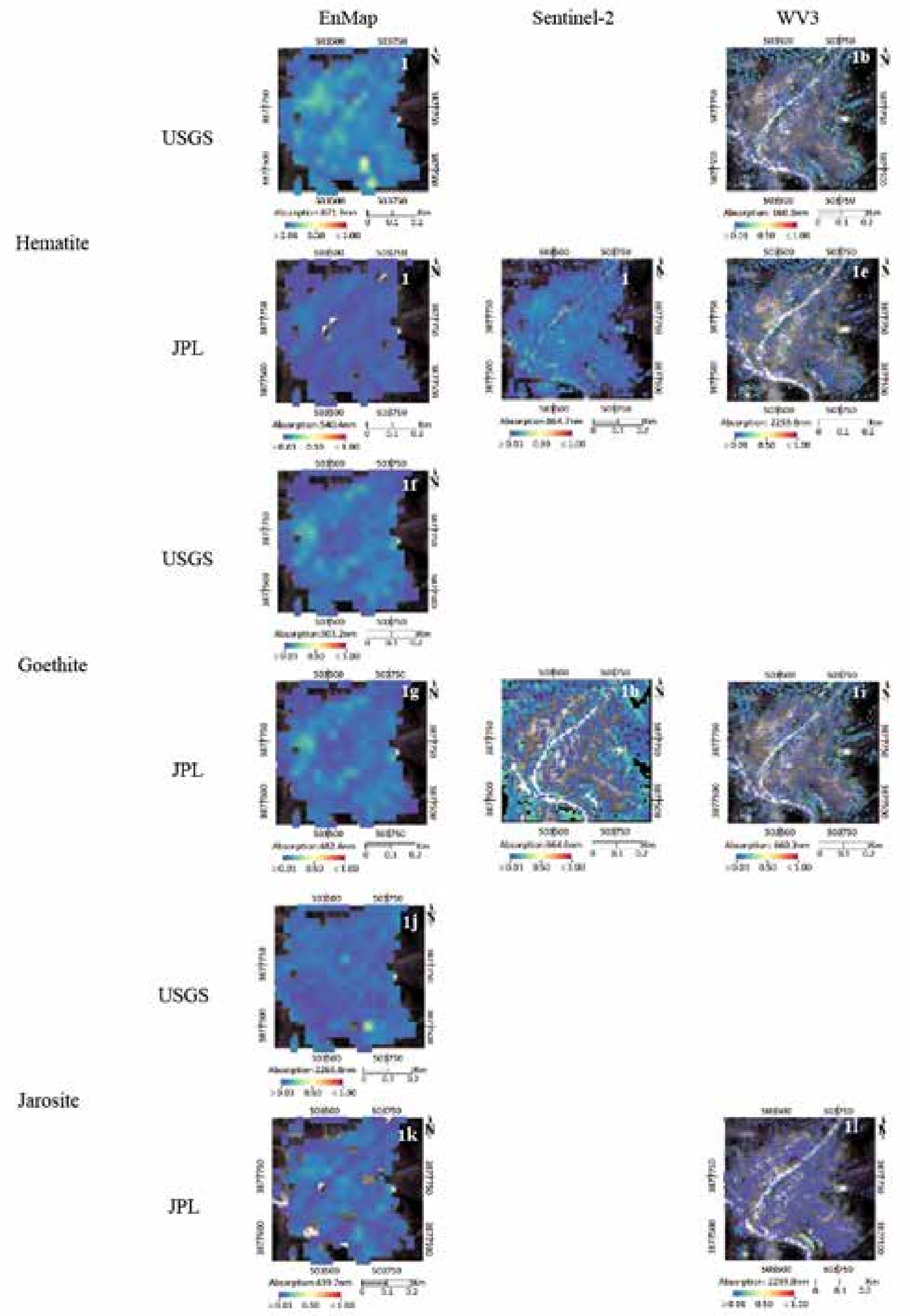

Figure 3. Absorption (1- CR) maps: Hematite-USGS (a) EnMap (2024/07/14) centred at 871.7nm; (b) WV3 (2020/2018) centred at 660.3nm. Hematite- JPL (c) EnMap (2024/07/26) centred at 540.4nm; (d) Sentinel-2 (2024/07/26) at 864.7nm; (e) WV3 (2020/2018) at 546.6nm. Goethite – USGS (f) EnMap (2024/07/14) centred at 501.2nm. Goethite -JPL (g) EnMap (2024/07/14) centred at 482.4nm; (h) Sentinel-2 (2024/07/26) centred at 664.6nm (i) WV3 (2020/2018) centred at 660.3nm. Jarosite-USGS (j) EnMap (2024/07/14) centred at 2265.7nm. Jarosite-JPL (k) EnMap (2024/07/14) centred at 439.7nm; and (l) WV3 (2020/2018) at 2259.8nm. The values range from 0.01 to 1 with 0.01 corresponding to minimum absorption and 1.0. to maximum absorption. The background image is the TCI of Sentinel-2 (2024/07/26)

SAM classification maps: Concerning SAM using the USGS endmembers (Figure 4), we mapped goethite, jarosite, copiapite, and schwertmannite with EnMap data with a threshold angle of 0.35, we mapped jarosite and copiapite with Sentinel-2 data using a threshold angle of 0.40, and all minerals with WV3 with a threshold angle of 0.25, except from hematite. Concerning SAM using the JPL endmembers, we mapped hematite, goethite, and jarosite with EnMap data using a threshold angle of 0.30, we mapped hematite and jarosite with Sentinel-2 data using a threshold angle of 0.40, and we mapped hematite, goethite, and jarosite with WV3 data using a threshold angle of 0.25. Hematite and jarosite were mapped with all three datasets.

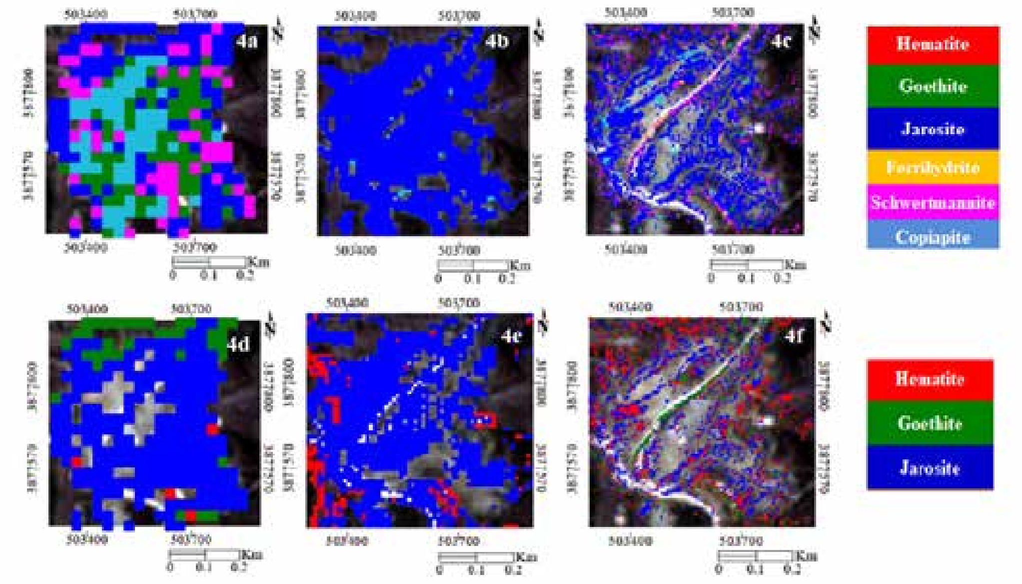

Figure 4. SAM classification maps. In the top row, SAM classification maps using the USGS endmembers for (a) EnMap (2024/07/14); (b) Sentinel-2 (2024/07/26); and (c) WV3 (2020/2018). In the bottom row, the SAM classification maps using JPL endmembers for (d) EnMap (2024/07/26); (e) Sentinel-2 (2024/07/26); and (f) WV3 (2020/2018). The background image is the TCI of Sentinel-2 (2024/07/26).

Overall, ferric iron, ferric oxides, and ferrous iron were mapped with EnMap, Sentinel-2, and WV3 data (SI method) (Figure 2). The presence of ferric iron could be considered as an indicator for the presence of several iron oxide/ hydroxides minerals such as hematite, goethite, and ferrihydrite while the ferrous index for copiapite. In this case study, ferric and ferrous iron seem to be present within the entire study area but the highest SI values were observed in pixels corresponding to the weathered slope areas of the tailings. As expected, the SI maps issued from WV3 data provide more details due to the high spatial resolution of the dataset (3.7m). The observed higher ferrous iron values compared with the ferric iron ones could be attributed to the copiapite presence. It must be noted here, that the higher the value, the higher the probability of the mineral's presence within the pixel.

Based on the analysis of the characteristic absorption features (BD analysis), concerning the USGS endmembers, in EnMap data the higheest absorptions (1-CR) were observed for hematite (0.41), jarosite (0.39), and copiapite (0.40), and the lowest ones for goethite (0.23) and schwertmannite (0.23). In WV3, the corresponding hematite absorption is 0.50. As for the JPL endmembers, we identified hematite (0.11), goethite (0.23), and jarosite (0.15) with EnMap, hematite (0.23) and goethite (0.33) with Sentinel-2, and hematite (0.53), goethite (0.60), and jarosite (0.35) with WV3. The highest absorption values were obtained for hematite, goethite, and jarosite using WV3 data but for a relatively small number of pixels within the image located mainly at the weathered slope areas and in certain flat areas (the same locations observed in the SI maps). Among the JPL-endmembers, hematite and goethite were detected in all three types of datasets and among the USGS-endmembers, only hematite and jarosite were identified using EnMap and WV3.

In the case of SAM using USGS endmembers, we note that jarosite and copiapite were mapped using EnMap, Sentinel-2, and WV3. Goethite and schwertmannite were also mapped using EnMap and WV3 but by applying a different threshold angle. Jarosite seems to be the spatially dominant mineral in the Sentinel-2 image. In the case of SAM using the JPL endmembers, jarosite also seems to be present within most image pixels followed by hematite and goethite.

The multispectral and hyperspectral images were acquired under optimal conditions: between late spring and early autumn with high sun elevation and no precipitation weather conditions. The temporal pattern of the data does not affect the results while there were no terrain modifications (e.g., human interventions) in the area during the study period. Results were not affected by possible vegetation changes while a) bare soil dominates the study area, b) a 0.25 NDVI threshold was applied to mask the sparse vegetation, or c) remained unchanged which cross-validated with historical Google Earth imagery. Finally, the viewing angle of each satellite is practically vertical and combined with the smooth terrain slopes in the study area, resulting in no shadow effects on one or more images.

Concluding, the detection of the specific minerals (using USGS or JPL endmembers) at different wavelengths using EnMap, Sentinel-2, and WV3 data seems to be influenced by each sensors' specifications (e.g. band wavelength position, spectral range, spectral band, spatial resolution, acquisition date etc.) and the inherent physical properties of the samples the spectral signatures of which are retrieved from the spectral library and used as endmembers (e.g. particle size, specific chemistry, environmental context). The SI, BD, and SAM indicate the presence of AMD-related minerals in the study area revealing higher values within the mine area. This is an ongoing work. The verification of the obtained results using in-situ samplings, chemical and mineral laboratory analyses, and in-situ spectral measurements is currently under study.

Acknowledgements

Funded by the European Union

"m4mining" project is funded by the European Union's Horizon Europe programme under Grant Agreement ID 101091462.

References

Adamides, N.G., 2010. Mafic-dominated volcanogenic sulphide deposits in the Troodos ophiolite, Cyprus Part 2-A review of genetic models and guides for exploration. Applied Earth Science 119, 193–204.

Baldridge, A.M., Hook, S.J., Grove, C.I., Rivera, G., 2009. The ASTER Spectral Library Version 2.0. Remote Sensing of Environment, 113, 711-715.

Ge, W., Cheng, Q., Jing, L., Fei, W., Zhao, M., & Ding, H. (2020). Assessment of the capability of Sentinel-2 imagery for iron-bearing minerals mapping: A Case Study in the Cuprite area, Nevada. Remote Sensing, 12(18), 3028.

Hannington, M.D., Galley, A.G., Herzig, P.M., Petersen, S., 1998. Comparison of the tag mound and stockwork with Cyprus-type massive sulfide deposits. Proceedings of the ocean drilling program, scientific results, 158

Hildebrand, J.C., 2022. Acid Mine Drainage and Tailing Monitoring using Satellite Imagery for VMS-type deposits in the Republic of Cyprus MSc. Thesis, (Scientific Technical Report STR; 22/08), Potsdam: GFZ German Research Centre for Geosciences, 16p.

Meerdink, S.K., Hook, S.J., Roberts, D.A.,Abbott, E.A., 2019. The ecostress spectral library version 1.0. Remote sensing of environment, 230(111196), 1–8.

Kokaly, R.F., Clark, R.N., Swayze, G.A., Livo, K.R, Hoefen, T.M., Pearson, N.C., Wise, R.A., Benzel, W.M., Lowers, H.A., Driscoll, R.L., Klein, A.J., 2017. USGS Spectral Library Version 7, Data series 1035

Parvaz, D.B., 2014. Oxidation Zones of Volcanogenic Massive Sulphide Deposits in the Troodos Ophiolite, Cyprus: Targeting Secondary Copper Deposits. Ph.D. Thesis, University of Exeter, Exeter, 58 p.

Sykioti, O., Ganas, A., Vasilatos, C., Kypritidou, Z., 2023. Investigating the capability of Sentinel-2 and Worldview-3 VNIR satellite data to detect mineralized zones at an igneous intrusion in the Koutala islet (Lavreotiki, Greece) using laboratory mineralogical analysis, reflectance spectroscopy and spectral indices. Bulletin of the Geological Society of Greece, 59, 175–213.

van der Meer, F.D., van der Werff, H.M.A., van Ruitenbeek, F.J.A., 2014. Potential of ESA's Sentinel-2 for geological applications. Remote Sensing of Environment 148, 124–133.

17th INTERNATIONAL CONGRESS
of the Geological Society of Greece

BULLETIN OF THE GEOLOGICAL SOCIETY OF GREECE, SP. PUBL.

EXTENDED ABSTRACT 181

A Novel Approach to Flood and Drought Management in Arid Regions using Multi-Agent Systems

Kravari K.[1], Emmanouloudis D.[1]

(1) UNESCO Chair for the Conservation and Ecotourism of Riparian and Deltaic Ecosystems, Democritus University of Thrace, Greece, kkravari@affil.duth.gr; kkravari@csd.auth.gr

Research Highlights

Multi-Agent Systems offer a promising decentralized approach for integrated flood and drought management in arid Greek regions, enabling more effective responses to extreme weather events. A conceptual case study demonstrates the potential of this framework to improve real-time decision-making and promote sustainable water resource management in the face of climate change.

Introduction

In Greece, like worldwide, arid and semi-arid regions face the alternating challenge of water scarcity and erratic rainfall patterns (Kourgialas, 2021; Nabinejad et al., 2023; El-Hamid et al., 2024). Hence, they are highly vulnerable to both droughts and floods. Unfortunately, the frequency and intensity of such extreme weather events are increasing, making traditional management methods obsolete. As a result, both the scientific community and society are now looking for more dynamic and adaptive approaches. This paper studies a novel approach to integrated flood and drought management using Multi-Agent Systems (MAS), an Artificial Intelligence technology. The proposed MAS framework consists of a network of intelligent agents, each responsible for a specific aspect of water resource management, including real-time data collection, flood prediction, drought monitoring, water allocation, and infrastructure control. This distributed and adaptive approach enables autonomous agents to have common goals, allowing them to interact and cooperate to achieve them. As a result, they will contribute to effective responses in case of extreme weather events, promoting sustainable water resource management. More specifically, Intelligent Agents in the context of a water resource management system, can integrate diverse data sources, support real-time decision-making, and enable responses to floods and droughts. The rest paper presents the architecture of the proposed MAS, including the types of agents, their interactions, and the data they utilize. A case study for a representative arid region presents the added value of the proposed approach.

The Challenge of Flood and Drought Management

It is known that arid regions have a low rainfall average and limited water resources. Yet, something is changing revealing serious challenges. The frequency and intensity of droughts are constantly increasing but at the same time, extreme precipitation events are more frequent nowadays. This is quite confusing for the traditional approaches that are often based on historical data and centralized control. On one side, droughts create a shortage of water for agriculture and industry besides domestic use, on the other side, flooding destroys infrastructure and causes loss of life, while even water sources can be polluted. The aim, therefore, of this paper is to deal with such challenges, proposing an integrated MAS approach that will be able to deal with both flood and drought management at the same time. To this end, a complex architecture with various intelligent agents is needed. Agents like Sensor Agents, Prediction Agents, Decision-Making Agents, and Infrastructure Control Agents should be represented in the framework. Each of these agents types should have specific responsibilities and well-designed knowledge-based interaction strategies.

Multi-Agent Systems for Flood and Drought Management

Although Artificial Intelligence (AI) is not new, over the last few years it reached a broader audience since it seems to be everywhere. However, despite the available technology in so many fields, there is still a lack of scientific approaches that could be used effectively in environmental real-life problems. Typically, AI approaches tend to enable machines to perform tasks that typically require human intelligence. But what we really need is approaches that can think, act and decide like humans when there are complex phenomena, unusual pattern and urgent situations (Chen, 2022; Sarker, 2022). In this context, an AI technology that is promising is the intelligent agents (Anshuka, 2022). An intelligent agent is an autonomous entity that can monitor its environment through sensors and act upon that to achieve its goals. The simplest type of agents is the reactive agents but here we need the complex cognitive agents those that are equipped with knowledge base and inference capabilities. These agents are able to know facts about their environment, when needed they can use this knowledge for reasoning and decision-making. In atypical form, a knowledge base includes facts, rules, and other forms of structured information. This allow agents to deal with complex cases, learn from their experience, and even explain their actions. Hence, this type of agents is appropriate for the needs of a water resource management systems, since they are capable of understanding complex hydrological processes and take critical decisions under uncertainty, and as such they are adopted in the current proposed approach.

The Architecture of the Multi-Agent System Approach

As already discussed, multi-agent systems are a promising solution for flood and drought management. The proposed MAS approach consists of a diverse network of intelligent agents, representing different roles and assigned with different responsibilities. The architecture of the system consists of five agent types (Figure 1); namely Sensor Agents, Prediction Agents, Decision-Making Agents, Infrastructure Control Agents, and Communication Agents.

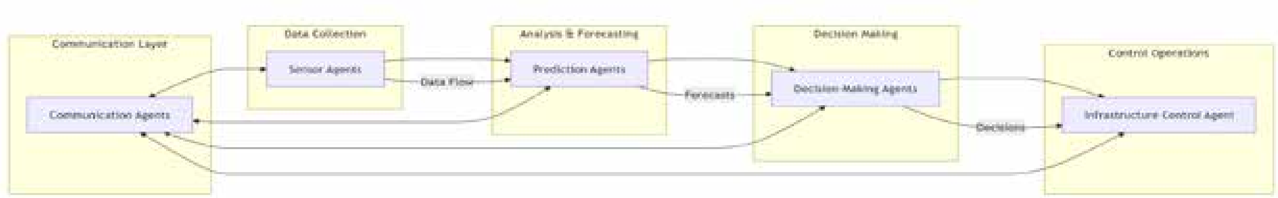

Figure 1. Agent types in the Multi-Agent System approach.

Sensor Agents are able to collect real-time data from various sources. These may include weather stations, river gauges, soil moisture sensors, and reservoir levels. Prediction Agents then receive the data and feed hydrological models or machine learning algorithms to forecast, for instance, flood risks and drought severity. Later, the Decision-Making Agents based on these predictions and some pre-defined rules could make decisions depending on the case. The decision could be related to water allocation, reservoir operation, or flood control measures. Of course, these decisions should somehow be implemented, hence, the Infrastructure Control Agents will follow by implementing the decisions made by the decision-making agents. They could for instance control pumps, gates, and other infrastructure components. Finally, the Communication Agents are responsible for keeping the team informed and functioning by sharing the necessary information between agents. It is worth mentioning here that there are approaches where agents communicate and negotiate with each other without the need for communication agents, however, in this approach we adopted their use to ensure smooth information sharing, making the already complex architecture of the system more light. In this context, consider the following example; during a heavy rainfall event, sensor agents collect data on rainfall intensity and river levels. Prediction agents use this data to forecast flood risk. Decision-making agents then determine the appropriate flood control measures, such as opening floodgates or diverting water to retention basins. Infrastructure control agents execute these decisions.

The mathematical background of the proposed approach is quite complex since the Multi-Agent System (MAS) should deal with different cases of flood and drought. The agents should be able to provide specific functionalities complying with different upcoming events to remain flexible and efficient. Figure 2 presents the mathematical components for each agent type but it should be clear that in a specific use case or scenario, only some of these components are triggered based on the agents' strategies and some pre-defined rules that depict the potential case. More specifically, Sensor Agents primarily deal with data. Hence, their case is quite straightforward. For calibration purposes, they use linear or non-linear functions to convert raw sensor readings into meaningful units, such as voltage to water level. For purposes of filtering, they use some statistical methods like Kalman and Savitzky-Golay filters to reduce noise in the data. Finally, they can use common statistical measures like mean, median, and standard deviation for aggregation since they have to summarize data from multiple sensors or time steps. On the other hand, Prediction Agents are responsible for hydrological modeling and, in some cases, machine learning. Hence, they are the most mathematically intensive agents in the system. As far as it concerns the hydrological models, the approach is based on sound physical laws, like conservation of mass, momentum, and energy, and some empirical relationships which is more difficult to incorporate in the system. Some of the examples that are studied are the rainfall-runoff models, in an attempt to use equations for describing how rainfall translates into streamflow. The unit hydrograph theory is the core theory here but the Horton's infiltration equation will follow. Of course, these models are not enough, hence, hydraulic models are also studied in an attempt to describe water flow in rivers and channels. Manning's and Saint-Venant's equations are some of the studied approaches. In the cases in which machine learning is needed, namely, cases where we have plenty of datasets, linear, polynomial, and support vector regression are the core cases. These models learn patterns from data and can be used to predict water level or flow. Sometimes, we need to classify cases and predict the type of an event. In such cases, the decision trees, random forests, and neural networks are mainly used to predict flood risk in terms of low, medium, or high. It should be mentioned that optimization is not part of this approach yet but gradient descent, genetic algorithms, or particle swarm optimization seem promising for the aforementioned hydrological and machine learning models.

The following simplified example explains better the approach; a prediction agent that uses historical data to estimate the values of a and b using the least squares regression method. The agent has to predict river flow (Q) based on rainfall (R). A simple linear regression model used by this agent is $Q = a + bR + \varepsilon$, where Q is the predicted river flow, R is the rainfall, a is the intercept, and b is the slope which represents the relationship between rainfall and flow, and ε is the error term. Now consider a more complex event like heavy rainfall. During the event, Sensor Agents collect data on rainfall intensity, river levels, and soil moisture. Prediction Agents have to use this data to forecast river flow and flood risk. Later the Decision-Making Agents will determine appropriate flood control measures, such as opening floodgates. For this example, the rainfall intensity r(t) will be constant at 20 mm/hr for 3 hours. So, r(t) = 20 mm/hr for $0 \leq t \leq 3$ hours, and r(t) = 0 otherwise. We also assume that the river water level h(t) is initially h(0) = 1.5 m while the initial soil moisture is s(0) = 60%. For demonstration purposes, we assume that it remains relatively constant during the short period of the rainfall event. Firstly, we use a simplified unit hydrograph with a peak of 10 $m^3/s/hr$ at t = 2 hours and a base width of 4 hours. For simplicity, we assume also that all the rainfall becomes excess rainfall r_e(t). So, r_e(t) = r(t) = 20 mm/hr for $0 \leq t \leq 3$ hours. We need to convert this to consistent units with the unit hydrograph (m^3/s), assuming a catchment area of 1 km^2 (10^6 m^2). So, r_e(t) = (20 mm/hr) * (1 m/1000 mm) * (10^6 m^2) * (1 hr/3600 s) = 5.56 m^3/s for $0 \leq t \leq 3$ hours. Based on the aforementioned simplified assumptions, the direct runoff will rise linearly to a peak and then fall linearly. Peak flow q_peak = r_e * (area under unit hydrograph) = 5.56 m^3/s * (0.5 * 4 hr * 10 $m^3/s/hr$) = 111.2 m^3/s and time to peak 2 hours. Hence, the direct runoff q(t) will be a triangle, rising linearly from 0 to 111.2 m^3/s in 2 hours, then falling linearly back to 0 over the next 2 hours. Now, the machine learning model, an LSTM Network, will follow. Here we assume that the network is trained, so given the rainfall initial river level and soil moisture, predicts a peak flow of 120 m^3/s at t = 2.5 hours. The agent trusts the LSTM slightly more in this heavy rainfall scenario and uses weights $w_1 = 0.4$ for the unit hydrograph model, and $w_2 = 0.6$ for the LSTM. Hence, at the LSTM peak time, t = 2.5 hours, the fused prediction is q_fused(2.5) = (0.4 * 111.2 m^3/s) + (0.6 * 120 m^3/s) = 44.48 m^3/s + 72 m^3/s = 116.48 m^3/s. Finally, the agent proceeds with the flood risk assessment which is simplified for the example since in real cases many factors beyond just river flow should be taken into account. Yet, in the context of the example. We set a flood warning threshold of 100 m^3/s. so, since q_fused(2.5) > 100 m^3/s, the agent outputs a fused river flow forecast with a peak of approximately 116.5 m^3/s around 2.5 hours and gives a flood warning, like "High Flood Risk" or similar.

Following the work conducted from the prediction agents, Decision-Making Agents are responsible for decision making, proposing specific actions. These agents have to use the predictions provided by the aforementioned agents along with some pre-defined rules. Although, there various technologies that can be used, in this approach the agents are rule-based. This means that they are based mainly on if-then-else rules and thresholds. For instance, a simple example is "If water level > X, then open floodgate Y". Hence, these agents are actually based on logic, pretty much like humans, making the decision-making process transparent and explainable. More specifically, the core of these agents is their knowledge base, which consists of a set of rules. Each rule has a set of conditions and an action. Typically, the conditions are comparisons between predicted values, like water level and flow rate, and predefined thresholds. The actions are specific guidelines like opening floodgates or adjusting pump rates. A typical rule is in the form of *IF (Condition 1) AND (Condition 2) AND ... AND (Condition N) THEN (Action)*. Below are presented some examples for purposes of better understanding. R1 and R2 are related to flood control, R3 and R4 are related to drought management while are related to water allocation.

R1: IF (Predicted Water Level > Flood Warning Threshold) AND (Rainfall Intensity > Heavy Rainfall Threshold) THEN (Open Floodgate Y to Level Z)

R2: F (Predicted River Flow > Critical Flow Rate) THEN (Activate Emergency Flood Protocol)

R3: IF (Soil Moisture < Drought Threshold) AND (Reservoir Level < Low Reservoir Threshold) THEN (Implement Water Restrictions – Level 1)

R4: IF (Groundwater Level < Critical Groundwater Level) THEN (Issue Drought Warning to Farmers)

R5: IF (Reservoir Level > Optimal Level) AND (Downstream Flow Requirements Met) THEN (Increase Water Release for Irrigation)

R6: IF (Water Demand Forecast > Available Water) THEN (Implement Water Conservation Measures)

It is clear from these examples that thresholds are crucial, since they define the boundaries that trigger specific actions. These thresholds can be pre-defined and fixed or dynamic, adjusted on real-time conditions or historical data. For example, the "Flood Warning Threshold" might be a fixed water level, or it could be dynamically adjusted based on the current river flow and downstream conditions. Sometimes Decision-Making Agents have to also use logical operators like AND, OR, and NOT to create complex rules with multiple conditions, like in the following example.

R7: IF (Predicted Water Level > Flood Warning Threshold) AND (Rainfall Intensity > Heavy Rainfall Threshold) AND (Downstream Reservoirs Not Full) THEN (Open Floodgate Y to Level Z)

Of course, all these rules would be useless without the proper inference engine. The inference engine checks the conditions of each rule and if they are met, the rule is "fired," and the corresponding conclusion is extracted. Hence, this agent type is equipped with proper inference engines. Currently, explainability is not included in the system but it is still quite easy to understand why a particular action was taken because the rules are clearly defined. It is also worth mentioning that rules can be easily added, modified, or removed, making the system adaptable to changing conditions or new knowledge. This approach is actually mainly based on rules because rule-based systems provide a good balance between complexity and performance which is convenient for many water resource management problems.

Next, Infrastructure Control Agents will take the conclusions and turn them into actions. For this purpose, depending on the available infrastructure, equations describing the behavior of pumps, gates, and other infrastructure components are used when there is an automation possibility. In cases where this is not possible, the information provided by the prediction agents can be used by humans to manually take the necessary actions. Finally, the Communication Agents will handle the information exchange throughout the whole procedure. Typically, they use graphs to create a communication network between agents allowing them to reach each other more easily.

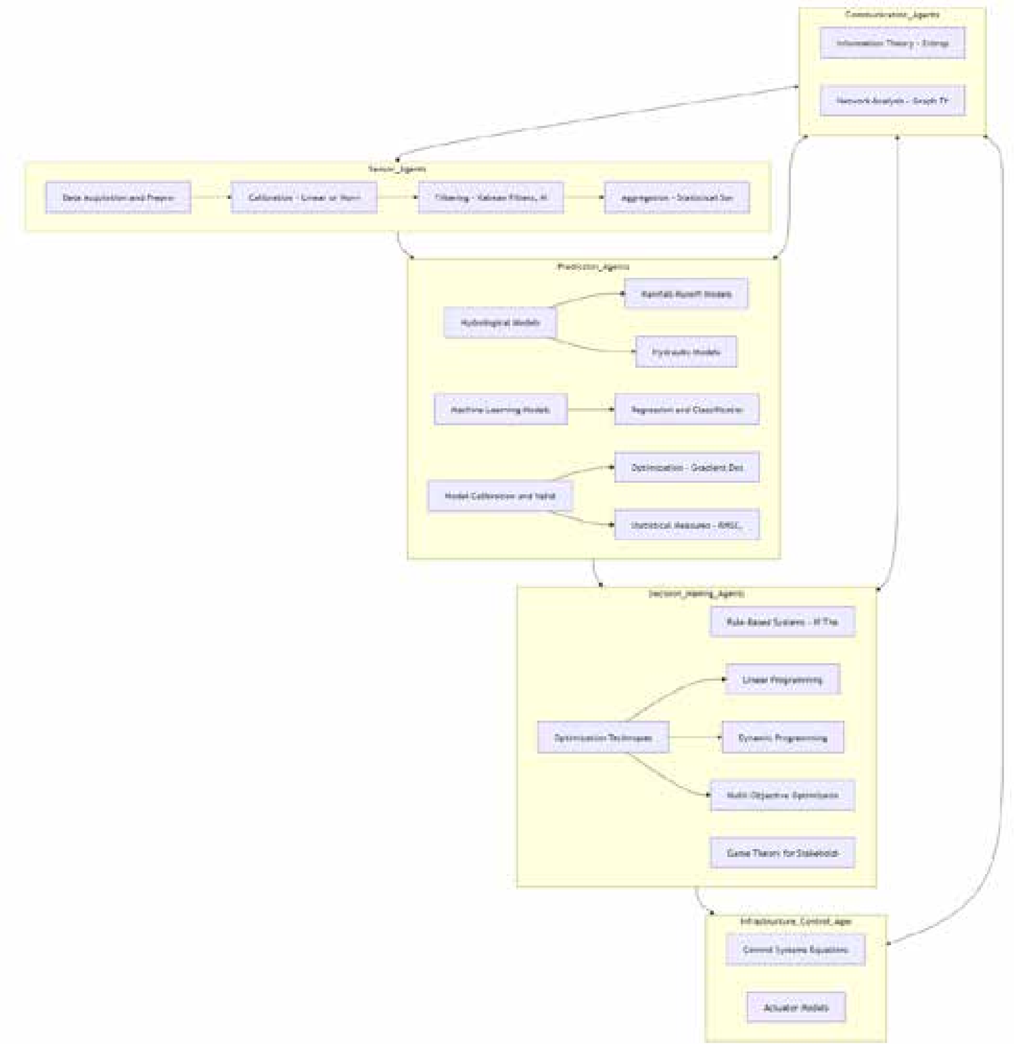

Figure 1. Background of the agent types.

The Technical Implementation of the Multi-Agent System

This section discuss core concepts of the technical implementation of the proposed Multi-Agent System. The chosen implementation language is Python which provided flexibility with several libraries for data handling, numerical computation, allowing integration with hydrological and machine learning models. The system implements the five aforementioned agent types as follows.

Each SensorAgent is initialized with a sensor_type, like “rainfall” or “river_level”, and a location identifier. For simulation purposes, the collect_data() method simulates the data acquisition process, generating a random value within a realistic range for the specified sensor type but in case of real datasets the method will process sensor data. Additionally, this method adds a timestamp to each data point, enabling temporal analysis which important when we have to adapt to pattern changes.

Each PredictionAgent is initialized with model_weights, allowing for flexible configuration of the weighting between different prediction models. The predict_flood_risk() method combines the outputs of a simplified unit hydrograph calculation and a placeholder machine learning prediction. The unit hydrograph calculation is simplified for research purposes but it could be replaced with a proper SWAT model integration using a library like pyswat in a real application. Libraries like TensorFlow or PyTorch (Ansel et al., 2024) are used here. The outputs from the simplified unit hydrograph and the placeholder are combined using a weighted average, controlled by the model_weights.

Each DecisionMakingAgent is initialized with a set of rules. The make_decision() method iterates through the rules, evaluating the conditions using Python's eval() function. This allows for flexible definition of conditions using comparison operators and logical connectives. However, using eval() can pose security risks if the rules are defined by untrusted sources. Hence, in the future a safer rule evaluation method will be implemented. The agent returns the action associated with the first rule whose conditions are met. The rules as discussed are designed to trigger actions based on predicted flood risk, soil moisture levels, and river levels.

Each InfrastructureControlAgent uses the execute_action() method to receive the action as input and prints a simulated execution message or in cases that there is an APIs or hardware control interface this method can interface with the physical infrastructure like floodgates or pumps.

Each CommunicationAgents uses the broadcast_message() method to allow agents to communicate with each other. The log_data() method is also crucial for recording the simulation results. It uses the json library to store the data in a structured JSON format, making it easy to parse and analyze the results later.

The interactions between the agents follow a defined sequence where Sensor Agents collect data, which is then used by Prediction Agents to forecast flood risk. Decision-Making Agents use these forecasts and their rule base to determine appropriate actions. Finally, Infrastructure Control Agents execute these actions. The Communication Agent logs all relevant data at each time step.

Mention that sensor data is stored as a list of dictionaries within each SensorAgent. Each dictionary contains the timestamp, value, and location of the sensor reading while the CommunicationAgent uses the json library to log the data from all agents in a structured JSON format.

The current implementation uses placeholder values for the hydrological and machine learning models. Later, when the system will be used in real-world scenario some integrations will be needed such as the integration with SWAT by using a Python library like pyswat to interact with the SWAT model or the integration with a pre-trained LSTM network by loading the trained model, i.e. from a saved file, into the PredictionAgent. Libraries like TensorFlow or PyTorch are already used and could support this. For the current research phase, the simulation loop consists of a predefined number of time steps. At each time step, sensor data is collected, predictions are made, decisions are taken, actions are executed, and all relevant data is logged. This loop structure allows for simulating the system's behavior over time and analyzing its response to different events.

Conceptual Case Study: Thessaly, Greece

A conceptual case study for the Thessaly region in Greece demonstrates the added value of the proposed Multi-Agent System (MAS) approach. Thessaly is a representative arid region which is characterized by limited water resources, rainfall patterns, and a high vulnerability to both drought and flood events. This conceptual case study discusses how the MAS approach can address the challenges in the area by integrating real-time data, employing intelligent prediction, and facilitating coordinated decision-making. More specifically, thessaly is an agricultural region, heavily reliant on irrigation. Its water resources are under significant pressure due to increasing demand and decreasing rainfall. The region experiences frequent droughts, leading to water shortages and economic losses. Yet, the last years intense rainfall events triggered flash floods, causing life losses, damage to infrastructure and agricultural lands. This makes Thessaly a really complex hydrological case (Xafoulis, 2023).

The proposed MAS can integrate data from existing meteorological and hydrological networks in Thessaly since there are ready installed stations there. This includes mainly rainfall data from weather stations, but also some river level data from gauging stations, soil moisture data from dedicated sensors, and reservoir level data. Of course, additional sensor deployments in strategic locations would be needed to cover the area. For the purposes of this case study, the agents within the MAS are trained using historical data from these sources. This historical data are used to calibrate the hydrological models and train the machine learning modelsemployed by the Prediction Agents. In real-life, real-time data streams would continuously update the models and inform the decision-making process. For now, a simulated heavy rainfall event, similar in magnitude to historical flood events in Thessaly, is introduced into the model. The Sensor Agents collect "real-time" rainfall data, which are transmitted to the Prediction Agents. The Prediction Agents, utilizing the calibrated hydrological and machine learning models, forecast the river flow and potential flood inundation areas. The Decision-Making Agents, based on pre-defined rules and the flood forecast, then optimize reservoir operations, determining the appropriate release rates to minimize downstream impacts. Simultaneously, the MAS generate timely warnings to local communities through communication channels like, SMS alerts. The Infrastructure Control Agents execute the reservoir operation decisions, adjusting gate openings and water releases.

This simulation takes into account three locations, Larissa, Trikala, and Volos, where the Sensor Agents record the rainfall intensities during a simulated heavy rainfall event as depicted in Table 1.

Table 1. Simulation values for the heavy rainfall event.

Time (hours)	Larissa (mm/hr)	Trikala (mm/hr)	Volos (mm/hr)
0	5	7	3
1	15	20	10
2	25	30	18
3	20	25	15
4	10	12	8

Based on this rainfall data and other relevant inputs, the Prediction Agent predicts a peak river flow of 280 m³/s at 4 hours. Part of the Decision-Making Agent knowledge base is presented below.

Rule1: IF (Predicted River Flow > 250 m³/s) AND (Reservoir Level < 90%) THEN (Open Floodgate A to 70% and Floodgate B to 50%)

Rule2: IF (Predicted River Flow > 200 m³/s) AND (Reservoir Level < 80%) THEN (Open Floodgate A to 50%)

Rule3: IF (Predicted River Flow > 150 m³/s) THEN (Issue Flood Warning to Larissa and Trikala)

Hence, since the predicted river flow exceeds 250 m³/s, and assuming that the reservoir level is at 85%, Rule1 is triggered. The Decision-Making Agent instructs the Infrastructure Control Agent to open Floodgate A to 70% and Floodgate B to 50%. A flood warning is also issued to Larissa and Trikala (Rule3). As a result, the floodgates are opened, reducing the peak flow downstream to 220 m³/s.

Conclusion and Future Work

This paper proposed an integrated approach towards flood and drought management within an arid area using a MAS. The MAS framework consists of Sensor, Prediction, Decision-Making, Infrastructure Control, and Communication Agents presents a novel, decentralized solution for mitigating the challenges imposed by extreme weather events. The Python implementation of the MAS was developed in a flexible language with extensive libraries, detailing both the functionalities of each agent type and how they interact. A conceptual case study for the Thessaly region in Greece showcased the potential benefits from the MAS in managing a flood scenario. The obtained results were promising, although there are a number of limitations regarding the present research. The existing implementation is using simplified models and placeholder values. A subsequent step would be to embed real-world hydrological models, such as SWAT, along with the trained machine learning models, like LSTMs, into the Prediction Agents. This will involve access and processing of real-world datasets from the Thessaly region or elsewhere, including historical rainfall, river flow, soil moisture, and other relevant variables. Furhermore, the rule-based decision-making could be further enriched with fuzzy logic or defeasible logic, to handle uncertainties and increase the accuracy of decision-making. Interaction between agents may be explored further either by implementing negotiation protocols or other collaborative mechanisms. The Infrastructure Control Agents need to be connected with the real physical infrastructure through APIs or hardware interfaces, enabling automated control of floodgates, pumps, and other devices.

References

Kourgialas, N.N., 2021. A critical review of water resources in Greece: The key role of agricultural adaptation to climate-water effects. Science of The Total Environment. 775, 145857.

El-Hamid, H.F., Zeleňáková, M., Soľáková, T., Saleh, O.K., El-Dakak, A.M., 2024. Monitoring flood and drought risks in arid and semi-arid regions using remote sensing data and standardized precipitation index: A case study of Syria. Journal of Flood Risk Management 17(1), e12961. https://doi.org/10.1111/jfr3.12961

Nabinejad, S., Schüttrumpf, H., 2023. Flood Risk Management in Arid and Semi-Arid Areas: A Comprehensive Review of Challenges, Needs, and Opportunities. Water, 15(17), 3113. https://doi.org/10.3390/w15173113

Xafoulis, N., Kontos, Y., Farsirotou, E., Kotsopoulos, S., Perifanos, K., Alamanis, N., Dedousis, D., Katsifarakis, K., 2023. Evaluation of Various Resolution DEMs in Flood Risk Assessment and Practical Rules for Flood Mapping in Data-Scarce Geospatial Areas: A Case Study in Thessaly, Greece. Hydrology, 10(4), 91. https://doi.org/10.3390/hydrology10040091

Sarker, I.H. , 2022. AI-Based Modeling: Techniques, Applications and Research Issues Towards Automation, Intelligent and Smart Systems. SN COMPUT. SCI. 3, 158. https://doi.org/10.1007/s42979-022-01043-x

Chen, J., Sun, J., & Wang, G., 2022. From Unmanned Systems to Autonomous Intelligent Systems. Engineering, 12, 16–19. https://doi.org/10.1016/j.eng.2021.10.007

Ansel, J., Yang, E., He, H., Gimelshein, N., Jain, A., Voznesensky, M., ... & Chintala, S., 2024. PyTorch 2: Faster Machine Learning Through Dynamic Python Bytecode Transformation and Graph Compilation. In Proceedings of the 29th ACM International Conference on Architectural Support for Programming Languages and Operating Systems, 2, 929–947. Association for Computing Machinery. https://doi.org/10.1145/3620665.3640366

Anshuka, A., van Ogtrop, F.F., Sanderson, D.,Leao Z. S., 2022. A systematic review of agent-based model for flood risk management and assessment using the ODD protocol. Nat Hazards 112, 2739–2771. https://doi.org/10.1007/s11069-022-05286-y

17th INTERNATIONAL CONGRESS of the Geological Society of Greece

BULLETIN OF THE GEOLOGICAL SOCIETY OF GREECE, SP. PUBL.

EXTENDED ABSTRACT 182

Contemporary distributed block deformation in the South Aegean Sea (Greece), deduced by the analysis of continuous GNSS measurements

Kravvariti Ph.[1], Tzanis, A.[1], Sakkas, V.[1], Kranis H.[2]

(1) Section of Geophysics and Geothermy, Department of Geology and the Geo-environment, National and Kapodistrian University of Athens; atzanis@geol.uoa.gr.

(2) Section of Dynamic, Tectonic and Applied Geology, Department of Geology and the Geo-environment, National and Kapodistrian University of Athens

Introduction / Background

The south Aegean Sea and its adjacent areas are a highly segmented tectonically active domain, characterised by high-rate extension and severe crustal thinning. The different segments (blocks) that make up the south Aegean crust are bounded by significant fault zones and/or dislocation surfaces whose relative motion varies in size and direction. Over the past several decades, the recorded seismicity of the S. Aegean was sparse, scarce, and of generally low intensity. Thus, it cannot assist in adequately resolving regional tectonics.

Hitherto knowledge of tectonic regime was mainly based on the sparse earthquake record, a significant number of shallow marine seismic surveys, minimal use of geophysical potential field data, bathymetry and Differential GPS measurements. All these efforts achieved remarkable results for the methods employed and some resulted in block tectonic models. One of the first approaches by McClusky et al. (2000) identified a South Aegean microplate and determined its motion. Later, Nyst and Thatcher (2004), observed NW-SE trending extension on the Dodecanese Islands, proposing as well that the Peloponnese and the Central and South Aegean belong to a block with internal deformation zones. Reilinger et *al*. (2006) suggested that the kinematics of the south Aegean could be explained by a three-microplate model. Floyd et *al*. (2010) introduced a 15-block model and Briole et *al*. (2021) a 5-block model consistent with known regional-scale structures of the area, but is also rather coarse and with awkwardly shaped blocks (e.g. that of the Central Aegean. Finally, by interpreting a combination of GPS and palaeomagnetic data Lazos et *al*. (2022) propose the existence of an NNE-SSW 'boundary' extending from the west coast of Chios Island and through Paros Island terminating offshore to the south of western Crete; this is referred to as the Mid-Cycladic Lineament and is suggested to delimit areas rotating clockwise to its west counterclockwise to it east.

Herein, we use Differential GNSS measurements augmented with Seismotectonic information and geophysical data to outline the regional tectonic structure and kinematics of the South Aegean Region. Most hitherto work based on GNSS data has studied the deformation of the S. Aegean area by *referring* the velocity or displacement vectors to *remote* locations, usually in Eurasia (e.g. Potsdam, Germany), or the ITRF system as in Fig. 2). While this approach is informative and very useful in studying the *large-scale (whole-plate)* deformation of the Aegean, *it fails* to *resolve* the kinematics/pattern of relative block motions at local- and regional-scales and, therefore, assist in understanding the regional tectonics regime(s). The present study *departs* from this norm by attempting to inquire about *relative block motions* using *local reference points*, thus assisting in understanding the regional pattern(s) of tectonic deformation. Along this vein, if the regional tectonic structure comprises a mosaic of moving rigid blocks separated by active major faulting, it is straightforward to study the motion of any given block *relative* to others by letting some fixed observation point on the immobile block define the origin of a *local reference frame* and subtracting the velocity vectors of *all* other observations points from the velocity vector of the origin. Effectively, the present work expands on that of Sakkas et al. (2020) but incorporates additional cGNSS measurements, strain field computations and seismotectonic information. The resulting tectonic model has significant similarities to that of Sakkas et *al*. (2020), albeit with differences in the configuration and boundaries of the crustal blocks.

Data and Methods

We use data from 54 permanent, continuously recording GNSS stations (cGNSS), all of which are onshore and distributed over the Cyclades, Dodecanese, Crete, Eastern Peloponnese, Attica and Euboea as shown in Fig. 1. They belong to several networks operated by different institutions and agencies. Specifically, two belong to the network of the National and Kapodistrian University of Athens; www.remsenslab.geol.uoa.gr), one to the COMET network (Centre for the Observation and Modelling of Earthquakes, Volcanoes and Tectonics; comet.nerc.ac.uk/), eight to the NCAD (National Cadastre and Mapping Agency S.A. (www.hepos.gr), nine to the NOANET (Geodynamic Institute of National Observatory of Athens; Ganas *et al*., 2008; Chousianitis *et al*., 2021) and 32 to the private sector METRICA S.A. network (www.metrica.gr/diktyo-hxgn-smartnet). All data sets span a mean period of five (5) years, but their majority exceeds three years with many spanning almost one decade. The primary data were processed with the Bernese v5.2 software (Dach et *al*., 2015) to generate high-precision time series of daily coordinates. We also considered (processed) displacement time series from two stations of the Geodetic Laboratory of Nevada (MAGNET + Global GPS Network Map (unr.edu)). The annual velocity of each station was obtained from the slope of the least-squares line best fitting the coordinate time series.

The observed velocity field in the ITRF 2008 reference frame was subjected to strain analysis using the *grid*_strain package by Pesci and Teza (2007), a grid with a cell dimension of 30km and no interpolation. The results are shown in Fig. 6. The recovered strain values correspond to high and mid-significance, so that only points sufficiently close to the cGNSS stations would be included in the calculations. This prevented the introduction of potentially misleading information in areas with sparse or no station coverage. Even so, in cases where the distribution of GNNS stations is one-sided, the calculated strain values should be interpreted with caution.

Finally, to further constrain the relative motion between blocks and the resulting tectonic model, we included seismotectonic information in the form of 1147 focal mechanisms of *crustal* (less than 30km deep) earthquakes with $M_w \geq 4$, spanning the period 1904–2022. This dataset is a combination of the data bank used by Kassaras *et al.* (2016), which covers the period 1904-2016, as augmented by the first Author to the year 2022 using the same criteria to ensure homogeneity. The focal mechanisms are also illustrated in Fig. 6.

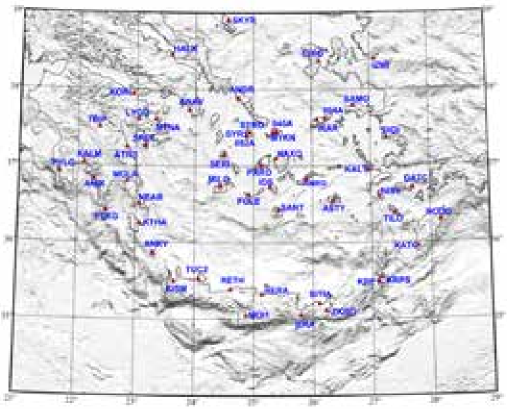

Figure 1. The continuously recording permanent GNSS network used in the analysis. See text for details.

Results

Motion Relative to the ITRF 2008 Reference Frame: The horizontal velocity vectors relative to the ITRF 2008 reference frame are shown in Figure 2. Error ellipses are drawn at the tips of the velocity vectors at the 95% confidence level (used throughout). In this frame, the motion of the entire South Aegean area appears quasi-uniform in a south-westerly direction and at rates of the order of 20mm/year. Minor local differentiations are evident in the rate and/or direction of the velocity vectors, but their interpretation in terms of local to regional kinematics is not easy, if at all possible. The same difficulty arises when the velocity is referred to a remote point on the surface, located in Eurasia or Africa. The local differentiations in crustal deformation can be resolved by using local reference points: herein we use the stations ASTY (Astypalaea Island in the Dodecanese), NAXO (Naxos Island in the Cyclades), ANAV (Anavyssos, Attica).

Motion Relative to ASTY (25.38°E, 37.10°N) on Astypalaea Island (Figure 3): Significant changes in the sense of motion can be observed (a) Relative to a NE-SW line joining the islands of Kos, Astypalaea (ASTY) and Anafi (ANF), and b) relative to a line between Anafi (ANF) and Kasos islands, extending in a NW-SE direction between Crete and Karpathos (KRP). In addition, the stations located in the north and west sectors of the study area *diverge* from those in the south and east sectors. Moreover, and importantly, the SE Dodecanese (Nisyros, Tilos, Rhodes etc.) appears to comprise a block moving to the east-northeast relative to the KOS-ASTY-ANF and ANF-Kasos lines in a sense *sinistral* with respect to the KOS-ASTY-ANF line. Accordingly, the KOS-ASTY-ANF and ANF–KASOS lines appear to be parts of significant tectonic boundaries.

Motion Relative to NAXO (25.38°E, 37.10°N) on Naxos Island (Figure 4): Here we observe a *very* significant change in the sense of motion relative to a NE-SW line joining Kalymnos (KALY), Amorgos (AMRG) and Santorini (SANT). The southeastern part of this line coincides with the southern boundary of the Anhydros Basin, forming between Amorgos and Santorini. All stations located in the Cyclades Archipelago generally drift with very low relative velocities associated with significant error ellipses that hinder their interpretation, while they exhibit significantly non-uniform orientations. These may be attributed partly to their proximity to the local reference point (small displacement/ large error) and partly to small-scale distributed internal deformation in the “Cyclades Block” (non-uniform orientations). Exceptions to this pattern appear to be the islands Santorini (SANT) and Folegandros (FOLE), which diverge from the rest of the Cyclades relative to an NW-SE line extending between the islands Anafi (ANF) and Ios (IOS). In addition, there is evidence of convergence between east Crete (TUC2) - Anthikethyra (ANKY)and Kythera (KTHA) on one hand, and Santorini (SANT) – Folegandros (FOLE) on the other. Finally, the SE Dodecanese, to the south of the KOS-ASTY-ANF and east of the ANF-KASOS lines respectively, *diverges* from the areas to the north and west of these boundaries at *very high rates*.

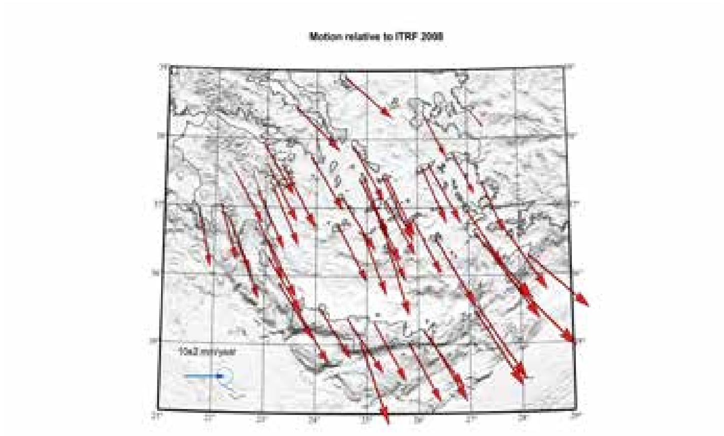

Figure 2. Horizontal velocities of the GNSS stations data in the ITRF2008 reference frame.

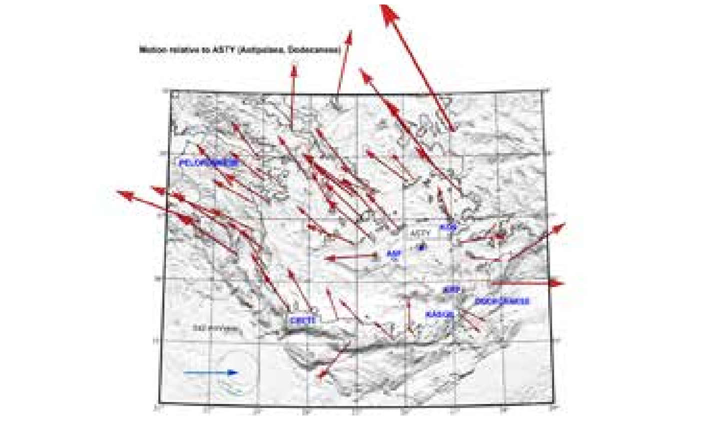

Figure 3. Horizontal velocities of the GNSS relative to the ASTY station.

Motion Relative to ANAV (23.91°E, 37.74°N) at Anavyssos, Attica (Figure 5): It is evident that in this local reference frame, the line Ikaria (IKAR) – Naxos (NAXO) – Paros (PARO) – Milos (MILO) defines a boundary so that: a) Stations to the north of the line and the west of longitude W of 24°E describe mainly NE-SW trajectories, approximately parallel to the south branches of the westward extension of the North Anatolian Fault into the Aegean; b) stations to the north of the line diverge northwards and, c) stations in the vicinity of this line describe NE-SW to E-W trajectories. Significantly, all stations south of the KOS-ASTY-ANF line and east of the ANF-KASOS lines, i.e. the Dodecanese, *diverge* rapidly in a South-Easterly direction. Because all stations located to the south of the Peloponnese and on western Crete are relatively stationary relative to ANAV, the trajectories of MILO, FOLE and SANT, as well as of all stations in eastern Crete indicate that the area within MILO, FOLE, SANT, western Crete, KASOS and ANF may undergo *counterclockwise rotation* which can only be effected by sinistral NW-SE and dextral NE-SW faulting along the KASOS-ANF line. Accordingly, it appears that the horizontal sense of NW-SE faulting changes from *dextral* north of the KALY-AMRG-SANT line to *sinistral* south of the KOS-ASTY-ANF line.

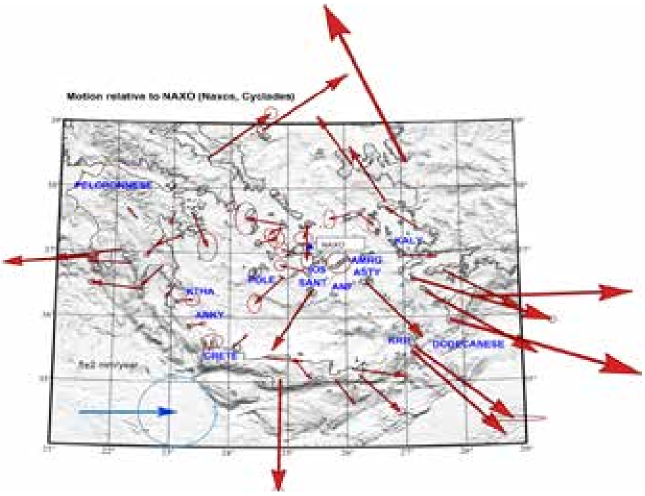

Figure 4. Horizontal velocities of the GNSS relative to the ASTY station.

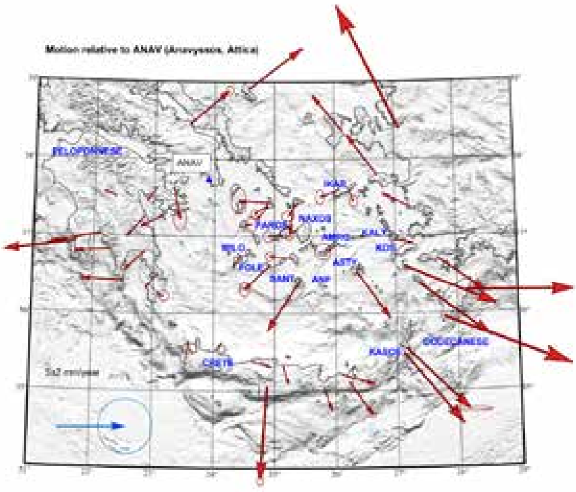

Figure 5. Horizontal velocities of the GNSS relative to the ANAV station.

Strain analysis and focal mechanisms: The calculated two-dimensional strain rate tensor is presented in Fig. 6. Extension (positive eigenvalues) is indicated with blue vectors and compression (negative eigenvalues) with red. The Cyclades Islands and the western coasts of Anatolia are characterized by an almost N-S extensional field, which rotates to NNW-SSE south of IKAR (Ikaria) – NAXO (Naxos) – Paros (PARO) – MILO (Milos) line discussed earlier. This counterclockwise rotation of the extensional field continues to the south and southeast, with the transition apparently associated with KOS (Kos) – ASTY (Astypalaea) – ANF (Anafi) line also discussed above. The Dodecanese Islands experience NW-SE to NNW-ESE extension. This changes to NE-SW compression in Crete. The transition appears to be almost abrupt and occurs just west of an (obvious in the focal mechanism distribution) NNE-SSW oriented extensional feature between the Kasos (KASOS)/ Karpathos (KPR) and Nisyros/Kos (KOS) islands, which we tentatively dub “the *Karpathos – Nisyros detachment*”, as well as west of the Kasos – Anafi line which is hereby confirmed. Minor differentiations in the strain field are also evident near Santorini and Folegandros Islands, confirming their separation from the rest of the Cyclades bounded by a line through Santorini (SANT) and Ios/Folegandros (FOLE). Finally, Euboea and the eastern part of central Greece are characterized by NNE-SSW extension, while the south Peloponnese is dominated by E-W extension. Similar findings concerning the Peloponnese, the eastern part of the central Aegean and Euboea were also reported by Chousianitis *et al.* (2015). The results of our strain analysis agree remarkably well with the crustal stress field derived from the inversion of earthquake focal mechanisms, e.g. as reported by Kassaras *et al.* (2020).

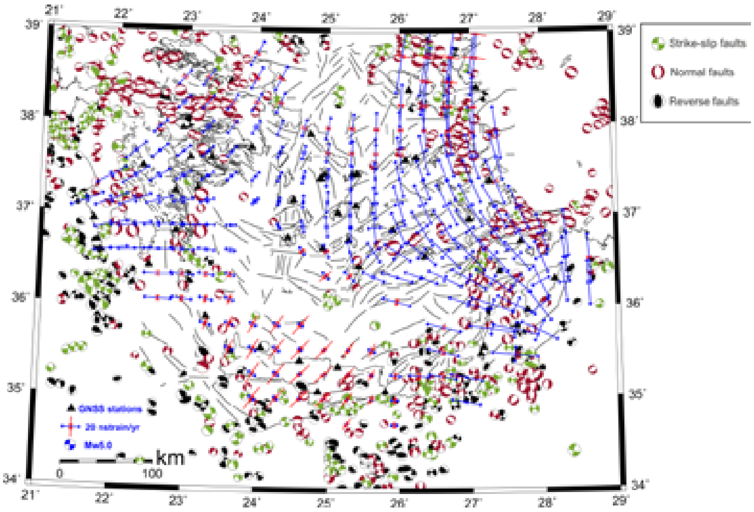

Figure 6. The strain field derived by inversion of the regional velocity field and focal mechanisms of crustal earthquakes with M≥4 over the period 1904-2022. The locations of the cGNSS stations are also indicated with black triangles.

Conclusions

The joint evaluation of all the above information confirms the distributed block deformation of the South Aegean and allows for the tentative identification of 7 major crustal blocks, of which block 1 is further partitioned into three sub-blocks. These are illustrated in Fig. 7 and are numbered from 1 to 7, with the sense of *horizontal* relative motion at their interfaces being as follows:

Block 1a: This includes the area to the north of the Ikaria – Paros/Naxos – Milos line and to the east of longitude 24°E. It is separated from Block 1b by a tentative, N-S oriented, apparently right-lateral discontinuity approximately extending along a line passing east of the Milos and Serifos islands and between the Euboea – Andros strait. It is also separated from Block 2 by a right-lateral and apparently aseismic discontinuity.

Block 1b: The Myrtoan Sea, separated from Block 1a by the Milos – Serifos – Andros line. The western boundary of this block exhibits null horizontal displacement as it comprises the NNW-SSE normal faults bounding the east coast of the Peloponnese. Moreover, the nature of its interface with Block 5 (Cretan Sea) remains undetermined.

Block 2: This comprises the southern Cyclades except for the island east of the Santorini – Ios line, Ikaria, Samos and others. It is separated from Block 1b by the Ikaria – Paros/Naxos – Milos line to the north, from Block 3 by the Kalymnos – Amorgos – Santorini line and from Block 4 by the Santorini – Ios line. The first interface has tentatively been identified as right lateral, the second appears to be normal with a left-lateral horizontal component and the third is tentatively identified as right lateral.

Block 3: The northern part of the Dodecanese. It is separated from Block 2 by the Kalymnos – Amorgos – Santorini line, to the east by the Kasos/Karpathos – Nisyros/Kos line and to the west by the Kasos Anafi line. The sense of horizontal motion here changes abruptly from left-lateral to practically null at the normal faults of the Kasos/Karpathos – Nisyros/Kos line (*Karpathos–Nisyros detachment*). The interface with Block 5 appears to be right lateral.

Block 4: Located at the southeast end of the Cyclades, it includes the islands Santorini, Sikinos, Folegandros. It is separated from Block 2 by the NNE-SSW right-lateral Santorini – Ios line, from Block 1a by the NW-SE right-lateral Paros/Naxos – Milos line and from Block 5 by the continental slope of the Cretan Sea, which is assumed to comprise normal faults with some right-lateral horizontal component. If this configuration is correct, Block appears to experience south-westward translation with simultaneous counterclockwise rotation.

Block 5 is the Cretan Sea. As indicated above, the eastern half of this block may undergo counterclockwise rotation effected by NW-SE left-lateral displacement and NE-SW right-lateral faulting.

Block 6 includes the southeast Dodecanese, Karpathos and Kasos. It is bounded to the southeast by the left lateral faulting of the Aegean – African plates interface and to the west by the normal faults of the Karpathos – Nisyros detachment.

Block 7 is the Karpathos – Nisyros detachment.

In a final comment, it is noted that this configuration and relative motion of crustal block amply explains the geographical configuration of the Cycladic islands.

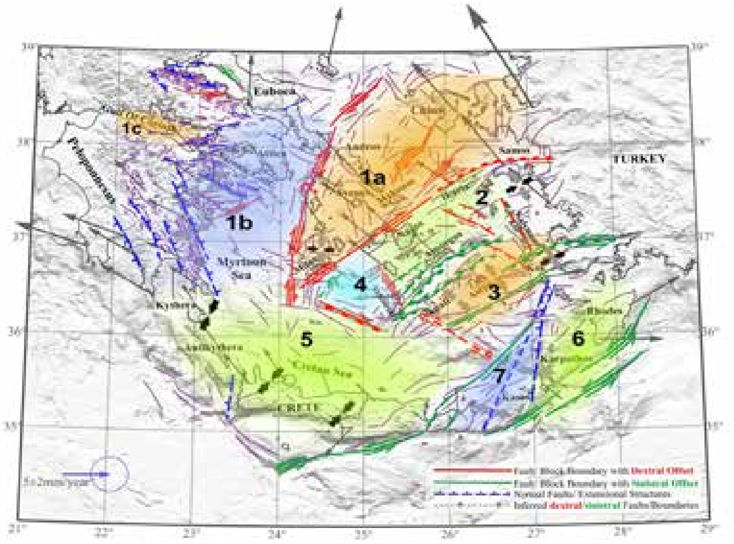

Figure 7. A model of contemporary distributed block deformation in the South Aegean.

Acknowledgements

This research was supported by the Hellenic Foundation for Research and Innovation (HFRI) under the HFRI PhD Fellowship grant (Fellowship Number: 841).

References

Briole, P., Ganas, A., Elias, P. and Dimitrov, D., 2021. The GPS velocity field of the Aegean: new observations, contribution of the Earthquakes, crustal blocks model, *Geophys. J. Int.*, 226, 468–492, doi:10.1093/gji/ggab089.

Chousianitis, K., Ganas, A. and Evangelidis, C.P., 2015. Strain and rotation rate patterns of mainland Greece from continuous GPS data and comparison between seismic and geodetic moment release, *J. Geophys. Res.*, Solid Earth, 120, 3909–3931, doi:10.1002/2014jb011762.

Chousianitis, K., Papanikolaou, X., Drakatos, G. and Tselentis, G-A, 2021. NOANET: A continuously operating GNSS network for solid-earth sciences in Greece, *Seismol. Res. Lett.*, 92, 2050–2064, doi:10.1785/0220200340.

Floyd, M.A. et *al*., 2010. A new velocity field for Greece: Implications for the kinematics and dynamics of the Aegean, *J. Geophys. Res.: Solid Earth*, 115, doi:10.1029/2009jb007040.

Ganas, A. et *al*., 2008. NOANET: The new permanent GPS network for Geodynamics in Greece: *Geophys. Res. Abs*., 10, EGU2008-A-04380, SRef-ID: 1607-7962/gra/EGU2008-A-04380.

Kassaras, I., Kapetanidis, V. and Karakonstantis, A., 2016. On the spatial distribution of seismicity and the 3D Tectonic stress field in Western Greece, *Phys. Chem. Earth*., *Parts A/B/C*, 95, 50–72, doi:10.1016/j.pce.2016.03.012.

Kassaras, I. et *al*., 2020. The New Seismotectonic Atlas of Greece (v1.0) and its implementation, *Geosci. J.*, 10, 447, doi:10.3390/geosciences10110447.

Lazos, I. et *al*., 2022. Temporal evolution of crustal rotation in the Aegean region based on primary geodetically-derived results and palaeomagnetism, *Acta Geod. Geophys.* , 57, 317–334, doi:10.1007/s40328-022-00379-3.

McClusky, S. et *al*., 2000. Global Positioning System constraints on plate kinematics and dynamics in the eastern Mediterranean and Caucasus, *J. Geophys. Res*., 105, 5695–5719, doi:10.1029/1996jb900351.

Nyst, M. and Thatcher, W., 2004. New constraints on the active tectonic deformation of the Aegean, *J. Geophys. Res.: Solid Earth*, 109, doi:10.1029/2003jb002830.

Pesci, A. and Teza, G., 2007. Strain rate analysis over the central Apennines from GPS velocities: the development of a new free software, *Bollettino di Geodesia e Scienze Affini*, 56, 69–88.

Reilinger, R. et *al*., 2006. GPS constraints on continental deformation in the Africa□Arabia□Eurasia continental collision zone and implications for the dynamics of plate interactions, *J. Geophys. Res.: Solid Earth*, 111, doi:10.1029/2005jb004051.

Sakkas, V. et *al*., 2020. Contemporary kinematics of the South Aegean area (Greece) detected with continuous GNSS measurements: *Proc., 2020 EGU General Assembly*, No EGU2020-7656, doi:10.5194/egusphere-egu2020-7656.

17th INTERNATIONAL CONGRESS
of the Geological Society of Greece

BULLETIN OF THE GEOLOGICAL SOCIETY OF GREECE, SP. PUBL.

EXTENDED ABSTRACT 183

Geophysical investigation of landslide phenomena in the Perivoli area, Grevena, using the electrical resistivity tomography method.

Krotka K.[1], Fikos I.[1], Papathanasiou G.[2]

(1) Laboratory of Applied Geophysics Aristotle University of Thessaloniki, Thessaloniki, Greece,
konstantinakrkt2000@gmail.com , ifikos@geo.auth.gr
(2) Laboratory of Engineering Geology & Hydrogeology, School of Geology, Aristotle University of Thessaloniki, Greece,
gpapath@geo.auth.gr

Introduction

This study focuses on the identification of the boundaries of a landslide in a remote but inhabited area, laterally and in depth, as well as analyzing the characteristics of it using geoelectrical surveying methods. The landslade is located on the provincial road of Grevena - Vovousa (Fig. 1), limiting access to the country's main road network from remote areas. This study emphasizes on the importance of further investigetion, since the landslade often reactivates, damaging the road and posing a threat to the people of the area. The results showcase the geometry of the landslide's subsurface and the thickness of the layers comprising it.

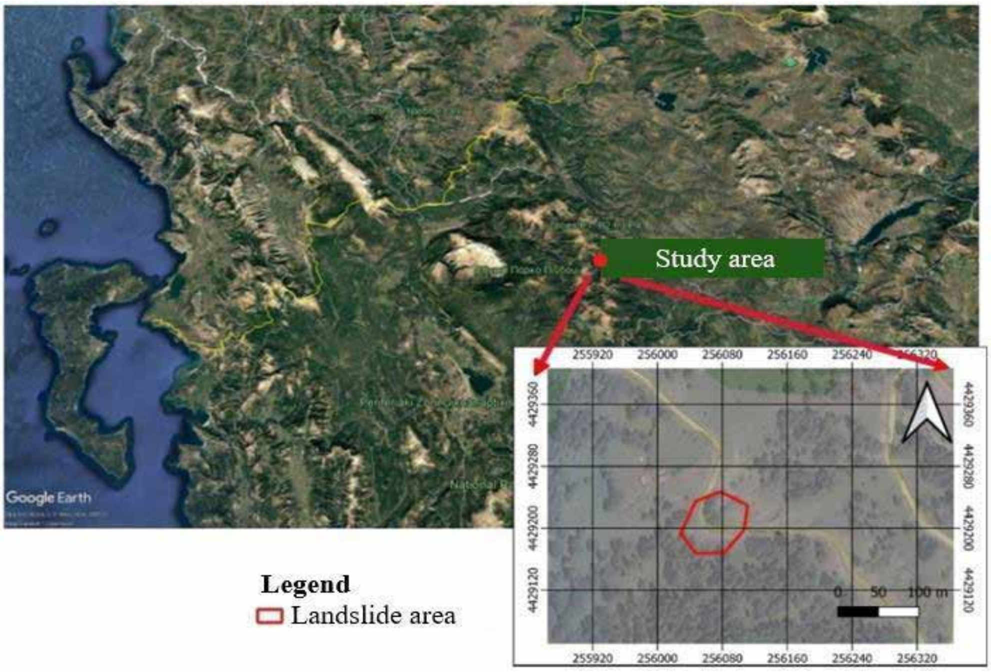

Figure 1: Location of the landslide (Google earth with modifications).

Geological Setting

The investigated area is part of the External Hellenides and more specifically it is located in the tectonostratigraphic zone of Pindos. The dominant formations of this zone are flysch, limestones and platy limestones. The Pindos flysch is divided into two layers, the 1st and 2nd flysch, both consisting of clastic sediments. The 1st is characterized by alterations of pebbles, sandstones and marls and was deposited during the Lower Cretaceous, while the 2nd has a calcareous-marl composition and was formed between the Danian and the Upper Eocene (Mountrakis, 2020). In the geologic map of Pentalofos (IGME, 1977) it can be seen that the landslide is entirely located in the area's flysch (Fig. 2), which overlies the limestone. The flysch in the area occurs with a chaotic structure, sandy and clayey composition and the limestones in the area are white (Mountrakis, 2020). The geological map also shows that the main formations include the undivided Pindos flysch (Danian-Eocene), which coexists with sandstone masses, marls and clay slates. In addition, Mesozoic limestones are found, either as platy/well-stratified ashy or reddish limestones, or as white limestone masses. Peridotites, serpentinites, dolerites and microlithic rocks also occur in the area, either individually or in combinations.

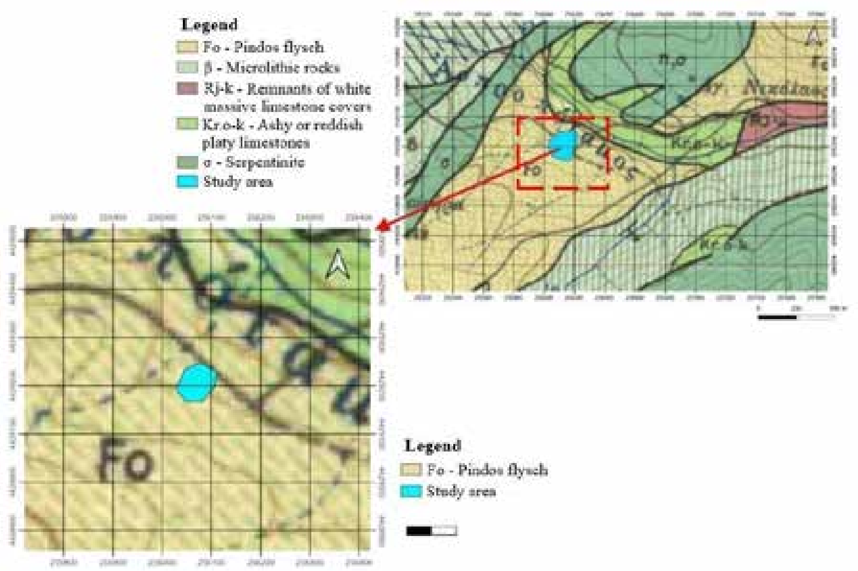

Figure 2: Geologic map of the area (IGME 1977, with modifications).

During the field research a stream was found acting as a natural boundary between the superficial geological formations (flysch and limestone). Flysch appears SE of the stream, while limestone predominates the NW side of it (fig. 3). This holds great importance, as it offers a clear view of the layers comprising the landslide. The subsurface consists of remnants of white limestone covers (Rj-k, Fig. 2), followed by a metabase layer. The upper layer/weathering mantle, which is the moving part of the landslide, consists of Pindos flysch. (Mountrakis D., 2020)

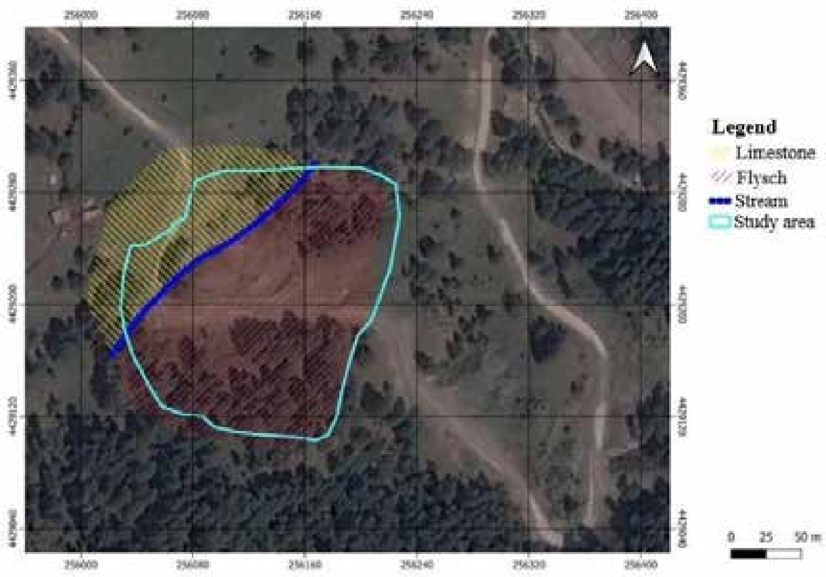

Figure 3: Stream as a natural boundary between the formations (Google earth with modifications).

Geotechnical characteristics

The flysch in the Perivoli area was geotechnically classified as category XI, characterized as strongly sheared siltstone or clayey shale with chaotic structure and clay pockets. It includes thin layers of sandstone that have been transformed into small fragments, making it particularly unstable and associated with landslide phenomena in areas of Western Greece. Its mechanical behaviour is characterised by great anisotropy, due to the degree of weathering, the orientation of discontinuities, high slope gradients and the presence of water. Furthermore, category XI flysch has increased clay content which creates impermeable and semi-permeable barriers, causing slope stability problems (Marinos *et al.*, 2013). Limestone on the other hand, has high strength values due to its natural state. It is particularly vulnerable to erosion due to the presence of water, which can lead to karstification and decrease its durability. The geotechnical characteristics of it depend on the degree of weathering, secondary relaxation and the presence of water. The weathering mantle occuring in the composition of the landslide, has a loose structure and the grain size of the material varies. Its mechanical strength values are lower than those of the original rock, while its limestone composition makes it permeable to groundwater, contributing to the occurrence of failures in the area.

Applied methodology

The geophysical method used in this study is electrical resistivity tomography (ERT). This offers a detailed depiction of the geological formations underground and provides insight on changes or possible movements in the landslide, helping to comprehend the phenomenon better. The arrangements used were the dipole-dipole, for the definition of the lateral boundaries, and the multi-gradient, for the definition of the landslide's depth. This combination provided a more complete depiction of the subsurface structure (Tsourlos P., 2021). A differential GPS (Trimble GNSS System) was used for the precise placement of the electrodes and the measurements were taken with the Syscal Pro instrument (IRIS Instruments). The first tomography (ERT1) was carried out along the movement axis of the landslide (Fig. 4). Its purpose was to determine the depth of the slip surface and the upper limit of the landslide. A limestone outcrop was observed in the southern part, which posed the question of whether it was the crown or just an eyebrow of the landslide. The tomography was 115 meters long and 23 electrodes were used (due to the road network) with 5 meters spacing in between. No increase in resistance was observed at a depth of 20 meters in ERT1, which affected the decisions regarding the length of the next two tomographies ERT2 & ERT3. The second tomography (ERT2) was carried out across the movement axis of the landslide (east to west) and a few meters north of the limestone outcrop mentioned earlier (Fig. 4). After a quick view of the preliminary results of ERT2, signs of clear increase in the resistivity were not identified, therefore this tomography was also 115 meters long in order to provide insight as deep as possible. As in the case of ERT1, 24 electrodes were used with 5 meters spacing in between. The third tomography (ERT3) was almost parallel with ERT2 at the landslide's foot area (Fig. 4). The tomography was 92 meters long and 24 electrodes were used with 4 meters spacing in between, providing slightly better resolution at expense of the maximum depth of investigation.

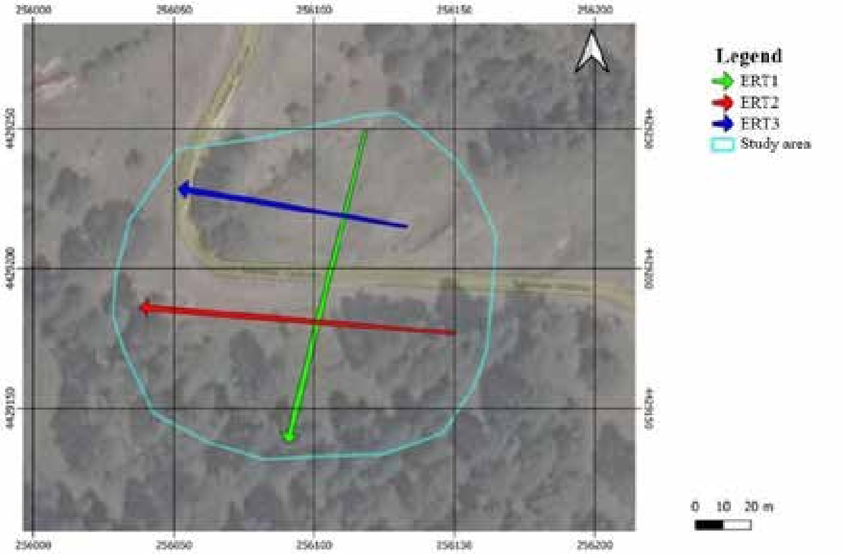

Figure 4: Orientation of the tomographies (Google earth with modifications).

Afterwards the results were subjected to mathematical inversion in the ResIPy open source software. Specifically, this software processed, filtered and finally modeled the geoelectrical data from the tomographies. The results of this process were easy to interpret images, depicting the layers' resistivity in representative colours.

Results

The inversion program ResIPy created two-dimensional models depicting the specific electrical resistivities of the subsurface (Fig. 5, 6, 7). The scale in the models ranges from dark blue for low resistivity values, to dark red for the highest resistivity values. In ERT1 (Fig. 5) 642 values were used by merging both the dipole-dipole and multi-gradient arrangements and the final error (RMS) was 2.36%. The analysis of the results shows that the subsurface can be divided into three main layers. The first layer (Fig.5, blue area) had the lowest resistivity (20-45 Ohmm) and was about 10 meters thick throughout the entire tomography, except for the area between the 11th and 13th electrodes, where there was a lack of data due to the road network. The second layer (Fig. 5, green and yellow area) had a resistivity of 45-75 Ohm*m and was also 10 meters thick, which remained the same through the entire tomography, with the same anomaly on the road area.

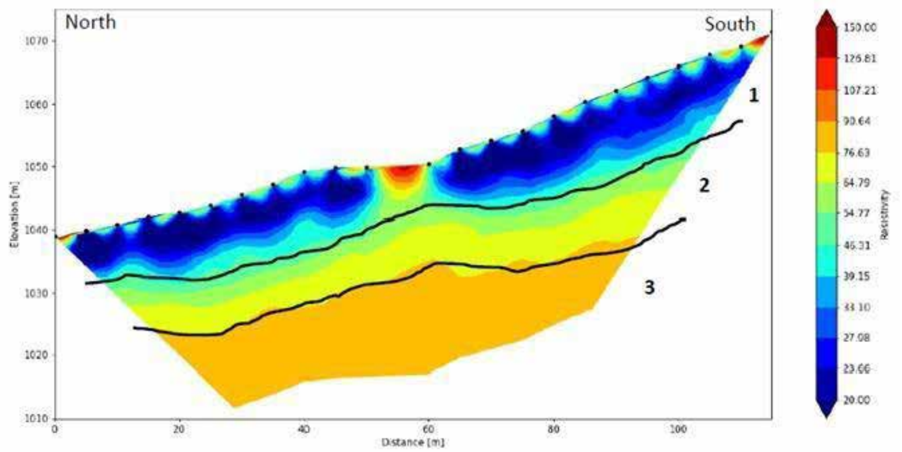

Figure 5: ERT1 resistivity distribution model.

In ERT2 (Fig. 6), 792 values were used by merging the dipole-dipole and multi-gradient arrangements and the final error (RMS) was 2.42%. The subsurface was divided into three main layers with different specific electrical resistivity. The first layer (Fig. 6, blue area), had the lower resistivity values (20-45 Ohmm) and was about 10 m thick. There were no obstacles, and all 24 electrodes were used this time. In this area, increased electrical resistivity values were observed at two points: eastern, between the 1st and 3rd electrode (90 – 105 Ohm*m) and between the 3rd and 4th electrode (45-75 Ohm*m) and western, between the 21st and 24th electrode (45-105 Ohm*m). In the central part of the section, between the 4th and 21st electrodes, the first layer dominates, which probably corresponds to the moving mass of the landslide. The second layer (Fig. 6, green and yellow area) had intermediate resistivity values (45-75 Ohm*m) and was also about 10 meters thick. In areas of increased resistivity, the second layer is locally thicker. Finally, at a depth of about 20 meters, a third layer appeared, which had higher resistivity values (75 to 90 Ohm*m) and was observed uniformly along the entire length of the tomography.

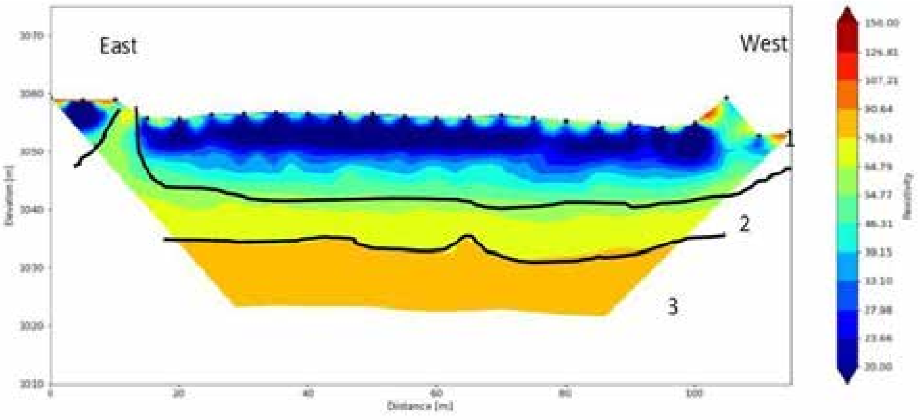

Figure 6: ERT2 resistivity distribution model.

In ERT3 (Fig. 7) 693 values were used by merging the dipole-dipole and multi-gradient arrangements and the final inversion error (RMS) was 2.92%. In this tomography only 23 electrodes were recording, due to the presence of the road network. As previously, three main layers are identified based on the specific electrical resistivities. The first layer is characterized by low resistivity values (20-45 Ohm*m), uniformly observed over most of the section, with the thickness being around 10

m. However, in the western part of the tomography, local variations are recorded, with increased resistivity values reaching 125 Ohmm between the 17th and 18th electrodes, and 45-90 Ohmm values in other areas. In the western part, where the tomography crosses the provincial road network, even higher resistance values were observed, reaching 150 Ohmm. The second layer, located at a depth of 10 meters, has intermediate resistivity values (45-75 Ohm*m), while its thickness reached 15 m locally, mainly in the area between the 6th and 10th electrode. Finally, the third layer appears at a depth of about 20 meters where higher resistivity values (75-90 Ohmm) are observed throughout the entire length of the tomography.

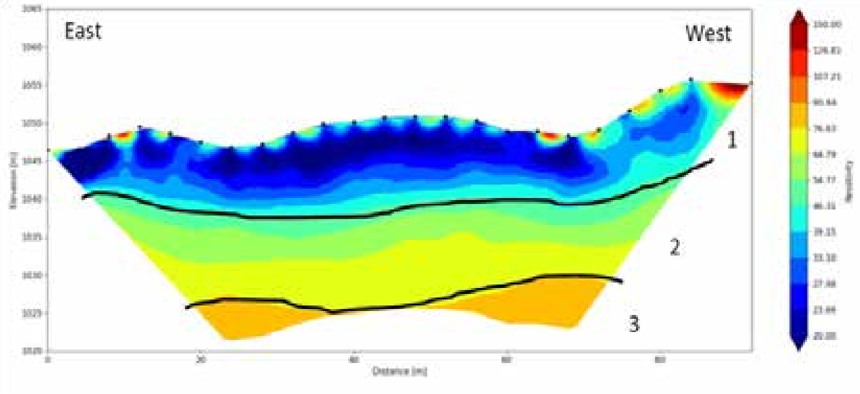

Figure 7: ERT3 resistivity distribution model.

The study of the area through three electrical tomographies (ERT1, ERT2, ERT3), revealed three main geoelectric layers corresponding to geological layers: the flysch (low resistivity values), the weathering mantle (intermediate resistivity values) and the limestone (high resistivity values). These geoelectric characteristics are directly related to the geotechnical properties of the formations, such as their strength, with limestone having the highest strength and flysch having the lowest. The analysis of ERT1 revealed ground subsidence, but it has not appeared as the main crown of the landslide. Instead, it is attributed to the heterogeneity of the flysch. Sections ERT1, ERT2 and ERT3 are cross each other at points used to confirm the validity of the results and to better understand the subsurface of the area. As the ERT1 was vertical to the other electrical tomographies (ERT2 & ERT3), there are two intersection points. The first one (Fig. 7), between ERT1 and ERT2, is located at the absolute altitude of 1.055 meters. On ERT1 this one is found between the 14th and 15th electrode and on the ERT2 it is found between the 9th and 10th electrode. For this common area were found both similar geoelectrical characteristics of the formations and thicknesses of them all, flysch was found 13 meters thick and weathering mantle 10 meters. The limestone basement is found at 23 meters depth.

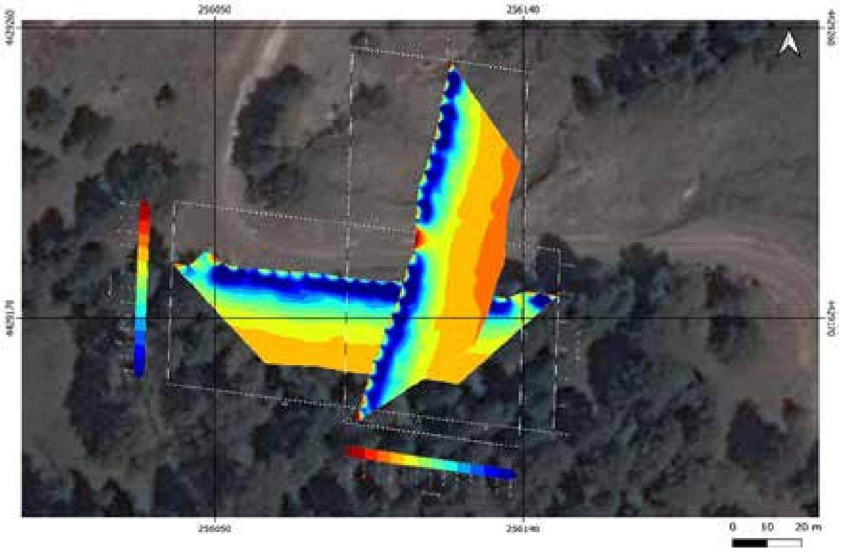

Figure7: Intersection point between ERT1 and ERT2

The second intersection point (Fig. 8), between ERT1 and ERT3, is located at the absolute altitude of 1.046 meters. This point is found between the 7th and 8th electrode on both first and third electrical tomography. At this intersection point the flysch appears with only 10 meters thickness and the weathering layer with 11 meters. The limestone basement is found at 21 meters depth.

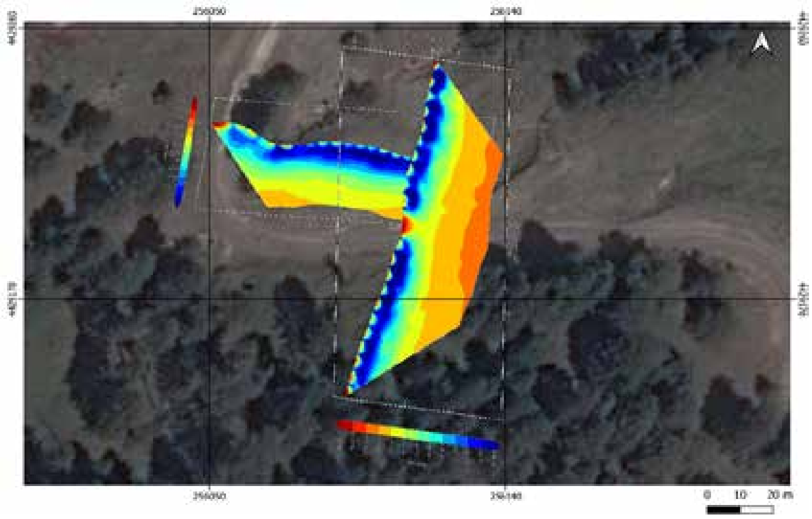

Figure 8: Intersection point between ERT1 and ERT3

Tomographies ERT2 & ERT3 were almost parallel and therefore provide data about the three formations on different elevations of the landslide. On ERT2 the subsurface flysch is found at 1046 meters altitude and on ERT3 at 1037 meters while the weathering layer is located at 1046 meters and 1037 meters and the base layer of limestone is located at 1035 meters altitude on ERT2 and at 1025 meters on ERT3. It becomes clear that the thickness of all the formations remain the same in the examined area even though the altitude decreases constantly, the distance between the two parallels is 37.5 meters.. According to these data, the altitude difference and the distance between the parallels, it follows the total slope of the landslide which is calculated as 13,5 degrees.

References

Brunn, J., 1977. Geological Map of Greece 1:50.000, Sheet Pentalofos. I.G.M.E., Athens.

Marinos, V., Kilias A., Makedon Th. & Thomaidou E., 2013. Guide to Field Trip West Macedonia - Epirus - Central Greece, Technical Geology, Aristotle University of Thessaloniki, Thessaloniki, Greece.

Mountrakis, D., 2020. Geology and Geotectonic Evolution of Greece, 2nd Edition, Part 1, Chapter A’, 25-28, Thessaloniki, Greece.

Mountrakis, D., 2020. Geology and Geotectonic Evolution of Greece, 2nd Edition, Part 1, Chapter D’, 153, Thessaloniki, Greece.

Tsourlos, P., 2021. Electromagnetic Methods of Geophysical Surveys, Notes, Aristotle University of Thessaloniki, Greece

17th INTERNATIONAL CONGRESS
of the Geological Society of Greece

BULLETIN OF THE GEOLOGICAL SOCIETY OF GREECE, SP. PUBL.

EXTENDED ABSTRACT 184

A holistic proposition for assessing reference station conditions

Olga-Joan Ktenidou[1], Antonia Papageorgiou[12], Fevronia Gkika[1], Erion-Vasilis Pikoulis[1], Kalliopi Fragouli[1], Fanis Chalaris[1], Spyros Liakopoulos[1], Ziya Cekinmez[13], Panagiotis Savvaidis[14], Christos Evangelidis[1]

[1] National Observatory of Athens, Greece
[1] University of Patras, Greece
[1] National Technical University of Athens, Greece
[1] Aristotle University of Thessaloniki, Greece

Introduction and background

The assumption of reference station conditions is an important one, yet is often taken for granted, especially at seismological stations or those presumably lying on rock. Stations are not always installed on true bedrock or in ideal free-field conditions, and –what is more– rock formations do not always exhibit negligible amplification, as assumed. In Greece, few site effects studies or field surveys have been conducted to characterise seismic networks in their entirety. Here, we first investigate broadband and accelerometric stations from the HL network, run by the National Observatory of Athens (NOA) throughout mainland and island Greece. We propose a solution that does not need significant nationwide resources (time and funding at a massive scale) such as would be required for in-situ geophysical campaigns. Instead of waiting for a time when funding and personmonths will be available at a massive scale to characterise all stations with measurements on site, we propose efficient desk studies that capitalize on the existing recordings collected so far, supplemented by additional desk work and existing knowledge that network operators have acquired from their site visits already. There are 60 such stations with publicly available data streams in the period 2012-2024 which are thought to lie on rock. We address the reference station question compiling a wide variety of parameters: waveform-derived (site-specific amplification characteristics), operator-derived (on-site observations from station visits and walk-overs), and external sources (geological maps and literature). We co-evaluate all these factors to propose a transparent scheme for assessing reference stations for the HL network. Finally, we propose the extension of this pilot study to include other networks, in the region of Macedonia and Thrace, as they can be of use in studying seismicity and seismic hazard in the Kavala-Prinos area, in the framework of EU project COREu.

Methodology

We follow the methodology set forth in detail in Ktenidou et al. (2024). We compile all types of information to create a comprehensive, systematic and holistic set of station metadata as follows.

1. We first compile all publicly available information from external sources. These include notes on geology and topography from the literature (e.g. the ESM ORFEUS website, (https://esm-db.eu/; Lanzano et al., 2021 & Luzi et al., 2016; the NOA/GEIN website, https://accelnet.gein.noa.gr/; Margaris et al., 2021 – M2021). We then collect and analyse geological maps to provide a consistent description of geological unit and geological age. We mostly use geological maps (1:50,000 scale) published by the Hellenic Survey of Geology and Mineral Exploration (HSGME). We then combine this with observations by the operators regarding the geology, topography, and the installation and housing conditions on site, which are attributed high accuracy and reliability owing to the site visits. These parameters are shown in Tables 1, 2 and 3. We acknowledge the limitations of using this kind of geological map, where the scale is more appropriate for nationwide studies than site-specific ones, where inconsistencies are likely between map sheets due to them having been compiles by different persons and even with several decades' time difference, and where simplifications are likely made in the presence of complexities. But there is no other readily available resource for deriving geological information homogeneously across the country, and in this sense the geological information we compile suffers from issues of granularity for the sake of some –relative- consistency and homogeneity.
2. The second and most demanding stage of this study is to create a strong-motion database to study amplification. We collect waveforms available from the past decade from events with M4 and above, and we perform a detailed analysis to estimate the local site response per station. To do this, the dataset first goes through quality control by visually inspecting and meticulously processing the data on a waveform-specific basis, both in the time and frequency domain. Single-station amplification functions are then estimated from the dataset using the horizontal-to-vertical spectral ratio (HVSR) technique of Lermo and Chavez-Garcia (1993). A good reference station should have low and flat amplification, as e.g. some of the Northern Greece stations shown in Figure 1. Moreover, it should exhibit no significant azimuthal variation, and to assess this we not only assess the features of the mean HVSR per station but also its directional sensitivity as per Ktenidou et al. (2016), which serves as a means to identify departure from the 1D assumption (Figure 2 shows the low sensitivity for two of those stations). We propose that three values of standard deviation at different frequency ranges (0.3-30 Hz, 1-10 Hz, and fo) can be used as approximate indicators of the azimuthal stability of site response. These parameters are shown in Table 4.

We evaluate each criterion independently and assess whether each station can be considered a reference station from the point of view of geology, topographic relief, installation conditions, Vs30, and the characteristics of the HVSR in terms of mean amplification level and shape as well as in terms of directional stability. These assessments are shown in the following tables for the three stations in Northern Greece, which ranked very high among the 60 Greek stations studied.

It is well known that the amplification (A_0, A_1 in table 4) is usually underestimated by HVSR, since the vertical component is of course amplified to an unknown degree yet assumed unaffected. We also attempt some preliminary corrections to the amplitude based on the methodology of Ito et al. (2020), which however was calibrated on regional data from Japan, and so may not reflect vertical amplification levels in Greece. Hence we show these results only in an indicative capacity. Figure 3 shows examples of the Ito correction of the mean HVSR shown in Figure 1, and Table 4 also includes characteristics of resonance (e.g. A0_corr) based on these corrections. Clustering was also performed based on corrected HVSRs and similar clusters were found (more details in Ktenidou et al., 2024).

Table 1. Parameters describing housing/installation conditions and Vs30 for 3 example stations.

Station code	Building type (GEIN)	Installation con-dition	Potential reference (Inst/on)?	EC8 (ESM)	Vs30 (ESM)	Vs30 geology (M2021)	Vs30 terrain (M2021)	Preferred Vs30 (M2021)	Potential reference site (Vs30)?
KVLA	2-floor RC	Not free field	**no**	B	782	528	475	501	**yes (ESM)**
NVR	1-floor RC	free field	**yes**	A	955	556	475	514	**yes - ESM**
PLG	1floor RC	Vault in building	**yes**	B	608	492	519	506	**no**

Table 2. Parameters describing topography and slope for 3 example stations.

Station code	Station elevation (m)	Topographic code (ESM)	Slope angle (ESM)	Slope angle (M2021)	Slope (M2021)	Assessment from site visit	Potential reference site (Topography)?
KVLA	122	T1	9	7	0.122	Flat/shallow (<15) within 200 m	**yes**
NVR	627	T1	15	0.259	15	Flat/shallow (<15) within 200 m	**yes**
PLG	566	T1	5	4	0.073	Flat/shallow (<15) within 200 m	**yes**

Table 3. Parameters describing geological conditions for 3 example stations.

Station code	Geologic description (GEIN)	Description (M2021)	Geologic Age (M2021)	Geologic unit - this study	Geologic age - this study	Reference map used (HSGME)	Potential reference site?
KVLA	limestone	Alluvial deposits	Oligocene	Kavala granite	Quartenary	Kavala Sheet	**yes**
NVR	sandstone	Scree and Talus Cones	Pleistocene		Metamorphic rocks/upper series (schists, schist-gneisses, gneisses, amphibolites and marbles)	Oligocene - Miocene	**yes**
PLG	gneiss	Basal Conglome-rate Series	Upper Miocene -Lower Pliocene	Quartzites and quartzitic sandstones of Svoula group	Triassic - middle Jurassic	Polygyros Sheet	**yes**

Table 4. Waveform-derived parameters for 3 example stations.

Station code	f0 inspected >2.7 (Hz)	A0	Peaky / flat?	f1 (Hz)	A1	f0_corr if not seen in HVSR (Hz)	A0_corr (/ A1_corr)	Potential reference site (HV mean)?
KVLA	-	-	f	-	-		-	**yes**

NVR	-	-	**p**	-	-	5.0	4	**ok**
PLG	-	-	f	-	-		-	**yes**
Station code	**SD (1-10 Hz)**	**SD (0.3-30 Hz)**	**Directional variability < 10 Hz**	**Directional variability - HF**	**Cluster no. from mean HV**	**Cluster no. from HV_corr**	**Response description (mean HV)**	**Potential reference site (HV directionality)?**
KVLA	1.04	1.07	Low		6	5	Reference station	**yes**
NVR	1.05	1.09	Low		5	5	Flat, near-reference	**yes**
PLG	1.05	1.09	Low		6	5	Reference station	**yes**

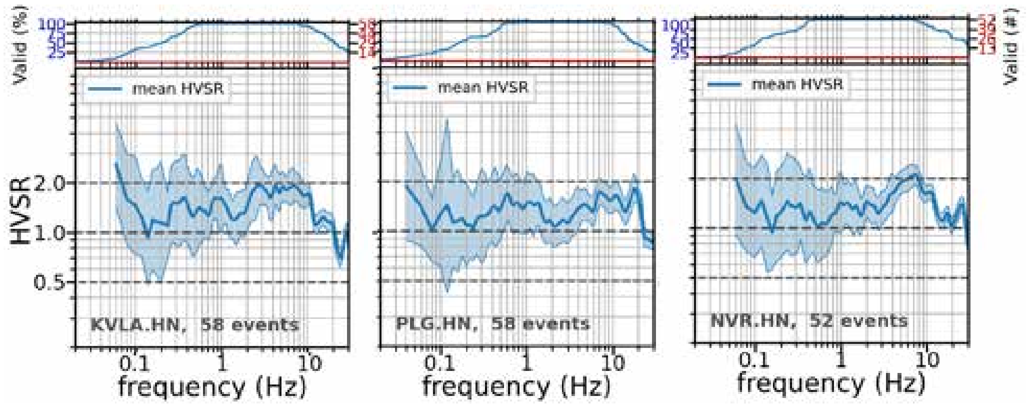

Figure 1. Mean HVSR ± 1 standard deviation for 2 stations in Northern Greece (left to right: HL.KVLA, HL.PLG and HL.NVR); inset on top indicates the number of available recordings per frequency.

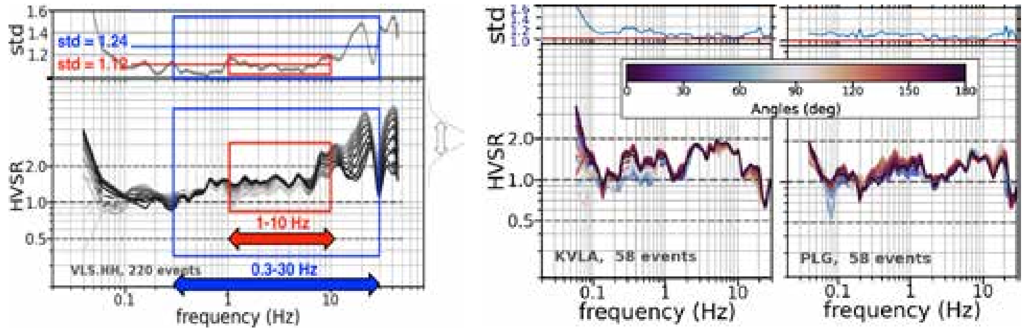

Figure 2. HVSR per component for 2 stations (left to right: HL.KVLA, HL.PLG), as those are rotated by 10º intervals from North to East; inset on top indicates the standard deviation (hence, directional sensitivity or variability) per frequency.

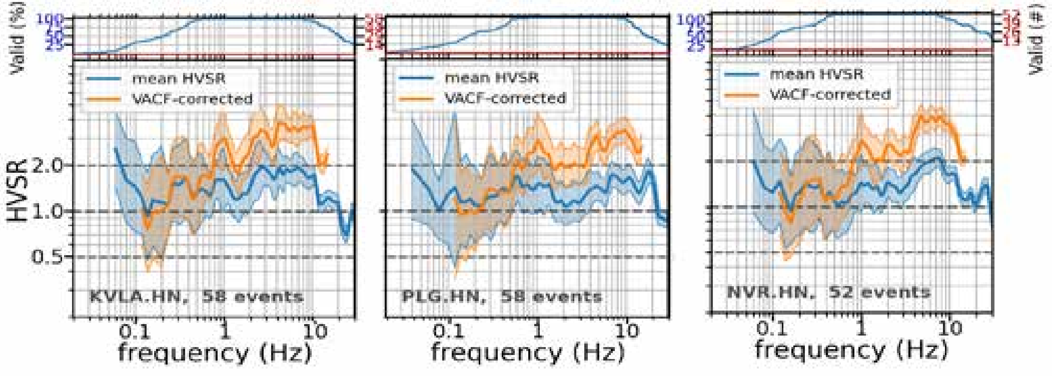

Figure 3. Mean HVSR±1 standard deviation (in blue) for 3 stations in Northern Greece (left to right: HL.KVLA, HL.PLG and HL.NVR) and corrected HVSR using Ito et al. (2020) correction function for the vertical component (in orange). The latter is only computed within the method's range of applicable frequencies and is offered in an indicative quality; inset on top indicates the number of available recordings per frequency.

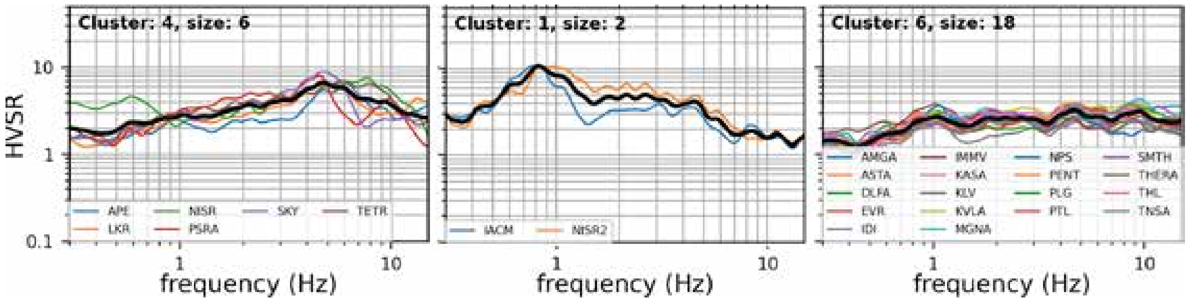

Figure 4. Example station clusters with different style of HVSR response.

Finally, we use clustering techniques to group stations with different response characteristics (Figure 4) and finally combine this data-derived characterization with the previously compiled metadata to evaluate the stations' overall capacity as reference sites.

Results and discussion

In this study, we compiled several descriptors from literature, geological maps and direct network operator observations from site visits and we also derived site-specific amplification characteristics from strong-motion data analysis. We brought everything together to co-evaluate the overall potential of our stations as reference stations. We proposed a solution that does not need significant nationwide resources (time and funding at a massive scale) such as would be required for in-situ geophysical campaigns. Instead of waiting for a time when funding and personmonths will be available at a massive scale to characterise all stations with measurements on site, we propose efficient desk studies that capitalize on the existing recordings collected so far, supplemented by additional desk work and existing knowledge that network operators have acquired from their site visits already. We acknowledge the limitations of HVSR, namely the underestimation of amplification level, and hence propose that our amplification results be regarded as potential lower-bounds. However we do stress that even with a full-blown budget for geophysical campaigns, the resulting Vs profiles would still suffer from that method's own drawbacks – they would be non-unique and any forward site response modeling using them would also heavily rely on the 1D assumption: this, HVSR does not – it actually reveals at least some of nature's departure from it.

This work has been completed for all HL network stations that lie on rock and is currently underway for stations from other networks in the regions of Macedonia and Thrace. The special focus on this region intends to add value and help decrease epistemic uncertainties for future applications that will take place within the European project COREU (https://coreu.eu/), which will involve seismic monitoring and hazard assessment in the Kavala-Prinos area in the framework of a CCS pilot study.

Acknowledgements

All waveforms and station metadata are freely accessible at https://eida.gein.noa.gr/, the regional node of EIDA hosted by the Institute of Geodynamics of the National Observatory of Athens (NOA). Event parameters come from the seismic catalogue of NOA, freely accessible here: https://eida.gein.noa.gr/fdsnws/availability/1. We gratefully acknowledge partial financial support from EU project COREU.

References

Ito, E., Nakano, K., Nagashima, F. and Kawase H. (2020): A Method to Directly Estimate S-Wave Site Amplification Factor from Horizontal-to-Vertical Spectral Ratio of Earthquakes (eHVSRs), Bull. Seismol. Soc. Am., 110, 2892–2911, doi: 10.1785/0120190315.

Ktenidou, O.-J., Pikoulis, E.-V., Papageorgiou, A., Gkika, F., Liakopoulos, S., Cekinmez, Z., Savvaidis, P., Fragouli, K., and Evangelidis, C. P. (2024): The quest for reference stations at the National Observatory of Athens, Greece, Nat. Hazards Earth Syst. Sci. Discuss. doi:10.5194/nhess-2023-233

Ktenidou, O.-J., Chávez-García, F.J., Raptakis, D. and Pitilakis, K.D. (2016): Directional dependence of site effects observed near a basin edge at Aegion, Greece, Bull. Earth. Eng., 14(3), 623-645, doi:10.1007/s10518-015-9843-x.

Lanzano, G., Luzi, L., Cauzzi, C., Bienkowski, J., Bindi, D., Clinton, J., Cocco, M., D'Amico, M., Douglas, J., Faenza, L., Felicetta, C., Gallovic, F., Giardini, D., Ktenidou, O-J. and 12 others: Accessing European Strong-Motion Data: An Update on ORFEUS Coordinated Services, Seismol. Res. Letts, 92, 1642–1658

Lermo, J., and Chávez-García, F.G. (1993): Site effect evaluation using spectral ratios with only one station, Bull. Seismol. Soc. Am., 83,1574–1594.

Luzi, L., Puglia, R., Russo, E., D’Amico, M., Felicetta, C., Pacor, F., Lanzano, G., Çeken, U., Clinton, J., Costa, G., Duni, L., Farzanegan, E., Gueguen, P., Ionescu, C., Kalogeras, I., Özener, H., Pesaresi, D., Sleeman, R., Strollo, A. and Zare, M.: The engineering strong motion database: A platform to access pan‐European accelerometric data, Seismol. Res. Letters, 87, 987–99

Margaris, B.E., Scordilis, M., Stewart, J.P., Boore, D.M., Theodulidis, N., Kalogeras, I., Melis, N., Skarlatoudis, A., Klimis, N. and Seyhan, E. (2021). Hellenic strong-motion database with uniformly assigned source and site metadata for period of 1972-2015, Seismol. Res. Letts, 92, 2065-2080.

National Observatory of Athens, Institute of Geodynamics, Athens – NOA-GI (1975). National Observatory of Athens Seismic Network [Data set]. International Federation of Digital Seismograph Networks. https://doi.org/10.7914/SN/HL

17th INTERNATIONAL CONGRESS
of the Geological Society of Greece

BULLETIN OF THE GEOLOGICAL SOCIETY OF GREECE, SP. PUBL.

EXTENDED ABSTRACT 185

The Xerias Window near Argos (Peloponnesus)

Dipl.-Geol. Dr. Erwin Kunz, retired geologist, Bad Oeynhausen, Germany

Introduction and methodology

The area considered in this paper comprises a section of the mountains that separate the regions of Argolis and Arcadia. This mountain range is part of the Hellenides, and it is built up by the rock sequences of Tripolitza and Pindos Zone. Its tectonic architecture is deeply exposed in the Xerias Window (Jacobshagen 1986) (fig. 1). Key structures (Schwan 1964) are worked out for every lithological unit, for clarifying the large-scale architecture of the mountains.

Varying geodynamic stress fields

The nappe-shaped position of the Pindos Zone is obvious in the frame of the Xerias Window. The vergence of the key structures of the latter varies everywhere between W and SW, which proves a relative transport of the Pindos Zone as a whole in that direction.

In contrast, the Tripolitza Zone does not show evidence for such a transport. The folds and overthrusts within Tripolitza Carbonates and Flysch around Krya Vrysi trend resp. strike from WNW to ESE with their vergence to the NNE, which can be explained only by a compressional stress in this direction. Also, at the contact between Phyllite-Quartzite Series and Tripolitza Carbonates south of the Xerias valley, corresponding tectonic structures can be found.

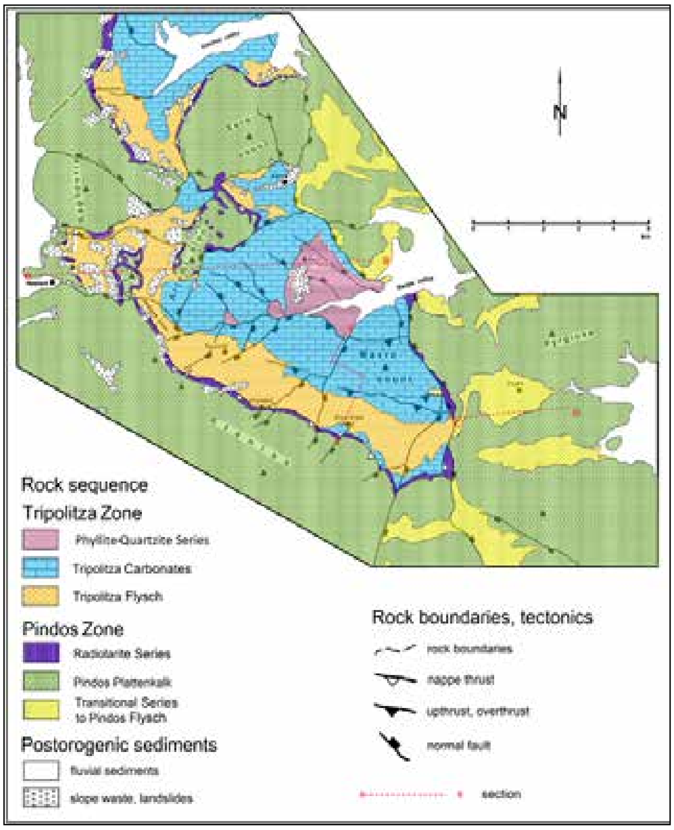

Fig. 1: Generalised geological map of the Xerias Window and its frame

Round about since Upper Miocene, the compressive stress was followed by young extensional tectonics, which continues until today. Its influence on the development of the Xerias Window and on the forming of its frame is described. The important faults created in this time (Xerias faults) show clear parallels to the Corinthian and the Argolic Gulf.

References

Dercourt, J., Wever, P. de, Fleury, J.-J., 1976. Données sur le style tectonique de la nappe de Tripolitza en Péloponnèse septentrional (Grèce). *Bull. Soc. Géol. France,* 7e s., t. XVIII, no. 2, p. 317 – 326.

Doert, U., Richter, D., Mariolakos, I., 1977. Ein tektonisches Querprofil durch die Olonos-Pindos-Zone im Gebiet südwestlich Argos und seine Bedeutung für den Gebirgsbau des Peloponnes (Griechenland). *Ann. Géol. Pays Hellén.,* 28, p. 368 – 386.

Eckl, H., 1979. Beitrag zum Gebirgsbau des NE-Peloponnes im Grenzbereich Olonos-Pindos-Zone/Gavrovo-Tripolitza-Zone. *Z. dt. geol. Ges.,* 130, p. 347 – 351.

Fleury, J.-J., 1980. Les zones de Gavrovo-Tripolitza et du Pinde-Olonos (Grèce continentale et Péloponnèse du Nord). Evolution d'une plate-forme et d'un bassin dans leur cadre alpin. 2 vol. *Soc. Géol. du Nord,* publ. no. **4**: 651 pp.

Jacobshagen, V., 1986. Geologie von Griechenland. – *Beitr. reg. Geol. d. Erde*, vol. 19, 363 pp., Borntraeger, Berlin, Stuttgart.

Papanikolaou, D. I. 2021. The Geology of Greece. – 345 pp., 293 fig., Springer, Cham/Schweiz.

Schwan, W. 1964. Begriff und Bedeutung der Leitstrukturen. Ein Beitrag zur tektonischen Forschungsmethodik. *Geotekt. Forsch.,* 19, p. 1 – 47, 7 pl., 6 fig.

Xypolias, P., Doutsos, T. 2000. Kinematics of rock flow in a crustal-scale shear zone: Implication for the orogenic evolution of the southwestern Hellenides. *Geol. Mag.,* 137 (1), p. 81 – 96.

17th INTERNATIONAL CONGRESS
of the Geological Society of Greece

BULLETIN OF THE GEOLOGICAL SOCIETY OF GREECE, SP. PUBL.

EXTENDED ABSTRACT 186

Mineralogy and Geochemistry of the Non-Sulfide Zinc-Lead Deposits, Thasos Island, North Aegean, Greece

Kyriakos A.[1], Sakellaris G.A.[1], Melfos V.[1], Stergiou C.L.[1,2], Papadopoulou L.[1], Kantiranis N.[1]
(1) School of Geology, Aristotle University of Thessaloniki, Greece, axkyriak@geo.auth.gr (2) Chemical Process & Energy Resources Institute (CPERI), Centre for Research and Technology Hellas (CERTH), 50200 Ptolemaida, Greece

Introduction

Thasos Island has long been recognized as an important mining center with its prehistoric ochre mines in the area of Tzines representing some of the earliest mining activities in Europe, dating back to 20,000 BCE (Koukouli *et al.,* 1988). The island was also renowned for its gold, silver, copper and lead production, referenced by Herodotus and Strabo. Due to its abundant Zn occurrences, and particularly calamine ore (smithsonite), Thasos witnessed significant mining activity in the early 20th century. On that time, calamine, a non-sulfide type of zinc ore, was the primary source of Zn worldwide. In 1902, the German company “Minengesellschaft Fr. Speidel” established a mining complex in the Limenaria town to exploit zinc and argentiferous lead ores. However, operations ceased in 1913 due to declining ore grades. In 1925, a subsidiary of the Belgian company “Société des Mines et Fonderies de Zinc de la Vieille Montagne” undertook the restoration and the expansion of the mining facilities. Despite these efforts, the global economic crisis of the 1930s along with the development of flotation and smelting processes for zinc sulfide ores (sphalerite), resulted in cease of the lead-zinc mining activity on the island (Epitropou, 2005). Further exploration on the island during the 1970s and 1980s failed to locate new significant resource of either non-sulfide or sulfide zinc mineralization.

Non-sulfide zinc deposits in Europe were used since Roman times for the production of brass (zinc-copper ± tin alloy). These ores are mostly secondary and form through supergene oxidation of primary sulfide deposits (Boni and Large, 2003). According to Large (2001), the non-sulfide zinc deposits are classified into three main groups based on their geologic characteristics: a) calamine-dominated deposits formed through supergene oxidation of primary sulfides in carbonate environments, often preserved as karst cavity infillings, with main minerals smithsonite ($ZnCO_3$), hydrozincite, and hemimorphite; b) willemite-dominated (Zn_2SiO_4) deposits of primary hydrothermal origin, associated with fault zones and brecciation, and; c) supergene zinc deposits formed by residual surface oxidation, hydromorphic dispersion, and precipitation in carbonate environments, with a complex mineralogy including smithsonite, sauconite, and hydrozincite.

This research work investigates the most important non-sulfide zinc-lead-silver deposits, as well as, the iron-manganese deposits of Thasos. Despite the extensive studies on the metamorphic lithologies and core complex structures of Thasos, these deposits have remained understudied, and no comprehensive data regarding the processes of formation and the characteristics of primary mineralization exist. The aim of this work is to classify the mineralization in respect to mineralogy, the metal concentrations, and the correlations between major and trace elements, contributing to a better understanding of their genesis and economic potential.

Geological Context

Thasos Island located in the northern Aegean Sea, Greece, is geologically part of the Rhodope Metamorphic Core Complex. This complex comprises Paleozoic to Mesozoic high-grade metamorphic rocks that were exhumed during the Late Oligocene to Miocene extension (Wawrzenitz & Krohe, 1998). The metamorphic complex of Thasos is divided into three units (Brun & Sokoutis, 2007): a) a lower unit of marbles (Profitis Ilias), and dolomitic marbles with intercalations of paragneisses and mica schists (Potamia series), which covers the eastern part of the island; b) an intermediate slab of orthogneisses with paragneisses, mica schists (Maries series), and marbles (Kastro), which dominates the western and central part and; c) an upper unit of Tertiary conglomerates and non-mylonitic metamorphic rocks, migmatites and pegmatoids, with minor amphibolites and marbles in southwestern Thasos (Figure 1). These tectonic units are separated by two major southwest-dipping, low-angle extensional fault systems. These low-angle faults were originally thrust faults that transported the migmatites and the overlying intermediate unit over the lower unit. However, during the Miocene, these faults were reactivated as detachment faults. Most of the zinc deposits are located in the western part of the island, within the intermediate marble-gneissic unit along the major detachment faults and can be characterized as stratabound.

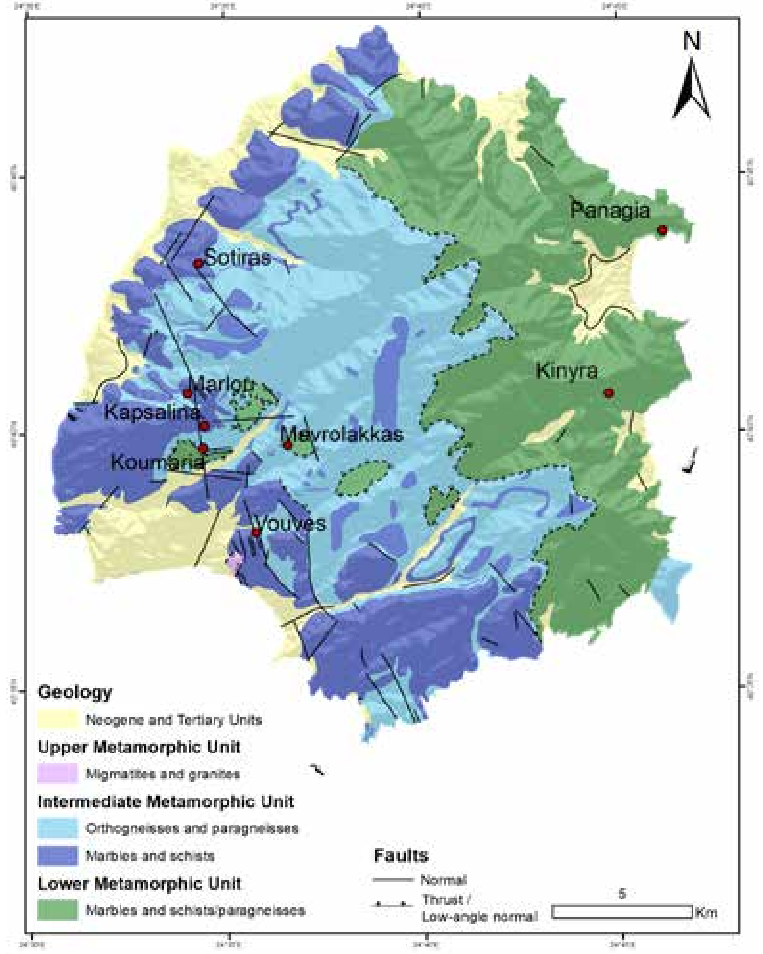

Figure 1. Geological map of Thasos illustrating the locations of the most significant zinc-lead and iron-manganese mines visited and sampled on the island, modified after Brun & Sokoutis (2007).

Samples and Methods

Representative hand specimens were collected from outcrops at the former (ancient and modern) mining sites of Sotiras, Koumaria, Kapsalina, Maries, and Vouves zinc-lead-silver deposits, as well as Mavrolakkas iron-manganese deposit during a two-day field work. Polished thin sections were prepared for microscopic examination using a Zeiss Axioscope 40 Pol, and by backscattered electron imaging (BSE) with a JEOL JSM- 6390LV scanning electron microscope (SEM) equipped with an OXFORD INCA 300 energy-dispersive X-ray spectroscopy (EDS). Powdered samples were proceeded for chemical analysis of major and trace elements, utilizing a wavelength-dispersive X-ray fluorescence (WD-XRF) spectrometry system. The instrument employs a Rhodium (Rh) X-ray tube with a Zirconium (Zr) filter, a three-crystal system (LiF(200), PET, RX25), and two detectors. The X-ray beam operated at high energy, with settings of 50 kV and 4 mA. The oxides measured include: Na_2O, MgO, Al_2O_3, SiO_2, P_2O_5, SO_3, K_2O, CaO, TiO_2, MnO, Fe_2O_3, and trace elements: Cl, Cu, Zn, Sr, Ag, Ba, and Pb (Table 1). All sample preparation and analytical procedures were carried out in the laboratory facilities of the Department of Mineralogy-Petrology-Economic Geology at the School of of Geology, Aristotle University of Thessaloniki.

Results

1. Structural setting

All visited zinc-lead-silver deposits are localized within certain layers of the marble units (Kastro) along major low-dipping detachment faults that bring the gneiss in contact to the marble (Figure 1). The geometry of deposits is highly dependent on the structural setting, with common morphologies including stratabound, stratiform, karst-hosted, lenticular, breccia-hosted, and tabular forms. The stratiform bodies are typically 1 to 3 meters thick extending for several 100s of meters to kilometers within the detachment zones (Figure 2).

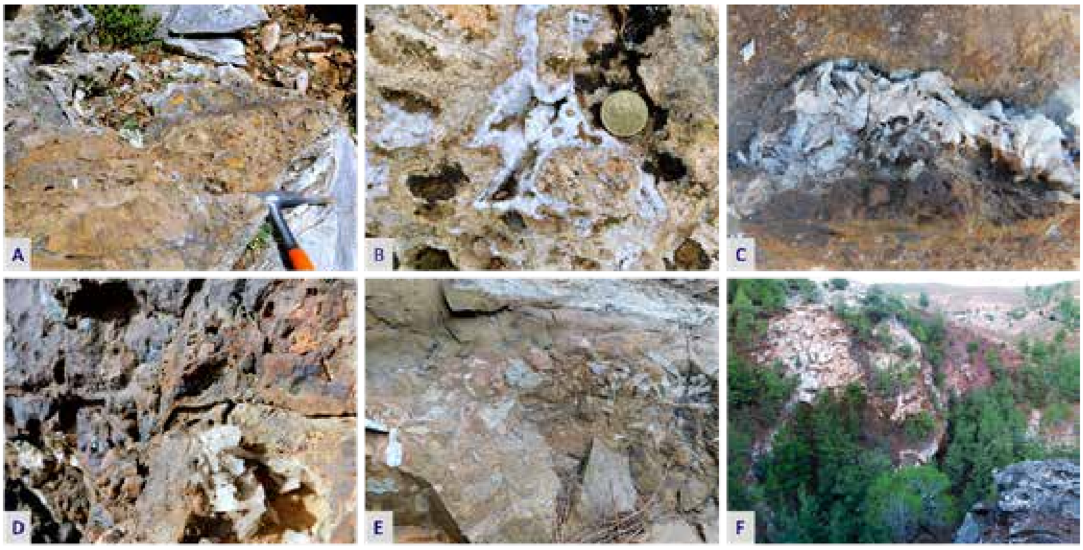

Figure 2. (A) Brecciated Zn-Pb mineralization within a low-angle detachment fault in marble at the contact with gneiss (Sotiras mine). (B) Zinc-rich aragonite filling fractures at the Sotiras mine. (C) Tabular barite crystal aggregates within Zn-Pb mineralization (Koumaria mine). (D) Well-formed barite crystals associated with massive stratiform Zn-Pb mineralization (Kapsalina outcrop). (E) Angular marble fragments within iron oxides-Zn-Pb breccia (Vouves mine). (F) Karst-hosted Fe-Mn (±Cu) mineralization within marbles (Mavrolakkas mine).

2. Mineralogy

The paragenesis of zinc-lead (±copper) minerals in all studied deposits consists predominately of the secondary carbonate minerals smithsonite ($ZnCO_3$) and cerussite ($PbCO_3$), and lesser lead-rich aragonite ($CaPbCO_3$), malachite ($Cu_2CO_3(OH)_2$), and azurite ($Cu_2(CO_3)_2(OH)_2$) (Figure 3). Notably, except Koumaria, where traces of sphalerite (ZnS) and galena were recognized, in none of the samples, primary sulfides were identified. Barite is a major gangue mineral constituent in most ore zones. More detailed:

Sotiras Zn-Pb mine:

The most abundant mineral phases in the ore samples are iron oxides enriched in Zn, smithsonite, and cerussite. Pure smithsonite or smithsonite with elevated Ca contents (up to 20%), is found as dispersed crystals in calcite-aragonite that replace dolomitic marble within breccia (Fig.2a,b and 3a,b).

Vouves Zn-Pb mine:

Mineralogical zoning within the ore breccia zones (Figure 2e) includes: a) a core zone with large euhedral crystals of barite, b) a botryoidal zone with Pb-rich calcite-aragonite, iron oxides enriched in lead, zinc, and occasionally in As and Si, as well as, calcite, c) an outer zone characterized by zinc-rich aragonite. Tiny flakes (less than 5 μm) of jarosite ($KFe_3(SO_4)_2(OH)_6$) and calcium-jarosite (jarosite with calcium impurities) are locally abundant within calcite, occurring between barite crystals. Additionally, concentric zoning in dolomite features iron-rich, Zn-rich and Pb-rich zones. An interesting mineral which occurs in botryoidal form is cesarolite, a rare secondary Pb-Mn oxide phase with the formula $PbMn_4O_6(OH)_2$ (Figure 3c, d).

Koumaria Zn-Pb mine:

Mineralization appears in breccia, consisting of cerussite, iron oxides, and Fe- and Zn-rich cesarolite, with frequent occurrences of barite veins (Figure 2c). The iron oxides are enriched in Pb, Zn, Si, and Mn, and, together with cesarolite, form euhedral structures related with the dissolution of primary mineral phases. Cesarolite appears as irregularly shaped and dispersed grains, suggesting its formation either as a secondary oxidation product or a replacement phase derived from earlier Pb-Mn-bearing minerals (Figure 3e,f). The iron oxides exhibit zoning and irregular morphologies, potentially indicating the oxidation of primary Fe-rich minerals. Their strong enrichment in Pb, Zn, Si, and Mn suggests remobilization and incorporation of these elements during post-depositional processes.

Mavrolakkas Fe-Mn mine:

The karst-filling mineralogy of this deposit within marble follows a distinct zoned pattern with an inner zone dominated by Mn-rich and Si-rich iron oxides, prismatic barite crystals, and quartz; and an outer zone composed of barren calcite/dolomite with minimal Fe and Mn enrichment (Figure 2f). The Fe oxides exhibit distinctive structures at the boundaries of what are likely primary crystals that have undergone oxidation. Additionally, apatite ($Ca_5(PO_4)_3(OH,F,Cl)$) crystals are occasionally observed among the Fe oxides.

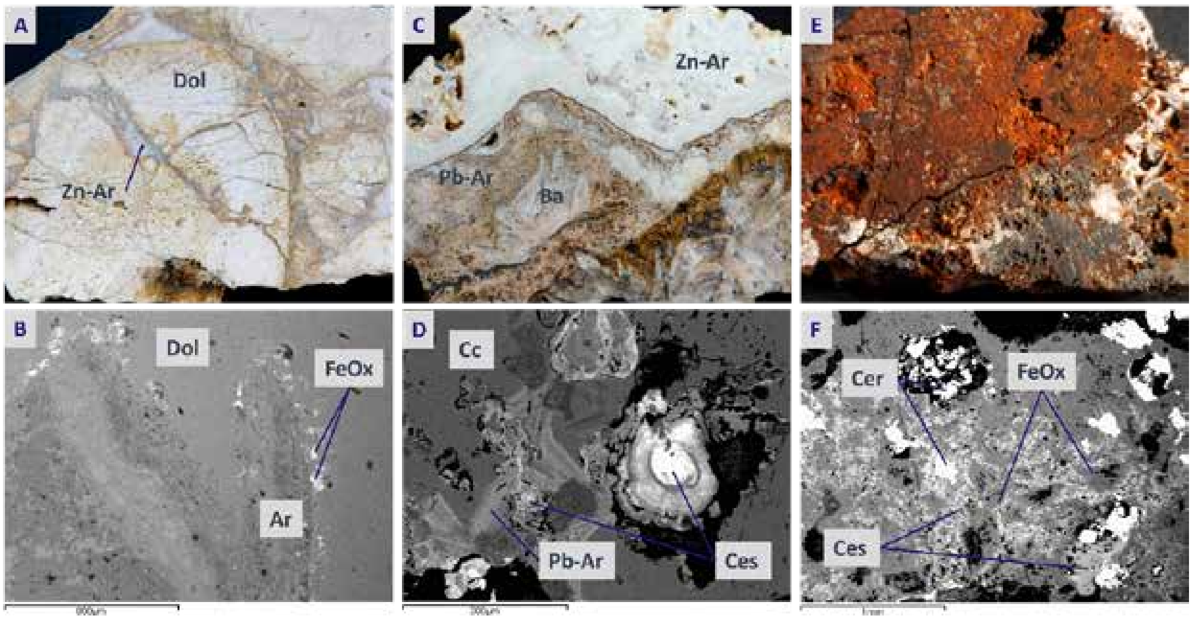

Figure 3. (A) Specimen from Sotiras showing Zn-rich aragonite veins within dolomite breccia. (B) BSE image from Sotiras depicting an aragonite vein within dolomite, with iron oxides forming along the contact zone. (C) Sample from Vouves displaying distinct mineralogical zonation. (D) Botryoidal cesarolite associated with Pb-rich aragonite. (E) Brecciated formation from Koumaria featuring a barite vein. (F) Typical Koumaria mineralization, characterized by cerussite, iron oxides, and cesarolite forming euhedral structures related to primary mineral phases. Mineral abbreviations: Cer: Cerussite, Ces: Cesarolite, Cc: Calcite, Ar: Aragonite, Pb-Ar: Pb-rich aragonite, Zn-Ar: Zn-rich aragonite, FeOx: Iron oxides, Dol: Dolomite.

3. Geochemistry

All samples from the Zn-Pb-Ag deposits exhibit several notable similarities, including consistently low bulk concentrations of Na, K, Al, Si, and Ti, while being enriched in Ca. This suggests a limited contribution from silicate phases and reinforces the strong association of the mineralization with carbonate-dominated host rocks.Sotiras Zn-Pb mine:

Elevated Mg and Ca concentrations are attributed to the presence of carbonates. Copper, Pb, and S exhibit the lowest amounts among all samples, with 0.002 wt.% Cu, 0.05 wt.% Pb, and 0.1 wt.% SO_3. Zinc is present at 0.48 wt.% Zn. Unlike all other samples, Ba was not detected, as its levels were below the detection limit. Iron and manganese concentrations are 1.37 wt.% Fe_2O_3 and 0.084 wt.% MnO, respectively.

Koumaria Zn-Pb mine:

The Koumaria samples are notable for the exceptionally high lead concentration, reaching 43 wt.% Pb, and the highest quantities of zinc (up to2.12 wt.% Zn) and manganese (up to 2.65 wt.% MnO), along with significant amounts of iron (up to 29 wt.% Fe_2O_3). Additionally, it contains notable silver (Ag) values up to 0,137 wt.% and the highest recorded copper (Cu) concentration of 0,104 wt.% among all analyzed samples. In contrast, calcium is the lowest among all samples at 1.05 wt.% Ca. Silicon and sulfur are present at similar levels, with 1.76 wt.% SiO_2 and 0.93 wt.% SO_2, respectively.

Vouves Zn-Pb mine:

The Vouves samples, similar to those from Sotiras, display high Ca and Mg concentrations (due to calcite-aragonite and dolomitic marble) along with notable amounts of zinc and lead. Zinc content ranges from 0.6 to 1.6 wt.%, while Pb varies from 0.25 to 0.64 wt.%. These samples also exhibit the highest recorded levels of barium and sulfur, reaching up to 16 wt.% Ba and 8 wt.% SO_3. Copper concentrations reach up to 0.049 wt.% Cu, while Fe and Mn are present in significant amounts, with values up to 4.12 wt.% Fe_2O_3 and 0.445 wt.% MnO.

Mavrolakkas Fe-Mn mine:

This site exhibits the highest iron and silicon quantities, exceeding 32.5 wt.% Fe_2O_3 and 11.1 wt.% SiO_2, respectively. Additionally, significant amounts of barium 10.5 wt.% Ba, sulfur 5.6 wt.% SO3 are observed, Manganese was measured at 1.8 wt.% MnO. In contrast, copper and zinc concentrations are relatively low at 0.007 wt.% Cu and 0.047 wt.% Zn, while lead is present at 0.36 wt.% Pb.

Table 1. Representative concentrations of major oxides and trace elements (wt.%), using X-ray fluorescence (WD-XRF).

Wt.%	Sot1	Vouv1	Vouv2	Vouv3	Koum1	Mavr1
Na2O	0.07	0.09	0.21	bdl	bdl	0.15
MgO	6.1	0.85	1.13	5.29	0.09	0.78
Al2O3	0.06	0.09	0.08	0.09	0.11	0.85
SiO2	0.24	0.32	0.25	0.36	1.76	11.1
P2O5	0.04	0.06	0.06	0.04	0.05	0.02
SO3	0.10	0.23	8.0	3.43	0.93	5.6
Cl	0.02	0.02	0.03	0.01	bdl	0.01
K2O	0.03	0.06	0.09	0.06	0.16	0.31
CaO	47.3	52.86	38.0	39.47	1.05	19.50
TiO2	0.003*	0.01	0.06	0.04	0.01	0.06
MnO	0.08	0.02	0.02	0.45	2.65	1.8
Fe2O3	1.37	0.23	3.90	4.12	29.0	32.5
Cu	0.002*	0.03	0.049*	0.002*	0.10	0.007*
Zn	0.48	0.60	1.17	1.67	2.12	0.047*
Sr	0.005*	0.03	0.26	0.13	bdl	0.13
Ag	bdl	bdl	bdl	bdl	0.137*	bdl
Ba	bdl	0.65	16.0	7.34	2.30	10.5
Pb	0.05	0.25	0.64	0.57	43.0	0.36
LOI	43.95	43.33	28.94	35.54	14.68	14.94

* For the above samples, rounding was maintained to the third decimal place.

Discussion and conclusions

Most non-sulfide Zn-Pb deposits in Europe are classified as “calamine” ores, defined as concentrations of oxidized Zn and Pb minerals formed through deep weathering of carbonate-hosted primary sulfide ores (Large, 2001). These calamine-type ores are predominantly composed of smithsonite and hydrozincite, which result from the interaction of low-pH, Zn-rich groundwater with carbonate host rocks. Lead-bearing minerals, such as anglesite and cerussite, may also be present if the primary sulfide paragenesis contains galena (Hitzman et al., 2003).

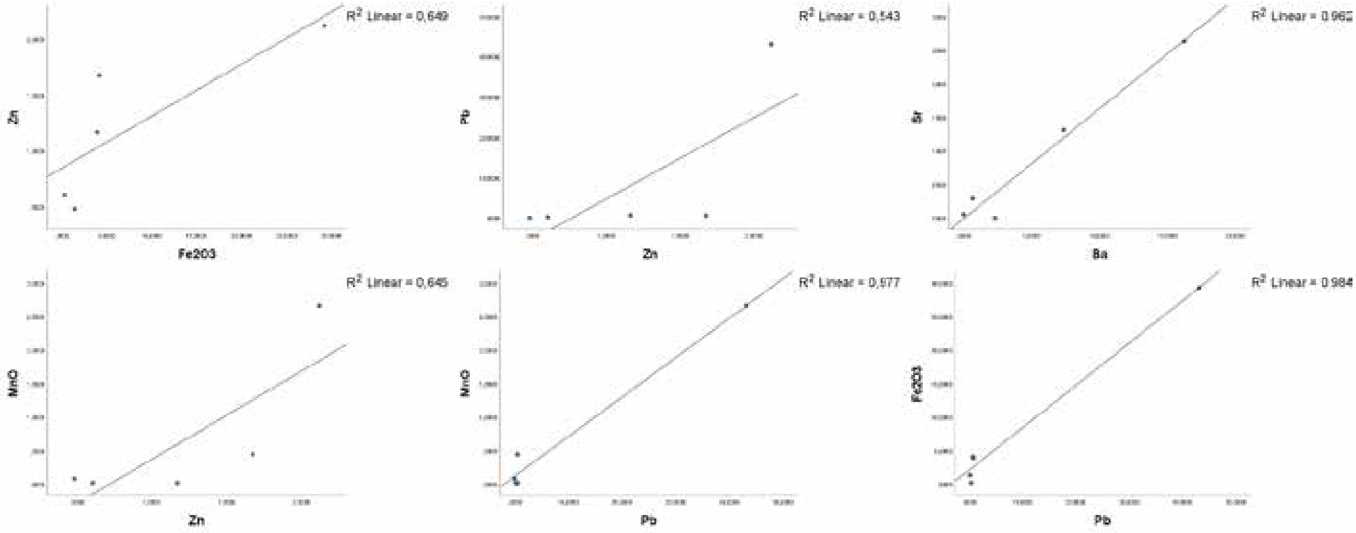

Figure 4. Positive correlation diagrams between major oxides and trace elements of the samples from Sotiras, Vouves and Koumaria.

The smithsonite and cerussite mineralization on Thasos Island is primarily hosted within breccia along large scale low-dipping (0–20°) detachment faults, which are likely of Middle Eocene to Early Miocene age, according to the studies of Brun and Sokoutis (2018) on the Kerdilion detachment fault. The ores are predominantly found within marbles at the contact zones with gneisses of the intermediate unit. The related Fe-oxides are enriched in Mn, Pb, and Zn, as well as As, Si. Other minerals include cesarolite, Pb-bearing aragonite-calcite, jarosite, and barite.

Chemical analyses reveal significant bulk concentrations of zinc and lead across the studied deposits, with Koumaria showing in addition to very high Zn and Pb content, notable enrichment in silver and copper (malachite, azurite). The correlation diagrams in Figure 4 provide insights into the geochemical relationships between different elements in the analyzed non-sulfide Zn-Pb deposits. The strong correlations of Pb with Fe and Mn oxides (Fe_2O_3 and MnO) suggest that lead was significantly remobilized (from oxidation of galena) and precipitated in oxidation zones either as cesarolite ($PbMn_4O_6(OH)_2$) and cerussite or was adsorbed onto Fe oxides/hydroxides. Moderate correlation of Zn with Fe and Mn oxides indicates that zinc liberated through oxidation from sphalerite and was partly incorporated into smithsonite and partly within the iron oxides (Fe-Zn-Si-As oxides). The moderate correlation between Pb and Zn indicates that these metals may have been liberated, transported and deposited together, although their geochemical behavior differs during formation of e.g., smithsonite vs. cerussite. The near-perfect correlation between Sr and Ba indicates the barite ($BaSO_4$) mineralization, with Sr substituting for Ba in the crystal lattice. In conclusion, the geochemistry supports a supergene enrichment model in which primary sulfides (galena, sphalerite) have undergone oxidation, leading to the formation of secondary carbonates (smithsonite, cerussite) and Pb-Mn oxides (cesarolite).

According to Hitzman *et al.* (2003), three main genetic models are considered as potential proto-ore types: Mississippi Valley Type (MVT), SEDEX, and Carbonate Replacement. Thasos deposits share almost all the typical characteristics of MVT Zn–Pb deposits. These include: a) carbonate sedimentary (dolomite) host rock, b) lead (Pb) and zinc (Zn) mineralization, with copper (Cu), silver (Ag), c) the presence of barite, d) stratiform morphology, and f) spatial relation with shale platform that contains hydrocarbon reservoir (Prinos oil district).

The development of the supergene mineralization may be attributed to the oxidation of the primary sphalerite-galena deposits which likely occurred through the infiltration of meteoric waters along post-Messinian normal faults. According to Boulvais *et al.* (2007) two distinct fluid flow events are associated with the normal faulting of Thasos: a) an early-stage, high-temperature fluid, likely of hydrothermal origin, and a later-stage, low-temperature fluid, possibly meteoric in nature, which appears to have driven the oxidative mineralization.

References

Boni, M., & Large, D. 2003. Non-sulfide zinc deposits: A new classification scheme based on geological and metallogenic criteria, Economic Geology 98(4), pp. 685–714.

Boulvais, P., Tistarelli, D., Laignel, B., and Lévêque, F., 2007. Fluid flow and supergene alteration in the Thasos Zn-Pb deposits, Greece: Evidence from fluid inclusions and stable isotope data. Geofluids 7(2), pp. 122-141.

Brun, J.P. & Sokoutis, D. 2007. Kinematics of the southern Rhodope core complex (North Greece), International Journal of Earth Sciences 96(6), pp. 1079–1099.

Brun, J. P., & Sokoutis, D. (2018). Core complex segmentation in North Aegean, a dynamic view. *Tectonics*, *37*(6), 1797-1830.

Epitropou, P. 2005. Historical overview of mining activity in Thasos.

Hitzman, M.W., Large, R.R., and Ludden, J.N., 2003. The Mississippi Valley-type deposits: A summary of their genesis and significance. Economic Geology 98(4), pp. 639-668.

Koukouli, E., Liritzis, I. & Zacharias, N. 1988. The prehistoric ochre mines of Tzines, Thasos, Greece: A mineralogical and geochemical approach, Archaeometry 30(2), pp. 231–243.

Large, R.R., 2001. The genesis of calamine deposits and their role as an indicator of supergene enrichment. Mineralium Deposita 36(5), pp. 392-409.

Wawrzenitz, N., & Krohe, A. 1998. Exhumation and doming of the Thasos metamorphic core complex (S Rhodope, Greece): structural and geochronological constraints. Tectonophysics 285(3-4), 301-332.

17th INTERNATIONAL CONGRESS
of the Geological Society of Greece

BULLETIN OF THE GEOLOGICAL
SOCIETY OF GREECE, SP. PUBL.

EXTENDED ABSTRACT 187

Study of the geochemical distribution of uranium and thorium in the soils of the Sarigiol Basin, Ptolemais, and their environmental significance.

Ladas, A.[1], Melfos, V.[2], Papadopoulou, L.[3], Kantiranis, N.[4]

(1) Aristotle University of Thessaloniki, Thessaloniki, Greece, anastladas@geo.auth.gr, (2) Aristotle University of Thessaloniki, Thessaloniki, Greece, melfosv@geo.auth.gr, (3) Aristotle University of Thessaloniki, Thessaloniki, Greece, lambrini@geo.auth.gr, (4) Aristotle University of Thessaloniki, Thessaloniki, Greece, kantira@geo.auth.gr

Introduction

The region of Kozani-Ptolemaida-Amynteo Basin hosts the largest lignite deposits in Greece. For decades, lignite has been extracted, stockpiled, and subsequently burned in the thermal power plants (TPPs) of the area. During combustion, many potentially trace elements, with some of them being harmful, are enriched in the fly ash dispersed into the broader region (Kassoli-Fournaraki et al., 1993; Sahanidis et al., 2001). Although previous research indicates that few elements from the region's fly ash exhibit a high degree of leaching, environmental concerns may arise due to the large volume of the fly ash produced (Georgakopoulos et al., 2002b).

The aim of this study was to investigate the geochemical distribution of uranium (U) and thorium (Th) in the soils of the Sarigkiol Basin, SE of Ptolemais town, as well as to evaluate their potential environmental impact. Additionally, an important environmental question addressed in this study is whether the origin of these two trace elements is lithogenic or anthropogenic.

Materials and Methods

For the purposes of this study, 24 soil samples were collected from the Sarigkiol Basin, Ptolemais. Eleven (11) of these samples were provided by Kantiranis et al. (2016) as part of research on assessing the origin of Cr(VI) in the groundwater supplying the municipal districts of Akrini, Agios Dimitrios, and Ryaki in the Municipality of Kozani. The data for these samples derived from the same study. The remaining thirteen (13) samples were collected in October 2023 for the purposes of this study. The sampling locations for each sample can be found in Table 1.

Table 1. Sampling locations for each sample (WGS 84, in decimal degrees).

Sample Name	Longitude	Latitude	Sample name	Longitude	Latitude
2A	329990.19	4471289.72	**15A**	323098.45	4474913.69
4A	326645.56	4471952.36	**52A**	313162.93	4473818.06
5A	326071.14	4471191.24	**54A**	315574.01	4473258.98
8A	323297.78	4475566.17	**55A**	315932.25	4471924.25
11A	322602.77	4477489.33	**56A**	314824.76	4470738.92
12A	321720.56	4476578.47	**57A**	317918.63	4470747.89
Sample name	**Longitude**	**Latitude**	**Sample name**	**Longitude**	**Latitude**
59A	318922.41	4473486.02	**36A**	320025.63	4472172.87
45A	315863.21	4469271.60	**30A**	322677.43	4473964.08
43A	317280.18	4468718.66	**38A**	322902.25	4471394.86
41A	319251.14	4470284.69	**39A**	323945.05	4470281.23
13A	321552.29	4475650.68	**19A**	325023.98	4473946.03
35A	321139.5	4473371.16	**23A**	324758.48	4472070.20

The sampling area and the sample locations are presented in Figure 1. Sampling was conducted using an "Edelman" auger from the top, 10-cm-thick soil horizon. The samples were subsequently dried in an oven at 110°C for 24 hours, then grinded with a mechanical grinder, quartered with a mechanical splitter, and final grinded using an agate mortar.

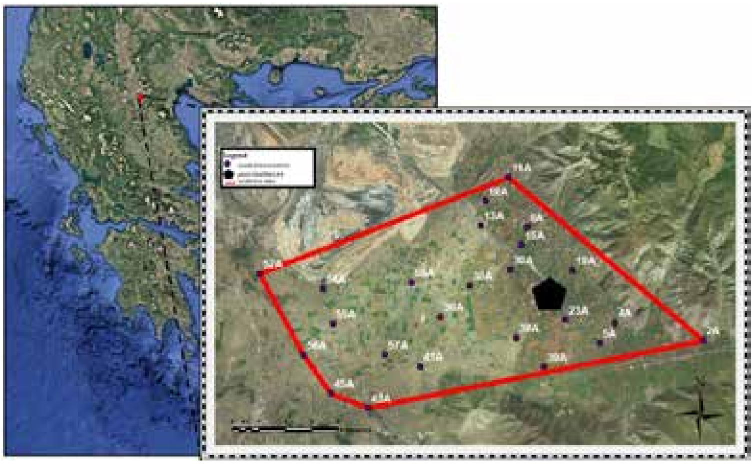

Figure 1. The sampling area and sampling sites (map taken from Google Earth).

The mineralogical analysis was performed using the X-ray diffraction (XRD) on randomly oriented powder preparations. A D8 ADVANCE diffractometer by BRUKER, housed in the Department of Mineralogy–Petrology–Economic Geology at the School of Geology, Aristotle University of Thessaloniki (AUTH), was used for this purpose. For the chemical analysis, the X-ray fluorescence (XRF) spectrometry was employed, using an S1 Titan 600 fluorometer by BRUKER, also located in the Department of Mineralogy–Petrology–Economic Geology at AUTH. The concentrations of the major oxides SiO_2, TiO_2, Al_2O_3, Fe_2O_3, MnO, MgO, CaO, K_2O, P_2O_5, SO_3, as well as the trace elements Cr, Ni, Cu, Zn, As, Rb, Sr, Y, Zr, Ba, Pb, Th and U were determined. Loss on ignition was determined as the percentage weight loss after heating 1 g of each sample at 1050/2h. The concentrations of the chemical elements were calculated using the Geoexploration reference curves integrated into the fluorosimeter. The accuracy of the values was ensured through the measurement of standard samples and the creation of calibration curves, with R^2 exceeding 0.9 in all cases.

The pre-existing measurements were conducted by the internationally certified and reliable Canadian Activation Laboratories LTD, located at 1336 Sandhill Drive, Ancaster, Ontario, Canada L9G 4V5 (http://www.actlabs.com). The following methods were applied: Inductively Coupled Plasma Optical Emission Spectrometry (ICP-OES) on fused pellets prepared with lithium metaborate ($LiBO_2$) and lithium tetraborate ($Li_2B_4O_7$) fusion; Inductively Coupled Plasma Mass Spectrometry (ICP-MS) on fused pellets prepared similarly; Instrumental Neutron Activation Analysis (INAA); and ICP after total digestion in a solution of $HClO_4$, HNO_3, HCl, and HF at 200°C (Kantiranis et al., 2016).

Due to the small number of samples, simple statistical processing was applied, and correlations of U and Th were performed with mineral phases, major oxides, and trace elements. Correlation diagrams were created, and the correlation coefficient R^2 was calculated. Finally, geochemical distribution maps were created in the ArcGIS 10.8.1 environment using the geostatistical Natural Neighbor (NN) method. Additionally, prediction models were generated using the deterministic Inverse Distance Weighted (IDW) method.

Results and Discussion

The mineralogical analysis of the soil samples identified the major mineral phases as calcite, quartz, dolomite, and feldspars. Chlorite, muscovite, amphiboles, serpentine, talc, pyroxenes, and clay minerals were also contained in the soils of the basin in minor amounts. A summary of their statistical distribution is provided in Table 2. The presence of these minerals is largely attributed to the lithology of the area, originating from the carbonate and ophiolitic rocks surrounding the mountainous regions of the basin (Kazakis et al., 2017, 2018), which enrich the detrital material in the study area, a region being now a drained mire (Pavlidis, 1985; Kazakis et al., 2018). Part of the calcite, quartz, feldspars, as well as pyroxenes and dolomite, is also attributed to lignite combustion (Filippidis and Georgakopoulos, 1992; Filippidis et al., 1996; Kolovos et al., 2002; Kostakis, 2009).

Table 2. Descriptive statistics of the mineralogical analysis (%w/w).

	Qz	Cc	Do	F	Ch	M	Am	Serp	Ta	Px	Cl
Mean	30.3	33.3	9.1	10.7	4.8	6.0	1.2	1.9	1.4	0.2	1.0
Median	22.0	25.3	2.3	9.6	3.7	3.1	0.8	0.6	1.2	-	-
STDev	17.6	23.4	12.7	6.6	3.6	7.5	1.4	2.3	1.5	0.8	2.2
Max	76	78.9	47.7	29.1	12.1	27.6	4.2	8	4.7	3.4	10.3
Min	51	-	-	-	-	-	-	-	-	-	-

1: STDev: standard deviation; Max: Maximum Value; Min: Minimum Value; Qz; quartz, Cc: calcite; Do: dolomite; F: feldspar (plagioclase + K-feldspar); Ch: chlorite and kaolinite; M: mica; Am: amphiboles; Serp: serpentine; Ta: talc; Px: pyroxenes; Cl: clay minerals.

Tables 3 and 4 present the summary statistics of the chemical analyses of major oxides and trace elements, respectively. Additionally, the following trace elements were analyzed: Cr, Ni, Cu, Zn, As, Rb, Sr, Zr, Ba, and Pb. The presence of major oxides is attributed to the mineralogical composition of the soil. Nickel (Ni) exhibits a lithogenic origin, while arsenic (As), the third most enriched element, has a mixed origin (Nanos et al., 2015; Kantiranis et al. 2016). All other trace elements, including Cr, Cu, Zn, Rb, Sr, Y, Zr, Ba, Pb, Th, and U, have been identified in previous studies as being present in the region's lignites, as well as in the fly ash and bottom ash produced by the area's thermal power stations (Georgakopoulos et al., 1996; 2002a,b;c). For each major oxide and trace element, the pollution coefficient was calculated by comparing the results to the global average soil values (Hansford and Boerngen, 1984; Kabata-Pendias, 2011).

Table 3. Descriptive statistics of the major oxides (%w/w) of the samples studied.

	SiO_2	TiO_2	Al_2O_3	MnO	MgO	CaO	K_2O	P_2O_5	SO_3	LOI
Mean	41.68	0.62	10.73	5.89	0.12	5.79	15.32	1.63	0.23	0.17
Median	39.75	0.63	10.86	5.49	0.12	4.19	16.55	1.43	0.22	0.14
STDev	10.58	0.18	2.65	1.39	0.03	3.39	8.22	0.62	0.08	0.16
Max	65.31	1.06	15.37	8.71	0.21	13.55	33.25	2.93	0.38	0.75
Min	23.87	0.34	6.40	3.73	0.06	1.25	1.28	0.78	0.08	0.00

1: STDev: standard deviation

Table 4. Descriptive statistics of the trace elements contents (in mg/kg) of the samples studied.

	Cr	Ni	Cu	Zn	As	Rb	Sr	Y	Zr	Ba	Pb	Th	U
Mean	593.3	287.1	33.1	68.7	9.8	80.7	103.7	24.8	183.1	246.5	16.6	7.9	3.3
Median	395.0	248.5	32.0	67.5	9.0	65.5	103.0	24.0	175.0	196.0	17.0	8.3	2.2
STDev	516.4	163.8	9.5	17.4	5.3	54.5	26.8	8.2	82.8	137.7	6.3	2.4	3.4
Max	2230.0	803.0	52.0	105.0	26.0	220.0	167.0	48.0	438.0	803.0	32.0	12.1	12.0
Min	33.0	80.0	16.0	41.0	2.0	15.0	14.0	13.0	72.0	107.0	3.0	4.0	0.5

1: STDev: standard deviation

The pollution coefficients calculated for U and Th (Table 5) showed relatively low values. In the case of Th, most samples had pollution coefficient values below 1, classifying them as non-polluted. Additionally, six samples had values between 1 and 3, characterizing them as moderately polluted. Similarly, U exhibited pollution coefficient values <1 for the majority of the samples, classifying them as non-polluted. Two samples showed values between 1 and 3, indicating moderate pollution, while four samples had pollution coefficient values between 3 and 6, classifying them as significantly polluted for U.

The correlation of U and Th concentrations with mineral phases, major oxides, and trace elements revealed environmentally significant trends. Initially, U correlated with Th, yielding an R^2 value of 0.42, indicating a mild correlation and suggesting a partially common origin. Both radioactive elements showed positive correlations with quartz and feldspars but negative correlations with calcite and dolomite, with no correlation observed with other mineral phases.

For quartz, U had an R^2 value of 0.48 and Th an R^2 of 0.46 (mild correlations), while for feldspars, U showed R^2 = 0.46 and Th R^2 = 0.43 (mild correlations). Consequently, due to their positive correlations with quartz and feldspars, both elements also exhibited positive correlations with the major oxides SiO_2, Al_2O_3, and K_2O. For U, the R^2 values for these oxides were 0.50, 0.41, and 0.46 (mild correlations), respectively, while for Th, the R^2 values were 0.59, 0.60, and 0.63 (strong correlations), respectively. Positive correlations were also observed for Fe_2O_3 and TiO_2, although with lower correlation values. The other major oxides exhibited negative or negligible correlations with U and Th.

Regarding trace elements, U had the strongest correlation with Zr, Y, and Zn, with R^2 values of 0.75, 0.56, and 0.41, respectively (strong to mild correlations). Other trace elements showed weaker positive or negligible correlations. Th exhibited its highest correlation with Zn, Ba, Y, and Pb, with R^2 values of 0.72, 0.50, 0.48, and 0.44, respectively (strong to mild correlations). Figure 2 presents correlation diagrams for U and Th with various minerals, major oxides, and trace elements.

Table 5. Pollution coefficient for U and Th of the samples studied.

Sample	**2A**	**4A**	**5A**	**8A**	**11A**	**12A**	**15A**	**52A**	**54A**	**55A**	**56A**	**57A**
C.U (ppm)	12	1	0.5	2.2	0.5	0.5	11	2.2	1.6	2	10	9
P.C.	4	0.33	0.17	0.17	0.73	0.17	3.67	0.73	0.53	0.67	3.33	3
C.Th (ppm)	9	8	8	4	5	4	11	9	6	10	9	9
P.C	0.98	0.87	0.87	0.43	0.54	0.43	1.2	0.98	0.65	1.09	0.98	0.98
Sample	**59A**	**45A**	**43A**	**41A**	**13A**	**35A**	**36A**	**30A**	**38A**	**39A**	**19A**	**23A**
C.U (ppm)	1.2	2.6	0.5	2.5	4.9	1.2	1.5	3.9	2.6	2.5	1.3	2.1
P.C.	0.4	0.87	0.17	0.83	1.63	0.4	0.5	1.3	0.87	0.83	0.43	0.70
C.Th (ppm)	4	11.4	6.8	9.3	6.8	4.7	6.8	9	11.4	12.1	6.1	8.6
P.C.	0.43	1.24	0.74	1.01	0.74	0.51	0.74	0.98	1.24	1.32	0.66	0.93

C.U: uranium concentration in ppm; C.Th: thorium concentration in ppm; P.C.; pollution coefficient

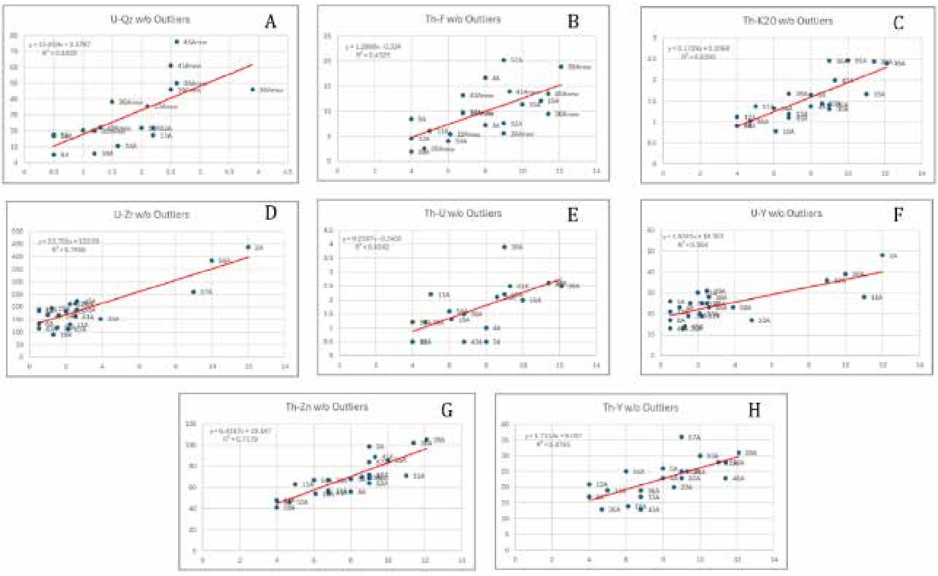

Figure 2. Correlation of U and Th. A) U with quartz, B) Th with feldspar, C) Th with K_2O, D) U with Zr, E) Th with U, F) U with Y, G) Th with Zn και H) Th with Y.

Finally, geochemical distribution maps were created for U, Th, and all other determined major oxides and trace elements. Alongside these distribution maps, predictive models were constructed for all chemical elements analyzed in the soils of the studied area.

The distribution maps for U and Th are presented in Figures 3 and 4, respectively. Additionally, the predictive model for K_2O is presented in Figure 5, which demonstrates very low errors (ME = -0.002 and RMSE = 0.6) based on the method applied.

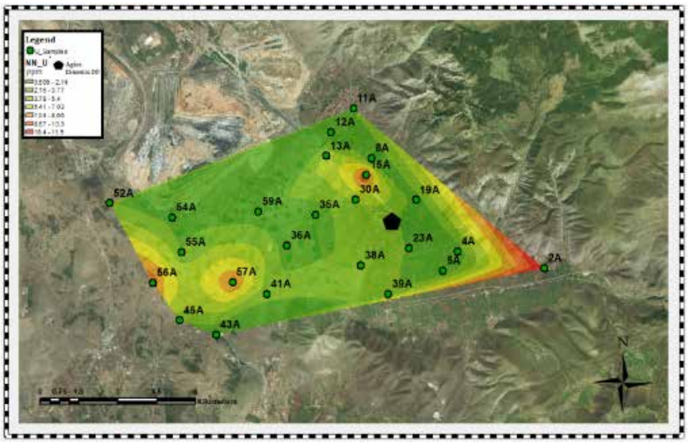

Figure 3. Geochemical distribution map of U using the NN method.

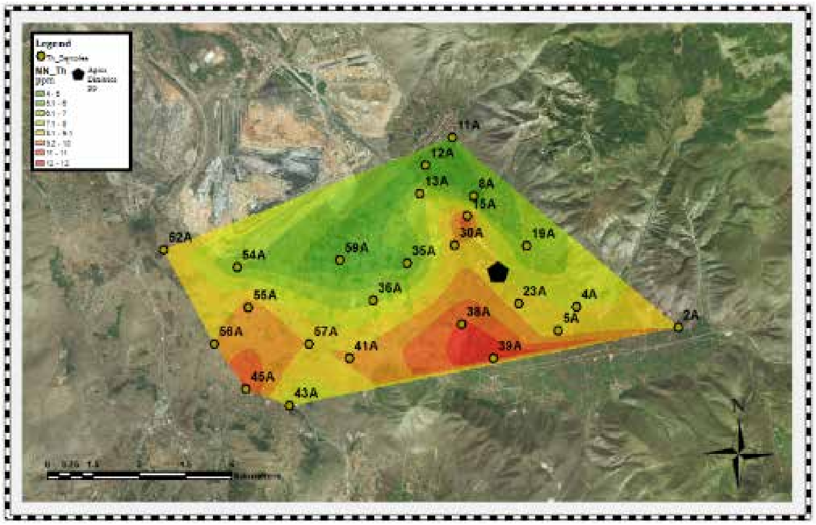

Figure 4. Geochemical distribution map of Th using the NN method.

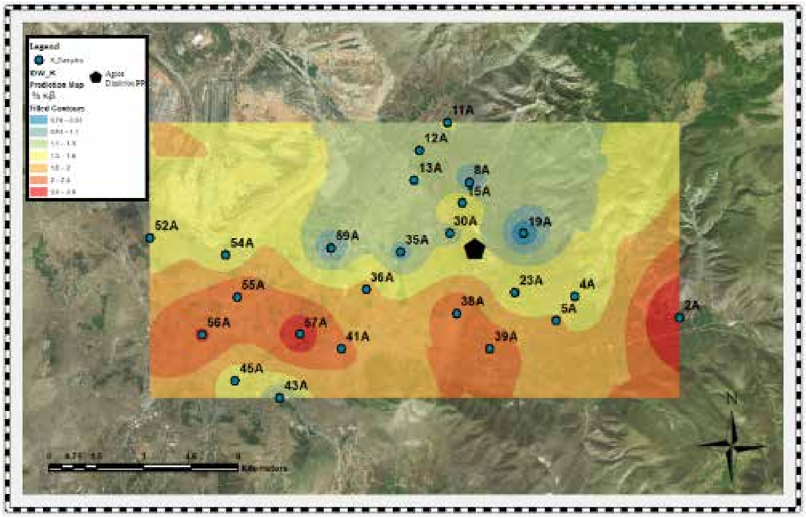

Figure 5. Geochemical distribution map of K_2O using the IDW method.

Conclusions

The results of this study present the geochemical distribution of U and Th in the soils of the Sarigiol Basin in the Ptolemais region, as well as their environmental significance. The main conclusions are as follows:

- Both radioactive elements, U and Th, are present in the basin's soils and show strong correlations with minerals such as quartz and feldspars, as well as with the oxides SiO_2, Al_2O_3, and K_2O.
- A strong correlation was observed between U and Th with the trace elements yttrium (Y), zirconium (Zr), zinc (Zn), and lead (Pb). These four trace elements exhibited a similar distribution pattern in the basin to this of U and Th and are primarily of anthropogenic origin, as they have been linked to industrial activities by previous studies, especially coal burning for energy production as they present high enrichment factors in fly ash.
- The high correlation values of these minerals, major oxides, and trace elements with U and Th, along with their geochemical distribution—showing higher concentrations near industrial activities—indicate anthropogenic activity, likely including lignite combustion and the dispersion of fly ash.
- According to the predictive models, K_2O could serve as a guiding element for identifying elevated concentrations of both radioactive elements.
- The concentrations of U and Th were considered relatively low based on the pollution index for each sample. However, their levels are not negligible, as both elements are radioactive and toxic at high concentrations, necessitating ongoing monitoring of their levels.

References

Filippidis, A., Georgakopoulos, A., 1992. Mineralogical and chemical investigation of fly ash from the Main and Northern lignite fields in Ptolemais, Greece. Fuel 71(4), 373-376.

Filippidis, A., Georgakopoulos, A., Kassoli-Fournaraki, A., 1996. Mineralogical components of some thermally decomposed lignite and lignite ash from the Ptolemais basin, Greece. International Journal of Coal Geology 30, 309-311.

Georgakopoulos, A., Fillipidis A., Kassoli-Fournaraki A., Fernandez-Turiel J.L., Llorens J.F., 1996. The content of some trace elements in surface soils and fly ash of Ptolemais lignite basin, Macedonia, Greece. 3rd International Conference on Environmental Pollution, 16-20/09/1996, Thessaloniki, 114-118.

Georgakopoulos, A., Filippidis, A., Kassoli-Fournaraki, A., Iordanidis, A., Fernandez-Turiel, J.L., Llorens, J.F., Gimeno, D., 2002a. Environmentally Important Elements in Fly Ashes and Their Leachates of the Power Stations of Greece. Energy Sources 24, 83-91.

Georgakopoulos, A., Filippidis, A., Kassoli-Fournaraki, A., Fernandez-Turiel, J.L., Llorens, J.F., Mousty, F., 2002b. Leachability of Major and Trace Elements of Fly Ash from Ptolemais Power Station, Northern Greece, Energy Sources 24(2), 103-113.

Georgakopoulos, A., Filippidis, A., Fernandez-Turiel, J.L., Kasoli-Fournaraki, A., Iordanidis, A., 2002c. Lithogenic and anthropogenic origin of trace elements in surface soils of the lignite-bearing basin of Amyntaio-Ptolemaida-Kozani. 6th Panhellenic Geographic Conference, Proceedings, 03-06/10/2002, Thessaloniki, pp. 335-344.

Hansford, T.S., Boerngen, G.J., 1984. Element Concentrations in Soils and Other Surficial Materials of the Conterminous United States. U.S. Geological Survey, Professional paper 1270, 105p.

Kabata-Pendias, A., 2011. Trace Elements in Soils and Plants. 4th ed., Taylor and Francis Group, LLC, U.S.A, p. 37-45, 50, 82-83, 158-164, 505.

Kantiranis, N., Mitrakas, M., Filippidis, A., Vargemezis, G., Zoumboulis, A., Tsourlos, P., Fikos, H., Vamvakaris, D., Karagianni, E., Paradeisopoulou, P., Kazakis, N., Vogiatzis, D., Kaprara, E., Kalaitzidou, K., Drakoulis, A., Ioannidis, M., Kollias, P., Georgiou, I., 2016. Assessment of the origin of Cr(VI) in the groundwater supplying the Municipal Districts of Akrini - Agios Dimitrios - Ryaki in the Municipality of Kozani. Final report, Aristotle University of Thessaloniki, Department of Chemical Engineering, Department of Geology, and Department of Chemistry, pp. 7-32, 85-105, 135-243.

Kassoli-Fournaraki, A., Georgakopoulos, A., Michailidis, A., Filippidis, A., 1993. Morphology, mineralogy and chemistry of the respirable-size (<5μm) fly ash fraction from the Main and Northern lignite fields in Ptolemais, Macedonia, Greece. In: Current Research in Geology Applied to Ore Deposits (P. Fenoll Hach-Ali, J. Torres-Ruiz, F. Gervilla, eds), La Guioconda. Second Biennial SGA Meeting, Granada, Spain, 727-730.

Kazakis, N., Kantiranis, N., Kalaitzidou, K., Kaprara, E., Mitrakas, M., Frei, R., Vargemezis, G., Tsourlos, P., Zouboulis, A., Filippidis, A., 2017. Origin of hexavalent chromium in groundwater: The example of Sarigkiol Basin, Northern Greece. Science of the Total Environment 593-594, 552-566.

Kazakis, N., Kantiranis, N., Kalaitzidou, K., Kaprara, E., Mitrakas, M., Frei, R., Vargemezis, G., Vogiatzis, D., Zouboulis, A., Filippidis, A., 2018. Environmentally available hexavalent chromium in soils and sediments impacted by dispersed fly ash in Sarigkiol basin (Northern Greece). Environmental Pollution 235, 635-637.

Kolovos, N., Georgakopoulos, A., Filippidis, A., Kavouridis, C., 2002. Environmental Effects of Lignite and Intermediate Steriles Coexcavation in the Southern Lignite Field Mine of Ptolemais, Northern Greece. Energy Sources 24(6), 561-573.

Kostakis, G., 2009. Characterization of the fly ashes from the lignite burning power plants of northern Greece based on their quantitative mineralogical composition. Journal of Hazardous Materials 166(2–3), 972-977.

Nanos, N., Grigoratos, T., Rodríguez Martín, J.A., Samara, C., 2015. Scale-dependent correlations between soil heavy metals and As around four coal-fired power plants of northern Greece. Stoch Environ Res Risk Assess 29, 1531–1543.

Pavlides, S., 1985. Neotectonic evolution of the Florina–Vegoritis–Ptolemaida basin (Western Macedonia). PhD Thesis, Department of Geology, Aristotle University of Thessaloniki, pp. 38-45 [Παυλίδης, Σ., 1985. Νεοτεκτονική εξέλιξη της λεκάνης Φλώρινας – Βεγορίτιδας – Πτολεμαΐδας (Δ. Μακεδονία), Διδακτορική Διατριβή, Τμήμα Γεωλογίας ΑΠΘ, σελ 38-45.].

Sahanidis, Ch., Georgakopoulos, A., Filippidis, A., Kasoli-Fournaraki, A., 2001. Trace element content of marl layers in the lignite-bearing basin of Ptolemaida-Amynteon, Western Macedonia. Bulletin of the Geological Society of Greece 34(3), 1115-1122.

17th INTERNATIONAL CONGRESS
of the Geological Society of Greece

BULLETIN OF THE GEOLOGICAL
SOCIETY OF GREECE, SP. PUBL.

EXTENDED ABSTRACT 188

Flood Dredge Spoils Mapping with the Use of UAS and GIS: The Case of 2020 Evia Flood

Lida Lakidi[1], Nafsika Ioanna Spyrou[1], Michalis Diakakis[2], Christos Filis[1], Evelina Kotsi[1], Spyridon Mavroulis[1], Emmanuel Skourtsos[1], Haralambos Kranis[1] and Efthymios Lekkas[1]

(1) Department of Dynamic, Tectonic, Applied Geology, Faculty of Geology and Geoenvironment, School of Sciences, National and Kapodistrian University of Athens, 15784 Athens, Greece

(2) Department of Geography and Climatology, Faculty of Geology and Geoenvironment, School of Sciences, National and Kapodistrian University of Athens, 15784 Athens, Greece

Introduction / Background

Natural disasters increasingly threaten human health, the environment, and the economy over time. The rise in frequency is attributed to two key factors: climate change and escalating human activity. Climate change intensifies natural phenomena, while human activity disrupts landscapes, leading to environmental imbalances. In 2023 alone, over 400 natural disasters were recorded globally, resulting in the deaths of 93 million people and damages amounting to

$498 billion USD. As shown in the accompanying image, from 1970 to 2024, the number of disasters has increased, with an average of 266.26 events per year (Burgueño Salas, 2024).

Dredge Spoils refers to the collection of solid and organic materials transported through water, which either flow in the watercourse and on the land surface or accumulate at the bottom of it. The accumulation of materials in aquatic environments is caused by factors such as urban development, agriculture, natural disasters, tidal effects, etc.

Flash floods carry a lot of dredged spoils due to the passage of water through vast areas, which then accumulate in floodplains, causing significant damage. They can roll boulders, cut trees, destroy buildings, and carry fabrics and metals. The resulting materials are transported to water channels and eventually to floodplains, leading to the contamination of the natural environment and acting as waste (Rao, 2017). Dredge materials are divided into two categories: Debris and Solid waste.

The flow of debris is one of the most destructive processes and can be defined as a rapid movement of mass composed of granular solids, water, and air (Varnes, 1978). The usual conditions for debris flow activity include steep slopes, loose materials, and wet conditions (Varnes, 1978). Debris flows can travel long distances and carry large amounts of debris along the way (Zimmermann & Haeberli, 1992). Moreover, in coastal environments, large volumes of debris are created and deposited after natural disasters such as tropical storms, floods, volcanic activity, earthquakes, fires, or explosions (Zimmermann & Haeberli, 1992).

Debris can sometimes be caused by human intervention due to uncontrolled land occupation and deforestation. For example, in Japan, most debris flows are created because of deforestation for building homes and temples. Acid rain could also be a factor, as seen in the Cubatáo area (Zimmermann & Haeberli, 1992).

The main types of debris are (Luther, 2006) (TCEQ Regulatory Guidance, 2017):

(a) Trees, shrubs, and other plant materials
(b) Building or demolition debris, such as construction materials, drywall, timber, treated wood, plastics, etc.
(c) Furniture and appliances such as carpets, furniture, mattresses, plumbing fixtures.
(d) Household hazardous waste such as cleaners, vehicle products, paints, oils, pesticides, solvents, etc.
(e) White goods like refrigerators, freezers, washing machines, dryers, stoves, water heaters, air conditioners
(f) Electronic waste such as computers, televisions, printers, stereos, DVD players, phones.

Other debris may include urban solid waste, including animal carcasses and trash that can cause unpleasant odors as they decompose.

Solid waste refers to any discarded material that is neither in a gaseous nor liquid phase. They can be defined as all discarded household, non-hazardous, industrial, and commercial waste. Additionally, construction waste, street garbage, agricultural waste, and all other non-hazardous, non-toxic waste are included. However, it does not include human excrement. They are produced by activities related to households, healthcare, agriculture, industry, commerce, and mineral extraction, and are piled on municipal streets and other public spaces (Goel, 2017).

Solid waste can generally be categorized as follows (Goel, 2017):

(a) Industrial and mining waste: Metal extraction and related industries represent significant factors for the economic development of many countries, and thus, mining waste represents most of the mining waste.
(b) Urban solid waste: City centers and commercial, institutional, residential, and municipal activities create this waste. This category is the most visible part, although it represents comparatively a small portion of the total solid waste produced.
(c) Hazardous waste: Refers to any waste considered toxic, reactive, radioactive, corrosive, flammable, or infectious. This category of waste also includes biomedical waste, plastics, and electronic waste. Hazardous waste is produced in relatively

small quantities compared to other categories of waste. This category has significant impacts on public health and the environment and is thus considered the most dangerous type of waste.

(d) Ash from thermal power plants: Thermal power plants that use coal are the primary source of electricity worldwide, although renewable energy sources are continuously increasing. Large amounts of ash are produced from coal combustion in thermal power plants. Thus, a significant solid waste management issue today is the management and disposal of this ash.

(e) Agricultural and related industries: Large amounts of agricultural waste are produced by these economic activities during harvesting and in food processing industries.

Other waste streams include oil waste, packaging waste, medical waste, scrap metal, and waste from tires and batteries. Cleaner manufacturing machinery can be developed to minimize waste at the point of production. Additionally, the environmental impact of solid waste can be reduced by sorting and processing waste before final disposal of the various components (Goel, 2017).

Disasters can generate enormous volumes of dredge spoils. During a debris flow, a liquefied mass of rocks, gravel, sand, soil, and other materials travel rapidly over long distances, causing severe destruction and intense erosion along its path. In most cases, the environmental consequences are significant. In terms of natural ecosystems, debris flows can devastate land and vegetation. Additionally, local populations may suffer fatalities, injuries, and displacement due to property loss (Kanji, 2001).

After a disaster, the removal of dredge spoils presents numerous challenges. The process often takes a long time, sometimes years—to complete. The most difficult aspect is finding effective management solutions. The dredge spoils management process should first address existing conditions and then gradually improve as follows ((ILO-OSH), 2001):

- Reduction of industrial, commercial, and household waste
- Increase in waste reuse and recycling
- Promotion of waste collection, processing, and disposal

Case Study

Between August 5 and 9, 2020, the storm “Thalia” struck Greece. This storm was caused by a cut-off low-pressure system in the mid and upper troposphere, located over the southern Adriatic and Ionian Seas. On August 8, the storm’s center was over the Ionian Sea before moving southeast toward the central Aegean on August 9.

By 19:00 UTC on August 8, thunderstorm clouds formed over Evia and organized into a severe storm within two hours. By 05:00 UTC, the storm began to weaken and soon dissipated. The main flooding event in Evia occurred on Sunday, August 9, with the Steni meteorological station recording 75 mm of rain from 23:20 to 02:40, 24 mm from 02:40 to 03:30, 200 mm from 03:30 to 07:30 and a total rainfall of 299 mm (Lekkas E., 2020).

The August 2020 flash floods primarily affected two riverbeds in the Politika area and the floodplain/coastal plains of the Lilandas and Messapios rivers. This study focuses on regions along the Lilandas River (Golubovic - Deligianni M., 2019), (Lekkas E., 2020).

According to the National Observatory of Athens, the storm resulted from a nearly stationary cut-off low-pressure system over the southern Adriatic and Ionian Seas. Early on August 8, 2020, the storm’s center was over the Ionian Sea, later moving southeast across mainland Greece. By the morning of August 9, 2020, the system’s center was detected over the central Aegean Sea (Lekkas E., 2020).

Methodology

The mapping of dredge spoils was based on field data collected by the research team from the Department of Dynamic, Tectonic, and Applied Geology at the University of Athens (NKUA). Immediately after the flood events, the team assessed the disaster’s impact. Data collection took place on August 9-10, 2020, using aerial imagery, videos, and ground-based photographs.

For aerial documentation, a Mavic 2 drone was deployed, flying at an altitude of 20-40 meters, depending on research needs, under sunny conditions.

The data collected was analyzed to identify and categorize dredge spoils in the study area. The categories observed included:

- Trees, shrubs, and other vegetation
- Construction and demolition debris
- Vehicles
- Mud, gravel, and boulders
- Waste
- Furniture and appliances

These categories slightly differ from those referenced in existing literature.

Google Earth was used to compare the aerial data with existing maps and determine the exact locations of the dredge spoils. Each identified deposit was outlined with a polygon to represent its occurrence. These polygons were then exported as Keyhole Markup Language (KML) files for use in Geographic Information Systems (GIS).

For final mapping and visualization, ArcGIS Pro was utilized. The KML file was imported into GIS and converted into a Feature Class, where descriptive data was processed, and each dredge spoil was classified based on its type and size.

Two separate layers were created, one illustrating sediment categories and another representing sediment sizes

To enhance visualization, the base map included Google Maps and a Digital Elevation Model (DEM), which provided elevation data for realistic terrain representation.

Results

The results present the mapping of dredge spoils through a series of maps, which illustrate the subregions within the study area to enhance the visualization of dredge spoils. These subregions, shown in figure 1, include Lilantas Delta, Lefkanti, Bourtzi, Vasiliko, Fylla, Afrati, Afrati/Pissonas, Pissonas, Pissonas/Pournos, and Pournos. For each subregion, two maps have been created, one categorizing the dredge spoils (a) and another representing their sizes (b).

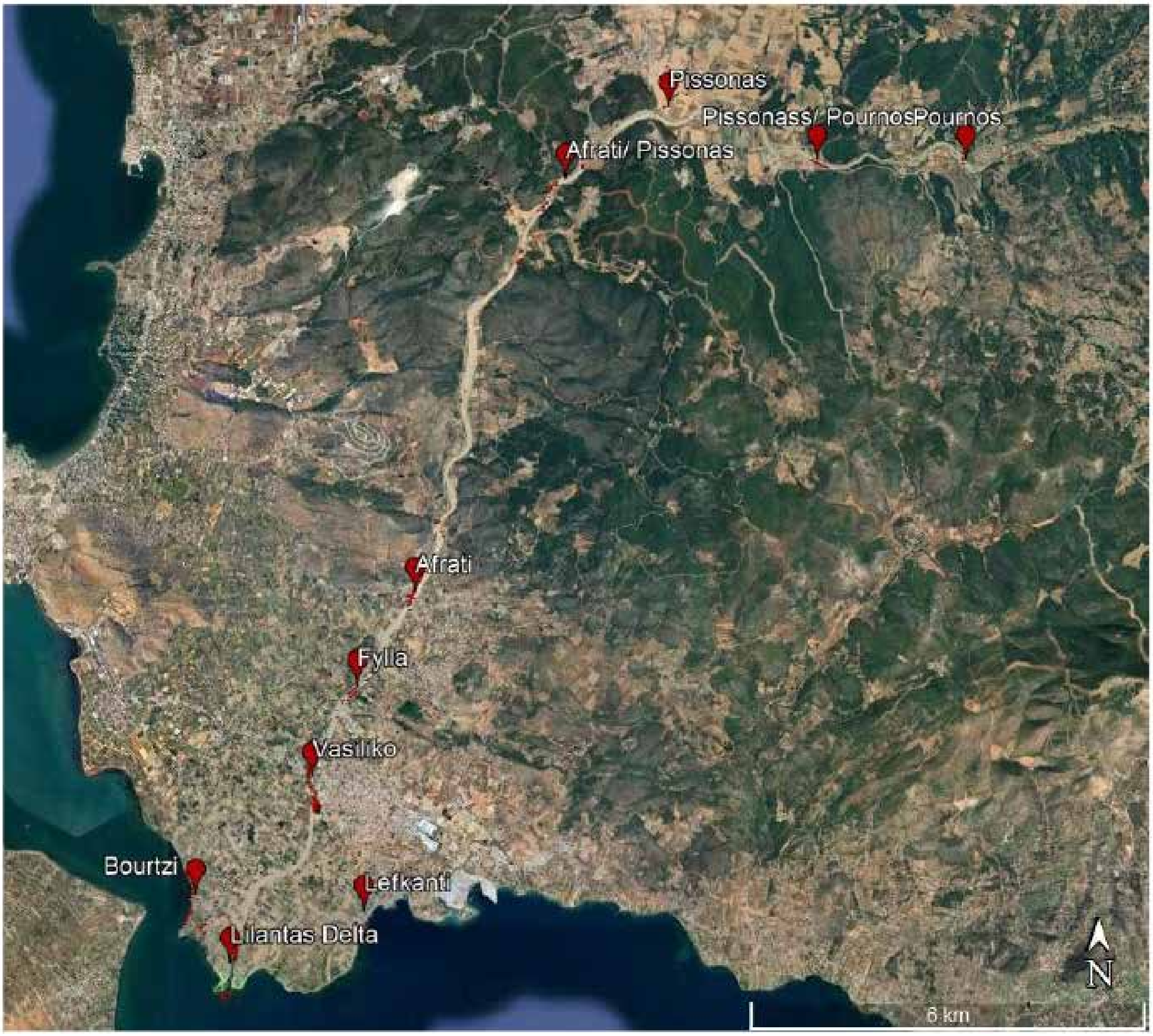

Figure 1. Map of subregions

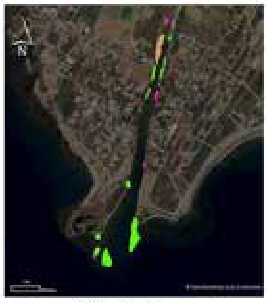
Figure 2a.


Figure 2b.

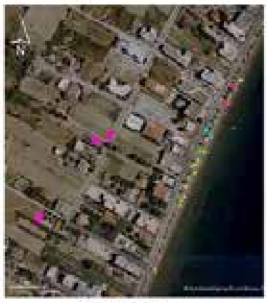
Figure 3a.


Figure 3b.


Figure 4a.


Figure 4b.


Figure 5a.


Figure 5b.


Figure 6a.


Figure 6b.

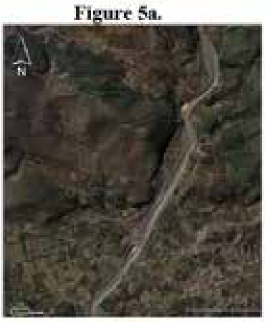
Figure 7a.

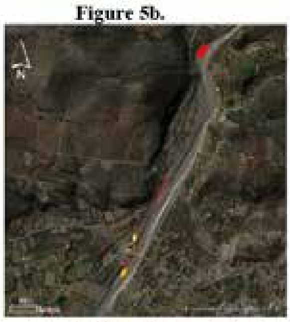
Figure 7b.


Figure 8a.

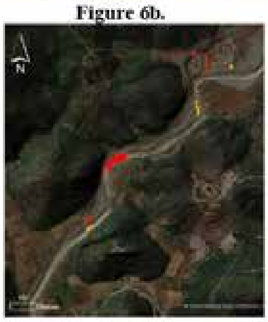
Figure 8b.


Figure 9a.


Figure 9b.


Figure 10a.


Figure 10b.


Figure 11a.


Figure 11b.

Categories

🟩 Plant materials
🟪 Construction debris
🟫 Mud, gravel, boulders
🟦 Waste
🟥 Vehicles
🟨 Furniture, appliances

Sizes

🟨 Small
🟧 Medium
🟥 Large

Table 1: Captions of figures 2-11.

Figures	Captions
Figure 2a	Map of dredge spoils by category in the area “Lilantas Delta”.
Figure 2b	Map of dredge spoils by size in the area “Lilantas Delta”.
Figure 3a	Map of dredge spoils by category in the area “Lefkanti”.
Figure 3b	Map of dredge spoils by size in the area “Lefkanti”.
Figure 4a	Map of dredge spoils by category in the area “Bourtzi”.
Figure 4b	Map of dredge spoils by size in the area “Bourtzi”.
Figure 5a	Map of dredge spoils by category in the area “Vasiliko”.
Figure 5b	Map of dredge spoils by size in the area “Vasiliko”.
Figure 6a	Map of dredge spoils by category in the area “Fylla”.
Figure 6b	Map of dredge spoils by size in the area “Fylla”.
Figure 7a	Map of dredge spoils by category in the area “Afrati”.
Figure 7b	Map of dredge spoils by size in the area “Afrati”.
Figure 8a	Map of dredge spoils by category in the area “Afrati/Pissonas”.
Figure 8b	Map of dredge spoils by size in the area “Afrati/Pissonas”.
Figure 9a	Map of dredge spoils by category in the area “Pissonas”.
Figure 9b	Map of dredge spoils by size in the area “Pissonas”.
Figure 10a	Map of dredge spoils by category in the area “Pissonas/Pournos”.
Figure 10b	Map of dredge spoils by size in the area “Pissonas/Pournos”.
Figure 11a	Map of dredge spoils by category in the area “Pournos”.
Figure 11b	Map of dredge spoils by size in the area “Pournos”.

From this study, the following conclusions can be drawn dredge spoils of various sizes are observed across different locations. In Lilandas Delta, small materials at the river delta increase in size upstream. The spoils are predominantly “Trees, Shrubs, and Other Vegetation”, along with “Construction or Demolition Debris”, “Mud, Gravel, and Boulders”, and “Vehicles”. In Lefkanti, small to medium-sized dredge spoils are mainly “Construction or Demolition Debris” and “Furniture and Appliances”, with some “Waste” and “Trees, Shrubs, and Other Vegetation”. In Bourtsi, dredge spoils of all sizes are mostly “Construction or Demolition Debris”, plus “Trees, Shrubs, and Other Vegetation”, “Mud, Gravel, and Boulders”, “Waste”, and “Vehicles”. In Vasiliko, dredge spoils of various sizes are mainly “Construction or Demolition Debris” and “Trees, Shrubs, and Other Vegetation”, with some “Mud, Gravel, and Boulders” and “Waste”. In Fylla, all sizes of dredge spoils are present, primarily “Construction or Demolition Debris” and “Trees, Shrubs, and Other Vegetation”, plus some “Mud, Gravel, and Boulders”. In Afrati, large-sized dredge spoils predominate, mainly “Construction or Demolition Debris” and “Trees, Shrubs, and Other Vegetation”, with some “Mud, Gravel, and Boulders”. In the Afrati/Pissonas area, medium and large dredge spoils are mostly “Mud, Gravel, and Boulders”, followed by “Construction or Demolition Debris” and “Trees, Shrubs, and Other Vegetation”. In Pissonas, medium and large spoils are mainly “Trees, Shrubs, and Other Vegetation” and “Mud, Gravel, and Boulders”. In the Pissonas/Pournos area, large amounts of medium and large “Construction or Demolition Debris” are observed. In Pournos, medium and large spoils are mainly “Mud, Gravel, and Boulders”, with “Trees, Shrubs, and Other Vegetation” and “Construction or Demolition Debris”.

Conclusions / Discussion

Dredge spoils of various sizes are observed across different locations, with materials ranging from small debris in river deltas to larger deposits upstream. The most observed categories include “Trees, Shrubs, and Other Vegetation,” “Construction or Demolition Debris,” and “Mud, Gravel, and Boulders.” In some areas, “Vehicles,” “Furniture and Appliances,” and “Waste” are also present. Larger spoils dominate locations like Afrati and Pissonas, while smaller to medium-sized materials are prevalent in places like Lefkanti and Vasiliko. Effective management and strategic land use planning are essential to mitigate risks associated with dredge spoil accumulation.

The state and relevant authorities must be aware of the extent of the destruction to reduce the likelihood of a similar future event. Identifying high-risk areas is crucial for implementing appropriate measures. Land use should be modified where necessary, such as prohibiting construction near riverbeds to prevent erosion risks. A rapid response is essential, including the removal of debris and financial recovery for affected environments. Protecting human life, health, safety, and the environment must be a priority. Public health risks should be minimized to ensure a swift return to normal activities. Additionally, securing basic needs and creating immediate short-term employment opportunities will support recovery efforts. Enhancing governmental preparedness and establishing sustainable debris management systems are key to long-term resilience and disaster prevention.

Acknowledgements

I would like to express my sincere gratitude to all those who contributed to the completion of this research. First and foremost, I am deeply thankful to Professor Dr. Efthymios Lekkas and Nafsica-Ioanna Spyrou, for their invaluable guidance, support, and expertise throughout the course of this project. Their insights and encouragement have been instrumental in shaping the direction and quality of my work. A special thanks to the members of the scientific team, who gathered the primary data, as without their efforts none of this could have been possible.

References

(ILO-OSH), I. L. (2001). Guidelines on Occupational Safety and Health Management.

Burgueño Salas, E. (2024). *Statista*. Retrieved from https://www.statista.com/statistics/510959/number-of-natural-disasters-events- globally/

Goel, S. (2017). Advances in Solid and Hazardous Waste Management. *Springer*.

Golubovic - Deligianni M., P. S. (2019). *Investigation of the causes of the flooding in the karst areas.* Govotsis Publishing Co.

Kanji, M. A. (2001). Environmental effects of debris flows and their protection measures. *In: The International Conference On Soil Mechanics and Geotechnical Engineering, AA Balkema Publishers*, pp. 1913-1916.

Lekkas E., S. N.-I.-E.-N. (2020). The August 9, 2020 Evia (Central Greece) Flood. *Newsletter of Environmental, Disaster, and Crises Management Strategies*.

Lewin, J., & Warburto, J. (1994). Debris flows in an alpine environment. *Geography*(79), pp. 98-107.

Luther, L. (2006). Disaster Debris Removal After Hurricane Katrina: Status and Associated Issues. *Congressional Research Service, The Library of Congress, USA*.

Rao, S. (2017). Ground water managment in river flood plains. *In: Sustainable Holistic Water Resources in a Changing Climate*, pp.
401-415.

Research Planning, I. (2014). Best Management Practices for Removal of Debris From Wetlands and Other. *Columbia SC, USA*, p.
29201.

TCEQ Regulatory Guidance. (2017). Managing Debris from Declared Disasters. *TCEQ publication RG-518*.

Urio, A., & Brent, A. (2006). Solid waste management strategy in Botswana : The reduction of construction waste. *Journal of the South African Institution of Civil Engineering, 48*, pp. 18-22.

Varnes, D. (1978). Slope Movement Types and Processes. *Special Report No. 176, National Academy of Sciences, Washington, DC, USA*, pp. 11-33.

Zimmermann, M., & Haeberli, W. (1992). Climatic change and debris flow activity in high-mountain areas. *Catena Supplement*(22),
pp. 59-72.

17th INTERNATIONAL CONGRESS
of the Geological Society of Greece

BULLETIN OF THE GEOLOGICAL
SOCIETY OF GREECE, SP. PUBL.

EXTENDED ABSTRACT 189

Contribution to the neotectonic study of West Lesvos.

Lamprakopoulos Aggelos[1], Zouros Nikolaos[1,2]
(1) Department of Geography, University of the Aegean, Lesvos, Greece, geod20007@geo.aegean.gr
(2) Natural History Museum of the Lesvos Petrified Forest, Lesvos, Greece

Introduction / Background

Lesvos island, located on the Northeast Aegean region, Greece, is characterized by active tectonics associated with the evolution and deformation of the broader Northeast Aegean Sea.

The Northeast Aegean region is characterized by complex tectonics controlled by interplay of moving tectonic plates in the broader area. The area is affected by the dextral strike-slip movement of the North Anatolian fault, which ends in the Aegean basin and creates significant tectonic structures such as the North Aegean trough and the Skyros trough. The area is also affected by E-W trending normal faults.

Several studies show that the region of the Northeast Aegean region is characterized by complex transtensional stress pattern due to the influence of the NAF, which in combination with the N-S extension stress field of the Aegean micro-plate, creates several secondary faults. (Pavlides & Caputo, 1994; Bellier et al., 1997; Kiratzi, 2002; Flerit et al., 2004; McNeill et al., 2004; Chatzipetros et al., 2013; Konstantinou, 2017; Sakellariou et al., 2017). Except from the well-developed NE-SW faults, the reflection profiles also show the existence of E-W and NW-SE oriented faults which were interpreted as Riedel fractures resulting from the transtensional character of the stress field (Pavlides & Tranos, 1991; Chatzipetros et al., 2013; Konstantinou, 2017).

The tectonic structure of Lesvos Island, both offshore and onshore, is similar to the overall regional deformation of the North Aegean area, where the two main strands of the western prolongation of the North Anatolian Fault form the North Aegean and the Skyros basins. In the Northeast Aegean region there are several E-W trending normal faults due to the active N-S extension stress field, but also there are several other strike-slip faults which are compatible that created in combination of the North Anatolian Fault that pass very close to Lesvos Island. These strike-slip faults have primarily NE-SW orientation and secondarily a NW-SE orientation (Chatzipetros et al., 2013; Kiratzi, 2018; Nomikou et al., 2021).

Figure 1: Seismic and active faults map of the Lesvos Island (Zouros et al., 2008).

The neotectonic studies in Lesvos Island have identified and mapped the major active tectonic structures of the island which are both normal and strike-slip strike (Zouros et al., 2008, 2011; Chatzipetros et al., 2013, Mourouzidou, 2021). In Lesvos Island are represented three neotectonic stages from since the Miocene. A) The recent active stage since the Pleistocene forms E-W trending normal faults (fig. 2&3), B) the second one took place in the Pliocene and formed normal faults of NW–SE strike, as well as strike–slip faults of NNE–SSW strike and finally, C) the earliest one of Upper Miocene age, based on its relation to synchronous volcanism and associated rocks, and formed strike–slip faults of E–W to ENE–WSW (fig. 4) strike (Chatzipetros et al., 2013).

In the area of west Lesvos there is a gap in tectonic data, due to the lithology which make difficult to identify fault traces. Since the relief is directly affected by erosional processes, among other factors, its intensity is associated with the age of faulting: younger activity generally produces steeper relief. Therefore, geomorphic structures associated with faulting are indicative of relatively recent age (Chatzipetros et al., 2013).

Intense volcanic activity appeared on Lesvos Island during Lower Miocene (23.5 to 16 million years ago) and the volcanic rocks are covering the 2/3 of the island's surface. Several volcanic rock units have been identified (Pe-Piper and Piper, 1993).

West Lesvos is covered mainly by pyroclastic material of the Sigri pyroclastic formation (Pe-Piper et al, 2019). Pyroclastic formations are easily eroded and thus the geomorphological indicators related with the recent tectonic activity are not well-preserved in the relief.

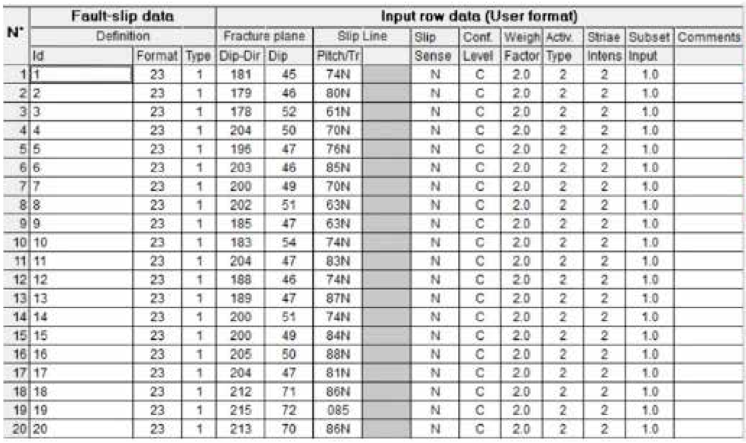

N°	Fault-slip data			Input row data (User format)										
	Definition			Fracture plane		Slip Line		Slip	Conf.	Weigh	Activ.	Striae	Subset	Comments
	Id	Format	Type	Dip-Dir	Dip	Pitch/Tr		Sense	Level	Factor	Type	Intens	Input	
1	1	23	1	181	45	74N		N	C	2.0	2	2	1.0	
2	2	23	1	179	46	80N		N	C	2.0	2	2	1.0	
3	3	23	1	178	52	61N		N	C	2.0	2	2	1.0	
4	4	23	1	204	50	70N		N	C	2.0	2	2	1.0	
5	5	23	1	196	47	76N		N	C	2.0	2	2	1.0	
6	6	23	1	203	46	85N		N	C	2.0	2	2	1.0	
7	7	23	1	200	49	70N		N	C	2.0	2	2	1.0	
8	8	23	1	202	51	63N		N	C	2.0	2	2	1.0	
9	9	23	1	185	47	63N		N	C	2.0	2	2	1.0	
10	10	23	1	183	54	74N		N	C	2.0	2	2	1.0	
11	11	23	1	204	47	83N		N	C	2.0	2	2	1.0	
12	12	23	1	188	46	74N		N	C	2.0	2	2	1.0	
13	13	23	1	189	47	87N		N	C	2.0	2	2	1.0	
14	14	23	1	200	51	74N		N	C	2.0	2	2	1.0	
15	15	23	1	200	49	84N		N	C	2.0	2	2	1.0	
16	16	23	1	205	50	88N		N	C	2.0	2	2	1.0	
17	17	23	1	204	47	81N		N	C	2.0	2	2	1.0	
18	18	23	1	212	71	86N		N	C	2.0	2	2	1.0	
19	19	23	1	215	72	085		N	C	2.0	2	2	1.0	
20	20	23	1	213	70	86N		N	C	2.0	2	2	1.0	

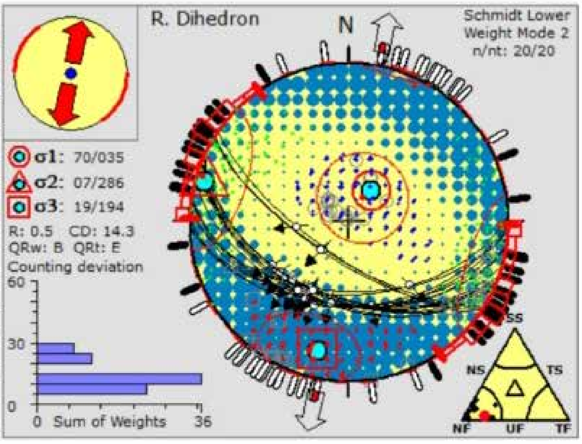

Figure 2: W – E to WNW – ESE trending normal faults affecting the Miocene lavas along the Voulgaris gorge.

Extensive field work was carried out for the study of tectonic structures in order to identify the tectonic deformation in the broader area, according to the new data.

Our study was based on the observations of the fresh road cuts created due to public works for the reconstruction of the new Kalloni – Sigri road. Lots of new tectonic data in the area of West Lesvos, were revealed. The fault planes affecting the volcanic formations consist significant indicators for the tectonic deformation in the area.

Objectives and Methodology

The extensive field work and study on several new faults in the western peninsula of Lesvos Island gave us the opportunity to identify active tectonic structures in a broad area. The faults in the study area are variable in strike and character. Their activity level is determined based on their geological, geometrical and geomorphological characteristics.

The faults of West Lesvos affecting the volcanic rocks present various orientations and types of striking with very clear striations on their fault surfaces.

The tectonic analysis of field data was conducted using Win Tensor 5.9.0 software (Delvaux & Sperner, 2003) to determine the kinematic axes of the main stress pattern in the area. Developed by Damien Delvaux, this software defines stress fields based on geological data, including faults, fractures, and striations, as well as earthquake focal mechanisms.

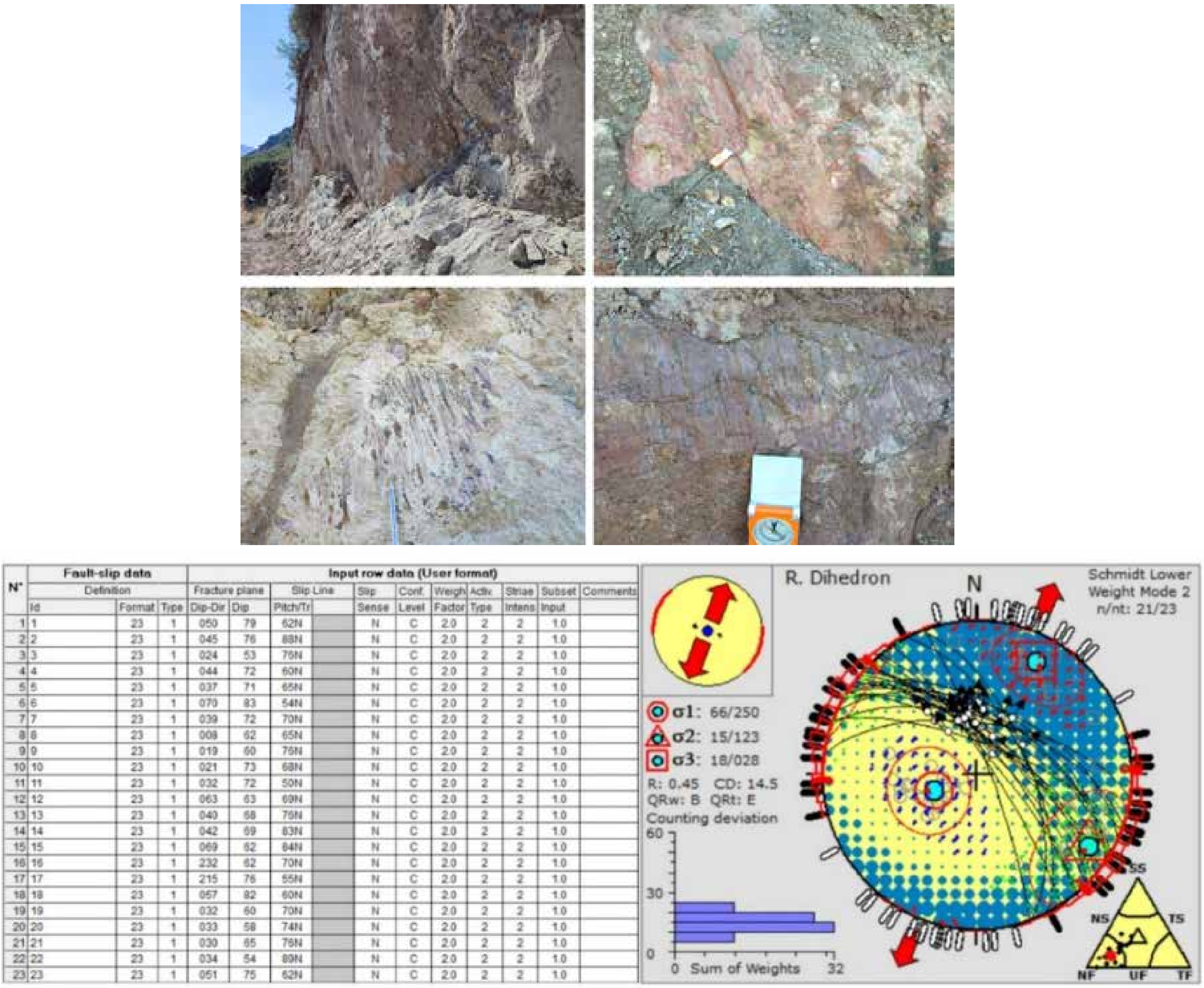

N°	Fault-slip data			Input row data (User format)										
	Definition			Fracture plane		Slip Line		Slip	Conf.	Weigh	Activ.	Striae	Subset	Comments
	Id	Format	Type	Dip-Dir	Dip	Pitch/Tr		Sense	Level	Factor	Type	Intens	Input	
1	1	23	1	050	79	62N		N	C	2.0	2	2	1.0	
2	2	23	1	045	76	88N		N	C	2.0	2	2	1.0	
3	3	23	1	024	53	76N		N	C	2.0	2	2	1.0	
4	4	23	1	044	72	60N		N	C	2.0	2	2	1.0	
5	5	23	1	037	71	65N		N	C	2.0	2	2	1.0	
6	6	23	1	070	83	54N		N	C	2.0	2	2	1.0	
7	7	23	1	039	72	70N		N	C	2.0	2	2	1.0	
8	8	23	1	008	62	65N		N	C	2.0	2	2	1.0	
9	9	23	1	019	60	75N		N	C	2.0	2	2	1.0	
10	10	23	1	021	73	68N		N	C	2.0	2	2	1.0	
11	11	23	1	032	72	50N		N	C	2.0	2	2	1.0	
12	12	23	1	063	63	69N		N	C	2.0	2	2	1.0	
13	13	23	1	040	68	75N		N	C	2.0	2	2	1.0	
14	14	23	1	042	69	83N		N	C	2.0	2	2	1.0	
15	15	23	1	069	62	84N		N	C	2.0	2	2	1.0	
16	16	23	1	232	62	70N		N	C	2.0	2	2	1.0	
17	17	23	1	215	76	55N		N	C	2.0	2	2	1.0	
18	18	23	1	057	82	60N		N	C	2.0	2	2	1.0	
19	19	23	1	032	60	70N		N	C	2.0	2	2	1.0	
20	20	23	1	033	58	74N		N	C	2.0	2	2	1.0	
21	21	23	1	030	65	76N		N	C	2.0	2	2	1.0	
22	22	23	1	034	54	89N		N	C	2.0	2	2	1.0	
23	23	23	1	051	75	62N		N	C	2.0	2	2	1.0	

Figure 3: WNW – ESE to NW – SE trending normal faults affecting the Miocene lavas along the Voulgaris gorge.

Initially, tectonic data are entered into a worksheet, specifying the dip direction, dip angle, pitch angle and orientation. The fault type (normal, reverse, or strike-slip), certainty factor, and striation intensity are also assigned.

In the processing stage, the software generates rose diagrams, statistical summaries of fault surfaces, and applies the Right Dihedron method for stress analysis.

Also, Dextral Strike-Slip faults were also identified and measured with NE – SW orientation and less Sinistral Strike-Slip faults with NW – SE orientation (fig. 4 & 5).

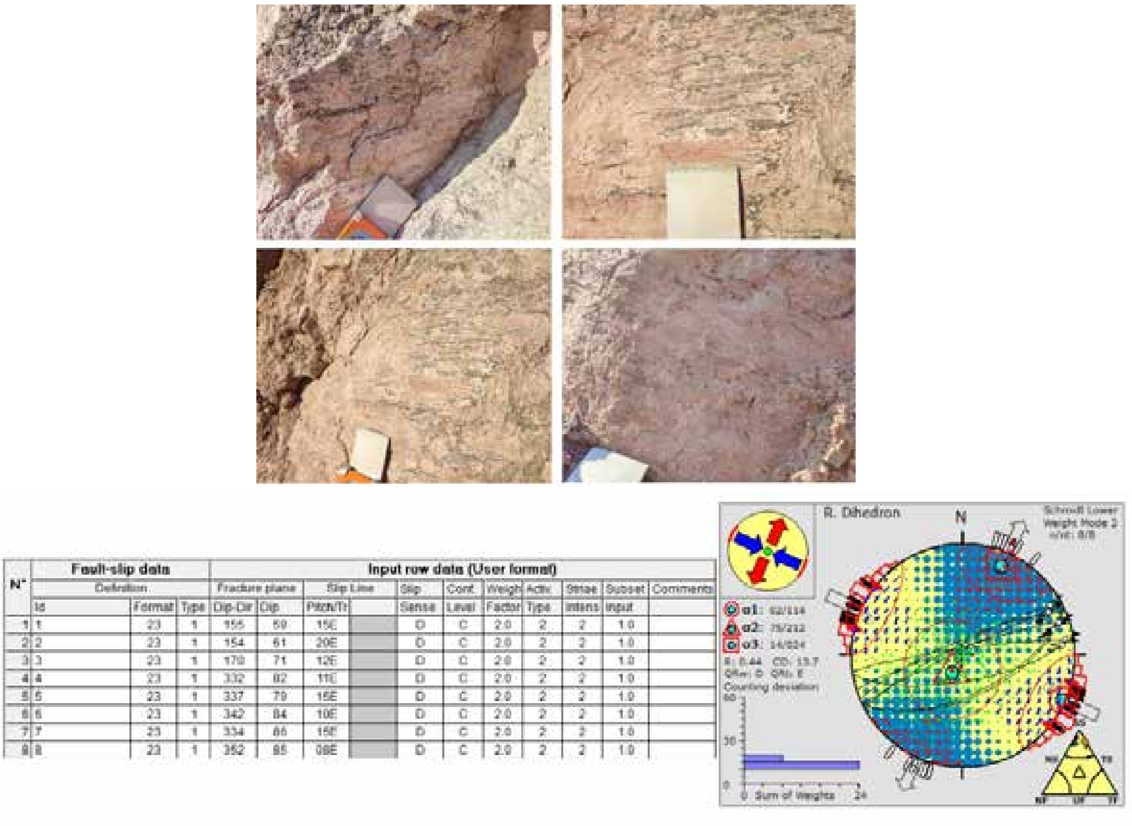

N°	Fault-slip data			Input row data (User format)										
	Definition			Fracture plane		Slip Line		Slip	Conf.	Weigh	Activ.	Striae	Subset	Comments
	Id	Format	Type	Dip-Dir	Dip	Pitch/Tr		Sense	Level	Factor	Type	Intens	Input	
1	1	23	1	155	59	15E		D	C	2.0	2	2	1.0	
2	2	23	1	154	61	20E		D	C	2.0	2	2	1.0	
3	3	23	1	170	71	12E		D	C	2.0	2	2	1.0	
4	4	23	1	332	82	11E		D	C	2.0	2	2	1.0	
5	5	23	1	337	79	15E		D	C	2.0	2	2	1.0	
6	6	23	1	342	84	10E		D	C	2.0	2	2	1.0	
7	7	23	1	334	86	15E		D	C	2.0	2	2	1.0	
8	8	23	1	352	85	08E		D	C	2.0	2	2	1.0	

Figure 4: NE – SW trending strike-slip faults with dextral component faults.

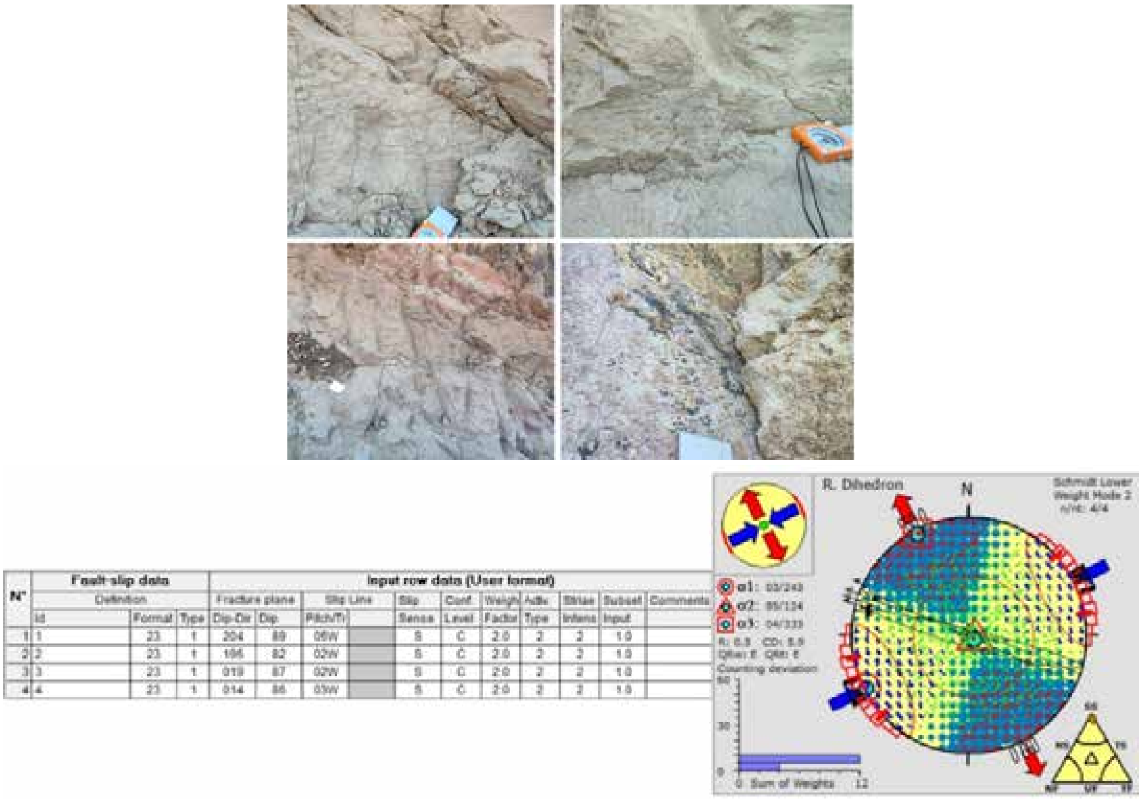

N°	Fault-slip data			Input row data (User format)										
	Definition			Fracture plane		Slip Line		Slip	Conf.	Weigh	Activ.	Striae	Subset	Comments
	Id	Format	Type	Dip-Dir	Dip	Pitch/Tr		Sense	Level	Factor	Type	Intens	Input	
1	1	23	1	204	89	06W		S	C	2.0	2	2	1.0	
2	2	23	1	196	82	02W		S	C	2.0	2	2	1.0	
3	3	23	1	019	87	02W		S	C	2.0	2	2	1.0	
4	4	23	1	014	86	03W		S	C	2.0	2	2	1.0	

Figure 5: NW-SE trending strike-slip faults with sinistral component.

Results and Conclusions

The neotectonic evolution of Lesvos Island reflects the complex interplay of regional tectonic forces in the NE Aegean. The North Anatolian Fault (NAF), a major dextral strike-slip fault, exerts significant influence, generating numerous secondary strike-slip faults. Simultaneously, the general N-S extension of the Aegean microplate has led to the formation of large W-E trending normal faults (Chatzipetros et al., 2013). This interaction results in a transtensional stress field, producing a diverse array of tectonic structures.

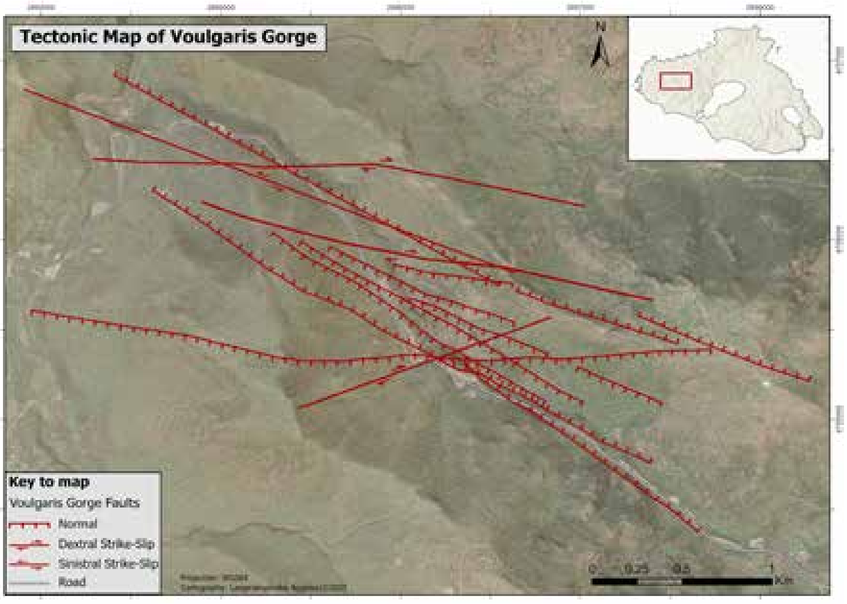

Figure 6: Tectonic map of Voulgaris Gorge area, where 3 different types of faults are presented. Can be observed E-W and NW-SE Normal faults, E-W and NE-SW Dextral Strike-Slip Faults, as well as NW-SE Sinistral Strike-Slip Fauts.

The transtensional field of NE Aegean region is formed by the dextral strike-slip fault of NAF and its stress pattern creates a variety of secondary tectonic structures (Fig. 6), such as secondary NW – SE strike-slip faults which are compatible with the active tectonics of the NE Aegean.

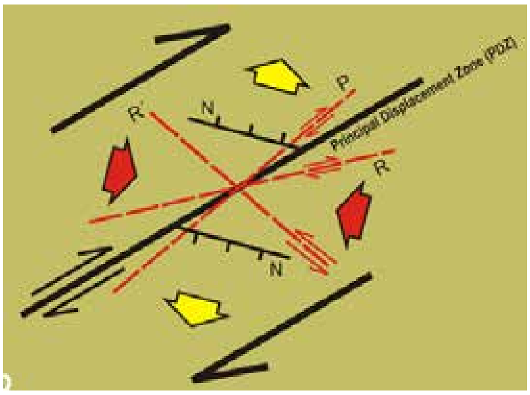

Figure 7: Schematic diagram showing the angular relationships between Riedel shears and the Principal Displacement Zone (PDZ) in a dextral strike–slip deformation zone R, R and P shears are strike slip faults, while N are normal faults perpendicular to the maximum extensional stress. This is a typical arrangement of faulting pattern in the close area of major strike–slip faults; not all types of faults however are always formed in such a setting (Chatzipetros et al., 2013).

In addition to W-E normal faults and NE-SW dextral strike-slip faults, a secondary set of sinistral strike-slip faults has been identified. These faults, which were previously underestimated, can now be considered potentially active structures within the broader stress regime. Their presence suggests a more intricate fault network than previously recognized, influencing seismic hazard assessments and regional tectonic models.

Findings from this study further indicate that the island's extensive tectonic activity has played a crucial role in shaping significant geological formations, such as Voulgaris Gorge. The gorge, along with similar landforms, is likely the result of long-term fault activation and progressive deformation under the prevailing transtensional stress field. These observations highlight the dynamic nature of Lesvos' neotectonic landscape and its ongoing structural evolution.

References

Bellier, O., Over, S., Poisson, A., Andrieux, J. (1997). Recent temporal change in the stress state and Modern Stress Field along the North Anatolian Fault Zone (Turkey). Geophysical Journal International, 131(1), pp. 61–86. doi:10.1111/j.1365-246x.1997.tb00595.x.

Chatzipetros, A., Kiratzi, A., Sboras, S., Zouros, N., & Pavlides, S. (2013). Active faulting in the north-eastern Aegean Sea Islands. Tectonophysics, 597–598, 106–122. https://doi.org/10.1016/j.tecto.2012.11.026.

Delvaux, D. and Sperner, B. (2003). Stress tensor inversion from fault kinematic indicators and focal mechanism data: the TENSOR program. In: New Insights into Structural Interpretation and Modelling (D. Nieuwland Ed.). Geological Society, London, Special Publications, 212, 75-100.

Flerit, F., Armijo, R., King, G., Meyer, B. (2004). The mechanical interaction between the propagating North Anatolian Fault and the back-arc extension of the Aegean. Earth and Planetary Science Letters, 224, 347–362.

Kiratzi, A. A. (2002). Stress tensor inversions along the westernmost North Anatolian Fault Zone and its continuation into the North Aegean Sea. Geophysical Journal International, 151(2), 360–376. https://doi.org/10.1046/j.1365-246X.2002.01753.x.

Kiratzi, A. (2018). The 12 June 2017 Mw 6.3 Lesvos Island (Aegean Sea) earthquake: Slip model and directivity estimated with finite-fault inversion. Tectonophysics 724–725 (2018) 1–10.

Kiratzi, A., Louvari, E. (2003). Focal mechanisms of shallow earthquakes in the Aegean Sea and the surrounding lands determined by waveform modelling: a new database. Journal of Geodynamics 36, 251–274.

Konstantinou, K.I. (2017). Accurate relocation of seismicity along the North Aegean Trough and its relation to active tectonics. Tectonophysics, 717, pp. 372–382. doi:10.1016/j.tecto.2017.08.021.

McNeill, L.C., Mille, A., Minshull, T. A., Bull, J. M., Kenyon, N. H. (2004). Extension of the North Anatolian Fault into the North Aegean Trough: Evidence for transtension, strain partitioning, and analogues for sea of marmara basin models. Tectonics, 23(2). doi:10.1029/2002tc001490.

Mourouzidou, O. (2021). Neotectonics of NE Aegean (Lesvos- Edremit Fault), Faculty of Sciences, Geology. Ph.D. Thesis, Aristotle University of Thessaloniki, Thessaloniki, 284 p.

Nomikou, P., Papanikolaou, D., Lampridou, D., Blum, M., & Hübscher, C. (2021). The active tectonic structures along the southern margin of Lesvos Island, related to the seismic activity of July 2017, Aegean Sea, Greece. Geo-Marine Letters, 41(4). https://doi.org/10.1007/s00367-021-00723-6.

Pavlides, S. B., & Tranos, M. D. (1991). Structural characteristics of two strong earthquakes in the North Aegean: Ierissos (1932) and Agios Efstratios (1968). Journal of Structural Geology, 13(2), 205–214. doi:10.1016/0191-8141(91)90067-s.

Pavlides, S. and Caputo, R. (1994). The north aegean region: A tectonic paradox?. Terra Nova, 6(1), pp. 37–44. doi:10.1111/j.1365-3121.1994.tb00631.x.

Pavlides, S., Mountrakis, D., Kilias, A., Tranos, M. (1990). The role of strike-slip movements in the extensional area of Northern Aegean (Greece). A case of transtensional tectonics. Annales Tectonicae.

Pavlides S, Tsapanos Th, Zouros N, Sboras S, Koravos G, Chatzipetros A. (2009) Using active fault data for assessing seismic hazard: a case study from NE Aegean sea, Greece. Earthquake Geotechnical Engineering Satellite Conference XVIIth International Conference on Soil Mechanics & Geotechnical Engineering 2–3. 10. 2009, Alexandria, Egypt.

Pe-Piper, G., & Piper, D. J. W. (1993). Revised stratigraphy of the Miocene volcanic rocks of Lesbos, Greece. Neues Jahrbuch für Geologie und Paläontologie - Monatshefte, 1993(2), 97–110. https://doi.org/10.1127/njgpm/1993/1993/97.

Pe-Piper, G., Piper, D., Zouros, N., Anastasakis, G. (2019). Age, stratigraphy, sedimentology and tectonic setting of the Sigri Pyroclastic Formation and its fossil forests, Early Miocene, Lesbos, Greece. Basin Research, 31(6), pp. 1178–1197. doi:10.1111/bre.12365.

Sakellariou, D., Mascle, J., Lykousis, V. (2017). Strike slip tectonics and transtensional deformation in the Aegean region and the Hellenic Arc: Preliminary results. Bulletin of the Geological Society of Greece, 47(2), p. 647. doi:10.12681/bgsg.11098.

Soulakellis, N., Novak, I., Zouros, N., Lowman, P., Yates, J. (2006). Fusing Landsat-5/TM imagery and shaded relief maps in tectonic and geomorphic mapping: Lesvos Island, Greece. Photogrammetric Engineering & Remote Sensing 6, 693–700.

Zouros, N., Pavlides, S., Kiratzi, A., Kakakaisis, G., Drakatos G., Soulakellis, N., Vaitis, M., Tsapanos, Th., Chatzipetros, A., Ganas, A., Sboras, S., Koravos, G., Koukourouvli, N., Lampaki, O., Valiakos, I., 2008. Active fault and seismicity maps of the North Aegean region (6 maps, 1:200.000, 1:100.000). Research project: use of modern research tools in geosciences for seismic hazard management in NE Aegean islands, Natural History Museum of the Lesvos Petrified Forest, Mytilene, Lesvos, Greece.

Zouros, N., Pavlides, S., Soulakellis, N., Chatzipetros, A., Vasileiadou, K., Valiakos, I., & Mpentana, K. (2011). Using active fault studies for raising public awareness and sensitisation on seismic hazard: A case study from Lesvos petrified forest Geopark, NE Aegean sea, Greece. Geoheritage, 3(4), 317–327. https://doi.org/10.1007/s12371-011-0044-y.

17th INTERNATIONAL CONGRESS
of the Geological Society of Greece

BULLETIN OF THE GEOLOGICAL
SOCIETY OF GREECE, SP. PUBL.

EXTENDED ABSTRACT 190

Field-Work Methods in Speleology: A Multidisciplinary Training Approach

Lazaridis G.[1,*], Onac B. P[2], De Waele J.[3], Vouvalidis K.[1], Gkelis S.[1], Gerovasileiou V.[4], Trimmis P. K.[5], Papadimitriou K.[6], Georgiakakis P.[7], Paragamian K.[8], Dora D.[1], Paragkamian S.[8], Digenis M.[4], Sdraka F.[1], Alexandropoulou C.[9], Alikakou T.[9], Arvaniti C.[9], Chatzinikolaou N.[9], Chavanidis K.[9], Georgopoulou X.[9], Giannopoulou A.[9], Koumparelou D.[9], Lytra C.[9], Simoglou I.[9]

*(1) Faculty of Sciences, Aristotle University of Thessaloniki (AUTH), 54124 Thessaloniki, Greece, *geolaz@geo.auth.gr*
(2) School of Geosciences, University of South Florida, 4202 Tampa, FL, 33620, USA
(3) Department of Biological, Geological and Environmental Sciences, Bologna University, 40126 Bologna, Italy
(4) Department of Environment, Faculty of Environment, Ionian University, 29100 Zakynthos, Greece
(5) School of Forestry and Natural Environment, Aristotle University of Thessaloniki, 54124 Thessaloniki, Greece
(6) School of Rural and Surveying Engineering, Aristotle University of Thessaloniki, Thessaloniki, 54124, Greece
(7) Natural History Museum of Crete, University of Crete, 71409 Heraklion, Greece
(8) Hellenic Institute of Speleological Research, 71306 Heraklion, Greece
(9) (participant) Center for Education and Lifelong Learning, AUTH, 54124 Thessaloniki, Greece

Research Highlights

This paper introduces a newly developed 55-hour educational program designed for higher education graduates to bridge knowledge gaps in speleology. The multidisciplinary course covered geosciences, biology, and archaeology, combining theoretical learning with practical fieldwork and advanced technologies. Emphasizing safety, data collection, and interdisciplinary methodologies, the program prepared participants for comprehensive cave research. Offering 4 ECTS credits and a specialized certificate, it significantly advanced speleological education while promoting sustainable research practices.

Introduction

Speleology, the scientific study of caves, requires a multidisciplinary approach to address the unique challenges of cave environments. This paper outlines a newly implemented educational program designed to bridge knowledge gaps and provide participants with practical and theoretical expertise. Based on the absence of dedicated training programs for cave studies highlights the need for such initiatives. This led to the development of a comprehensive curriculum that integrates various disciplines and ensures sustainability and safety in speleological research. Under the title “Field-Work Methods in Speleology”, a 55 instructional hours program, including synchronous and asynchronous components was created. The target audience consisted of graduates from higher education institutions who were interested in acquiring specialized skills in cave research.

Educational Framework

The program was structured around three key thematic units:

1. Geosciences: Covering cave morphology, stratigraphy, sampling and dating methods, paleoenvironmental reconstructions, and safety protocols along with topographic and geomorphological knowledge.
2. Biology: Focusing on terrestrial and aquatic cave ecosystems and organisms, sampling techniques, and data management.
3. Archaeology and Paleontology: Addressing excavation methodologies, anthropological artifact handling, and technological tools for research; cave clastic sediments and paleontological finds with emphasis on processes and taphonomy.

This educational package was developed in accordance with the Regulation of Studies of the Center of Education and Lifelong Learning of the Aristotle University of Thessaloniki (Greece). It underwent a peer-review evaluation process, which was approved to officially invite participants. The final program of the course provided 4 ECTS (European Credit Transfer System) and awarded a certificate of specialized training.

Methodology and outcomes

The program employed a blended learning approach that combined interactive lectures by leading experts with hands-on exercises in real-world cave settings. Participants actively engaged with advanced technologies to enhance their learning experience. By completing the program, they gained a comprehensive understanding of cave environments and processes while developing practical skills in data collection, analysis, and, most importantly, interpretation. This preparation equipped the participants to confidently and expertly address complex research questions in speleology.

Field-work guide – the scientific approach

As a measure of the course's success, we developed an evaluation scheme designed to produce a field protocol for working in caves, based on the participants' understanding. By integrating the correct answers and addressing specific aspects, we created a comprehensive general guide outlined below.

1. Basic steps for preparing cave field research: Cave fieldwork preparation involves several steps to ensure safety and thorough data collection. Initially, the research objectives and the team involved should be determined. This includes gathering relevant background data from cave maps, previous studies and local knowledge (non-scientific). Equipment preparation is crucial, ensuring that suitable tools are available. Additionally, safety should be prioritized, including evaluating the cave's morphology, checking atmospheric conditions, and having proper first aid kits. Lastly, obtaining permits and considering logistical factors, like weather forecasts and cave access, should be addressed.
2. Determining cave mapping routes: Mapping cave routes accurately is essential for understanding the cave's internal structure. As caves often feature intricate branches and complex passageways, it is crucial to track changes in direction and elevation with precision. By using a laser meter and clinometer, surveyors can obtain accurate measurements of distances and angles. In addition, photogrammetry has revolutionized cave surveying, providing high-accuracy three-dimensional (3D) models of cave systems. Softwares like Polycam, allow precise spatial data collection. These 3D models are not only useful for research but also provide an interactive way for others to explore the cave virtually. This technology can save considerable time and effort while ensuring that the resulting data is accurate and comprehensive.
3. The role of geological research in cave exploration: Geological mapping in caves provides crucial data for understanding the processes that shape cave formation. By documenting sediment layers, mineral deposits, and other geological features, researchers gain insights into past environmental conditions and the processes that have shaped the cave's structure. They identify areas of particular interest for further study, such as areas with rare deposits or specific speleothems. The information gathered during geological research can also aid in conservation efforts. After data are collected, the next step is their analysis. This involves synthesizing measurements, observations, and geological data to create a comprehensive report. The report should include maps, diagrams, and photographs that illustrate the cave's features and structure. This report is an essential document for both scientific research and future cave evaluation from a conservation perspective, as it ensures that the cave's layout and characteristics are intact. For geological recording, several tools are necessary, such as measuring tools (e.g., clinometers, distance meters, compass), recording tools (e.g., gas detectors, data loggers), documentation tools (e.g., camera, notebook) and as technology progresses, apps such as FieldMove Clino assist in collecting and recording data, while LiDAR-based apps help in creating 3D models.
4. Assessing safety: Safety during cave exploration requires assessing weather conditions, especially in cases where rising water levels could be a risk. It is vital to monitor cave stability to avoid collapses, which could result in injury or entrapment. Atmospheric conditions should be regularly monitored using gas detectors for oxygen, carbon dioxide, hydrogen sulfide etc. In certain caves, radon meters may also be used. Descending and climbing in caves demands special training and equipment.
5. Importance of documenting the location and characteristics of deposits: Deposits in caves, including chemical, clastic, and biogenic, offer significant insights into the cave's geological and environmental history. Recording their location, size, shape, color etc. is vital for understanding various processes. For example, clastic deposits provide information about their origin and the conditions under which they accumulated. Speleothems, on the other hand, provide evidence about airflow, microbial activity, precipitation, paleoenvironment etc.
6. Data to record geomorphological features in caves: For geomorphological cave features, data should be collected on the size, shape, color, and location of features like dissolution forms, notches, and sediment deposits. The relationship of these features to other geological elements such as fault lines or water supply sources must be recorded. Information about mesomorphological features, such as passage shapes and their relationship to water levels, is also essential. When recording these data, it is crucial to take detailed measurements, considering the three-dimensional distribution.
7. Following a sampling protocol for geological studies: clear guidelines for selecting, collecting, and storing samples, with the aim of representing the geological diversity of the cave. Sampling should follow strict rules to avoid contamination or alteration. Data regarding the exact location, date, and conditions at the time of sampling must be recorded. Furthermore, documentation of the sampling site on cave maps and in photos with scales is needed.

8. Sampling protocol for excavation research: careful documentation of sample locations, with special attention to the sites of archaeological/paleontological finds. In particular, the stratigraphy of findings is essential for understanding historical periods and their chronological framework. Aadditionally, documentation of the type of findings (e.g., ceramics, tools, bones) and the method of storage, preservation, and analysis are important.
9. Use of maps and topographic measurements in cave studies: These are essential tools for understanding the structure of a cave. The use of topographic maps allows for precise representation of cave formations and the creation of 3D models that facilitate study.
10. Ensuring accuracy in cave observations requires precise measurement of geometric characteristics and the appropriate use of specialized instruments. Measuring instruments must be calibrated and regularly checked to avoid errors during research. Additionally, the use of GIS software for storing and analyzing data aids in recording and verifying observations based on geometric parameters and geological models.
11. Key data in cave studies and their management: In cave studies, the data typically recorded include geological parameters (such as rock types and formations), geometric characteristics (width, height, depth), and ecological data (abiotic factors and cave biological communities). Managing this data requires the use of digital tools and databases for categorizing, storing, and extracting it for analysis, as well as fostering collaboration among scientists.
12. Key features and requirements of biological research in caves: Biological research in caves requires documentation of species inhabiting the caves, the assessment of ecological conditions, and evaluating the conservation needs. Key features include the utilization of specialized instruments and techniques for abiotic data acquisition, biological sampling, sample preservation, and subsequent laboratory procedures for species identification and analysis.

Interdisciplinary relationships – a synthesis

Multiple questions were tested during and at the end of course; a summary of which is given in the following section by providing a relevance scale of scientific fields to cave research (Table 1) along with a key table about the utilization of research fields in multidisciplinary studies (Table 2).

The relevance scale was created to assess and compare the significance of various scientific fields in the study of cave environments. It is based on seven key criteria, each designed to evaluate the contribution of each field to understanding different aspects of caves. These criteria are: 1) Contribution to understanding the processes that created and influenced the evolution of the cave; 2) Contribution to describing the structures and forms found within the cave; 3) Contribution to reconstructing the paleoenvironment and broader geophysical environment that influenced the cave; 4) Understanding the conditions (e.g., pH, temperature, nutrient levels) prevailing in the cave; 5) Contribution to developing a protection plan for caves as natural and cultural landscapes; 6) Understanding the impact of humans on the evolution of caves; and 7) Provision of technologies, methods, and data that facilitate cave study. For each field of study (Geology, Geomorphology, Mineralogy-Geochemistry, Paleontology, Biology, Topography, and Archaeology), scores were assigned based on how well the field meets these criteria. The scale provides a clear, comparative analysis of the relevance of each discipline in cave research. It serves as a guide for prioritizing which aspects of cave studies are most central to specific research objectives (such as geological, geomorphological, or biological studies), but it should not be interpreted as suggesting that fields with lower scores are unimportant. Each field plays an integral role in providing a comprehensive understanding of caves and their significance, both scientifically and culturally.

In this relevance scale, the “total” represents the average score for each scientific field in relation to the criteria established. Higher values indicate a strong relevance of a field to the corresponding criteria, while lower values indicate weaker relevance.

Table 1. Relevance scale for scientific fields to speleology.

Scientific fields	Criterion 1	Criterion 2	Criterion 3	Criterion 4	Criterion 5	Criterion 6	Criterion 7	Total
Geology	5	5	4	4	5	4	5	4.6
Geomorphology	5	5	4	5	5	3	5	4.6
Mineralogy-Geochemistry	4	5	5	5	3	5	5	4.6
Paleontology	3	4	5	5	3	4	4	4.1
Biology	4	4	4	4	5	3	4	4.0
Topography	3	5	3	2	4	1	5	3.3
Archaeology	2	3	4	2	5	5	1	3.1

Cave studies are a prime example of interdisciplinary research, where various scientific fields converge to offer a more comprehensive understanding of cave environments, their formation, evolution, and their preservation. Research from different disciplines contribute their unique methods, knowledge, and insights, allowing for the exploration of caves from multiple perspectives. Table 2 demonstrates the interaction among scientific disciplines and their contributions to cave research, showcasing how one field's tools or methods can yield valuable outcomes for another. Fields such as geology, biology, archaeology, and paleontology, play crucial roles in addressing different scientific questions and broader environmental, historical, and ecological contexts.

Table 2. Interdisciplinary connections between scientific fields and their contribution to cave research, highlighting how tools and insights from one discipline enhance the understanding and study of caves.

Utilization of	Applied on	Result
Geology	Geomorphology	Understanding the structural, petrographic and hydrologic conditions that led to the formation of specific landforms.
Geology	Archaeology	Use of stratigraphy for the relative dating of cultural artifacts; understanding processes; interpreting formation of spaces and deposition of sediments.
Geomorphology	Biology	Correlation of geomorphological structures and microhabitats with the distribution of various species inside the cave.
Mineralogy – Geochemistry	Archaeology	Determining the origin of raw materials used in artifacts and their processing techniques. This study provides information about human activities (e.g., presence of organic remains); identifying human use of fire, spaces, materials etc.
Archaeology	Geology	Study of the impact of human activity on cave formation and dating of classic sediments through archaeological findings.
Topography	Geology	Cave mapping to understand the creation and evolution of the cave; cave morphometrics; marking sample site.
Topography	Geomorphology	3D representation and survey of caves, landforms and dissolution and depositional features.
Paleontology	Archaeology	Study of fossils can provide information about the relationship between humans, animals and the environment (e.g., hunters, gatherers, domestication of animals) and their dietary habits.
Paleontology	Biology	Comparative study of anatomical structures and ancient DNA (aDNA) to draw conclusions about the evolution and adaptations of organisms in the cave environment and through time.
Biology	Archaeology	Study of the corrosive effect of microorganisms on archaeological finds.
Biology	Geomorphology	Influence of various biological factors on the formation of geological cave structures (e.g., guano-related minerals; biologically mediated deposits, dissolution structures).

Conclusive remarks

This program marks a significant advancement in speleological education, equipping participants with the essential tools and knowledge to thrive in this specialized field. Future iterations will focus on enhancing international collaborations and incorporating emerging technologies.

The program's multidisciplinary approach ensures participants to be prepared for diverse applications, from scientific research to heritage conservation. It also emphasizes sustainable practices to protect fragile cave ecosystems.

The relevance scale serves as a practical tool to prioritize efforts in cave-related research, with the importance of each scientific discipline varying based on the context and specific research goals.

The interdisciplinary nature of cave studies is clearly demonstrated, with various scientific fields working together to provide valuable insights that enrich and support one another. This highlights how methods and tools from one discipline can yield crucial outcomes for other areas, fostering a more integrated understanding of cave environments.

Acknowledgements

This educational program is offered by the Center for Education and Lifelong Learning at Aristotle University of Thessaloniki. We would like to thank the reviewers and staff for their approval and support of the course.

BULLETIN OF THE GEOLOGICAL SOCIETY OF GREECE, SP. PUBL.

EXTENDED ABSTRACT 191

Evaluation of karst geosites in Grevena-Kozani UNESCO Global Geopark

Lazaridis G.[1,*], Sdraka F.[1], Georgiadou M. E.[1], Batsi A.[2], Ghikas D.[2], Dora D.[1], Trimmis K. P.[3]
*(1) Faculty of Sciences, Aristotle University of Thessaloniki (AUTH), 54124 Thessaloniki, Greece, *geolaz@geo.auth.gr*
(2) Grevena-Kozani UNESCO Global Geopark, Grevena 51100, Greece
(3) School of Forestry and Natural Environment, Aristotle University of Thessaloniki, 54124 Thessaloniki, Greece

Research Highlights

This study undertakes a comprehensive assessment of karst landforms within the Grevena-Kozani UNESCO Global Geopark, focusing on scoring and analyzing the area's speleological features. By applying six evaluation criteria—scientific, ecological, cultural, aesthetic, economic, and potential utilization—previously used in Crete's Psiloritis and Lasithi Mountains (Fasoulas et al., 2011), the study employs a multidisciplinary methodology to explore management prospects for these unique landforms. It also aims to promote sustainable use and geoconservation of the geopark's caves, aligning with principles advocated by the European Geoparks and the International Union for Conservation of Nature (IUCN).

Introduction

There is a growing global interest in sustainable and alternative tourism that leverages natural and cultural resources. This trend has emerged as a reaction to the challenges of urban lifestyle. The term "Geotourism" refers to a type of alternative tourism that highlights the geological heritage of a location, offering visitors educational and nature-focused experiences. It addresses to individuals interested in geology and the geological processes that created landforms such as caves, gorges valleys, fossil sites and more. Importantly, the study of geosites extends beyond geological interest, contributing to a broader understanding of the environmental conditions in these areas. These conditions have significantly influenced historical human events as well as the evolution of other species and habitats (Rassios & Grieco, 2021).

Caves hold substantial importance within the tourism industry and have historically been the primary geological features of interest to tourists and they continue to be among the most popular geological sites. Cave tourism gained significant popularity in Europe during the 18th century, and today, caves worldwide attract hundreds of thousands of visitors annually (Theodosiadis, 2020). Greece is rich in carbonate rocks, the majority of which have undergone karstification, leading to the formation of thousands of caves across the country. Landforms of karst are of interest not only for natural and geological sciences, but also in other multidisciplinary fields. From a geological perspective caves provide invaluable insights into the conditions that led to their formation, their impressive internal features and their unique microclimate (Mammola et al., 2019). Biologists study caves as habitats, focusing on biodiversity and the ecosystems they sustain (Culver & Pipan, 2019). Fundamental is also the relationship of caves with anthropocentric sciences such as archaeology since caves are considered the earliest human habitation, while from a religious standpoint, caves remain significant as sites of worship and spiritual reverence (Trimmis, 2015).

UNESCO Global Geopark Grevena-Kozani geological settings

The Grevena-Kozani Geopark has been assigned as the UNESCO Global Geopark since 2021. Spanning an area of 2,486 km2 across five regional units in the geographic region of Western Macedonia,the geopark is renowned for its significant geological phenomena related to the formation processes of the Hellenic Orogeny. The area features Greece's oldest rocks, dated at 1 billion years, located in the Deskati region. These formations reveal the geological history and rifting processes that marked the formation of the Tethyan Ocean and the emergence of Europe as a distinct continental landmass. Oceanic crust rocks of the Tethys Ocean are found in Mount Vourinos, alongside sedimentary rocks of the Mesohellenic Trough.

The study area consists of rocks of the Pelagonian and Sub-Pelagonian geological zones (Mountrakis, 1985). The Pelagonian zone comprises Alpine and pre-Alpine rocks, originating from the Paleozoic, Mesozoic and Tertiary periods, which form the bedrock of the region. Overlying these bedrock formations are post-alpine formations, including the molassic sediments of the Mesohellenic Trough and the Plio-Pleistocene terrestrial deposits found in the Kozani-Servia and Grevena basins. These formations are the most recent deposits, consisting primarily of alluvial fans and younger river sediments.

The carbonate rocks of the area were formed during the main sedimentation that took place during the Triassic-Jurassic period. In the Vourinos area, these rocks are represented by crystalline, thickly layered, and tectonized limestones with interbedded layers of dolomites and dolomitic limestones. They form the carbonate cover on which the ophiolites were deposited. Upper Jurassic limestones which were formed in relatively shallow environments, are not distinctly separated from the overlying Cretaceous limestones and are typically mapped as a single unit. These massive carbonate formations are found in contact with the underlying ophiolithic rocks and the overlying Cretaceous limestones (Batsi, 2011).

Data and Methods

The methodological approach employed in this study combined fieldwork, bibliographic research and the application of the evaluation criteria proposed by Fassoulas et al. (2011). Karstic landforms in the area were studied in situ and documented. In specific cases, such as the Crystal Cave, which exhibits vertical development, specialized rope equipment was required for descent and documentation. A detailed catalog of all caves in the area was created, providing an extensive overview of the locations and landforms within Geopark. Precise cave mapping was performed using a Light Detection and Ranging (LiDAR) sensor Numerous 3D models of previously scanned caves, are available on the project website "Virtual speleological field trip in Greece" (Fig. 1).

According to Fassoulas et al. (2011), a systematic methodology for evaluating and assessing geotopes was developed to standardize scoring and minimize subjectivity in geological heritage management. This method categorizes evaluation criteria into six primary groups: scientific, ecological, cultural, aesthetic, economic, and potential for use. Each group is further subdivided into specific criteria that assess attributes such as geological history, ecological impact, cultural significance, landscape visibility, visitor appeal and future use potential. Scores are assigned on a scale from 1 to 10, incorporating qualitative and quantitative factors to account for intangible heritage elements.

This scoring system (Table 1) identifies geotopes of national and international significance, aligning with previous assessments (Grandgirard 1995; Rivas et al. 1997; Pralong, 2005; Zouros, 2007; Reynard et al., 2007). Based on the scores from different groups of criteria, three value indices were developed (Fassoulas et al, 2011): touristic value (Vtour), educational value (Vedu), and protection-need value (Vprot). Each index uses weighted coefficients to reflect the importance of different criteria. For example, Vedu prioritizes scientific value, while Vtour emphasizes aesthetic appeal, reflecting their respective focuses in education and tourism. The Vprot index incorporates scientific scores, integrity, and ecological risk factor, balancing ecological impact with protection status to assess conservation priorities.

- V_{tour} =0.4 Aesthetic + 0.2 Cultural + 0.2 Potential of Use + 0.2 Economic
- V_{edu}=0.4 Scientific + 0.2 Cultural + 0.2 Aesthetic + 0.2 Ecological
- V_{prot}= {Scientific + F_{ecol} + (11-Integrity)}/3

This methodology advances geotope evaluation by incorporating weighting coefficients, enabling a nuanced understanding of geotopes' multifaceted values. It supports sustainable tourism, education, and geoconservation, offering a replicable framework for assessing geological heritage in diverse contexts.

An inventory of caves in the area was compiled based on an unpublished archive of public documents provided by the late speleologist Konstantinos Ataktidis to Georgios Lazaridis. A total of 53 caves were reported, 10 of which are located within the municipality of Siatista, with the majority being potholes. The predominant rock in the broader region where the caves are located is limestone from the Pelagonian zone. The caves exhibit a variety of characteristics, including vertical and horizontal formations, as well as a range of sizes from small to large caves, with some featuring notable speleothems. However, many of these caves remain unexplored or insufficiently studied. This study focuses on analyzing four of these caves: Keli Kalogrias, Kalogria Cave, Orliakas Cave, and Vainaki Cave in the vicinity of the Geopark. These caves were selected for their unique and significant features, as well as the fact that they have been more thoroughly studied compared to others in the region.

Keli Kalogrias

Keli Kalogrias is a rock shelter formed in the limestone of the western banks of the Venetikos River, situated within the Portitsa Canyon. The shelter is located in close proximity to the historic village of "Spilaio" and derives its name, "Keli Kalogrias" (Nun's Cell), from a local legend suggesting that a nun once lived there. This characteristic enhances the cultural value of the landform. The cave is adorned with various speleothems, adding to its scientific and aesthetic significance.

Kalogrias Cave

This cave is located in the slopes of Orliakas Mt. It is small, a few meters long with an ascending branch that exits to a small opening. It is mainly fracture guided and displays a few common speleothems. It is also a cave of significant cultural and religious importance, deeply rooted in the local traditions of the area.

Table 1. Explanation of criteria and scoring system used in the evaluation framework for geosites as proposed in Fassoulas et al (2011).

Criteria	Explanation	Score 1	Score 10
1.1 Geologic history	Diversity of geological history represented at the site.	Simple type history	Tells the whole local story
1.2 Representativeness	How well the site exemplifies typical geological processes or features.	No representativeness	Very high representativeness
1.3 Geodiversity	Proportion of geological elements present.	<5%	>75%

1.4 Rarity	Frequency of similar features in the region or globally.	>7 (least rare)	Unique (most rare)
1.5 Integrity	Preservation state of the geosite	Almost destroyed	Intact
2.1 Ecological impact	Ecological significance of the geosite	No impact	Very high impact
2.2 Protection status	Level of ecological protection measures in place.	No protection	Complete protection
3.1 Ethics	Ethical value of the site.	No ethical significance	Very high significance
3.2 History	Historical importance of the site.	No historical relevance	Very high relevance
3.3 Religious	Spiritual or religious significance of the site.	No religious significance	Very high significance
3.4 Art and culture	Artistic and cultural relevance of the site.	No significance	Very high relevance
4.1 Viewpoints	Number of viewpoints the site offers.	None	>4
4.2 Landscape difference	Degree of visual contrast in the landscape.	No difference	Very high diversity
5.1 Visitors	Annual visitor number	<5,000	>75,000
5.2 Attraction	Site's appeal to visitors	No attraction	International recognition
5.3 Official protection	Level of official protection	International protection	No official protection
6.1 Intensity of use	Extent of site usage and potential overuse.	Very intense	No use
6.2 Impacts	Degree of human-induced impacts.	Very high impact	No impact
6.3 Fragility	Susceptibility to damage	No fragility	Very high fragility
6.4 Accessibility	Proximity to infrastructure	Close to hiking trail	Close to highway or town
6.5 Acceptable changes	Tolerance of the site to change.	No acceptable change	Very high tolerance

Orliakas Cave

The Orliakas Pothole (Fig.1), also known as the Cave of Crystals, is located to the west of the col of Mount Orliakas and reaches a depth of about 15 meters. Its entrance comprises two openings at nearly the same elevation, both of similar size and elliptical in shape. Transparent scalenohedral calcite crystals are adorn the walls and the ceiling of the cave. These crystals are remarkable in size, exceeding 30 cm in length. The cave is formed within Upper Cretaceous reef limestones, which unconformably overlain by sediments from the Mesohellenic Trough (Lazaridis, 2024).

Vainaki

Vainaki cave (Fig.1) comprises a phreatic passage now located several tens of meters above the current water table of the region. It is partially eroded and features two entrances, one at each end. The side walls retain well-defined scallops (Fig.1), offering valuable insights into the paleoflow and specifically the velocity and the flow direction that led the formation of the scallops within the passage.

Figure 1. 3D models of caves: Left – Orliakas Cave, Right – Vainaki Cave, Below – Close-up view of the Vainaki Cave 3D model showcasing well-defined scallop formations. (Source: https://speleology8.wordpress.com).

Results

Results According to the methodology outlined by Fasoulas et al. (2011), the corresponding scoring values for these geosites are presented in Table 2. As shown, the highest educational values are attributed to Orliakas Cave, due to its rarity and uniqueness in the area, its distinct morphology and its high integrity. Remarkably high ecological impact of Orliakas Cave reflects the geotope's role in supporting the development of specific ecotopes or the presence of endemic species in the region. Orliakas cave also receives the highest score for protection-need value because of its significant ecological impact, and its low actual protection status and preservation. The greatest potential for tourism development is attributed to Kalogrias Cave, which is known as a religious site. Its connection with local traditions and historical events in the region is of considerable importance.

Table 2. Evaluation results of geosites in the Grevena-Kozani UNESCO Global Geopark using the Fassoulas et al. (2011) method.

Cave Name	Keli Kalogrias	Kalogrias Cave	Orliakas Cave	Vainaki
1. Scientific score	2.9	2.9	7	5.5
1.1 Geological history	2.5	2.5	7.5	5
1.2 Representativeness	2.5	2.5	5	5
1.3 Geodiversity	1	1	5	2.5
1.4 Rarity	1	1	10	7.5
1.5 Intergrity	7.5	7.5	7.5	7.5
2. Ecological score	4.25	4.25	5.5	4.25
2.1 Ecological impact	7.5	7.5	10	7.5
2.2 Protection status	1	1	1	1
3. Cultural score	7.5	7.5	1.75	4.63
3.1 Ethics	10	10	2.5	10
3.2 History	7.5	7.5	2.5	5
3.3 Religious	10	10	1	1
3.4 Art and culture	2.5	2.5	1	2.5
4. Aesthetic score	5.5	5.5	5.5	6.25
4.1 Viewpoints	1	1	1	2.5
4.2 Landscape difference	10	10	10	10
5. Economic score	2	2	2	2
5.1 Visitors	1	1	1	1
5.2 Attraction	2.5	2.5	2.5	2.5
5.3 Official protection	2.5	2.5	2.5	2.5
6. Potential use score	5.7	6.5	4.7	6.5
6.1 Intensity of use	7.5	7.5	7.5	7.5
6.2 Impacts	7.5	7.5	2.5	7.5
6.3 Fragility	10	10	10	10
6.4 Accessibility	1	5	1	5
6.5 Acceptable changes	2.5	2.5	2.5	2.5
Fecol[1]	7.5	7.5	10	7.5
Vedu[2]	4.61	4.61	5.35	5.23
Vprot[3]	4.63	4.63	6.83	5.5
Vtour[4]	5.24	5.4	3.89	5.13

[1]Fecol: ecological factor, [2]Vedu: educational value, [3]Vprot: protection-need value, [4]Vtour: touristic value

Discussion

The evaluation was conducted on 8% of the caves within the geopark territory. Observing the analysis results, it appears that the economic, aesthetic, and ecological scores exhibit the greatest uniformity in their values. Specifically, the low ecological score is attributed to the limited tourist visitation, as these caves are considered local destinations, are not widely known, and some of them are difficult to access. Regarding the aesthetic score, there are small variations in values, with the average score across all caves exceeding 5. This indicates moderate landscape contrast, which evaluates differences in shape, color, or morphology between the geotope and its surroundings. Additionally, limited viewpoints are considered, focusing on visibility from roads or trails a few meters apart. The ecological score generally displays moderate to low values due to the high ecological impact and low protection status, as these caves are categorized as having no protection.

The most significant variations are observed in the cultural score. The Kalogrias Cave and Keli Kalogrias are religious sites of historical importance, and together with the Vainaki cave, they highlight the traditions and customs of the region. In contrast, no sufficient evidence has been found for Orliakas Cave to provide information supporting such an evaluation.

Previous work by Fasoulas et al. (2011) has provided information and analysis from caves in the Cretan region, allowing us to compare our results and form a more comprehensive picture. Especially at Psiloritis Geopark, the main tourist attractions in the area and the most suitable geotopes for educational activities are Idaion Andro and Sfentoni caves. These sites are already used for various educational programs and initiatives organized by the Geopark and local educational centers. It is important to note that the low tourist value score attributed to the aforementioned geotopes, is either due to restrictions on visitor numbers, or due to the site's fragility (Sfentoni cave) or ongoing excavations (Idaion Andro Cave). Compared to the touristic score values of Grevena-Kozani Geopark, similarly low value scores are observed, as they are limited to the local level.

At Lassithi Mountain most of the studied geosites lack proper protection or are inadequately managed due to the absence of centralized oversight. As a result, they face significant risks and threats. Many of these geotopes are deeply tied to the history and culture of Crete, such as the renowned Diktaion Andro, mythologically known as the birthplace of Zeus, and hold importance for both educational and tourism purposes. Notably, Dikation Andro, the area's most popular attraction with approximately 70.000 visitors annually, receives a tourism value score of only 4.8. This low score is primarily due to severe discoloration of stalagmites and stalactites caused by decades of improper lighting.

Conclusions

The application of evaluation frameworks is an invaluable tool for geopark management authorities, facilitating informed decision-making, sustainable exploitation, and the effective protection of natural resources and landforms. While criteria such as Scientific, Cultural, and Aesthetic scores largely depend on the natural characteristics of the geosite and its surroundings, Ecological, Economic, and Potential of Use criteria are significantly influenced by management practices and the applicable regional legislation. This distinction emphasizes dual dependency on both natural features and human interventions in the evaluation process.

The uniqueness of the Scientific criterion lies in its potential for enhancement, as it is directly tied to the extent and quality of interdisciplinary research conducted on the geosite. For example, incorporating advanced studies in geology, biology, and cultural heritage can elevate its scientific value. Similarly, the viewpoints of a geosite have a profound impact on its Aesthetic score. Although this factor is an inherent part of the landscape, it can be significantly improved through targeted management initiatives, such as the development of well-planned trails and the installation of strategically positioned viewpoints. These efforts not only enhance the visual appeal but also improve Accessibility scores, ultimately contributing to the geosite's Potential of Use.

The karstic geosites within the Grevena-Kozani UNESCO Global Geopark demonstrate strong performance in Cultural, Aesthetic, and Potential of Use categories. These promising results provide a solid foundation for more detailed investigations into the geosites, aimed at further promoting and showcasing their unique features. A comparative analysis of parameter values between the Grevena-Kozani Geopark and other geoparks reveals that these caves possess significant potential to be recognized as key geotopes within the geopark. Their inclusion would undoubtedly contribute to the geopark's enrichment and global significance.

Upon closer analysis of the applied criteria, it becomes clear that more specialized metrics are necessary for the comprehensive evaluation of karstic landforms, particularly karstic caves. Essential criteria include the accessible length of the cave, the level of technical expertise required for entry, and the suitability of its atmosphere for safe exploration. These parameters are critical for determining the potential for sustainable utilization while ensuring the protection of these fragile environments.

In conclusion, the evaluation frameworks not only serve as a cornerstone for effective geosite management but also underscore the necessity of refining assessment tools to address the specific needs of karstic caves. This step-by-step approach will enable more accurate evaluations, fostering both conservation and sustainable tourism development, and ultimately contributing to the long-term success of geoparks.

Acknowledgements

The authors would like to express their sincere gratitude to Iraklis Kalogeropoulos and Antonis Kleisiaris for their valuable contributions to the fieldwork. 3D cave scans conducted as part of the 'Virtual Speleological Field Trip in Greece' project, formally supported by the International Union of Speleology (UIS).

References

Batsi A., 2011. Tectonic evolution of the area of Rodiani, West Macedonia. MSc Thesis, Aristotle University of Thessaloniki, Thessaloniki.

Culver, D. C., Pipan, T., 2019. The biology of caves and other subterranean habitats. 2nd ed. Oxford University Press. Oxford.

Fassoulas, C., Mouriki, D., Dimitriou, P. D., Iliopoulos, G., 2011. Quantitative assessment of geotopes as an effective tool for geoheritage Management. Geoheritage, 4(3), 177–193.

Grandgirard, V., 1995. Méthode pour la réalisation d'un inventaire de geotopes géomorphologiques. UKPIK Cahiers de l'Institut de Géographie de l'Université de Fribourg 10:121–137.

Lazaridis, G. T., 2024. Formation conditions of hypogene caves in the Hellenic orogen: mineralogy, geochemistry, stable isotopes (C, O, S), fluid inclusions. .Ph.D Thesis, Aristotle University of Thessaloniki, Thessaloniki.

Mammola, S., Piano, E., Cardoso, P., Vernon, P., Domínguez-Villar, D., Culver, D. C., Pipan, T., Isaia, M., 2019. Climate change going deep: The effects of global climatic alterations on cave ecosystems. The Anthropocene Review, 6(1–2), 98–116.116.

Mountrakis, D., 1985. Geology of Greece, University Studio Press, Thessaloniki.

Pralong, J. P., 2005. A method for assessing the touristic potential and use of geomorphological sites. Geomorphologie: Relief, Processus, Environment 3:189–196.

Rassios, A. E., Grieco, G., 2021. Is geoheritage a “cutting-edge” science? Promotion of an extension to the definition of geoheritage with emphasis as a significant discipline in geosciences with cultural and societal relevance. In Geological Society of America eBooks, pp. 37–53.

Reynard, E., Fontana, G. D., Kozlik, L., Scapozza, C., 2007. A method for assessing “scientific” and “additional values” of geomorphosites. Geographica Helvetica, 62(3), 148–158. https://doi.org/10.5194/gh-62-148-2007

Rivas, V., Rix, K., Frances, E., Cendrero, A., Brunsden, D., 1997. Geomorphological indicators for environmental impact assessment: consumable and non-consumable geomorphological resources. Geomorphology 18:169–182.

Theodosiadis, T., 2020. Cave Tourism. International Developments and Greek Reality, with Emphasis on the Maara Cave in Drama, Alistratis Cave in Serres, and Vlychada Cave in Diros, Laconia MSc Thesis, Hellenic Open University, Greece.

Trimmis, K. P., 2015. Hidden Treasures in Forgotten Archives: Exploring the Archaeology of Greek Caves into the archives and the bulletin of the Hellenic Speleological Society. Chronika, 5, 32-41.

Zouros, N., 2007. Geomorphosite assessment and management in protected areas of Greece. Case study of the Lesvos Island-coastal geomorphosites. Geographica Helvetica 62(3):69–180.

17th INTERNATIONAL CONGRESS
of the Geological Society of Greece

BULLETIN OF THE GEOLOGICAL SOCIETY OF GREECE, SP. PUBL.

EXTENDED ABSTRACT 192

Utilizing Information and Communication Technology for geosite development: The case of sulfuric acid caves in the Vikos-Aoos UNESCO Global Geopark

Lazaridis G.[1,*], Stergiou C. L.[1,2], Chatzipetros A.[1], Stamoulis K.[3], Dora D.[1], Georgopoulou X.[4], Vouvalidis K.[1], Nikolaou E[5], Paschos P.[5], Kitsaki G.[6], Papaioannou H.[6]

*(1) Faculty of Geology, Aristotle University of Thessaloniki (AUTH), 54124 Thessaloniki, Greece, *geolaz@geo.auth.gr*
(2) Chemical Process & Energy Resources Institute (CPERI), Centre for Research and Technology Hellas (CERTH), 50200 Ptolemaida, Greece
(3) Archaeometry Center, University of Ioannina, 45110 Ioannina, Greece
(4) Department of Theatre Studies, National and Kapodistrian University of Athens, 15784 Ilissia, Greece
(5) Hellenic Survey of Geology and Mineral Exploration, Region of Epirus, Eleonas, 48100 Preveza, Greece
(6) Vikos-Aoos UNESCO Global Geopark - Development Agency of Epirus S.A. (EPIRUS S.A.), Ioannina, Greece

Research Highlights

Recent research within the Vikos-Aoos UNESCO Global Geopark and neighboring Albania has highlighted the significance of sulfuric acid speleogenesis (SAS) caves, drawing the attention of explorers and researchers alike. Collaborative efforts by the Geopark and the School of Geology at Aristotle University of Thessaloniki focus on mapping these caves and investigating their unique processes. Their presence in a Greek Geopark underscores their scientific importance and potential for fostering awareness and sustainable tourism. However, the challenges posed by toxic atmospheres and fragile ecosystems necessitate strict protection measures, advocating for innovative approaches such as Information and Communication Technologies (ICT) to ensure responsible geosite development.

The Geopark

The Vikos-Aoos Geopark, located in Epirus, Greece, spans 1,200 sq. km across the municipalities of Zagori and Konitsa and includes 62 villages whose residents primarily engage in tourism, agriculture, livestock farming, forestry, and small-scale manufacturing. Dominated by the Vikos and Aoos Gorges, the towering mountains of Northern Pindos, and rivers like Aoos, Voidomatis, and Sarantaporos, the geopark showcases a geologically diverse history starting 200 million years ago. Comprising sedimentary, metamorphic, and igneous rocks, including ophiolitic formations from the Tethys Ocean, the area reflects tectonic processes of the Alpine Orogeny and extensive faulting during the Quaternary, which shaped its rugged karstic landscape (Telbisz et al., 2019). Recognized as a UNESCO Global Geopark since 2010, it supports conservation, education, and sustainable development while protecting unique ecosystems and fostering public engagement through its exceptional geological and natural heritage.

The diverse geological processes in the Vikos-Aoos Geopark are reflected in its landforms and geomorphology, offering unique insights into the geological evolution of Greece. The park features 51 geosites classified into seven categories: springs, tectonic structures (faults and folds), river terraces, rock shelters, panoramic viewpoints, karstic formations, and glacial landforms. These sites showcase significant geological interest, rarity, and beauty.

Classic caves, such as the vertical shafts of "Vulture's Hole" (Geosite 39, -584m depth, 650m length), and "Chasm of Epos" (Geosite 40, -455m depth), and Gailotrypa (Geosite 44, -155 m deep), exemplify the dissolution of limestone along fractures and faults. Additionally, smaller rock shelters like Boila (Geosite 25), Kleidi (Geosite 24), and Megalakkos served as Paleolithic refuges for hunter-gatherers

While classic caves are well-recognized geosites within the park, SAS caves do not form a distinct category, emphasizing the broad diversity and representation of geological phenomena in the Geopark, and suggesting future actions on geoheritage recognition and preservation.

The SAS geosites of the Geopark

Landforms associated with sulfuric acid dissolution within the geopark include notable caves and springs (Fig.1 & Fig.2). Among them is the Skordyli Cave, situated on the northern bank of the Sarantaporos River, close to the Albanian border and approximately 2.5 km west-southwest of the Kavasila thermal springs. The cave entrance serves as the outlet for an underground sulfuric river that traverses a series of large chambers connected by smaller passages. Extending about half a kilometer from the underground spring to the outlet, the cave's sidewalls are coated with gypsum and native sulfur. Its ecosystem is remarkable for the presence of chemoautotrophic microorganisms and a high level of endemism (Sarbu et al., 2024).

Pixaria Cave, located east-northeast of the Kavasila thermal springs in a limestone outcrop, is similarly influenced by sulfur springs near its entrance, which lies close to the Sarantaporos River. The cave features fracture-guided passages forming a maze-like pattern, with a slightly inclined floor and median feeders. The walls of the passages are covered with gypsum, reflecting its speleogenetic processes.

Neles Cave is found near the Neles spring in Kleidonia Village, at the escarpment of the Konitsa Fault that borders Papigo Mountain to the west. The cave entrance is aligned along a fault plane, leading to a vertically developed passage. At its deepest point, 13 meters below the entrance, a horizontally oriented passage carries a stream of sulfuric water. The atmosphere is rich in hydrogen sulfide, and gypsum coats the walls and boulders. Although the cave and the spring appear interconnected, a direct link has yet to be confirmed.

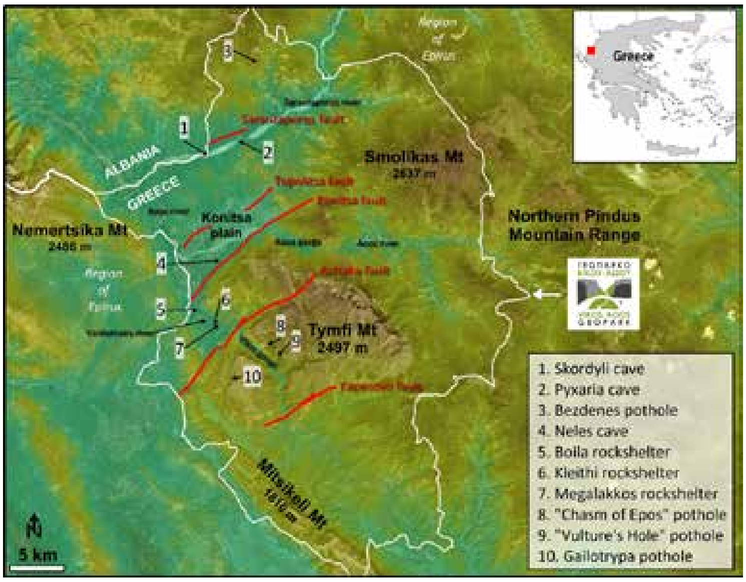

Figure 1. A map of the Vikos-Aoos Geopark showing the locations of the major caves, faults, mountains and rivers of the region (modified after Chatzipetros et al., 2024).

Lastly, Bezdenes Pothole, near the Amarantos thermal springs, is preliminarily included due to gypsum-like deposits found in its deeper sections. This impressive vertical void has a reported depth of 268 meters. Ongoing research aims to confirm its sulfuric acid dissolution origin and further clarify its speleogenetic context.

Figure 2. Entrances of Sulfuric Acid Speleogenesis caves in the Vikos-Aoos UNESCO Global Geopark: A. Skordyli sulfur Cave; B. Pixaria Cave; C., Neles Cave; D., Neles Spring; E. Bezdenes Pothole.

Application of Information and Communication Technologies

Information and Communication Technologies (ICT) have been utilized to support the study and promotion of sulfuric acid speleogenesis (SAS) geosites. Tools such as multimedia, data management systems, and virtual reality (VR) facilitate map creation, data analysis, and immersive public experiences. Their application varies across SAS geosites, addressing site-specific challenges while prioritizing safety.

In the field, a flexible suite of tools—primarily mobile-based applications—has been utilized. These tools facilitate the capture of georeferenced photographs of cave entrances, springs, and related features, as well as 3D scans of the caves. These scans form the foundation for VR or augmented reality (AR) experiences. Notable applications include FieldMove Clino by Midland Valley (specialized in petroleum engineering and structural geology software) for structural data collection and Polycam for 3D scanning. Polycam utilizes LiDAR (Light Detection and Ranging) technology, which works by emitting laser pulses and calculating the time taken for the light to bounce back, generating a precise 3D map of the cave. Advanced machine learning algorithms refine the scans, while AI plays a crucial role in enhancing 3D models by cleaning them, optimizing textures, and filling in missing data. The combined use of these applications, already validated in scientific cave research (Lazaridis et al., 2024), produces cave maps that meet the highest standards as defined by mapping grades (Häuselmann, 2011).

In the Vikos-Aoos Geopark, various 3D models have been developed to document the key features of SAS geosites. At the Neles location, two models were created to capture the spring and the cave, offering ground plans and depth measurements of the vertically developed cave. Similarly, at Pixaria Cave m (Fig.3), three models were produced: one documenting the entrance area with distinct dissolution forms, another capturing a passage characterized by a median sulfuric feeder, and a partial scan of the cave's initial section, highlighting its maze-like pattern of passages with consistent size and morphology.

Some of these scans are featured on the webpage "Virtual Speleological Field Trip in Greece" (https://speleology8.wordpress.com/pixaria-cave/) and are linked to related publications (e.g., Lazaridis et al., 2024). This makes these significant landforms accessible to a broad audience, including researchers, cavers, and the general public.

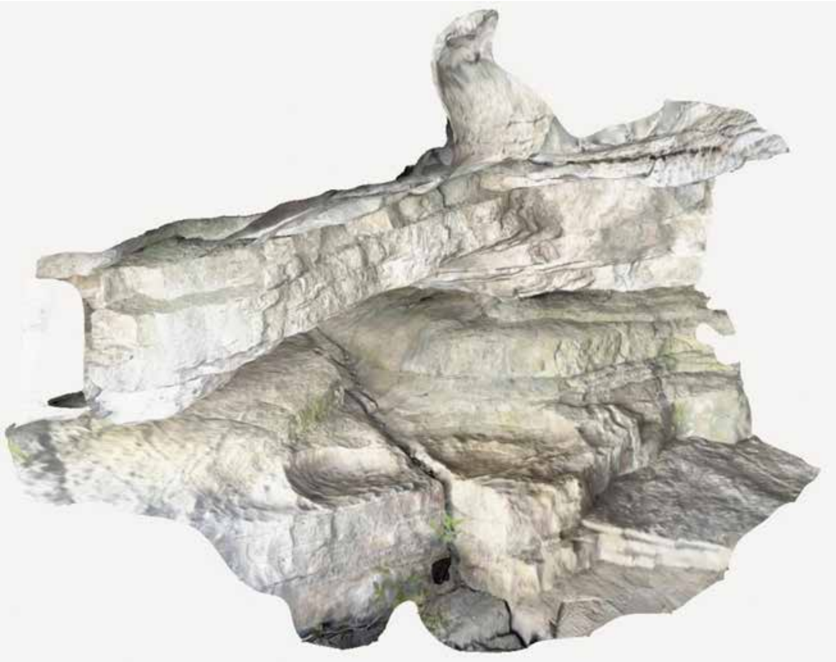

Figure 3. Example of a 3D-model from the entrance area of Pixaria Cave in Kavasila thermal springs of the Vikos-Aoos UNESCO Global Geopark.

Discussion

During the initial phase of this project, several challenges were encountered in applying ICT for geosite development. The primary concerns were identifying a time-efficient, safe, and cost-effective method capable of providing accurate data. To address these concerns, well-trained field participants were involved, equipped with real-time gas detectors and data loggers for monitoring radon levels. The use of smartphone-based tools proved to be an effective solution, helping minimize factors such as equipment costs and the time required for data acquisition. While this approach sometimes results in lower resolution or precision—such as in the point cloud data from 3D scans—it is a necessary trade-off, as safely entering these caves with highly specialized instruments is virtually impossible.

The fieldwork techniques employed in this study enabled the efficient collection of data and the development of a solid methodology that can be adapted for use in other karst geosites. The combination of ICT tools allowed the team to gather data quickly, facilitating the creation of comprehensive datasets while maintaining a rigorous approach to scientific research.

The implementation of ICT offers several advantages for overcoming speleological challenges and addressing preservation needs, while simultaneously promoting public engagement. In particular, the toxicity of hydrogen sulfide in the cave atmosphere and the elevated radon levels present significant obstacles for fieldwork, increasing the need for safety equipment and monitoring, especially for non-trained visitors. Furthermore, caves with vertical extents, such as Bezdenes Pothole and Neles Cave, pose accessibility challenges for both researchers and the public.

ICTs provide a way for the authorities of the Vikos-Aoos Geopark to offer virtual access to these geosites, enabling the public to explore them remotely while ensuring their protection. Moreover, these technologies support the creation of a management plan that safeguards both the caves and the sensitive ecosystems they contain, which are home to unique species with high levels of endemism. In addition to enhancing visitor safety, the geopark fulfills its role in the conservation and protection of these valuable geological sites.

The integration of ICT in geosite development not only advances scientific research but also provides a sustainable method for preserving these delicate ecosystems. By offering virtual access to otherwise inaccessible caves, such as Bezdenes Pothole and Neles Cave, the Vikos-Aoos Geopark can engage a wider public without compromising safety or the integrity of the sites (e.g. Evelpidou et al., 2021). This virtual experience, coupled with 3D scanning and augmented reality tools, allows visitors to explore these caves remotely, fostering greater awareness and interest in their preservation. The successful application of ICT in this context could serve as a model for other geosites, demonstrating the potential for technological advancements to enhance both public engagement and conservation efforts. Looking ahead, the continued use and advancement of these technologies will help ensure the long-term protection of these valuable natural resources, while also supporting local communities through increased tourism and educational opportunities (see for example Lazaridis et al., 2023).

The sulfuric acid caves in the Vikos-Aoos Geopark are the only known examples of this type of speleogenesis in Greece that are located in the area of an UNESCO Global Geopark, adding critical value to the promotion of these landforms. Their unique morphology also makes them ideal for educational purposes.

Finally, this work aligns with UNESCO's policies by fostering sustainable development, education, and cultural heritage preservation. By utilizing ICT to provide virtual access to inaccessible geosites, we promote inclusivity, enabling broader public engagement while protecting fragile ecosystems. The project supports education through innovative tools like 3D scanning and augmented reality, which enhance understanding of unique geological features. Additionally, our efforts contribute to local communities by encouraging geotourism and raising awareness about the importance of conserving these natural and cultural assets, reflecting UNESCO's goals of balancing accessibility, education, and preservation.

Conclusions

The use of ICT in the Vikos-Aoos Geopark has proven effective in overcoming challenges like toxic cave environments and limited accessibility. Smartphone-based tools and virtual technologies allowed for efficient data collection while keeping costs and time in check. These technologies not only helped gather accurate data but also enabled virtual access to caves, ensuring public safety while promoting awareness of these unique geological sites.

By offering virtual experiences, the Geopark can engage the public without compromising preservation efforts. This approach, using 3D scanning and augmented reality, sets a good example for other geosites looking to balance access and protection. Continued use of ICT will help safeguard these fragile ecosystems, support local tourism, and provide educational opportunities. The sulfuric acid caves in the geopark are particularly valuable for educational purposes and conservation, offering a unique opportunity for both research and public engagement.

This work supports UNESCO's policies by promoting sustainable geosite management, enhancing public engagement through virtual access, and fostering education and conservation of unique geological and cultural heritage.

Acknowledgements

Cave visits for this work have been approved by the Greek Ministry of Culture – Ephorate of Paleoanthropology and Speleology. Special thanks to the cavers who participated in the various expeditions for research in the area. 3D cave scans conducted as part of the 'Virtual Speleological Field Trip in Greece' project, formally supported by the International Union of Speleology (UIS).

References

Audy, M., Bouda, R., Bruthans, J., Rÿžiÿka, V., 2022. Albanian hypogene caves in the area of Vromoner thermal springs on the Sarandaporo River. Speleoforum, 41, 42–49.

Audy, M., Bruthans, J., Mareš, J., Sarbu, S., Galdenzi, S., Bouda, R., 2024. Sulfur 2023, hypogenni jeskyne Albanie a Recka Kavasila, Vromoner, Langarica. Speleoforum, 43, 104–111.

Benassi, A., 2024. Lengarices 2023: inseguendo il Soffi o del Drago (Albania). Speleologia, 89: 4-6.

Chatzipetros, A., Stergiou, C.L., Papaioannou, H., 2024. Seismic hazard in an actively uplifting area: the case of Vikos-Aoos UNESCO Global Geopark, NW Greece. In: Pellicer, M.X., Aytac, A., Amorfini, A., Delaby, S., (Eds.), Geohazards in European Geoparks, Akademisyen Yayınevi Kitabevi, Ankara, Turkey, pp. 150-153.

De Waele, J., D'Angeli, I. M., Audra, P., Plan, L., Palmer, A. N., 2024. Sulfuric acid caves of the world: A review. Earth-Science Reviews, 104693.

Evelpidou, N., Karkani, A., Saitis, G., Spyrou, E., 2021. Virtual field trips as a tool for indirect geomorphological experience: A case study from the southeast part of the Gulf of Corinth, Greece. Geoscience Communication Discussions, 2021, 1-16.

Kovařík, F., Audy, M., Sarbu, S.M., Fet, V., 2023. Euscorpius sulfur sp. n. (Scorpiones: Euscoriidae), a new cave scorpion from Albania and northwestern Greece. Euscorpius, 376:1-14.

Lazaridis, G., Dora, D., Sdraka, F. and Vouvalidis, K., 2023. Virtual speleological field trip in Greece – project report. UIS Bulettin, 61-1: 46-48.

Lazaridis, G., Melfos, V., Papadopoulou, L., 2011. The first cave occurrence of orpiment (As□S□) from the sulfuric acid caves of Aghia Paraskevi (Kassandra Peninsula, N. Greece). International Journal of Speleology, 40(2), 6.

Lazaridis, G., Melfos, V., Papadopoulou, L., Onac, B., Stergiou, Ch., Maravelis, A., Voudouris, P., Dora, D., Fitros, M., Papaioannou, H., Vouvalidis, K., 2024. Sulfuric acid speleogenesis in Greece. Acta Carsologica, 53/2-3, 127-144.

Lazaridis, G., Trimmis, K.P., Drnić, I., Brkić Drnić, K., 2024. Deciphering rock surface origins in a karst cave: insights from the Rača Cave, Lastovo, Croatia. Geologia Croatica, 77(3), pp.235-242.

Polymenakou, P., Mandalakis, M., Dailianis, T., Dimitriadis, C., Medvecky, M., Magoulas, A., Gerovasileiou, V., 2018. Preliminary assessment of methanogenic microbial communities in marine caves of Zakynthos Island (Ionian Sea, Greece). Mediterranean Marine Science, 19(2), 284-289.

Sarbu, S.M., Brad, T., Băncilă, R.I., Stefan, A., 2024. Exploring Biodiversity and Food Webs in Sulfur Cave in the Vromoner Canyon on the Greek–Albanian Border. Diversity 16, 477.

Telbisz, T., Stergiou, C.L., Mindszenty, A., Chatzipetros, A., 2019. Karst features and related social processes in the region of the Vikos gorge and Tymphi mountain (Northern Pindos National Park, Greece). Acta Carsologica 48(1), 29-42.

17th INTERNATIONAL CONGRESS
of the Geological Society of Greece

BULLETIN OF THE GEOLOGICAL SOCIETY OF GREECE, SP. PUBL.

EXTENDED ABSTRACT 193

Management of solid wastes from offshore oil drilling, based on their geochemical properties: A case study from the Prinos facilities in the Northern Aegean Sea.

Lianou Vasiliki[1], Tsakiridis Petros[2]
(1) National and Kapodistrian University of Athens, Athens, Greece, vlianou@geol.uoa.gr (2) National Technical University of Athens, Athens, Greece

Introduction

The increasing growth of the oil and gas industry has resulted in the generation of huge amounts of waste, most of which is produced during the drilling of wells for the exploration, extraction and production of hydrocarbons. The solid phase of drilling waste, also known as drill cuttings or DCs, is a major concern for oil companies, mainly due to the organic and inorganic contaminants it contains (Onwukwe & Nwakaudu, 2012). Increasing regulations and environmental concerns require the proper treatment and disposal of this waste (EU, 2013). However, the complexity, slow pace, and high cost of traditional debris remediation methods have, in recent years, shifted research focus toward its use as a raw material for manufacturing various products. The reuse of drilling waste in various applications, particularly in the construction sector, aligns with the principles of the circular economy and serves as a key solution for sustainable development (Asim *et al*., 2021). Research has already presented various proposals for the use of DCs, but choosing the appropriate solution is not an easy task. Each case is unique and demands a thorough understanding of the waste material's physical and chemical properties.

In Greece, the management of drill cuttings from hydrocarbon extraction has not been thoroughly studied. A significant challenge in exploring alternative management solutions is the lack of data on the composition and microstructure of this debris. Addressing this gap, this paper takes an initial step in analyzing and characterizing the geochemical properties of solid drilling cuttings from the country's sole hydrocarbon production facility.

Materials and Methods

A series of laboratory tests were carried out on a sample of DCs from Prinos facilities (fig. 1), using advanced X-ray (XRF and XRD) and scanning electron microscope (SEM) analysis methods to investigate its physical/mechanical properties, measure its hydrocarbon content (as these are its major contaminants) and determine its geochemical composition.

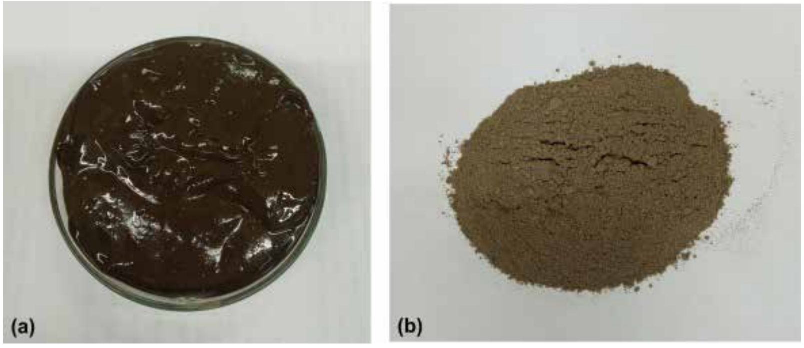

Figure 1. Sample of the study material: (a) coated with drilling mud, and (b) after drying at 110 °C for 24 hours.

Results

The results showed that the physical properties as well as the chemical and mineralogical composition of the DCs from Prinos depend on the rocks of the mining area, mainly on the calcium sources and the residual drilling mud. The debris material was characterized as silt, with the main oxides in its composition being BaO (21.98%), CaO (16.1%), SiO2 (14.21%) and SO3 (8.54%). The sample had a high loss on ignition (LOI ≈25.83% w/w) and contained organic material at 10.04% w/w and total petroleum hydrocarbons (TPH with C>12) at 7.34% w/w (fig. 3). It was also contaminated with polyaromatic hydrocarbons (PAHs: ≈180 mg/kg) (fig. 2). In terms of mineralogical composition, it contained: quartz (SiO2), calcite (CaCO3), dolomite [CaMg(CO3)2], anhydrite (CaSO4), barite (BaSO4) and alite (NaCl), with the dominant phase being quartz (excluding barite).

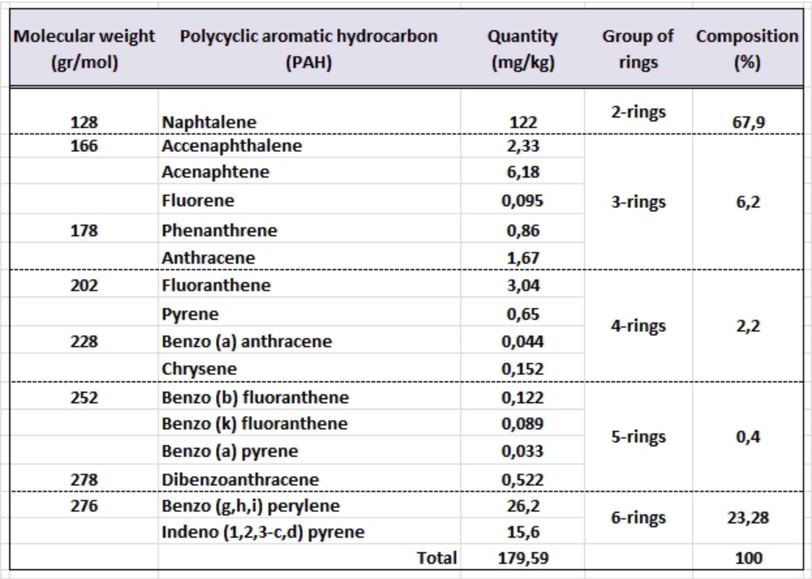

Molecular weight (gr/mol)	Polycyclic aromatic hydrocarbon (PAH)	Quantity (mg/kg)	Group of rings	Composition (%)
128	Naphtalene	122	2-rings	67,9
166	Accenaphthalene	2,33	3-rings	6,2
	Acenaphtene	6,18		
	Fluorene	0,095		
178	Phenanthrene	0,86		
	Anthracene	1,67		
202	Fluoranthene	3,04	4-rings	2,2
	Pyrene	0,65		
228	Benzo (a) anthracene	0,044		
	Chrysene	0,152		
252	Benzo (b) fluoranthene	0,122	5-rings	0,4
	Benzo (k) fluoranthene	0,089		
	Benzo (a) pyrene	0,033		
278	Dibenzoanthracene	0,522		
276	Benzo (g,h,i) perylene	26,2	6-rings	23,28
	Indeno (1,2,3-c,d) pyrene	15,6		
	Total	179,59		100

Figure 2. PAHs concentrations and percentage distribution of their fractions based on their ring group, in the sample.

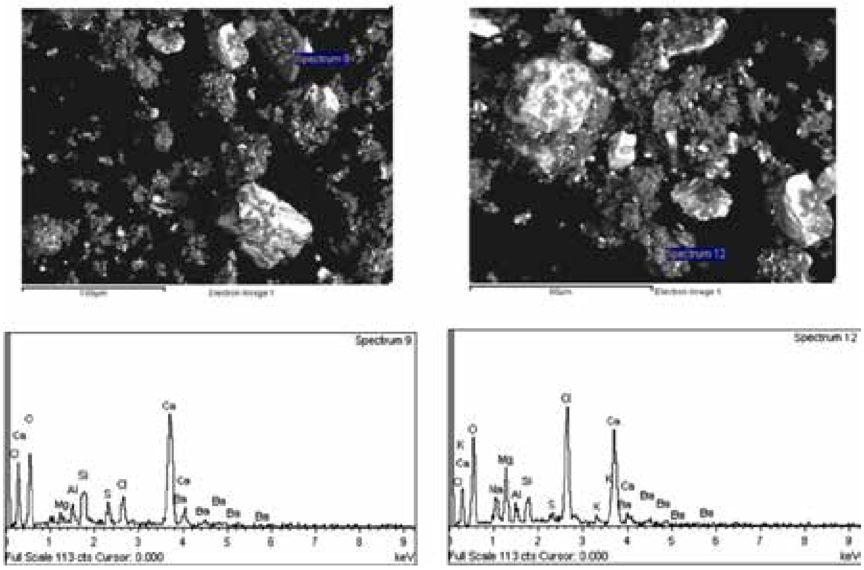

Figure 3. Characteristic mineral phases of the DCs sample from Prinos.

Conclusions

The main conclusions from the study of the results are summarized as follows: (a) the inorganic phases identified indicate that the material under consideration is of evaporite origin, (b) the very high percentage of Ba indicates the presence of drilling mud residues in the sample, (c) the contents of the remaining elements can be attributed mainly to the rocks of the mining area, and (d) the concentrations of trace elements in the DCs are probably controlled by the composition of the individual grains, with the exception of strontium, which is probably associated with the barite in the drilling mud.

Finally, to support the reuse and recycling of DCS, this study also explored three potential scenarios for utilizing Prinos drill cuttings. While the analysis was theoretical, the findings indicate promising opportunities for incorporating this type of solid waste into various products, demonstrating viable alternatives for its management.

Acknowledgements

I extend my gratitude to ENERGEAN OIL & GAS – ENERGIAKI AEGEAN S.A., with special thanks to Mr. V. Tsetoglou and Mr. P. Kokkini for supplying the material necessary for this study.

References

Asim, N., Badiei, M., Torkashvand, M., Mohammad, M., Alghoul, M.A., Gasaymeh, S.S., Sopian, K., 2021. Wastes from the petroleum industries as sustainable resource materials in construction sectors: Opportunities, limitations, and directions. Journal of Cleaner Production, 284, 125459.

EU, 2013. The Council Decision of 17 December 2012 on the accession of the European Union to the Protocol for the Protection of the Mediterranean Sea against pollution resulting from exploration and exploitation of the continental shelf and the seabed and its subsoil https://eur-lex.europa.eu/legal-content/EN/TXT/?uri=CELEX%3A32013D0005.

Onwukwe, S.I., Nwakaudu, M.S., 2012. Drilling wastes generation and management approach. Int J Environ Sci Dev 3(3), 252–257.

17th INTERNATIONAL CONGRESS of the Geological Society of Greece

BULLETIN OF THE GEOLOGICAL SOCIETY OF GREECE, SP. PUBL.

EXTENDED ABSTRACT 194

Palaeobotanical study of the Vrisaki flora from the Lesvos Petrified Forest

Eleni M. Liapi[1,2], George Iliopoulos[3], Nikolaos Zouros[1,2]

(1) Natural History Museum of the Lesvos Petrified Forest, Sigri/Lesvos, Greece, geod22002@aegean.gr (2) Department of Geography, University of the Aegean, Mytilene/Lesvos, Greece (3) Department of Geology, University of Patras, Rio/Patras, Greece

Research highlights

New insights into the plant palaeoassemblages from the Petrified Forest of Lesvos Island are revealed through the documentation and taxonomic determination of the leaf macro-remains from Vrisaki fossiliferous locality.

Background

The Petrified Forest, located at the western peninsula of the Lesvos Island, Greece, and recognized as a UNESCO Global Geopark, plays a pivotal role in preserving and showcasing the natural heritage of the Lesvos Island through efforts in scientific research, geo-conservation, geo-education and geo-tourism.

The recent construction of the new Kalloni-Sigri road, crossing the protected area of the Lesvos Petrified Forest in Western Lesvos, has exposed a remarkable wealth of plant fossil sites (Fig. 1). Especially, twelve fossiliferous localities were identified and excavated along the road, carefully protected, and studied to ensure their preservation and to advance knowledge. The findings include a wide variety of fallen and in situ fossilized tree trunks along with mass occurrences of leaf macro-remains revealing the great palaeobotanical richness of the region (Zouros, 2021). The unearthed fossil material surpasses all prior expectations establishing the Lesvos Petrified Forest as one of the most significant areas for scientific investigations worldwide. Recent studies on both wood anatomy and leaf macro-morphology have provided new insights into the preserved volcanic flora of the broader protected area of the Petrified Forest (Velitzelos et al., 2019; Iamandei et al., 2022, 2024; Kafetzidou et al., 2022; Tsitsou et al., 2022; Liapi et al., 2022, 2023, 2024; Zhu et al. 2024).

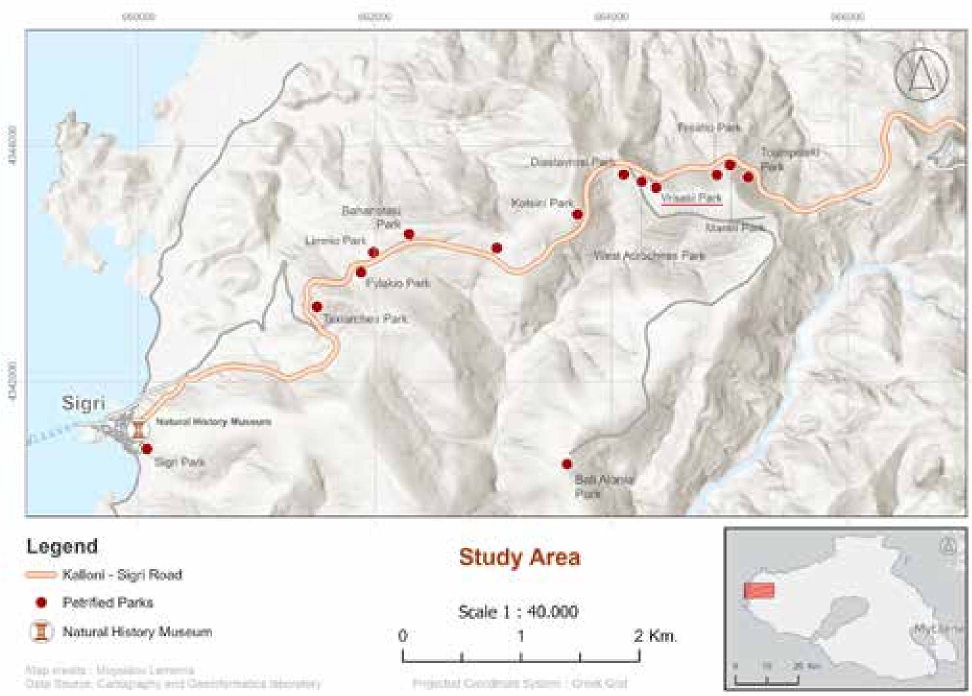

Figure 1. Location map of Western Lesvos where several new fossiliferous localities have been unearthed in the broader area of the Akroheiras hill range along Kalloni-Sigri road. The studied fossil material originates from Vrisaki Park (underlined on the map).

Objectives

The primary objective of this work is to enhance the study of the palaeobotanical record of the Petrified Forest through the documentation and taxonomic determination of leaf macro-remains from the new fossil sites along the Kalloni-Sigri road which traverses the Akrocheiras hill range (Fig. 1). In this context, several leaf macro-remains from Vrisaki fossiliferous locality have been examined, described and determined. Additionally, the palaeoecological signals of the plant taxa have been assessed to reconstruct the environmental conditions that prevailed during the Early Miocene.

Material and Methods

The studied material consists 500 fossiliferous slabs comprising over 6930 leaves and a small number of reproductive organs. These remains have been preserved within different fine- to coarse-grained tuff layers, occurring both as leaf litter accumulated in the fine tuff layers, and as scattered leaves intermixed with pyroclastic material. The slabs were collected, conserved and cataloged by the research and technical team of the Natural History Museum of the Lesvos Petrified Forest (Zouros et al., 2022). The fossils were evaluated, with the majority of the material examined under an OPTIKA SLX-5 stereomicroscope. The taxonomic determination was conducted following the manual of leaf architecture with a focus on the key macro-morphological features of the fossils, including margin type, apex and base shapes, as well as venation architecture (Ellis et al., 2009).

Preliminary Results

To date, the palaeoflora of Vrisaki consists of at least one bryophyte, three ferns and more than 50 different angiosperm taxa, 21 of which are determined at a high taxonomic rank (family, genus and/or species). The determined taxa based on foliage include Bryophyta gen. et sp. indet., Thelypteridaceae gen. et sp. indet., aff. *Rumohra recentior* (Unger) Barthel, *Daphnogene polymorpha* (A. Braun) Ettingshausen, *Laurophyllum* sp. 1, *Laurophyllum* sp. 2, *Smilax weberi* P.Wessel, *Phoenicites* sp., *Calamus* sp., Zingiberaceae gen. et sp. indet., aff. Zingiberales, Fagaceae gen. et sp. indet. 1, Fagaceae gen. et sp. indet. 2, Juglandaceae gen. et sp. indet., *Alnus* vel *Rubus*, *Rubus* sp., aff. *Celtis japeti* Unger, *Populus* sp., *Nerium* sp., *Myrtophyllum* sp., and *Pungiphyllum cruciatum* (A. Braun) Frankenhäuser & V. Wilde. Additionally, the leaf material has been grouped into several distinct morphotypes, each requiring further investigation for a more detailed classification (Fig. 4, 4.4–4.7). Based on reproductive organs, the flora includes a solely infructescence of *Alnus* ?*kefersteinii* (Göppert) Unger, winged fruits of *Acer* sp. and cf. *Acer* sp., and a few buds probably of lauraceous affinity. Different representative plant taxa of the studied area are illustrated in Figures 2–4, underscoring the floral diversity of Vrisaki.

Discussion

The enormous quantities of leaf macro-remains and the numerous petrified tree trunks preserved in various fossiliferous localities within the pyroclastic rocks of the Lesvos Petrified Forest provides a great opportunity to decipher the Early Miocene subtropical history of the island. This ongoing research focuses on the documentation and systematic taxonomy of the abundant leaf material from the fossiliferous locality of Vrisaki. So far, more than 54 plant taxa have been documented and analyzed based on their macro-morphological characteristics. The palaeoflora of the Vrisaki fossiliferous locality represents a diverse array of vegetation types, ranging from riparian habitats to lowland and upland mesophytic forest regions. The determined taxa are linked to one or more vegetation units, reflecting the ecological diversity and complexity of the palaeoenvironment. Evidence of a riparian plant association is suggested by taxa such as aff. *Rumohra recentior*, *Daphnogene polymorpha*, *Phoenicites* sp., *Alnus* ?*kefersteinii*, *Alnus* vel *Rubus*, *Populus* sp. and possibly *Pungiphyllum cruciatum*. The occurrence of members of the Lauraceae and Fagaceae families, Juglandaceae gen. et sp. indet., aff. *Celtis japeti* and *Nerium* sp. is indicative of well-drained forests. Herbaceous monocots, including members of Zingiberales, were likely adapted to the shaded understory beneath the forest canopy of the riparian or well-drained forests. In addition, lianas such as *Smilax weberi* and *Calamus* sp. may have been part of riparian or well-drained forests, suggesting a forest structure with multiple layers. The preliminary results from the systematic taxonomy of the Vrisaki fossiliferous locality reveal sufficient floristic similarities with the West Akrocheiras fossiliferous locality from the Akrocheiras hill (Kafetzidou et al., 2022; Tsitsou et al., 2022; Liapi et al., 2022, 2023). Both palaeofloras share plant taxa such as Thelypteridaceae gen. et sp. indet., *Daphnogene polymorpha*, *Laurophyllum* sp. 1, *Smilax weberi, Phoenicites* sp., *Calamus* sp., Zingiberaceae gen. et sp. indet., Fagaceae gen. et sp. indet. 1, *Rubus* sp., aff. *Celtis japeti*, *Populus* sp., *Acer* sp., *Nerium* sp., *Myrtophyllum* sp., and *Pungiphyllum cruciatum*. Notably, the Vrisaki palaeoflora appears to exhibit a greater diversity based on fruit remains, including *Alnus* ?*kefersteinii*, *Acer* sp. and cf. *Acer*.

Despite the progress that has been made in recent years, further investigation is required as several morphotypes still remain under study. The systematic taxonomy of the plant macro-remains from Akrocheiras hill poses challenges due to the extensive abundance of collected specimens and the overlapping morphological features exhibited by certain leaf types. Completing the systematic classification in the future will provide a more comprehensive floristic knowledge and offer valuable insights into the palaeoenvironmental history of the Early Miocene of Lesvos.

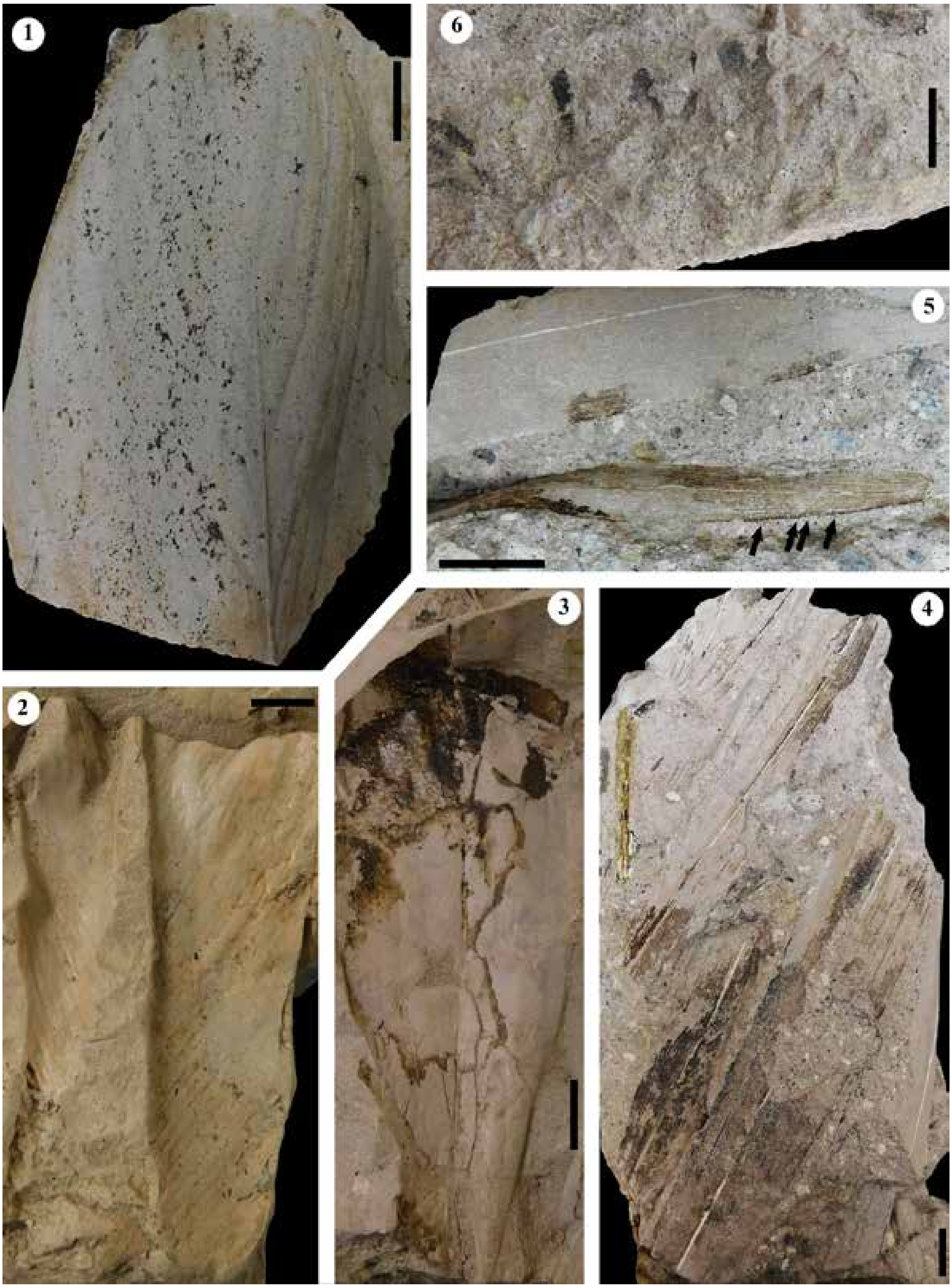

Figure 2. Characteristic plant taxa from the Vrisaki fossiliferous locality of the Lesvos Petrified Forest: 1. aff. Zingiberaceae gen. et sp. indet., leaf, BPΦ1805; 2. aff. Zingiberaceae gen. et sp. indet., leaf, BPΦ2371; 3. Monocotyledoneae fam. gen. et sp. indet. (aff. Zingiberales) leaf, BPΦ467; 4–5. *Calamus* sp., leaf, BPΦ1814, 4. Two leaflets attached to a rachis at the top of the figure, 5. Close up of the leaflets where the black arrows show the distinctive spines in the margin; 6. Bryophyta gen. et sp. indet., thallus, BPΦ2130.
Scale bars equal 2 cm (1, 3, 4–5) and 1 cm (2, 6).

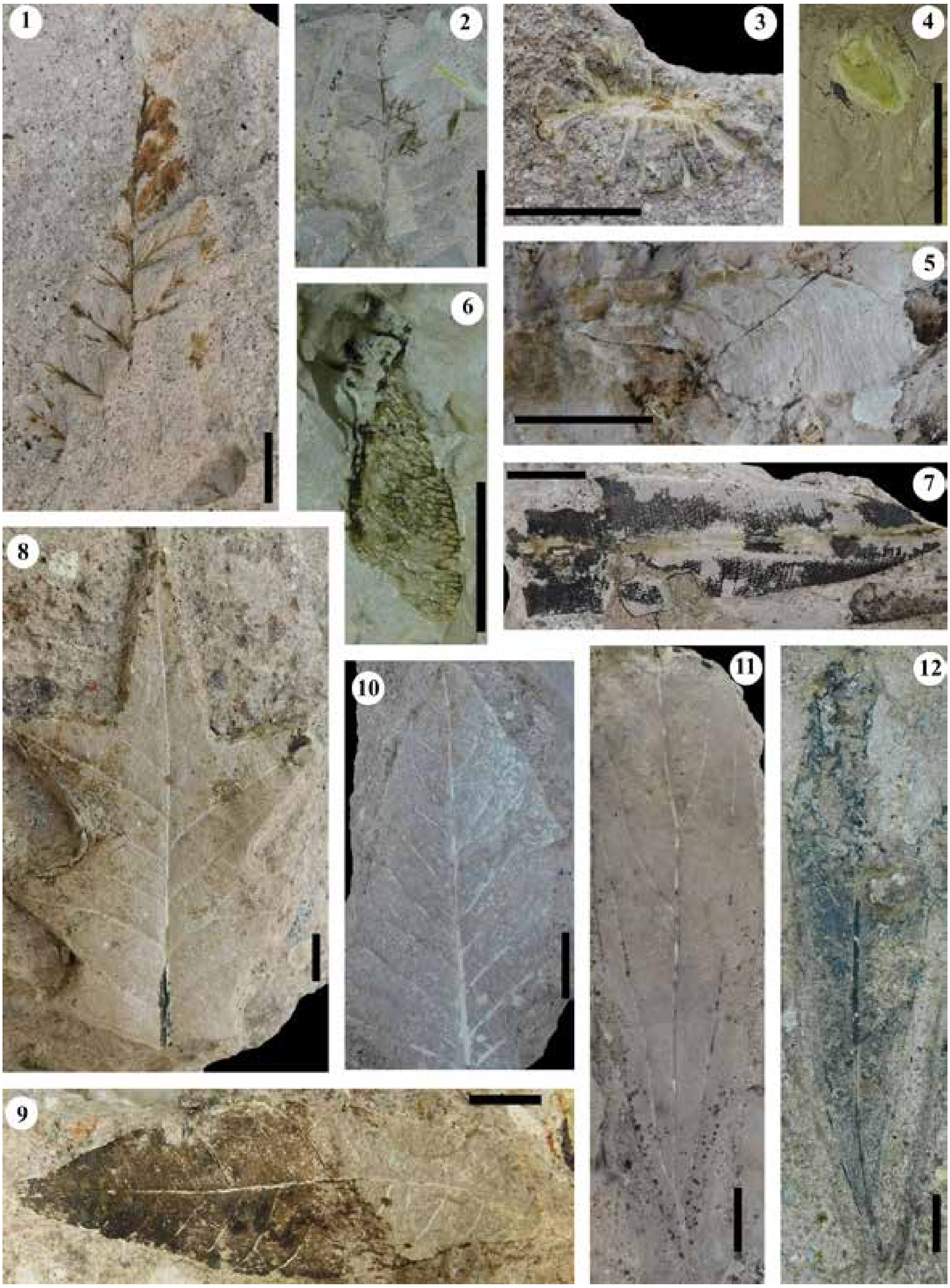

Figure 3. Characteristic plant taxa from the Vrisaki fossiliferous locality of the Lesvos Petrified Forest: 1. aff. *Rumohra recentior*, frond, ΒΡΦ880; 2. Thelypteridaceae gen. et sp. indet., frond, ΒΡΦ317; 3. *Alnus ?kefersteinii*, infructescense, ΒΡΦ1805; 4–5. *Acer* sp., winged fruits, ΒΡΦ1739, 4. Preserved nutlet, 5. Samara; 6. cf. *Acer* sp., winged fruit, ΒΡΦ763; 7. *Nerium* sp., leaf, ΒΡΦ823; 8. *Pungiphyllum cruciatum*, leaf, ΒΡΦ2461A; 9. Fagaceae gen. et sp. indet. 1, leaf, ΒΡΦ2099; 10. Fagaceae gen. et sp. indet. 2, leaf, ΒΡΦ1070; 11. *Daphnogene polymorpha*, leaf, ΒΡΦ2394; 12. *Laurophyllum* sp. 1, leaf, ΒΡΦ349.
Scale bars equal 1 cm.

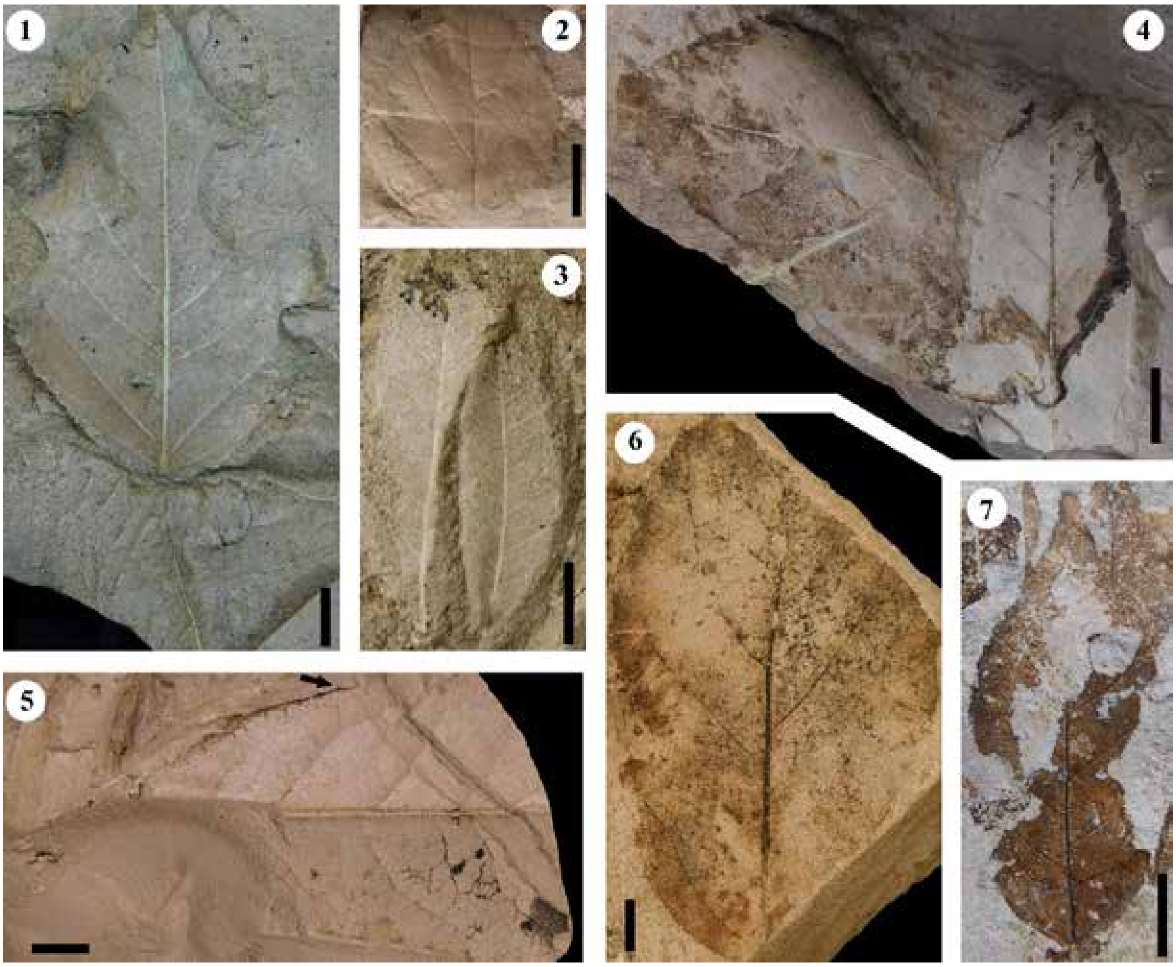

Figure 4. Diverse plant taxa from the Vrisaki fossiliferous locality of the Lesvos Petrified Forest: 1. *Populus* sp., leaf, ΒΡΦ915; 2. *Rubus* sp., leaf, ΒΡΦ2371; 3. *Myrtophyllum* sp., leaf, ΒΡΦ469; 4–7. Dicotyledonous angiosperms of unknown systematic affinity, 4. Leaves, ΒΡΦ1915; 5. Leaf (black arrow indicates the small glandular teeth), ΒΡΦ758; 6. Leaf, ΒΡΦ2199; 7. Leaf, ΒΡΦ1890.
Scale bars equal 1 cm.

Acknowledgments
The authors would like to express appreciation to the research and technical team of the Natural History Museum of the Lesvos Petrified Forest for their contribution and support to the current palaeobotanical research.

References

Ellis, B., Daly, D.C., Hickey, L.J., Johnson, K.R., Mitchell, J.D., Wilf, P., Wing, S.L., 2009. Manual of Leaf Architecture. Cornell University Press, New York.

Iamandei, S., Iamandei, E., Velitzelos, D., Velitzelos, E., 2022. Palaeoxylotomical studies in the Cenozoic petrified forests of Greece. Part two – conifers. Acta Palaeontologica Romaniae 18 (1), 65–111.

Iamandei, S., Iamandei, E., Velitzelos, D., Velitzelos, E., 2024. Palaeoxylotomical studies in the Cenozoic petrified forests of Greece. Part three – dicots. Acta Palaeontologica Romaniae 20 (2), 61–96.

Kafetzidou, A., Kouli, K., Zidianakis, G., Kostopoulos, D., Zouros, N., 2022. The early Miocene angiosperm flora of Akrocheiras in Lesvos Petrified Forest (North Aegean, Greece) – Preliminary results. Review of Palaeobotany and Palynology 296, 104559.

Liapi, E., Zidianakis, G., Tsitsou, E., Iliopoulos, G., Zouros, N., 2022. New floristic data of the Early Miocene Lesvos Petrified Forest − Part A: Non-vascular plants, ferns and monocots from the West Akrocheiras outcrop. Bulletin of Geological Society of Greece Sp. Publ. 10, 64–65.

Liapi, E., Tsitsou, E., Iliopoulos, G., Zouros, N., 2023. Taxonomic investigations of the West Akrocheiras plant assemblage of the Lesvos Petrified Forest. 8th Agora Paleobotanica Meeting, abstracts volume, Belver de Cerdanya, pp. 39–40.

Liapi, E., Iliopoulos, G., Zouros, N., 2024. Documenting the leaf flora of a new fossiliferous locality from the Lesvos Petrified

Forest. Folia Musei Rerum Naturalium Bohemiae Occidentalis - Geologica et Paleobiologica 58 (1), 29–33.

Tsitsou, E., Zidianakis, G., Liapi, E., Iliopoulos, G., Zouros, N., 2022. New floristic data of the Early Miocene Lesvos Petrified Forest − Part B: Dicotyledon taxa from the West Akrocheiras outcrop. Bulletin of Geological Society of Greece Sp. Publ. 10, 66–67.

Velitzelos, D., Iamandei, S., Iamandei, E., Velitzelos, E., 2019. Palaeoxylotomical studies in the Cenozoic petrified forests of Greece. Part one – palms. Acta Palaeobotanica 59 (2), 289–350.

Zhu, Y.B., Li, Y., Zhang, J.P., Wang, Y.D., Zouros, N., 2024. A new species of *Pseudotsuga* (Pinaceae) from the lower Miocene of Lesvos, Greece, and its palaeogeographical and palaeoclimatic implications, Palaeoworld 34, 100852.

Zouros, N.C., 2021. The Miocene petrified forest of Lesvos, Greece: Research and geoconservation activities. Geoconservation Research. 4 (2), 635–649.

Zouros, N., Soulakellis, N., Valiakos, I., Bentana, K., Theodorou, E., Zgournios, E., Antonakis, E., Lamprakopoulos, A., 2022. Enhancement and promotion of the new fossiliferous sites along the new Kalloni Sigri road–An example of good practice of geoconservation in Lesvos Island UNESCO Global Geopark Greece. Bulletin of Geological Society of Greece Sp. Publ. 10, 849–850.

17th INTERNATIONAL CONGRESS
of the Geological Society of Greece

BULLETIN OF THE GEOLOGICAL
SOCIETY OF GREECE, SP. PUBL.

EXTENDED ABSTRACT 195

Preliminary results of the fluid geochemistry surveillance campaigns on Santorini island (Greece) after the 2025 Anydros seismic sequence

Liuzzo M.[1], Federico C.[1], Grassa F.[1], Kanellopoulos Ch.[2], Kyriakopoulos K.[1,3], Lalechos S.[4], Manousaki M.[4], Nisi B.[5], Tamburello G.[6], Tassi F.[5,7], Vaselli O.[5,7], Vougioukalakis G.[2], Paonita A.[1], Bianco F.[8], D'Alessandro W.[1]

(1) Istituto Nazionale di Geofisica e Vulcanologia, Palermo, Italy, marco.liuzzo@ingv.it; walter.dalessandro@ingv.it (2) Hellenic Survey of Geology and Mineral Exploration, Acharnae, Greece (3) National and Kapodistrian University of Athens, Athens, Greece (4) Earthquake Planning & Protection Organization of Greece, Athens, Greece (5) Consiglio Nazionale delle Ricerche (IGG), Italy (6) Istituto Nazionale di Geofisica e Vulcanologia, Bologna, Italy (7) University of Florence, Florence, Italy (8) Istituto Nazionale di Geofisica e Vulcanologia, Naples, Italy

Recent seismic activity in the Santorini region has attracted global attention and raised concerns about ongoing volcanic hazards. Santorini, a large volcanic caldera featuring the central islets of Nea Kameni and Palea Kameni, has a complex eruptive history spanning approximately 650,000 years, including the catastrophic eruption (~1560 B.C.) linked to the decline of the Minoan civilization. Since 27 January 2025, the region has experienced a major seismic crisis, with over 2,000 earthquakes recorded, including 14 events with magnitudes ≥5.0 and a maximum magnitude of 5.3. Seismicity has been concentrated approximately 25 km northeast of Santorini and 25 km southwest of Amorgos.

We present the results of two geochemical surveys conducted between March and April 2025, involving water sampling from 10 wells, measurements of soil CO_2 fluxes and d^{13}C-CO_2 values in Santorini and Nea Kameni, as well as sampling of fumarolic gases at Nea Kameni and bubbling gases at Palea Kameni. These data provide a preliminary assessment of the current degassing dynamics of the area. Comparison and integration with existing literature indicate that the post-seismic volcanic phase following the January–February 2025 seismic crisis is marked by an increased degassing rate in the Nea Kameni region. However, the chemical and isotopic compositions of the gases ($^3He/^4He$ and d^{13}C values) exhibit only minor variations relative to pre-crisis measurements reported in previous studies.

Although preliminary, these findings underscore the critical need for continuous monitoring of the Santorini volcanic system, in order to deliver timely and reliable information to the local community and to support effective volcanic risk mitigation strategies.

17th INTERNATIONAL CONGRESS
of the Geological Society of Greece

BULLETIN OF THE GEOLOGICAL
SOCIETY OF GREECE, SP. PUBL.

EXTENDED ABSTRACT 196

Automated Seismic signals' identification: A statistical criterion for decreasing the false alarm rate; Implementation on synthetic data.

Lois A.[1], Giannopoulos D.[1], Sokos E.[1]
(1) University of Patras, Department of Geology, Patras, Greece, lois@upatras.gr

Abstract

Algorithms dealing with the problem of the identification of micro-earthquakes constitute a topic of ongoing research. The development of methodologies dealing with the specific problem has gained considerable attention during the last decades in the context of research, appearing at the same time to be the central issue in various application areas. The extraction and efficient analysis of the useful information from continuous recordings are of great importance, since it is a prerequisite for reliable interpretations. Nevertheless, such processes usually suffer from a number of false alarms, which tends to be significantly increased in extremely noisy environments. In this paper, we propose a "decision-making" scenario to be applied on the extracted intervals, for the purpose of decreasing the probability of false alarms. The specific statistical criterion can be implemented regardless of the detection algorithm that has been applied for the identification of the seismic events and its efficiency is confirmed by its application on a series of experiments on synthetic data.

Introduction

The most widely used algorithms, mainly due to their simplicity and the low computational resources that they demand, are the energy-based algorithms, which are also referred to in the literature as STA/LTA detectors. In its simplest form, the STA/LTA algorithm processes the initial recordings, or some characteristic function derived from raw data, using two moving windows and compares their absolute values' ratio to a user-defined threshold value, to declare a seismic event. This idea was firstly adopted by Allen (1978), who applied energy criteria on the characteristic function that resulted from the signal's positive envelope. Baer & Kradolfer (1987) proposed a modified and improved version of Allen's method, aiming in overcoming specific drawbacks that characterize the latter, which are mainly associated to the user-defined parameters of the technique, such as the selection of the appropriate characteristic function, as well as the threshold value, in order to increase the detection rate. Another class of techniques that are commonly used for the solution of the seismic event detection problem, as well as the picking of phase arrivals are the methodologies which utilize autoregressive modeling along with the Akaike Information Criterion (AIC) (Leonard & Kennett 1999). The basic assumption constituting the base of these algorithms is that the seismic recordings can be segmented into locally stationary parts, which can be described by autoregressive models of different orders. This property can be used as a diagnostic tool to discriminate useful information from the background noise. Moreover, several methodologies based on classical statistical concepts, such as the maximum likelihood, hypothesis testing scenarios, higher order statistics etc., were introduced as possible solutions for the signal identification problem. Since the statistical properties of seismic noise are not easily predictable, as it is widely reported (Arrowsmith et al. 2008) Lois et al. (2013, 2019) proposed the solution of the problem under examination, using a thresholding type technique, which is applied under a non–strict hypothesis testing framework. Higher order statistics (HOS) also constitute an important tool that has been exploited by geoscientists, during the last two decades, for the purpose of solving the event detection problem, as well as the accurate estimation of the phase arrival times (Saragiotis et al. 2002). Apart from the above-mentioned techniques, which mainly rely on classical seismic signal analysis applied on either 1C or 3C data, there are also more sophisticated approaches that are referred to in the literature, using artificial neural networks (Mousavi et al. 2018), machine learning (Chen 2018), fuzzy logic theory (Chu & Mendel 1994), etc. Nevertheless, it is obvious that the above-listed methodologies are affected by several factors, such as the source type, the instrument response, the noise level of the study area, the epicentral distance of the recorded events etc. Thus, the development of robust algorithms that provide stable results for general situations is of vital importance. In this study we propose a statistical criterion serving as an "outcome control" process, adopted to refine the initial outcome acquired by any detection algorithm.

Methodology

Once the extraction of the segments of the seismic record is achieved (using any of the well-known detection algorithms), the main effort of the proposed methodology is focused in performing the implementation of a mechanism capable to control the results by retaining the useful, for our analysis, information and eliminating the intervals corresponding to false alarms. In that scope, pure seismic noise is initially isolated, using energy criteria, and, thereafter, we introduce a "decision-making" criterion, based on the comparison among autoregressive models estimated on the isolated seismic noise, as well as the detected segments resulting from the application of the detection algorithm.

Let us consider that $\mathfrak{B}$ is a set containing *I* blocks $\boldsymbol{b}_i$of length *L* that have been drawn independently and with replacement from the initial stationary record $\mathbf{z}_n$, corresponding to the vertical component, that is:

$$\mathfrak{B} = \{\boldsymbol{b}_1, \boldsymbol{b}_2, \dots, \boldsymbol{b}_I\},\ \boldsymbol{b}_i = [z_i, z_{i+1}, \dots, z_{i+L-1}], i \in [1, N-L+1]. \quad (1)$$

It is clear that the *i*–th element $\boldsymbol{b}_i$of the set $\mathfrak{B}$ is a block of length *L* consisting of consecutive samples, with its starting index *i* being a uniformly distributed discrete random variable ensuring equiprobable selection of each *L*-length block from the available $N-L+1$ that are contained in the initial record $\mathbf{z}_n$ (Lois et al 2013). Apparently, $\mathfrak{B}$ can also be formulated as a $I \times L$ matrix, having in its *i*–th row the block $\boldsymbol{b}_i$.

Having formed the set $\mathfrak{B}$ by applying the previously mentioned sampling procedure, the goal now is to identify blocks consisting solely of noise samples. This constitutes a clustering problem that can be addressed using various approaches. For instance, Lois et al. (2013) proposed the application of a modified "k-median" algorithm that exploits as input autoregressive models estimated on blocks $\boldsymbol{b}_i$, instead of the blocks themselves, in order to reduce the dimensionality of the problem. Following the specific approach, a robust separation among "noise" and "signal" models is achieved, but in general high computational resources are demanded, due to the modeling procedures that have to be applied on each block that is selected during the sampling process. In this work, a simple energy-based procedure is applied in order to establish the desirable isolation of the noise blocks. In general, given a stationary recording, samples forming a noise block are expected to be characterized by insignificant fluctuations in amplitude, thus resulting in low values of the block's variation. On the other hand, the presence of a seismic signal or part of it in a block causes an increase in the block's variation, due to high fluctuations among the samples within the block. Therefore, the selection of the desirable intervals is based on the comparison of their standard deviations to a predefined value.

More particularly, assuming that $\mathcal{S}$ is a set including the standard deviations of the blocks $\boldsymbol{b}_i\boldsymbol{b}_i$:

$$\mathcal{S} = \{\sigma(\boldsymbol{b}_i)\}_{i \in [1,I]} = [\sigma(\boldsymbol{b}_1), \sigma(\boldsymbol{b}_2), \dots, \sigma(\boldsymbol{b}_I)], \quad (2)$$

the desirable set $\mathfrak{B}_{noise} \subseteq \mathfrak{B}$, containing the noise blocks is selected using the following relation:

$$\mathfrak{B}_{noise} = \{\boldsymbol{b}_i \in \mathfrak{B}; \sigma(\boldsymbol{b}_i) \leq median(\mathcal{S})\} \quad (3)$$

It is apparent that since the median value of the set $\mathcal{S}$ constitutes the "middle observation" of its sorted values, the latter can equally be formulated as an $\frac{I}{2} \times L$ or $\left(\frac{I}{2} + 1\right) \times L$ matrix, depending on whether *L* is an odd or an even number. What we need now is to calculate a time series, representative of the noise characteristics of the given recording, in order to use it as a "reference vector" for the next step of our analysis. In that scope, we calculate and denote as $\bar{\boldsymbol{b}}_n\bar{\boldsymbol{b}}_n$ the average of the noise blocks, calculated column-wise, such as:

$$\bar{\boldsymbol{b}}_n = \left[\frac{1}{r}\sum_{j=1}^{r}\mathfrak{B}_{noise}^{j}(1), \frac{1}{r}\sum_{j=1}^{r}\mathfrak{B}_{noise}^{j}(2), \dots, \frac{1}{r}\sum_{j=1}^{r}\mathfrak{B}_{noise}^{j}(L)\right] \quad (3)$$

where the first element of the reference vector is the average of the first column of matrix $\mathfrak{B}_{noise}$, the second element is the average of the second one etc. and *r* equals to $\frac{I}{2} \times L$ or $\left(\frac{I}{2} + 1\right) \times L$, depending on whether *L* is an odd or an even number, as it has already been mentioned. Index jj refers to each selected noise block that fulfils eq. (2).

Since the "average" noise block has been isolated using the above-mentioned energy-based procedure, our goal is to estimate the stochastic models that best describe both the noise and the "candidate" seismic signals. These models will be the tools that will permit the elimination of any "false" information that may have been included in the initial results. To this end, we apply autoregressive (AR) modeling procedures to the specific time series, selecting the optimal model orders by using the corrected Akaike Information Criterion (*AICc*). In general, the *AICc* for finite sample sizes and for a model order *P* is defined as follows:

$$AICc = 2P - 2\ln\{l(\theta^*)\} + \frac{2P(P+1)}{L-P-1} \quad (4)$$

where $l(\theta^*)l(\theta^*)$ is the achieved maximum of the likelihood function $l(\theta)$ and θ^* is the maximum likelihood parameter estimator of length *P*, resulting from the solution of the following optimization problem:

$$\theta^* = arg \max_{\theta}\{l(\theta)\} \quad (5)$$

Moreover, it is known that *AIC* (so *AICc*) provides a means of model selection by estimating the amount of information that is lost by a given model. Hence, the less information a model loses, the higher the quality of that model is. Therefore, given a set of models, the optimum model is the one corresponding to the minimum value of the *AICc*, so if $P_i, P_i \in \mathbb{P} \subseteq \mathbb{N}$ are the candidate AR model orders, then the optimum order *P* is estimated by:

$$P = arg \min_{P_i \in \mathbb{P}} \{AICc(P_i)\} \quad (6)$$

Now, we can formulate the average PP-order noise model $\bar{m}_n\bar{m}_n$ which is described as follows:

$$\bar{x}_t = c + \sum_{j=1}^{P} \varphi_j \bar{x}_{t-j} + \varepsilon_t, \quad \varepsilon_t \sim N(0, \sigma_\varepsilon^2) \quad (7)$$

where c is a constant value, φ_j are the parameters of the model and ε_t is white noise with zero mean value and variation equal to σ_ε^2.

Furthermore, assuming that the algorithm has detected *k* segments in the initial recording, we derive in the same way *k* AR(Q_i) models, where the *i*-th model m_i of order Q_i is given by:

$$x_t^i = c^i + \sum_{j=1}^{Q_i} \theta_j^i x_{t-j}^i + \varepsilon_t^i, \quad \varepsilon_t^i \sim N\left(0, \sigma_{\varepsilon^i}^2\right) \quad (8)$$

where c^i is a constant value, θ_j^i are the parameters of each model m_i and ε_t^i is again a process of white noise with zero mean and variation equal to $\sigma_{\varepsilon^i}^2$. Apparently, the model orders Q_i are also computed using the *AICc*. The remaining step, in order to complete the presentation of the proposed algorithm, is a “Decision-Making” criterion which will allow controlling the outcome of detection algorithm, thus ensuring the best possible final result. The general idea lies on the fact that, given the AR models describing the average noise block, as well as the detected intervals from the initial record, we can conclude on the “nature” of each candidate segment by examining whether it converges to the estimated noise model or not. Here, the concept of convergence implies the notion of the distance among these models. In other words, in an ideal case, a model describing a detected segment, which is close to the estimated noise model, is more likely to correspond to a false detection, than to a seismic signal. Alternatively, a model that deviates sufficiently from the noise model probably corresponds to a microseismic event or to any other signal with dynamical characteristics that differ from the characteristics of the background noise. The main question arising from the proposed approach concerns the measure of similarity or the appropriate criterion that must be adopted in order to conclude to secure results. For example, Picolo (2010) proposed the autoregressive metric for comparing time series models, by introducing the Euclidean distance between the coefficients of their AR formulations. Even though the specific distance is a well-defined measure of structural dissimilarity between two stochastic models, its implementation to models associated with passive seismic data leads to unstable conclusions, especially in extremely noisy environments.

Taking into consideration the fact that changes in both the order and the values of the AR coefficients are diagnostic of the differences between noise and signal (Leonard & Kennett 1999), we propose the following scenario in order to decide about the “nature” of the detected intervals under investigation:

$$(P \leq Q_i) \cap \left(\sigma(|\boldsymbol{\varphi}|) < \sigma\left(|\boldsymbol{\theta}^i|\right)\right), \forall\, i \epsilon [1, k], k \epsilon \mathbb{Z} \quad (9)$$

where $\sigma(.)$ refers to the standard deviation of the quantities $\boldsymbol{\varphi} = [\varphi_1, \varphi_2, \dots, \varphi_P]$, which is the vector containing the coefficients of the noise model, and $\boldsymbol{\theta}^i = [\theta_1^i, \theta_2^i, \dots, \theta_{Q_i}^i]$ is the respective vector corresponding to the *i*–th detected interval.

Experimental Results

The simulations with synthetic data were performed using two different noise process scenarios. To this end, two first-order AR processes were utilized (denoted by AR1 and AR2 respectively) with poles of different magnitude, in order to simulate, as realistically as possible, a “normal” case (pole magnitude = 0.73), as well as an extreme case (pole magnitude = 0.9), where the assumption of stationarity almost fails. For each of the two noise process scenarios, 500 records of synthetic seismic data were constructed (each having a duration of 10 min and a sampling rate of 100 Hz), containing a total number of 2500 events. More specifically, to construct each data record, we initially created the noise process, using the above-mentioned AR processes, and then 5 synthetic seismic events, with the desired SNR in the range [-5, 5] dB, were superimposed. The SNR was estimated using a window of 100 samples (1s) in the vicinity of the first arrival of each seismic event. Moreover, the seismic events were created according to Lois et al. (2013). Initially, a window of white Gaussian noise was low-pass filtered and the resulting sequence was multiplied by a half-Gaussian window of the same length, for the purpose of simulating the exponential decay (attenuation) of the signal’s amplitude. Then, the vector representing the seismic signal was multiplied by a constant gain, in order to control the SNR in the desirable range. The detected segments were acquired using an improved 3C version of the well-known STA/LTA algorithm (STA/LTA$_{3C}$). According to the classical approach (STA/LTA), the ratio between a short-term average (STA) and a long-term average (LTA) window is usually calculated using data from the vertical component. In our experiments (STA/LTA$_{3C}$), in order to increase the SNR of the ratio function and, consequently, its capability to detect small-magnitude events, we exploit information from all three components of the recorded signal, using their L_2–norm, that is:

$$f_i^{sl} = \sum_{i=1}^{N}\left(\sqrt{z_i^2 + x_i^2 + y_i^2}\right) \quad (10)$$

where z_i corresponds to the vertical component, while x_i and y_i to the East-West and North-South horizontal components, respectively. The results regarding the false alarm rate prior and after the application of the proposed statistical criterion is presented in table 1.

Table 1. False alarm rate prior and after the application of the proposed statistical criterion on synthetic data

False Alarm Rate	AR[1]		AR[2]	
SNR (dB)	Prior (%)	After (%)	Prior (%)	After (%)
-5	33.87	14.47	66	37.33
-2	15.13	8.07	52.63	28.97
0	7.92	1.96	25.15	16.79
2	4.03	0.86	13.35	7.38
5	0.39	0	6.74	2.03

1: Results from the application of the proposed "Decision Making" criterion on the two different noise process scenarios.

By inspecting the results presented in table 1, associated with both noise scenarios it becomes evident that the implementation of the proposed criterion significantly reduces the false alarm rate of the initial outcome derived by (any) detection algorithm. Regarding the first noise scenario and for noise levels down to 2 dB the results are acceptable even without the application of the "decision – making" scenario. But for extreme noise levels, corresponding to negative values of SNR the proposed technique provides a reduction of almost 50% to false detections. Moreover, for the second noise scenario where the useful information is buried to strongly correlated synthetic seismic noise, the attempt is focused on testing the performance of the method in cases where basic assumptions, such as the stationarity, almost fail. Nevertheless, and by considering the extremely noisy environment (-2 and -5 dB), the rate of false signal identifications reduced significantly, approaching again a reduction of 50%.

Conclusions

In this study, we introduce a statistical criterion which can be applied on the initial outcome obtained by the implementation of each well-known detection algorithm on seismic data. This "Decision-Making" scheme relies on stochastic modeling applied on both the detected intervals and a signal representative to the recorded seismic noise. Comparisons among the calculated models provide us an indication about the nature of the "candidate" seismic signals. The advantages of the proposed approach were confirmed through a series of experiments, using synthetic seismic data, providing a significant reduction of the false alarm rate even in extremely noise environments.

References

Allen, R. V., 1978. Automatic earthquake recognition and timing from single traces, Bull. seismol. Soc. Am.68, 1521–1532.

Arrowsmith, S. J., Whitaker, R., Taylor, S. R., Burlacu, R., Stump, B., Hedlin, M., Randall, G., Hayward, C. & ReVelle, D., 2008. Regional monitoring of infrasound events using multiple arrays: Application to Utah and Washington State, Geophys. J. Int., vol. 175(1), pp. 291–300, https://doi.org/10.1111/j.1365-246X.2008.03912.x.

Baer, M. & Kradolfer, U., 1987. An automatic phase picker for local and teleseismic events, Bull. seismol. Soc. Am., 77, 1437–1445.

Chen, Y., Hill, J. C., Lei, W., Lefebvre, M., Bozdag, E., Komatitsch, D. & Tromp, J., 2017. Automated time-window selection based on machine learning for full-waveform inversion, 87th Annual International Meeting, SEG, Expanded Abstracts, 1604-1609.

Chu, C. K., & Mendel, J., 1994. First break refraction event picking using fuzzy logic systems, IEEE T FUZZY SYST., 2, 255–266,doi: 10.1109/91.324805.

Lois, A. E., Psarakis, E. Z. & Pikoulis, E., 2013. A new thresholding type technique for the detection of seismic events, 21st European Signal Processing Conference (EUSIPCO 2013), Marrakech, 1-5.

Lois, A., Sokos, E., Martakis, N, Paraskevopoulos, P. & Tselentis, G.-A., 2013. A new automatic S-onset detection technique: Application in local earthquake data, Geophysics, 78, KS1–KS11.

Leonard, M. & Kennet, B. L. N., 1999. Multi-component autoregressive techniques for the analysis of seismograms, PHYS EARTH PLANET IN, 113, 247–263, doi: 10.1016/S0031-9201(99)00054-0.

Mousavi, S. M., Zhu, W., Sheng, Y., & Beroza, G. C., 2019. CRED: A Deep Residual Network of Convolutional and Recurrent Units for Earthquake Signal Detection, Sci. Rep., 9(1), doi:10.1038/s41598-019-45748-1.

Piccolo, D., 2010. The Autoregressive metric for comparing time series models, Statistica, Department of Statistics, University of Bologna, 70(4), 459-480.

Saragiotis, C., Hadjileontiadis, L. & Panas, S., 2002. Pai-S/K: A robust automatic seismic p phase arrival identification scheme, IEEE T GEOSCI REMOTE, 40(6), 1395–1404.

17th INTERNATIONAL CONGRESS
of the Geological Society of Greece

BULLETIN OF THE GEOLOGICAL SOCIETY OF GREECE, SP. PUBL.

EXTENDED ABSTRACT 197

Mapping the active Faults affecting Ionians Islands, Western Hellenic Arc

Loreto M.F.[1], Ferrante V. [1], Ligi M.[1], Muccini F.[2,3], Palmiotto C.[1], Petracchini L.[3], Romano S.[1], Ganas A.[4], Argnani A.[1], Conti A.[3], Cuffaro M.[3], Pensa A.[5], Kothri S.[6], Lampridou D.[6], Merino I.[7], Ranero R.C.[8,9] and Nomikou P.[6]

(1) CNR, Istituto di Scienze Marine (ISMAR), Bologna, Italy, mariafilomena.loreto@cnr.it
(2) Istituto Nazionale di Geofisica e Vulcanologia (INGV), Roma, Italy
(3) CNR, Istituto di Geologia Ambientale e Geoingegneria (IGAG), Roma, Italy
(4) Institute of Geodynamics - National Observatory of Athens (NOA), Greece
(5) Italian Institute for Environmental Protection and Research, Rome, Italy
(6) Department of Geography and Climatology - National and Kapodistrian University of Athens (NKUA), Greece
(7) Faculty of Geosciences, University of Bremen, Bremen, Germany
(8) Institució Catalana de Recerca i Estudis Avançats (ICREA), Barcelona, Spain
(9) Barcelona Center for Subsurface Imaging, ICM, CSIC, Barcelona, Spain

Introduction / Background

The area offshore the central Ionian Islands (Cephalonia, Lefkada, Zakynthos, and Ithaca), western Greece (Fig. 1A; 1B), is within the Mediterranean regions one with the highest seismic activity and tsunamigenic potential (Fig. 1C). Here, the Hellenic frontal thrust system stops against the right-lateral Cephalonia Transform Fault, a fault more than 100 km-long (Louvari et al. 1999), to step back towards Corfu (Sachpazi et al., 2000). In recent decades, this area experienced several destructive events, such as the 1953 Cephalonia earthquakes (three M6+ events) and the more recent the Mw 6.8 Zakynthos event occurred the 28 October 2018 (Ganas et al., 2020) and the swarm of moderate size events ranging from 5.3 to 5.7 occurred in 2006 (Papadimitriou et al. 2012). Although this area has a high exposure to geological risk, offshore remains little explored. In order to improve the knowledge on shallow deformation, fault geometry and on the hazard potential of tsunamigenic faults, we carried out two oceanographic cruises, in May 2022 (aboard of the R/V G. Dallaporta supported by the Italian National Research Council - CNR) and in June 2023 (aboard of the R/V L. Bassi from the National Institute of Oceanography and Applied Geophysics - OGS in the frame of the POSEIDON project supported by the Eurofleet+ Program). During these two cruises we collected a multidisciplinary and multiscale dataset composed of geophysical (e.g., bathymetry, multichannel seismic data, magnetometry) and geological data (gravity cores).

Results

The newly collected high-resolution multichannel seismic data (Fig. 1B), integrated with high-resolution swath bathymetry, allowed us to define the sediment deformation patterns at the intersection between the Cephalonia Fault and the thrust fronts of the Hellenic Arc. To south of Cephalonia, the high-resolution multichannel seismic profile highlights a series of small bulges with internal discontinuities close to small drops of the seafloor (Fig. 2) interpreted as reverse faults bounding positive flower structures dipping toward southeast. Amongst two well-imaged flower structures, a shallow layer of sediments is dislocated by E-verging thrusts forming reverse structures. More eastward, the Argostoli Ridge is bounded on its west side by a strike-slip fault with inverse component, interpreted as a west-verging transpressive fault. The ridge internally is affected by a series of minor compressive faults, as revealed by the dislocations of sedimentary layers L1 and L2, and by a series of minor normal faults related to gas escape that have generated a Giant Pockmark. Further south, the Cephalonia Fault still shows this transpressive character and the Argostoli Ridge looks bounded even on its east side by a strike-slip fault with inverse component (Fig. 3).

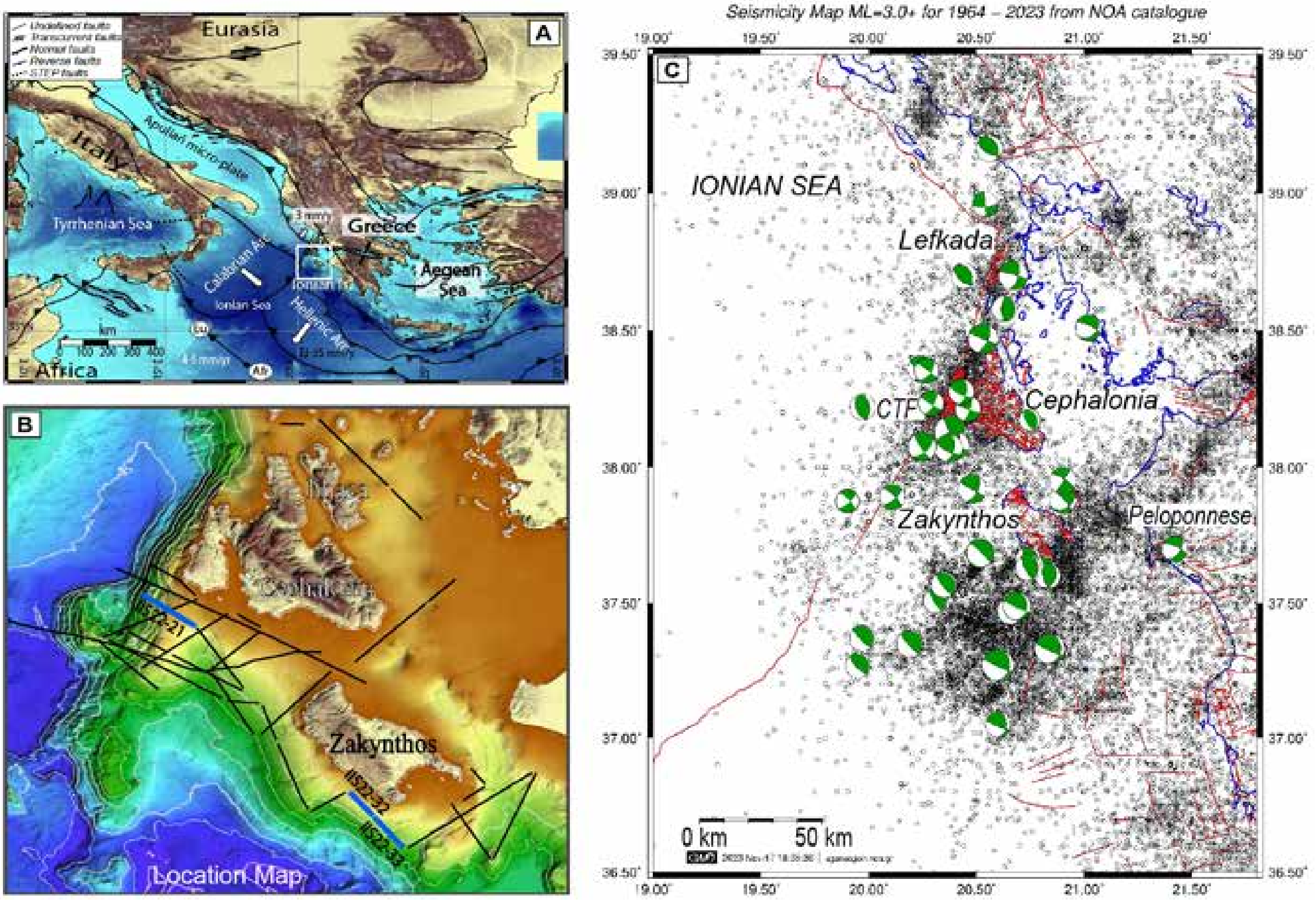

Figure 1. A) Tectonic map of the central Mediterranean showing location of the study area (white box). Mediterranean structural sketch modified after an online Tectonic Map (Woudloper - Own work, CC BY-SA 1.0) and by Loreto et al., (2021). B) Relief map of the study area. It shows the dataset collected during the IONIANS2022 survey. The multichannel seismic profiles shown in this abstract are pointed out with thick blue lines. Bathymetry data were downloaded from EMODnet portal (https://emodnet.ec.europa.eu/en/bathymetry#bathymetry-approach) and gridded using GMT software (Wessel et al., 2019). Inset (upper right): GPS velocity vectors map from https://www.unavco.org/. C) Map showing the distribution of the instrumental seismicity (black dots) with focal mechanisms (beachballs; events with 5.5 ≤ M ≤ 6.8; period 1959 - 2022). Green beachballs are focal mechanisms downloaded from the Global Centroid Moment Tensor database (www.globalcmt.org). Seismicity data collected from 1964 to 2023 by the NOA Institute of Geodynamics (only events with local magnitude M≥3 are shown; https://www.gein.noa.gr/en/services-products/earthquake-catalogs/). Faults are after Ganas et al. (2013, 2018). Map projection is geographic, Datum WGS84.

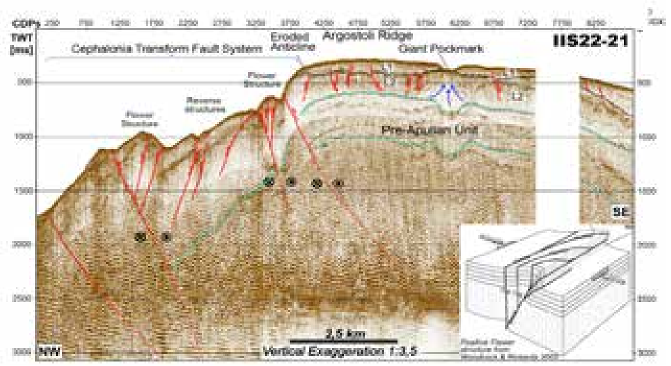

Figure 2. High-resolution multichannel seismic profiles crossing IIS22-21 the Cephalonia Transform Fault system. Faults are marked with red lines, while the kinematics (normal, reverse) are inferred by arrows direction. Blue lines mark the multiple signals. Black lines bound two sedimentary units. A sketch of a strike-slip fault with compressive component modified by Woodcock & Rickards (2003) has been included.

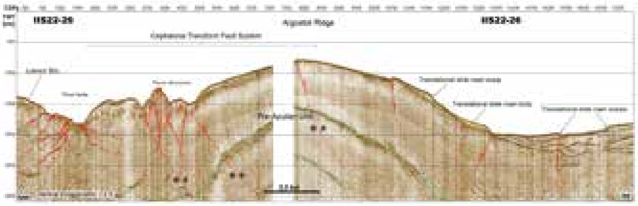

Figure 3. High-resolution multichannel seismic profiles crossing IIS22-26 the Cephalonia Transform Fault system further south of Cephalonia Isl. Faults are marked with red lines, while the kinematics is inferred by arrows direction. Light blue lines mark multiple signals.

South of Zakynthos, the deformation setting changes with respect to the CTF system zone. Here a well-stratified shallow unit, likely of Plio-Quaternary age, overlies a unit internally low reflective facies; we interpreted belonging to the Pre-Apulian unit (Fig. 4). The sedimentary unit is cut by widespread SE and NW dipping faults with extensional kinematics. Some of these faults affect the stratified unit and part of the underlaying Pre-Apulian Unit. These faults frequently reach the seafloor forming small steps. A series of sedimentary unconformities and a deep graben filled by sediments have been mapped in the surroundings of this gentle anticline. This complex setting suggests that there is a strong interplay between tectonics and sedimentary processes.

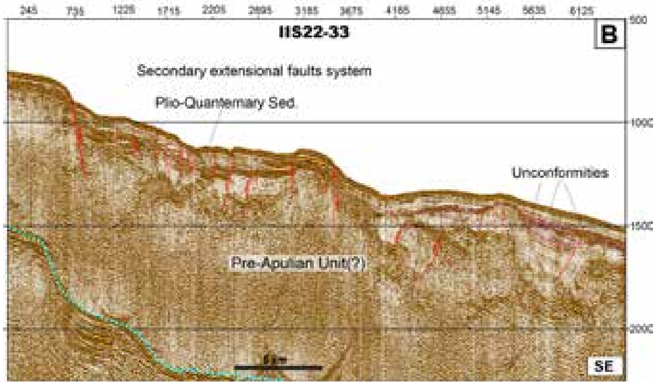

Figure 4. High-resolution multichannel seismic profiles IIS22-33 crossing the slope offshore Zakynthos. Faults are marked with red lines, while the kinematics is inferred by arrows direction. Light blue lines mark the multiple signals.

Discussion

The morphotectonic setting of the CTF fault system results show more complexity than previously mapped (Fig. 2, 3 4). Shallow sediment deformation in the central sector of the CTF system is controlled by a series of strike-slip faults with a compressive component, locally expressed by positive flower structures, generally E-dipping. The Cephalonia fault system splays into several branches, similar to a compressive strike-slip duplex (Woodcock and Fischer, 1986), and changes size passing from ~6 km (Fig. 1B), to west of Cephalonia Is., to 25 km-wide in the southern part. Our new findings completely change the previous published interpretation of the geometry of CTF system, inferred only from seismological data and modelling (Louvari et al., 1999; Papadimitriou et al., 2021). Given that the single fault "widens" into a fault system, the overall slip rate (~17 mm/yr; Tsironi et al. 2024) is partitioned, which might decrease the earthquake magnitude over several active faults and increases the distribution of events over a large area, as inferred from recorded seismicity (Fig. 2 and Fig. 4 in Kassaras et al., 2016). This new fault anatomy, with a multi-segment geometry, should have an effect over the seismological models proposed in the future for the CTF system. Southwest of Zakynthos, a series of normal faults dissecting the shallow marine sediments SE-ward (Fig. 4) indicate that this area is dominated by extensional stress. However, this area has been struck during last decades by several earthquakes, most of which with thrust mechanisms (Figs. 1c and 2a; Kassaras et al., 2016). Combining MCS data (Fig. 4) with swath bathymetry (fig. 1B) and seismological data (Fig. 1C) and considering the orientation of faults with respect to the morphologic features of the area (Fig. 4), we interpret these extensional structures as a secondary system that is able also to trigger earthquakes. This idea is also supported by some focal mechanisms with extensional kinematics recorded on-land (see Figs. 4 and 7 in Kassaras et al., 2016). This extensional secondary system may accommodate deformation induced by a deep compressive fault system, whose orientation remains still to be determined, or may result by a local extensional stress field controlled by gravitational instability, suggested by the large slump and morphological steps along the slope (Figs. 1B, 3 and 4).

Conclusions

The new geophysical data, including high-resolution and high-penetration multichannel seismic data and high-resolution swath bathymetry, allowed us to map the anatomy of the Cephalonia Transform Fault system in its southern sector and deformation affecting the slope to south of Zakynthos. We studied the sediment deformation patterns at the intersection between the Cephalonia strike-slip fault and the thrust fronts of the Hellenic System revealing a larger system and more complex structure than anticipated from previous works. The main outcome of the present work is a new morpho-structural map of Cephalonia and Zakynthos offshore. South of Cephalonia Island, the CTF "widens" to a 25 km-wide system of splays composed of elongated sigmoidal, positive-flower structures, possibly merging at depth into a single strike-slip fault. To west of Cephalonia Island, CTF narrows into a 6 km-wide strike-slip structure. Our data supports a dominant strike-slip kinematics with compressive component of the CTF. South of Zakynthos, the tectonic regime in the shallow sediments is dominated by extension, possibly representing a secondary tectonic system controlled by a local extensional stress field associated with a gravitational instability.

Acknowledgements

Seismic data interpretation was carried out using the Kingdom Suite software (S&P Global), freely available under the S&P Global University Grant Program. Geophysical data were collected during the IONIANS cruise supported by internal CNR funding (https://www.ismar.cnr.it/web-content/rapporto-tecnico-n-11/) and aboard of the R/V L. Bassi – INOGS during POSEIDON cruise supported by the Eurofleet+ program (http://eurofleet.maris2.nl/cds-report/25). The open source for seismological data is https://www.gein.noa.gr/en/services-products/earthquake-catalogs/

References

Ganas, A., Briole, P., Bozionelos, G., Barberopoulou, A., Elias, P., Tsironi, V., Valkaniotis S., Moshou A., Mintourakis, I., 2020. The 25 October 2018 Mw= 6.7 Zakynthos earthquake (Ionian Sea, Greece): A low-angle fault model based on GNSS data, relocated seismicity, small tsunami and implications for the seismic hazard in the west Hellenic Arc. Journal of Geodynamics, 137, 101731. https://doi.org/10.1016/j.jog.2020.101731

Ganas, A., Oikonomou, I.A., Tsimi, C. 2013. NOAfaults: a digital database for active faults in Greece, *Bull. Geological Society of Greece 47* (2), 518–530. https://doi.org/10.12681/bgsg.11079 .

Ganas, A., Tsironi, V., Kollia, E., Delagas, M., Tsimi, C., Oikonomou, A. 2018. Recent upgrades of the NOA database of active faults in Greece (NOAFAULTs), In: Proceedings of the 19th *General Assembly of WEGENER*, pp. 10–13. Grenoble, France.

Kassaras, I., Kapetanidis, V., Karakonstantis, A. 2016. On the spatial distribution of seismicity and the 3D tectonic stress field in western Greece, *Physics and Chemistry of the Earth, 95*, 50–72. https://doi.org/10.1016/j.pce.2016.03.012 .

Loreto, M. F., Zitellini, N., Ranero, C. R., Palmiotto, C., & Prada, M. 2021. Extensional tectonics during the Tyrrhenian back-arc basin formation and a new morpho-tectonic map. *Basin Research*, *33*(1), 138-158.

Louvari, E., Kiratzi, A. A., & Papazachos, B. C. 1999. The Cephalonia transform fault and its extension to western Lefkada Island (Greece). Tectonophysics, 308(1-2), 223-236.

Papadimitriou, P., Chousianitis, K., Agalos, A., Moshou, A., Lagios, E., & Makropoulos, K. 2012. The spatially extended 2006 April Zakynthos (Ionian Islands, Greece) seismic sequence and evidence for stress transfer. *Geophysical Journal International*, *190*(2), 1025-1040.

Papadimitriou, P., Kapetanidis, V., Karakonstantis, A., Spingos, I., Pavlou, K., Kaviris, G., ... & Voulgaris, N. 2021. The 25 October 2018 Zakynthos (Greece) earthquake: seismic activity at the transition between a transform fault and a subduction zone. *Geophysical Journal International*, *225*(1), 15-36.

Sachpazi, M., Hirn, A., Clément, C., Haslinger, F., Laigle, M., Kissling, E., ... & Ansorge, J. 2000. Western Hellenic subduction and Cephalonia Transform: local earthquakes and plate transport and strain. Tectonophysics, 319(4), 301-319.

Tsironi, V., Ganas, A., Valkaniotis, S., Kouskouna, V., Sokos, E., Koukouvelas, I. 2024. Active shortening and aseismic slip along the Cephalonia Plate Boundary (Paliki Peninsula, Greece): Evidence from InSAR and GNSS data, *Tectonophysics, 884*, 230400. https://doi.org/10.1016/j.tecto.2024.230400

Wessel, P., Luis, J. F., Uieda, L., Scharroo, R., Wobbe, F., Smith, W. H. F., & Tian, D. 2019. The Generic Mapping Tools Version 6, *Geochemistry, Geophysics, Geosystems*, 20(11), 5556–5564. https://doi.org/10.1029/2019GC008515.

Woodcock, N. H., & Fischer, M. 1986. Strike-slip duplexes. *Journal of structural geology*, *8*(7), 725-735.

Woodcock, N. H., & Rickards, B. 2003. Transpressive duplex and flower structure: Dent fault system, NW England. *Journal of Structural Geology*, *25*(12), 1981-1992.

17th INTERNATIONAL CONGRESS
of the Geological Society of Greece

BULLETIN OF THE GEOLOGICAL
SOCIETY OF GREECE, SP. PUBL.

EXTENDED ABSTRACT 198

The Early Pleistocene vertebrate fauna of Vatera, Lesbos, Greece

George Lyras[1], Athanassios Athanassiou[2], Alexandra van der Geer[3], George Kontakiotis[1], Evangelia Besiou[1], Asimina Antonarakou[1]

(1) Department of Historical Geology-Paleontology, Faculty of Geology and Geoenvironment, School of Earth Sciences, National and Kapodistrian University of Athens, Panepistimiopolis, Zografou, 15784 Athens, Greece, glyras@geol.uoa.gr (2) Hellenic Ministry of Culture, Superintendence of Palaeoanthropology–Speleology, Athens, Greece (3) Naturalis Biodiversity Center, Leiden, the Netherlands.

Background and objectives

Fossil-rich areas are found around the area of Vatera near Vrissa, about 6 km south of the town Polichnitos in the southern region of Lesbos Island. Systematic excavations were conducted here between 1996 and 2007 (Lyras & van der Geer, 2007). Fossil remains from these excavations were deposited in a local museum, alongside fish fossils (Drinia *et al*., 2007) and plant remains (Mantzouka *et al*., 2013) collected from the broader Polichnitos area. This year, renewed interest in Vatera's fossil record has brought the University of Athens back to the region. This contribution aims to provide a context and rationale for the new project in the light of the current knowledge on the terrestrial vertebrate fossils discovered thus far at Vatera.

The Vatera sites and fauna

The terrestrial vertebrate fossils at Vatera were discovered within the fluvial deposits of the Vatera Formation. This formation comprises alternating layers of breccia-conglomerates, sandy clays, sandy conglomerates, and silt. A total of 630 vertebrate fossils have been recovered from seven sites (Figure 1), coded with E, F, DS, H, T, U, and V for the different sites. The mammalian fauna includes the papionine monkey *Paradolichopithecus arvernensis* (van der Geer & Sondaar, 2002), the raccoon dog *Nyctereutes megamastoides*, the badger *Meles thorali*, the scimitar-toothed cat cf. *Homotherium latidens*, the rhinoceros *Stephanorhinus* cf. *etruscus*, the gomphothere *Anancus arvernensis*, the southern mammoth *Mammuthus meridionalis*, the giraffid *Palaeotragus* cf. *inexspectatus*, the small Tegelen deer cf. *Metacervocerus rhenanus*, the antelope *Gazellospira torticornis*, and the large bovine *Leptobos* sp. (de Vos *et al*., 1997). Additional finds include two horse morphotypes: *Equus stenonis* and *Equus* sp. (Eisenmann, 2002), three species of gazelle (*Gazella aegaea*, *G.* cf. *bouvrainae*, and *G.* aff. *borbonica*) (Athanassiou, 2002), and birds. Furthermore, remains of the spur-thighed tortoise (*Testudo graeca*), and a giant tortoise (*Titanochelon* sp.) (de Lapparent de Broin, 2002) were also described.

The monkey of Vatera

Paradolichopithecus arvernensis is a large Old-World monkey. In morphology, it resembles macaques cranially but baboons postcranially (Szalay & Delson, 1979). Among the material thus far excavated at Vatera is a juvenile male mandible (van der Geer & Dermitzakis, 2008), an adult female mandible, an upper canine and, notably, several postcranial elements (van der Geer & Sondaar, 2002). This species is known from several European localities, including three in Greece (van der Geer & Sondaar, 2002; Kostopoulos *et al*., 2018; Sianis *et al*., 2023). However, significant insights into its postcranial morphology are provided by only two sites: Vatera and Valea Grăunceanului (Romania). The postcranial elements suggest that *Paradolichopithecus* was a highly terrestrial monkey, exhibiting a notable frequency of bipedalism in its daily locomotor behavior (Sondaar & van der Geer, 2002; Sondaar et al., 2006).

The giant tortoise of Vatera

A rare and exceptional find in the fauna of F-site is a sample of limb bones and osteoderms, which may belong to a single individual of a giant tortoise. The recovered skeletal elements represent a very large form with an estimated carapace length of approximately 186 cm, one of the largest individuals known in the fossil record (de Lapparent de Broin, 2002). Taxonomically, the giant tortoise from Vatera was originally referred to the species cf. *Cheirogaster* aff. *schafferi*. A recent revision of the fossil Testudines from Greek localities reclassified it to the genus *Titanochelon*, refraining from a species-level attribution (Vlachos, 2022). Given the current biochronological placement of F-site (see below), the Vatera form represents the last giant tortoise of Europe.

Palaeoenvironment and age

The presence of horses, a palaeotragine giraffe, and four bovid species indicates a relatively dry and open landscape. Additionally, the terrestrial characteristics observed in the postcranial elements of *Paradolichopithecus* further support the idea of an open savanna /bushland environment. Based on the faunal composition the sites have been attributed to the biozone MN 17, or the Saint-Vallier Faunal Unit, or the Dafnero Faunal Unit (middle Villafranchian, earliest Pleistocene) (de Vos *et al*., 2002; Konidaris & Kostopoulos, 2024). However, the presence of two horse species is puzzling and may suggest that more than one faunal assemblage is represented at Vatera (Eisenmann, 2002).

Figure 1. Location of the fossil sites of the Vatera Formation

Conclusion and future work

Vatera is a key locality, because here the remains of two rare and puzzling creatures have been found together: the highly terrestrial macaque *Paradolichopithecus arvenensis* and the giant tortoise *Titanochelon sp.*, one of the largest tortoises in the world. Our future work will focus on reconstructing in detail (a) the stratigraphy of the Vatera sites, (b) the relation between the individual sites, and (c) the palaeoenvironment(s) of Vatera, in order to build a robust local biochronological–biostratigraphic scheme that can be integrated in the broader Eurasian context.

Acknowledgements

We are thankful to Michael Dermitzakis, Konstandinos Taxidis, John de Vos, Jan van der Made and the late Paul Sondaar for making the excavations and the research in Vatera possible.

References

Athanassiou, A., 2002. A new gazelle species (Artiodactyla, Bovidae) from the Late Pliocene of Greece. Annales Géologiques des Pays Helléniques 39, 299-310.

Drinia, H., Dermitzakis M.D., Kouli, K., Tsourou, T., 2002. Sedimentary facies analysis and paleoenvironmental interpretation of Vatera Formation, Lesvos Island, Greece. Annales Géologiques des Pays Helléniques 39, 15-35.

De Lapparent de Broin, F., 2002. A giant tortoise from the late Pliocene of Lesvos Island (Greece) and its possible relationships. Annales Géologiques des Pays Helléniques 39, 99-130.

De Vos, J., van der Made, J., Athanassiou, A., Lyras, G., Sondaar, P., Dermitzakis, M.D., 2002. Preliminary note on the Late Pliocene fauna from Vatera (Lesvos, Greece). Annales Géologiques des Pays Helléniques 39, 37-70.

Eisenmann, V., 2002. The primitive horses of the Vatera formation (Lesvos). Annales Géologiques des Pays Helléniques 39, 131-153.

Konidaris, G.E., Kostopoulos, D.S., 2024. The Late Pliocene–Middle Pleistocene Large Mammal Faunal Units of Greece, Quaternary, 7(2), 27.

Kostopoulos, D.S., Guy, F., Kynigopoulou, Z., Koufos, G.D., Valentin, X., Merceron, G., 2018. A 2Ma old baboon-like monkey from Northern Greece and new evidence to support the *Paradolichopithecus – Procynocephalus* synonymy (Primates: Cercopithecidae). Journal of Human Evolution 121, 178-192.

Lyras, G.A., van der Geer, A.A.E., 2007. The Late Pliocene vertebrate fauna of Vatera (Lesvos Island, Greece). Cranium 24 (2), 11-24.

Mantzouka, D., Sakala, J., Kvaček, Z., Karakitsios, V., 2013. Palaeobotanical study of Polichnitos region, southern part of Lesbos island, Greece (preliminary results on angiosperm wood). Proceedings of the 13th International Congress of the Geological Society of Greece, Chania, Sept. 2013, Bulletin of the Geological Society of Greece, 47 (1), 204-015.

Sianis, P.D., Athanassiou A., Kostopoulos D.D., Roussiakis, S., Kargopoulos, N., Iliopoulos, G., 2023. The remains of a large cercopithecid from the Lower Pleistocene locality of Karnezeika (southern Greece). Earth and Environmental Science Transactions of the Royal Society of Edinburgh 114 (sp. issue 1-2), 177-182.

Sondaar, P.Y., van der Geer, A.A.E., 2002. Arboreal and terrestrial traits as revealed by the primate ankle joint. Annales Géologiques des Pays Helléniques 39, 87-98.

Sondaar P.Y., van der Geer, A.A.E., Dermitzakis, M., 2006. The unique postcranial of the Old World monkey *Paradolichopithecus*: more similar to *Australopithecus* than to baboons. Hellenic Journal of Geosciences 41 (1), 19-28.

Szalay, F.S., Delson, E., 1979. Evolutionary history of the Primates. Academic Press.

Van der Geer, A.A.E., Dermitzakis, D.M., 2008. Dental eruption sequence in the Pliocene Papionini *Paradolichopithecus arvernensis* (Mammalia: Primates) from Greece. Journal of Vertebrate Paleontology 28 (4), 1238-1244.

Van der Geer, A.A.E., Sondaar, P.Y., 2002. The postcranial elements of *Paradolichopithecus arvernensis* (Primates, Cercopithecidae, Papionini) from Lesvos, Greece. Annales Géologiques des Pays Helléniques 39, 71-86.

Vlachos, E., 2022. The fossil record of turtles and tortoises (Reptilia: Testudines) in Greece, in Vlachos, E. (Ed.), Fossil Vertebrates of Greece, vol. 1: Basal Vertebrates, Amphibians, Reptiles, Afrotherians, Glires, and Primates, 245-281.

17th INTERNATIONAL CONGRESS
of the Geological Society of Greece

BULLETIN OF THE GEOLOGICAL SOCIETY OF GREECE, SP. PUBL.

EXTENDED ABSTRACT 199

Assessing the impact of climate change on olive cultivation in the Peloponnese, Greece: A long-term analysis using climate indices

P. Machaira[1,2], E. Kostopoulou[2], M. Gratsea[1], G. Kitsara[1], C. Giannakopoulos[1]
(1) Institute for Environmental Research and Sustainable Development, National Observatory of Athens, Greece, p.machaira@noa.gr (2) Department of Geography, University of Aegean, Greece

Introduction

Climate change is expected to significantly impact olive cultivation in the Peloponnese, through rising temperatures and decreasing rainfall. Additionally, geological processes, such as soil erosion and changes in hydrological conditions, may intensify the effects of climate change on olive trees. This study aims to evaluate the long-term impacts of climate change on olive cultivation in the region, utilizing climate indices related to temperature and rainfall patterns.

The Peloponnese, a key olive-producing area, is particularly vulnerable to the combination of future climatic changes and geological processes, which could disrupt olive cultivation. Rising temperatures and shifts in rainfall patterns are anticipated to affect flowering dates, irrigation needs, and overall production. Changes in hydrological conditions and soil erosion may negatively affect soil quality and water absorption, further stressing cultivation. The reduction in winter rainfall is expected to negatively impact on olive yields, while an increase in hot days may influence the phenology of olive trees, leading to higher irrigation requirements.

Moreover, climate change, along with increased CO_2 concentrations, is expected to have extensive impacts on olive cultivation. These changes will affect water availability and distribution, pest and disease occurrences, and overall socio-economic development. Key variables likely to be most affected include the duration of phenological stages, crop evapotranspiration, irrigation demands, and biomass growth and yield. These projected changes underscore the importance of adapting agricultural practices to the new climatological and geological conditions to ensure the sustainability of olive oil production in the region.

Material and Methods

Study Area

The Mediterranean has been identified as a climate change "hot-spot" and the impacts are expected to be particularly intense (IPCC, 2021). This specific area is warming 20% faster than the global average (MedECC, 2020). The olive tree (Olea europaea L.) is one of the most significant crops in the Mediterranean basin, which accounts for almost 95% of the global olive oil production. It also holds considerable importance in the Peloponnese region, representing approximately 40% of Greece's olive production. The Peloponnese features a predominantly Mediterranean climate, characterized by mild, wet winters and hot, dry summers. However, significant climatic variation occurs with altitude. Coastal areas experience milder conditions, while mountainous regions, such as Arcadia, have lower temperatures and higher rainfall. These altitudinal gradient influences local agricultural practices, including olive cultivation.

Climate data

For this study, a three-member GCM-RCM sub-ensemble from the Euro-Cordex database (Jacob *et al*., 2014), with a horizontal resolution of 0.11° was used for the study area (Table 1). Daily climate data, including precipitation and temperature, were obtained for three climate periods: historical (1971-2000), near future (2031-2060), and distant future (2071-2100). These data were evaluated under two future emission scenarios: RCP4.5 (a medium mitigation scenario) an RCP8.5 (a high emissions scenario without climate mitigation policies) (Moss *et al*., 2010). The model data were validated against observational data from local meteorological stations, confirming its suitability for this study

Table 1. Three-member GCM-RCM sub-ensemble from the Euro-Cordex database.

Institute	Institute Code	Regional Climate Model (RCM)	Global Climate Model (GCM)	GCM, RCM Pair as Used
Swedish Meteorological and Hydrological Institute	SMHI	RCA4	MPI-ESM-LR	1.MPI-ESM-LR_r1i1pi_ RCA4 rca4-mpi-lr
Swedish Meteorological and Hydrological Institute	SMHI	RCA4	HadGEM2-ES	2.HadGEM2-ES_r1i1pi_ RCA4 rca4-mohc
Royal Netherlands Meteorological Institute, De Bilt, The Netherlands	KNMI	RACMO22E	HadGEM2-ES	2.HadGEM2-ES_r1i1pi_ RACMO22E racmo22e-mohc

Climate indices

For the assessment of the impacts of climate change on olive cultivation, climatic indices based on temperature and precipitation were used. These indices were identified by agricultural sector scientists as appropriate for the olive sector within the framework of the MedGold project. The selection of these indices is in accordance with previous studies on the impact of climate change on olive cultivation in Mediterranean agricultural environments, such as research conducted in Andalusia (Gratsea *et al*., 2022). Specifically, the climatic indices used to assess the impacts of climate change on olive cultivation include the SPRTX index, which is related to the average maximum temperature during the spring months (April-May) and is considered the best indicator for the flowering period of olive trees, aiding in decisions regarding irrigation and management of the olive fruit fly (Perez-Lopez *et al.,* 2008). The SPR32 index, calculated as the number of days with Tmax >32° C in May and June, is linked to early flowering and increased pest and disease risk, providing crucial information for plant management and yield prediction (Ribeiro *et al.,* 2009). The SU38 and SU40 indices, representing the number of days with Tmax >38°C and Tmax >40°C, respectively, are associated with early olive ripening , influencing decisions on harvesting, pest control, and additional irrigation. Additionally, SU40 negatively affects the photosynthesis rate of olive trees (Garcia-Inza *et al.,* 2014). Finally, the WINRR index, which calculates total precipitation from October to May, is crucial for water availability and crop yield. Water deficits during winter and early spring have been shown to reduce yield, while also influencing soil management and long-term crop variety selection (Aissaoui *et al.,* 2016).

Results

Climate indices are essential for characterizing climate variability and investigating the impacts of climate change on olive crops. The effects of climate change on olive cultivation were assessed by analyzing the relationships between primary production, temperature, precipitation, and water availability. Water availability is critical before flowering, while temperature affects fruit development. High summer temperatures can damage fruit surfaces, accelerate ripening and affect overall yield. Climatic indices were calculated annually for three climate periods (historical period, near and distant future) under two emission scenarios (RCP4.5, RCP8.5), focusing on spatial distributions and mean differences. These simulations allow comparison of emission scenario impacts on olive crops and support future agricultural decisions.

Regarding the SPRTX index, it represents the average maximum temperature during spring (April–May), calculated as the mean of daily maximum temperatures between April 1 and May 31. It is a key indicator for olive tree flowering, linked to evapotranspiration and pest development. Warmer climates may accelerate flowering, potentially requiring new varieties or relocation to cooler areas. Higher temperatures will increase evapotranspiration, necessitating more irrigation. While pests and diseases may rise, the olive fly is expected to decrease. In the Peloponnese, the average increase for the near future is about 2°C for RCP4.5 and 3°C for RCP8.5, and for the distant future, 3°C and 5°C, respectively (Figure 1). Similar results were observed by Fraga et al. (2019) for the average temperature of the growing season in the Peloponnese.

Concerning the SPR32 index, it refers to the number of spring days (May and June) with Tmax >32° C. It is linked to early flowering, increasing the risk of pests and diseases (Ribeiro *et al.,* 2009). Rising temperatures will impact flowering and necessitate adjustments in cultivation practices. At temperatures above 35° C, stomatal closure hinders crop growth and productivity (Mavromatis *et al*., 2022). Adaptations such as improved soil management, pruning and increased irrigation during spring will be essential for olive cultivation. Based on the RCP8.5 scenario, the greatest increase in the number of spring days with Tmax >32° C is projected for the distant future (Figure 2), consistent with Mavromatis *et al*. (2022). Specifically, an additional 10 and 14 days with Tmax >32° C per year are projected for the near future under RCP4.5 and RCP8.5, respectively, and 12 and 24 days for the distant future.

The SU38 and SU40 indices represent the number of summer (June, July, August) days with Tmax >38° C and Tmax >40° C, respectively. They are calculated as the annual number of days exceeding these temperature thresholds. Increases in these indices are linked to earlier olive ripening (Garcia-Inza *et al.,* 2014). Notably, SU40 is associated with reduced photosynthetic capacity due to heat stress. Olive production is negatively affected by summer drought, as this is when fruit formation and growth occur (Mavromatis *et al*., 2022). Mitigation measures include adjusting harvest timing, pest control treatments and additional irrigation to support plant resilience. The number of summer days with maximum temperatures exceeding 38° C is expected to increase. The most significant rise is projected for the distant future under the RCP8.5 scenario (Figure 3). Specifically, for the near future, an additional 10 (RCP4.5) and 13 (RCP8.5) days per year are anticipated, while for the distant future, the increase is projected at approximately 15 (RCP4.5) and 40 (RCP8.5) additional days per year, mainly impacting coastal zones. Extreme heat stress, as indicated by the SU40 index, is projected to increase during summer months. The largest rise is expected under the RCP8.5 scenario in the distant future (Figure 4). Average increases for the near future are about 3 (RCP4.5) and 4 (RCP8.5) additional days per year, while for the distant future, the SU40 index is projected to rise by approximately 5 (RCP4.5) and 22 (RCP8.5) additional days annually. Similar to the SU38 index, these changes will primarily impact coastal areas.

Regarding the WINRR index, it refers to the total rainfall from October to May and is closely related to crop yield, as water availability is a crucial factor for the physiological activity of olive trees (Aissaoui *et al.,* 2016). Negative impacts of reduced winter rainfall include increased irrigation demands, decreased water availability due to prolonged droughts, changes in soil fertility and higher risks of soil erosion associated with droughts and extreme precipitation variability. Projected reductions during winter and early spring are significant for decision-making related to crop yield, soil management and long-term changes in crop varieties (Gratsea *et al*., 2022). The WINRR index is projected to decline in both the near and distant future. The most significant reductions are expected on the western side of the Peloponnese, with largest decreases projected under the RCP8.5 scenario (Figure 5), consistent with Fraga *et al.* (2019). Specifically, for the near future, average reductions are estimated at 9% (RCP4.5) and 16% (RCP8.5). The greatest declines (>20%) are projected for southern-western Peloponnese (Messenia), while the north-eastern regions (Corinthia) may experience smaller reductions (5-10%).

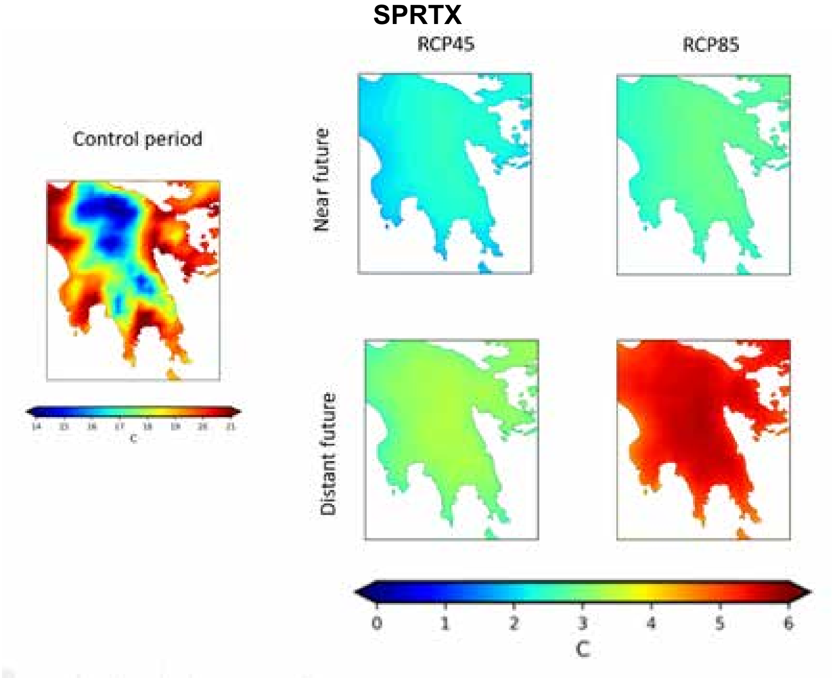

Figure 1. Absolute differences of spring (April-May) maximum temperature, between the reference period and the near or distant for two climate scenarios (RCP4.5, RCP8.5)

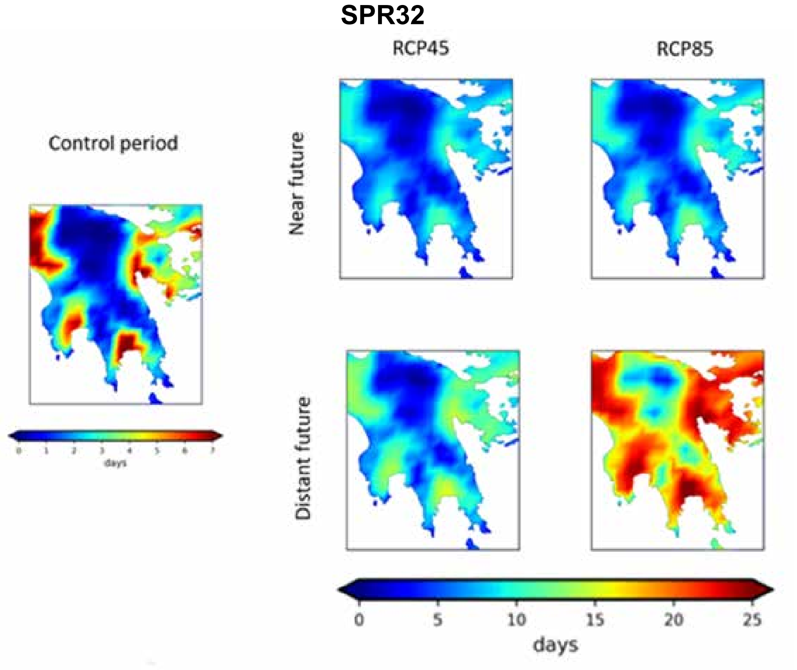

Figure 2. Absolute differences of the number of spring heat days (Tmax>32°C), between the reference period and the near or distant for two climate scenarios (RCP4.5, RCP8.5)

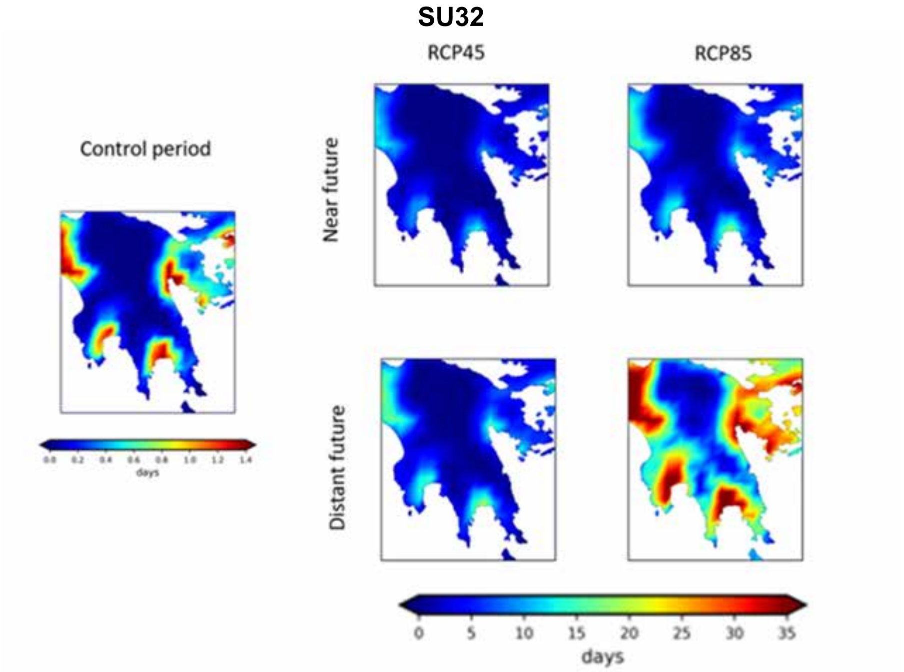

Figure 3. Absolute differences of the number of summer heat days (Tmax>38°C), between the reference period and the near or distant for two climate scenarios (RCP4.5, RCP8.5)

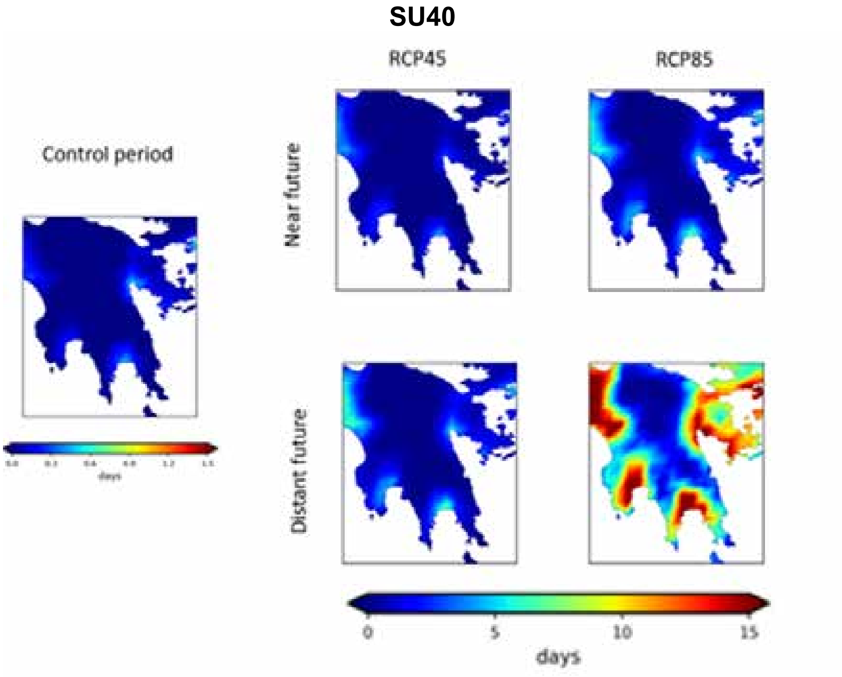

Figure 4. Absolute differences of the number of summer heat days (Tmax>40°C), between the reference period and the near or distant for two climate scenarios (RCP4.5, RCP8.5)

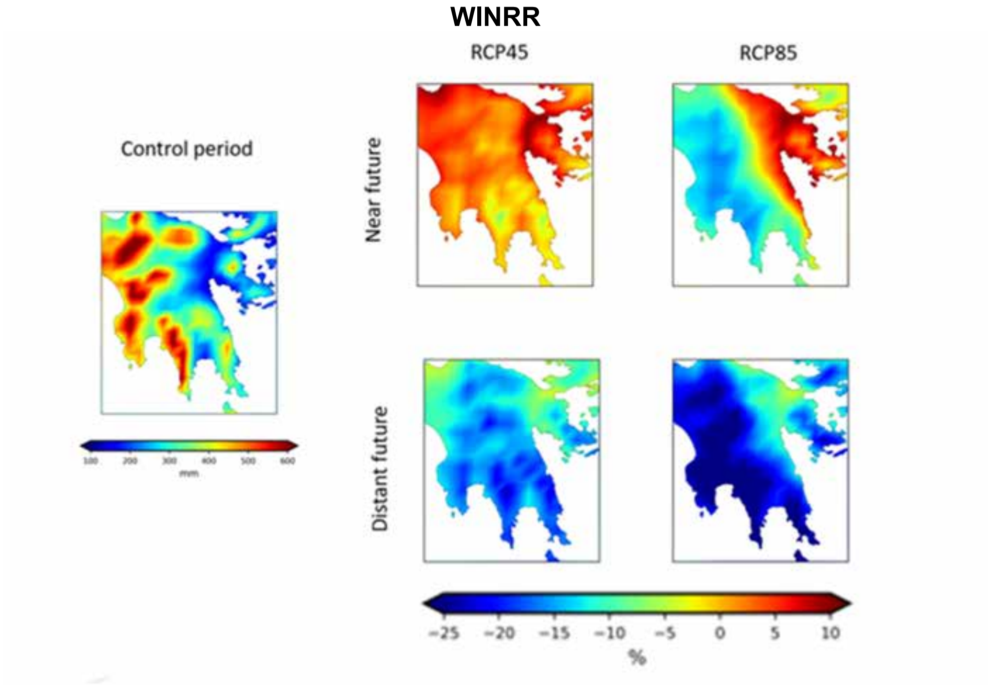

Figure 5. : Relative differences for total winter (Oct-May) precipitation, between the reference period and the near or distant for two climate scenarios (RCP4.5, RCP8.5)

Conclusions

The assessment of climate change impacts on olive cultivation in the Peloponnese, using adapted climate indices highlights significant future challenges. Temperature-related indices, SPRTX and SPR32, show projected increases, indicating accelerated flowering, particularly in coastal areas. Mitigation measures include introducing olive varieties with lower chilling requirements, relocating cultivation to cooler regions, enhancing irrigation and adopting soil conservation practices. Elevated summer temperatures, linked to the SU40 index, are expected to reduce fruit weight (Garcia-Inza *et al.,* 2014), and photosynthetic capacity, particularly in erosion-prone coastal areas, emphasizing the need for additional irrigation and land management strategies. The WINRR index, associated with winter precipitation, is crucial for olive yield. Projected reductions, exceeding 20% in the south-western Peloponnese, highlight the need for integrated water and soil management to sustain cultivation under evolving climatic and geological conditions. Based on these projections, the cultivation requirements of olive trees will change, requiring adaptation to future climate conditions. High temperatures are expected to negatively impact growth and, consequently, productivity. Adaptation strategies will include modifying cultivation practices and land management practices introducing olive varieties with lower chilling requirements or relocating production to cooler areas may become necessary. Water availability is critical during pre-flowering stages (Aissaoui et al., 2016), and reduced annual rainfall is expected to increase water demand. Effective management of soil fertility and optimized irrigation practices will be crucial for sustaining olive cultivation, ensuring both productivity and resilience under changing climatic conditions.

The overall impact of climate change on the expected yields of olive cultivation is expected to be negative, primarily due to rising temperatures and decreasing rainfall. Elevated temperatures are expected to cause heat stress on crops, negatively impacting their growth and development. Heatwaves can damage sensitive crops, reduce yields, and affect the quality of olive products. Additionally, climate change is likely to alter rainfall patterns, potentially leading to droughts and fluctuations in soil moisture levels, which will affect crop growth and irrigation needs. As a result, agricultural production is projected to decline, with an increased risk of diseases and pests. Moreover, the growing frequency and intensity of extreme weather events may cause significant damage to olive trees and their production. Consequently, climate change is expected to affect the dynamics of olive cultivation, with the projected yield losses leading to significant changes in the sector’s economy across the Peloponnese, potentially resulting in social impacts.

Short-term adaptation strategies in olive cultivation aim to mitigate the immediate impacts of climate change. Improved water resource management through efficient irrigation systems, the implementation of early warning systems for diseases, and the adoption of sustainable agricultural practices contribute to maintaining productivity.

Additionally, farmers' access to climate information enables the adjustment of cultivation practices to changing conditions, enhancing the sector's sustainability. These strategies provide immediately applicable solutions which, in combination with long-term interventions, can significantly contribute to preserving the productivity and quality of olive production.

Acknowledgements

We acknowledge the use of data from the Copernicus Climate Change Service (C3S) and the Climate Data Store (CDS), specifically the CORDEX-EUR-11 climate model data.

References

Aissaoui, F., Chehab, H., Bader, B., Salem, A. B., M'barki, N., Laamari, S., Chihaoui, B., Mahjoub, Z. and Boujnah, D., 2016. Early water stress detection on olive trees (Olea europaea L. cvs "chemlali" and "Chetoui") using the leaf patch clamp pressure probe. Computers and Electronics in Agriculture, 131, 20–28. doi:10.1016/j.compag.2016.11.007.

Fraga, H., Pinto, J. G., Viola, F. and Santos, J. A., 2019. Climate change projections for olive yields in the Mediterranean Basin. International Journal of Climatology. doi:10.1002/joc.6237.

García-Inza, G. P., Castro, D. N., Hall, A. J., and Rousseaux, M. C., 2014. Responses to temperature of fruit dry weight, oil concentration, and oil fatty acid composition in olive (Olea europaea L. var. "Arauco"). European Journal of Agronomy, 54, 107–115. doi:10.1016/j.eja.2013.12.005.

Gratsea, M., Varotsos, K. V., López-Nevado, J., López-Feria, S. and Giannakopoulos, C., 2022. Assessing the Long-Term Impact of Climate Change on Olive Crops and Olive Fly in Andalusia, Spain, through Climate Indices and Return Period Analysis. Climate Services, vol. 28, no. October, https://doi.org/10.1016/j.cliser.2022.100325.

IPCC, 2021: Climate Change 2021. The Physical Science Basis. Contribution of Working Group I to the Sixth Assessment Report of the Intergovernmental Panel on Climate Change [Masson-Delmotte, V., et al.]. Cambridge University Press, Cambridge, United Kingdom and New York, NY, USA, 2391 pp.

Jacob, D., Petersen, J., Eggert, B., Alias, A., Christensen, O.B., Bouwer, L.M., Braun, A., Colette, A., Déqué, M.; Georgievski, G., et al., 2014. EURO-CORDEX: New high-resolution climate change projections for European impact research. Reg Environ. Change 14, 563–578.

Mavromatis, T., Georgoulias, A. K., Akritidis, D., Melas, D. and Zanis, P., 2022. Spatiotemporal Evolution of Seasonal Crop-Specific Climatic Indices under Climate Change in Greece Based on EURO-CORDEX RCM Simulations. Sustainability, 14, 17048. https://doi.org/10.3390/ su142417048.

MedECC, 2020. Climate and Environmental Change in the Mediterranean Basin – Current Situation and Risks for the Future. First Mediterranean Assessment Report [Cramer, W., Guiot, J., Marini, K. (eds.)]. Union for the Mediterranean, Plan Bleu, UNEP/MAP, Marseille, France, 632 pp., ISBN: 978-2-9577416-0-1.

Moss, R.H., Edmonds, J.A., Hibbard, K.A., Manning, M.R., Rose, S.K., Van Vuuren, D.P., Carter, T.R., Emori, S., Kainuma, M., Kram, T., 2010. The next generation of scenarios for climate change research and assessment. Nature 463, 747–756.

Pérez-López, D., Ribas, F., Moriana, A., Rapoport, H. F., & De Juan, A., 2008. Influence of temperature on the growth and development of olive (Olea europaea L.) trees. The Journal of Horticultural Science and Biotechnology, 83(2), 171–176. https://doi.org/10.1080/14620316.2008.11512366.

Ribeiro, H., Abreu, L. and Cunha, M., 2009. A bioclimatic model for forecasting olive yield. Journal of Agricultural Science 147, 647–656, https://doi.org/10.1017/ s0021859609990256.

17th INTERNATIONAL CONGRESS
of the Geological Society of Greece

BULLETIN OF THE GEOLOGICAL SOCIETY OF GREECE, SP. PUBL.

EXTENDED ABSTRACT 200

A WebGIS platform for the multiparametric monitoring of ground deformation and critical infrastructures under the name PROION

Efthymios Magkoufis[1], Athanassios Ganas[2], Konstantinos Nikolakopoulos[3], Betty (Vasiliki) Charalampopoulou[1]
(1) Geosystems Hellas S.A., 11632 Athens, Greece, e.magkoufis@geosystems-hellas.gr
(2) Institute of Geodynamics, National Observatory of Athens, 11810 Athens, Greece, aganas@gein.noa.gr
(3) Department of Geology, University of Patras, 26504 Patra, Greece, knikolakop@upatras.gr

Introduction

Both the modern human-made and natural environment face numerous challenges and risks that have direct and indirect consequences on their sustainability and security. Climate change, combined with the accumulated pressures, ageing infrastructure, and the impact of natural hazards, contributes to the rising frequency of phenomena and events that demand effective and intelligent responses (Kyriou *et al.*, 2023). In this context, the need for a modern, multiparametric framework to monitor and provide up-to-date information on the pressures affecting both the environment and critical infrastructure led to the proposal and successful implementation of the research project, "PROION". The project was based on innovative technologies and methodologies that make use of the latest available infrastructure and development tools. From the perspective of optimal observation of critical infrastructure and the surrounding physical environment, the PROION project aimed to acquire, process, organise and make available measurement data both through the use of in-situ sensors and free satellite products that provide valuable information on the ground deformation, as well as the stability of critical infrastructure. Receiving co-funding from the European Union and the Greek Government, PROION (T2EDK-02396) was invited to implement its vision in the region of Achaia (Fig. 1), part of the Enceladus Hellenic Supersite (EHS).

Methodology

The three main study areas were, i) the building of the Department of Geology at the University of Patras campus, ii) the Asterion dam and iii) an active landslide that includes the boundaries of the mountainous settlement of Krini.

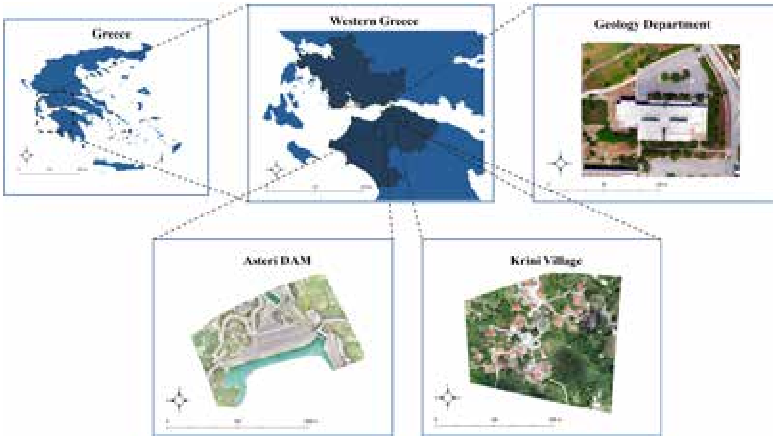

Figure 1. The three sites selected for monitoring in the framework of the PROION project.

In addition, in order to provide the best quality of the final ground displacement products, three SAR triangular aperture reflectors were designed, constructed and installed in the project study areas. For the observation of the study areas, SAR satellite data from the European Sentinel-1 space mission (Tsironi et al. 2022) as well as low-cost GNSS (Ganas *et al.*, 2024) in-situ sensors and accelerometers were used to record local micro-vibrations and seismic events in a timely and accurate manner (Nikolakopoulos *et al.*, 2023). With the acquisition of the multidimensional observations, the InSAR interferometry method was exploited to produce time-series of displacements with 6-12 days repeatability, while GNSS measurements were used to observe the 3-D change in the precise position of the ground and reflectors. In order to accurately render and observe the study areas, regular mapping of these areas was carried out using TLS and UAVs to produce point clouds of high geometric accuracy (Nikolakopoulos *et al.*, 2023). Subsequently, aiming to fully exploit the available information, fuzzy logic algorithms capable of adapting to the temporal behaviour of the observed points and ultimately achieving accurate predictions of their future position were developed. The following graphs (Fig. 2) illustrate the GNSS measurements of the Department of Geology station, acquired and processed for the period of July 2022 to December 2024.

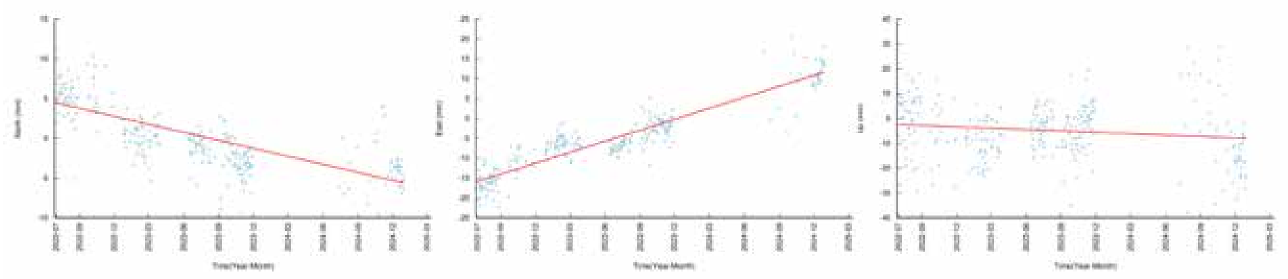

Figure 2. The GNSS measurements of the Department of Geology station from July 2022 to December 2024.

For the success of the overall system, a geospatial database was created both for the organisation and storage of the collected observations and for the subsequent retrieval of these through the compilation of complex spatio-temporal queries. The need for a powerful high-performance relational database led to the use of PostgreSQL with PostGIS software extension to manage spatial information and optimally retrieve it by applying specialised techniques such as spatial indexing (Ďuračiová *et al.*, 2018).

WebGIS platform

Subsequently, to offer an integrated framework for the disposal and visualisation of the generated data, a modern WebGIS platform for multiparametric monitoring was designed and implemented following the most advanced technological standards and specifications. Utilising cutting-edge technologies and modern libraries for the development of web-based geographic information systems, such as Mapbox GL JS, Deck GL, React JS, Chart.js, Flask, etc., a web platform capable of retrieving, managing and visualising spatially and diagrammatically the generated project data in an optimal and user-friendly way was developed. The platform was developed in Software-as-a-Service (SaaS) architectural standard (Capodiferro, *et al.*, 2024), offering easy access and interaction, also achieving easy maintenance and deployment both throughout the project and after its completion. Recognising the advantages of using 3D data visualisation methods for maximum understanding of the projected information, the Mapbox GL JS library was chosen (Zunino *et al.*, 2020), achieving the most complete 3D representation of the observed information through its direct correlation with the topography and morphology of the wider area (Fig. 3).

Figure 3. Illustration of the possibilities for end-user interaction and visualisation with the provided datasets in a cartographic environment. Coloured dots represent Copernicus SAR data (Sentinel-1 time series).

In addition, the platform offers tools for spatio-temporal analysis of longitudinal observations, geospatial data overlay as well as near real-time earthquake epicentres, achieving optimal monitoring of areas of high interest. Finally, in pursuit of a more complete user experience, the Deck GL library was exploited to represent cloud points within the cartographic environment, offering an additional dimension to the observation and understanding of the specific conditions governing each area and infrastructure of interest (Fig. 4), through direct spatial correlation with the ground deformation, geology and seismic phenomena that may occur within or near them.

Figure 4. The point cloud of the Department of Geology on the 3D map environment.

Platform Accessibility and Future Prospects

The PROION's WebGIS platform, developed through this project, represents a significant advancement in presenting and analysing ground deformation data to end users. Considering the sensitive insights provided by the platform and the commercialisation of the overall product, the accessibility of the platform remains strict, allowing only authorised users to access the provided data. Therefore, interested parties are able to request access to an online demo of the platform by contacting the authors of the current publication directly via the provided e-mails. Furthermore, the platform shows strong potential for integration into future scientific research or operational monitoring systems, particularly in critical infrastructures and geohazard-prone regions. Its adaptability and scalability could support ongoing efforts in early warning and near-real-time infrastructure monitoring, while further integration of Machine Learning techniques has been explored to expand the current capabilities, aiming to serve as a supporting tool for data-driven decision-making.

Results and Conclusions

The successful implementation of the PROION project and the development of the WebGIS platform have resulted in the provision of a highly relevant system for the monitoring and evaluation of the longitudinal territorial behaviour and mobility of the areas of high interest. In conclusion, the continuous evolution of Remote Sensing and the creation of new and more powerful software technologies extend the possibilities of designing and implementing a sophisticated tool of higher performance and greater added value for the shielding of Greek territory.

Acknowledgements

This research has been co-financed by the European Regional Development Fund of the European Union and Greek national funds through the Operational Program Competitiveness, Entrepreneurship and Innovation, under the call RESEARCH – CREATE – INNOVATE (project code: T2EΔK-02396 Multiparametric monitoring platform with micro-sensors of eNceladus hellenIc supersite).

References

Capodiferro, C., De Maria, M., Mazzei, M., Spreafico, M., Bik, O.V., Palma, A.L., Solovyeva, A.V., 2024. Cultural itineraries generated by smart data on the Web. ISPRS Int. J. Geo-Inf. 13(2), 47.

Ďuračiová, R., Faixová Chalachanová, J., 2018. Fuzzy spatio-temporal querying the PostgreSQL/PostGIS database for multiple criteria decision making. In: Lecture Notes in Geoinformation and Cartography, Springer International Publishing, pp. 81-97.

Ganas, A., Mavropoulos, G., Karamitros, I., Nikolakopoulos, K., Charalampopoulou, V., Anastasiou, D., Athanassopoulos, T., Kyriou, A., Tsironi, V., 2024. A new low-cost GNSS instrument for monitoring of ground motions and critical infrastructures within the Greek "Supersite." EGU General Assembly 2024, Vienna, Austria, 14–19 Apr 2024, EGU24-10188, https://doi.org/10.5194/egusphere-egu24-10188

Kraak, M.-J., Ormeling, F., 2023. Cartography: Visualization of Geospatial Data, Fourth Edition, 4th ed. CRC Press, London, England.

Kyriou, A., Mpelogianni, V., Nikolakopoulos, K., Groumpos, P., 2023. Review of Remote Sensing Approaches and Soft

Computing for Infrastructure Monitoring. Geomatics 3, 367-392.

Nikolakopoulos, K., Kyriou, A., Sokos, E., Bousias, S., Strepelias, E., Groumpos, P., Mpelogianni, V., Roumelioti, Z., Serpetsidaki, A., Paliatsas, D., Ganas, A., Charalampoulou, V. (Betty), Athanasopoulos, T., 2023. Synergy of accelerometer, GNSS, InSAR and TLS measurements in the light of PROION Project.

Nikolakopoulos, K.G., Kyriou, A., 2023. Creation of 3D infrastructure model from UAV and TLS data in the frame of PROION project. In: Themistocleous, K., Michaelides, S., Hadjimitsis, D.G., Papadavid, G. (Eds.), Ninth International Conference on Remote Sensing and Geoinformation of the Environment (RSCy2023). SPIE, p. 10.

Tsironi, V., Ganas, A., Karamitros, I., Efstathiou, E., Koukouvelas, I., Sokos, E. 2022. Kinematics of Active Landslides in Achaia (Peloponnese, Greece) through InSAR Time Series Analysis and Relation to Rainfall Patterns. Remote Sens., 14(4), 844. https://doi.org/10.3390/rs14040844

Zunino, A., Velázquez, G., Celemín, J., Mateos, C., Hirsch, M., Rodriguez, J., 2020. Evaluating the performance of three popular Web mapping libraries: A case study using Argentina’s life quality index. ISPRS Int. J. Geo-Inf. 9(10), 563.